Atmosphere, Earth, Ocean & Space

Chen-Tung Arthur Chen
Xinyu Guo *Editors*

Changing Asia-Pacific Marginal Seas

Springer

Atmosphere, Earth, Ocean & Space

The series Atmosphere, Earth, Ocean & Space (AEONS) publishes state-of-art studies spanning all areas of Earth and Space Sciences. It aims to provide the academic communities with new theories, observations, analytical and experimental methods, and technical advances in related fields. The series includes monographs, edited volumes, lecture notes and professional books with high quality. The key topics in AEONS include but are not limited to: Aeronomy and ionospheric physics, Atmospheric sciences, Biogeosciences, Cryosphere sciences, Geochemistry, Geodesy, Geomagnetism, Environmental informatics, Hydrological sciences, Magnetospheric physics, Mineral physics, Natural hazards, Nonlinear geophysics, Ocean sciences, Seismology, Solar-terrestrial sciences, Tectonics and Volcanology.

More information about this series at http://www.springer.com/series/16015

Chen-Tung Arthur Chen · Xinyu Guo
Editors

Changing Asia-Pacific Marginal Seas

Springer

Editors
Chen-Tung Arthur Chen
Department of Oceanography
National Sun Yat-sen University
Kaohsiung, Taiwan

Xinyu Guo
Center for Marine Environmental Studies
Ehime University
Matsuyama, Japan

ISSN 2524-440X ISSN 2524-4418 (electronic)
Atmosphere, Earth, Ocean & Space
ISBN 978-981-15-4885-7 ISBN 978-981-15-4886-4 (eBook)
https://doi.org/10.1007/978-981-15-4886-4

This Springer imprint is published by the registered company Springer Nature Singapore Pte Ltd.
The registered company address is: 152 Beach Road, #21-01/04 Gateway East, Singapore 189721, Singapore

Contents

Chapter 1
Introduction

Chen-Tung Arthur Chen and Xinyu Guo

Marginal seas are among the most productive marine environments in the world, and they are known to have undergone rapid environmental changes in recent decades. These include the marginal seas of the Asia-Pacific. Since the livelihoods of billions of people depend on them, many changes, such as warming seawater, rising sea levels, eutrophication, deoxygenation, and acidification, threaten to have severe consequences. Many studies have been published in this important field but almost no review is internationally available.

This book introduces temporal changes over time scales from years to decades in the marginal seas in the Northwest Pacific (Fig. 1.1), ranging from the northernmost Arctic/Subarctic Bering Sea to the tropical South China Sea (SCS). The relevant physical variables include sea level, sea surface temperature, water mass index, current and transport, and local issues, such as sea ice and tidal mixing, as well as other processes and dynamics govern them. Trends are also discussed. The biogeochemical variables include nutrient concentrations, oxygen concentration, pH, ocean acidification, eutrophication, and productivity.

This monograph comprehensively reviews long-term changes in the physical and biogeochemical variables for six marginal seas and two related western boundary currents. The focus on Asia-Pacific marginal seas is especially important because of their extensive exploitation and the urgent need for adaptive management strategies

C.-T. A. Chen (✉)
Department of Oceanography, National Sun Yat-sen University, Kaohsiung 804, Taiwan
e-mail: ctchen@mail.nsysu.edu.tw

State Key Laboratory of Satellite Ocean Environment Dynamics, Second Institute of Oceanography, Ministry of Natural Resources, Hangzhou 310012, China

Ocean College, Zhejiang University, Zhoushan 316021, China

X. Guo
Center for Marine Environmental Study, Ehime University, Matsuyama, Ehime, Japan
e-mail: guoxinyu@sci.ehime-u.ac.jp

C.-T. A. Chen and X. Guo (eds.), *Changing Asia-Pacific Marginal Seas*, Atmosphere, Earth, Ocean & Space, https://doi.org/10.1007/978-981-15-4886-4_1

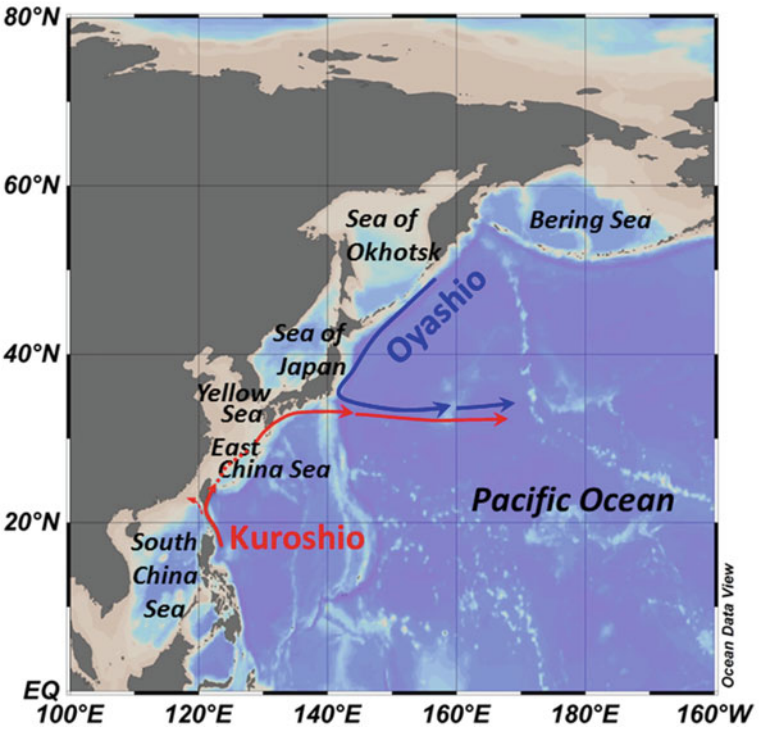

Fig. 1.1 Map of the Asia Pacific marginal seas (drawn using ODV, Schlitzer, R., Ocean Data View, https://odv.awi.de, 2018)

in their coastal areas. Readers in most oceanographic fields will find the newest information on long-term changes in these marginal seas in a single book. For instance, satellite-derived chlorophyll concentration, a proxy for primary productivity, has increased in several seas over the last two decades, whereas it has declined in open oceans. This fact is of interest both because the underlying dynamics are likely to differ and because inferences drawn from open ocean data may not apply to coastal areas, which may be considerably more economically and socially important. This book provides a holistic overview of what has changed and warns readers of what is likely to change in the Asia-Pacific marginal seas in the future.

The subarctic Bering Sea is the northernmost marginal sea in the Asia-Pacific region. The Okhotsk Sea, although located in a temperate zone, has subarctic characteristics such as ice cover in winter. Like other seas at high latitudes, both are changing rapidly. One of the most notable changes is that the sea surface temperature (SST), which for the Bering and Okhotsk Seas between 1998 and 2016, increased by approximately 5.5 °C/century ($p = 0.14$) and by about 4.5 °C/century ($p = 0.41$), respectively; these rates are much higher than the reported global rate of 1.5 °C/century between 2000 and 2010. During the former period, the chlorophyll concentration in both seas increased significantly by about 1 μg/L per century. The

Secchi disk depth (SDD) did not significantly change in the Bering Sea but increased by 1.8 m/century in the Okhotsk Sea. Unlike in tropical oceans, both the SST and the chlorophyll concentration in these high-latitude seas increased, revealing the different responses of phytoplankton in those seas to oceanic warming. These changes in the SST, chlorophyll concentration and the SDD may affect physical and biological processes as well as carbon sequestration in these seas. Yet, these two seas are only weakly affected by the land directly as the surrounding areas are thinly populated.

Biogeochemical processes in the East China Sea (ECS) are heavily influenced by densely populated China. Phytoplankton became dramatically more abundant between 1958 and 2016 in both the Changjiang (Yangtze River) estuary and the ECS as a result of an increase in outflows of N and P from rivers. Consequently, hypoxia and anoxia have begun to become severe problems around the river mouth at Changjiang. Additionally, prior to the 1980s, diatoms were overwhelmingly dominant but in recent years dinoflagellate and cyanobacteria concentrations have been increasing. The relative drop in the diatom concentration may be related to the doubling of the N/Si ratio from around 0.5 in the 1980s to approximately 1 in the 2000s.

In between the ECS and the Okhotsk Sea is the Sea of Japan, which is increasingly vulnerable to inputs of anthropogenic nutrients from China through the Tsushima Strait between Korea and Japan. The Sea of Japan is unique in having its own thermohaline circulation, so it acts like a miniature ocean. In recent decades, water column ventilation has waned, consistent with global warming. This weakening of ventilation has reduced the transport of dissolved oxygen and anthropogenic CO_2 from the surface to the interior of the sea, but accelerated the acidification of deep waters in the basin.

The tropical/subtropica SCS is the largest marginal sea in the world. Like other warm bodies of water, its SST is rising, albeit more slowly (1.2 °C/century between 1998 and 2016) than that of cold-water regions at high latitudes. The chlorophyll concentration increased at 0.12 μg/L per century from 1998 to 2016, and the SDD increased by 3.5 m/century. Changes in SST, chlorophyll concentration and SDD in the SCS exhibited high temporal-spatial variability, and these parameters varied in opposite directions during the periods 1998–2008 and 2008–2016. The first period witnessed declining SST and SDD and increasing chlorophyll concentration. The second period witnessed increasing SST and SDD but declining chlorophyll concentration.

The aforementioned Asia-Pacific marginal seas are affected not only by the land but also by ocean currents, such as the Oyashio and the Kuroshio. The low-temperature Oyashio-influenced region northeast of Japan is an important area for the formation of the North Pacific Intermediate Water (NPIW), which carries anthropogenic CO_2 into the interior of the North Pacific Ocean. In the Oyashio region between the 1960s and the 2010s, the seawater fCO_2 increased at a rate of 2.86 $\pm$ 0.92 uatm/yr, which is significantly greater than the rate of increase of atmospheric fCO_2 of 1.95 $\pm$ 0.03 uatm/yr. This difference may be due to reduced primary production as a result of increased water column stratification in the Oyashio region.

The warm Kuroshio is the strongest current in the North Pacific Ocean and hugely influences the SCS, ECS and the Yellow Sea. Enhanced intrusion of the oligotrophic (with low nutrient concentrations) Kuroshio surface water into the SCS apparently reduced the productivity and, therefore, the fluxes of sinking particles in the SCS between 2013 and 2017. However, the productivity in the SCS increased during a large-scale Kuroshio intrusion in 1998–2006, revealing that other factors were also involved. The Kuroshio has undergone a reduction in both DO and pH in its intermediate layer, most likely as a result of reduced ventilation in the NPIW. Since the Kuroshio Intermediate Water (KIW) is an important component of the bottom water on the ECS shelf, a reduction in DO and pH in the KIW might have contributed to the enlargement of the hypoxia area and the severity of acidification close to the Changjiang river mouth.

The physical processes that are associated with the above-mentioned interannual variations and long-term trends in these marginal seas can be separated into two groups. The first comprises local processes, such as air-sea heat flux, river discharge and precipitation, wind stresses and wind curl, all of which act on the sea surface or land-side boundary. Not only water temperature and salinity but also surface current, sea level, and even sea ice, respond to these local changes. The second consists of remote processes that act on the lateral boundary of the marginal seas with the open ocean. These remote processes are caused by changes in the Kuroshio and Oyashio that are themselves caused by the westward propagation of barotropic and baroclinic Rossby waves from the interior ocean and or the advection of signals from the upstream areas of two western boundary currents. Readers should keep these two types of process in mind as they read the following chapters.

Chapter 2
Changes in Temperature, Chlorophyll Concentration, and Secchi Disk Depth in the Bering Sea from 1998 to 2016

Chen-Tung Arthur Chen, Shujie Yu, Ting-Hsuan Huang, Yan Bai, and Xianqiang He

Abstract The subarctic Bering Sea is the northernmost marginal sea in the Asia-Pacific region and, like other seas at high latitudes, it is changing rapidly. One of the most notable changes is the sea surface temperature (SST), which increased by approximately 5.5 °C/century ($p = 0.14$) from 1998 to 2016—a much higher rate than the reported global rate of 1.5 °C/century between 2000 and 2010. During the former period, the chlorophyll concentration increased significantly by 0.011 μg/L per year ($p = 0.03$). However, the Secchi disk depth did not significantly change. Unlike in tropical oceans, both SST and chlorophyll concentration in the Bering Sea increased, revealing the different responses of phytoplankton to oceanic warming.

Keywords Bering sea · Sea surface temperature · Chlorophyll concentration · Secchi disk depth · Temporal changes

2.1 Introduction

The Bering Sea (2.269×10^6 km^2) is the third largest marginal sea in the world after the South China Sea and the Mediterranean Sea, and the second largest in the North Pacific. It is divided about equally into a wide shelf in the northeast and a deep basin

C.-T. A. Chen (✉) · T.-H. Huang
Department of Oceanography, National Sun Yat-Sen University, Kaohsiung 804, Taiwan
e-mail: ctchen@mail.nsysu.edu.tw

T.-H. Huang
e-mail: thhuang@mail.nsysu.edu.tw

S. Yu · Y. Bai · X. He
State Key Laboratory of Satellite Ocean Environment Dynamics, Second Institute of Oceanography, Ministry of Natural Resources, Hangzhou 310012, China
e-mail: yvshujie@126.com

Y. Bai
e-mail: baiyan@sio.org.cn

X. He
e-mail: hexianqiang@sio.org.cn

C.-T. A. Chen and X. Guo (eds.), *Changing Asia-Pacific Marginal Seas*, Atmosphere, Earth, Ocean & Space, https://doi.org/10.1007/978-981-15-4886-4_2

with a maximum depth of over 5000 m in the southwest. The mean water depth of the 500 km-wide shelf is less than 50 m with a shelf break at a water depth of 100–200 m. Ice covers the shelf from November to May. The Bering Strait is around 85 km wide and less than 50 m deep. It is the only northern gateway through which water of Pacific origin flows into the Arctic Ocean and finally enters the Atlantic. Alaska lies to the northeast and the east of the Bering Sea. To its south, the Aleutian Islands separate the Bering Sea from the North Pacific Ocean; to the west and northwest lie the Russian Far East and the Kamchatka Peninsula (Chen et al. 2004).

The Bering Sea is more nutrient-rich than the open oceans, and its primary productivity (PP), even in the deep basin, is almost double that in the Gulf of Alaska immediately south of the Aleutian Islands (Tsunogai et al. 1979; Takahashi 1995; Takahashi et al. 2002). Accordingly, the Bering Sea has one of the highest biological productivities in the world and supplies 40% of the fish catch of the U.S. (Walsh et al. 1989; Wiese et al. 2012). Despite of the shallowness of the Bering Strait it transported 0.7 Sv (10^6 m^3 s^{-1}) of seawater to the Arctic Ocean in 1995. The transport increased to 1.2 Sv in 2015 (Woodgate 2018), and accounted for 19% of the dissolved organic carbon there (Roach et al. 1995; Wheeler et al. 1997). Takahashi (1999) claimed that "… Much of the biological production of organic matter and associated nutrients that flow into the Arctic Ocean today is due to this northerly current direction". This current has intensified in recent years (Woodgate et al. 2012), so has the outflow from the Yukon River, which is a major river entering the Bering Sea (Ge et al. 2013).

Since marine ecosystems are very sensitive to environmental changes, and especially long-term perturbations that are caused by anthropogenic activities and global environment change, many investigations have reported that global warming may reduce primary productivity and global phytoplankton biomass. This is mainly because warming of the surface layer makes the surface seawater lighter, hence higher stability of the water column. As a result, the nutrient-laden subsurface water becomes more difficult to upwell to the nutrient-poor euphotic zone, thus lower primary productivity (McClain et al. 2004; Behrenfeld et al. 2006; Polovina et al. 2008; Irwin and Oliver 2009; Steinacher et al. 2010; Boyce et al. 2010). However, marginal seas are highly variable and different regions thereof may respond to global change on various time scales (Siegel et al. 2013; Bai et al. 2018). The Bering Sea is a notable example of variability. For example, the shelf water has a pCO_2 of approximately 100 μatm below saturation in winter, mainly because of cooling. However, the rate of air-sea exchange is probably low in winter because of the coverage of the continental shelf with sea ice. Near the shelf break, vertical mixing causes pCO_2 supersaturation (Chen 1993). In summer, the shelf area is highly undersaturated with a pCO_2 as low as 125 μatm because of high productivity—especially of siliceous shell-bearing plankton such as diatoms (Codispoti et al. 1986; Takahashi 1999; Chen et al. 2014). Unlike $CaCO_3$ shells, which emit CO_2 upon formation siliceous shells do not emit CO_2 so siliceous shell-bearing plankton are more efficient in absorbing CO_2 than are $CaCO_3$ shell-bearing plankton.

Phytoplankton convert CO_2 to dissolved inorganic carbon, dissolved organic carbon and particulate organic carbon, and transport them to the deep basin mainly by way of sinking particles. As a result of rising atmospheric CO_2 levels since the

Industrial Revolution, the air-sea exchange of CO_2 of the Northeastern shelf may have switched during the last 250 years from being a CO_2 source to being a CO_2 sink simply because the CO_2 concentration in the atmosphere has increased (Walsh and Dieterie 1994). Chen (1993) reported that the excess CO_2 in the Bering Sea penetrates to at least 1000 m. The penetration is deeper in the eastern and southern basin, and slightly shallower off the Kamchatka Peninsula. Tritium and freons exhibit similar penetration, but the 14C concentration does not level off until a slightly greater depth is reached (Warner and Roden 1995). It should be pointed out, however, that we are not implying that dense, subsurface water is formed on the Bering Sea shelf and carries excess CO_2, tritium, freons and bomb-produced radiocarbon to the deep basin. All these signals have actually been imported from the North Pacific Ocean. Because higher CO_2 results in lower pH which favors the dissolution of $CaCO_3$, the carbonate deposits on the vast Bering Sea shelves may provide a large sink for excess CO_2 in the near future. The shelf waters are currently about 210 and 150% saturated with calcite and aragonite, respectively. Owing to the small depth of the shelves (less than 200 m) relative to the saturation horizons of calcite (400 m) and aragonite (350 m), the upward migration of these saturation horizons as a result of excess CO_2 input (Feely and Chen 1982; Sharma et al. 1999) has probably not affected the dissolution rates of carbonates.

An increase of approximately 200 μatm in pCO_2, however, would make the shelf water undersaturated with aragonite and high-magnesium calcite, which would then dissolve and neutralize the excess CO_2. Note the pCO_2 in the Bering Sea has increased at a rate about twice the global rate of 2 μatm/yr (Wang et al. 2017). A doubling of the current CO_2 level in the atmosphere by the second half of the next century would cause the calcites on the shelves to dissolve, providing another large CO_2 sink (Chen 1993).

Temperature and biological productivity are two factors that strongly influence the air-sea exchange of CO_2, which is the chief culprit in global environmental change. SST has been increasing and the amount of sea ice decreasing over the last few thousand years (Stabeno et al. 2012; Wang et al. 2012; Harada et al. 2014) but this investigation is concerned only with recent changes. Because of the lack of field observations, the following considers decadal changes in temperature, chlorophyll concentration, and the related Secchi disk depth (SDD) in the Bering Sea based on satellite data. Specifically, time series of data from 1998 to 2016 from the SeaWiFS (Sea-Viewing Wide Field-of-View Sensor) onboard the SeaStar satellite and Aqua/MODIS (Moderate Resolution Imaging Spectroradiometer) onboard the Agua satellites are used. Mean climatological conditions, long-term changes and spatial variations, are provided.

2.2 Sea Surface Temperature

Climate models predict that the Arctic, including the Bering Sea, will become warmer, with nearly ice-free summers by 2050 (Wang and Overland 2009). This

section concerns the temperature trend from 1998 to 2016. The sea surface temperature data (SST) were taken from the AVHRR_OI dataset, which is a product of the Group for High-Resolution Sea Surface Temperature (GHRSST) and can be obtained from National Centers for Environmental Information (NCEI), NOAA (https://data.nodc.noaa.gov/ghrsst/L4/GLOB/NCEI/AVHRR_OI/). It is a level-4 product that is derived from the Advanced Very High-Resolution Radiometer (AVHRR) with a spatial resolution of 0.25°. NCEI provides global daily SST data from 1981 to 2016. Data are averaged monthly from 1998 to 2016 as the monthly data field. The monthly mean was obtained by averaging daily data. Trends were assessed by subtracting monthly climatological mean values from mean data for each month to remove the seasonal signal, and linear trends were identified using regression analysis. Pixels were removed when the number of available data was less than half of the total number of data (228 monthly data). The statistical significance of the trends (expressed as a P value, where $P < 0.1$ indicates the existence of a trend at a confidence level of over 90%) was assessed using the F-test. The colored pixels on the trend map represent where the available data is greater than 80 (that is, there are more than 80 months during 1998–2016 when data of this pixel is available) and shows a significant trend. Note for some areas the data may indicate ice surface temperature (Fig. 2.1).

The climatological SST was lowest, below approximately 3 °C, in the northeastern part of the Bering Sea that covers the continental shelf. The temperature is slightly higher, but still below around 5 °C, off Eastern Siberia, and reaches around 6 °C

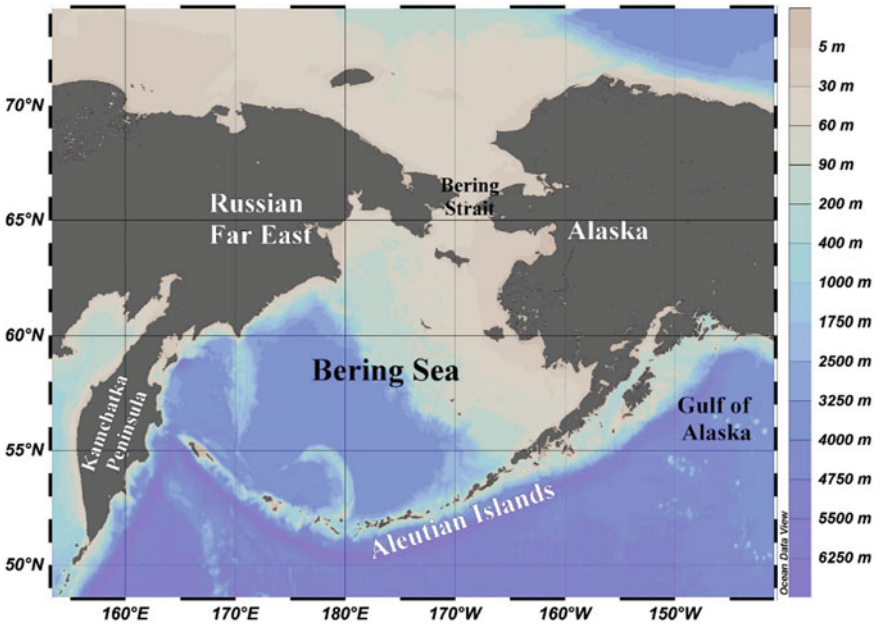

Fig. 2.1 Map of the Bering Sea (drawn using ODV, Schlitzer, R., Ocean Data View, https://odv.awi.de, 2018)

further south. South of Aleutian Is. the SST jumps to above 7 °C (Fig. 2.2a). The SST exhibits a large seasonal variation from approximately 1 °C in February to about 10 °C in August (Fig. 2.3). Indeed. The timeseries data show sinusoidal-wave like trend. The annual mean SST shows a warming trend between 1999 and 2003, and between 2012 and 2016. But, between 2003 and 2012 the mean SST seems to be decreasing. Overall, however, throughout the Bering Sea the SST increased by 5.5 °C/century ($p = 0.14$) from 1998 to 2016 in both the Bering Sea Basin and coastal zones (Fig. 2.4). The most intense warming occurred in the west of the basin, reaching 6–8 °C/century, similar to those in other high-latitude seas (Screen and Simmonds 2010; He et al. 2017). By way of comparison, the global SST increased by 1.5 °C/century ($p = 0.001$) from 2000 to 2010 (He et al. 2017). Such an increase in SST may promote the growth of phytoplankton in the Bering Sea.

Bai et al. (2018) examined the SST of 12 marginal seas around the Eurasian continent between 2003 and 2014 but they did not include the Bering Sea. The 12 seas exhibited an increase in temperature of <3 °C/century for the South China Sea, Java-Banda Sea, Bay of Bengal and Arabian Sea, reaching the relatively high rate of 9 °C/century for the Japan Sea and the East China Sea. The Black Sea exhibited the greatest increase (19 °C/century), followed by the Baltic Sea (10 °C/century). Bai et al. (2018) noted that enclosed seas warmed more than open seas. The Bering Sea is semi-enclosed and its warming rate (5.5 °C/century) found in this study is moderate. Whereas Bai et al. (2018) used a period of 12 years, this investigation considered a period of 19 years (1998–2016), possibly reducing the rate of change.

Chen et al. (2020a, 2020b) investigated the rate of SST change in the Okhotsk Sea and South China Sea (SCS) for the same duration. For the former, also a high latitude sea, the SST increased by 4.5 °C/century, only slightly lower than the 5.5 °C/century found for the Bering Sea. For the subtropical and tropical SCS, however, the increase was only 1.2 °C/century. Belkin (2009) reported that the East Bering Sea warmed by 1.1 °C/century between 1982 and 2006. How much of the larger increase of 5.5 °C/century from 1998 to 2016 that was estimated herein was caused by enhanced warming after 2006 is unclear considering the complicated relationship between the SST, sea ice and the oceanic and atmospheric patterns. For instance, the strong advection of warm water through the Aleutian Islands from the Gulf of Alaska (Stabeno et al. 2017).

2.3 Chlorophyll Concentration

The chlorophyll concentration data that are used herein were obtained from the Ocean Color project of the ESA Climate Change Initiative (CCI) (http://www.esa-oceancolour-cci.org), which provides a high number of observations, and yields long-term multi-sensor time-series of satellite ocean-color data primarily for use in climate studies. Monthly L3S chlorophyll data (version 3.1) with a spatial resolution of 4 km that covered the study areas and the period 1998–2016 were used. Trends were assessed pixel by pixel and reported as average percentage values per year

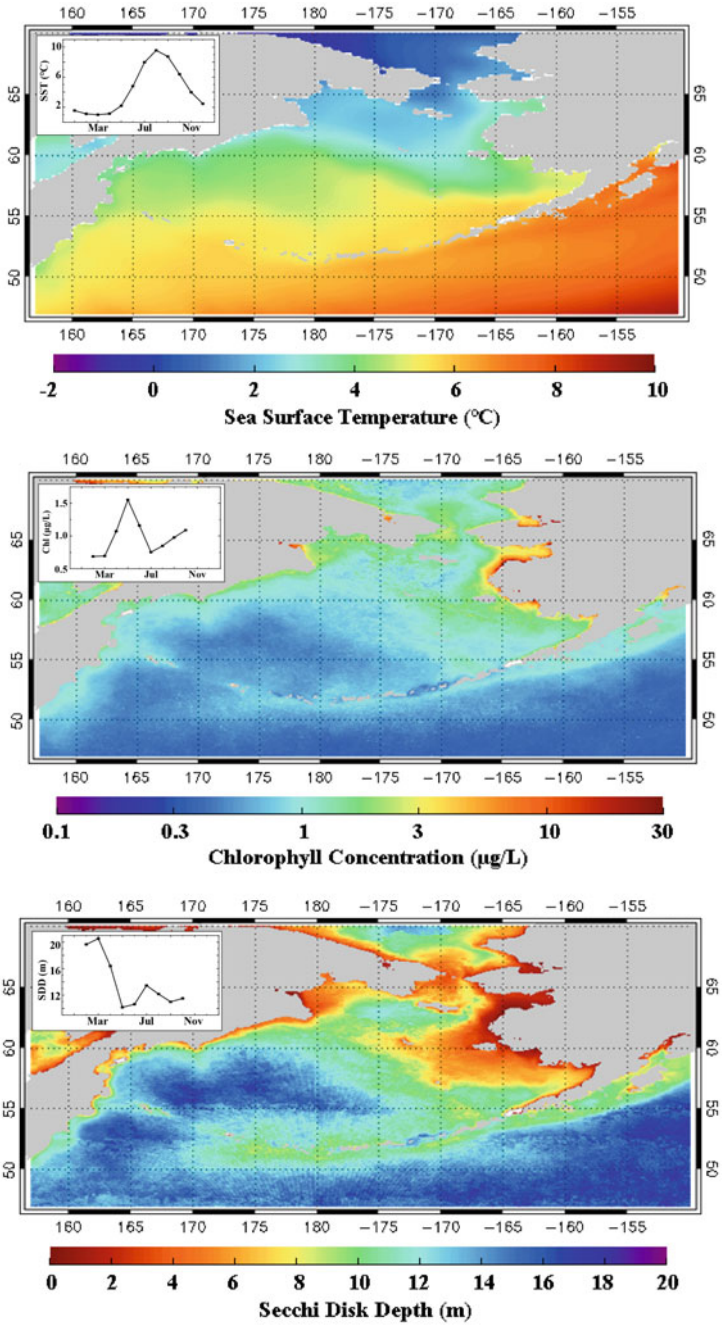

Fig. 2.2 Climatological Map and monthly mean of **a** SST, **b** chlorophyll concentration and **c** SDD in the Bering Sea. The insets are climatological monthly mean curves in the enclosed area

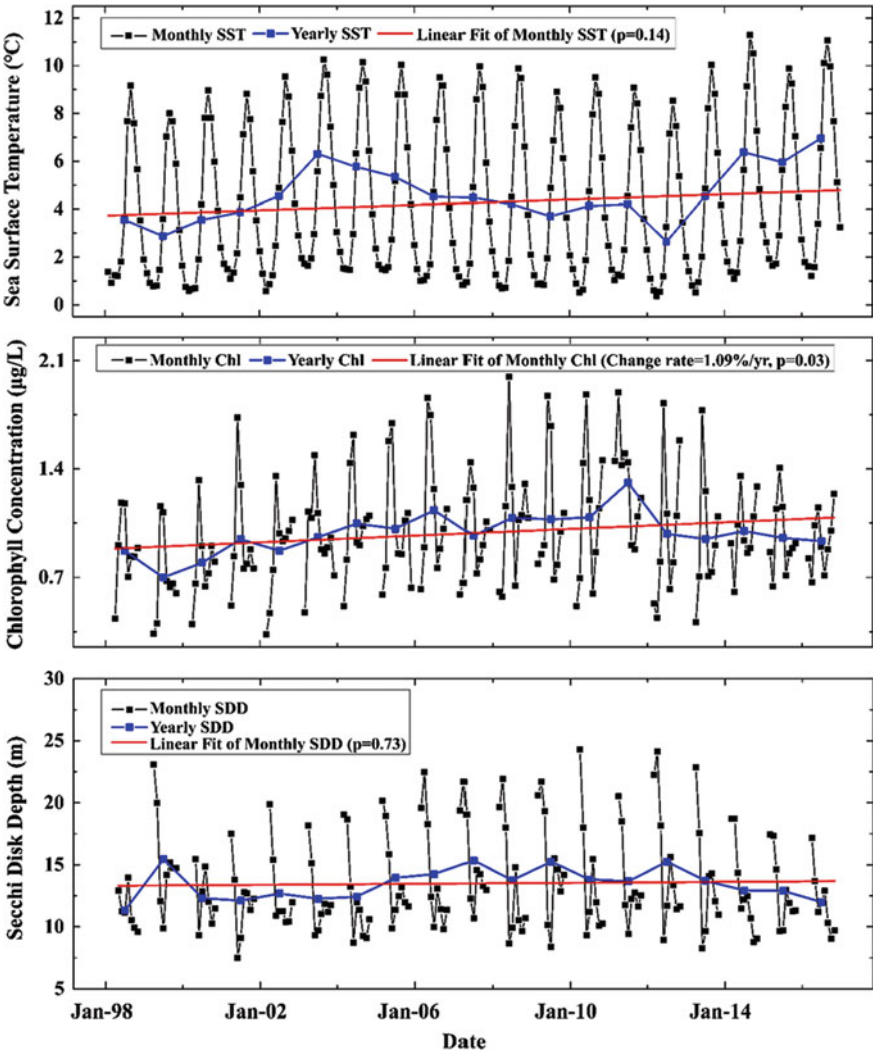

Fig. 2.3 Time series of **a** SST, **b** chlorophyll concentration and **c** SDD for the Bering Sea from 1998 to 2016

averaged over the whole period, obtained from a linear slope as presented in Fig. 2.3b. Satellite-derived chl-a data may have high uncertainty in Case-II waters. Therefore, in the statistics of this study, we have dropped the turbid waters pixels with remote sensing reflectance at 555 nm larger than 0.1 sr^{-1} to diminish this effect.

We have also recognized the influence of sea ice and cloud on the data availability for the ocean color satellite records. To diminish this effect, we have used the monthly composited products instead of daily or 8-days composited products. In fact, the monthly products almost have full data availability in the whole regions in summer.

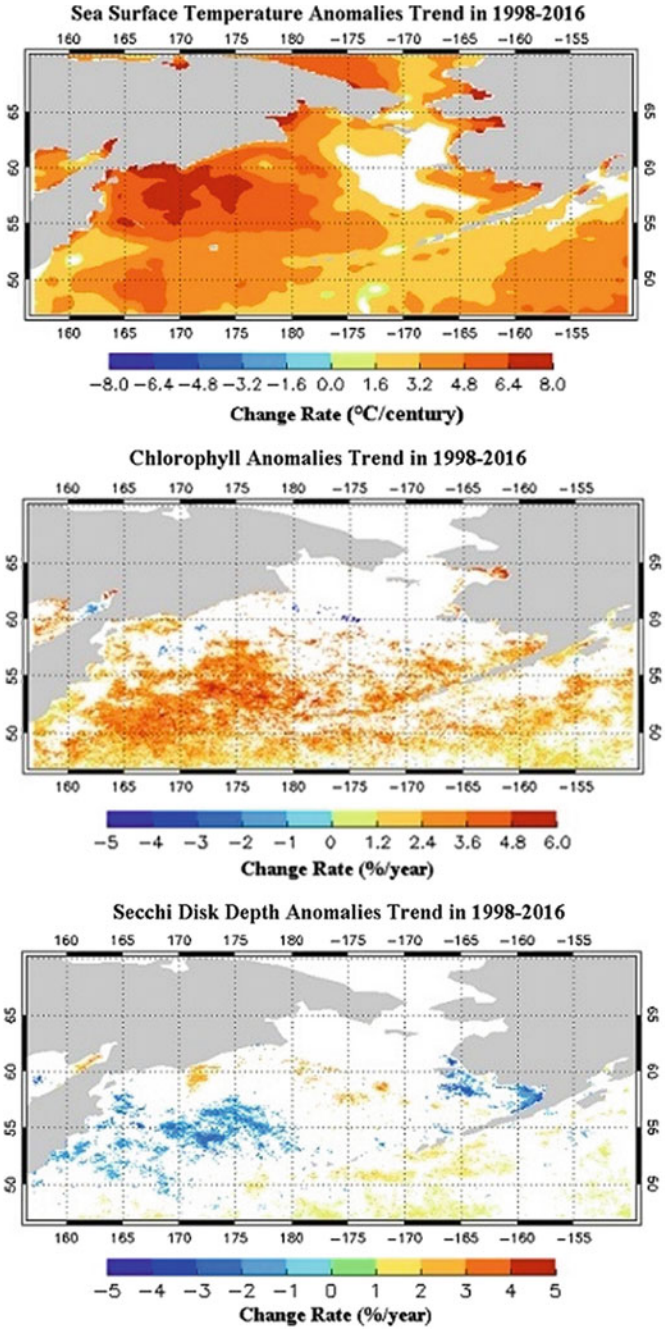

Fig. 2.4 Trend maps of **a** SST, **b** chlorophyll concentration and **c** SDD in the Bering Sea from 1998 to 2016. Only pixels that satisfy the significance criterion $P < 0.1$ are shown in bright colors

Moreover, the satellite chl-a data used in this study were from the ESA CCI product, which is a multiple-satellite merged dataset with much higher data availability than dataset from single satellite.

Figure 2.2b presents the climatological distribution of chlorophyll. Chlorophyll concentrations are as high as 10 μg/L in the bays in western Alaska, falling to between 1 and 3 μg/L on the shelf and off Eastern Siberia. In the Bering Sea Basin, the chlorophyll concentration is typically below 1 μg/L (Fig. 2.2b). From 1998 to 2016, the chlorophyll concentration in the Bering Sea increased at a rate of 0.011 μg/L (1.09%) per year ($p = 0.03$; Fig. 2.3b), slightly higher than the rate reported by He et al. (2017). The increase in chlorophyll concentration in the southern Bering Sea was a significant 4–5% per year. Yet, the change was almost insignificant in the region of the continental shelf (Fig. 2.4b) except for the coastal region and the bay north of the Yukon Delta where the increase reached 5%/yr. Gregg et al. (2005) also reported an increases of 6%/yr between 1998 and 2003. Note that there are three eddies along the Kamchatka coast from 55°N to 60°N and chl-a has somehow increased at the periphery of the eddies (Mizobata and Saitoh 2004; Mizobata et al. 2006).

By way of comparison, the chlorophyll concentration increased by 0.01 μg/L/yr (1%) in the Okhotsk Sea during the same period as this study (Chen et al. 2020a). This is almost the same as what was found for the Bering Sea. On the other hand, Chen et al. (2020b) found that the chlorophyll concentration increased by only 0.0012 μg/L/yr during the same period in the warm South China Sea.

Note that in open ocean waters, the uncertainty of the satellite-derived Chla is about 35%. On the other hand, regarding the statistics trend, the most important thing is the stability of the dataset itself instead of the absolute accuracy. In other word, the trend analysis is based on the relative change. Based on this point, satellite products can still be used for long-term change analysis even with high uncertainty. For example, even for the high accuracy product, such as the SST, we know the uncertainty of satellite-derived SST has the absolute error of around 0.5 K, however, the uncertainty of the SST trend is only around 0.02 K per year.

A higher SST generally causes stronger stratification of the water column, disfavoring the supply of nutrients from nutrient-rich deep oceans to the generally nutrient-deficient surface euphotic zone. Accordingly, primary productivity and chlorophyll concentration are lowered. Indeed, Siegel et al. (2013) reported that the area-mean chlorophyll concentration decreased significantly (0.18%/yr) between 1998 and 2011 over the warm regions of the world with a climatological SST of greater than 15 °C. Interestingly, they found that the chlorophyll concentration increased significantly (0.83%/yr) in the Southern Hemisphere with an SST of less than 15 °C. However, they found no significant trend in the Northern Hemisphere with an SST of less than 15 °C. Giesbrecht et al. (2018) also reported no clear trends in the Bering Sea from 2006 to 2016. Thomas et al. (2012) suggested that the optimal temperature for phytoplankton growth in mid- and high latitudes typically exceeds the local ambient temperature. Therefore, any increase in SST causes the ambient temperature to become closer to the optimal temperature for certain phytoplankton species, possibly increasing their growth rate and correspondingly increase the surface chlorophyll concentration. Moreover, a global increase in temperature may also cause pole-ward shifts of

phytoplankton communities from mid- and low latitudes, increasing phytoplankton biomass and primary productivity at mid-high latitudes. As stated above, the SST of the Bering Sea increased during the period of interest. Increasing SST reduces the solubility of oxygen. Warming also raises metabolic rates, thus accelerating the rate of oxygen consumption. On the other hand, increasing chlorophyll concentration enhances the rate of oxygen production. The end result of these conflicting effects is that the oxygen content in most of the Bering Sea surface water has declined since 1960 (Schmidtko et al. 2017; Ito et al. 2017; Breitburg et al. 2018).

2.4 Secchi Disk Depth

The SDD is a measure of water transparency, and reflects the clarity of water or the attenuation of light as it penetrates the water column. The SDD is easy to measure and has been measured for over a century (He et al. 2013a, 2013b, 2014, 2017). Satellite ocean color remote sensing has enabled SDD to be obtained globally in recent decades. Transparency data (Secchi disk depth) from the Globcolour project (http://globcolour.info/), which began in 2005 as an European Space Agency Data User Element (DUE) project, were utilized to provide a continual dataset of multi-sensor level-3 satellite ocean color products. Monthly L3m SDD data (Doron et al. 2011) with a spatial resolution of 4 km, covering the study areas in the period 1998–2016, were used. Trends were assessed pixel by pixel and reported as percentage change per year averaged over the period of interest, computed from a linear slope as shown in Fig. 2.2. See Bai et al. (2018) for details.

Figure 2.2c shows the climatological SDD. Generally, a continental shelf is associated with a low SDD because there the turbidity and phytoplankton biomass are higher than those in the deeper ocean basin. A marked 2–3% decrease in SDD per year is evident in the southeastern part of the Bering Sea Basin and off southwest Alaska, possibly as a result of increases in chlorophyll concentration. However, the northern part of the Bering Sea Basin and the continental slope witnessed increases in SDD (Fig. 2.4c). On average, the Bering Sea exhibited a statistically insignificant increase in SDD (0.02 m/yr, $p = 0.73$) between 1998 and 2016. This increase is about the same as that found for the Okhotsk Sea (0.018 m/yr; Chen et al. 2020a), but it smaller than that found for the South China Sea (0.036 m/yr; Chen et al. 2020b). All 12 marginal seas that were examined by Bai et al. (2018) exhibited larger rates of increase between 2003 and 2014; they were as high as 0.35 m/yr ($p < 0.007$) for the Java-Banda and Arabian Seas, followed by 0.25 m/yr ($p = 0.0003$) for the Persian Gulf. The South China Sea had the lowest rate of increase of 0.05 m/yr ($p = 0.49$). Tropical and subtropical oceans exhibited a significant increase of SDD and a decrease of chlorophyll concentration (Siegel et al. 2013). This is because the SDD is basically correlated negatively with the chlorophyll concentration (Fig. 2.5). In the Bering Sea, despite of a significant increase in chlorophyll concentration at a rate of 0.011 μg/L per year ($p = 0.03$), no significant change of SDD was observed throughout.

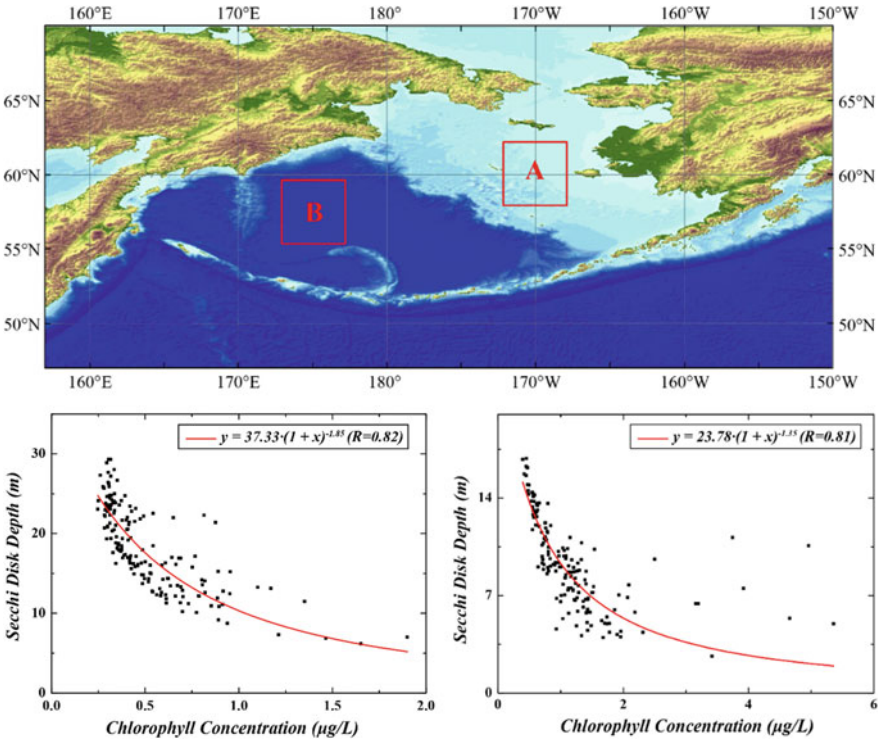

Fig. 2.5 Chlorophyll concentration versus SDD in selected areas

Note subarctic seas in the Northern Hemisphere are basically very productive and are turbid. Even the phytoplankton growth rate is decreased, suspended sediment is still abundant especially in the shelf region. This may explain why no significant change of SDD was observed throughout.

2.5 Conclusions

In this study, time-series satellite-derived records were used to elucidate long-term changes in the surface water temperature, chlorophyll concentration, and Secchi disk depth in the Bering Sea from 1998 to 2016. Overall, SST increased at a rate of 5.5 °C/century ($p = 0.14$) and chlorophyll concentration increased at a rate of 0.011 μg/L per year ($p = 0.03$). However, the Secchi disk depth did not significantly change on the average although in the southwestern deep basin the SDD decreased, perhaps reflecting enhanced intrusion of the more transparent North Pacific water. These results demonstrated that oceanic warming might have enhanced chlorophyll concentration in the Bering Sea, contrary to the widely reported conclusion that a

higher SST corresponds to a lower chlorophyll concentration in tropical and subtropical oceans. Validation of the above, however, must be done with field data in the future.

Note the trend analysis is based on the relative change. From this point, satellite products can still be used for long-term change analysis even with high uncertainty.

Acknowledgments The authors would like to thank the Ministry of Science and Technology of the Republic of China, Taiwan, for financially supporting this research under contract MOST 107-2611-M-110-006, 107-2611-M-110-021 and 107-2611-M-110-012 and the Ministry of Education (Higher Education Sprout Program) of Republic of China. Two anonymous reviewers provided very comprehensive and constructive comments which helped strengthening the manuscript.

References

Bai Y, He XQ, Yu SJ, Chen CTA (2018) Changes in the ecological environment of the marginal seas along the Eurasian continent from 2003 to 2014. Sustainability 10(3):635. https://doi.org/10.3390/su10030635

Behrenfeld MJ, O'Malley RT, Siegel DA, McClain CR, Sarmiento JL, Feldman GC, Milligan AJ, Falkowski PG, Letelier RM, Boss ES (2006) Climate-driven trends in contemporary ocean productivity. Nature 444:752–755. https://doi.org/10.1038/nature05317

Belkin IM (2009) Rapid warming of large marine ecosystems. Prog Oceanogr 81(1–4):207–213

Boyce DG, Lewis MR, Worm B (2010) Global phytoplankton decline over the past century. Nature 466(7306):591–596

Breitburg D, Levin LA, Oschlies A, Gregoire M, Chavez FP, Conley DJ, Garcon V, Gilbert D, Gutierrez D, Isensee K, Jacinto GS, Limburg KE, Montes I, Naqvi SWA, Pitcher GC, Rabalais NN, Roman MR, Rose KA, Seibel BA, Telszewski M, Yasuhara M, Zhang J (2018) Declining oxygen in the global ocean and coastal waters. Science 359(6371):eaam7240. https://doi.org/10.1126/science.aam7240

Chen CTA (1993) Carbonate chemistry of the wintertime Bering Sea marginal ice-zone. Cont Shelf Res 13(1):67–87. https://doi.org/10.1016/0278-4343(93)90036-w

Chen CTA, Andreev A, Kim KR, Yamamoto M (2004) Roles of continental shelves and marginal seas in the biogeochemical cycles of the North Pacific Ocean. J Oceanogr 60(1):17–44

Chen CTA, Yu SJ, Huang TH, Bai Y, He XQ (2020a) Changes in temperature, chlorophyll concentration, and Secchi disk depth in the Okhotsk Sea from 1998 to 2016. In Chen CTA, Guo XY (eds) Changing Asia-Pacific Marginal Seas. Springer International Publishing (in press)

Chen CTA, Yu SJ, Huang TH, Lui HK, Bai Y, He XQ (2020b) Changing biogeochemistry in the South China Sea. In Chen CTA, Guo XY (eds) Changing Asia-Pacific marginal seas. Springer International Publishing (in press)

Chen LQ, Gao ZY, Sun H, Chen BS, Cai WJ (2014) Distributions and air-sea fluxes of CO_2 in the summer Bering Sea. Acta Oceanol Sin 33(6):1–8. https://doi.org/10.1007/s13131-014-0483-9

Codispoti LA, Friederich GE, Hood DW (1986) Variability in the inorganic carbon system over the Southeastern Bering sea shelf during Spring 1980 and Spring summer 1981. Cont Shelf Res 5(1–2):133–160

Doron M, Babin M, Hembise O, Mangin A, Garnesson P (2011) Ocean transparency from space: Validation of algorithms using MERIS, MODIS and SeaWiFS data. Remote Sens Environ 115(12):2986–3001. https://doi.org/10.1016/j.rse.2011.05.019

Feely RA, Chen CTA (1982) The Effect of Excess CO_2 on the calculated calcite and aragonite saturation Horizons in the Northeast Pacific. Geophys Res Lett 9(11):1294–1297. https://doi.org/10.1029/gl009i011p01294

Ge SQ, Yang DQ, Kane DL (2013) Yukon River Basin long-term (1977–2006) hydrologic and climatic analysis. Hydrol Process 27(17):2475–2484. https://doi.org/10.1002/hyp.9282

Gregg WW, Casey NW, McClain CR (2005) Recent trends in global ocean chlorophyll. Geophys Res Lett 32(3):L03606. https://doi.org/10.1029/2004gl021808

Harada N, Katsuki K, Nakagawa M, Matsumoto A, Seki O, Addison JA, Finney BP, Sato M (2014) Holocene sea surface temperature and sea ice extent in the Okhotsk and Bering Seas. Prog Oceanogr 126:242–253. https://doi.org/10.1016/j.pocean.2014.04.017

He XQ, Bai Y, Chen CTA, Hsin YC, Wu CR, Zhai WD, Liu ZL, Gong F (2014) Satellite views of the episodic terrestrial material transport to the southern Okinawa Trough driven by typhoon. J Geophys Res-Oceans 119(7):4490–4504. https://doi.org/10.1002/2014jc009872

He XQ, Bai Y, Pan DL, Huang NL, Dong X, Chen JS, Chen CTA, Cui QF (2013a) Using geostationary satellite ocean color data to map the diurnal dynamics of suspended particulate matter in coastal waters. Remote Sens Environ 133:225–239. https://doi.org/10.1016/j.rse.2013.01.023

He XQ, Bai Y, Pan DL, Chen CTA, Cheng Q, Wang D, Gong F (2013b) Satellite views of the seasonal and interannual variability of phytoplankton blooms in the eastern China seas over the past 14 yr (1998–2011). Biogeosciences 10(7):4721–4739. https://doi.org/10.5194/bg-10-4721-2013

He XQ, Pan DL, Bai Y, Wang TY, Chen CTA, Zhu QK, Hao ZZ, Gong F (2017) Recent changes of global ocean transparency observed by SeaWiFS. Cont Shelf Res 143:159–166. https://doi.org/10.1016/j.csr.2016.09.011

Irwin AJ, Oliver MJ (2009) Are ocean deserts getting larger? Geophys Res Lett 36(18):L18609. https://doi.org/10.1029/2009GL039883

Ito T, Minobe S, Long MC, Deutsch C (2017) Upper ocean O_2 trends: 1958–2015. Geophys Res Lett 44(9):4214–4223. https://doi.org/10.1002/2017gl073613

McClain CR, Signorini SR, Christian JR (2004) Subtropical gyre variability observed by ocean-color satellites. Deep-Sea Res Pt II 51(1–3):281–301

Mizobata K, Saitoh S (2004) Variability of Bering Sea eddies and primary productivity along the shelf edge during 1998-2000 using satellite multisensor remote sensing. J Marine Syst 50(1–2):101–111. https://doi.org/10.1016/j.jmarsys.2003.09.014

Mizobata K, Wang J, Saitoh SI (2006) Eddy-induced cross-slope exchange maintaining summer high productivity of the Bering Sea shelf break. J Geophys Res-Oceans 111:C10017. https://doi.org/10.1029/2005jc003335

Polovina JJ, Howell EA, Abecassis M (2008) Ocean's least productive waters are expanding. Geophys Res Lett 35(3):L03618. https://doi.org/10.1029/2007GL031745

Roach AT, Aagaard K, Pease CH, Salo SA, Weingartner T, Pavlov V, Kulakov M (1995) Direct measurements of transport and water properties through the Bering Strait. J Geophys Res-Oceans 100(C9):18443–18457. https://doi.org/10.1029/95jc01673

Schmidtko S, Stramma L, Visbeck M (2017) Decline in global oceanic oxygen content during the past five decades. Nature 542(7641):335–339. https://doi.org/10.1038/nature21399

Screen JA, Simmonds I (2010) The central role of diminishing sea ice in recent Arctic temperature amplification. Nature 464(7293):1334–1337. https://doi.org/10.1038/nature09051

Sharma S, Barrie LA, Plummer D, McConnell JC, Brickell PC, Levasseur M, Gosselin M, Bates TS (1999) Flux estimation of oceanic dimethyl sulfide around North America. J Geophys Res-Atmos 104(D17):21327–21342

Siegel DA, Behrenfeld M, Maritorena S, McClain CR, Antoine D, Bailey SW, Bontempi PS, Boss ES, Dierssen HM, Doney SC, Eplee RE, Evans RH, Feldman GC, Fields E, Franz BA, Kuring NA, Mengelt C, Nelson NB, Patt FS, Robinson WD, Sarmiento JL, Swan CM, Werdell PJ, Westberry TK, Wilding JG, Yoder JA (2013) Regional to global assessments of phytoplankton dynamics from the SeaWiFS mission. Remote Sens Environ 135:77–91

Stabeno PJ, Duffy-Anderson JT, Eisner LB, Farley EV, Heintz RA, Mordy CW (2017) Return of warm conditions in the southeastern Bering Sea: Physics to fluorescence. PLoS One 12(9):e0185464. https://doi.org/10.1371/journal.pone.0185464

Stabeno PJ, Kachel NB, Moore SE, Napp JM, Sigler M, Yamaguchi A, Zerbini AN (2012) Comparison of warm and cold years on the southeastern Bering Sea shelf and some implications for the ecosystem. Deep-Sea Res Pt II 65–70:31–45

Steinacher M, Joos F, Frolicher TL, Bopp L, Cadule P, Cocco V, Doney SC, Gehlen M, Lindsay K, Moore JK, Schneider B, Segschneider J (2010) Projected 21st century decrease in marine productivity: a multi-model analysis. Biogeosciences 7(3):979–1005. https://doi.org/10.5194/bg-7-979-2010

Takahashi K (1995) Opal particle flux in the subarctic Pacific and Bering Sea and sidocoenosis preservation hypothesis. In Proceedings of 1994 Sapporo IGBP Symposium, Sapporo, Japan, pp 458–466

Takahashi K (1999) The Okhotsk and Bering Seas: Critical marginal seas for the land-ocean linkage. In: Land-Sea Link in Asia, Proceedings of an International Workshop on Sediment Transport and Storage in Coastal Sea-Open System, Tsukuba, Japan, pp 341–353

Takahashi K, Fujitani N, Yanada M (2002) Long term monitoring of particle fluxes in the Bering Sea and the central subarctic Pacific ocean, 1990–2000. Prog Oceanogr 55(1–2):95–112

Thomas MK, Kremer CT, Klausmeier CA, Litchman E (2012) A global pattern of thermal adaptation in marine phytoplankton. Science 338(6110):1085–1088. https://doi.org/10.1126/science.1224836

Tsunogai S, Kusakabe M, Iizumi H, Koike I, Hattori A (1979) Hydrographic features of the deep-water of the Bering sea—sea of silica. Deep-Sea Res 26(6):641–659

Walsh JJ, Dieterle DA (1994) CO_2 Cycling in the Coastal Ocean.1. A Numerical-Analysis of the Southeastern Bering Sea with Applications to the Chukchi Sea and the Northern Gulf-of-Mexico. Prog Oceanogr 34(4):335–392

Walsh JJ, Mcroy CP, Coachman LK, Goering JJ, Nihoul JJ, Whitledge TE, Blackburn TH, Parker PL, Wirick CD, Shuert PG, Grebmeier JM, Springer AM, Tripp RD, Hansell DA, Djenidi S, Deleersnijder E, Henriksen K, Lund BA, Andersen P, Mullerkarger FE, Dean K (1989) Carbon and Nitrogen Cycling within the Bering/Chukchi Seas: Source regions for organic matter effecting AOU demands of the Arctic Ocean. Prog Oceanogr 22(4):277–359

Wang HJ, Hu XP, Cai WJ, Sterba-Boatwright B (2017) Decadal fCO_2 trends in global ocean margins and adjacent boundary current-influenced areas. Geophys Res Lett 44(17):8962–8970. https://doi.org/10.1002/2017gl074724

Wang MY, Overland JE (2009) A sea ice free summer Arctic within 30 years? Geophys Res Lett 36:L07502. https://doi.org/10.1029/2009gl037820

Wang MY, Overland JE, Stabeno P (2012) Future climate of the Bering and Chukchi Seas projected by global climate models. Deep-Sea Res Pt II 65–70:46–57. https://doi.org/10.1016/j.dsr2.2012.02.022

Warner MJ, Roden GI (1995) Chlorofluorocarbon evidence for recent ventilation of the deep Bering Sea. Nature 373(6513):409–412

Wheeler PA, Watkins JM, Hansing RL (1997) Nutrients, organic carbon and organic nitrogen in the upper water column of the Arctic Ocean: implications for the sources of dissolved organic carbon. Deep-Sea Res Pt II 44(8):1571–1592

Wiese FK, Van Pelt TI, Wiseman WJ (2012) Bering Sea linkages introduction. Deep-Sea Res Pt II 65–70:2–5. https://doi.org/10.1016/j.dsr2.2012.03.001

Woodgate RA (2018) Increases in the Pacific inflow to the Arctic from 1990 to 2015, and insights into seasonal trends and driving mechanisms from year-round Bering Strait mooring data. Prog Oceanogr 160:124–154. https://doi.org/10.1016/j.pocean.2017.12.007

Woodgate RA, Weingartner TJ, Lindsay R (2012) Observed increases in Bering Strait oceanic fluxes from the Pacific to the Arctic from 2001 to 2011 and their impacts on the Arctic Ocean water column. Geophys Res Lett 39. https://doi.org/10.1029/2012gl054092

Chapter 3
Long-Term Trend and Interannual to Decadal Variability in the Sea of Okhotsk

Takuya Nakanowatari and Humio Mitsudera

Abstract In this article, we describe physical aspects of long-term variations in the Sea of Okhotsk. The maximum sea ice extent (MSIE) in the Sea of Okhotsk decreased at a rate of $-8.7 \pm 2.5\%$ per decade from 1979 to 2010, which is the second largest fraction of ice reduction in the marginal seas of the Northern Hemisphere. The Okhotsk Sea Intermediate Water (OSIW) on the isopycnal surface of $27.0\sigma_\theta$ exhibits a remarkable warming trend, with a maximum value of 0.62 ± 0.18 °C over the last 50 years. Salinity of the dense shelf water (DSW) is a key parameter of the OSIW warming; DSW salinity decreases at a rate of -0.12 ± 0.08 over the last 50 years, caused by freshening of the surface salinity in the subarctic North Pacific, as well as reduction in ice production in the Sea of Okhotsk. Besides, interannual-to-decadal scale variations are evident in the MSIE, DSW salinity and OSIW temperature, and their mechanisms are discussed. Further, the sea level along the coast of the Sea of Okhotsk, correlated with the wind-driven coastal current, exhibits coherent interannual variations. Effects of the 18.6-year-period nodal tide cycle, caused by strong tides along the Kuril Islands, are also discussed.

Keywords Sea ice · Dense shelf water · Salinity · Warming of the Okhotsk Sea intermediate water · Coherent sea level variations · 18.6-year-period nodal tide

3.1 Background

The Sea of Okhotsk is a marginal sea located in the subpolar region of the western North Pacific. In this chapter, interannual to decadal variations and long-term trends of the physical aspects of the Sea of Okhotsk, such as sea ice, temperature, salinity

T. Nakanowatari
Hokkaido National Fisheries Research Institute, Japan Fisheries Research and Education Agency, Kushiro, Japan
e-mail: nakanowataritakuya@affrc.go.jp

H. Mitsudera (✉)
Pan Okhotsk Research Center, Institute of Low Temperature Science, Hokkaido University, Nishi 8, Kita 19, Sapporo, Japan
e-mail: humiom@lowtem.hokudai.ac.jp

C.-T. A. Chen and X. Guo (eds.), *Changing Asia-Pacific Marginal Seas*, Atmosphere, Earth, Ocean & Space, https://doi.org/10.1007/978-981-15-4886-4_3

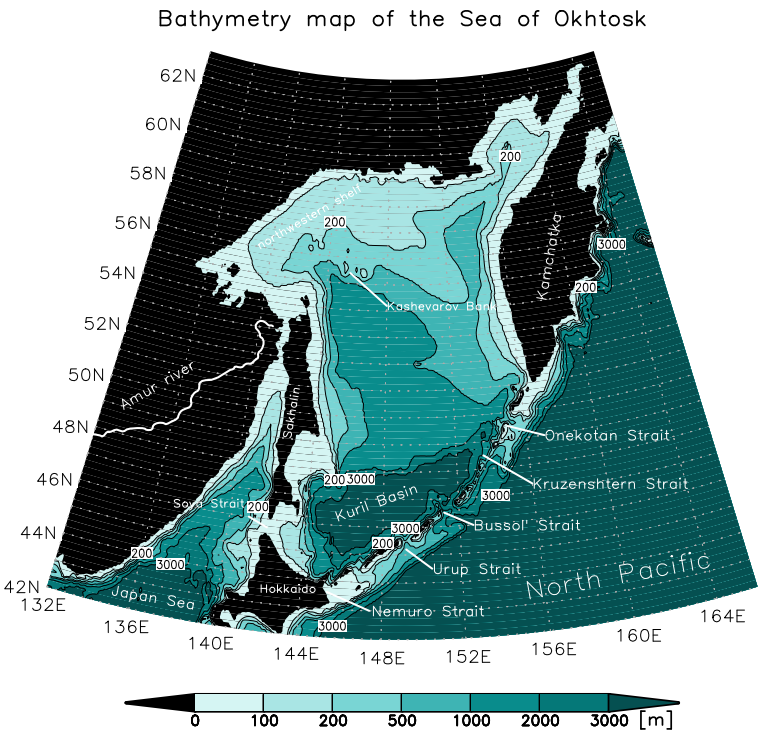

Fig. 3.1 Bathymetry map of the Okhotsk Sea. The bathymetry data are derived from ETOPO5

and currents, are described based on hydrographic observations and numerical model simulations. As a background, we first briefly describe the mean field and seasonal variations in this introductory section.

Geometric features are depicted in Fig. 3.1 The Sea of Okhotsk has an area of 1,530,000 km^2. The central part of the basin is typically 1000 m deep, surrounded by wide continental shelves with a depth of less than 200 m. The Kuril Basin in the southern part exceeds a depth of 3000 m. The Sea of Okhotsk connects to the North Pacific Ocean through straits along the Kuril Islands, such as the Bussol Strait (approximately 2300 m deep) and the Kruzensterna Strait (approximately 1800 m deep). The sea also connects to the Japan Sea through the Soya Strait, where the sill depth is approximately 50 m. Substantial water exchange occurs through these straits (Fig. 3.2). On the other hand, the Okhotsk Sea collects a large amount of freshwater from one of the top 10 largest rivers in the world, the Amur River, which has an area of 2,130,000 km^2 and is 4400 km in length, as well as other rivers along the coast of the Okhotsk Sea and local precipitation. Because of the large amount of various freshwater inputs, the surface water of the Okhotsk Sea is the freshest in the western region of the North Pacific, whereas the freshness is diluted by the inflow of relatively saline waters through the straits from the North Pacific (Ohshima et al. 2010; Uehara et al. 2014; Matsuda et al. 2015) and the Japan Sea (Talley and Nagata

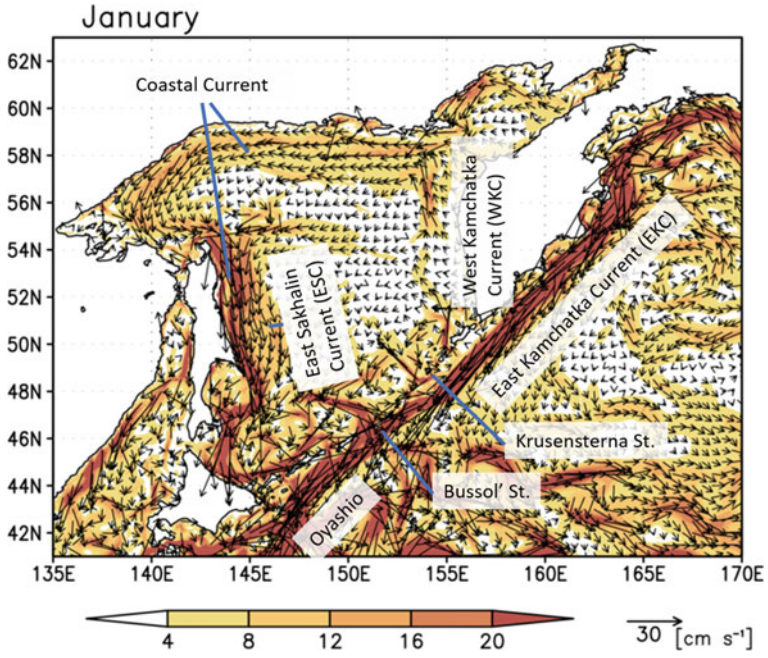

Fig. 3.2 Surface currents in January produced from the Matsuda et al. (2015) model

1995). Various nutrients and materials, such as iron, are also discharged from the Amur River to the Sea of Okhotsk (Nishioka et al. 2014) and transported out to the Oyashio region (Nishioka et al. 2007, 2011, 2013; Nishioka and Obata 2017). High primary production in the Oyashio region (e.g., Yasunaka et al. 2014, 2016) may be attributed to iron transport from the Sea of Okhotsk (Nishioka et al. 2013; Uchimoto et al. 2014; Nakanowatari et al. 2017; Nishioka and Obata 2017).

Surface currents are cyclonic in the central part of the basin (Fig. 3.2). Northward baroclinic transport relative to 1000 m (or the bottom in shallow areas) is 3.5 Sv, which agrees with the Sverdrup transport when the wind stress curl is integrated over the domain where the depth of the ocean exceeds 500 m (Ohshima et al. 2004). The baroclinic structure persists throughout the year. On the other hand, the transport of the East Sakhalin Current (ESC), a western boundary current of the Sea of Okhotsk (Fig. 3.2), is 6.7 Sv on average, having a large seasonal variation of 12.3 Sv in winter and 1.2 Sv in summer (Mizuta et al. 2003). Furthermore, coastal currents also form on shallow continental shelves. The volume transport is evaluated well by the arrested topographic waves (Ohshima et al. 2002; Simizu and Ohshima 2002; Nakanowatari and Ohshima 2014). In the eastern part of the Sea of Okhotsk, a northward current is observed (Uehara et al. 2014; Matsuda et al. 2015). Here, we refer to this current as the West Kamchatka Current (WKC). The WKC is important for the sea surface temperature (SST) and sea ice extent (Nakanowatari et al. 2010) as well as the sea surface salinity in the Sea of Okhotsk (Uehara et al. 2014) because the WKC advects

anomalies from the North Pacific through the Kuril straits, e.g., the Krusensterna Strait (Fig. 3.2).

A prominent feature of the Sea of Okhotsk is the presence of sea ice in winter; this sea is recognized as the lowest-latitude marginal sea ice area in the Northern Hemisphere. Sea ice begins forming in late November over the northwestern continental shelf when cold westerly winds begin to blow from the continent in association with the wintertime East Asian Monsoon. Sea ice exhibits the maximum extent in late February or early March and melts in June (https://www.data.jma.go.jp/kaiyou/db/seaice/okhotsk/okhotsk_annual.html). Normally, sea ice covers the western part of the Sea of Okhotsk, where the East Sakhalin Current flows southward, whereas the sea surface is open in the eastern part (Fig. 3.3) because of the warm and saline water inflow from the North Pacific Ocean that is advected by the WKC. Large interannual to decadal variations, as well as long-term trends, have been observed in the maximum sea ice extent (MSIE), which is defined by the sea ice area averaged from February to March (Nakanowatari et al. 2010).

The sea ice formation and the consequent brine rejection results in the production of dense shelf water (DSW), which is generally characterized by cold (−1 °C) and oxygen-rich water mass with a potential density larger than 26.8σ_θ over the northwestern shelf region (Shcherbina et al. 2003, 2004a, b).[1] The largest amount of ice production occurs over the northwestern and northern shelves in the Okhotsk Sea, where ice production exceeds 10 m during winter (Nihashi et al. 2009). The DSW formation drives overturning circulation by ventilating the surface water, which originates in the North Pacific, to the intermediate layer as deep as 300–500 m (Gladyshev et al. 2000; Itoh et al. 2003; Uehara et al. 2012; Vigan et al. 2019). The intermediate-layer water flows along the coast of Sakhalin Island and is mixed with the ambient water from the Pacific Ocean and Japan Sea to form the Okhotsk Sea Intermediate Water (OSIW) (Itoh et al. 2003) or Okhotsk Sea Mode Water (Yasuda 1997), which has a core density of 26.8σ_θ. The OSIW finally flows out from the Kuril straits to the Oyashio region and spreads to the basin area as a major source water for North Pacific Intermediate Water heavier than 26.8σ_θ (You et al. 2000). The DSW salinity is an important parameter used to measure the strength of the overturning circulation (Matsuda et al. 2015). The DSW salinity varies as a result of sea ice formation fluctuations (Martin et al. 1998; Ohshima et al. 2014; Kashiwase et al. 2014), as well as sea surface salinity anomalies advected by the coastal current from the North Pacific Ocean (Nakamura et al. 2006a, b; Matsuda et al. 2009; Uehara et al. 2014). Freshwater input from rivers and precipitation may also be important for DSW salinity (Nakamura et al. 2006a, b; Uehara et al. 2014). Recently, the intermediate layer is substantially warming (Nakanowatari et al. 2007), which is likely caused by weakened DSW ventilation (Nakanowatari et al. 2007; Kashiwase et al. 2014; Ohshima et al. 2014; Uehara et al. 2014; Nakanowatari et al. 2015a).

[1] In Sect. 3.3, DSW is defined as water colder than −1.5 °C that is located below a depth of 100 m and is detected at each observed profile over the northern shelves in the Sea of Okhotsk (Uehara et al. 2012, 2014). Density range is typically 26.8–26.9σ_θ with this definition.

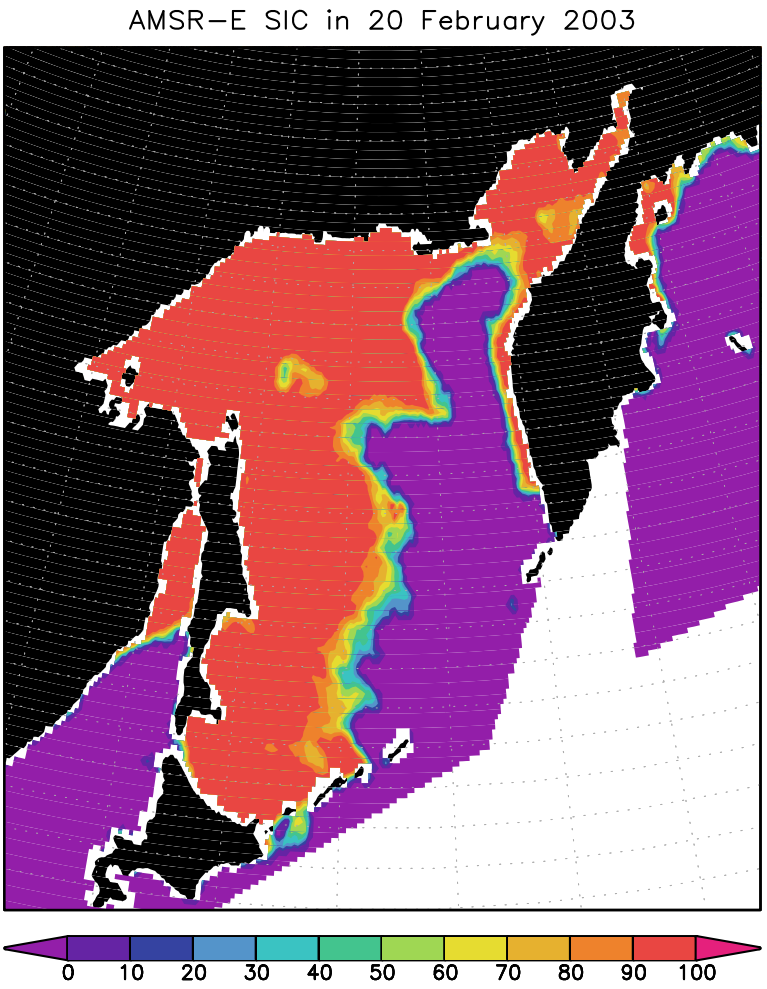

Fig. 3.3 Spatial distribution of daily mean sea ice concentration (%) of AMSR-E on 20 February 2003

Tides cause strong diapycnal mixing along the Kuril Islands and straits because of strong tidal currents interacting with ridged bottom topography (e.g., St. Laurent et al. 2002; Yagi et al. 2014 and reference therein). Vertical diffusivity along the Kuril Islands is estimated to be 10–100 $\times$ 10^{-4} m^2 s^{-1}, which is 2–3 orders of magnitude larger than the background diffusivity (~0.1 $\times$ 10^{-4} m^2 s^{-1}) in the ocean interior far from the ridged topography. Surface water is mixed with the intermediate layer up to 27.4σ_θ in the Kuril Straits (Yamamoto-Kawai et al. 2004; Uchimoto et al. 2014). This mixing brings saline and nutrient-rich water from the intermediate layer to the surface layer, implying that the mixing is important for the overturning circulation (Nakamura et al. 2006a, b; Matsuda et al. 2009; Kawasaki and Hasumi 2010) and

material circulations (Nishioka et al. 2011) in the Sea of Okhotsk and western North Pacific. Modulation of tidal mixing occurs in association with the lunar nodal tide with a period of 18.6 years (Yasuda et al. 2006; Osafune and Yasuda 2006). The 18.6-year modulation is expected to be stronger for diurnal tides (e.g., the K_1 is modulated by $\pm 14\%$ and the O_1 by $\pm 18\%$) than semidiurnal tides (e.g., the M_2 is modulated by $\pm 4\%$ and the S_2 by 0%) (Ray 2006). Bidecadal variations are observed in various nutrients and materials in the Oyashio and North Pacific Ocean (Ono et al. 2001; Watanabe et al. 2003), which may be attributed to the 18.6-year period nodal tide cycle.

In this chapter, we first describe variations in sea ice and SST and their interactions in Sect. 3.2. Long-term variations in the DSW and overturning circulation will be discussed in Sect. 3.3. In Sect. 3.4 the coherent sea level variations along the coast of the Sea of Okhotsk are described, and these variations may be related to variability in the warm and saline inflow from the North Pacific. The effects of the 18.6-year period nodal tide will be discussed in Sect. 3.5.

3.2 Sea Ice and SST

Accompanied by the extreme decrease in Arctic sea ice extent during summer over the last decades, surface air temperature warming has also been amplified during winter with a maximum of approximately 2.0 °C for the past 50 years over the Eurasian continent (Serreze and Barry 2011). Since the sea ice and water mass formations in the Sea of Okhotsk are controlled by the severe northwesterly winds blowing from the Eurasian continent in winter (Martin et al. 1998, Ohshima et al. 2003, Nihashi et al. 2009), it is likely that the sea ice and ocean environment are strongly influenced by polar amplification. From the beginning of satellite observations using Special Sensor Microwave Imager (SSM/I), the sea ice cover area in the winter season shows a decreasing trend ($-8.7 \pm 2.5\%$ per decade) from 1979 to 2010 (Cavalieri and Parkinson 2012), which is the second largest fraction behind the Barents and Kare Seas ($-9.2 \pm 1.6\%$ per decade) in the Arctic sea ice area. Since the sea ice cover has an insulation role in the heat exchange that occurs between the ocean and atmosphere (e.g., Inoue et al. 2003), the decrease in the sea ice cover in the Sea of Okhotsk changes the heat flux distribution and could affect the winter climate in the downstream region through large-scale atmospheric fluctuations (Honda et al. 1999, Screen 2017).

The mechanism of interannual variability in the sea ice area of the Okhotsk Sea has been investigated in terms of its relationship to large-scale atmospheric conditions (Cavalieri and Parkinson 1987; Parkinson 1990; Tachibana et al. 1996; Yamazaki 2000; Ogi and Tachibana 2006; Sasaki et al. 2007). In the mid-winter stage, when the Aleutian low is strengthened, the northwesterly wind and ESC have a main role in the southward transport of sea ice. Kimura and Wakatsuchi (1999) showed that the extent of wintertime sea ice is well explained by the free drift theory (2% of the geostrophic wind speed). On the other hand, during the onset stage, sea ice formation

is well determined by the local heat flux of the preceding autumn (Ohshima et al. 2006). A Singular Value Decomposition analysis between the sea ice concentration and atmospheric variables related to sea ice formation showed that the autumn atmospheric cooling influence affects the sea ice extent in late winter as atmospheric preconditioning (Sasaki et al. 2007) (Fig. 3.4). The predicted sea ice extent during February-March from the air temperature at 850 hPa in East Eurasia (52.5°N, 135°E), which is the most sensitive to sea ice variability, is highly correlated with the observed data (r = 0.67) (Fig. 3.5).

The ocean heat flux originates from the East Kamchatka Current (EKC) is also the major determinant factor for the interannual variability in the sea ice cover in late winter because the southeastern part of the Okhotsk Sea is not covered by sea ice in every winter (Fig. 3.3). Nakanowatari et al. (2010) statistically examined the ocean temperature variability in and around the Sea of Okhotsk and found that the MSIE,

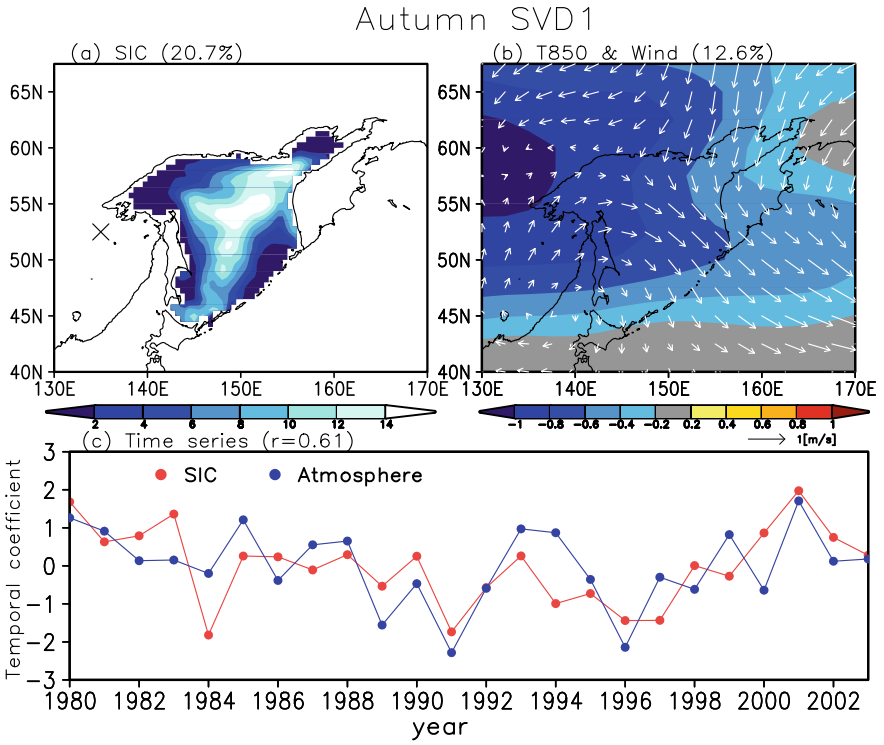

Fig. 3.4 First SVD mode between sea ice concentrations (SICs) in February–March from 1980 to 2003 and four-month leading atmospheric anomalies combined with zonal and meridional wind speeds at 1000-hPa and T850 in October-November from 1979 to 2002. Regression maps for **a** SIC and **b** 1000-hPa wind speed (arrows) and (b) T850 (contours) with the time series of atmospheric anomalies and SICs of SVD1, respectively. **c** Time series of SICs and SVD1 atmospheric anomalies (after Sasaki et al. 2007, modified). In panel a, the location of East Eurasia is indicated by a cross symbol

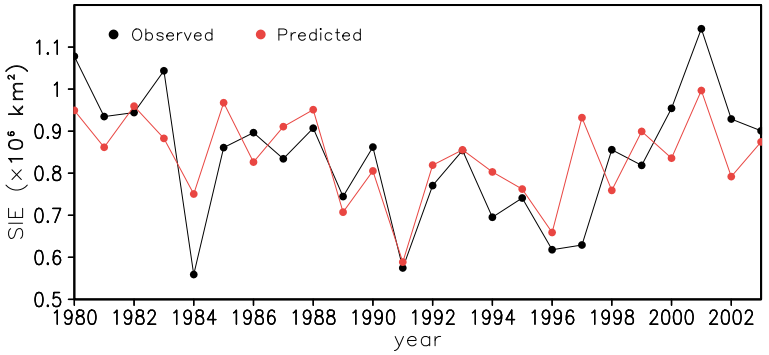

Fig. 3.5 Time series of the observed February–March mean sea ice extent in the Okhotsk Sea (black line) and predicted sea ice extent (red line) using the regression model of air temperature at 850 hPa (T) at 52.5°N, 135°E (shown in Fig. 3.4a) in October-November (Y = 9.47 − 6.90 T) (after Sasaki et al. 2007, modified)

which is the sea ice area from February to March, is significantly correlated with the sea surface temperature in the EKC during the preceding autumn (November-December) (Fig. 3.6). The lag correlation analysis between the MSIE and SSTs in the EKC region (rectangular box shown in Fig. 3.6) shows that the negative correlation between these factors becomes the highest (r = −0.72) when the SSTs lead the MSIE by 2–3 months. The SST and upper ocean temperature anomalies in the EKC

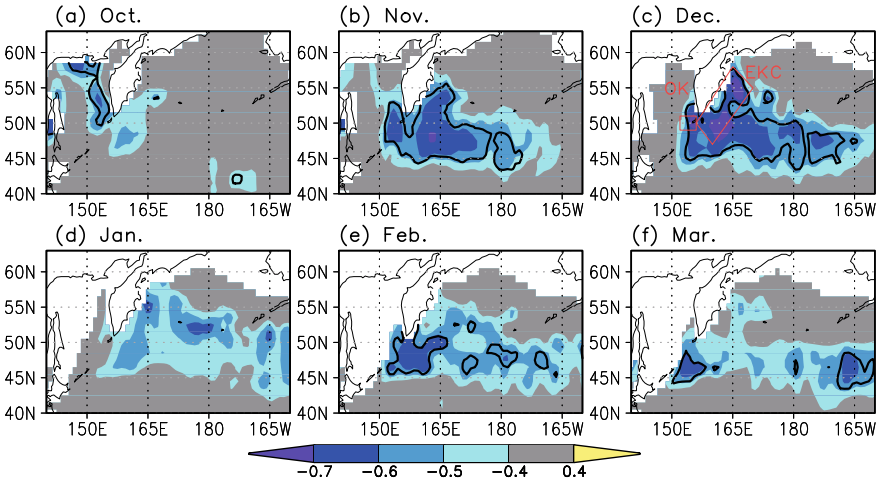

Fig. 3.6 Lag correlations (colored) between the MSIE and SST in the preceding October–March from 1980 to 2006. The SST data are derived from the Hadley Center sea Ice and Sea Surface Temperature data set version 1 (HadISST) (Rayner et al. 2003). Thick contours indicate areas where the correlation exceeds the 99% confidence level, estimated by a Monte Carlo simulation (after Nakanowatari et al. 2010, modified)

show that the ocean heat condition in the mixed layer is a good indicator of the MSIE anomalies on an interannual timescale. For example, the minimum value of the ocean temperature anomaly in November-December 2000 is consistent with the largest MSIE anomaly in 2001 (Fig. 3.7a).

Since the HadISST data are relatively low resolution (1°), the signal of ocean heat advection is obscure in the southeastern part of the Okhotsk Sea in January (Fig. 3.6d). However, the influence of the EKC on the ocean heat condition in the Sea of Okhotsk is supported by high-resolution (0.25°) satellite-based SST data (Reynolds et al. 2007). In January, the SST time series in the southeastern part of the Okhotsk Sea, which corresponds to the pathway of the EKC inflow water, is highly correlated with the MSIE ($r = -0.49$, significant at the 95% confidence level) (Fig. 3.7b). The high correlation relationship between SST and MSIE is also obtained in February ($r = -0.57$), which is higher than that in January. Thus, the ocean temperature anomaly in the EKC does not disappear after autumn and persists until late winter within the Sea of Okhotsk.

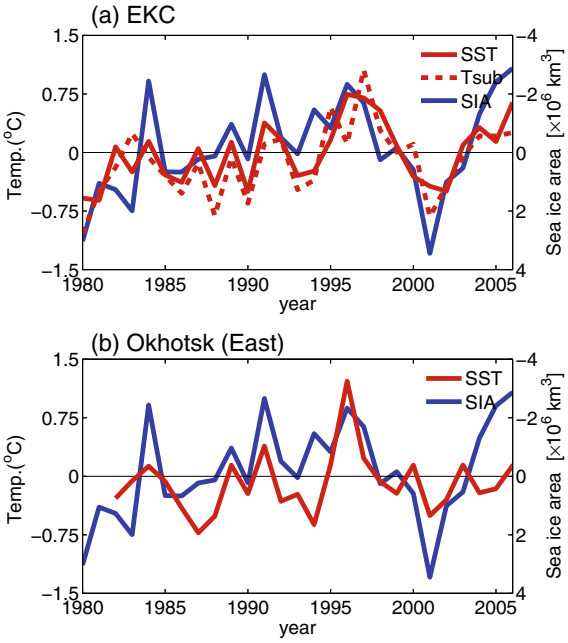

Fig. 3.7 **a** Time series of HadISST anomalies (solid red), ocean temperature anomalies at 20 m depth (broken red) averaged in the EKC region (rectangular box in Fig. 3.6c) in November–December and the MSIE anomalies (blue). The time series of SST and ocean temperature anomalies are shifted by 1 year (preceding year). The scale of the MSIE anomalies is indicated on the right axis and is inverted. The ocean temperature data were derived from in situ oceanographic observations from the World Ocean Database 2005. **b** Time series of the satellite-based SST anomalies averaged in the southeastern part of the Okhotsk Sea (rectangular box in Fig. 3.6c) in January (solid red) and the MSIE anomalies (blue) (after Nakanowatari et al. 2010, modified)

Although there are no direct measurements of inflow water from the Pacific, the dynamic topography of the surface layer (Nakanowatari et al. 2010), seasonal change in sea surface height (Nakanowatari and Ohshima 2014), and earlier surface drifter data (Ohshima et al. 2010) support the idea that the EKC inflow from the Pacific Ocean is strengthened during the winter season and influences the sea ice advance in the eastern part of the Okhotsk Sea. The EKC has an average surface velocity of 20 to 40 cm/s in December-February based on satellite tracked drifting buoy data (Stabeno et al. 1994). Since the ocean temperature anomaly in the EKC can be advected to the Sea of Okhotsk in a month or two at this current speed, the EKC water in the northern part of the Kuril Strait must be transported by the WKC to the northeastern part of the Okhotsk Sea in a month or two to explain the 3-month time lag between the MSIE and EKC-SST. The surface current data of the recent model simulation based on the eddy-resolving (2–10 km grid) OGCM of the North Pacific (Matsuda et al. 2015) also supports that such a surface current of 10 cm/s (WKC) exists along the western side of the Kamchatka Peninsula in winter (Fig. 3.2).

The lead-lag relationship between MSIE and SST in the EKC has the benefit of the long-term prediction of MSIE in the Sea of Okhotsk. Nakanowatari et al. (2010) explored the predictability of MSIE with the SST data in the EKC during the preceding November-December using an empirical method. In this analysis, the air temperature at 850 hPa over East Eurasia in the preceding October-November (T850) is also adopted as the predictor of the MSIE because this meteorological variable is known to be a good indicator of autumn atmospheric preconditioning in the Sea of Okhotsk (Sasaki et al. 2007). The wintertime atmospheric index is defined by the NW-SE component of the geostrophic wind (V_g) over the Sea of Okhotsk (50°N–60°N, 145°E–165°E) in December-February, following Kimura and Wakatsuchi (1999). The correlation relationships among the MSIE, SST in the EKC region (T-EKC) in the preceding November-December, T850, and V_g are summarized in Table 3.1. The correlation of the T850 with the MSIE is −0.71 (significant at the 95% confidence level), which is consistent with the findings of Sasaki et al. (2007). This high correlation is comparable to that between the MSIE and the T-EKC (−0.72). These two factors seem to be somewhat related to each other but not strongly (the correlation is 0.46). V_g is positively correlated with the MSIE ($r = 0.41$), but the correlation is much smaller than those of T-EKC and T850.

Table 3.1 Correlations among the MSIE, SST, T850, and Vg during 1980–2006[a]

	MSIE	EKC-SST	T850	Vg
MSIE	–	−0.72	−0.71	0.41
EKC-SST	–	–	0.46	0.14
T850	–	–	–	0.39

[a]SST, T850, and Vg are defined by the sea surface temperature averaged over the EKC region in the preceding November–December; air temperature at 850 hPa in the preceding October–November at 52.5°N, 135°E; and the offshore component of the wintertime geostrophic wind (December-February) over the Sea of Okhotsk (50°–60°N, 145°E–165°E), respectively. Bold numbers indicate the correlations exceeding the 95% confidence level based on a Monte Carlo simulation

If the autumn atmospheric preconditioning (T850) and ocean thermal conditions in the EKC (T-EKC) are adopted for the multiple linear regression model of the MSIE from 1980 to 2006, we obtain the following equation:

$$MSIE(t) = -0.20T\text{-}EKC(t-1) - 0.05T850(t-1) + 1.08 \qquad (3.1)$$

The correlation between the predicted and observed MSIEs becomes 0.84 (71% of the total variance in the MSIE is explained by the two variables), which is 20% higher than the value of 0.71 (50% of the total variance) from the prediction that uses only T850. Based on the prediction scheme constructed during 1980–2006, the recent MSIE is diagnostically predicted using T-EKC and T850 data from 2007 to 2018 (Fig. 3.8). During the first several years, the predicted MSIE is comparable to the observed value (e.g., 2010). However, in the latter half of these years, the predicted MSIE fails to follow the observed value (e.g., 2017 and 2018). This result is partly related to the weak contribution of T850 in this prediction scheme because the correlation between the observed MSIE and T850 during the entire period (from 1980 to 2018) becomes worse ($r = -0.40$) compared to the value ($r = -0.71$) from 1980 to 2006. On the other hand, the correlation between the observed MSIE and T-EKC during the whole period is -0.63, which is still significant at the 95% confidence level. When the MSIE is predicted based on the prediction scheme of T-EKC, the predicted MSIE is improved and close to the low level of the observed MSIE (Fig. 3.8). Thus, during 2011–2018, the decrease in the MSIE may be related to the

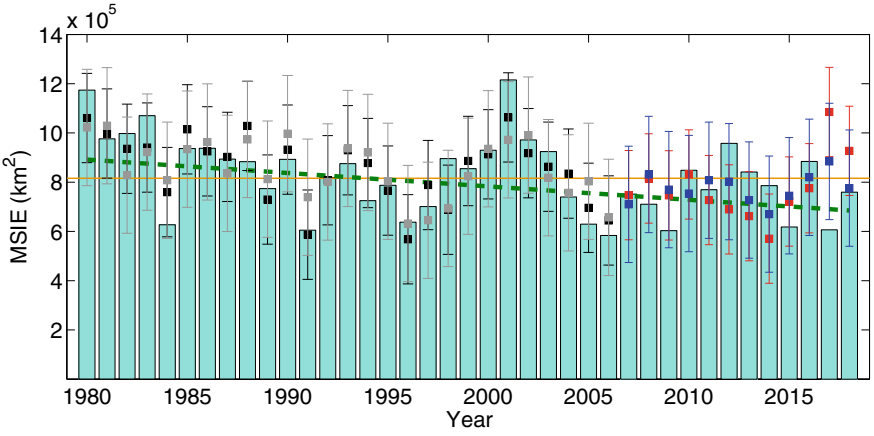

Fig. 3.8 **a** Time series of the observed MSIE (sea ice area averaged from February to March) (magenta bars) and predicted MSIE by the multiple linear regression model using T850 and the EKC-SST (black squares) from 1980 to 2006. The MSIE predicted by the regression models of both T850 and EKC-SST (red) is plotted from 2007 to 2018. Gray and blue squares indicate the predicted MSIE based on only EKC-SST data. Error bars indicate the 95% confidence interval of the RMSE. The climatological value of MSIE is shown in the yellow solid line. The green dashed line indicates the linear regression line of the observed MSIE during 1980–2018 (after Nakanowatari et al. 2010, modified)

ocean temperature warming in the EKC region. However, even this prediction scheme could not precisely predict the extreme minimum value in 2017. Since the change in the ocean current speed is not considered in this prediction scheme, this assumption may not be appropriate during 2011–2018 because the Aleutian low strength, which is closely related to the Pacific inflow water (Ohshima et al. 2010; Nakanowatari and Ohshima 2014), has gradually decreased during early winter (Nakanowatari et al. 2015a). Furthermore, the weakening of the Aleutian low also leads to modulation of the storm track pathway (Rodionov et al. 2007), which may result in the migration of cyclones into the Sea of Okhotsk and retreat of the sea ice area by the southeasterly wind. In fact, multiple synoptic-scale cyclones that formed along the southern Japan coast migrated into the Sea of Okhotsk in January-February 2017. During this season, the autumn atmospheric preconditioning was favorable for the advance of sea ice area (T850 in the preceding autumn shows the minimum temperature (−14.6 °C)), but the MSIE was below normal (Fig. 3.8). Thus, there is a large uncertainty in the future projection of sea ice areas in the Sea of Okhotsk under the drastically changing climate.

3.3 Long-Term Trends and Variations in Dense Shelf Water and Intermediate-Layer Water

The signal of long-term climate change is obvious in the intermediate water mass properties in the Sea of Okhotsk. According to the analysis of the historical hydrographic observations archived in the World Ocean Database 2001 and additional data obtained under the Japan-Russia-United States international collaborative study since the late 1990s and 2000s in the Sea of Okhotsk, the water temperature at 26.8–27.2σ_θ (300–700 m depth) has significantly increased during the past 50 years (1955–2004), with a maximum value of 0.62 ± 0.18 °C at 27.0σ_θ (Fig. 3.9a). The warming trend is remarkable along the ESC, which is the western boundary current of the Okhotsk Sea, and spreads to the western subarctic region (Fig. 3.10a). In this water mass, the dissolved oxygen has also significantly decreased by −0.58 ± 0.35 ml/l over the past 45 years (1960–2004) (Fig. 3.9b). Most of the changes in the dissolved oxygen are explained by the apparent oxygen utilization, and thus, the changes in saturation rate due to the water temperature changes have minor effects. Since the intermediate water temperature in the Sea of Okhotsk is maintained by the supply of cold and oxygen-rich DSW formed over the northwestern shelf region (Fig. 3.10b, c), the trend signals of these hydrographic data imply that the ventilation of the North Pacific Intermediate Water, which originates from the Sea of Okhotsk, has decreased. Since the updated analysis of the dissolved oxygen data through 2015 shows that the dissolved oxygen has significantly decreased around the Sea of Okhotsk, it is expected that the weakening of the ventilation in the Okhotsk Sea has continued (Ito et al. 2017).

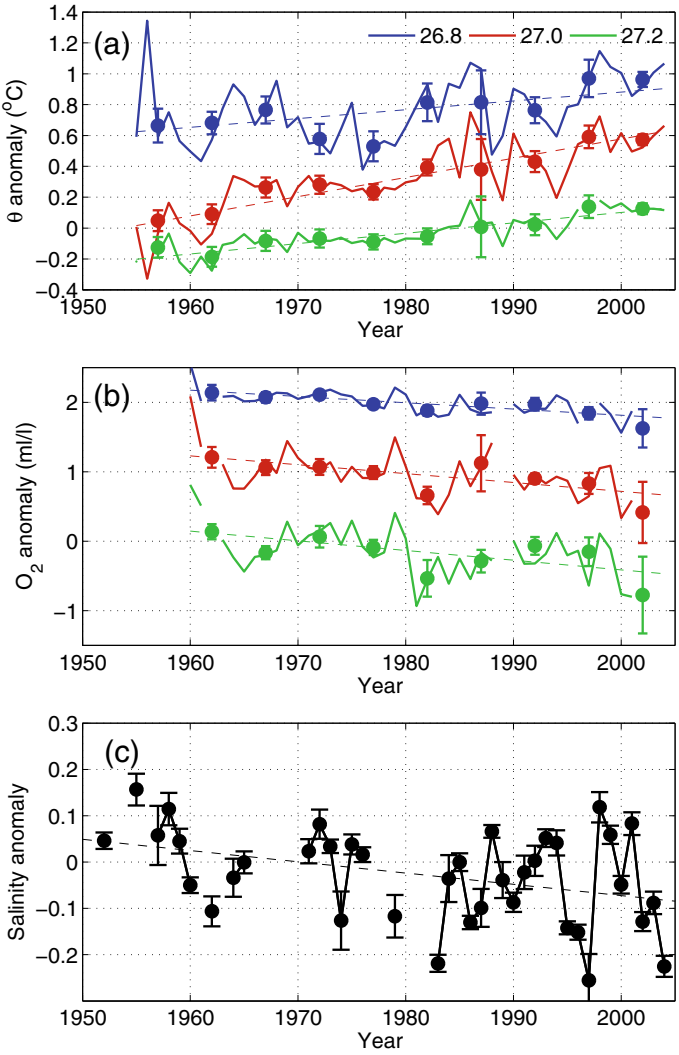

Fig. 3.9 Time series of **a** annual mean potential temperature (°C) and **b** dissolved oxygen (ml/l) anomalies at 26.8, 27.0, and 27.2σ_θ averaged over the Sea of Okhotsk from 1955 to 2004 (for dissolved oxygen, the data are plotted since 1960). Closed circles show the 5-yr averaged anomalies with errors at the 95% confidence interval for the 5-yr averages (after Nakanowatari et al. 2007, modified). **c** Time series of the annual mean salinity anomaly of DSW from 1950 to 2005. The standard errors are shown in each plot, and the years in which the data are less than 5 points are ignored (after Uehara et al. 2014, modified). The linear regression line for each time series is indicated by a dashed line

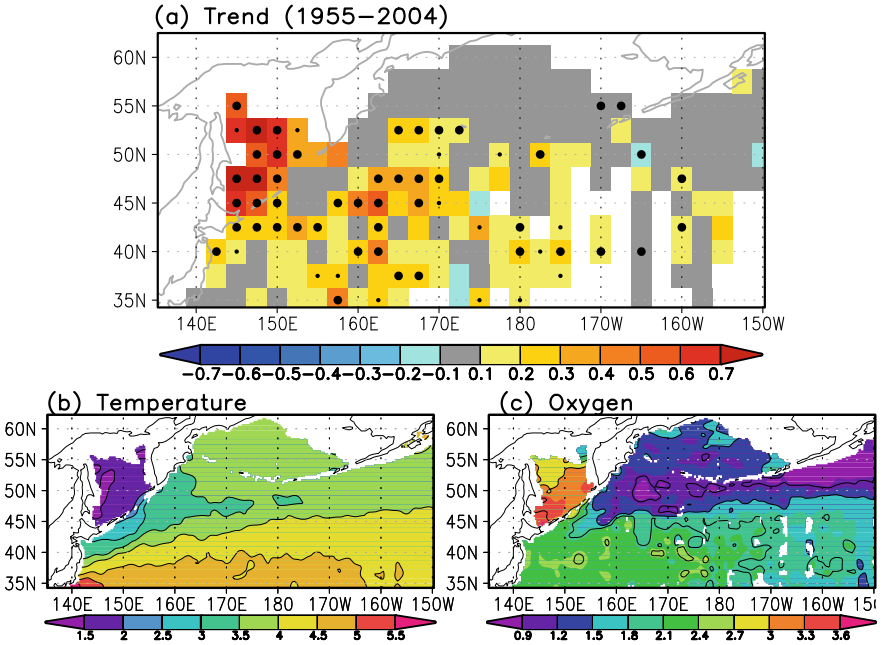

Fig. 3.10 **a** Linear trends (colors in °C/50-yr) of potential temperature anomalies at 27.0σ_θ from 1955 to 2004. Large and small dots indicate grid boxes in which the linear trend is significant at the 95% and 90% confidence levels, respectively. White color indicates the grid boxes in which annual temperature anomalies are not available for more than 10 years throughout the analyzed period (after Nakanowatari et al. 2007, modified). Climatologies of **b** potential temperature (°C) and **c** dissolved oxygen at 27.0σ_θ

Direct evidence of the long-term changes in DSW formation was shown by Uehara et al. (2014). They examined the extensive hydrographic database in the Sea of Okhotsk compiled by the Far Eastern Regional Hydrometeorological Research Institute (FERHRI), including all available hydrographic data. In their study, the DSW was detected as a water mass colder than −1.5 °C at depths deeper than 100 m over the northwestern shelf, where the density is 26.8–26.9σ_θ, which is nearly the core density of DSW. The temporal variation in the DSW volume was evaluated as the salinity value (Uehara et al. 2012). It was found that the DSW salinity produced in winter has significantly decreased by -0.12 ± 0.08 during the last 50 years (1950–2005) (Fig. 3.9c). Since the water properties of the DSW are quite sensitive to the salinity value because the temperature is near the freezing point (−1.8 °C) under sea ice production, the salinity reduction in the DSW indicates a decrease in the DSW volume at heavier density. This result is consistent with the highest warming of water temperature being found in the heavier density range of 27.0σ_θ rather than the core density (26.8σ_θ) of the Okhotsk Sea Intermediate Water (OSIW) (Nakanowatari et al. 2007).

Based on the hydrographic dataset of the Sea of Okhotsk from 1930 to 2009 derived from the World Ocean Database 2001 and additional hydrographic observation data and profiling float data from the latter period, the volume change in OSIW at 26.8, 26.9, 27.0, and 27.1σ_θ is estimated to be +14.0, −2.4, −7.4, and −2.2 × 10^3 km^3, respectively, which accounts for +16, −3, −11, and −4% of the climatological value, respectively (Ohshima et al. 2014). Assuming that OSIW is formed by the isopycnal mixing of DSW and the North Pacific water and assuming that the volume of the North Pacific water is steady, it is suggested that the mixing ratio of OSIW at 26.9–27.0σ_θ is shifted to warm and saline water properties due to the decrease in heavier DSW input. Thus, the warming signal of OSIW at a heavier density surface can be interpreted by the change in the mixing ratio of DSW and North Pacific water.

Another possible mechanism of the warming signal at an isopycnal surface is the apparent effects due to water column freshening, which is likely to have a primary role in lighter density (e.g., 26.8σ_θ) because the warming signal at this density cannot be explained by the mixing ratio change. DSW density varies solely by salinity changes because it is produced at freezing temperature, ~ −1.8 °C. Therefore, ventilation of freshened DSW causes pure freshening of the pycnocline water (according to a definition of Bindoff and McDougall 1994) below the winter mixed-layer base at a depth of ~100 m. This results in warming on isopycnal surfaces in the OSIW pycnocline. More specifically, let us look at the relationship between OSIW freshening and warming at a depth of 300 m, where the potential density of the water is approximately 26.8σ_θ (Fig. 3.11). The water exhibits freshening at a depth of 300 m from 1955 to 1977 and from 1978 to 2014. Then, the warming occurs along the isopycnal surface 26.8σ_θ, since the T-S relationship changes from the blue curve to

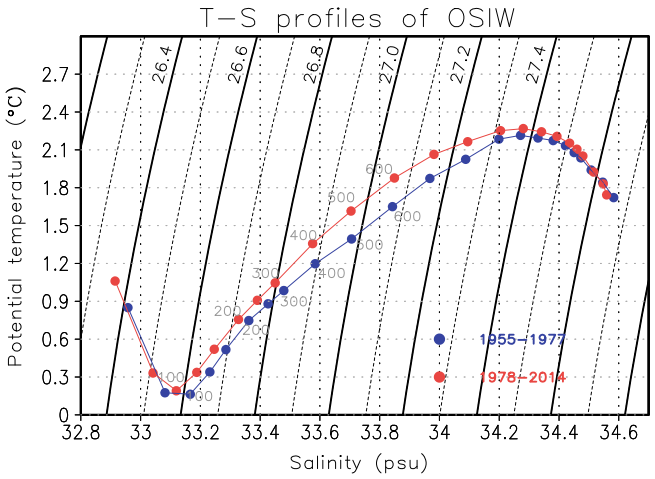

Fig. 3.11 The observed T-S curve averaged over the Sea of Okhotsk from 50 to 2500 m depth. The blue and red circles denote the past (1955–1976) and present (1977–2004) mean values (after Nakanowatari et al. 2015b, modified). The depth information from the sub-surface to intermediate depth (100–600 m) is shown

the red curve shown in Fig. 3.11 (also see Ohshima et al. 2014; Nakanowatari et al. 2015b).

Decadal-scale variability has recently been discovered within the OSIW temperature in the Okhotsk Sea (Osafune and Yasuda 2006; Ohshima et al. 2010; Uehara et al. 2014). Such a decadal-scale variability is also found in biogeochemical variables such as AOU in the Kuril Basin and western subarctic gyre (Andreev and Kusakabe 2001) and phosphate concentration in adjacent regions (Ono et al. 2001). These observational studies speculated that the decadal fluctuations in the area are related to the strength of the Aleutian lows through the change in the ventilation and/or exchange between the Sea of Okhotsk and North Pacific. The hypothesis that the water exchange is regulated by the strength of the Aleutian low is supported by the profiling float and satellite altimeter data (Ohshima et al. 2010). Furthermore, Uehara et al. (2014) found that the decadal variability in the DSW salinity is significantly correlated with the salinity anomalies propagating from the Bering Sea and even from the subarctic North Pacific (Fig. 3.12), which we will discuss later in this section. They also found that the DSW salinity is negatively correlated with decadal variations in the OSIW temperature at $27.0\sigma_\theta$, implying that the surface salinity change also substantially influences the intermediate water property through the DSW formation and changes the overturning circulation. On the other hand, Osafune and Yasuda (2006) examined the influence of 18.6-yr tidal modification on the decadal fluctuation of the OSIW properties and found that the water mass property changes can be explained by the diapycnal mixing induced by the strong tides in the Kuril Strait.

The causes of the DSW reduction have been investigated from the standpoint of the thermohaline and wind-driven circulations, both of which are important for the overturning circulation (Matsuda et al. 2009; Nakanowatari et al. 2015a). In the following subsections, we discuss the effects of sea ice production and sea surface salinity on DSW reduction. We also discuss the cause and impacts of the DSW reduction by describing the numerical modeling results.

3.3.1 Sea Ice Production

DSW forms as a result of brine rejection when sea ice is produced. Sea ice production has been estimated using satellite microwave and infrared radiometers over coastal polynyas, combined with heat flux calculations (e.g., Ohshima et al. 2003; Nihashi et al. 2009). Kashiwase et al. (2014) retrieved the ice production over the northern continental shelves in the Sea of Okhotsk for 21 years using a thin ice algorithm derived from the Special Sensor Microwave/Imager (SSM/I), based on a comparison with high-resolution ice-thickness estimates from the Advanced Very High Resolution Radiometer (AVHRR) infrared images. They further examined the rate of change in the sea ice production rate over the northwestern shelf before the era of microwave satellite missions based on the observed meteorological variables utilizing a multiple regression coefficient analysis. The reconstructed ice production

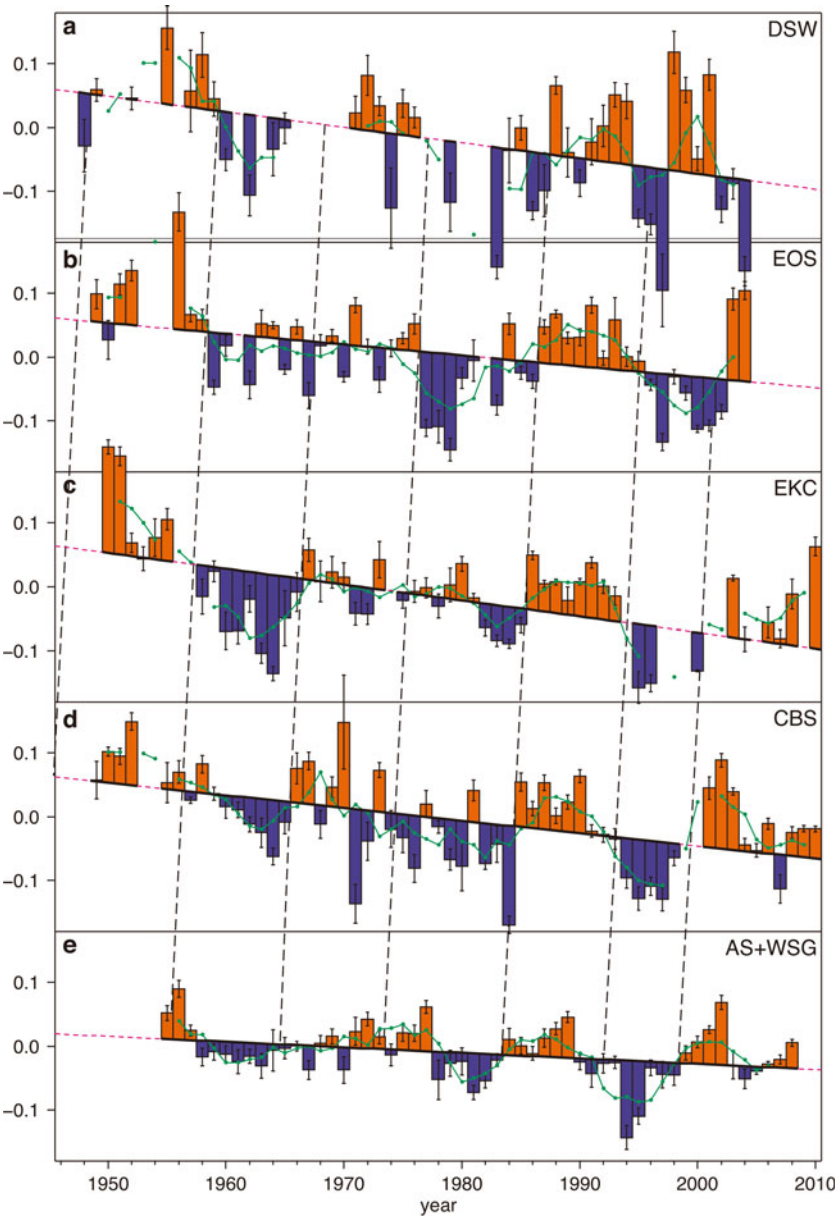

Fig. 3.12 **a** Time series of DSW salinity anomalies. **b**–**d** Time series of the upper layer salinity anomalies (averaged over depths of 0–100 m) in **b** eastern Okhotsk Sea (EOS), **c** EKC, and **d** central Bering Sea (CBS). (e) Regressed time series of the upper layer salinity anomalies in the western Subarctic Gyre (WSG) and Alaskan Stream (AS) with respect to that in the CBS. Red and blue bars denote positive and negative deviations from the linear trend (magenta dashed line), respectively, with standard errors indicated (whiskers). Green lines and dots represent the time series low-pass filtered by 5-year running mean. Propagations of salinity anomalies are suggested by dashed lines (after Uehara et al. 2014, license No. 4563970987463 by Elsevier)

indicates an 11.4% decrease over the past 34 years (1974–2008). It was shown that air temperature warming has a large contribution to the decrease in sea ice production. They suggested that the ice production decrease causes OSIW warming. Interannual variations in ice production are also correlated with OSIW temperature variations, where the correlation coefficient is −0.57 at $27.0\sigma_\theta$. Furthermore, a composite map of potential temperature at $27.0\sigma_\theta$ during high ice-production years showed a cold anomaly pathway of DSW along the coast of Sakhalin.

3.3.2 Sea Surface Salinity

The salinity of the DSW is a key factor that determines the ventilation strength of the overturn. The DSW is produced when water reaches freezing temperature (i.e., approximately −1.8 °C), so the density is determined solely by salinity. Upper ocean salinity decreases in recent decades influences the DSW salinity. Uehara et al. (2014) used a hydrographic dataset expanded with those of FERHRI after quality control of the historical data archives was performed, and these data include the World Ocean Database (WOD) and those of the Japan Oceanographic Data Center. The researchers showed evidence of a freshening trend in the DSW at a rate of -0.12 ± 0.08 for the past 50 years (1950–2005) as well as decadal salinity variations with a typical magnitude of ~0.1 over the northwestern Okhotsk Sea (Fig. 3.9c). The DSW's trend is comparable to the surface freshening in the subpolar gyre, which has an average magnitude estimated at 0.10–0.12 psu over a 50-year period (Durack and Wijffels 2010; Durack et al. 2012). Uehara et al. (2014) also found that decadal DSW variations are affected by salinity anomalies in the mixed layer (upper 100 m), and these anomalies propagate a long distance from the Bering Sea via the East Kamchatka Current and the eastern Okhotsk Sea (Fig. 3.12). It takes 2–3 years for the salinity anomaly to reach the northwestern shelf of the Sea of Okhotsk from the Bering Sea, which is consistent with the advective time scale across these regions (Matsuda et al. 2015). The decadal salinity anomalies may be traced farther upstream in the Alaskan Stream and the western subpolar gyre.

Local precipitation over the Sea of Okhotsk also exhibits a significant correlation with the variability in the DSW salinity (Uehara et al. 2014). Figure 3.13a presents the correlation and regression map of annual mean precipitation from the Climate Prediction Center (CPC) Merged Analysis of Precipitation (CMAP; Xie and Arkin 1997) with the DSW salinity time series (Fig. 3.9c), when the former leads the latter by 1 year. The area exhibiting a significant negative correlation is located over the northeastern part of the Sea of Okhotsk and the Kamchatka Peninsula. The variations in precipitation can account for changes of approximately 0.03 in the upper layer salinity, assuming that a freshwater flux of 10 mm month^{-1} affects the salinity of the mixed layer up to a depth of 100 m. They also examined other precipitation datasets and found similar results for the interannual variability (Fig. 3.13b–d). Therefore, local precipitation is likely influential in DSW salinity.

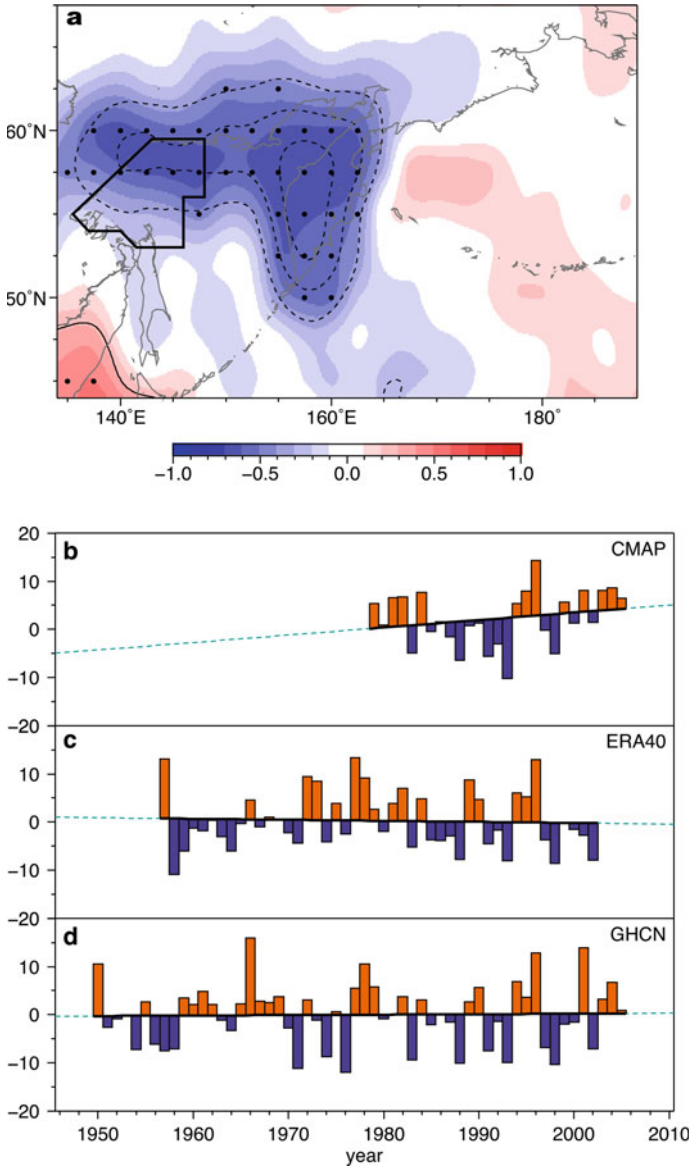

Fig. 3.13 **a** Map of the correlation (color shade) and regression (contours) coefficients between the time series of annual mean precipitation from CMAP and those of the DSW salinity anomalies in Fig. 3.9c. The former leads the latter by 1 year. The solid and dashed contours indicate positive and negative regression coefficients, respectively, and their intervals are 2 mm month^{-1}. The region with significant correlations ($p < 0.05$) is hatched. **b**–**d** The time series of the precipitation anomalies (mm month^{-1}) from **b** CMAP (Xie and Arkin 1997), **c** the European Centre for Medium-Range Weather Forecasts (Uppala et al. 2005; referred to as ERA40) and **d** the National Climatic Data Center (NCDC) Global Historical Climatology Network (GHCN) precipitation (Peterson and Vose 1997). The time series were constructed using the data in the region with significant correlations ($p < 0.05$) (after Uehara et al. 2014, license No. 4563970987463 by Elsevier)

3.3.3 Numerical Modeling Results

Nakanowatari et al. (2015a) performed a hindcast experiment from 1979 to 2008 using an ice-ocean coupled model forced with atmospheric reanalysis data and qualitatively simulated the observed warming trend of intermediate water temperature in and around the Sea of Okhotsk, which is characterized by significant warming along the ESC and subarctic frontal region (Fig. 3.14a). The time series of the annual mean of potential temperature anomalies in the OSIW showed a remarkable warming signal that began in the 1990s. The simulated warming trend seems to be overestimated compared to the observed time series (Fig. 3.14b), which is likely related to the excess cold anomaly in the 1980s. Because this period corresponds to the phase of strong tidal mixing due to the 18.6-yr nodal cycle (Yasuda et al. 2006; Osafune and Yasuda 2006), this overestimation may be related to the deficiency in the tidal mixing effect in this simulation.

According to the perturbed experiments on the atmospheric forcing, where the interannual variations in the atmospheric forcing were restricted to turbulent heat flux (HEAT), freshwater (precipitation minus evaporation) flux (WFLX), and wind stress (WSTR), the recent OSIW warming is mostly explained by the reduction in the DSW due to surface cooling weakening and precipitation excess (Fig. 3.15), which are consistent with the results of earlier observational studies (Kashiwase et al. 2014; Uehara et al. 2014). The simulated reduction rate of sea ice production is -0.63×10^{11} m^3/30 yr, which accounts for approximately 14% of the climatology of the annual sea ice production and is comparable to the observed estimation (Kashiwase et al. 2014). Additional sensitivity experiments on each component of the turbulent heat flux showed that the sea ice reduction is prominent in December (-21.7%) and March (-33.6%), as these components are sensitive to the air temperature change (i.e., warming signal) (Table 3.2). Therefore, the duration of sea ice production has been shortened rather than cooling rate weakening in January-February. The trend pattern of atmospheric circulation in March during 1980–2008 reveals significant weakening in the Aleutian low and Siberian high and thus weakening of the wintertime monsoon in Far East Asia (Fig. 3.16). On the other hand, this period (1980–2008) also corresponds to the phase shift in the Pacific Decadal Oscillation from a positive to a negative phase in which the Aleutian low has weakened (Bond et al. 2003). Therefore, the internal climate variability inherent to the Earth climate system may also be related to wintertime monsoon weakening, which has led to the remarkable OSIW warming trend in recent decades.

In this simulation, the impact of the freshwater flux change on the OSIW warming trend should be carefully considered because the atmospheric reanalysis data have a large uncertainty in the interannual variability. However, recent observational evidence shows that significant freshening of surface water has occurred within the Sea of Okhotsk over the past several decades (Hill et al. 2003; Uehara et al. 2014; Ohshima et al. 2014). A multidecadal-scale decrease in sea surface salinity was also observed in the subarctic North Pacific, and water circulation enhancement is suggested under global warming (Hosoda et al. 2009; Durack and Wijffels 2010; Durack et al. 2012).

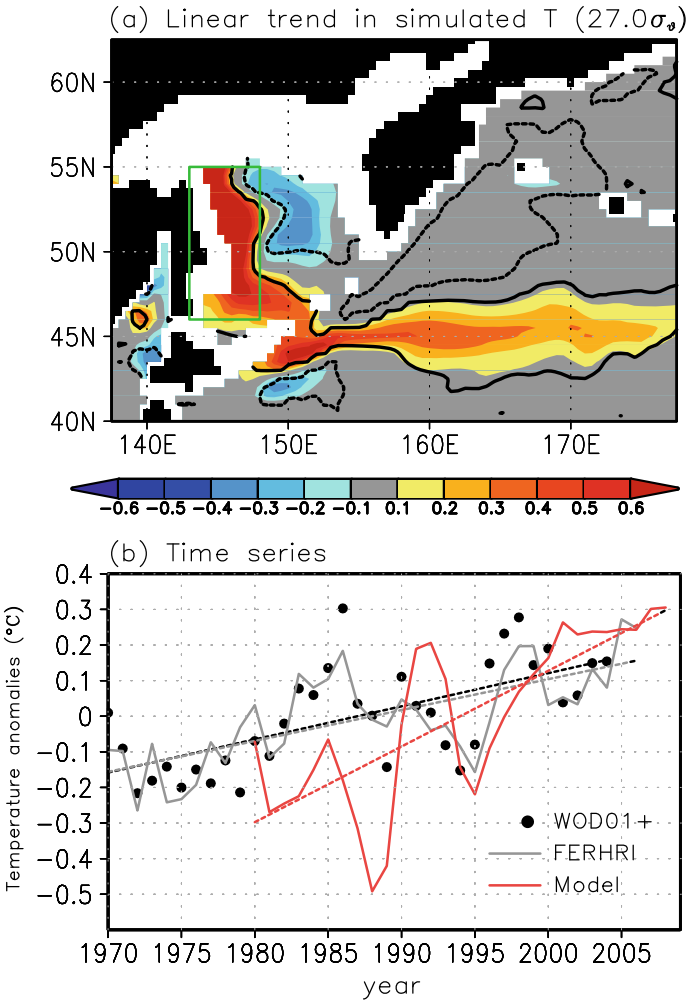

Fig. 3.14 **a** The spatial distribution of the linear trend (°C/30 years) in the annually averaged potential temperature at 27.0σ_θ in the hindcast experiment from 1980 to 2008. The white-colored regions represent water that is lighter than the corresponding density. The contour indicates the regions where the linear trend is significant at the 90% confidence level. The significance of the linear trend estimate is based on a Student's t distribution (after Nakanowatari et al. 2015a, modified). **b** Time series of the annual mean of OSIW potential temperature anomalies at 27.0σ_θ for the hindcast data (red line). The OSIW region for the hindcast data is defined by the green rectangular area in panel a. The time series of the observed potential temperature anomalies of OSIW derived from the World Ocean Database 2001, including additional intensive observations in the Sea of Okhotsk from 1998 to 2004 (closed circles) (Nakanowatari et al. 2007) and from the Far Eastern Regional Hydrometeorological Research Institute (FERHRI) databases (gray line) (Uehara et al. 2014), are also shown in panel b. Linear regressions of the annual time series are indicated by dashed lines (after Nakanowatari et al. 2015a, modified)

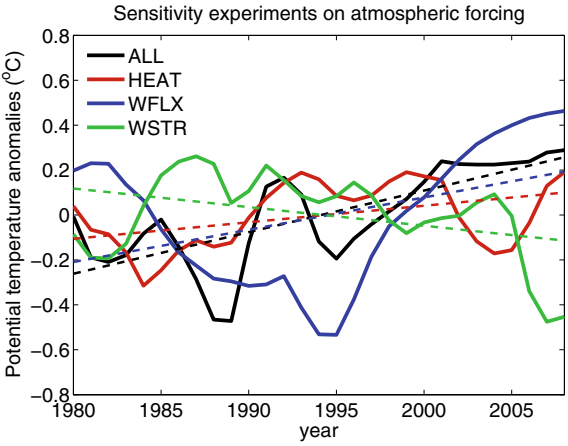

Fig. 3.15 Time series of the annual mean of potential temperature anomalies at $27.0\sigma_\theta$ over the western part of the Okhotsk Sea (shown in Fig. 3.14a), derived from the hindcast experiment (black) and perturbation experiments for turbulent heat flux (HEAT), fresh water flux (WFLX), and wind stress (WSTR). Linear regression for each time series is indicated by a dashed line (after Nakanowatari et al. 2015a, modified)

Table 3.2 Change rates (%) in the monthly means sea ice production from 1980 to 2008 ($\times 10^{11}$ m^3/30 years) relative to the climatological value in the sensitivity experiments on turbulent heat flux (HEAT), air temperature (HEAT-T), specific humidity (HEAT-Q), and wind speed (HEAT-W)

	HEAT	HEAT-T	HEAT-Q	HEAT-W
December	−21.7	−22.0	−7.3	6.3
January	−11.0	−11.5	−1.7	2.4
February	−4.3	−6.4	−0.7	3.1
March	−33.6	−32.8	−7.4	5.1

[a]HEAT-T, HEAT-Q, and HEAT-W are the abbreviations for the sensitivity experiments in the heat flux calculation where the interannual variations are restricted to air temperature, specific humidity, and scalar wind speed, respectively

The low-salinity water inflow from the North Pacific Ocean may also lead to surface freshening in the Sea of Okhotsk. Thus, although there are possible causes of surface freshening in the Sea of Okhotsk, the impact and principle mechanism have not yet been clarified. To determine the future state of the thermohaline circulation in the Sea of Okhotsk and its adjacent ocean, it is necessary to appropriately evaluate the long-term change in freshwater flux, including rainfall and river runoff, as well as to examine the degree of polar amplification in sea ice productivity.

3.4 Coherent Sea Level Variations in the Coastal Area

Because most of the sea surface in the Sea of Okhotsk is covered by sea ice during the winter season, the ocean current study based on satellite altimeter data is limited to the warm season (Ebuchi 2006) and southern part, which is not covered by sea ice even in winter (Uchimoto et al. 2008). According to these studies, the sea surface

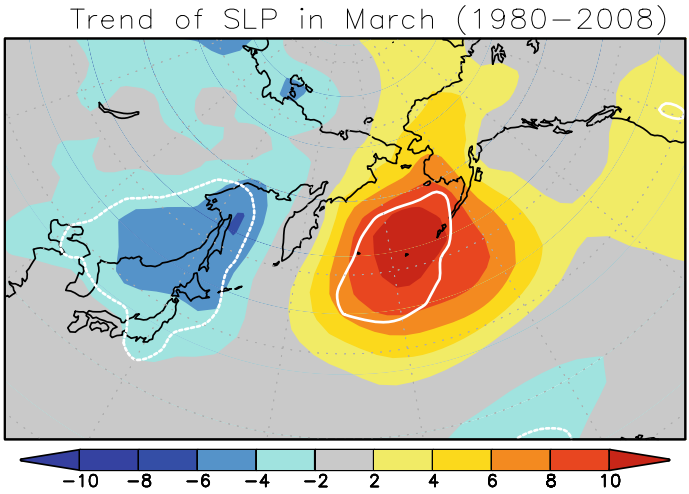

Fig. 3.16 Linear trends in sea level pressure (hPa/30 yrs) in March, as calculated from NCEP-NCAR reanalysis data from 1980 to 2008. Shading indicates regions where trends are significant at the 95% confidence level, based on the t-test (after Nakanowatari et al. 2015a, modified)

height in the Sea of Okhotsk is dominated by the seasonal variation related to wind-driven circulations, such as the ESC and the movement of mesoscale eddies, which are independent of the thermosteric height signal due to the annual cycle of shortwave radiation flux. The seasonal cycle of dynamic sea surface height change is also found in the point sea level data available from tide-gauge measurements. Itoh and Ohshima (2000) examined the tide-gauge data along the northern coast of Hokkaido Island and showed remarkable seasonal variations with a peak in winter and minimum in summer. Isoguchi et al. (1997) and Isoguchi and Kawamura (2006) showed that the coastal sea level rises in winter and lowers in summer in accordance with the strength of the EKC, which is based on tide gauge and satellite altimeter data.

By utilizing both tide-gauge observations provided by FERHRI and the Permanent Service for Mean Sea Level (PSMSL) and satellite altimeter data, Nakanowatari and Ohshima (2014) clearly showed that the sea level fluctuates coherently along the coastal region in and around the Sea of Okhotsk with a maximum in winter and minimum in summer, which cannot be explained by the annual cycle of thermosteric and pressure effects (Fig. 3.17a), except for some regions around the Soya Strait where seasonal variations in the Soya warm current are prominent with the maximum occurring in September (Fig. 3.17b). Based on the altimetry data, this seasonal cycle is dominant in and around the Sea of Okhotsk (Fig. 3.17a) and confined to the coastal area. The seasonal sea level variation has a large amplitude at the southern edge of Sakhalin Island with an amplitude of 20 to 30 cm. The spatiotemporal phases of the seasonal sea level variations along Sakhalin Island are explained by the dynamic response to the ocean current of the Arrested Topographic Waves (ATWs), which

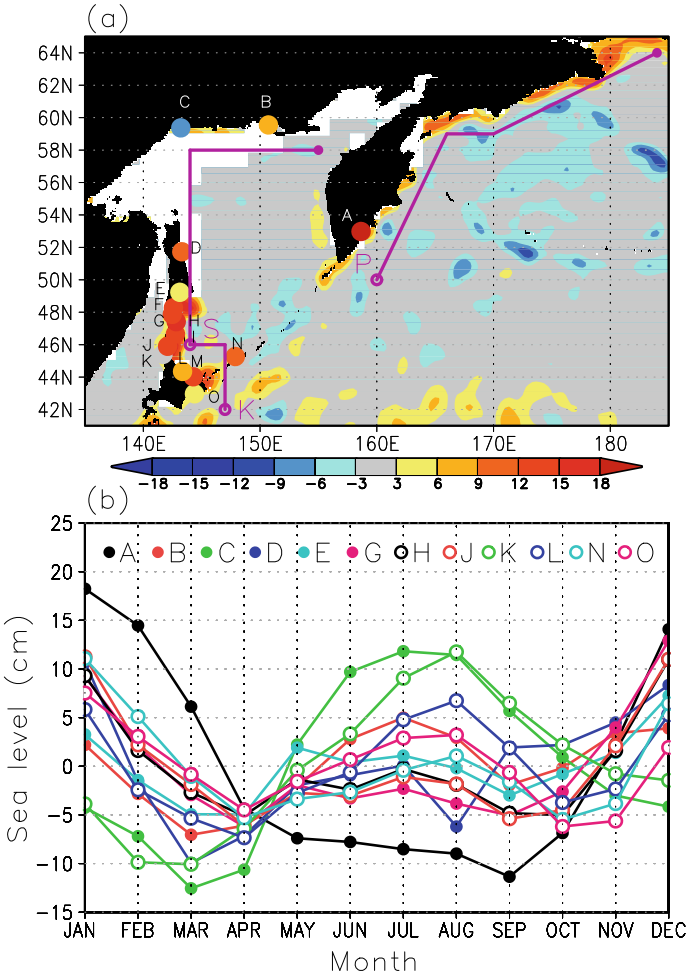

Fig. 3.17 **a** Climatological sea level difference (cm) between December and May for 15 tide gauge data (circles) during and satellite altimeter data (shaded). The integral routes for ATW calculation are shown by the purple line from the corresponding starting points (closed circles) to the target area labelled with S, P, and K, which indicates the Sakhalin, Petropavlovsk-Kamchatsky, and Kushiro stations, respectively. **b** Monthly mean climatology of sea level calculated from the tide gauge data (see panel a for the locations of the tide gauges) from which the thermosteric components related to surface heat flux and the inverse barometer effect caused by atmospheric pressure are removed (after Nakanowatari and Ohshima 2014, modified)

are calculated by the integration of alongshore wind stress from the upstream region (Csanady 1978).

$$V_{ATW} = \int_{l_1}^{l_2} \frac{\tau_l}{\rho f} dl, \tag{3.2}$$

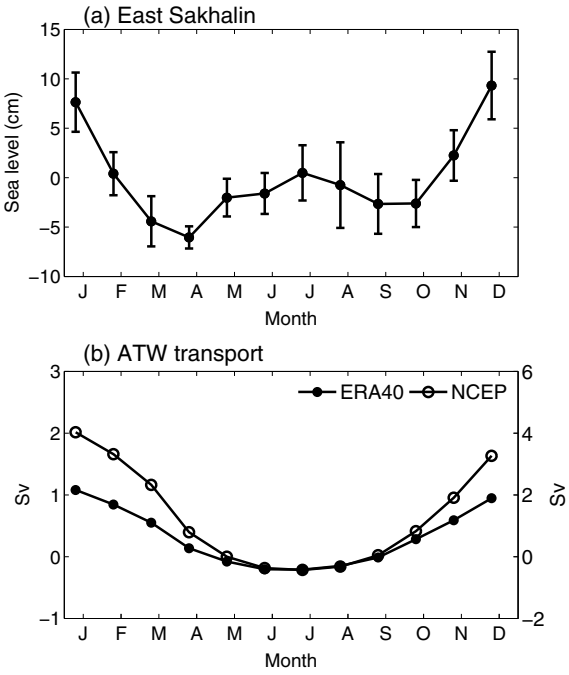

Fig. 3.18 **a** The monthly mean of the tide gauge sea level averaged along Sakhalin Island (D-J) and its standard deviation. **b** The monthly mean of the ATW transport integrated along Sakhalin Island from the northern shelf of the Okhotsk Sea (shown in Fig. 3.17a). In panel b, the closed and open circles indicate the ATW transports calculated from the ERA40 and NCEP-NCAR reanalysis data, respectively (after Nakanowatari and Ohshima 2014, modified)

where a right-handed coordinate system is used with the l axis along the coastline. τ_l is the alongshore component of the wind stress, ρ is the density of water, and f is the Coriolis parameter. The seasonal cycle of ATW transport for the integral route along Sakhalin Island and the northern part of the Okhotsk Sea (see Fig. 3.17a) based on the monthly mean wind stress data show that the timing and strength of the peaks correspond to those of the sea level anomalies averaged over the southern edge of Sakhalin Island on a seasonal timescale (Fig. 3.18a, b), although we note that the seasonal amplitude of the ATW transport for the NCEP-NCAR reanalysis data is somewhat larger than that of the ERA40 data. Assuming that the width and depth of this coastally trapped current are assumed to be 70 km and 100 m, the seasonal amplitude of the geostrophic volume transport derived from the sea level change (14 cm) is estimated to be 1.1 Sv, which is comparable to the theoretical value of the ATW transport (0.95 Sv).

On an interannual timescale, the coherent sea level variation is dominant in winter (December to February). The first EOF mode of the wintertime sea level explains 61% of the total variance with a large amplitude along Sakhalin Island (Fig. 3.19a, b). This coherent pattern of wintertime sea level variation is more evident in the satellite altimeter data, and the coherent sea level variation signal is confined to the shelf region where the water depths are shallower than 1000 m, and extended to the eastern shelf of the Kamchatka Peninsula and the southern coast of Hokkaido (Fig. 3.20). The interannual fluctuation in the wintertime sea level is also well explained by the ATW transport in the Sea of Okhotsk. The correlation between the wintertime

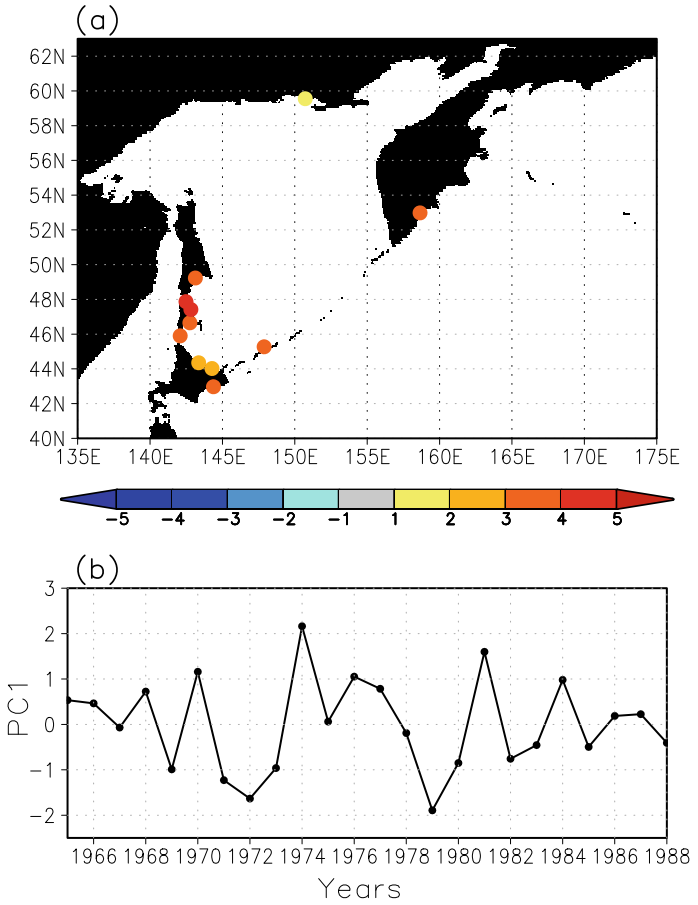

Fig. 3.19 **a** Spatial pattern of the EOF1 for 11 tide gauge sea levels in winter (December–February) from 1965 to 1988. **b** Time series of principle components of EOF1 (after Nakanowatari and Ohshima 2014, modified)

(December to February) sea level anomalies (solid line) averaged along Sakhalin Island (E, G, H, I, J) and the ATW transport anomalies is 0.66 from 1965 to 1988 (Fig. 3.21), which is higher than the correlation with the Sverdrup transport in the Sea of Okhotsk (Table 3.3). The influence of the ATW is also found in the sea level data along the upstream East Kamchatka and the southern coast of Hokkaido as the significant correlation with the ATW transport is calculated from the upstream region (Table 3.3).

On the Pacific side, the time-varying Sverdrup transport is considered to be a dominant factor for the interannual variations in EKC (Isoguchi and Kawamura 2006) and Oyashio (Ito et al. 2004). In fact, the wintertime sea level variations in these coastal areas, such as PK and Kushiro, are well correlated with the Sverdrup transport at 42°N in the North Pacific (Table 3.3). On the other hand, the wintertime

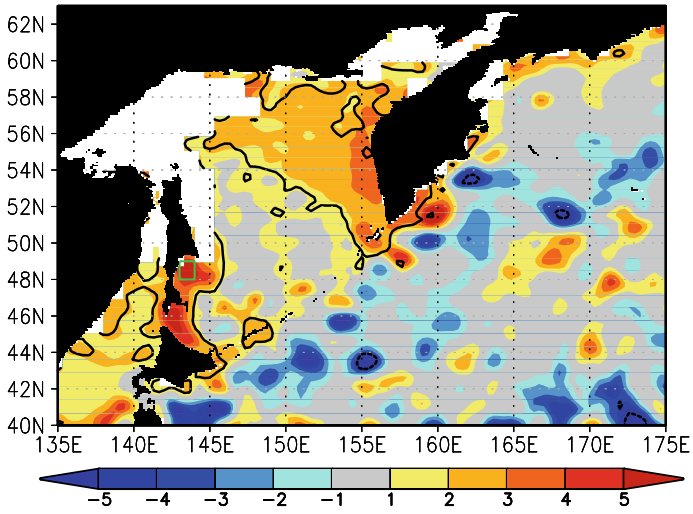

Fig. 3.20 Regression maps (colors) of the SSHAs in December onto the normalized SSHAs averaged over the area offshore of Sakhalin Island (48°–49°N, 143°–144°E; indicated as green square) from 1993 to 2009. Contours indicate the areas where the correlation exceeds the 95% confidence level. The regions in which the sea ice concentration is larger than 10% are masked out with white (after Nakanowatari and Ohshima 2014, modified)

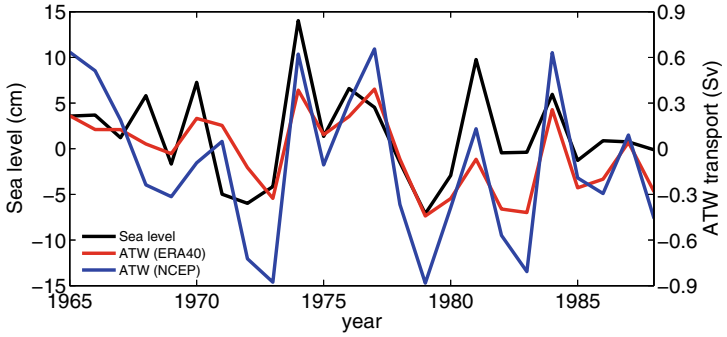

Fig. 3.21 Time series of the wintertime (December to February) sea level anomalies (black line) averaged along Sakhalin Island (E, G, H, I, J) (see Fig. 3.17a for the locations) and the ATW transport anomalies calculated from the northern part of the Okhotsk Sea (see Fig. 3.17a for the route location), which are calculated from the ERA40 (red) and NCEP-NCAR reanalysis (blue) data, respectively. The scale of the ATW transport anomalies is indicated on the right axis (after Nakanowatari and Ohshima 2014, modified)

ATW transport is also highly correlated with the interannual variations in coastal sea level changes. For the Kushiro, there is no significant correlation between the ATW transport and Sverdrup transport ($r = 0.15$). When a statistical regression model for the Kushiro sea level is applied using both the ATW and Sverdrup transports, the

Table 3.3 Correlation coefficients between the sea level along Sakhalin Island (E, G, H, I, and J), PK (A), and Kushiro (O) and the ATW transport and the Sverdrup transport integrated over the Sea of Okhotsk (OK) and North Pacific (NP) calculated using ERA-40 and NCEP-NCAR reanalysis data in winter (December to February)

	ATW	Sverdrup transport	Atmospheric data	Period
Sakhalin	0.66	0.64 (OK at 46–50°N)	ERA-40	1965–1988
	0.71	0.71 (OK at 46–50°N)	NCEP-NCAR	
PK	0.65	0.59 (NP at 51°N)	ERA-40	1958–2001
Kushiro	0.59	0.56 (NP at 42°N)	ERA-40	1958–2001

multiple correlation coefficient between the observed and predicted sea level reaches a significantly high value of 0.76 (Fig. 3.22). Thus, the ATW has a substantial impact on the wintertime sea level height and the resultant coastally trapped current strength in and around the Sea of Okhotsk on the interannual timescale.

It is suggested that wintertime increases in the sea level along the Okhotsk coast of Hokkaido (Itoh and Ohshima 2000) and the Oyashio coast (Isoda et al. 2003; Sakamoto et al. 2010; Kusaka et al. 2009) are related to the advent of lighter ESC water from the upstream region. In fact, although the wintertime peak is commonly found in December along Sakhalin Island (e.g., H), the timing of the peak along the southern coast of the Hokkaido (O) is delayed by one month (Fig. 3.17b). Thus, it is suggested that the advection of ESC water also contributes to the wintertime sea level change and its maintenance around the Hokkaido through the following baroclinic jet current in later stages (Sakamoto et al. 2010).

The atmospheric circulation patterns responsible for the wintertime coherent sea level variation are the prevailing northeasterly wind anomalies over the Sea of Okhotsk and the Bering Sea (Fig. 3.23a). These wind stresses enhance the Ekman transport over the coastal region and pile up the sea level along Sakhalin Island and the east coast of the Kamchatka Peninsula to generate ATWs. The northeasterly wind anomalies related to the wintertime coherent sea level are associated with the dipole pattern of high pressure over the Eurasian continent and low pressure over the subtropics (Fig. 3.23b). This anomalous sea level pressure pattern is related to both the Western Pacific (WP) pattern, which is characterized by the meridional dipole anomaly of atmospheric circulation over the western North Pacific (Horel and Wallace 1981) and the strength of the Aleutian low. The correlations between the PC-1 and the WP index of the Climate Prediction Center (Barnston and Livezey 1987) and the North Pacific Index (NPI), which is the Aleutian low strength defined as the sea level pressure averaged over a region from 30°–60°N and 160°E–140°W (Trenberth and Hurrell 1994), are −0.46 and −0.60, respectively (significant at the 90% and 95% confidence levels).

The coherent sea level variation around the Kamchatka Peninsula and the resultant ATWs also have a potential impact on the inflow water change from the Pacific and the sea ice shrinkage in mid-winter. The wintertime PC-1 has the highest negative

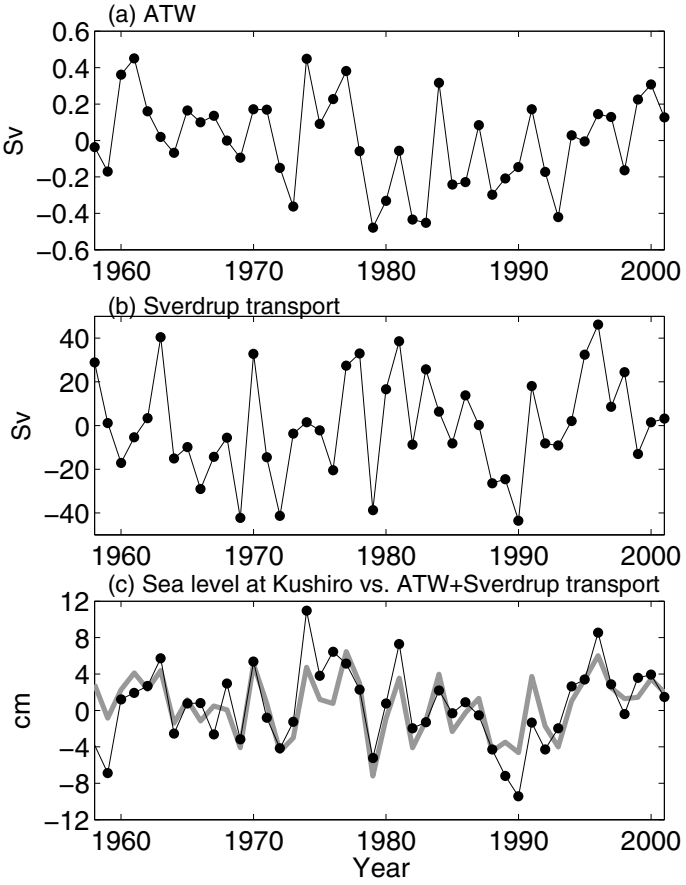

Fig. 3.22 Time series of **a** the wintertime (December to February) ATW transport anomalies integrated from the northern shelf of the Okhotsk Sea (see Fig. 3.17a for the route location), and **b** Sverdrup transport at 42°N, calculated by the wind stress data from ERA-40. **c** The sea level anomalies (solid line) along the Kushiro (see Fig. 3.17a for the location) and the predicted sea level from the multiple regression model of ATW and Sverdrup transports (gray)

correlation with the sea ice extent in January from 1971 to 1988 ($r = -0.67$, significant at the 95% confidence level), indicating that the ATW-related warmer coastal current from the Pacific suppresses the sea ice extent advance. Conversely, the correlations between PC-1 and sea ice extent in December and February are only -0.01 and -0.32, respectively. The weak statistical relationship in early and late winter seems to be related to other dominant factors, such as atmospheric heat conditions (Ohshima et al. 2006; Sasaki et al. 2007) and the remote effect of the EKC water (Nakanowatari et al. 2010). Thus, for the precise prediction of annual variability in the sea ice extent in the Sea of Okhotsk during the whole winter, it may be necessary

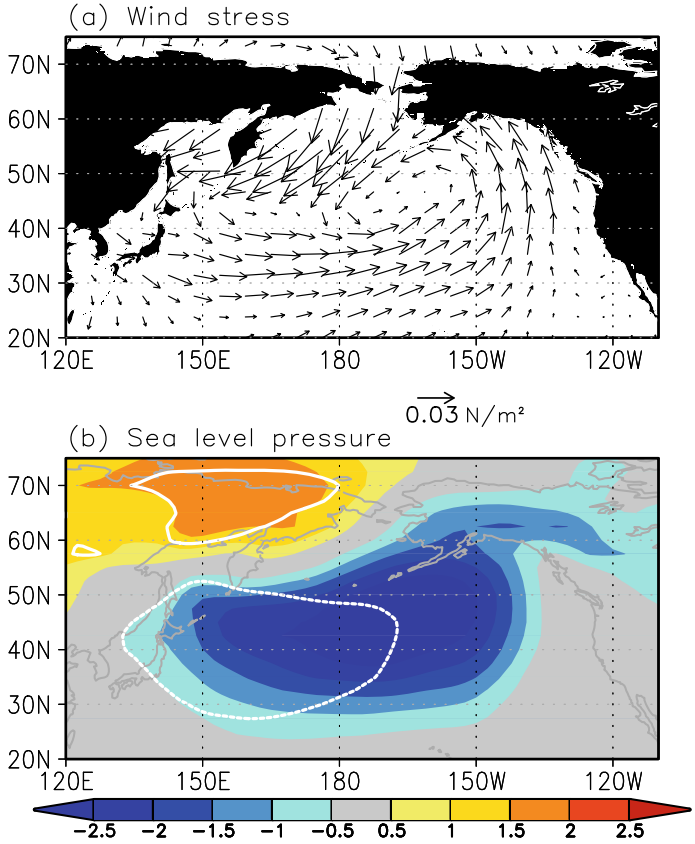

Fig. 3.23 Regression maps of **a** the wind stress (vectors) and **b** sea level pressure (colors) of ERA-40 onto the PC-1 of the sea levels in winter (December to February). In **a**, the standard vector length of 0.03 N/m^2 is shown at the bottom. Contours indicate the region in which the positive (negative) correlation is significant at the 95% confidence level (after Nakanowatari and Ohshima 2014, modified)

to consider the volume changes in inflowing water from the Pacific through shallow straits, such as the Onekotan Strait (Fig. 3.1).

3.5 18.6-yr Lunar Nodal Tide and Its Influence on Water Mass Property Changes

Bidecadal variations are frequently observed in various water mass properties and nutrients in the Sea of Okhotsk and adjacent seas (Ono et al. 2001; Watanabe et al. 2003; Osafune and Yasuda 2006; Yasuda et al. 2006; Tadokoro et al. 2009; Osafune and Yasuda 2012, 2013). The nodal tide with an 18.6-year period cycle is a likely

agent that causes bidecadal variations; the nodal tide occurs because of the lunar orbit inclination with respect to the Earth's equatorial surface. Tidal mixing is strong along the Kuril Islands (Nakamura and Awaji 2004; Nakamura et al. 2006a). The diurnal K_1 and O_1 tides are dominant in this region. Modulations of tidal current amplitude in K_1 and O_1 due to the nodal cycle are 11% and 19%, respectively. The nodal tide modifies the water properties bidecadally; in the Sea of Okhotsk, Osafune and Yasuda (2006) showed that the potential temperature in the $26.8\sigma_\theta$ layer exhibits bidecadal oscillation with maxima (minima) in the mid-1960s (1960 and the late 1970s), which corresponds well with the maxima (minima) of the nodal tide. The thickness between the $26.7\sigma_\theta$ and $27.0\sigma_\theta$ isopycnals also showed bidecadal variations with an amplitude of ± 17 m with respect to a mean thickness of 370 m. Table 3.4 summarizes the results of an analysis fitting to the lunar nodal tide in the Sea of Okhotsk after Osafune and Yasuda (2006). They also examined the effects of the nodal tide in the Oyashio and the EKC regions. Furthermore, using an atmosphere-ocean coupled model with vertical diffusivity estimated from the global tidal model, Tanaka et al. (2012) suggested that an SST anomaly with a period of 18.6 years would cause bidecadal climate fluctuations that are evident over the North Pacific Ocean (Minobe 1999). According to their results, the SST anomaly is generated locally around the Kuril Islands and subsequently appears in the Kuroshio-Oyashio Extension region; a positive (negative) SST anomaly tends to occur during strong (weak) tidal mixing. The SST anomaly is amplified through positive feedback due to midlatitude air-sea interactions and induces bidecadal climate oscillations resembling the Pacific Decadal Oscillation.

Here, we note the variability in salinity associated with the nodal tides because it may affect the overturning circulation described in Sect. 3.3. Surface salinity increases because of upward salt fluxes from the relatively saline intermediate layer due to enhanced vertical mixing (Nakamura and Awaji 2004; Nakamura et al. 2006a) during the stronger nodal tide period (Osafune and Yasuda 2006, 2012, 2013). Uehara et al. (2014) showed that the nodal tide exhibits significant correlations (at the 95% confidence level) with the upper-layer salinity anomalies in the Eastern Okhotsk Sea

Table 3.4 Parameters fit to the nodal tide obtained in the Sea of Okhotsk (after Osafune and Yasuda 2006)

	Mean	Amplitude	Lag	Correlation (n: number of data)
AOU at $27.0\sigma_\theta$ (ml/l)	4.4	0.17	−5.1 years	0.76 (n = 35)
PO_4 at $27.0\sigma_\theta$ (μM)	2.8	0.080	9.0 years	0.36 (n = 29)
θ at $26.8\sigma_\theta$ (°C)	0.87	0.15	−1.4 years	0.66 (n = 58)
Thickness between $26.7\sigma_\theta$ and $27.0\sigma_\theta$ (m)	370	17	3.2 years	0.64 (n = 27)
Depth at $26.6\sigma_\theta$ (m)	120	22	−6.7 years	0.80 (n = 61)
Depth at $26.8\sigma_\theta$ (m)	300	18	−4.4 years	0.66 (n = 58)
Sea surface salinity (psu)	0.0025	0.13	1.8 years	0.53 (n = 31)

(r = 0.50), the East Kamchatka Current (r = 0.55), and the Bering Sea (r = 0.42) along the salinity anomaly pathway (Fig. 3.12), when the nodal tide leads by 2, 3 and 0 years, respectively. However, the lag correlation between the DSW salinity in Fig. 3.9c and the nodal tide does not exhibit a very high correlation (r = 0.28). On the other hand, Osafune and Yasuda (2006) indicated that the salinity variations in this period are evident in the surface and intermediate layers of the Oyashio regions and the southern Okhotsk Sea adjacent to the Kuril Islands. Furthermore, the intermediate layer thickness is changed by the nodal tide as mentioned above, which significantly influences the intermediate-layer circulation and hence the overturning (Nakamura et al. 2006b). Therefore, it appears that the nodal tide influences the overturning circulation through the direct ventilation along the Kuril Islands due to mixing rather than through the DSW formation that occurs remotely over the northern shelves.

3.6 Summary

In this article, we presented the long-term trends and interannual to decadal variations in physical properties such as sea ice, temperature, salinity and currents in the Sea of Okhotsk. The subjects in this chapter are summarized as follows:

(1) Maximum sea ice extent (MSIE) in the Sea of Okhotsk has decreased at a rate of $-8.7 \pm 2.5\%$ per decade from 1979 to 2010, which is the second largest fraction in the Northern Hemisphere. Interannual variations also occur in the MSIE. With regard to the interannual variations, the MSIE is significantly correlated with the late fall preconditioning. Sea ice formation is largely determined by the local heat flux in the late fall, but the influence of autumn atmospheric cooling seems to be weak in recent decades. The ocean heat flux from the East Kamchatka Current to the eastern Okhotsk Sea in early winter is also a major determinant factor for the MSIE.

(2) The Okhotsk Sea intermediate water (OSIW) temperature shows a warming trend with a maximum value of 0.62 ± 0.18 °C at the isopycnal surface of $27.0\sigma_\theta$ for the last 50 years. One of the key parameters that determines the intermediate-layer temperature is the salinity of the dense shelf water (DSW). The DSW salinity decreases at a rate of -0.12 ± 0.08 over the last 50 years, which causes lightening of the DSW, resulting in warming at the $27.0\sigma_\theta$ density surface. The DSW salinity decrease is caused by freshening of the surface salinity in the subarctic gyre in the North Pacific Ocean, as well as the reduction in ice production in polynyas over the northern shelves in the Okhotsk Sea. Decadal variations are also evident in the OSIW temperature, which are correlated with variations in the DSW salinity and ice production.

(3) The sea level along the Sea of Okhotsk exhibits coherent variations from the east coast of the Kamchatka Peninsula to the eastern coast of Hokkaido Island. The sea level fluctuations correlate well with those of the coastal currents along the coast of the Sea of Okhotsk. The transport of the coastal currents is estimated

well by the arrested topographic waves. The coherent variations potentially influence the MSIE and DSW salinity by varying the inflow transport from the North Pacific.

(4) Strong mixing occurs as a result of the interaction between tidal currents and the ridged bottom topography in the straits along the Kuril Islands. An 18.6-year-period cycle associated with the nodal tide bidecadally modulates various water properties, such as temperature, salinity, layer thickness and nutrients, along the Kuril Islands.

As described in Sects. 3.2 and 3.3, the MSIE has decreased and the intermediate layer has warmed substantially in the past 50 years. Global warming is in progress according to the Intergovernmental Panel on Climate Change 5th assessment report, which implies that the temperature over the Eurasian continent would continue to increase, as would the temperature of the Okhotsk Sea. Furthermore, the hydrological cycle is likely intensified, and hence, an increase in precipitation is predicted at high latitudes. These predictions support the simple future projection such that the sea ice will be further reduced and the intermediate layer will be further warmed in the Sea of Okhotsk. On the other hand, the Multi-Model Ensemble (MME) of the fifth phase of the Coupled Model Intercomparison Project (CMIP5) indicates that the Aleutian low would strengthen and shift northward in response to global warming (Ogata et al. 2014; Gan et al. 2017). This may cause intensification of the northwesterly monsoon wind over the Okhotsk Sea. With this atmospheric condition, both the ice production in polynyas over the northern continental shelves and salt transport due to the wind-driven circulation from the southern part of the Sea of Okhotsk may increase. These are favorable conditions for DSW ventilation to the intermediate layer, which strengthens the overturning circulation. Itaki and Ikehara (2004) reconstructed the paleo-Okhotsk Sea and showed that the DSW ventilation substantially increased during a warm period between 7500 and 3500 years ago in the mid-Holocene and declined during a cold period (Neoglaciation) between 3000 and 2000 years ago. These paleo-oceanographic features are consistent with the atmospheric circulation of the CMIP5 MME predicted with the global warming projection. Further study is needed to better understand the response of the Sea of Okhotsk to global warming.

Acknowledgements AMSR-E data was supplied by Japan Aerospace Exploration Agency through the Arctic Data archive System (ADS), under the cooperation between National Institute of Polar Research and JAXA. We would thank Dr. Sasaki for providing us with data to redraw some figures. We would also thank Dr. Nishikawa for drawing figures. This work was supported by the Ministry of Education, Culture, Sports, Science and Technology, Japan, Grants-in-Aid for Scientific Research (17H01156 and JP18H04909).

References

Andreev AG, Kusakabe M (2001) Interdecadal variability in dissolved oxygen in the intermediate water layer of the Western Subarctic Gyre and Kuril Basin (Okhotsk Sea). J Geophys Res 28:2453–2456

Barnston AG, Livezey RE (1987) Classification, seasonality and persistence of lowfrequency atmospheric circulation patterns. Mon Weather Rev 115:1083–1126

Bindoff NL, McDougall TJ (1994) Diagnosing Climate Change and ocean ventilation using hydrographic data. J Phys Oceanogr 24:1137–1152

Bond NA, Overland JE, Spillane M, Stabeno P (2003) Recent shifts in the state of the North Pacific. Geophys Res Lett 30:2183. https://doi.org/10.1029/2003gl018597

Csanady GT (1978) The arrested topography wave. J Phys Oceanogr 8:47–62

Cavalieri DJ, Parkinson CL (1987) On the relationship between atmospheric circulation and fluctuations in the sea ice extents of the Bering and Okhotsk seas. J Geophys Res 92:7141–7162

Cavalieri DJ, Parkinson CL (2012) Arctic sea ice variability and trends, 1979–2010. The Cryosphere 6:g 881–889. https://doi.org/10.5194/tc-6-881-2012

Durack PJ, Wijffels SE (2010) Fifty-year trends in global ocean salinities and their relationship to broad-scale warming. J Clim 23:4342–4362. https://doi.org/10.1175/2010JCLI3377.1

Durack PJ, Wijffels SE, Matear RJ (2012) Ocean salinities reveal strong global water cycle intensification during 1950 to 2000. Science 336:455–458. https://doi.org/10.1126/science.1212222

Ebuchi N (2006) Seasonal and interannual variations in the East Sakhalin Current revealed by TOPEX/POSEIDON altimeter data. J Oceanogr 62:171–183

Gan B, Wu L, Jia F, Li S, Cai W, Nakamura H, Alexander MA, Miller AJ (2017) On the response of the Aleutian Low to greenhouse warming. J. Clim 30:3907–3925. https://doi.org/10.1175/JCLI-D-15-0789.1

Gladyshev S, Martin S, Riser S, Figurkin A (2000) Dense water production on the northern Okhotsk shelves: comparison of shipbased spring-summer observations for 1996 and 1997 with satellite observations. J Geophys Res 105:26,281–26,299. https://doi.org/10.1029/1999JC000067

Hill KL, Weaver AJ, Freeland HJ, Bychkov A (2003) Evidence of change in the Sea of Okhotsk: implications for the North Pacific. Atmos Ocean 41:49–63

Honda M, Yamazaki K, Nakamura H, Takeuchi K (1999) Dynamic and thermodynamic characteristics of atmospheric response to anomalous sea-ice extent in the Sea of Okhotsk. J Clim 12:3347–3358

Horel JD, Wallace JM (1981) Planetary-scale atmospheric phenomena associated with the Southern Oscillation. Mon Weather Rev 109:813–829

Hosoda S, Suga T, Shikama N, Mizuno K (2009) Global surface layer salinity change detected by Argo and its implication for hydrological cycle intensification. J Oceanogr 65:579–586. https://doi.org/10.1007/s10872-009-0049-1

Inoue J, Ono J, Tachibana Y, Honda M, Iwamoto K, Fujiyoshi Y, Takeuchi K (2003) Characteristics of heat transfer over the ice-covered Sea of Okhotsk during cold air outbreaks. J Meteorol Soc Jpn 81:1057–1067

Isoda Y, Kuroda H, Myousyo T, Honda S (2003) Hydrographic feature of coastal Oyashio and its seasonal variation. Bull Coast Oceanogr 41:5–12 (in Japanese with English abstract)

Isoguchi O, Kawamura H, Kono T (1997) A study on wind-driven circulation in the subarctic North Pacific using TOPEX/POSEIDON altimeter data. J Geophys Res 102:12,457–12,468

Isoguchi O, Kawamura H (2006) Seasonal to interannual variations of the western boundary current of the subarctic North Pacific by a combination of the altimeter and tide gauge sea levels. J Geophys Res 111:C04013. https://doi.org/10.1029/2005JC003080

Itaki T, Ikehara K (2004) Middle to late Holocene changes of the Okhotsk Sea Intermediate Water and their relation to atmospheric circulation. Geophys Res Lett 31:L24309. https://doi.org/10.1029/2004GL021384

Ito T, Minobe S, Long MC, Deutsch C (2017) Upper ocean O2 trends: 1958–2015. Geophys Res Lett 44:4214–4223. https://doi.org/10.1002/2017GL073613

Ito S, Uehara K, Miyao T, Miyake H, Yasuda I, Watanabe T, Shimizu Y (2004) Characteristics of SSH anomaly based on TOPEX/POSEIDON altimeter and in situ measured velocity and transport of Oyashio on OICE. J Oceanogr 60:425–437

Itoh M, Ohshima KI (2000) Seasonal variations of water masses and sea level in the southwestern part of the Okhotsk Sea. J Oceanogr 56:643–654

Itoh M, Ohshima K, Wakatsuchi M (2003) Distribution and formation of Okhotsk Sea intermediate water: an analysis of isopycnal climatological data. J Geophys Res 108:3258. https://doi.org/10.1029/2002JC001950

Kashiwase H, Ohshima KI, Nihashi S (2014) Long-term variation in sea ice production and its relation to the intermediate water in the Okhotsk Sea. Prog Oceanogr 126:22–32

Kawasaki T, Hasumi H (2010) Role of localized mixing around the Kuril Straits in the Pacific thermohaline circulation. J Geophys Res 115:C11002. https://doi.org/10.1029/2010JC006130

Kimura N, Wakatsuchi M (1999) Processes controlling the advance and retreat of sea ice in the Sea of Okhotsk. J Geophys Res 104:11,137–11,150

Kusaka A, Ono T, Azumaya T, Kasai H, Oguma S, Kawasaki Y, Hirakawa K (2009) Seasonal variations of oceanographic conditions in the continental shelf area off the eastern Pacific coast of Hokkaido, Japan. Oceanogr Jpn 18: 135–156 (in Japanese with English abstract)

Martin S, Drucker R, Yamashita K (1998) The production of ice and dense shelf water in the Okhotsk Sea polynyas. J Geophys Res 103:27,771–27,782

Matsuda J, Mitsudera H, Nakamura T, Uchimoto K, Nakanowatari T, Ebuchi N (2009) Wind and buoyancy driven intermediate-layer overturning in the Sea of Okhotsk. Deep-Sea Research I 56:1401–1418

Matsuda J, Mitsudera H, Nakamura T, Sasajima Y, Hasumi H, Wakatsuchi M (2015) Overturning circulation that ventilates the intermediate layer of the Sea of Okhotsk and the North Pacific: the role of salinity advection. J Geophys Res Oceans 120. http://dx.doi.org/10.1002/2014JC009995

Minobe S (1999) Resonance in bidecadal and pentadecadal climate oscillations over the North Pacific: role in climatic regime shifts. Geophys Res Lett 26:855–858

Mizuta G, Fukamachi Y, Ohshima KI, Wakatsuchi M (2003) Structure and seasonal variability of the East Sakhalin Current. J Phys Oceanogr 33:2430–2445

Nakamura T, Awaji T (2004) Tidally induced diapycnal mixing in the Kuril Straits and its role in water transformation and transport: a three-dimensional nonhydrostatic model experiment. J Geophys Res 109:C09S07. http://dx.doi.org/10.1029/2003JC001850

Nakamura T, Toyoda T, Ishikawa Y, Awaji T (2006a) Enhanced ventilation in the Okhotsk Sea through tidal mixing at the Kuril Straits. Deep-Sea Res I 53:425–448

Nakamura T, Toyoda T, Ishikawa Y, Awaji T (2006b) Effects of tidal mixing at the Kuril Straits on North Pacific ventilation: adjustment of the intermediate layer revealed from numerical experiments. J Geophys Res 111:C04003. https://doi.org/10.1029/2005JC003142

Nakanowatari T, Ohshima KI, Wakatsuchi M (2007) Warming and oxygen decrease of intermediate water in the northwestern North Pacific, originating from the Sea of Okhotsk. 1955–2004. Geophys Res Lett 34:L04602. http://dx.doi.org/10.1029/2006GL028243

Nakanowatari T, Ohshima KI, Nagai S (2010) What determines the maximum sea ice extent in the Sea of Okhotsk? Importance of ocean thermal condition from the Pacific. J Geophys Res 115:C12031. https://doi.org/10.1029/2009jc006070

Nakanowatari T, Ohshima KI (2014) Coherent sea level variability in and around the Sea of Okhotsk. Prog Oceanogr 126:58–70

Nakanowatari T, Nakamura T, Uchimoto K, Uehara H, Mitsudera H, Ohshima KI, Hasumi H, Wakatsuchi M (2015a) Causes of the multidecadal-scale warming of the intermediate water in the Okhotsk Sea and Western Subarctic North Pacific. J Clim 28:714–736

Nakanowatari T, Mitsudera H, Motoi T, Ishikawa I, Ohshima KI, Wakatsuchi M (2015b) Multidecadal-scale freshening at the salinity minimum in the Western part of North Pacific:

importance of wind-driven cross-gyre transport of subarctic water to the subtropical gyre. J Phys Oceanogr 45:988–1008. https://doi.org/10.1175/JPO-D-13-0274.1

Nakanowatari T, Nakamura T, Uchimoto K, Nishioka J, Mitsudera H, Wakatsuchi M (2017) Importance of Ekman transport and gyre circulation change on seasonal variation of surface dissolved iron in the western subarctic North Pacific. J Geophys Res 122:4364–4391. https://doi.org/10.1002/2016JC012354

Nihashi S, Ohshima KI, Tamura T, Fukamachi Y, Saitoh S (2009) Thickness and production of sea ice in the Okhotsk Sea coastal polynyas from AMSR-E. J Geophys Res 114:C10025. https://doi.org/10.1029/2008JC005222

Nishioka J, Ono T, Saito H, Nakatsuka T, Takeda S, Yoshimura T, Suzuki K, Kuma K, Nakabayashi S, Tsumune D, Mitsudera H, Johnson WK, Tsuda A (2007) Iron supply to the western subarctic Pacific: importance of iron export from the Sea of Okhotsk. J Geophys Res 112:C10012. https://doi.org/10.1029/2006JC004055

Nishioka J, Ono T, Saito H, Sakaoka K, Yoshimura T (2011) Oceanic iron supply mechanisms which support the spring diatom bloom in the Oyashio region, western subarctic Pacific. J Geophys Res 112:C10012. https://doi.org/10.1029/2010JC006321

Nishioka J, Nakatsuka T, Watanabe YW, Yasuda I, Kuma K, Ogawa H, Ebuchi N, Scherbinin A, Volkov YN, Shiraiwa T, Wakatsuchi M (2013) Intensive mixing along an island chain controls oceanic biogeochemical cycles. Glob Biogeochem Cycles 27. http://dx.doi.org/10.1002/gbc.20088

Nishioka J, Nakatsuka T, Ono K, Volkov YN, Scherbinin A, Shiraiwa T (2014) Quantitative evaluation of Fe transport processes in the Sea of Okhotsk. Prog Oceanogr 126:1–7

Nishioka J, Obata H (2017) Dissolved iron distribution in the western and central subarctic Pacific: HNLC water formation and biogeochemical processes. Limnol Oceanogr 62:2004–2022

Ogata T, Ueda H, Inoue T, Hayasaki M, Yoshida A, Watanabe S, Kira M, Ooshiro M, Kumai A (2014) Projected future changes in the Asian monsoon: a comparison of CMIP3 and CMIP5 model results. J Meteorol Soc Jpn Ser II 92:207–225

Ogi M, Tachibana Y (2006) Influence of the annual Arctic Oscillation on the negative correlation between Okhotsk Sea ice and Amur River discharge. Geophys Res Lett 33:L08709. https://doi.org/10.1029/2006GL025838

Ohshima KI, Wakatsuchi M, Fukamachi Y, Mizuta G (2002) Near-surface circulation and tidal currents of the Okhotsk Sea observed with satellite-tracked drifters. J Geophys Res 107:3195. https://doi.org/10.1029/2001JC001005

Ohshima KI, Watanabe T, Nihashi S (2003) Surface heat budget of the Sea of Okhotsk during 1987–2001 and the role of sea ice on it. J Meteorol Soc Jpn 81:653–677. https://doi.org/10.2151/jmsj.81.653

Ohshima KI, Simizu D, Itoh M, Mizuta G, Fukamachi Y, Riser SC, Wakatsuchi M (2004) Sverdrup balance and the cyclonic gyre in the Sea of Okhotsk. J Phys Oceanogr 34:513–525

Ohshima KI, Nihashi S, Hashiya E, Watanabe T (2006) Interannual variability of sea ice area in the Sea of Okhotsk: importance of surface heat flux in fall. J Meteorol Soc Jpn 84:907–919

Ohshima KI, Nakanowatari T, Riser S, Wakatsuchi M (2010) Seasonal variation in the in- and outflow of the Okhotsk Sea with the North Pacific. Deep Sea Res II 57:1247–1256. https://doi.org/10.1016/J.DSR2.2009.12.012

Ohshima KI, Nakanowatari T, Riser S, Volkov YN, Wakatsuchi M (2014) Freshening and dense shelf water reduction in the Okhotsk Sea linked with sea ice decline. Prog Oceanogr 126:71–79

Ono T, Midorikawa T, Watanabe YW, Tadokoro K, Saino T (2001) Temporal increases of phosphate and apparent oxygen utilization in the surface waters of western subarctic Pacific from 1968 to 1998. Geophys Res Lett 28:3285–3288

Osafune S, Yasuda I (2006) Bidecadal variability in the intermediate waters of the northwestern subarctic Pacific and the Okhotsk Sea in relation to 18.6 year period nodal tidal cycle. J Geophys Res 111:C05007. http://dx.doi.org/10.1029/2005JC003277

Osafune S, Yasuda I (2012) Numerical study on the impact of the 18.6-year period nodal tidal cycle on water masses in the subarctic North Pacific. J Geophys Res 117:C05009. http://dx.doi.org/10.1029/2011JC007734

Osafune S, Yasuda I (2013) Remote impacts of the 18.6 year period modulation of localized tidal mixing in the North Pacific. J Geophys Res Oceans 118:3128–3137. https://doi.org/10.1002/jgrc.20230

Parkinson CL (1990) The impact of the Siberian high and Aleutian low on the sea-ice cover of the Sea of Okhotsk. Ann Glaciol 14:226–229

Peterson TC, Vose RS (1997) An overview of the global historical climatology network temperature database. Bull Am Meteorol Soc 78:2837–2848

Ray RD (2006) Decadal climate variability: is there a tidal connection? J Clim 20:3542–3560

Rayner NA, Parker DE, Horton EB, Folland CK, Alexander LV, Rowell DP, Kent EC, Kaplan A (2003) Global analyses of sea surface temperature, sea ice, and night marine air temperature since the late nineteenth century. J Geophys Res 108:4407. https://doi.org/10.1029/2002JD002670

Reynolds RW, Smith TM, Liu C, Chelton DB, Casey KS, Schlax MG (2007) Daily High-resolution-blended analyses for sea surface temperature. J Climate 20(22):5473–5496

Rodionov SN, Bond NA, Overland JE (2007) The Aleutian Low, storm tracks, and winter climate variability in the Bering Sea. Deep-Sea Res. Part II 54:2560–2577

Sakamoto K, Tsujino H, Nishikawa S, Nakano H, Motoi T (2010) Dynamics of the coastal Oyashio and its seasonal variation in a high-resolution Western North Pacific Ocean model. J Phys Oceanogr 40:1283–1301

Sasaki YN, Katagiri Y, Minobe S, Rigor IG (2007) Autumn atmospheric preconditioning for interannual variability of wintertime sea-ice in the Okhotsk Sea. J Oceanogr 63:255–265

Screen JA (2017) Simulated atmospheric response to regional and Pan-Arctic Sea ice loss. J Clim 30:3945–3962. https://doi.org/10.1175/JCLI-D-16-0197.1

Serreze MC, Barry RG (2011) Processes and impacts of Arctic amplification: a research synthesis. Glob Planet Change 77:85–96. https://doi.org/10.1016/j.gloplacha.2011.03.004

Shcherbina AY, Talley LD, Rudnick DL (2003) Direct observations of North Pacific ventilation: Brine rejection in the Okhotsk Sea. Science 302:1952–1955

Shcherbina AY, Talley LD, Rudnick DL (2004a) Dense water formation on the northwestern shelf of the Okhotsk Sea: 1. Direct observations of brine rejection. J Geophys Res 109:C09S08. https://doi.org/10.1029/2003JC002196

Shcherbina AY, Talley LD, Rudnick DL (2004b) Dense water formation on the northwestern shelf of the Okhotsk Sea: 2. Quantifying the transports. J Geophys Res 109:C09S09. https://doi.org/10.1029/2003JC002197

Simizu D, Ohshima KI (2002) Barotropic response of the Sea of Okhotsk to wind forcing. J Oceanogr 58:851–860

Stabeno PJ, Reed RK, Overland JE (1994) Lagrangian measurements in the Kamchatka Current and Oyashio. J Oceanogr 50:653–662

St. Laurent LC, Simmons HL, Jayne SR (2002) Estimating tidally driven mixing in the deep ocean. Geophys Res Lett 29:2106. https://doi.org/10.1029/2002GL015633

Tachibana Y, Honda M, Takeuchi K (1996) The abrupt decrease of the sea ice over the southern part of the Sea of Okhotsk in 1989 and its relation to the recent weakening of the Aleutian low. J Meteorol Soc Jpn 74:579–584

Tadokoro K, Ono T, Yasuda I, Osafune S, Shiomoto A, Sugisaki H (2009) Possible mechanisms of decadal-scale variation in PO4 concentration in the western North Pacific. Geophys Res Lett 36:L08606. https://doi.org/10.1029/2009GL037327

Talley LD, Nagata Y (1995) The Okhotsk Sea and Oyashio region. PICES Scientific Report No. 2, Sidney, B.C., Canada, 227 pp

Tanaka Y, Yasuda I, Hasumi H, Tatebe H, Osafune S (2012) Effects of the 18.6-yr modulation of tidal mixing on the North Pacific Bidecadal climate variability in a coupled climate model. J Clim 25:7625–7642

Trenberth KE, Hurrell JW (1994) Decadal atmosphere-ocean variations in the Pacific. Clim Dyn 9:303–319

Uchimoto K, Mitsudera H, Ebuchi N, Mizuta G (2008) Seasonal variations of the sea level in the eastern part of the Kuril Basin. Umi to Sora 84:93–99 (in Japanese with English abstract and figure captions)

Uchimoto K, Nakamura T, Nishioka J, Mitsudera H, Misumi K, Tsumune D, Wakatsuchi M (2014) Simulation of high concentration of iron in dense shelf water in the Okhotsk Sea. Prog Oceanogr 126:194–210

Uehara H, Kruts AA, Volkov YN, Nakamura T, Ono T, Mitsudera H (2012) A New climatology of the Okhotsk Sea derived from the FERHRI database. J Oceanogr 68:869–886

Uehara H, Kruts AA, Mitsudera H, Nakamura T, Volkov YN, Wakatsuchi M (2014) Remotely propagating salinity anomaly varies the source of the North Pacific ventilation. Prog Oceanogr 126:80–97

Uppala SM, Kållberg PW, Simmons AJ, Andrae U, da Costa Bechtold V, Fiorino M, Gibson JK, Haseler J, Hernandez A, Kelly GA, Li X, Onogi K, Saarinen S, Sokka N, Allan RP, Andersson E, Arpe K, Balmaseda MA, Beljaars ACM, Vande Berg L, Bidlot J, Bormann N, Caires S, Chevallier F, Dethof A, Dragosavac M, Fisher M, Fuentes M, Hagemann S, Hólm E, Hoskins BJ, Isaksen L, Janssen PAEM, Jenne R, McNally AP, Mahfouf J-F, Morcrette J-J, Rayner NA, Saunders RW, Simon P, Sterl A, Trenberth KE, Untch A, Vasiljevic D, Viterbo P, Woollen J (2005) The ERA-40 re-analysis. Q J R Meteorol Soc 131:2961–3012

Vigan M, Ohshima KI, Nakanowatari T, Riser S (2019) Seasonal changes of water mass, circulation and dynamic response in the Kuril Basin of the Sea of Okhotsk. Deep Sea Res Part I 144:115–131

Xie P, Arkin PA (1997) Global precipitation: a 17-year monthly analysis based on gauge observations, satellite estimates, and numerical model outputs. Bull Am Meteorol Soc 78:2539–2558

Yagi M, Yasuda I, Tanaka T, Tanaka Y, Ono K, Ohshima KI, Katsumata K (2014) Re-evaluation of turbulent mixing vertical structure in the Bussol' Strait and its impact on water masses in the Okhotsk Sea and the North Pacific. Prog Oceanogr 126:121–134. https://doi.org/10.1016/j.pocean.2014.04.023

Yamazaki K (2000) Interaction between the wintertime atmospheric circulation and the variation in the sea ice extent of the Sea of Okhotsk (in Japanese with English abstract). Seppyo 62:345–354

Yamamoto-Kawai M, Watanabe S, Tsunogai S, Wakatsuchi M (2004) Chlorofluorocarbons in the Sea of Okhotsk: ventilation of the intermediate water. Geophys Res 109. https://doi.org/10.1029/2003JC001919

Yasuda I (1997) The origin of the North Pacific intermediate water. J Geophys Res 102:893–910. https://doi.org/10.1029/96JC02938

Yasunaka S, Nojiri Y, Nakaoka S, Ono T, Whitney FA, Telszewski M (2014) Mapping of sea surface nutrients in the North Pacific: basin-wide distribution and seasonal to interannual variability. J Geophys Res Oceans 119:7756–7771. https://doi.org/10.1002/2014JC010318

You Y, Suginohara N, Fukasawa M, Yasuda I, Kaneko I, Yoritaka H, Kawamiya M (2000) Roles of the Okhotsk Sea and Gulf of Alaska in forming the North Pacific intermediate water. J Geophys Res Oceans 105:3253–3280. https://doi.org/10.1029/1999JC900304

Watanabe YW, Wakita M, Maeda N, Ono T, Gamo T (2003) Synchronous bidecadal periodic changes of oxygen, phosphate and temperature between the Japan Sea deep water and the North Pacific intermediate water. Geophys Res Lett 30:2273. https://doi.org/10.1029/2003GL018338

Yasuda I, Osafune S, Tatebe H (2006) Possible explanation linking 18.6-year period nodal tidal cycle with bi-decadal variations of ocean and climate in the North Pacific. Geophys Res Lett 33:L08606. https://doi.org/10.1029/2005GL025237

Yasunaka S, Ono T, Nojiri Y, Whitney FA, Wada C, Murata A, Nakaoka S, Hosoda S (2016) Long-term variability of surface nutrient concentrations in the North Pacific. Geophys Res Lett 43(7):3389–3397

Chapter 4
Changes in Temperature, Chlorophyll Concentration, and Secchi Disk Depth in the Okhotsk Sea from 1998 to 2016

Chen-Tung Arthur Chen, Shujie Yu, Ting-Hsuan Huang, Yan Bai, and Xianqiang He

Abstract The Okhotsk Sea is located in a subarctic zone with characteristics such as ice cover in winter. Like other high-latitude seas, the Okhotsk Sea is undergoing rapid changes. Notably, its sea surface temperature (SST) increased by about 4.5 °C/century between 1998 and 2016, exceeding the reported rate of increase of 1.3 °C/century between 1982 and 2006. During the same period (1998–2016), the chlorophyll concentration increased by 0.01 μg/L (0.99%) annually. The Secchi disk depth (SDD) slightly increased at 0.018 m/yr. These changes in the SST, chlorophyll concentration and Secchi disk depth lead to reduced oxygen content, and may affect other physical and biological processes as well as carbon sequestration in the Okhotsk Sea.

Keywords Okhotsk Sea · Sea surface temperature · Chlorophyll concentration · Secchi disk depth · Temporal changes

C.-T. A. Chen (✉) · T.-H. Huang
Department of Oceanography, National Sun Yat-Sen University, Kaohsiung 804, Taiwan
e-mail: ctchen@mail.nsysu.edu.tw

T.-H. Huang
e-mail: thhuang@mail.nsysu.edu.tw

S. Yu · Y. Bai · X. He
State Key Laboratory of Satellite Ocean Environment Dynamics, Second Institute of Oceanography, Ministry of Natural Resources, Hangzhou 310012, China
e-mail: yvshujie@126.com

Y. Bai
e-mail: baiyan@sio.org.cn

X. He
e-mail: hexianqiang@sio.org.cn

C.-T. A. Chen and X. Guo (eds.), *Changing Asia-Pacific Marginal Seas*, Atmosphere, Earth, Ocean & Space, https://doi.org/10.1007/978-981-15-4886-4_4

4.1 Introduction

The Okhotsk Sea has an area of 1.528×10^6 km^2, making it the sixth largest marginal sea in the world and the third largest in the North Pacific; it has a maximum depth of over three thousand meters. In the north and northwest of the Okhotsk Sea is the Russian Far East; in the west is Sakhlin Is.; in the south is Hokkaido Is., and in the southeast is the Kuril Islands. Shelves occupy 40% of its surface area. Although this sea is located at temperate/subarctic latitudes, it has many of the characteristics of a polar ocean, including large seasonal variations in water temperature and a subarctic water column structure. It also has seasonal ice cover from December through April and an areal coverage that is comparable to that of the Bering Sea. The Okhotsk Sea connects to the open North Pacific through the Kuril Island chain. In the northwestern shelf region, the Amur River, one of the largest rivers in the world, supplies fresh water, heat, nutrients, and organic matter to the Okhotsk Sea (Fig. 4.1).

The cold, fresh but dense Okhotsk Sea Intermediate Water is believed to be an important source of North Pacific Intermediate Water (Watanabe and Wakatsuchi

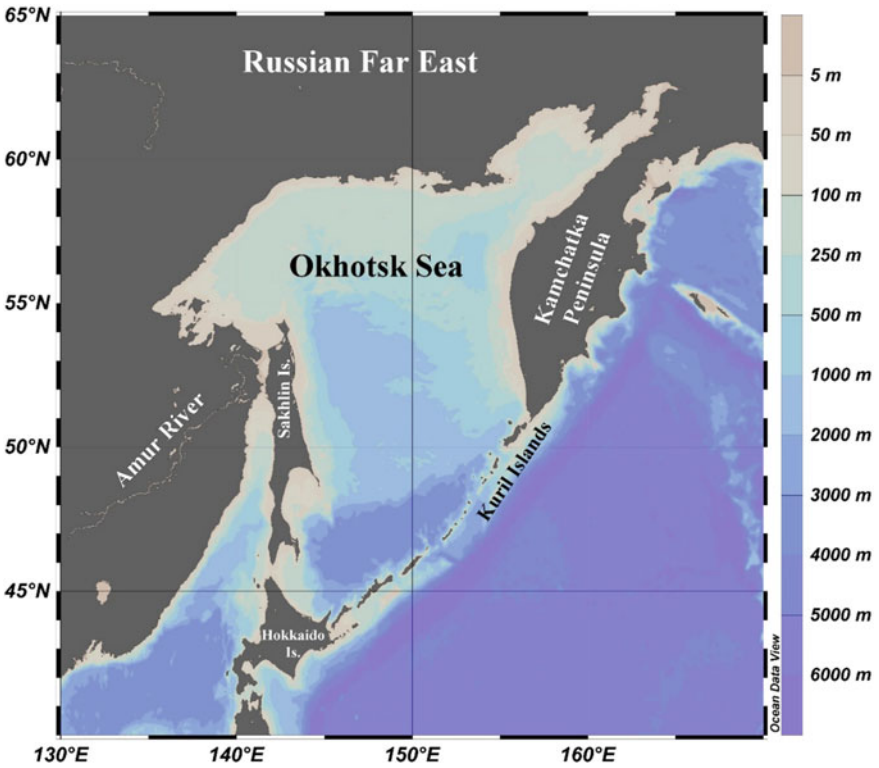

Fig. 4.1 Map of the Okhotsk Sea (drawn using ODV, Schlitzer, R., Ocean Data View, https://odv.awi.de, 2018)

1998). The SST is known to have increased and the sea ice cover has decreased over the last several thousand years following the Holocene Optimum (Harada et al. 2014), and the rates have accelerated (Nakanowatari and Mitsudera 2020). This investigation is concerned with only recent changes. Anthropogenic CO_2, tritium and chlorofluorocarbons (CFCs) have reportedly penetrated the Okhotsk Sea, and the pCO_2 of its surface water has been increasing, albeit at a slower rate due to the enhanced stratification (Wakita et al. 2003; Chen et al. 2004; Watanabe et al. 2013; Landschutzer et al. 2014). A brief review of the relevant literature follows. Then, the changes in SST, chlorophyll concentration and Secchi disk depth (SDD) between 1998 and 2016 are obtained from time series satellite records.

4.2 Known Temporal Changes

In summer, surface waters with pCO_2 between –20 and –90 μatm undersaturation are commonly observed in the Okhotsk Sea, whereas values ranging between –170 μatm undersaturated to 50 μatm supersaturated have also been reported. The lowest undersaturation of CO_2 has been measured along the eastern coast of Sakhalin and the northern shelf area. These undersaturations are attributed to enhanced phytoplankton productivity. Excess CO_2 penetrates to at least 1000 m (Chen and Tsunogai 1998; Andreev et al. 1999). Wong et al. (1998) reported that CFCs are present in the Okhotsk Sea Intermediate Water, which feeds into the North Pacific Intermediate Water, in which high concentrations of dissolved oxygen (DO), tritium, CFCs and excess CO_2 are detected (Tsunogai et al. 1995). Chen and Tsunogai (1998) reported an inventory of 0.18 ± 0.08 Gt excess carbon in the Okhotsk Sea. This value is not large but the export to the interior of the North Pacific, 0.011–0.18 Gt C yr^{-1}, is significant (Chen et al. 2004).

Strong winds that are coupled with intense vertical mixing and inter-leaving of waters in the winter increase the oceanic penetration of excess CO_2 in the Okhotsk Sea. Although this sea has a limited capacity to store this excess CO_2, it acts as a conveyer meaning that the dense shelf water that is formed in winter (Yamamoto-Kawai et al. 2004) flows out to the deep basins and enters the intermediate layer in the North Pacific. The water from the Sea of Japan also exports excess CO_2 into the intermediate layer of the Okhotsk Sea (Otsuki et al. 2003).

The Okhotsk Sea may have been affected by climate change. The warm Kamchatka Current Intermediate Water has reportedly warmed while the upper layer in the Oyashio and the Okhotsk Sea has cooled and become fresher (Rogachev 2000). Andreev and Kusakabe (2001) and Ito et al. (2017) demonstrated that the DO concentrations in the intermediate waters of the Okhotsk Sea and the western Subarctic Gyre have declined since the 1950s.

The above findings reveal that many biophysical parameters have changed in the Okhotsk Sea. Unfortunately, very few quantitative temporal variabilities based on field data have been obtained. The following concerns almost continuous time-series

satellite-derived SST, chlorophyll concentration and SDD values between 1998 and 2016.

4.3 Sea Surface Temperature

SST data for the period 1981–2016 were taken from the AVHRR_OI dataset, which is a product of the Group for High-Resolution Sea Surface Temperature (GHRSST) and can be obtained from National Centers for Environmental Information (NCEI), NOAA (https://data.nodc.noaa.gov/ghrsst/L4/GLOB/NCEI/AVHRR_OI/). Data were averaged each month between 1998 and 2016 to provide monthly climate data. Trends in SST were assessed by subtracting monthly climatological mean values from monthly mean data to remove the seasonal signal, and then performing linear regression analysis. Pixels were removed when the number of available data was less than half of the total number of data (228 monthly data). The statistical significance of the trends (expressed as a P value, where $P < 0.1$ indicates the existence of a trend at a confidence level of over 90%) was assessed using the F-test. Details can be found in Chen et al. (2020a).

The annual mean SST is less than 7 °C everywhere except at the very southern end of the sea, north of Hokkaido (Fig. 4.2a). The SST exhibits a large seasonal variation with a low of slightly below 0 °C in winter and a high of 13 °C in summer (Fig. 4.3a). Overall, the temporal SST change in the Okhotsk Sea, 4.5 °C/century, was not statistically significant ($p = 0.41$) in 1998–2016 (Fig. 4.4a) even though marked warming occurred in central and eastern regions of the Okhotsk Sea (Fig. 4.4a). Further, increasing trends of SST are found around Hokkaido, off Hokkaido (41~42° N, 146~147° E), and in the western subarctic gyre. On the other hand, decreasing trend of SST can be seen along the Kuril Islands and off Hokkaido (about 42° N, 149~153° E). Note this increase in SST is only slightly lower than found for the Bering Sea (5.5 °C/century), but is much higher than found for the warm South China Sea (1.2 °C/century; Chen et al. 2020b) for the same period (Chen et al. 2020a).

Based on the AVHRR_OI dataset, He et al. (2017) reported a similar rate of increase of about 5 °C/century between 1998 and 2010 but Belkin (2009) reported a much lower rate of increase of 1.3 °C/century between 1982 and 2006. Belkin (2009) used SST climatological data from the U.K. Meteorological Office Hadley Centre. Different sources of SST data and different time spans might have contributed to the different rates of SST increase. Generally, a longer time-series yields a rate of change of smaller magnitude as a result of temporal smoothing. Both sides of the Kamchatka Peninsula witnessed the most intense overall SST rise at a rate of 5–6 °C/century, which might have contributed to the increased growth of phytoplankton in recent years.

Further, increasing trends of SST are found around Hokkaido, off Hokkaido (41~42° N, 146~147° E), and in the western subarctic gyre. On the other hand, decreasing trend of SST can be seen along the Kuril Islands and off Hokkaido (about 42° N, 149~153° E).

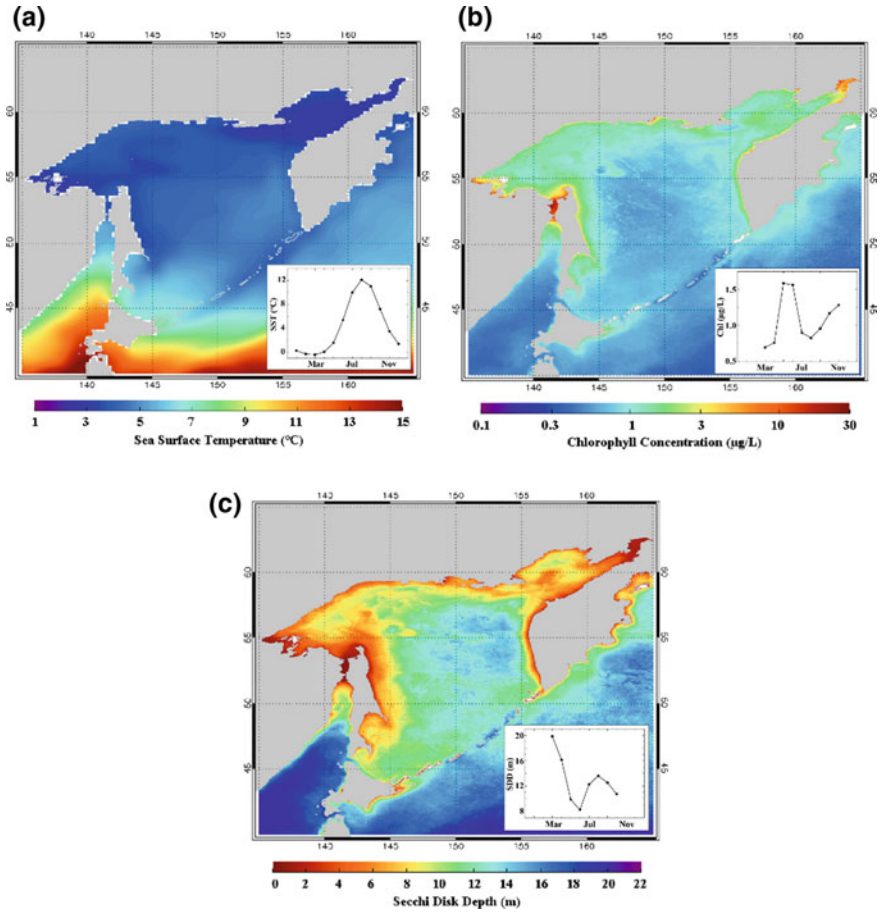

Fig. 4.2 Climatological map and monthly mean of **a** SST, **b** chlorophyll concentration and **c** SDD in the Okhotsk Sea. The insets are climatological monthly mean curves in the enclosed area

Bai et al. (2018) recently evaluated the rates of change of the SSTs of 12 marginal seas (not including the Okhotsk Sea) around the Eurasian continent from 2003 to 2014. The 12 seas exhibited increasing SSTs, with the Black Sea exhibiting the fastest warming (19 °C/century), followed by the Baltic Sea and the Mediterranean Sea (10 °C/century). The Sea of Japan, the East China Sea, and the Persian Gulf also exhibited rapid warming of about 9 °C/century. The low-latitude marginal seas, such as the South China Sea, the Java-Banda Sea, the Bay of Bengal, the Arabian Sea and the Red Sea have a low warming rate (~3 °C/century). Interestingly, the North Sea has a much lower warming rate (1.3 °C/century) than that of the Okhotsk Sea (4.5 °C/century), despite its similar latitude. Since the North Sea does not have ice cover, whether losing sea ice in the Okhotosk Sea leads to enhanced absorption of solar energy, hence higher warming rate, remains to be investigated.

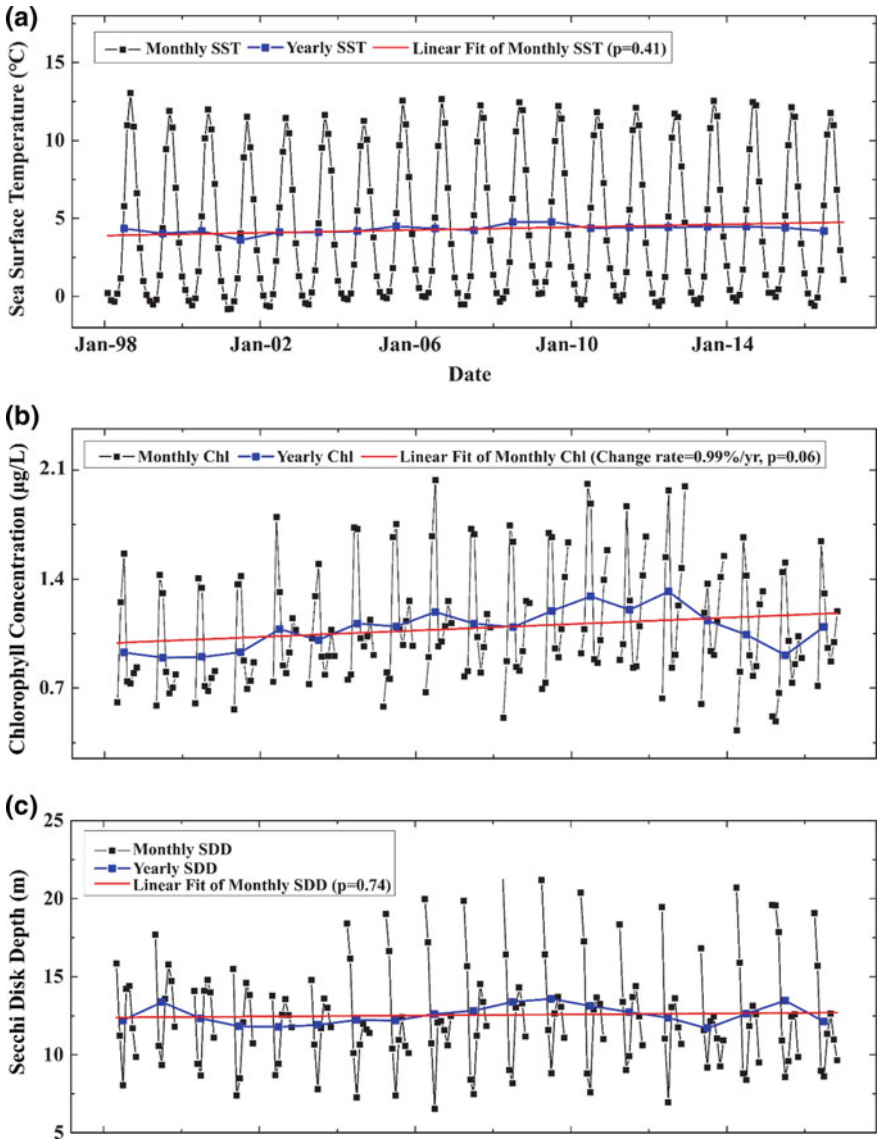

Fig. 4.3 Time series of **a** SST, **b** chlorophyll concentration, and **c** SDD in the Okhotsk Sea during 1998–2016

Note that the above is based on satellite data hence is concerned with only surface waters. The warming, however, is not limited to the surface layer. For instance, Nakanowatari and Mitsudera (2020) reported a warming trend as high as 0.62 ± 0.18 °C between 1955 and 2004 at the isopycnal surface of 27.0 σ_θ off the coast of Sakhalin.

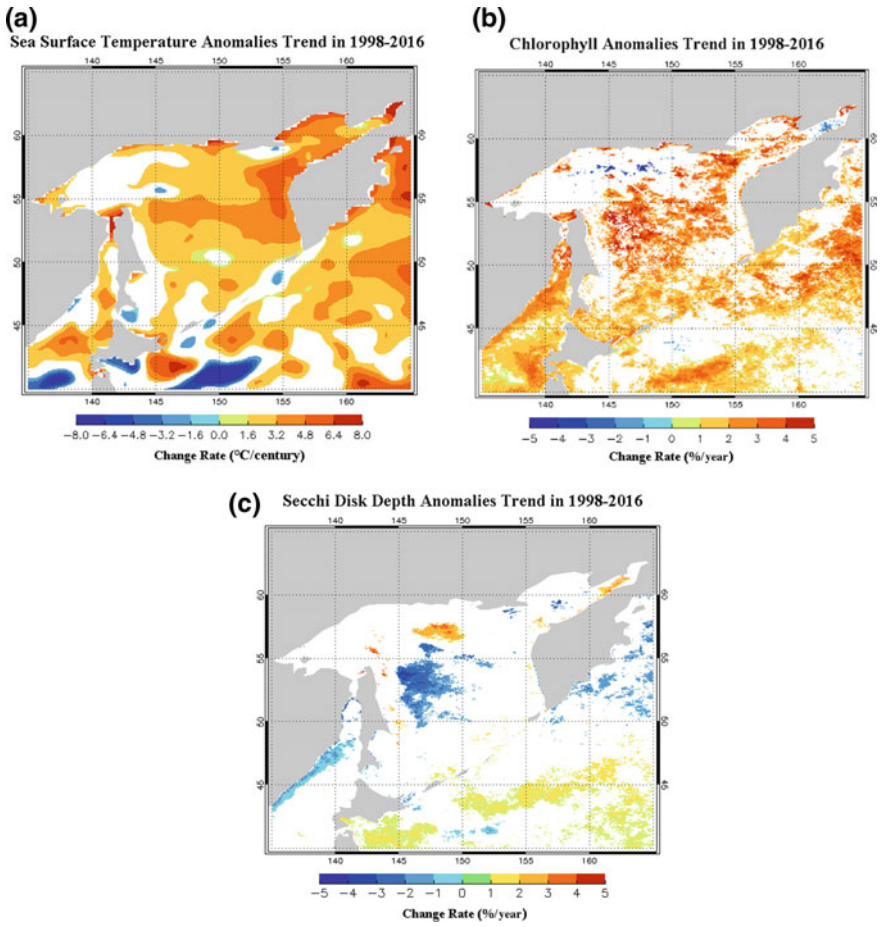

Fig. 4.4 Trend maps of **a** SST, **b** chlorophyll concentration, and **c** SDD in the Okhotsk Sea during 1998–2016. (Only pixels that satisfy the significance criterion $P < 0.1$ are indicated in bright colors)

4.4 Chlorophyll Concentration

The chlorophyll concentration data for the period of 1998–2016 were obtained from the Ocean Colour project of the ESA Climate Change Initiative (CCI) (http://www.esa-oceancolour-cci.org). These are merged data from multiple ocean color satellite sensors. Trends in chlorophyll concentration and SDD were assessed pixel by pixel and each was reported as a percentage per year, which is the ratio of the linear slope (as shown in Fig. 4.4b) to the average over the period. Details can be found in Chen et al. (2020a).

As elsewhere in the global oceans (Chen et al. 2008; Naik and Chen 2008; Dai et al. 2009), the chlorophyll concentration is highest in bays around the Okhotsk Sea

and in the plume off the Amur River (Fig. 4.2b). The chlorophyll concentration is also higher in coastal regions than in more open waters (Fig. 4.2b).

The chlorophyll concentration exhibits a large seasonal variation (Fig. 4.3b), typically peaking around May and reaching a minimum in December and January; this pattern is similar to that found in other high-latitude seas. This variation perhaps reflects the combined effect of limited available solar energy in winter and the blocking of light by sea ice, both not reflected in the satellite observations. Also, the chlorophyll concentration exhibits a large interannual variability, but also a generally increasing trend (Fig. 4.3b). This finding is consistent with the conclusion of Bai et al. (2018), who found that high-latitude marginal seas around the Eurasian continent generally had increasing chlorophyll concentrations between 2003 and 2014. The Baltic Sea had the highest rate of increase of 1.92%/yr (0.19 μg/L per year), followed by the Sea of Japan and the East China Sea (1%/yr). Between 1998 and 2016, chlorophyll concentration in the Okhotsk Sea increased at a similar rate of 0.99%/yr (or 0.01 μg/L per year) ($p = 0.06$), consistent with the result of He et al. (2017) for 1997–2010. The significant increases took place throughout the sea, except in the northwestern parts where sporadic declines occurred (Fig. 4.4b). The greatest rise of 4–5% per year occurred in the central basin and in the bay in the northeast. By way of comparison the Bering Sea also witnessed an increase of 0.011 μg/L/yr between 1998 and 2016 (Chen et al. 2020a) but the South China Sea witnessed only a small increase of 0.0012 μg/L/yr for the same period (Chen et al. 2020b).

Increasing chlorophyll concentration enhances oxygen production but the oxygen concentration in most of the Okhotsk Sea has fallen since 1960 (Schmidtko et al. 2017). Note that during wintertime, strong vertical mixing happens in the Okhotsk Sea. Also, strong tidal mixing near Kuril Islands occurs. Apparently, the increase in SST, which reduces oxygen solubility and increases the rate of oxygen-consuming metabolism, plays a greater role than increasing chlorophyll concentration in reducing the oxygen content in the Okhotsk Sea.

4.5 Secchi Disk Depth

The SDD is a good index of water transparency, which is related to light penetration, surface reflectance and suspended particulate matter and phytoplankton abundance, etc. (Fei 1986; Tilzer et al. 1994; Sanden and Hakansson 1996; Doron et al. 2007; He et al. 2017). Relevant data for the Okhotsk Sea over the period 1998–2016 were obtained from the Globcolour project (http://globcolour.info/). Details can be found in Chen et al. (2020a). Figure 4.2c displays a climatological map of the SDD. The spatial distribution is clearly influenced by the chlorophyll concentration (Fig. 4.2b): the SDD is generally low in the bays, near the coast, and in the area around the mouth of the Amur River. Notably, rivers export both nutrients and suspended sediments, and in nearshore areas, tidal movements and winds effective in disturbing bottom sediments and in moving nutrient-rich bottom waters to the euphotic zone. As a result, enhanced productivity (high chlorophyll concentration) but reduced transparency

(low SDD) run in tandem. In the central and southeastern Okhotsk Sea away from land masses, the SDD is high whereas the chlorophyll concentration is low.

During the period 1998–2016, the SDD in the Okhotsk Sea slightly but insignificantly increased by 0.018 m/yr (0.14%/yr) ($p = 0.74$; Fig. 4.3c). Yet, in the central basin, the SDD declined markedly at a rate of 3–4% per year (Fig. 4.4c), probably as a result of the increasing chlorophyll concentration. The distribution of patches with increased SDD broadly matches that of patches of reduced chlorophyll concentration (Fig. 4.4b). Note the SDD correlates negatively with chlorophyll concentration (Fig. 4.5).

By way of comparison, the 12 marginal seas of the Eurasian continent that were studied by Bai et al. (2018) all showed increasing SDD between 2003 and 2014. The Persian Gulf had the highest percentage increase (3.02%/yr, or 0.25 m/yr). The Java-Banda Sea and Arabian Sea also had high percentage increases of about 1.3%/yr or 0.35 m/yr in absolute terms. The other nine marginal seas had rates of increase of less than 1%/yr. However, even the lowest reported rate of 0.18%/yr (0.05 m/yr) for the South China Sea exceeded that of the Okhotsk Sea.

He et al. (2017) also reported a much higher rate of increase of SDD (~0.08 m/yr) between 1997 and 2010 for the Okhotsk Sea. The different durations of data coverage and different satellite records make meaningful comparisons of various results difficult. For instance, Bai et al. (2018) began with data for 2003—a year of rather low SDD, at least in the Okhotsk Sea (Fig. 4.3c)—and ended their analyses in the year 2014, after which the SDD exhibits a steady decline) (Fig. 4.3c). Limiting our analysis to 2003–2014 would have yielded a higher rate of increase in SDD. Moreover, both He et al. (2017) and Bai et al. (2018) used single satellite records from SeaWiFS and Aqua/MODIS, respectively, whereas the present study was based on merged records from multiple satellites. Nevertheless, all results reveal a net increase in the SDD in the Okhotsk Sea in the last two decades. Using the same method as this study, Chen et al. (2020a) found no significant change in SDD in the Bering Sea, but found an increase of 0.036 m/yr for the South China Sea (Chen et al. 2020b).

4.6 Conclusions

As one of the sources of the North Pacific Intermediate Water, the Okhotsk Sea plays an important role in carbon sequestration. In this study, which is based on time-series satellite records, changes in sea surface temperature, chlorophyll concentration and Secchi disk depth in the Okhotsk Sea from 1998 to 2016 were investigated. Overall, the SST, chlorophyll concentration and Secchi disk depth in the Okhotsk Sea all increased over that period. The SST increased at a rate of 4.5 °C/century—higher than the rate of increase of 1.3 °C/century over the period 1982–2006, reported elsewhere. The chlorophyll concentration and the SDD increased by 0.01 μg/L (0.99%) and 0.018 m per year, respectively. These changes in the SST, chlorophyll concentration and Secchi disk depth may alter the physical and biological processes in, as well as the carbon sequestration by, the Okhotsk Sea. These potential effects warrant future

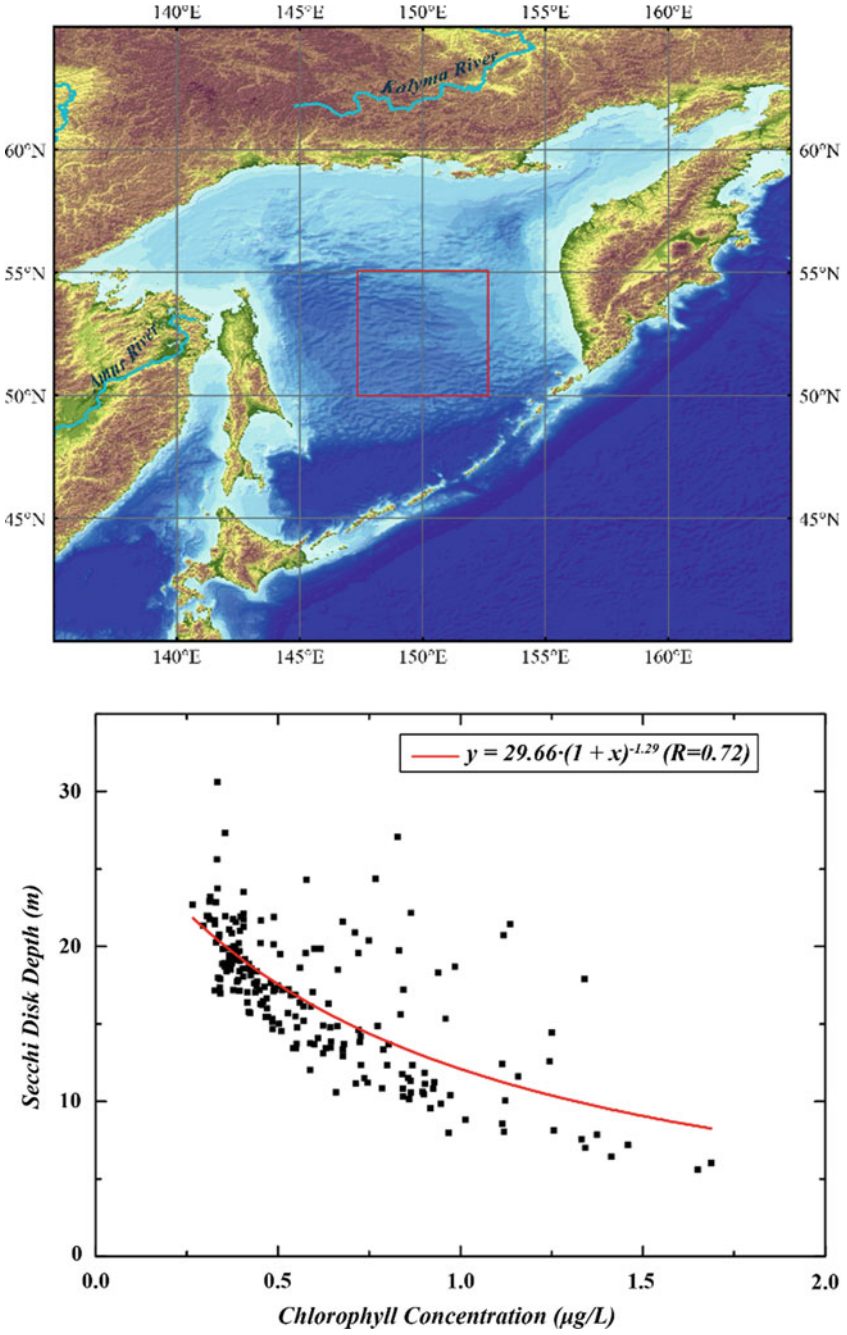

Fig. 4.5 Chlorophyll concentration versus SDD in the selected area

investigations. More importantly, validation of the above requires field data which are urgently needed.

Acknowledgements The authors would like to thank the Ministry of Science and Technology of the Republic of China, Taiwan, for financially supporting this research under contract MOST 107-2611-M-110-006, 107-2611-M-110-021 and 107-2611-M-110-012 and the Ministry of Education (Higher Education Sprout Program) of Republic of China. Two anonymous reviewers provided constructive comments which strengthened the manuscript.

References

Andreev AG, Kusakabe M (2001) Interdecadal variability in dissolved oxygen in the intermediate water layer of the Western Subarctic Gyre and Kuril Basin (Okhotsk Sea). Geophys Res Lett 28(12):2453–2456

Andreev AG, Bychkov AS, Zhabin IA (1999) Excess CO_2 penetration in the Okhotsk Sea. In: 2nd international symposium on CO_2 in the oceans, extended abstract, Tsukuba, 18–22 January 1999, pp 279–288

Bai Y, He XQ, Yu SJ, Chen CTA (2018) Changes in the ecological environment of the marginal seas along the Eurasian Continent from 2003 to 2014. Sustainability 10(3):635. https://doi.org/10.3390/su10030635

Belkin IM (2009) Rapid warming of large marine ecosystems. Prog Oceanogr 81(1–4):207–213

Chen CTA, Tsunogai S (1998) Carbon and nutrients in the ocean. In: Galloway N, Melillo JM (eds) Asia change in the context of global climate change. Cambridge University Press, pp 271–307

Chen CTA, Andreev A, Kim KR, Yamamoto M (2004) Roles of continental shelves and marginal seas in the biogeochemical cycles of the North Pacific Ocean. J Oceanogr 60(1):17–44. https://doi.org/10.1023/B:JOCE.0000038316.56018.d4

Chen CTA, Wang SL, Lu XX, Zhang SR, Lui HK, Tseng HC, Wang BJ, Huang HI (2008) Hydrogeochemistry and greenhouse gases of the Pearl River, its estuary and beyond. Quatern Int 186:79–90. https://doi.org/10.1016/j.quaint.2007.08.024

Chen CTA, Yu SJ, Huang TH, Bai Y, He XQ (2020a) Changes in temperature, chlorophyll concentration, and Secchi disk depth in the Bering Sea from 1998 to 2016. In: Chen CTA, Guo XY (eds) Changing Asia-Pacific marginal seas. Springer International Publishing (in press)

Chen CTA, Yu SJ, Huang TH, Lui HK, Bai Y, He XQ (2020b) Changing biogeochemistry in the South China Sea. In: Chen CTA, Guo XY (eds) Changing Asia-Pacific Marginal Seas. Springer International Publishing (in press)

Dai MH, Lu ZM, Zhai WD, Chen BS, Cao ZM, Zhou KB, Cai WJ, Chen CTA (2009) Diurnal variations of surface seawater pCO_2 in contrasting coastal environments. Limnol Oceanogr 54(3):735–745. https://doi.org/10.4319/lo.2009.54.3.0735

Doron M, Babin M, Mangin A, Hembise O (2007) Estimation of light penetration, and horizontal and vertical visibility in oceanic and coastal waters from surface reflectance. J Geophys Res 112:C6003. https://doi.org/10.1029/2006JC004007

Fei ZL (1986) Study on the water color and transparency in the Bohai Sea. J Oceanogr Huanghai Bohai Sea 2:26–29 (in Chinese with English abstract)

Harada N, Katsuki K, Nakagawa M, Matsumoto A, Seki O, Addison JA, Finney BP, Sato M (2014) Holocene sea surface temperature and sea ice extent in the Okhotsk and Bering Seas. Prog Oceanogr 126:242–253. https://doi.org/10.1016/j.pocean.2014.04.017

He XQ, Pan DL, Bai Y, Wang TY, Chen CTA, Zhu QK, Hao ZZ, Gong F (2017) Recent changes of global ocean transparency observed by SeaWiFS. Cont Shelf Res 143:159–166. https://doi.org/10.1016/j.csr.2016.09.011

Ito T, Minobe S, Long MC, Deutsch C (2017) Upper ocean O_2 trends: 1958–2015. Geophys Res Lett 44(9):4214–4223. https://doi.org/10.1002/2017GL073613

Landschutzer P, Gruber N, Bakker DCE, Schuster U (2014) Recent variability of the global ocean carbon sink. Global Biogeochem Cycles 28(9):927–949. https://doi.org/10.1002/2014GB004853

Naik H, Chen CTA (2008) Biogeochemical cycling in the Taiwan Strait. Estuar Coast Shelf Sci 78(4):603–612. https://doi.org/10.1016/j.ecss.2008.02.004

Nakanowatari T, Mitsudera H (2020) Long-term trend and interannual to decadal variability in the Sea of Okhotsk. In: Chen CTA, Guo XY (eds) Changing Asia-Pacific marginal seas. Springer International Publishing (in press)

Otsuki AS, Watanabe S, Tsunogai S (2003) Absorption of atmospheric CO_2 and its transport to the intermediate layer in the Okhotsk Sea. J Oceanogr 59(5):709–717

Rogachev KA (2000) Recent variability in the Pacific western subarctic boundary currents and Sea of Okhotsk. Prog Oceanogr 47(2–4):299–336

Sanden P, Hakansson B (1996) Long-term trends in Secchi depth in the Baltic Sea. Limnol Oceanogr 41(2):346–351. https://doi.org/10.4319/lo.1996.41.2.0346

Schmidtko S, Stramma L, Visbeck M (2017) Decline in global oceanic oxygen content during the past five decades. Nature 542(7641):335–339. https://doi.org/10.1038/nature21399

Tilzer MM, Gieskes WW, Heusel R, Fenton N (1994) The impact of phytoplankton on spectral water transparency in the southern-ocean—implications for primary productivity. Polar Biol 14(2):127–136. https://doi.org/10.1007/BF00234975

Tsunogai S, Watanabe S, Honda M, Aramaki T (1995) North Pacific Intermediate water studied chiefly with radiocarbon. J Oceanogr 51:519–536

Wakita M, Watanabe YW, Watanabe S, Noriki S, Wakatsuchi M (2003) Oceanic uptake rate of anthropogenic CO_2 in a subpolar marginal sea: The Sea of Okhotsk. Geophys Res Lett 30(24):2252. https://doi.org/10.1029/2003GL018057

Watanabe T, Wakatsuchi M (1998) Formation of 26.8-26.9 σ_θ water in the Kuril Basin of the Sea of Okhotsk as a possible origin of North Pacific Intermediate Water. J Geophys Res 103 (C2):2849–2865. https://doi.org/10.1029/97jc02914

Watanabe YW, Nishioka J, Nakatsuka T (2013) Decadal time evolution of oceanic uptake of anthropogenic carbon in the Okhotsk Sea. Geophys Res Lett 40(2):322–326. https://doi.org/10.1002/grl.50113

Wong CS, Matear RJ, Freeland HJ, Whitney FA, Bychkov AS (1998) WOCE line P1W in the Sea of Okhotsk: 2. CFCs and the formation rate of intermediate water. J Geophys Res 103(C8):15625–15642. https://doi.org/10.1029/98jc01008

Yamamoto-Kawai M, Watanabe S, Tsunogai S, Wakatsuchi M (2004) Chlorofluorocarbons in the Sea of Okhotsk: Ventilation of the intermediate water. J Geophys Res 109:C09S11. https://doi.org/10.1029/2003jc001919

Chapter 5
Long-Term Changes in the Abyssal Japan Sea (East Sea): A Physical View

Tomoharu Senjyu

Abstract The Japan Sea (East Sea) is of interest because it includes a local system for the formation of deep water and a thermohaline circulation system similar to that found in the Atlantic Ocean. A long-term trend of warming and decrease in the oxygen concentration have been reported in the deep layer of the Japan Sea, which are thought to be a result of global warming. Although the minimum oxygen decrease rate at approximately 1000 m suggests a relatively active supply of new deep water to the depths, the overall deep water formation has been stagnant since the 1970s throughout the water column. In addition to the gradual linear trends, decadal-scale variations in temperature and oxygen concentration have been reported in the abyssal Japan Sea. The correlation between the decadal-scale variation and the Arctic oscillation index indicates that the deep water formation in the Japan Sea is modulated by the Arctic oscillation via the sea surface temperature in the East China Sea. A weakening of the deep flow was suggested by a recent revisit observation of the northeastern Japan Sea, although no significant long-term trend has been reported of the deep flow in the southwestern basin.

Keywords Japan Sea Proper Water · Deep water formation · Warming trend · Decreasing oxygen concentration · Global warming · Decadal-scale variation · Arctic oscillation · Thermohaline circulation

5.1 Introduction

The Japan Sea (East Sea) is a marginal sea that is loosely isolated from the northwest of the North Pacific by the Japanese Islands and Sakhalin (Fig. 5.1). Four narrow shallow straits (the Tsushima, Tsugaru, Soya, and Mamiya Straits) connect the Japan Sea with the East China Sea, the North Pacific, and the Okhotsk Sea. Part of the subtropical water that originates in the Kuroshio is transported from the East China Sea to the subarctic North Pacific and the Okhotsk Sea via the Japan Sea. Therefore,

T. Senjyu (✉)
Research Institute for Applied Mechanics, Kyushu University, 6-1 Kasuga-Koen, Kasuga City, Fukuoka 816-8580, Japan
e-mail: senjyu@riam.kyushu-u.ac.jp

C.-T. A. Chen and X. Guo (eds.), *Changing Asia-Pacific Marginal Seas*, Atmosphere, Earth, Ocean & Space, https://doi.org/10.1007/978-981-15-4886-4_5

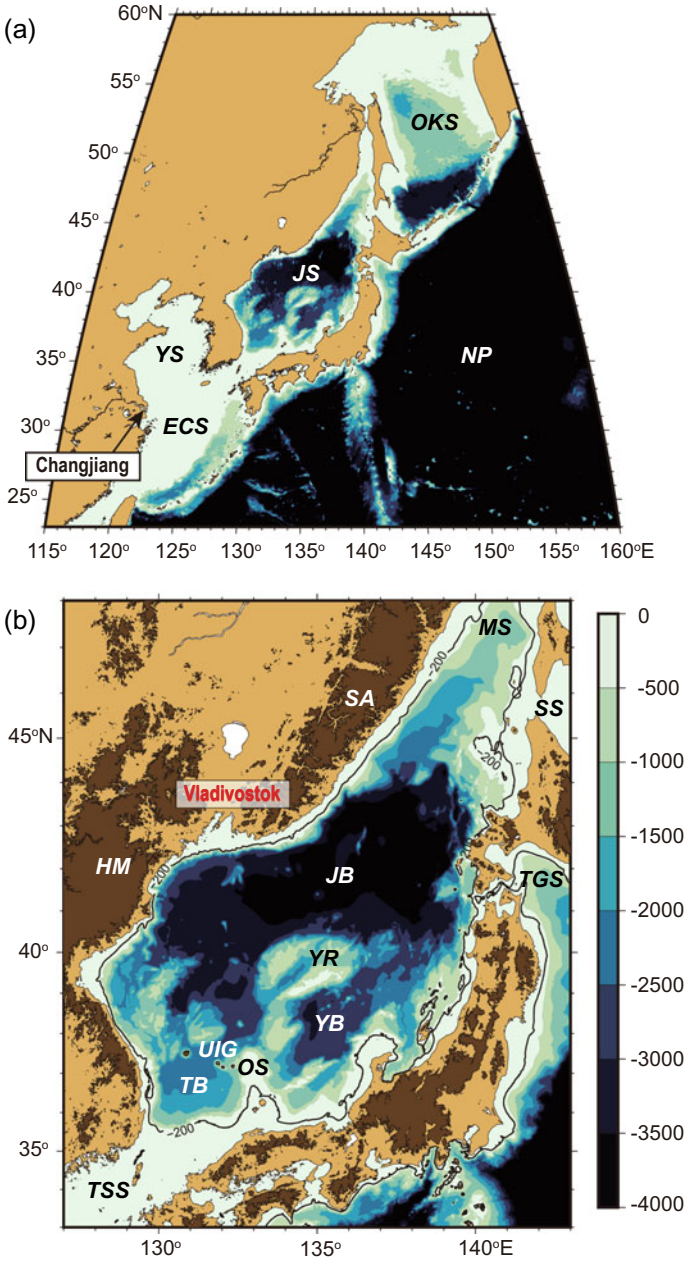
(a)
60°N
55°
50°
45°
40°
35°
30°
25°
115°
120°
125°
130°
135°
140°
145°
150°
155°
160°E
OKS
JS
YS
NP
ECS
Changjiang
(b)
45°N
40°
35°
130°
135°
140°E
MS
SA
SS
Vladivostok
HM
JB
TGS
YR
YB
UIG
OS
TB
TSS
200
0
-500
-1000
-1500
-2000
-2500
-3000
-3500
-4000

◀**Fig. 5.1** Bottom topography **a** around and **b** in the Japan Sea. (**a**) Abbreviations of OKS, JS, YS, ECS, and NP indicate the Okhotsk, Japan, Yellow, East China Seas, and the North Pacific, respectively. (**b**) The Tsushima, Tsugaru, Soya, and Mamiya Straits are indicated as TSS, TGS, SS, and MS, respectively. The 200 m isobaths are drawn to show the shallowness of the straits. Abbreviations of JB, YB, TB, YR, OS, and UIG denote the Japan, Yamato, Tsushima Basins, Yamato Rise, Oki Spur, and Ulleung Interplain Gap, respectively. Brown parts on the land show areas higher than 500 m from the sea level. The Shikhote-Alin and Hamgyong Mountains are indicated by SA and HM, respectively

the Japan Sea is an important pathway for the transportation of subtropical water to the subarctic regions (Talley et al. 2006).

The warm and saline subtropical water that flows into the Japan Sea is carried by the Tsushima Current and the East Korean Warm Current to the north (Fig. 5.2), together with low salinity water that is mainly derived from the freshwater of the Changjiang, the largest river in Asia (Fig. 5.1a) (Senjyu et al. 2006). The Japan Sea includes surface circulations in both the south and the north bound by a subarctic front that lies at about 40° N, similar to the subtropical and subarctic gyres in the North Pacific. The East Korean Warm Current is the western boundary current for the southern circulation. The Liman Current is another western boundary current for the northern circulation, which transports cold and less-saline water southwestwards along the Russian coast.

A unique feature of the Japan Sea, which is not seen in any other North Pacific marginal seas, is the self-contained thermohaline circulation system that includes the formation of deep water. The Japan Sea has the largest volume (1.690×10^6 km^3) and mean depth (1667 m) compared to the adjacent Okhotsk Sea and the East China and Yellow Seas, although the area and maximum depth of the other seas show comparable values to those of the Japan Sea (Table 5.1). However, the deep areas of both the Okhotsk Sea and the East China Sea are limited in the south (Fig. 5.1a). The Japan Sea is therefore seen as relatively deep in comparison. Contrary to the significant depth of the sea, the four straits connecting the Japan Sea with other seas are shallower than 120 m. This means that areas of the Japan Sea that are deeper than 200 m are completely isolated from the adjacent water (Fig. 5.1b). This bowl-like topography of the sea, a semi-enclosed deep basin with shallow sills, indicates that the deep water in the Japan Sea must be produced within the sea itself.

The Japan Meteorological Agency (JMA) reported that the sea surface temperature (SST) in the central part of the Japan Sea shows a significant warming trend at a rate of +1.71 °C per 100 years, which is the highest rate of warming around Japan and corresponds to 3.2 times the global mean of +0.54 °C per 100 years (http://www.data.jma.go.jp/gmd/kaiyou/english/long_term_sst_japan/sea_surface_temperature_around_japan.html). In addition to this long-term trend of warming, variability on interannual and decadal-scale has been reported for the temperature of both the sea surface and the upper ocean (e.g., Park and Oh 2000; Hong et al. 2001; Minobe et al. 2004; Na et al. 2012). Large-scale atmospheric variations such as the Southern Oscillation, Arctic Oscillation (AO), and the North

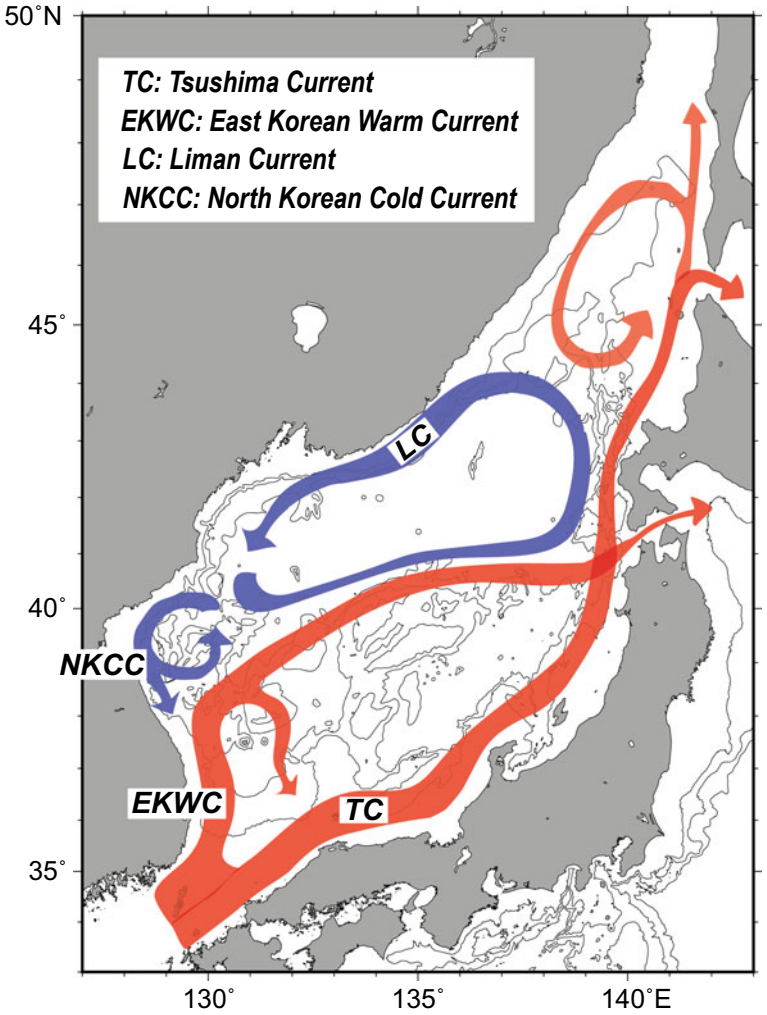

Fig. 5.2 Major surface currents in the Japan Sea. Red and blue colors indicate warm and cold currents, respectively

Table 5.1 Comparison of area, volume, maximum depth, and mean depth among the Okhotsk, Japan, and Yellow and East China Seas (National Astronomical Observatory of Japan 2018)

	Area (10^6 km^2)	Volume (10^6 km^3)	Max. depth (m)	Mean depth (m)
Okhotsk Sea	1.392	1.354	3372	973
Japan Sea	1.013	1.690	3796	1667
Yellow and East China Seas	1.202	0.327	2292	272

Atlantic Oscillation have been suggested as the cause for this long-term variability in temperature.

Long-term trends of temperature increase and decreases in dissolved oxygen (DO) concentration have also been reported in the deep layer of the Japan Sea, as well as decadal-scale variations, although any relationship with the variability in the upper ocean is unclear. Since there is a substantial volume of deep water in the Japan Sea as shown in the next section, any slight warming of the deep water indicates a significant increase in heat content, which means a structural change of the sea. Therefore, in this chapter, we introduce these changes found in the Japan Sea, focusing on the deep water. With regards to the variability in the upper ocean, an excellent review written by Park et al. (2016) is available.

5.2 The Japan Sea Proper Water

The deep basin of the Japan Sea is subdivided into three basins (the Japan, Yamato, and Tsushima (Ulleung) Basins) by a shallow central bank (the Yamato Rise) and a southern spur (the Oki Spur) (Fig. 5.1b).

As a typical example, the vertical profiles of potential temperature (PT), salinity, DO concentration, and potential density referred at the sea surface (σ_θ) in the Japan Basin are shown in Fig. 5.3. The layer below the main thermocline (>300 m) is occupied by a cold (<1.0 °C) and less saline (34.06–34.07) water mass. This water mass is known as the Japan Sea Proper Water (JSPW) and occupies more than 80% of the total volume of the Japan Sea (Uda 1934; Yasui et al. 1967). Worthington (1981) pointed out that the JSPW is one of the most homogeneous water masses in the world, although careful examination of its water characteristics revealed that the JSPW can be subdivided into three water masses (e.g., Nitani 1972; Kim et al. 2004). For this study, we refer to these as the upper portion of JSPW, Deep Water, and Bottom Water, in accordance with Senjyu and Sudo (1993, 1994) and Gamo and Horibe (1983). Another important characteristic of the JSPW is a high concentration of DO (approximately 200 μmol kg^{-1}).

The JSPW is formed in the northwestern Japan Basin in the winter by deep convection (Sudo 1986, Senjyu and Sudo 1993, 1994, 1996; Senjyu et al. 2002). The depth of the isopycnal surface which corresponds with the top of the JSPW ($32.00\sigma_1$, where σ_1 is a potential density referred to 1000 dbar, and the σ_1 surface coincides roughly with the $27.31\sigma_\theta$ surface in the Japan Sea (Senjyu and Sudo 1994)) during winter is shown in Fig. 5.4. An outcropping of the isopycnal surface appears to the southeast of Vladivostok where deep convection develops as a result of cooling at the sea surface. This process of convective formation accounts for the main features of the JSPW; the homogeneity, low temperature, and richness in DO.

Atmospheric disturbances play an important role in the formation of the JSPW. An example of atmospheric conditions favorable for the formation of JSPW is shown in Fig. 5.5, with a representation of the sea level pressure, the wind, and the air temperature during January 26–29, 2003 (Cui and Senjyu 2010). In this example, an

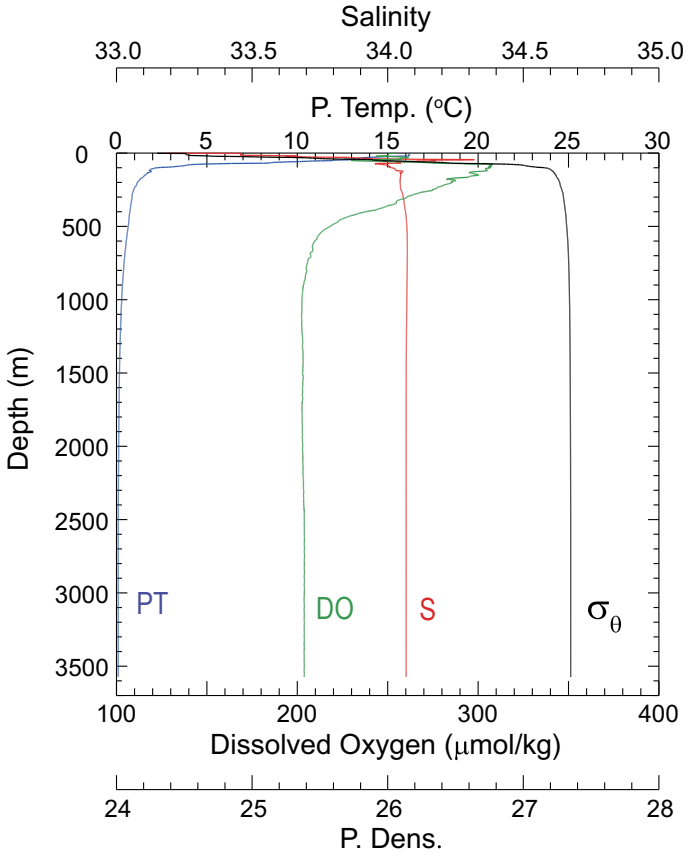

Fig. 5.3 Typical profiles of potential temperature (PT, blue), salinity (S, red), dissolved oxygen (DO, green), and potential density (σ_θ, black) in the Japan Sea, which were measured at 40° 49.34′ N 137° 59.18′ E in the Japan Basin on November 13, 2015 by the Japan Meteorological Agency

atmospheric low pressure occurred in the East China Sea on January 26, and at the same time weak easterly winds blew over the Japan Sea with the 0 °C air temperature contour located at 42–45° N. When the low pressure migrated into the Japan Sea on January 27, strong cyclonic winds prevailed over the sea. The low pressure reached the northern Japan Sea on January 28 and finally moved into the Okhotsk Sea on January 29. During this period, a northwesterly monsoon developed as a result of the strong northeast–southwest gradient in atmospheric pressure. Noteworthy is jet-like winds originating near Vladivostok, these are converged monsoon winds by the presence of two coastal mountain chains: the Shikhote-Alin Mountains and the Hamgyong Mountains (Fig. 5.1b) (Seung and Yoon 1995; Kawamura and Wu 1998). These strong winds brought cold air to the Japan Sea; on January 28–29, cold air with temperature lower than 0 °C (light-gray zone in the lower panels of Fig. 5.5) spread rapidly southwards, and air colder than −5 °C (dark-gray zone) appeared south of

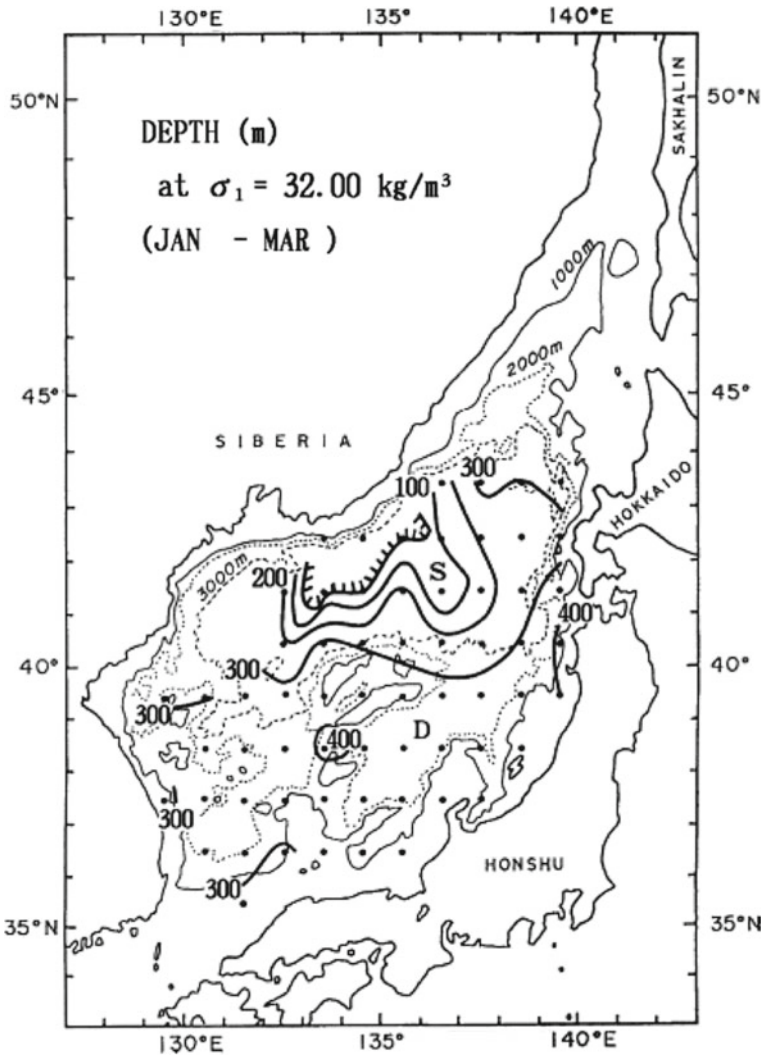

Fig. 5.4 Winter distribution of the isopycnal surface corresponding to the top of the JSPW ($32.00\sigma_1$) based on the climatological mean for 1964–1985 (Senjyu and Sudo 1996). The hatched area indicates outcropping onto the sea surface

Vladivostok. These occasional cold jets, the cold-air outbreaks, effectively cool the sea surface south of Vladivostok where the JSPW forms.

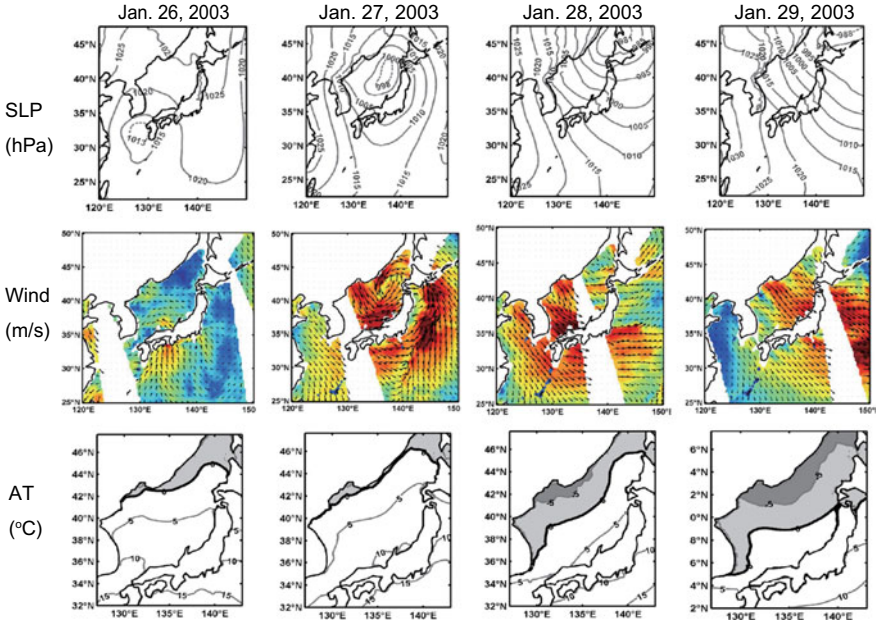

Fig. 5.5 Distributions of sea level pressure (upper), wind (middle), and air temperature (lower) during the period January 26–29, 2003 (Cui and Senjyu 2010). White gaps in the wind figures are due to missing data in the QuickScat observations

5.3 Long-Term Trends in the JSPW

Long-term trends of increasing PT and decreasing DO have been reported in the JSPW (Gamo et al. 1986; Minami et al. 1999; Kim et al. 2001). Time series of PT and DO at Sta. PM5 (37° 43′ N 134° 43′ E) in the Yamato Basin, which is the most frequently observed hydrographic station in the Japan Sea by the JMA, are shown in Fig. 5.6. The gradual warming of water and decrease in the DO over the recent decades have been recognized throughout the water column from 500 to 2500 m. Similar trends to those in the Yamato Basin have been confirmed in the eastern Japan Basin. These long-term trends in PT and DO are accompanied by structural changes to the Japan Sea. The JSPW is becoming lighter year by year due to gradual warming and modest variations in salinity (Kwon et al. 2004). In addition, the thickness of the Bottom Water, the densest part of the JSPW, is decreasing and a DO minimum layer at approximately 1000 m is becoming less clear (Gamo et al. 1986; Gamo 2011), although the re-activation of the Bottom Water formation since the 2000s has been proposed (Yoon et al. 2018).

Global warming has been suggested as a cause of both the warming and decrease in DO of the JSPW (Gamo 1999, 2011; Minami et al. 1999; Kim et al. 2001). Gamo et al. (2001) proposed that a mode shift has occurred in the water mass formation.

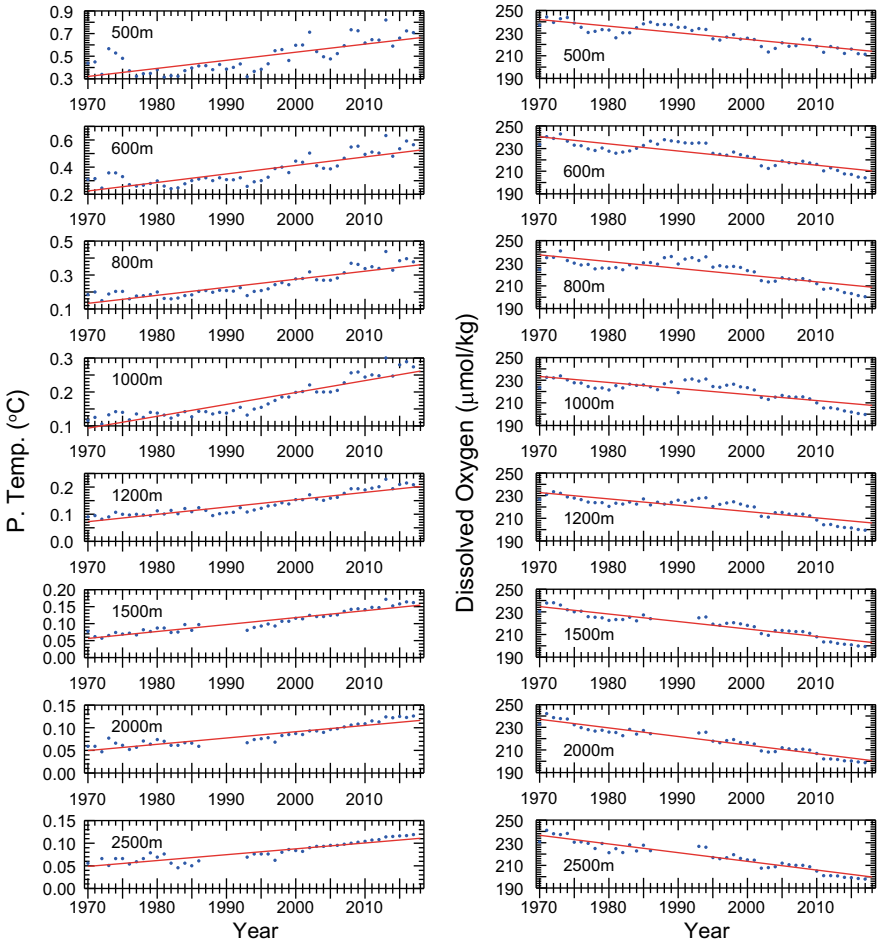

Fig. 5.6 Time series of PT (left) and DO (right) at Sta. PM5 (37° 43′ N 134° 43′ E) in the Yamato Basin from 500 to 2500 m. Blue dots denote the yearly mean observational data and red lines indicate the linear trends. Note that PT axes vary with subfigures

In the past, successive cold winters frequently caused the development of deep convection that reached down to the bottom layer, and a large volume of Bottom Water was thereby produced via this process every year. However, since at least the 1970s, moderate winters accompanied by global warming have reduced this deep convection, together with an enhancement in the formation of the upper portion of the JSPW at about ~1000 m. In fact, the winter air temperature at Vladivostok near the region of JSPW formation shows a clear increasing trend (Gamo 2011).

The warming rate of PT decreases monotonically with depth (Table 5.2). However, the rates of decrease in DO reaches a minimum at depths of between 1000 and 1200 m, with a loss of less than -0.6 μmol kg^{-1} per year, suggesting a relatively

Table 5.2 Linear trends of PT and DO with 95% confidence intervals at each layer shown in Fig. 5.6

Depth (m)	PT (°C year^{-1})	DO (μmol kg^{-1} year^{-1})
500	+0.0073 ± 0.0014	−0.5954 ± 0.0993
600	+0.0064 ± 0.0011	−0.6414 ± 0.1089
800	+0.0048 ± 0.0008	−0.6072 ± 0.1093
1000	+0.0036 ± 0.0006	−0.5441 ± 0.0971
1200	+0.0028 ± 0.0004	−0.5709 ± 0.0958
1500	+0.0021 ± 0.0004	−0.6747 ± 0.1129
2000	+0.0014 ± 0.0002	−0.7769 ± 0.1273
2500	+0.0013 ± 0.0002	−0.7846 ± 0.1299

active oxygen supply to the depths. Although this fact supports the mode shift of the water mass formation as suggested by Gamo et al. (2001), the overall formation of JSPW has been stagnant since the 1970s, as indicated by the trends in warming and the decreasing DO throughout the water column (Fig. 5.6 and Table 5.2) (Cui and Senjyu 2012).

5.4 Decadal-Scale Variations in the JSPW

In addition to the linear trends, a periodic interdecadal change in both PT and DO of the JSPW has been reported (Watanabe et al. 2003; Cui and Senjyu 2010, 2012). The time series for PT and DO at 1000 m in the Yamato Basin (Sta. PM5) depicts an almost out-of-phase variation (lower panel of Fig. 5.7). The observational data showed positive (negative) deviations from the linear trend in the 1970s and 2010s for PT (DO). However, negative (positive) deviations were prevalent for PT (DO) between 1985 and 2000. The correlation coefficient between the deviations in PT and DO is −0.58 ($p < 0.01$, $n = 48$). Similar decadal-scale fluctuations in PT and DO have also occurred throughout the range of 500–2500 m depth (Fig. 5.6).

A significant correlation between the decadal-scale variation in the JSPW and the Arctic oscillation index (AOI) has been pointed out (Fig. 5.7) (Cui and Senjyu 2010); the correlation coefficient between the low-pass filtered AOI and PT (DO) deviation from the linear trend is −0.46 (+0.60) ($p < 0.01$, $n = 44$). This fact indicates that the JSPW formation is modulated by the AO, which is a climatic oscillation pattern that shows an opposite polarity between the North Pole and mid-latitude areas (Thompson and Wallace 1998). Because the AO has positive polarity in the Aleutian low in the North Pacific and negative polarity in the Siberian High on the Eurasian Continent at mid-latitudes, the east–west atmospheric pressure gradient over the Japan Sea increases significantly during periods of negative AOI. This means that a strong winter monsoon tends to occur during periods of negative AOI, which is considered to be favorable for the formation of JSPW. However, PT (DO) tends to decrease (increase) unexpectedly in the periods when AOI is positive (Fig. 5.7).

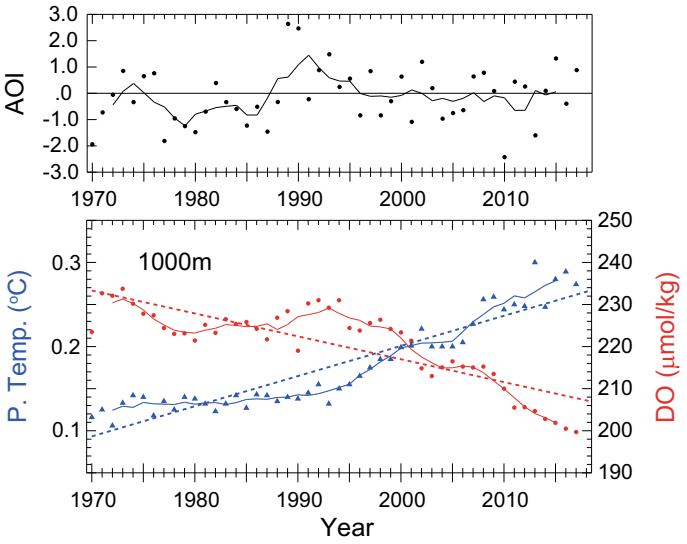

Fig. 5.7 Time series of winter-mean AOI (upper) and those of PT (blue) and DO (red) at 1000 m of Sta. PM5 in the Yamato Basin (lower). The thin lines indicate five-year running averages. The broken lines in the lower panel denote liner trends

As shown in the previous section, the JSPW is formed by atmosphere-ocean interaction. The development of atmospheric disturbances can be associated with the SST in the East China Sea (Isobe and Beardsley 2007). In years of positive AOI, the winter monsoon is weak. Accordingly, the SST in the East China Sea experiences an anomalous increase, which promotes the development of atmospheric disturbances above the sea. As a result, atmospheric disturbances frequently migrate into the Japan Sea, and cold-air outbreaks occur actively over the sea. Since sensible and latent heat fluxes between the sea surface and atmosphere depend largely on wind speed (Kawamura and Wu 1998; Tomita et al. 2016), these active cold-air outbreaks result in the formation of large volumes of JSPW. This is the reason why PT (DO) deviations from the linear trend in the JSPW correlate negatively (positively) with AOI (Cui and Senjyu 2010).

5.5 Changes in the Deep Flow Field

The JSPW that is produced during the winter sinks down to the deep and bottom layers in the northwestern Japan Sea, and then spreads over the whole of the sea as the lower part of the thermohaline circulation. The distribution of the mean flow vectors in the abyssal layers (>1000 m) from direct current observation is shown in Fig. 5.8; this is the updated version of Senjyu et al. (2005) with the addition of our

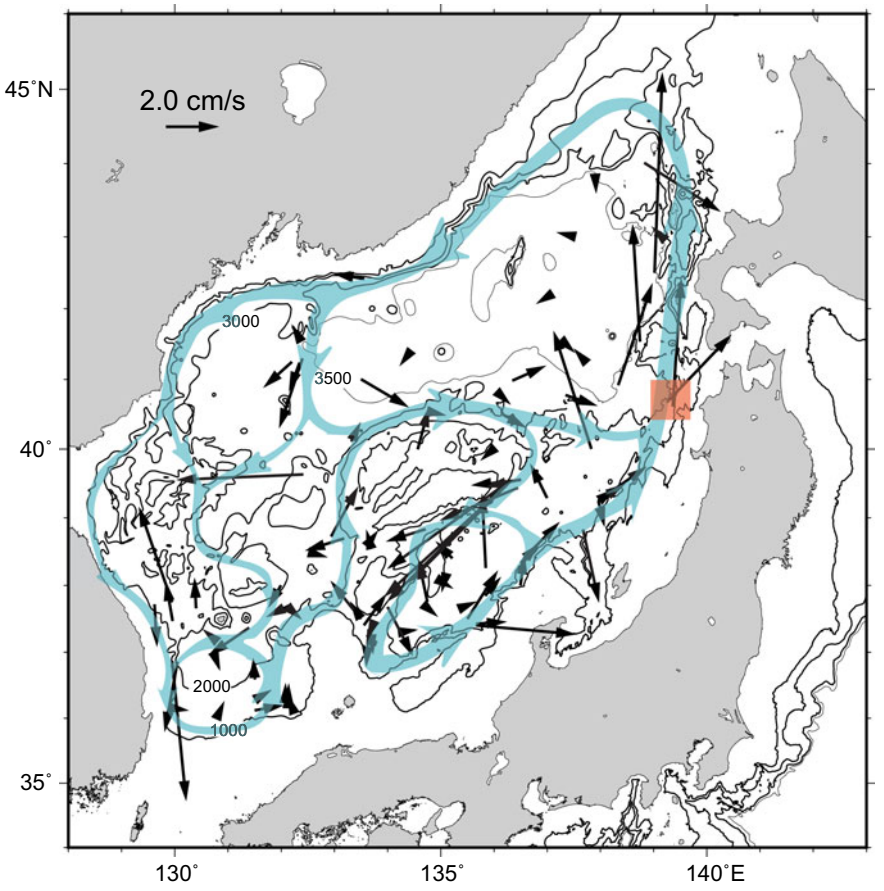

Fig. 5.8 Distribution of the mean flow vectors in the abyssal Japan Sea (1000 m–bottom) from direct current observations. A vector length of 2.0 cm s^{-1} is shown in the upper-left corner. Conceptual view of the abyssal circulation inferred from the mean flow vectors is superimposed. A red square in the eastern Japan Basin denotes the location of the revisit observation in Fig. 5.9

new data as well as that of Fukushima and Kojima (2011) and Teague et al. (2005). A conceptual view of the abyssal circulation that can be inferred from the mean flow vectors is superimposed. The circulation consists of relatively strong cyclonic flows along the basin periphery and sluggish flows in the interior region. Besides the cyclonic circulation over the whole of the basin, there are also closed cyclonic circulations within the Japan, Yamato, and Tsushima Basins. Similar circulation patterns can be found in the flow fields inferred from information collected using Argo floats (Park et al. 2004; Choi and Yoon 2010; Kang et al. 2016) and the output of numerical models (e.g., Hogan and Hurlburt 2000; Park et al. 2013).

The number of papers discussing long-term changes in the deep flow field is limited. Deep current in the central region of the Ulleung Interplain Gap (UIG) has

been observed for the first time since 1997 using moored current meters (Chang et al. 2002). Since the UIG is the only channel connecting the Tsushima Basin with the Japan Basin at depths below 2000 m, deep water exchange must be occurring between the basins through the gap (Fig. 5.1b). Records from current meters have revealed that the along-channel component of the flow (a southwestward flow towards the Tsushima Basin was dominant at this site) showed no significant trend during the period from 1997 to 2002; instead notable fluctuations with a period of 20–50 d prevailed (Chang et al. 2004). However, a warming trend observed in the abyssal UIG suggests an increase in the heat transport into the Tsushima Basin, although the southwestern volume transport is compensated for by a narrow fast northward flow in the eastern UIG (Chang et al. 2009).

Recently, revisit observations using moored current meters were conducted in the eastern Japan Basin during the period of July 2016 to May 2017 (Fig. 5.8) (Senjyu MS). At the same site, a deep flow observation with current meters was carried out from April 1994 to May 1995 (Mori et al. 2001). Comparing the records at approximately 2000 m from both observations, the flows in 2016–2017 appear to be weaker than those in 1994–1995 (Fig. 5.9). In fact, the mean flow speed in 2016–2017 was less than that in 1994–1995 by about 30%, although the direction of the mean flow was northwards for both periods (Table 5.3). In contrary, the standard deviation in the flow from both periods was almost the same, suggesting the same level of eddy activity. Using an idealized numerical model of the Japan Sea, Yoshikawa (2012) showed that the intensity of deep circulation depends mainly on the volume of newly formed deep water. The influence of reduction in the deep water formation is likely to

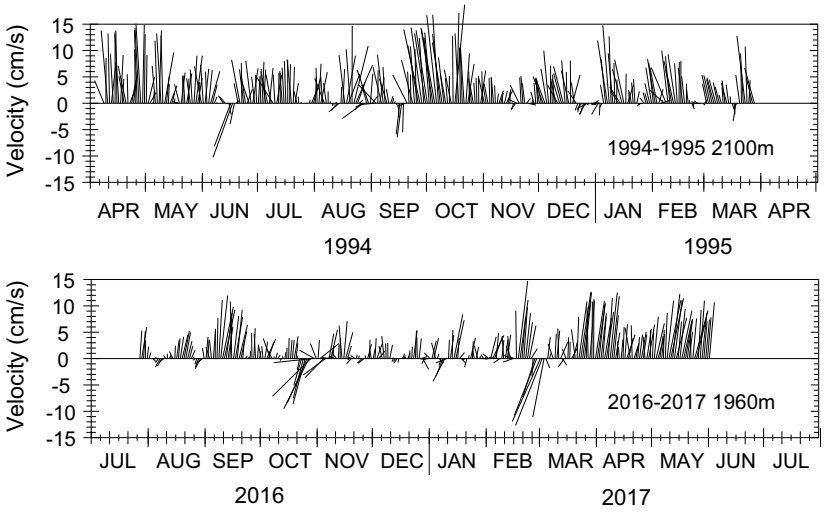

Fig. 5.9 Stick diagrams of deep flows measured in the eastern Japan Basin (Fig. 5.8) during the period of April 1994–March 1995 (upper) and July 2016–June 2017 (lower). The flows are resampled at 1 d intervals after low-pass filtering

Table 5.3 Means and standard deviations (SD) of flows measured in the eastern Japan Basin in 1994–1995 and 2016–2017. The values were calculated for 10 months (August–May) considering seasonal variation

Period	Mean (cm s^{-1})				SD (cm s^{-1})	
	Dir. (°T)	Speed	E-W	N-S	E-W	N-S
1994–1995	355.2	5.17	−0.43	5.15	1.00	4.64
2016–2017	2.6	3.29	0.15	3.28	1.30	4.43

appear firstly in the Japan Basin that includes the area of JSPW formation. Although more careful examination is required, the result of the revisit observations may be a signal of a weakening thermohaline circulation in the Japan Sea.

5.6 Concluding Remarks

Although the JSPW is known as a homogeneous water mass, its characteristics fluctuate depending on the conditions during its formation. Two types of long-term variation were found in the JSPW: a linear trend and a decadal-scale variation. The former seems to synchronize with the warming trend in the SST due to global warming. On the other hand, the latter is associated with the SST conditions in the East China Sea via the AO. This indicates that the Japan Sea and the East China Sea are a single system connected by the atmosphere. This is an example of a teleconnection system on a marginal sea scale. Recent studies using numerical models have suggested another example of the teleconnection system; the control of volume transport of the Tsushima Current by the wind stress in the downstream region over the Okhotsk Sea (Tsujino et al. 2008; Kida et al. 2016). The coexistence of global warming and teleconnection systems among marginal seas indicates that to consider the future of the Japan Sea, we have to take into account not only global conditions but also local conditions in the surrounding water and atmosphere.

The Japan Sea is often referred to as a "miniature ocean" because of its wind-driven and thermohaline circulations that are similar to these found in the Pacific and Atlantic oceans. The Fourth Assessment Report by the Intergovernmental Panel on Climate Change reported that owing to its limited size, the Japan Sea is easily subject to climate changes and responds quickly to such forced changes to the surface over the entire depth (Bindoff et al. 2007). This fact indicates that the Japan Sea can play an important role as "a canary in the coal mine" for the global oceans (Gamo 2011). To understand the influences of global warming and climate change on the oceans, continuous monitoring of the Japan Sea is desirable.

Acknowledgements Part of this study was supported by the Environment Research and Technology Development Fund of Ministry of the Environment, Japan (2-1604) and JSPS KAKENHI Grant Number JP18H03741.

References

Bindoff NL, Willebrand J, Artale V, Cazenave A, Gregory J, Gulev S, Hanawa K, Le Quéré C, Levitus S, Nojiri Y, Shum CK, Talley LD, Unnikrishnan A (2007) Observations: oceanic climate change and sea level. Climate change 2007: the physical science basis. Contribution of Working Group I to the fourth assessment report of the intergovernmental panel on climate change. Cambridge University Press, Cambridge, pp 385–432

Chang KI, Hogg N, Suk MS, Byun SK, Kim YG, Kim K (2002) Mean flow and variability in the southwestern East Sea. Deep-Sea Res I 49:2261–2279

Chang KI, Teague WJ, Lyu SJ, Perkins HT, Lee DK, Watts DR, Kim YB, Mitchell DA, Lee CM, Kim K (2004) Circulation and currents in the southwestern East/Japan Sea: overview and review. Prog Oceanogr 61:105–156

Chang KI, Kim K, Kim YB, Teague WJ, Lee JC, Lee JH (2009) Deep flow and transport through the Ulleung Interplain Gap in the southwestern East/Japan Sea. Deep-Sea Res I 56:61–72

Choi YG, Yoon JH (2010) Structure and seasonal variability of the deep mean circulation of the East Sea (Sea of Japan). J Oceanogr 66:349–361

Cui Y, Senjyu T (2010) Interdecadal oscillations in the Japan Sea Proper Water related to the arctic oscillation. J Oceanogr 66:337–348. https://doi.org/10.1007/s10872-010-0030-z

Cui Y, Senjyu T (2012) Has the upper portion of the Japan Sea Proper Water formation really been enhancing? J Oceanogr 68:593–598. https://doi.org/10.1007/s10872-012-0115-y

Fukushima S, Kojima T (2011) Characteristics of deep current observed near the bottom in the Sea of Japan. Report of hydrographic and oceanographic researches. Hydrographic and Dceanographic Department, Japan Coast Guard, vol 47, pp 32–43

Gamo T (1999) Global warming may have slowed down the deep conveyor belt of a marginal sea of the northwestern Pacific: Japan Sea. Geophys Res Lett 26:3137–3140

Gamo T (2011) Dissolved oxygen in the bottom water of the Sea of Japan as a sensitive alarm for global climate change. Trends Anal Chem 30:1308–1319

Gamo T, Horibe Y (1983) Abyssal circulation in the Japan Sea. J Oceanogr Soc Japan 39:220–230

Gamo T, Nozaki Y, Sakai H, Nakai T, Tsubota H (1986) Spatial and temporal variations of water characteristics in the Japan Sea bottom water. J Mar Res 44:781–793

Gamo T, Momoshima N, Tolmachyov S (2001) Recent upward shift of the deep convection system in the Japan Sea, as inferred from the geochemical tracers tritium, oxygen, and nutrients. Geophys Res Lett 28:4143–4146

Hogan PJ, Hurlburt HE (2000) Impact of upper ocean-topographical coupling and isopycnal outcropping in Japan/East Sea models with 1/8° to 1/64° resolution. J Phys Oceanogr 30:2535–2561

Hong CH, Cho KD, Kim HJ (2001) The relationship between ENSO events and sea surface temperature in the East (Japan) Sea. Prog Oceanogr 49:21–40

Isobe A, Beardsley RC (2007) Atmosphere and marginal-sea interaction leading to an interannual variation in cold-air outbreak activity over the Japan Sea. J Climate 20:5707–5714

Kang SK, Seung YH, Park JJ, Park JH, Lee JH, Kim EJ, Kim YH, Suk MS (2016) Seasonal variability in middepth gyral circulation patterns in the central East/Japan Sea as revealed by long-term Argo data. J Phys Oceanogr 46:937–946

Kawamura H, Wu P (1998) Formation mechanism of Japan Sea Proper Water in the flux center off Vladivostok. J Geophys Res 103:21611–21622

Kida S, Qiu B, Yang J, Lin X (2016) The annual cycle of the Japan Sea throughflow. J Phys Oceanogr 46:23–39

Kim K, Kim KR, Min DH, Vlokov Y, Yoon JH, Takematsu M (2001) Warming and structural changes in the East (Japan) Sea: a clue to future changes in global oceans? Geophys Res Lett 28:3293–3296

Kim K, Kim KR, Kim YG, Cho YK, Kang DJ, Takematsu M, Volkov Y (2004) Water masses and decadal variability in the East Sea (Sea of Japan). Prog Oceanogr 61:157–174

Kwon YO, Kim K, Kim YG, Kim KR (2004) Diagnosing long-term trends of the water mass properties in the East Sea (Sea of Japan). Geophys Res Lett 31:L20306. https://doi.org/10.1029/2004gl020881

Minami H, Kano Y, Ogawa K (1999) Long-term variations of potential temperature and dissolved oxygen of the Japan Sea Proper Water. J Oceanogr 55:197–205

Minobe S, Sako A, Nakamura M (2004) Interannual to interdecadal variability in the Japan Sea based on a new gridded upper water temperature dataset. J Phys Oceanogr 34:2382–2397

Mori K, Isoda Y, Murakami T, Ohtani K (2001) Low-frequency variations of the deep flow southwest of the Tsugaru Straits. Oceanogr in Japan 10:1–13

Na H, Kim KY, Chang KI, Park JJ, Kim K, Minobe S (2012) Decadal variability of the upper ocean heat content in the East/Japan Sea and its possible relationship to northwestern Pacific variability. J Geophys Res 117:C02017. https://doi.org/10.1029/2011jc007369

National Astronomical Observatory of Japan (2018) Rika Nenpyo (Chronological Scientific Tables 2019), Maruzen, Tokyo, 1022 pp

Nitani H (1972) On the deep and bottom waters in the Japan Sea. In: Shoji D (ed) Researches in hydrography and oceanography. Hydrographic Department of Japan Maritime Safety Agency, Tokyo, pp 151–201

Park WS, Oh IS (2000) Interannual and interdecadal variations of sea surface temperature in the East Asian Marginal Seas. Prog Oceanogr 47:191–204

Park YG, Oh KH, Chang KI, Suk MS (2004) Intermediate level circulation of the southwestern part of the East/Japan Sea estimated from autonomous isobaric profiling floats. Geophys Res Lett 31:L13213. https://doi.org/10.1029/2004gl020424

Park YG, Park JH, Lee HJ, Min HS, Kim SD (2013) The effects of geothermal heating on the East/Japan Sea circulation. J Geophys Res Ocean 118:1893–1905

Park JJ, Park KA, Kim YG, Yun JY (2016) Chapter 3: Water masses and their long-term variability. In: Chang KI, Zhang CI, Park C, Kang DJ, Ju SJ, Lee SH, Wimbush M (eds) Oceanography of the East Sea (Japan Sea). Springer, Switzerland, pp 59–86

Senjyu T, Sudo H (1993) Water characteristics and circulation of the upper portion of the Japan Sea Proper Water. J Mar Sys 4:349–362. https://doi.org/10.1016/0924-7963(93)90029-l

Senjyu T, Sudo H (1994) The upper portion of the Japan Sea Proper Water; its source and circulation as deduced from isopycnal analysis. J Oceanogr 50:663–690. https://doi.org/10.1007/bf02270499

Senjyu T, Sudo H (1996) Interannual variation of the upper portion of the Japan Sea Proper Water and its probable cause. J Oceanogr 52:27–42. https://doi.org/10.1007/bf02236531

Senjyu T, Aramaki T, Otosaka S, Togawa O, Danchenkov M, Karasev E, Volkov Y (2002) Renewal of the bottom water after the winter 2000–2001 may spin-up the thermohaline circulation in the Japan Sea. Geophys Res Lett 29. https://doi.org/10.1029/2001gl014093

Senjyu T, Shin HR, Yoon JH, Nagano Z, An HS, Byun SK, Lee CK (2005) Deep flow field in the Japan/East Sea as deduced from direct current measurements. Deep-Sea Res II 52:1726–1741. https://doi.org/10.1016/j.dsr2.2003.10.013

Senjyu T, Enomoto H, Matsuno T, Matsui S (2006) Interannual salinity variations in the Tsushima Strait and its relation to the Changjiang discharge. J Oceanogr 62:681–692. https://doi.org/10.1007/s10872-006-0086y

Seung YH, Yoon JH (1995) Some features of winter convection in the Japan Sea. J Oceanogr 51:61–73

Sudo H (1986) A note on the Japan Sea Proper Water. Prog Oceanogr 17:313–336

Talley LD, Min DH, Lobanov VB, Luchin VA, Ponomarev VI, Salyuk AN, Shcherbina AY, Tishchenko PY, Zhabin I (2006) Japan/East Sea water masses and their relation to the sea's circulation. Oceanography 19:32–49

Teague WJ, Tracey KL, Watts DR, Book JW, Chang KI, Hogan PJ, Mitchell DA, Suk MS, Wimbush M, Yoon JH (2005) Observed deep circulation in the Ulleung Basin. Deep-Sea Res II 52:1802–1826

Thompson DWJ, Wallace JM (1998) The Arctic Oscillation signature in the wintertime geopotential height and temperature fields. Geophys Res Lett 25(9):1297–1300

Tomita H, Senjyu T, Kubota M (2016) Evaluation of air-sea sensible and latent heat fluxes over the Japan Sea obtained from satellite, atmospheric reanalysis, and objective analysis products. J Oceanogr 72:747–760. https://doi.org/10.1007/s10872-016-0368-y

Tsujino H, Nakano H, Motoi T (2008) Mechanism of currents through the straits of the Japan Sea: mean state and seasonal variation. J Ocenogr 64:141–161

Uda M (1934) The results of simultaneous oceanographical investigations in the Japan Sea and its adjacent waters in May and June. J Imp Fish Exp Sta 5:57–190

Watanabe YW, Wakita M, Maeda N, Ono T, Gamo T (2003) Synchronous bidecadal periodic changes of oxygen, phosphate and temperature between the Japan Sea deep water and the North Pacific intermediate water. Geophys Res Lett 30:2273. https://doi.org/10.1029/2003gl018338

Worthington LV (1981) The water masses of the world ocean: some results of a fine-scale census. In: Warren BA, Wunsch C (eds) Evolution of physical oceanography. M.I.T. Press, Cambridge, pp 42–69

Yasui M, Yasuoka T, Tanioka K, Shiota O (1967) Oceanographic studies of the Japan Sea (1)–Water characteristics. Oceanogr Mag 19:177–192

Yoon ST, Chang KI, Nam SH, Rho TK, Kang DJ, Lee T, Park KA, Lobanov V, Kaplunenko D, Tishchenko P, Kim KR (2018) Re-initiation of bottom water formation in the East Sea (Japan Sea) in a warming world. Sci Rep 8:1576. https://doi.org/10.1038/s41598-018-19952-4

Yoshikawa Y (2012) An eddy-driven abyssal circulation in a bowl-shaped basin due to deep water formation. J Oceanogr 68:971–983

Chapter 6
Anthropogenic Perturbations of the Carbon and Nitrogen Cycles in the East Sea (Sea of Japan)

Kitack Lee, Eunil Lee, and Chang-Ho Lee

Abstract The dynamic overturning circulation in the East Sea facilitates the absorption of anthropogenic CO_2 by effectively transporting it from the surface to the interior of the sea. However, recent weakening of this overturning circulation has decreased the transport of anthropogenic CO_2 and O_2 from the surface to the interior of the sea, but accelerated the acidification of deep water in the basin; the rate of acidification in the deep water is higher than the rate at the surface. An emerging perturbation to the East Sea is an increase in the input of anthropogenic nitrogen. The concentration of surface nitrate (N) relative to that of phosphate (P) in the East Sea increased disproportionally over the period since 1980. The increase in the N concentration in the East Sea and adjacent seas has probably been driven primarily by deposition of pollutant nitrogen from atmospheric and riverine sources. A review of these critical results indicates that the East Sea provides insights into how future global warming and human perturbations might alter the nitrogen and carbon cycles and their interactions.

Keywords The East Sea · Anthropogenic CO_2 · Circulation · Water column · Ventilation · Anthropogenic nitrogen · N* (the seawater concentration of N relative to that of P)

K. Lee (✉) · C.-H. Lee
Division of Environmental Science and Engineering, Pohang University of Science and Technology, Pohang 37673, Korea
e-mail: ktl@postech.ac.kr

C.-H. Lee
e-mail: lch6261@postech.ac.kr

E. Lee
Ocean Research Division, Korea Hydrographic and Oceanographic Agency, Busan 49111, Korea
e-mail: elee@korea.kr

C.-T. A. Chen and X. Guo (eds.), *Changing Asia-Pacific Marginal Seas*, Atmosphere, Earth, Ocean & Space, https://doi.org/10.1007/978-981-15-4886-4_6

6.1 Introduction

Coastal and marginal seas bordering major continents potentially absorb considerable amounts of atmospheric CO_2 because high inputs of nutrients from adjacent continents decrease the surface water CO_2 concentration by increasing production of organic matter. This in turn drives the transfer of more CO_2 from the atmosphere to the ocean. Marginal seas also connect terrestrial and oceanic carbon reservoirs (Tsunogai et al. 1999; Choi et al. 2002; Thomas et al. 2004; Chen and Borges 2009; Cossarini et al. 2015; Bourgeois et al. 2016). However, the role of coastal and marginal seas as a sink of anthropogenic CO_2 has been overlooked because they account for only 7% of the total area of the world ocean. As a result, data regarding the amounts of anthropogenic CO_2 stored in coastal and marginal seas and its temporal variability are limited. More importantly, mechanisms responsible for the transfer of atmospheric CO_2 to the coastal and marginal seas, and eventually to the open ocean, are yet to be elucidated.

The East Sea (Sea of Japan) is bordered by Korea, Russia, and Japan, and only exchanges surface water with the western North Pacific Ocean, through three shallow (<150 m depth) straits (Fig. 6.1). Deep water formed on the continental shelf and slope off Vladivostok (Russia) is a unique overturning circulation of the East Sea, and as a result the East Sea basin is actively ventilated at all depths within decadal time scales (Kim and Kim 1996; Gamo et al. 2001; Kim et al. 2001; Talley et al. 2003; Chap. 5). This active overturning circulation is evident in the high O_2 concentration at 1000 m and greater depths. The concentrations of O_2 in the East Sea interior are higher than in the well ventilated South Pacific Ocean (Talley et al. 2006), where ventilation of intermediate water results in high O_2 content at 1000 m depth. The anomalous weak stability of the East Sea water column (in terms of density) is primarily responsible for this active ventilation (Kim and Kim 1996; Kim et al. 2001). As the various processes responsible for overturning circulation in the East Sea (subduction, open ocean convection, and brine rejection from sea ice formation) are subject to change in response to regional or global climate variations (e.g. Talley et al. 2006; Chap. 5), they can influence the intensity of the overturning circulation, and thereby the properties of deep waters including temperature and O_2 concentration.

A recent and less well documented perturbation in the East Sea is the increasing addition of anthropogenic nitrogen to the East Sea (Kim et al. 2011, 2013). The increased addition of anthropogenic nitrogen is particularly acute in the East Sea and the western North Pacific, where the rapid growth of populations and industrial activity in northeast Asian countries has increased the environmental loads of this pollutant (Jickells et al. 2017). These unparalleled perturbations in northeast Asia have markedly increased reactive nitrogen fluxes into the adjacent marine environment (Galloway 2000; Kim et al. 2011; Kim et al. 2014a), mainly through atmospheric transport by westerly winds and subsequent deposition. Increasing addition of reactive nitrogen to the oceans could lead to significant changes in nitrogen cycle and phytoplankton biomass in the upper ocean (Okin et al. 2011; Kim et al. 2014b). However, it has been suggested that the impact may not be detectable (e.g. Duce

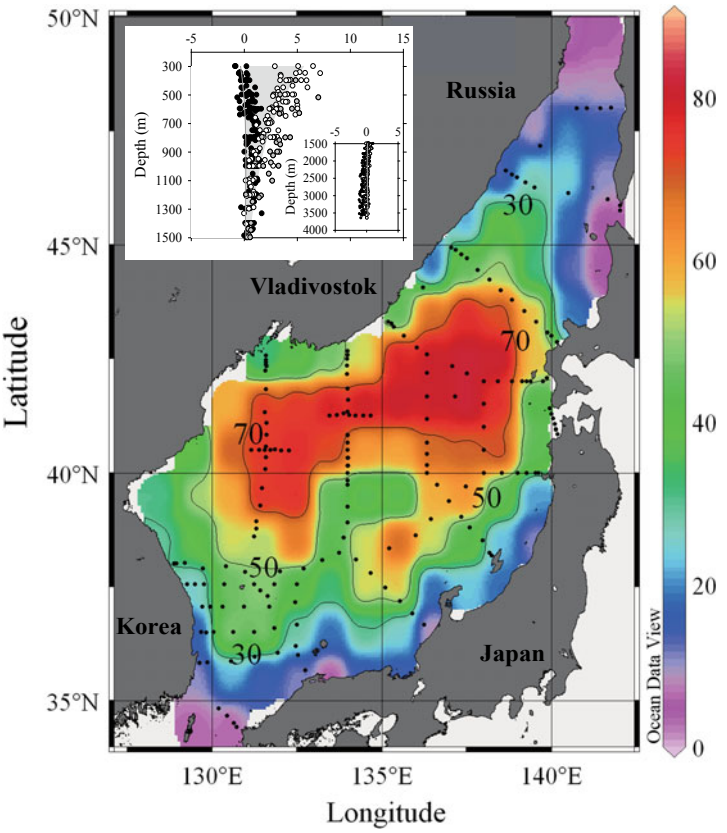

Fig. 6.1 Map of anthropogenic CO_2 column inventory per unit area (mol C m^{-2}) in the East Sea, as of 1999. The inset shows the amounts of anthropogenic CO_2 accumulated during the periods 1992–1999 (open circles) and 1999–2007 (solid circles) as a function of depth. The gray circles in the inset denote data within the anticyclonic eddies. Filled circles represent sampling locations occupied on the Russia R/V Khromov and sampling locations occupied on the U.S. R/V Roger Revelle. Modified from figures in Park et al. (2006, 2008)

et al. 2008), except in near-shore environments. A study by Kim et al. (2011), in which nutrient concentration measurements made over more than two decades were directly compared, showed that the seawater N concentration has increased in extensive areas of the northeast Asia marginal seas, and this increase has primarily been associated with the growing input of anthropogenic nitrogen (Kim et al. 2011, 2013; Kim et al. 2014a). As the East Sea is located downwind of the East Asian continent, the basin has received ever-increasing amounts of pollutant nitrogen deposited from the atmosphere, resulting from the use of fossil fuels and nitrogen fertilizers. The increasing loads of pollutant nitrogen will subsequently increase its concentration in seawater, and thereby the ratio of seawater N to P. These changes may alter the

composition of phytoplankton species, and eventually, the structure of the ecosystem of the East Sea.

Over the past century the East Sea underwent unprecedented changes that are manifested in the physical and chemical properties of its surface waters and deep interior (Chap. 5). As consequences of its changing nature and the many measurements made in the East Sea, this basin may be a useful site for investigating how ocean nutrient and carbon cycles respond to natural and anthropogenic perturbations over varying time scales. This chapter reviews key findings from the scientific literature, and highlights the footprints that the profound natural and anthropogenic perturbations have left in the East Sea.

6.2 Physical Properties of the Interior of the East Sea

Inter-decadal variations in water column ventilation of the East Sea are only detectable in waters shallower than 600 m (Talley et al. 2004; Min and Warner 2005). Both the decrease in the O_2 concentration and the concurrent increase in heat content in the deep East Sea (specifically Japan Basin located in the northern East Sea) between 1992 and 2007 are indicatives of a weakening of water column ventilation. The decrease in the O_2 concentration is also evident in the southern East Sea between 1965 and 2015 (Chen et al. 2017). This finding is broadly consistent with open ocean studies concluding that the reduction in the O_2 concentration in the open ocean has resulted from changes in ocean circulation (Joos et al. 2003; McDonagh et al. 2005; Deutsch et al. 2006; Schmidtko et al. 2017). Continual warming of waters below the permanent thermocline has also occurred since the 1960s. Over the period 1969–2007 the temperature increase at depths deeper than 2000 m was approximately 0.05 °C (0.013 °C decade^{-1}), which exceeds the global warming of 0.037 °C that occurred between 1955 and 1998 (0.009 °C decade^{-1}). The dissolved O_2 concentration in the waters deeper than 2000 m also decreased.

The rate of decrease in the O_2 inventory of the upper Proper Water (300–800 m) in the Japan basin of the East Sea was two-fold higher for the period 1999–2007 than for the period 1992–1999 (Fig. 6.2). The decrease in the O_2 inventory over the period 1999–2007 is probably because of weakening of upper Proper Water ventilation, given the constant rate of O_2 consumption arising from the oxidation of organic matter settling from the surface. Under this assumption, the weakened ventilation during the period 1999–2007 probably enabled bacterial consumption of O_2 to exceed its supply through movement of water parcels from the site of deep water formation to the observation point. This explanation is consistent with open ocean studies that have concluded that the observed reductions in O_2 concentration are largely driven by changes in ocean circulation (Joos et al. 2003; McDonagh et al. 2005; Deutsch et al. 2006; Schmidtko et al. 2017), and are less likely to be because of changes in the rate of O_2 demand from downward settling of organic matter. The two-fold increase in the rate of decrease in the East Sea water column O_2 inventory during the period 1999–2007 (relative to that during the period 1992–1999)

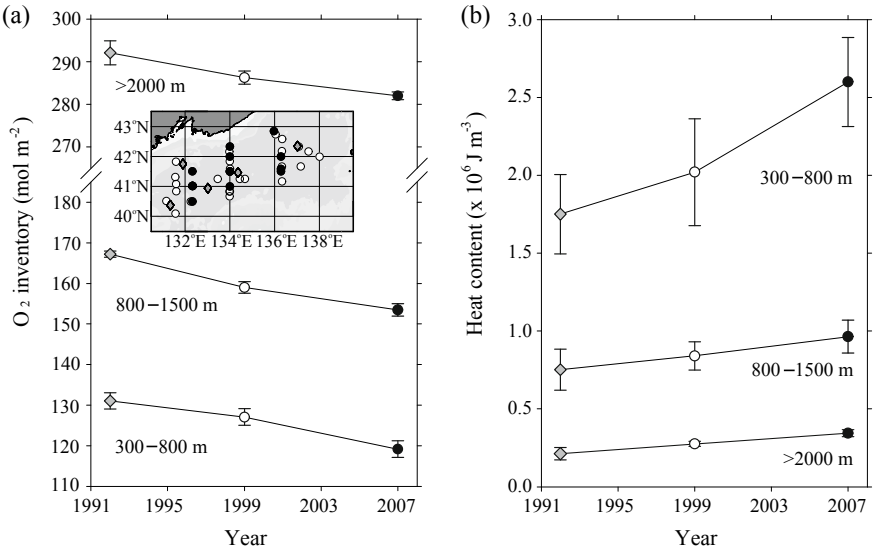

Fig. 6.2 Temporal variations in **a** water column O_2 inventories (mol m^{-2}) and **b** heat content (106 J m^{-3}) in the upper and lower Proper Water (300–800 m and 800–1500 m, respectively) and Deep Water (>2000 m) in the East Sea basin during the period 1992–2007. Error bars represent one standard deviation from the mean. Redrawn using data from Park et al. (2008)

may be undeniable evidence for comparable weakening of the upper Proper Water ventilation over the transition period. The cause of the more recent waning of water column ventilation remains undecided, although warming of the water column is a distinct possibility. This layer of water also contains most of the anthropogenic CO_2 that has been absorbed since 1992. The direct association between water column ventilation and water column inventory of anthropogenic CO_2 is more thoroughly discussed in the following section.

6.3 Anthropogenic CO2 in the East Sea

Methods for the measurement and calibration of seawater carbon parameter in field studies in 1992, 1999, and 2007 have been documented elsewhere (Chen et al. 1995; Talley et al. 2004; Park et al. 2006, 2008). The concentration of anthropogenic CO_2 in a given water parcel was determined using the ΔC^* method proposed by Gruber et al. (1996). In thermodynamic calculations of ocean carbon parameters involved in estimation of anthropogenic CO_2, we used the carbonic acid dissociation constants of Mehrbach et al. (1973), as refitted in more adequate forms of the equations by Dickson and Millero (1987) and other ancillary constants documented by Millero (1995). The B/Cl ratio of 0.2414 (Lee et al. 2010) was used to convert total alkalinity

to carbonate alkalinity, or vice versa. All these thermodynamic constants were shown to be consistent with seawater carbon data obtained from the laboratory (Lee et al. 1996) and field (Lee et al. 2000; McElligott et al. 1998; Millero et al. 2002) studies.

To estimate the rate of anthropogenic CO_2 uptake for the periods 1992–1999 and 1999–2007, extended multi-linear regression analysis was applied to the datasets of total dissolved inorganic C for 1992, 1999, and 2007, respectively (data collected for waters <300 m depth were excluded in this calculation to avoid seasonal variations). The uptake of anthropogenic CO_2 by the East Sea primarily depends on the formation of deep water (occurred primarily on the continental shelf and slope off Vladivostok, Russia), the weak water column stability of the East Sea relative to the open ocean, and the absence of transport of anthropogenic CO_2 via the exchange of intermediate and deep waters (containing anthropogenic CO_2) with the adjacent North Pacific (Chen et al. 2006; Lee et al. 2011). The weak stability of the East Sea also facilitates active deep convection, whereby surface water charged with anthropogenic CO_2 is effectively transported to the interior of the basin.

All three of the above factors collectively contributed to the accumulation of anthropogenic CO_2 in the interior of the East Sea (Figs. 6.1 and 6.3). The highest concentrations of anthropogenic CO_2 (50–60 μmol kg^{-1}) have been found in the southern upper East Sea (Fig. 6.3a, b). In the southern basin vertical mixing is

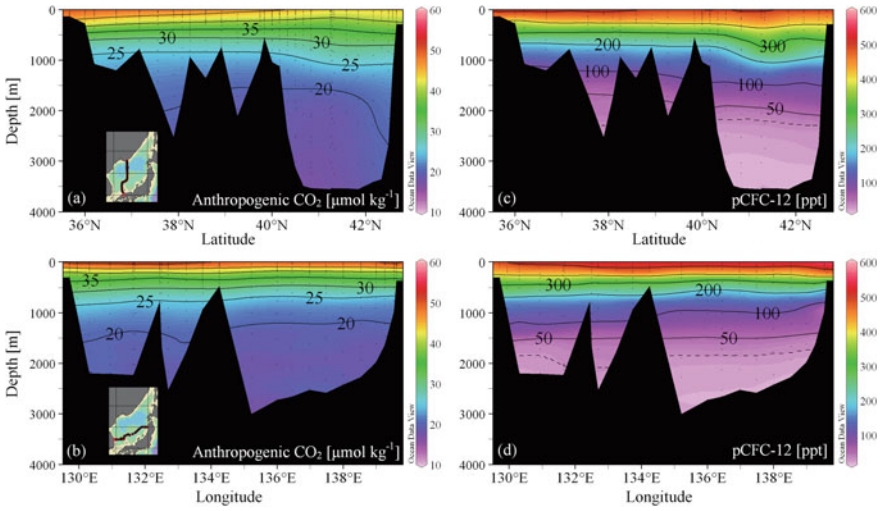

Fig. 6.3 **a**, **c** Meridional and **b**, **d** zonal sections of anthropogenic CO_2 and pCFC-12 nominally along 134°E and 38°N in the East Sea, respectively. Deep waters near the bottom (~3500 m depth) of the East Sea basin contain approximately 10–15 μmol kg^{-1} of anthropogenic CO_2. Anthropogenic CO_2 concentrations are not scaled down because corrections for the key systematic errors (inaccuracies in the assumption of the constant air-sea disequilibrium and the pCFC-12 age bias) differ for different water masses. Dotted lines represent water masses of approximately 40 years in age. Modified from a figure in Park et al. (2006)

largely suppressed by stronger stratification, which would cause greater accumulation of anthropogenic CO_2 in the upper ocean. In contrast, in the northern basin surface waters mix extensively with deep waters that contain lower levels of anthropogenic CO_2, thus lowering the anthropogenic CO_2 concentration in the upper ocean. Anthropogenic CO_2 penetrates to the bottom throughout the basin, and its concentration in deep waters reaches 10–15 μmol kg^{-1} (Fig. 6.3a, b). The partial pressure of CFC-12 (pCFC-12) tracer-derived ages of deep waters that contain 10–15 μmol kg^{-1} of anthropogenic CO_2 are approximately 40 years old (i.e. waters lost contact with the atmosphere approximately in the mid-1960s; Fig. 6.3c, d). There is a similarity in the meridional and zonal distributions of anthropogenic CO_2 concentration and pCFC-12, because both anthropogenic gases penetrate to deep depths via the same process (i.e. deep water formation). The formation of deep water effectively transports surface waters loaded with anthropogenic CO_2 (and CFCs) to the interior of the basin during the winter cooling period. This transport mechanism also operates in the North Atlantic, where anthropogenic CO_2 (CFCs) reaches depths exceeding 3000 m (Lee et al. 2003), whereas anthropogenic CO_2 at the same latitude in the North Pacific does not penetrate beyond 1500 m depth, largely because of the absence of deep water formation (Sabine et al. 2002; Gruber et al. 2019).

The rate of CO_2 uptake by the East Sea has changed in response to the waxing and waning of water column ventilation. The anthropogenic CO_2 found at specific density surfaces was substantial for the period 1992–1999, whereas for the period 1999–2007 only small amounts of anthropogenic CO_2 were present at these surfaces (inset in Fig. 6.1); virtually no increase in anthropogenic CO_2 was found in waters deeper than 300 m (close to the mean winter mixed layer depth) for the period 1999–2007. The rapid and substantial reduction in uptake of anthropogenic CO_2 during this period is probably because of the absence of transport of anthropogenic CO_2 to the interior of the East Sea (also indicating the near absence of overturning circulation) (Park et al. 2008). Several lines of evidence also support the weakening of the ventilation of the East Sea over the past half century (e.g. Gamo 1999; Kim et al. 2001; Kim et al. 2010b; Chap. 5).

There is also evidence for weakening of anthropogenic CO_2 uptake by the East Sea over recent periods. Given that approximately 80% of the total anthropogenic CO_2 emissions have largely occurred since 1950 (Marland et al. 2008), the mean CO_2 uptake rate by the East Sea during this 50-year period was approximately 1.2 mol C m^{-2} $year^{-1}$. This rate was calculated from the total column inventory of anthropogenic CO_2 (75 mol C m^{-2}) accumulated in the basin (Park et al. 2006) divided by 50 years. This rate is two-fold higher than the accumulation rate calculated for the period 1992–1999 (0.6 mol C m^{-2} $year^{-1}$), which approximates the lower end of the CO_2 uptake rate (0.6–1.3 mol C m^{-2} $year^{-1}$) reported for the major oceans over the past two decades (Peng et al. 1998, 2003; Murata et al. 2007; Quay et al. 2007). This confirms the finding of Chen et al. (2004), who showed that the uptake of anthropogenic CO_2 by the East Sea began to decrease during the 1990s or earlier.

Oceanic uptake of anthropogenic CO_2 has increased the dissolved inorganic C concentration in the East Sea, which is predicted to have influenced key ocean biogeochemical processes, including calcification (e.g. Riebesell et al. 2000; Iglesias-Rodriguez et al. 2008; Zhang and Cao 2016), organic matter production (e.g. Riebesell et al. 2007; Engel et al. 2014; Kim et al. 2018; Zhang et al. 2018) and trace gas production (e.g. Liss et al. 1993; Andreae and Crutzen 1997; Kim et al. 2010a). Both the accumulation of anthropogenic CO_2 and the reduction in water column ventilation (manifested in apparent O_2 utilization; the amounts of O_2 used as a result of organic matter oxidation) could have contributed to the acidification at various depths in the East Sea (Kim et al. 2010b; Chen et al. 2017). The contribution of anthropogenic CO_2 to ocean acidification is substantial above 500 m depth, but gradually decreases with increasing depth, whereas the contribution of reduction in water column ventilation to acidification increases with increasing depths; its contribution is greatest for waters deeper than 2000 m, and is five-fold that of anthropogenic CO_2 at the same depths (Fig. 6.4). This finding is surprising because no discernable sign of acidification has been found in the deep waters of the open oceans.

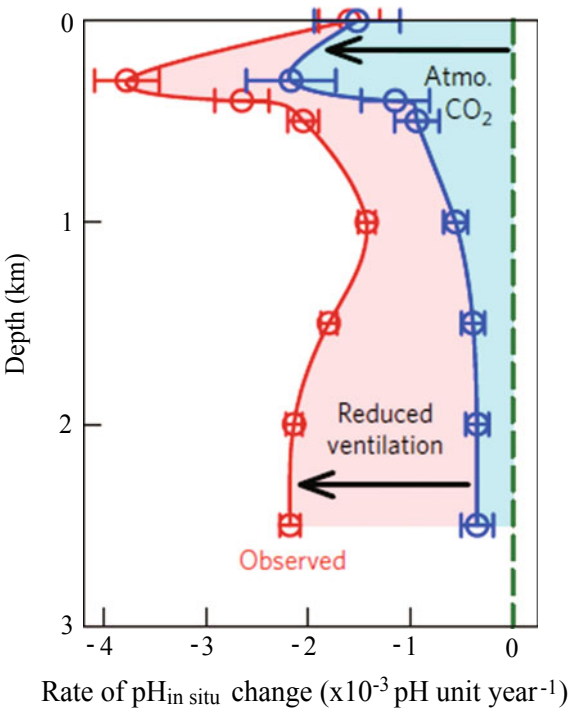

Fig. 6.4 Rate of temporal changes of pH at various depths between 1965 and 2015. The arrows and the colored regions represent the magnitudes of changes due to the increasing anthropogenic CO_2 and reducing seawater ventilation. The blue circles show the rate of pH change due to increasing anthropogenic CO_2, while the red circles show the results with additional considerations of the reduced seawater ventilation (Chen et al. 2017)

6.4 Anthropogenic Nitrogen

The data on seawater N and P concentrations presented in this section were derived from studies in coastal and marginal seas of the northwest Pacific since the 1980s, and archived at the Japan Meteorological Agency (JMA; https://www.jma.go.jp/jma/indexe.html). Data for the coastal waters of Korea since 1995 are archived at the Korea National Institute of Fisheries Science (NIF; http://www.nifs.go.kr/kodc/index.kodc). The NIF data only relate to shallow waters (<100 m), whereas the JMA dataset was derived from the entire water column in the East China Sea, the East Sea, and the Pacific coast of Japan. The methods for evaluation of data accuracy and consistency have been described elsewhere (Kim et al. 2011, 2013).

Over the past 3 decades the rate at which the seawater concentration of N relative to that of P (expressed as $N^* = N - R_{N:P} \times P$; where $R_{N:P}$ is the mean N:P ratio of 15:1 for deep waters) increased across the study area, but the rate of increase differed among locations and time periods (Fig. 6.5) (Kim et al. 2011). The rate of N* increase was highest downstream of the Changjiang River and in the coastal waters surrounding Korea. The rate of increase progressively declined eastward into the East Sea and further to the Pacific coast of Japan. The ocean areas showing an increase in N* were mostly downwind (to the east and southeast) of the East Asian continent, which is an indication that anthropogenic N input is an underlying cause of this trend. Anthropogenic nitrogen input over the western North Pacific has increased by a factor of 10 over the past 140 years (Jickells et al. 2017), which exceeds the global mean increase (a factor of 3.5; Galloway et al. 2004; Duce et al. 2008; Jickells et al. 2017). More recently, NO_x emissions from East Asia increased 65% over the period 1975–1987, and 230% over the following 15 years (Akimoto and Narita 1994; Ohara et al. 2007). As a result, anthropogenic nitrogen deposition over the Northwest Pacific marginal seas, including the East Sea, has been recognized as a significant external nitrogen source (Nakamura et al. 2005; Zhang et al. 2007; Onitsuka et al. 2009; Kang et al. 2010; Ren et al. 2017).

The seawater N concentration measured off the east coast of Korea (near Uljin) increased between 1986 and 2000, whereas the P concentration remained relatively unchanged (Fig. 6.6a). After a brief period of high N* values (2002–2005), the N^* levels decreased during the latter part of the 2000s (2007–2010) (Fig. 6.6a). The values of N and N* in the region east of Oki island in the East Sea increased steadily over the observational period, whereas the P concentration showed no sign of either increase or decrease (Fig. 6.6b). The observed patterns of seawater N* at the two sites were significantly correlated with those of total anthropogenic nitrogen deposition at the closest air monitoring stations for which both seawater N* and anthropogenic nitrogen deposition data were simultaneously available; these included at Uljin ($r = 0.83$; Fig. 6.7a, c) and on Oki island ($r = 0.88$; Fig. 6.7b, d) for the period (2002–2008). The correlations between seawater N* and the levels of anthropogenic nitrogen deposition at these locations indicate that increasing anthropogenic nitrogen deposition over the past 30 years is the most likely cause of the observed increase in the N concentration (and therefore N*) over the East Sea. By contrast, the near constant

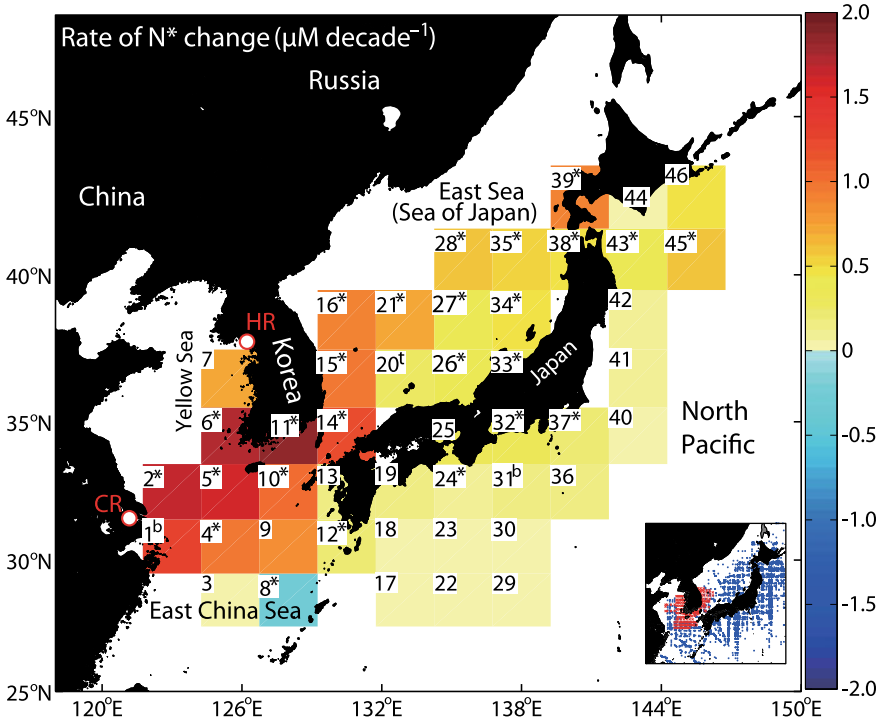

Fig. 6.5 Rate of change (μM decade^{-1}) of N* in surface waters (≤50 m) of the Yellow Sea, East China Sea and East Sea. The red and yellow boxes indicate regions in which the N* values tended to increase, and the blue box indicates a region in which N* decreased. Boxes with statistically significant N* trends are marked with an asterisk (indicating statistical significance based on both the t-test and bootstrapping methods) or with the characters t or b (indicating statistical significance based only on either the t-test or bootstrapping) next to the box number. CR and HR indicate the locations of the mouths of Changjiang and Han rivers, respectively. The inset shows the locations at which the data were sampled over the past 30 years, from the archive of the Korea National Fisheries Research and Development Institute (red) or the Japan Meteorological Agency (blue). Modified from a figure supplied by Kim et al. (2011)

level of P during the study period indicates that the input of P (predominantly via an entrainment of deep water) has been balanced by the removal of P (via organic matter production by phytoplankton).

Across the East Sea the rate of increase in the N inventory in the surface layer ($\Delta N^*/\Delta t \times 50$ m) ranged from 2 to 10 mmol m^{-2} year^{-1}, which accounts for only 5–10% of the anthropogenic nitrogen deposition (50–110 mmol N m^{-2} year^{-1}). This large difference indicates that most deposited anthropogenic nitrogen was either assimilated and exported to the interior as organic matter, or was mixed downward to depths exceeding the mixed layer. By comparing the amount of anthropogenic nitrogen deposition with estimates of export production based on an empirical model (Falkowski et al. 1998) and a coupled physical-ecosystem model (Onitsuka et al.

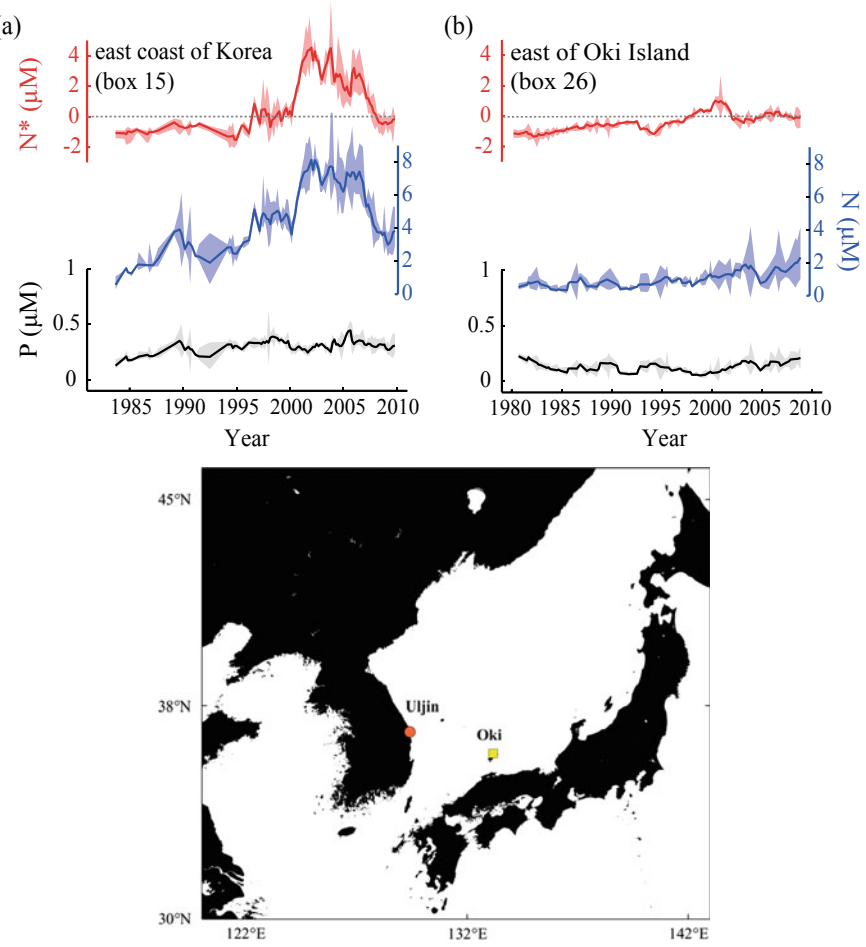

Fig. 6.6 Time-series of N* (μM) (red line), nitrate (N, μM) (blue line), and phosphorus (P, μM) (black line) **a** off the east coast of Korea (Uljin; box 15 in Fig. 6.5) and **b** in the region east of Oki Island (box 26 in Fig. 6.5). The color gradations indicate the confidence interval (p = 0.05) from the mean of the measurements collected over a 2-month interval. The dotted lines correspond to N* = 0 μM Modified from figures supplied by Kim et al. (2011)

2009), anthropogenic nitrogen deposition has been estimated to be a significant contributor to export production in this region, accounting for 10% of that occurring in the East Sea (Onitsuka et al. 2009; Kang et al. 2010).

The impact of anthropogenic nitrogen deposition on seawater N* is not confined to the surface layer, but extends to deeper layers of the East Sea (Fig. 6.8). Anthropogenic nitrogen deposition increased the N* values in waters to depths of 750 m, but the signals were rapidly attenuated at greater depth. The N* inventory in the East Sea was calculated by vertical integration of N* values between the surface and

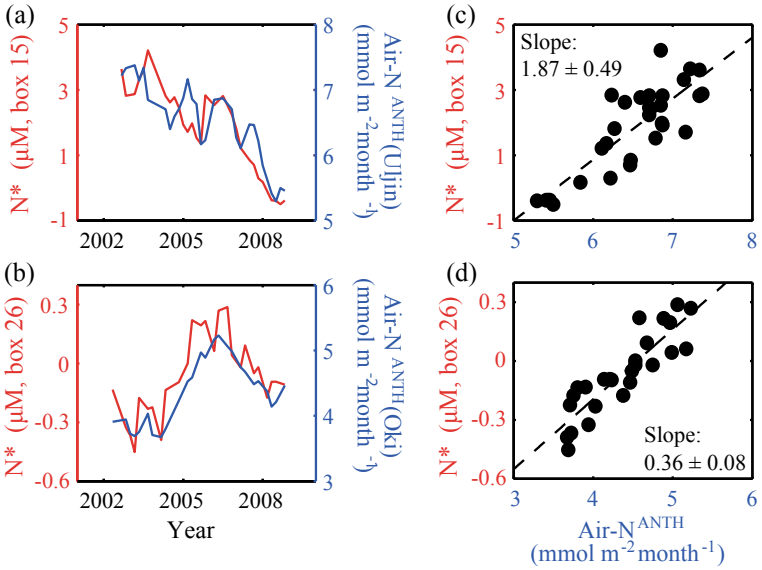

Fig. 6.7 **a**, **b** Time-series (left column) and **c**, **d** correlation (right column) plots of N* (μM) and the total (wet + dry) anthropogenic N deposition ($NO_3^- + NH_4^+$, mmol m^{-2} $month^{-1}$) measured at the two air monitoring stations (Uljin, east coast of Korea and east of Oki Island). For the time-series and correlation plots, 2-year moving averages of two measures were used, anthropogenic N deposition and seawater N*. The dashed lines in the correlation plots are least-squares linear fits. Modified from figures supplied by Kim et al. (2011)

750 m depth. The increase in N* over the past 3 decades was 0.68×10^{12} mol N, which is consistent with the integrated anthropogenic nitrogen deposition rate over this period (0.79×10^{12} mol N). The consistency between these values indicates that anthropogenic nitrogen deposition was sufficiently large to account for the observed increase in N* in the East Sea, and this conclusion is reinforced by the fact that no major river (a major N contributor) flows into the East Sea. Moreover, an additional P source (via atmospheric deposition) to the East Sea is insignificant (Xing et al. 2018) and thus do not contribute to change in the N* trend in the East Sea. The abundance of N relative to P in the East Seas has increased significantly since 1980. Anthropogenic nitrogen deposition has progressively reduced the deficiency of N relative to P over the extensive areas of the East Sea.

The findings presented in this chapter have far-reaching implications for marginal seas near other major continents. The observed trends can probably be extrapolated to the North, Baltic, South China, and Mediterranean Seas (Kim et al. 2014a; Moon et al. 2016), which have received increasing amounts of anthropogenic nitrogen via atmospheric deposition and riverine input. The findings further indicate that anthropogenic nitrogen is replacing the conventional paradigm of nitrate flux from nitrate-rich deep water as the primary driver of biological export production (Zhang et al. 2001; Duce et al. 2008).

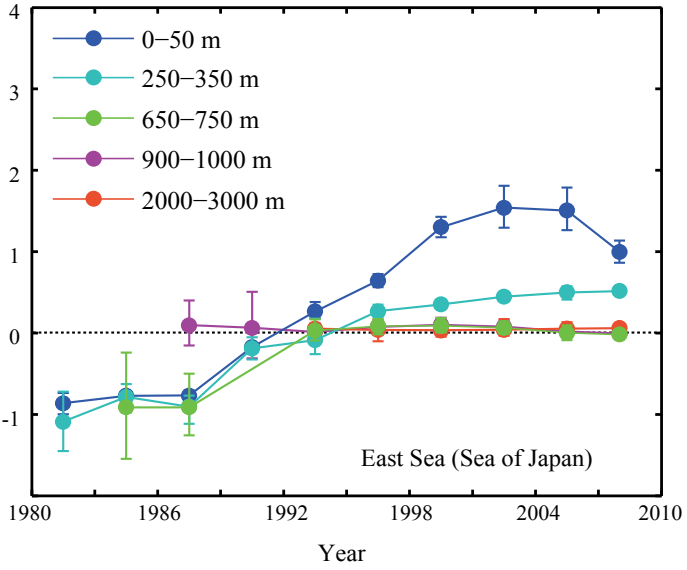

Fig. 6.8 Time-series of the 3-year mean N* (μM) for various depth ranges in the East Sea. The colors indicate the N* values derived from the data collected at the indicated depth ranges. The dotted lines correspond to N* = 0 μM. The error bars are the confidence interval of the resulting N*, for p = 0.05. Modified from a figure supplied by Kim et al. (2011)

6.5 Conclusions

The East Sea is actively ventilated from the surface to the bottom over decadal time scales. The distribution of anthropogenic CO_2 in the East Sea shows features that are consistent with the distribution found in the North Atlantic Ocean, where deep water formation occurs, particularly the high levels of anthropogenic CO_2 in the water column. However, the formation of sea ice is the source of deep and bottom waters in the East Sea. As future climate warming could greatly reduce or possibly eliminate sea ice in the East Sea, this could have profound impacts on the accumulation of anthropogenic CO_2 in its deep waters. The impact of the East Sea processes on the properties of waters of the North Pacific is not firmly established; however, it should not be overlooked. The decreasing salinity and cooling of the East Sea may affect the formation of North Pacific Intermediate Water by modifying the properties of the outflow entering the Sea of Okhotsk. Changes in North Pacific Intermediate Water formation directly impact the amount of anthropogenic CO_2 that is transported from the Sea of Okhotsk to the North Pacific Ocean.

In addition to climatic impacts, increasing inputs of anthropogenic nitrogen is affecting the nitrogen cycle of the East Sea. The impact of this is growing, and it will eventually affect the absorption and storage of anthropogenic CO_2 in the East Sea by increasing organic C production by phytoplankton. These two major perturbations

(warming and anthropogenic nitrogen loading) will probably shift the nitrogen and carbon cycles in the East Sea to unprecedented states in the coming decades.

Acknowledgments This work was primarily supported by Mid-career Researcher Program (No. 2018R1A2A1A19019281) of the National Research Foundation of Korea (NRF) funded by the Ministry of Science, ICT and Future Planning and by "Ieodo Ocean Research Station" project of the Korea Hydrographic and Oceanographic Agency, Ministry of Oceans and Fisheries.

References

Akimoto H, Narita H (1994) Distribution of SO_2, NO_x and CO_2 emissions from fuel combustion and industrial activities in Asia with $1° \times 1°$ resolution. Atmos Environ 28:213–225

Andreae MO, Crutzen PJ (1997) Atmospheric aerosols: biogeochemical sources and role in atmospheric chemistry. Science 276:1052–1058

Bourgeois T, Orr JC et al (2016) Coastal-ocean uptake of anthropogenic carbon. Biogeosciences 13:4167–4185

Chen CTA, Borges AV (2009) Reconciling opposing views on carbon cycling in the coastal ocean: Continental shelves as sinks and near-shore ecosystems as sources of atmospheric CO_2. Deep-Sea Res PT II 56:578–590

Chen CTA, Wang SL, Bychkov AS (1995) Carbonate chemistry of the Sea of Japan. J Geophys Res-Oceans 100:13737–13745

Chen CTA, Andreev A et al (2004) Roles of continental shelves and marginal seas in the biogeochemical cycles of the North Pacific Ocean. J Oceanogr 60:17–44

Chen CTA, Wang SL et al (2006) Carbonate chemistry and projected future changes in pH and $CaCO_3$ saturation state of the South China Sea. Mar Chem 101:277–305

Chen CTA, Lui HK et al (2017) Deep oceans may acidify faster than anticipated due to global warming. Nat Clim Change 7:890–894

Choi SD, Lee K, Chang YS (2002) Large rate of uptake of atmospheric carbon dioxide by planted forest biomass in Korea. Global Biogeochem Cy 16. https://doi.org/10.1029/2002GB001914

Cossarini G, Querin S, Solidoro C (2015) The continental shelf carbon pump in the northern Adriatic Sea (Mediterranean Sea): Influence of wintertime variability. Ecol Model 314:118–134

Deutsch C, Emerson S, Thompson L (2006) Physical-biological interactions in North Pacific oxygen variability. J Geophys Res-Oceans 111. https://doi.org/10.1029/2005JC003179

Dickson AG, Millero FJ (1987) A comparison of the equilibrium constants for the dissociation of carbonic acid in seawater media. Deep-Sea Res 34:1733–1743

Duce RA, Laroche J et al (2008) Impacts of atmospheric anthropogenic nitrogen on the open ocean. Science 320:893–897

Engel A, Piontek J et al (2014) Impact of CO_2 enrichment on organic matter dynamics during nutrient induced coastal phytoplankton blooms. J Plankton Res 36:641–657

Falkowski PG, Barber RT, Smetacek V (1998) Biogeochemical controls and feedbacks on ocean primary production. Science 281:200–206

Galloway JN (2000) Nitrogen mobilization in Asia. Nutr Cycl Agroecosys 57:1–12

Galloway JN, Dentener FJ et al (2004) Nitrogen cycles: Past, present, and future. Biogeochemistry 70:153–226

Gamo T (1999) Global warming may have slowed down the deep conveyor belt of a marginal sea of the northwestern Pacific: Japan Sea. Geophys Res Lett 26:3137–3140

Gamo T, Momoshima N, Tolmachyov S (2001) Recent upward shift of the deep convection system in the Japan Sea, as inferred from the geochemical tracers tritium, oxygen, and nutrients. Geophys Res Lett 28:4143–4146

Gruber N, Sarmiento JL, Stocker TF (1996) An improved method for detecting anthropogenic CO_2 in the oceans. Global Biogeochem Cy 10:809–837
Gruber N, Clement D et al (2019) The oceanic sink for anthropogenic CO_2 from 1994 to 2007. Science 363:1193–1199
Iglesias-rodriguez MD, Halloran PR et al (2008) Phytoplankton calcification in a high-CO_2 world. Science 320:336–340
Jickells TD, Buitenhuis E et al (2017) A reevaluation of the magnitude and impacts of anthropogenic atmospheric nitrogen inputs on the ocean. Global Biogeochem Cy 31:289–305
Joos F, Plattner GK, Stocker TF et al (2003) Trends in marine dissolved oxygen: Implications for ocean circulation changes and the carbon budget. EOS Trans AGU 84:197–201
Kang J, Cho BC, Lee CB (2010) Atmospheric transport of water-soluble ions (NO^{3-}, NH^{4+} and nss-SO_4^{2-}) to the southern East Sea (Sea of Japan). Sci Total Environ 408:2369–2377
Kim KR, Kim K (1996) What is happening in the East Sea (Japan Sea): Recent chemical observations during CREAMS 93–96. J Kor Soc Oceanogr 31:164–172
Kim JM, Lee K et al (2010a) Enhanced production of oceanic dimethylsulfide resulting from CO_2-induced grazing activity in a high CO_2 world. Environ Sci Technol 44:8140–8143
Kim TW, Lee K et al (2010b) Prediction of Sea of Japan (East Sea) acidification over the past 40 years using a multiparameter regression model. Global Biogeochem Cy 24. https://doi.org/10.1029/2009GB003637
Kim K, Kim KR et al (2001) Warming and structural changes in the east (Japan) Sea: A clue to future changes in global oceans? Geophys Res Lett 28:3293–3296
Kim TW, Lee K et al (2011) Increasing N abundance in the northwestern Pacific Ocean due to atmospheric nitrogen deposition. Science 334:505–509
Kim TW, Lee K et al (2013) Interannual nutrient dynamics in Korean coastal waters. Harmful Algae 30:S15–S27
Kim IN, Lee K et al (2014a) Increasing anthropogenic nitrogen in the North Pacific Ocean. Science 346:1102–1106
Kim TW, Lee K et al (2014b) Impact of atmospheric nitrogen deposition on phytoplankton productivity in the South China Sea. Geophys Res Lett 41:3156–3162
Kim JM, Lee K et al (2018) Phytoplankton do not produce carbon-rich organic matter in high CO_2 oceans. Geophys Res Lett 45:4189–4197
Lee K, Choi SD et al (2003) An updated anthropogenic CO_2 inventory in the Atlantic Ocean. Global Biogeochem Cy 17. https://doi.org/10.1029/2003GB002067
Lee K, Millero FJ, Campbell DM (1996) The reliability of the thermodynamic constants for the dissociation of carbonic acid in seawater. Mar Chem 55:233–245
Lee K, Millero FJ et al (2000) The recommended dissociation constants for carbonic acid in seawater. Geophys Res Lett 27:229–232
Lee K, Kim TW et al (2010) The universal ratio of boron to chlorinity for the North Pacific and North Atlantic oceans. Geochim Cosmochim Ac 74:1801–1811
Lee K, Sabine CL et al (2011) Roles of marginal seas in absorbing and storing fossil fuel CO_2. Energy Environ Sci 4:1133–1146
Liss PS, Malin G, Turner S (1993) Production of DMS by marine phytoplankton. Dimethylsulphide: oceans, atmosphere and climate. London: Kluwer Academic Publications, pp 1–14
Marland G, Boden TA, Andres RJ (2008) Global, regional, and national fossil fuel CO_2 emissions. Trends: A Compendium of Data on Global Change. Carbon Dioxide Information Analysis Center, Oak Ridge National Laboratory, U.S. Department of Energy, Oak Ridge, Tenn., U.S.A
Mcdonagh EL, Bryden HL et al (2005) Decadal changes in the South Indian Ocean thermocline. J Climate 18:1575–1590
Mcelligott S, Byrne RH et al (1998) Discrete water column measurements of CO_2 fugacity and pHT in seawater: a comparison of direct measurements and thermodynamic calculations. Mar Chem 60:63–73
Mehrbach C, Culberson CH et al (1973) Measurement of the apparent dissociation constants of carbonic acid in seawater at atmospheric pressure. Limnol Oceanogr 18:897–907

Millero FJ (1995) Thermodynamics of the carbon dioxide system in the oceans. Geochim Cosmochim Ac 59:661–677
Millero FJ, Pierrot D et al (2002) Dissociation constants for carbonic acid determined from field measurements. Deep-Sea Res PT I 49:1705–1723
Min DH, Warner MJ (2005) Basin-wide circulation and ventilation study in the East Sea (Sea of Japan) using chlorofluorocarbon tracers. Deep-Sea Res PT II 52:1580–1616
Moon JY, Lee K et al (2016) Temporal nutrient dynamics in the Mediterranean Sea in response to anthropogenic inputs. Geophys Res Lett 43:5243–5251
Murata A, Kumamoto Y et al (2007) Decadal increases of anthropogenic CO_2 in the South Pacific subtropical ocean along 32°S. J Geophys Res-Oceans 112. https://doi.org/10.1029/2005JC003405
Nakamura T, Matsumoto K, Uematsu M (2005) Chemical characteristics of aerosols transported from Asia to the East China Sea: an evaluation of anthropogenic combined nitrogen deposition in autumn. Atmos Environ 39:1749–1758
Ohara T, Akimoto H et al (2007) An Asian emission inventory of anthropogenic emission sources for the period 1980-2020. Atmos Chem Phys 7:4419–4444
Okin GS, Baker AR et al (2011) Impacts of atmospheric nutrient deposition on marine productivity: roles of nitrogen, phosphorus, and iron. Global Biogeochem Cy 25. https://doi.org/10.1029/2010GB003858
Onitsuka G, Uno I et al (2009) Modeling the effects of atmospheric nitrogen input on biological production in the Japan Sea. J Oceanogr 65:433–438
Park GH, Lee K et al (2006) Large accumulation of anthropogenic CO_2 in the East (Japan) Sea and its significant impact on carbonate chemistry. Global Biogeochem Cy 20. https://doi.org/10.1029/2005GB002676
Park GH, Lee K, Tishchenko P (2008) Sudden, considerable reduction in recent uptake of anthropogenic CO_2 by the East/Japan Sea. Geophys Res Lett 35. https://doi.org/10.1029/2008GL036118
Peng TH, Wanninkhof R et al (1998) Quantification of decadal anthropogenic CO_2 uptake in the ocean based on dissolved inorganic carbon measurements. Nature 396:560–563
Peng TH, Wanninkghof R, Feely RA (2003) Increase of anthropogenic CO_2 in the Pacific Ocean over the last two decades. Deep-Sea Res PT II 50:3065–3082
Quay P, Sonnerup R et al (2007) Anthropogenic CO_2 accumulation rates in the North Atlantic Ocean from changes in the $^{13}C/^{12}C$ of dissolved inorganic carbon. Global Biogeochem Cy 21. https://doi.org/10.1029/2006gb002761
Ren H, Chen YC et al (2017) 21st-century rise in anthropogenic nitrogen deposition on a remote coral reef. Science 356:749–752
Riebesell U, Zondervan I et al (2000) Reduced calcification of marine plankton in response to increased atmospheric CO_2. Nature 407:364–367
Riebesell U, Schulz KG et al (2007) Enhanced biological carbon consumption in a high CO_2 ocean. Nature 450:545–548
Sabine CL, Feely RA et al (2002) Distribution of anthropogenic CO_2 in the Pacific Ocean. Global Biogeochem Cy 16. https://doi.org/10.1029/2001GB001639
Schmidtko S, Stramma L, Visbeck M (2017) Decline in global oceanic oxygen content during the past five decades. Nature 542:335–339
Talley LD, Lobanov V et al (2003) Deep convection and brine rejection in the Japan Sea. Geophys Res Lett 30. https://doi.org/10.1029/2002GL016451
Talley LD, Tishchenko P et al (2004) Atlas of Japan (East) Sea hydrographic properties in summer, 1999. Prog Oceanogr 61:277–348
Talley LD, Min DH et al (2006) Japan/East Sea water masses and their relation to the sea's circulation. Oceanography 19:32–49
Thomas H, Bozec Y et al (2004) Enhanced open ocean storage of CO_2 from shelf sea pumping. Science 304:1005–1008

Tsunogai S, Watanabe S, Sato T (1999) Is there a "continental shelf pump" for the absorption of atmospheric CO_2? Tellus B 51:701–712

Xing J, Song J et al (2018) Water-soluable nitrogen and phosphorus in aerosols and dry deposition in Jianzhou Bay, North China: Deposition velocities, orignins and biogeochemical implications. Atmos Res 207:90–99

Zhang H, Cao L (2016) Simulated effect of calcification feedback on atmospheric CO_2 and ocean acidification. Sci Rep-UK 6:20284

Zhang JZ, Wanninkhof R, Lee K (2001) Enhanced new production observed from the diurnal cycle of nitrate in an oligotrophic anticyclonic eddy. Geophys Res Lett 28:1579–1582

Zhang G, Zhang J, Liu S (2007) Characterization of nutrients in the atmospheric wet and dry deposition observed at the two monitoring sites over Yellow Sea and East China Sea. J Atmos Chem 57:41–57

Zhang SH, Yu J et al (2018) Effect of elevated pCO_2 on trace gas production during an ocean acidification mesocosm experiment. Biogeosciences 15:6649–6658

Chapter 7
The Changing Bohai and Yellow Seas: A Physical View

Hao Wei, Haiyan Zhang, Wei Yang, Jianlong Feng, and Cuicui Zhang

Abstract The Bohai and Yellow Seas (BYSs) are the marginal seas in the Northwestern Pacific region. Consistent with the general trend of global warming, the BYSs are also changing rapidly which include the change of sea surface temperature (SST), water masses and sea level etc. These parameters are very sensitive to the global warming due to the shallow water depth of the BYSs. The SST in the BYSs shows an increasing trend of 0.8 to 2 °C per century, nearly twice of the globally averaged rate. Similarly, the Yellow Sea Cold Water Mass (YSCWM), which is one of the most prominent hydrologic features in the YS, also shows a clear warming trend in its northern part. Previous studies also found that the coastal sea level in the BYSs is increasing rapidly with the rising rate higher than the global average. Besides these long-term varying trend, there also exist strong interannual variations which sometimes can be regarded as responses to the large-scale climatic variations affecting the East Asian monsoon, such as the Arctic Oscillation (AO), the Pacific Decadal Oscillation (PDO) and the El Niño–Southern Oscillation (ENSO). Artificial coastline changing also induced the storm surge abnormal variation especially in the BS.

Keywords The Bohai and Yellow Seas · Sea surface temperature · Coastal sea level · Temporal changes

H. Wei · H. Zhang · W. Yang (✉) · C. Zhang
School of Marine Science and Technology, Tianjin University, Tianjin, China
e-mail: wei_yang@tju.edu.cn

H. Wei
e-mail: hao.wei@tju.edu.cn

H. Zhang
e-mail: haiyan_zhang@tju.edu.cn

C. Zhang
e-mail: cuicui.zhang@tju.edu.cn

J. Feng
College of Marine and Environmental Sciences, Tianjin University of Science and Technology, TEDA, Tianjin, China
e-mail: fjl181988@tust.edu.cn

C.-T. A. Chen and X. Guo (eds.), *Changing Asia-Pacific Marginal Seas*, Atmosphere, Earth, Ocean & Space, https://doi.org/10.1007/978-981-15-4886-4_7

7.1 Introduction

The Bohai and Yellow Seas (BYSs) are typical semi-closed marginal seas, located on the continental shelf of the Northwestern Pacific (Fig. 7.1). The Bohai Sea (BS) is connected with the Yellow Sea (YS) through the Bohai Strait. The BS covers an area of 7.7×10^4 km^2 with an average water depth of 18 m, and is usually divided into five parts: the Bohai Bay, the Laizhou Bay, the Liaodong Bay, the central BS, and the Bohai Strait. In the central BS, there exists a shallow area named as the Liaodong Bank. The Yellow Sea has an extent of 30.9×10^4 km^2 with an average depth of 44 m. It is divided into the North Yellow Sea (NYS) and the South Yellow Sea (SYS) by the line connecting the Chengshan Cape and Changsan-got. The 50 m isobaths defines a trough in the northwest-southeast direction, with the maximum depth reaching 110 m (Sun 2008).

The BYSs are located in the mid-latitudes and are influenced by the East Asian monsoon, thus have pronounced seasonal variations present in the physical environments. In winter the water temperature is low and stratification is mostly absent

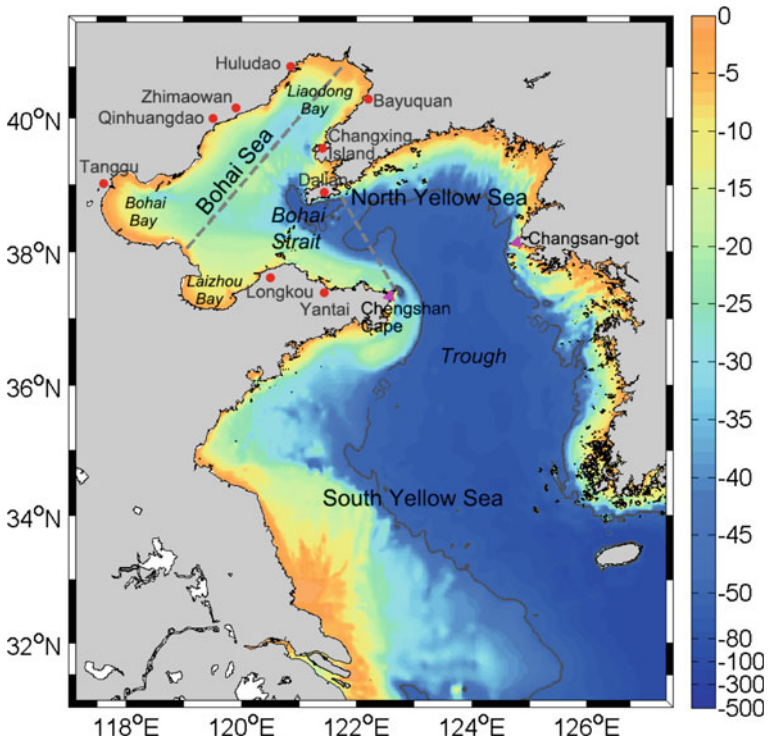

Fig. 7.1 Topography of the BYSs with color shading denoting depth in meter, and a solid black contour depicting the 50 m isobath. The dashed lines in the BS and NYS are the standard transects of hydrography observations

except when the saline and warm Yellow Sea Warm Current intrudes into the SYS. In summer a strong seasonal thermocline develops, with upper layer being warmer and the lower layer beneath the thermocline being still cold (He et al. 1959; Lin et al. 2006). In addition, strong tidal fronts exist in summer (Zhao 1987; Zhao et al. 2001). Climate variability and global warming have profound influences on the physical environments of the region. The construction of artificial coastline leads to changes of tides and localized anomalies of mean sea levels (Pelling et al. 2013).

7.2 Changes of Water Temperature

In winter, the water column is well mixed vertically, with temperature of −1.5–3.6 °C in the BS and 0–13 °C in the YS. In summer, the upper layer above the thermocline is occupied by warm water with temperature in the range of 24–27 °C. By contrast, below the thermocline the temperature is lower than 20 °C in the BS, mainly in the depressions around the Liaodong Bank; and lower than 10 °C in the YS, mainly in the trough and the adjacent deep areas (Sun 2008).

Consistent with global warming, sea surface temperature (SST) in the BYSs also shows an increasing trend. Based on observations during 1960–1997 at coastal stations (i.e., Longkou, Tanggu, Qinhuangdao, Zhimaowan, Bayuquan, and Changxing Island) around the BS, Lin et al. (2001) obtained the sea surface warming rates in the range of 0.001 °C/year(yr)–0.019 °C/yr, with the average rate being 0.011 °C/yr. Based on observations during a slightly shorter period (1965–1997) at coastal stations (Longkou, Tanggu, Qinhuangdao, Hulutao, Bayuquan, Dalian, Yantai), Fang et al. (2002) obtained a relatively higher warming rate of 0.015 °C/yr, which may be attributed to the exclusion of the extremely warm year of 1961. During this period, the coastal SST in the BS has increased by 0.48 °C, about two times of the amplitude of global ocean warming (Lau and Weng 1999). The higher warming rate in the BYSs can be related to the shallow water depth and small heat content, in comparison with the global ocean.

In the BS, water temperature observations have been made at grid-stations and along standard transects by the former State Oceanic Administration of China. Analyses have revealed that the temperature in different seasons shows prominently different variations at interannual and decadal time scales. Based on SST maps derived from observations at stations during 1960–1985, the surface temperature shows an increasing trend in spring (May) and a decreasing trend in summer (August) (He and Zhang 1990). Through analyzing observations along the standard transect that connects the Yellow River estuary and the head of the Liaodong Bay (dashed line in Fig. 7.1), Li et al. (2018) identified a warming trend in winter (February) during 1978–1999. However, through examining the winter-mean time series of SST during a longer period of 1976–2012, Shi (2013a, b) found that this warming trend became much less evident, in comparison with the pronounced interannual and decadal variations (Fig. 7.2). In summer, through analyzing the observational data

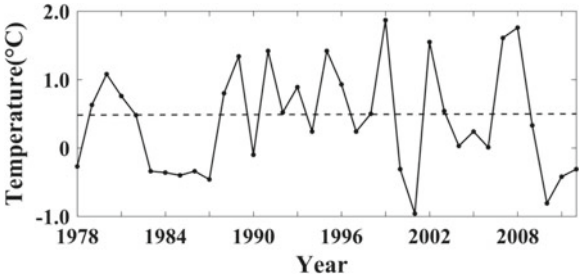

Fig. 7.2 Winter-averaged surface temperature (°C) along the standard transect in the BS. The dashed line represents the linear regression of temperature. Re-plotted from Shi (2013b)

along the standard transect during 1978–2014, Shi (2015) further confirmed the cooling trend, with a higher cooling rate of 0.029 °C/yr in the bottom layer. Specifically, cooling mainly occurred in the warm central BS, with an average cooling rate of 0.068 °C/yr during 1976–2003; while during the same period a warming trend of 0.036 °C/yr was found in the cold water adjacent to the depressions (Jia et al. 2008). Further studies are required to understand the decadal variations, the differences in long-term trends among the seasons, and the spatial variations of the trends in summer.

Similar to the BS, temperature in the YS also shows different trends in winter and summer. The winter temperature presents a warming trend, while in summer there is no clear warming or cooling trend beyond the interannual variations (Wei et al. 2010; Shi 2015). Based on observations along the standard transect that connects Dalian and the Chengshan Cape in the NYS (Fig. 7.1), the winter surface temperature shows an increasing trend of 0.048 °C/yr during 1977–2012 (Shi 2013a, b). Besides this overall warming trend, the winter temperature shows a cooling trend after 2008, and this also occurs in the SYS according to observations along the standard transect 36° N (Fig. 7.3; Shi 2013a, b, 2014). Moreover, based on winter temperature observations along several transects in the YS from 1977 to 1998, Wei et al. (2010) found distinct cold and warm phases before and after 1986.

In addition to in-situ observations, the SST data from satellite remote sensing and ocean reanalysis SST products have also been analyzed to reveal a basin-scale warming trend in the BYSs, although the estimated rates differ based on different

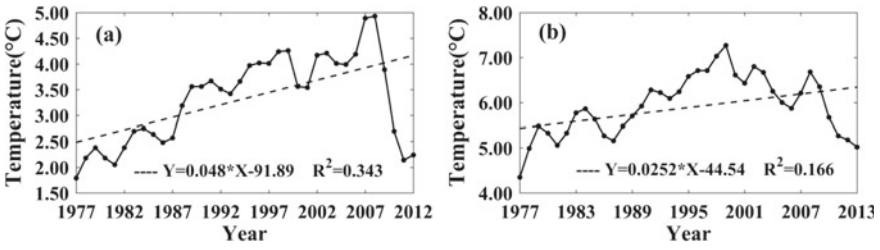

Fig. 7.3 Winter-averaged surface temperature along standard transects in **a** the NYS and **b** the SYS. Replotted from Shi (2013a) and (2014)

datasets. The averaged warming rate was 0.04 °C/yr based on the Advanced Very High Resolution Radiometer (AVHRR) data during 1981–2009 (Park et al. 2015), while was only 0.01 °C/yr based on the Hadley reanalysis data during 1985–2015 (Jiang et al. 2018). The difference between the two estimated rates is partly due to the exclusion of the cooling period after 2008 in the analysis of Park et al. (2015). Spatially, the SST warming rate is higher in the shallow waters of the YS than in that of the BS. The SST warming is accompanied by the strengthening of water column stratification (Park et al. 2015). Based on the AVHRR data of 1982–2011 that has been calibrated with observations, Luo et al. (2012) showed that, on decadal time scales, the winter SST in the YS changed from a cold phase to a warm phase during 1989–1990, and from a warm phase back to a cold phase during 2000–2001. Therefore, the SST in 1990s was the highest, 1.07 °C higher than that in the 1980s and 0.53 °C higher than in the 2000s. The warming before the 1990s and cooling after the 1990s were also confirmed by Kim et al. (2018).

In winter, variations of water temperature in the BYSs is mainly attributed to the turbulent (latent and sensible) components of the air-sea heat fluxes, and hence can be related to changes in surface winds and the large-scale atmospheric circulation. In the central YS in winter, the variations of the main axis of the Yellow Sea Warm Current (YSWC) can also induce an east-west difference in water temperature (Yuan 2011; Wei et al. 2013). Water temperature variations in the BYSs have also been related to large-scale climatic variations affecting the East Asian monsoon, such as the Arctic Oscillation (AO), the Pacific Decadal Oscillation (PDO) and the El Niño–Southern Oscillation (ENSO) (Fang et al. 2002; Wei et al. 2010; Yeh and Kim 2010; Yuan 2011; Luo et al. 2012; Park et al. 2015; Shi 2015; Kim et al. 2018). The winter warming in the BYSs can be mainly attributed to the weakening of the East Asian Winter Monsoon (EAWM) that corresponds to the reduction in heat loss from the ocean, and this can be further related to the positive AO index phase (Yuan 2011; Wei et al. 2013).

The first mode of the empirical orthogonal function (EOF) of the winter SST variability in the BYSs has a significant correlation with the AO index ($R = 0.50$, $p < 0.01$; Park et al. 2015), which is also correlated with the North Pacific Oscillation (NPO, Yeh and Kim 2010). More specifically, the first EOF mode has a significant correlation with the PDO index before the regime shift in the North Pacific (1982–1997), and has a weak correlation after the 1990s (Kim et al. 2018). In the BYSs in summer, variations of water temperature in the upper layer are primarily caused by variations in shortwave solar radiation that exhibit moderate correlations with the three indices of the atmospheric circulation pattern of the Western Pacific Subtropical High, namely its area, intensity and the western boundary; whereas water temperature variations in the bottom layer closely follow the variations of winter temperature (Wei et al. 2013).

7.3 The Yellow Sea Cold Water Mass and Tidal Fronts

One of the prominent features of hydrography in the YS is the existence of the Yellow Sea Cold Water Mass (YSCWM) in summer. It refers to a bulk of water mass with temperature lower than 10 °C that lies below the seasonal thermocline in the central of YS at depth exceeding 30 m (Fig. 7.4). Since the first observational evidence of the YSCWM was presented (Uda 1934), this unique water mass has been studied extensively. He et al. (1959) suggested that the YSCWM was formed locally in the YS during the summer season, and was in fact the remaining cold water mass of the previous winter. The bowl-like topography and the shallow water fronts induced by the strong tidal mixing also play a significant role in the maintenance of the cold water mass (Guan 1963; Zhao 1985). There are two low-temperature centers of the YSCWM located in the NYS and SYS, respectively. In some years, the YSCWM has another low-temperature center at the western part of the SYS (Weng 1988; Lee et al. 1998).

The seasonal evolution of the YSCWM is generally clear based on previous studies. In the late spring and early summer (April to June), the YSCWM begins to form along with the appearance of thermocline due to the rapid warming at the sea surface. The YSCWM is formed from July to August when the thermocline becomes strongest. The water column can be vertically separated into three layers during that period: the upper well-mixed warm water, a narrow thermocline, and the lower well-mixed cold water. Water temperature can change by 18 °C within a short distance across the thermocline. Due to the cooling of atmosphere from September to November, the thermocline weakens while the temperature of the central YSCWM begins to increase. From December to the next March/April, the thermocline disappears and the YSCWM becomes indistinct as the water is well-mixed in the vertical direction (Qiu et al. 1989; Ren and Zhan 2005; Zhang et al. 2008).

Besides the seasonal variation, the YSCWM also shows evident long term and interannual changes. Based on observations along a section across the northern part of the YSCWM, Jiang et al. (2007) revealed a slightly increasing trend of temperature from 1976 to 1999. Li et al. (2015a) found that the temperature in the center of the northern part of the YSCWM increased 0.026 °C/yr from 1976 to 2006, along with the weakening of the front in the northern part. This warming in the northern part of the YSCWM in summer can be related to the warming in the NYS in winter caused by the weakening of the East Asian Winter Monsoon during the same period (Li et al. 2015a). Limited by the length of the observations, the long term trend of temperature in the southern part of the YSCWM still remains unclear.

It is generally agreed that the interannual variations of the temperature of the YSCWM in summer are closely related to that of the local water temperature during the previous winter (Guan 1963; Hu and Wang 2004; Park et al. 2011; Yang et al. 2014). This relationship has been continuously applied to explain the observed interannual variations of the YSCWM temperature in summer (Li et al. 2015b; Zhu et al. 2018). However, unclarified details of the YSCWM variations still remain. For example, what percentage of the YSCWM originates from the coastal water? What

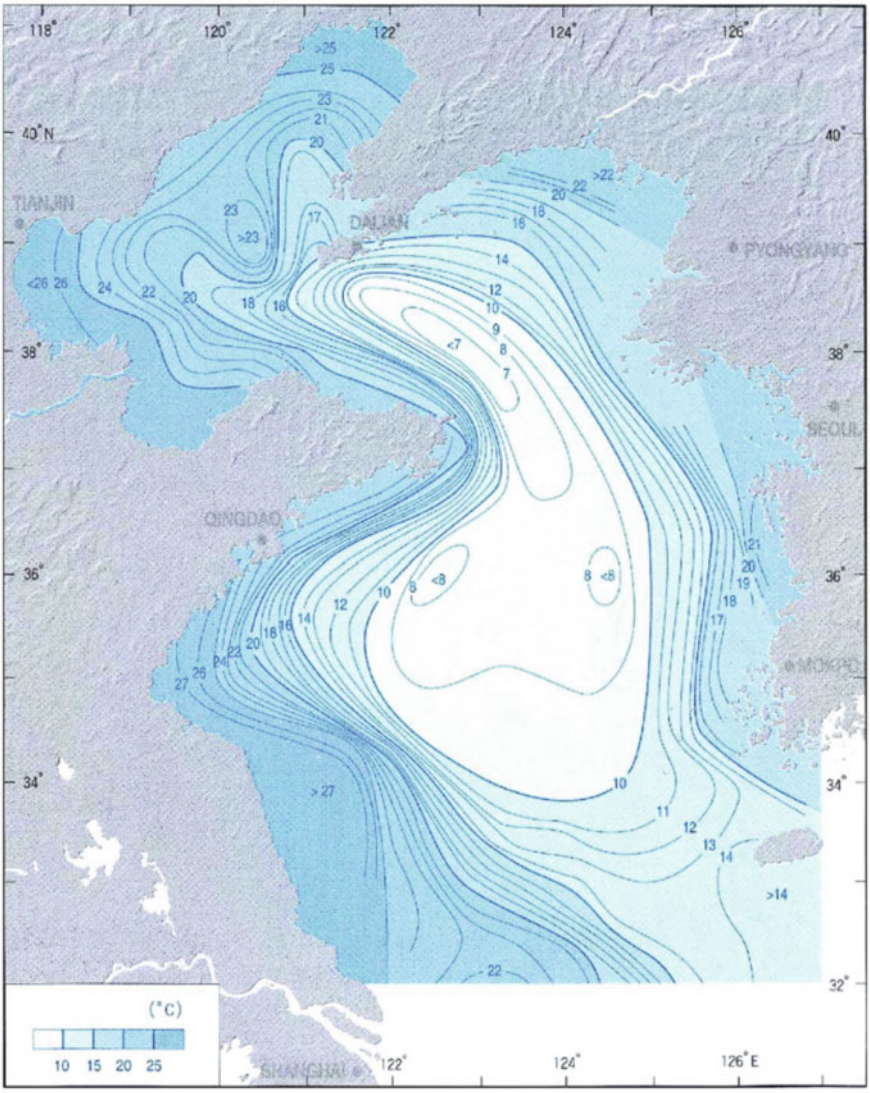

Fig. 7.4 Bottom water temperature of the Yellow Sea in August (1958–1988) Modified from Lee et al. (1998)

is the associated circulation pattern during the formation stage of the YSCWM? Further studies are needed to answer these questions.

The upper border line of the YSCWM takes the shape of a bowl being turned upside down to cover the topography, if looking from the side (Fig. 7.5b). Zhao (1985) pointed out that in summer the isothermal lines would be horizontally flat if only the wind-induced mixing were considered (see Fig. 7.5a). However, the presence of

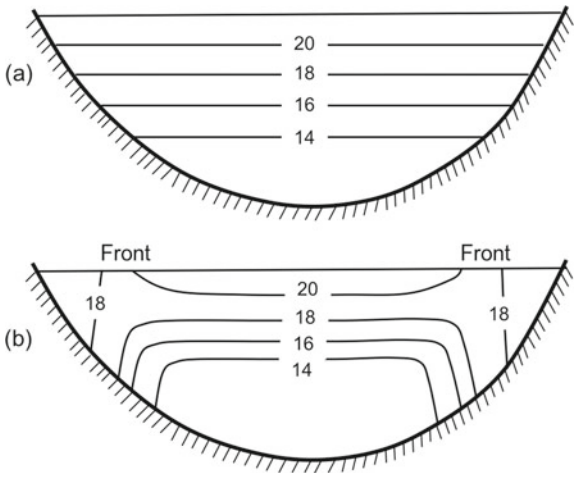

Fig. 7.5 The cross-section distribution of temperature **a** without and **b** with the tidal mixing effect being included

tidal mixing would break down the pycnocline in the coastal region and thus creating horizontal fronts that separate the coastal well-mixed water from the deeper stratified water. The locations of the fronts can be estimated by calculating the Simpson-Hunter number. Zhao (1985) found that the locations of the fronts coincided with the boundary of the YSCWM if the critical value of the Simpson-Hunter number was taken as 1.8–2. This implied that besides the surface heating in summer, the strong tidal mixing in coastal water is also an important factor during the formation of the YSCWM. Based on numerical model simulations, Ren and Zhan (2005) investigated the roles played by the thermocline, tidal mixing and the local topographic feature in the formation of the YSCWM and found a direct relationship between the amplitude of the tidal currents and the coverage area of the YSCWM. Xu et al. (2003) suggested that the strong boundary mixing in the YS played an important role in maintaining the dome-like feature of the thermocline which acted as the upper boundary of the YSCWM.

Based on mooring observations lasting for nearly 1 year in the western part of the SYS, Li et al. (2016) studied the declining stage of the YSCWM and found step-like increases of the near-bottom temperature in autumn. During each spring tide, the bottom temperature increased by nearly 2 °C. The causes of this step-like changing feature were not explored in previous studies. Based on the results of Ren and Zhan (2005), we suggest the changes in the positions of the fronts as a plausible interpretation. That is, as the coastal water cools down, the positions of the front shift to a deeper location due to tidal mixing during each spring tide; and the bottom water at the mooring location, after the front passes by to the deeper side, shall mix with the warm water in the upper layer hence its temperature increases. This interpretation needs to be validated with more comprehensive observations. Overall, it is reasonable to conclude that tidal mixing plays important roles in both the formation and decline of the YSCWM.

7.4 Changes of the Sea Levels: Rising Rate, Tides and Extremes

The sea levels of coastal areas of the BYSs have significant fluctuations, but also a generally increasing trend during the past 40 years. The rate of coastal sea level rise in the BYSs is higher than the global average during the same period. As summarized in Table 7.1, the rising rate has significant regional differences, and also shows acceleration in recent years (see also in Fig. 7.6).

Sea levels of the BYSs present significant seasonal, interannual and decadal variations (Feng et al. 2012; Pan et al. 2017), in particularly at periods of 1, 2, 4–7, 11 and 19 years. The range of the seasonal sea level variations decreases from north to south along the coast of China, from 60 cm in the Bohai Sea to 25 cm in the South China Sea. In the meanwhile, the occurrence of the maximum delays from north to south, from July in the Bohai Sea to November in the South China Sea (Fang et al. 1986). The seasonal sea level variations at tide gauges along the BS and YS are quite close to a sinusoidal function. The highest monthly mean sea level in the BS usually occurs in July–August (months with the highest air temperature and the lowest surface air pressure), and the lowest monthly mean usually occurs in January. The range of the seasonal variation is about 60 cm. In the YS, the highest monthly mean

Table 7.1 Rates of coastal sea level rise of the BYSs

References	Data	Period	Region	Rate (mm/yr)
China Sea Level Bulletin (2008)	Tide gauges	1979–2008	Bohai Sea	2.6
			Yellow Sea	2.3
Qiao and Chen (2008)	T/P Jason-1	1992–2004	Bohai Sea	3.6
			Yellow Sea	5.2
Liu et al. (2009)	AVISO	1992–2007	Bohai Sea and North Yellow Sea (37°–41° N, 117°–121° E)	3.3
			Middle of the South Yellow Sea (33°–37° N, 117°–125 E)	2.5
Zhan et al. (2009)	AVISO SLA	1993–2007	Yellow Sea	3.9
Wang et al. (2014)	AVISO SLA	1993–2011	Bohai and Yellow Sea	3.1
Zhang and Fang (2015)	AVISO	1993–2012	Bohai Sea	3.1
			Yellow Sea	2.9
Guo et al. (2015)	T/P Jason-1 Jason-2	1993–2012	Bohai Sea	4.4
			Yellow Sea	2.3
Chang et al. (2017)	GRACE AVISO Ishii	1993–2014	Bohai Sea	3.1
			Yellow Sea	2.6

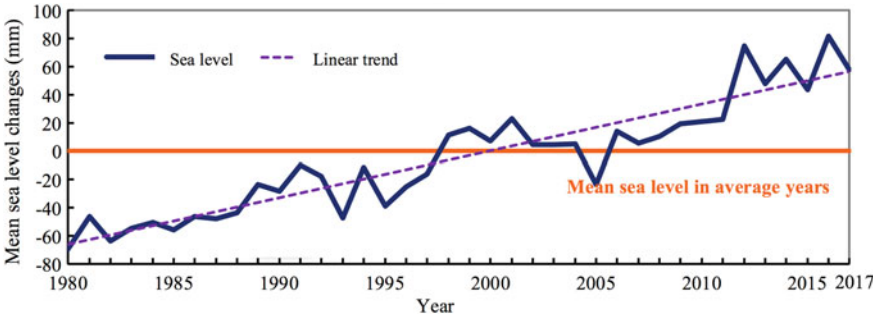

Fig. 7.6 Time series of the averaged sea level in the coastal areas of China from 1980 to 2017 (China Sea Level Bulletin 2017)

sea level usually occurs in August, and the lowest monthly mean usually occurs in January–February, with the range of the seasonal variation about 45 cm (Wang et al. 2012) (Fig. 7.7).

Due to the changes of mean sea level and changes in bathymetry, the amplitude of the M_2 tidal constituent in the BS decreased at the rate of 2.1 mm/yr since 1950, while the amplitude of the K_1 constituent showed little changes (Liu et al. 2017); while in the YS, the amplitude of the M_2 constituent increased at the rate of 4–7 mm/yr from 1954 to 2012 (Feng et al. 2015). From 1954 to 2012, the epoch of the semidiurnal

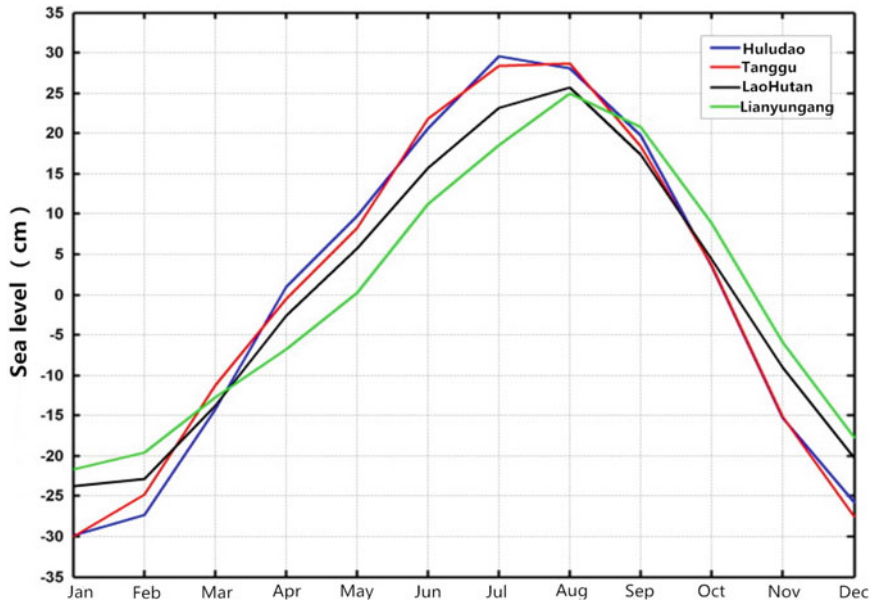

Fig. 7.7 The seasonal variations of the sea levels at tide gauges along the coast of the BYSs (Modified from Wang et al., 2012)

constituents decreased in the BS but increased in the YS. In the BS since 1950, the epoch of the M_2 constituent decreased at the rate of 0.11°/yr, and the epoch of K_1 constituent decreased at the rate of 0.09°/yr (Liu et al. 2017).

From 1970 to 1997, the mean tide range in the YS increased at the rate of 7.1 mm/yr. The mean tide range increased at the rate of 12.3 mm/yr at Lianyungang, and 3.0 mm/yr at Chengshantou. At both stations, the increasing rate of the mean tide range was 1.5–4 times that of the sea level rise (Zhang and Du 2000). At most tide gauges along the coast of China, the mean high tide shows significant rising trends, and the average rate is about 5.1 mm/yr. The rates are the largest from the northern YS to Hangzhoy Bay, of about 5–12 mm/yr; are the smallest along the southwestern part of the BS, of about 2–4 mm/yr (Zhang et al. 2018).

The extreme sea levels along the coast of China have increased (Feng and Tsimplis 2014). Ma et al. (2016) found that the maximum water levels at Tianjin estimated using the data from 1980–2012 were higher than that estimated using the data from 1950 to 1979. Feng et al. (2018b) found that the extreme sea levels at four tide gauges in the BS increased during the recent decades from 1980 to 2016, and this change of the extreme sea levels is highly affected by the sea level rise and of high tide levels (Fig. 7.8).

Based on numerical model simulation, Feng et al. (2014) showed that the storm surges at Qingdao would intensify under the conditions of sea level rise and the increasing sea surface temperature. Zhao and Jiang (2011) and Ding and Wei (2016)

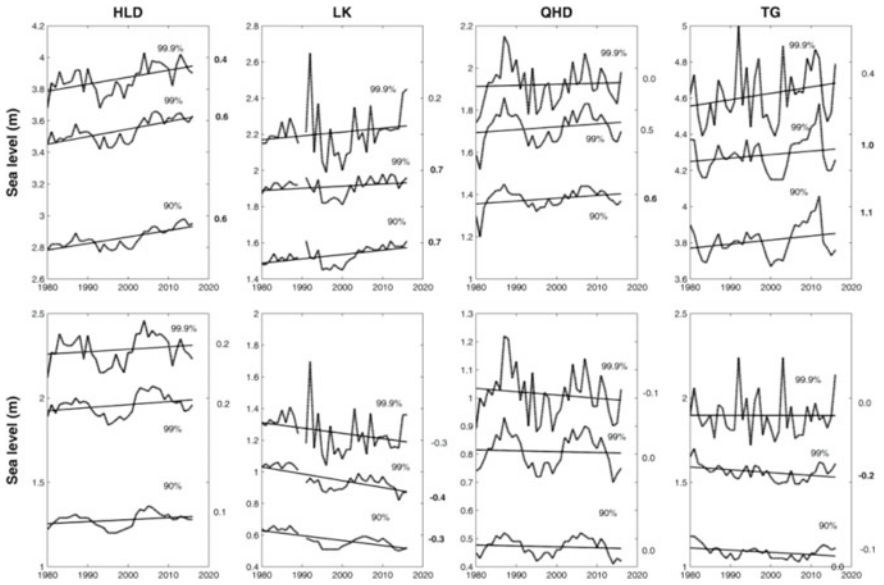

Fig. 7.8 Time series of percentiles of (upper) total and (lower) reduced (mean sea level) sea level height for HLD, LK, QHD and TG. The straight lines are the linear trends, and their change rates (cm/year) are listed at the right-side of each panel (Feng et al. 2018b). The 99.9% percentile level represent the 99.9% highest water level during a year

found that the land reclamation patterns and changes of the coastline can affect the storm surges in the BS. Using a numerical model, Feng et al. (2015) showed that along the coastline of the BS, the intensity of storm surges decreased from 1961 to 2006, especially at the Bohai Bay and Laizhou Bay. Using data from 4 tidal gauges (1980–2016), Feng et al. (2018a) further related the decadal and long-term changes of storm surges in the BS to the changes of the AO and the Siberian High.

7.5 Summary

The Bohai and Yellow Seas, as typical marginal seas in the Northwestern Pacific region, have changing physical environments under the influence of climate variability and global warming. In this study, we have reviewed theories, observations, and numerical simulations that are relevant to the topic of changing BYS. Three subjects are involved including the changes of water temperature, the most important regional water mass (the YSCWM), and sea levels.

Long-term observations show that the sea surface temperature in the BYSs shows an increasing trend, consistent with the global warming. Under this overall increasing trend, however, both the BS and YS show different variations in summer and winter. The warming trend is most obvious in winter with its controlling factors remaining unknown. The YSCWM, as the most prominent feature of hydrography in the summer stratified YS, also shows evident long term and interannual changes. The interannual variation of the temperature of the YSCWM is successfully related to the previous local water temperature during the previous winter. The northern part of YSCWM have been reported to experience warming trend with the southern part remain unclear. Further studies are required to understand the differences and mechanisms in long-term trends among the seasons, and also the oscillations with interannual to multi-decadal time scale. The sea levels of coastal areas of the BYSs also have a generally increasing trend during the past 40 years with a faster rising rate than the global average. Furthermore, observations show that the rising rate is now under acceleration trend in recent years which has significant regional differences.

Acknowledgments This study was supported by the National Key Research and Development Program of China (Grant No. 2017YFC1404403). H.Y. Zhang thanks the support from National Natural Science Foundation of China (NSFC, 41806018). W. Yang thanks the support from NSFC (41906006). J.L. Feng thanks the support from NSFC (41706020). C.C. Zhang thanks the support from NSFC (41806116).

References

Chang L, Qian A, Yi S, Xu C, Sun W (2017) Sea level change in China adjacent seas studied using satellite altimeter, satellite gravity, and thermohaline data. J Univ Chin Acad Sci 34(3):371–379 (in Chinese with English abstract)

China's State Oceanic Administration (2008) China sea level bulletin. China's State Oceanic Administration, Beijing

China's State Oceanic Administration (2017) China sea level bulletin. China's State Oceanic Administration, Beijing

Ding Y, Wei H (2016) Modeling the impact of land reclamation on storm surges in Bohai Sea, China. Nat Hazards 85:559–573. https://doi.org/10.1007/s11069-016-2586-4

Fang G, Chen Z, Zheng W et al. (1986) Analysis and prediction of tides and tidal current. China Ocean Press, Beijing, pp 474 (in Chinese)

Fang GH, Wang K, Guo FY, Wei ZX, Fan WJ, Zhang DS, Bi JH (2002) Long-term changes and interrelations of annual variations of the hydrographical and meteorological parameters of the Bohai Sea during recent 30 years. Oceanol Limnol Sin 33(5):515–525 (in Chinese with English abstract)

Feng X, Tsimplis MN (2014) Sea level extremes at the coasts of China. J Geophys Res-Oceans 119:1593–1608. https://doi.org/10.1002/2013JC009607

Feng W, Zhong M, Xu Z (2012) Sea level variations in the South China Sea inferred from satellite gravity, altimetry, and oceanographic data. Sci China-Earth Sci. https://doi.org/10.1007/s11430-01204394-3 (in Chinese with English abstract)

Feng J, Jiang W, Bian C (2014) Numerical prediction of storm surge in the Qingdao area under the impact of climate change. J Ocean U China 13(4):539–551

Feng X, Tsimplis MN, Woodworth PL (2015) Nodal variations and long-term changes in the main tides on the coasts of China. J Geophys Res-Oceans 120:1215–1232

Feng J, Li D, Li Y, Liu Q, Wang A (2018a) Storm surge variation along the coast of the Bohai Sea. Sci Rep 8:11309. https://doi.org/10.1038/s41598-018-29712-z

Feng J, Li D, Wang H, Liu Q, Zhang J, Li Y, Liu K (2018b) Analysis on the extreme sea levels changes along the coastline of Bohai Sea, China. Atmosphere 9:324. https://doi.org/10.3390/atmos9080324

Guan B (1963) A preliminary study of the variation of the temperature and the characteristics of the circulation of the Yellow Sea Cold Water Mass. Oceanol et Limnol Sin 5(4):255–284

Guo J, Wang J, Hu Z, Hwang C, Chen C, Gao Y (2015) Temporal-spatial variations of sea level over China seas derived from altimeter data of TOPEX/Poseidon, Jason-1 and Jason-2 from 1993 to 2012. Chin J Geophys-Chin Ed 58(9):3103–3120. https://doi.org/10.6038/cjg20150908 (in Chinese with English abstract)

He XM, Zhang YK (1990) Distribution and interannual variation of water temperature in spring, summer and autumn in central and southern Bohai Sea. Mar Forecasts 7(3):44–50 (in Chinese with English abstract)

He C, Wang Y, Lei Z, Xu S (1959) Preliminary study of the formation of Yellow Sea Cold Water Mass and its property. Oceanol et Limnol Sin 2(1):11–15 (in Chinese with English abstract)

Hu DX, Wang QY (2004) Interannual variability of the southern Yellow Sea Cold Water Mass. Chin J Oceanol Limnol 22(3):231–236

Jia RL, Su J, Hu XM, CAO Yong (2008) Structure of temperature and salinity and its variation along B1 section during summer. J Ocean U China 38(5):705–711 (in Chinese with English abstract)

Jiang BJ, Bao XW, Wu DX, Xu JP (2007) Interannual variations of temperature and salinity of northern Yellow Sea Cold Water Mass and its possible cause. Acta Oceanol Sin 29(4):1–10 (in Chinese with English Abstract)

Jiang WF, Yu LL, Yu QX, Jiang Y, Jiao Y (2018) Spatio-temporal analysis of the sea surface temperature in the Bohai and Yellow Seas under the background of climate change. J Guangxi Acad Sci 34(3):216–221 (in Chinese with English abstract)

Kim YS, Jang CJ, Yeh SW (2018) Recent surface cooling in the Yellow and East China Seas and the associated North Pacific climate regime shift. Cont Shelf Res 156:43–54. https://doi.org/10.1016/j.csr.2018.01.009

Lau KM, Weng H (1999) Interannual, decadal–interdecadal, and global warming signals in sea surface temperature during 1955–97. J Clim 12(5):1257–1267

Lee YC, Qin Y, Liu R (1998) Yellow Sea Atlas. HoKong Publishing Co, Seoul, Korea

Li XW, Wang XD, Chu P, Zhao DL (2015a) Low-frequency variability of the Yellow Sea Cold Water Mass identified from the China Coastal Waters and adjacent sea reanalysis. Adv Meteorol. https://doi.org/10.1155/2015/269859

Li A, Yu F, Diao XY, Si GC (2015b) Interannual variability of temperature of the northern Yellow Sea Cold Water Mass. Acta Oceanol Sin 37(1):30–42

Li JC, Li GX, Xu JS, Dong P, Qiao LL, Liu SD, Sun PK, Fan ZS (2016) Seasonal evolution of the Yellow Sea Cold Water Mass and its interactions with ambient hydrodynamic system. J Geophys Res-Oceans 121(9):6779–6792. https://doi.org/10.1002/2016JC012186

Li B, Zhao L, Wei S (2018) Inter-annual variations of dissolved oxygen and nutrients in the Bohai Sea and the North Yellow Sea (accepted). https://doi.org/10.13364/j.issn.1672-6510. 20170342

Lin CL, Su JL, Xu BR, Tang QS (2001) Long-term variations of temperature and salinity of the Bohai Sea and their influence on its ecosystem. Prog Oceanogr 49(1–4):7–19. https://doi.org/10.1016/S0079-6611(01)00013-1

Lin XP, Xie SP, Chen XP, Xu LL (2006) A well-mixed warm water column in the central Bohai Sea in summer: effects of tidal and surface wave mixing. J Geophys Res—Oceans 111(C11). https://doi.org/10.1029/2006JC003504

Liu X, Liu Y, Guo L, Gu Y, Liu Y, Ma Y (2009) Mean sea level change in East China Sea and its response to ENSO. Mar Sci Bull 28(05):34–42 (in Chinese with English abstract)

Liu KX, Wang H, Fu SJ, Gao ZG, Dong JX, Feng JL, Gao T (2017) Evaluation of sea level rise in Bohai Bay and associated response. Adv Climate Change Res 8:48–56. https://doi.org/10.1016/j.accre.2017.03.006

Luo XF, Wei H, Yuan CY (2012) Inter-annual and decadal variations of sea surface temperature in the Yellow Sea by satellite data. Periodical Ocean Univ China 42(10):19–25 (in Chinese with English abstract)

Ma XD, Zhang GY, Yuan DK, Li YY (2016) Analysis of the characteristics of storm surges in Tianjin coastal area. Adv Mar Sci 34(4):516–522 (in Chinese with English abstract)

Pan Y, Yue JP, Song YH, Peng GY, Zhang P (2017) Initial research on sea level change in the South China Sea from 1993 to 2015. Geospatial Inf 15(10):9–13 (in Chinese with English abstract)

Park S, Chu PC, Lee JH (2011) Interannual-to-interdecadal variability of the Yellow Sea Cold Water Mass in 1967–2008: characteristics and seasonal forcings. J Mar Syst 87(3–4):177–193. https://doi.org/10.1016/j.jmarsys.2011.03.012

Park KA, Lee EY, Chang E, Hong SV (2015) Spatial and temporal variability of sea surface temperature and warming trends in the Yellow Sea. J Mar Syst 143:24–38. https://doi.org/10.1016/j.jmarsys.2014.10.013

Pelling HE, Uehara K, Green JAM (2013) The impact of rapid coastline changes and sea level rise on the tides in the Bohai Sea, China. J Geophys Res—Oceans 118(7):3462–3472. https://doi.org/10.1002/jgrc.20258

Qiao X, Chen G (2008) A preliminary analysis on the China Sea level using 11 years'TOPEX/Poseidon altimeter data. Mar Sci 01:60–64 (in Chinese with English abstract)

Qiu DL, Zhou SL, Li CM (1989) Application of cluster analysis method in determining water mass of the Huanghai Sea. Acta Oceanol Sin 6(3):281–292 (in Chinese with English abstract)

Ren HJ, Zhan JM (2005) A numerical study on the seasonal variability of the yellow sea cold water mass and the related dynamics. J Hydrodyn 20(S1):887–896 (in Chinese with English abstract)

Shi Q (2013a) Climate response and spatial-temporal model of the inter-annual change of temperature and salinity in the north Yellow Sea in winter. Marin Sci Bull 32(6):633–640 (in Chinese with English abstract)

Shi Q (2013b) Climate response and spatial-temporal model on the inter-annual change of temperature-salinity in the Bohai Sea during winter. Marin Sci Bull 32(5):505–513 (in Chinese with English abstract)
Shi Q (2014) Climate response and spatial-temporal model of the inter-annual change of winter temperature-salinity in the South Yellow Sea. Mar Sci Bull 33(2):148–156 (in Chinese with English abstract)
Shi Q (2015) Climate response and spatio-temporal model on the interannual temperature-salinity changes in summer of Bohai Sea. J Appl Oceanogr 34(4):484–495 (in Chinese with English abstract)
Sun XP (2008) Regional marine in China Seas. China Ocean Press, Beijing (in Chinese with English abstract)
Uda M (1934) Hydrographical researches on the normal monthly conditions in the Japan Sea, the Yellow Sea and the Okhotsk Sea. J Imperial Fish Exp Stat 5:191–236
Wang H, Fan W, Gao Z (2012) Analysis on the sea level anomaly high in the coastal area of Bohai Sea and Yellow Sea. Mar Sci Bull 31(03):255–261 (in Chinese with English abstract)
Wang L, Wang J, Yang J (2014) The comprehensive analysis of sea-level change in the East China Sea. Acta Oceanol Sin 36(01):28–37 (in Chinese with English abstract)
Wei H, Shi J, Lu Y, Peng Y (2010) Interannual and long-term hydrographic changes in the Yellow Sea during 1977–1998. Deep-Sea Res Pt II 57(11–12):1025–1034
Wei H, Yuan C, Lu Y, Zhang Z, Luo X (2013) Forcing mechanisms of heat content variations in the Yellow Sea. J Geophys Res-Oceans 118(9):4504–4513
Weng XC, Zhang YK, Wang CM et al (1988) The variation characteristics of the Yellow Sea cold water mass. Oceanologia Limnologia Sinica 19(4):368–379 (in Chinese with English abstract)
Xu D, Yuan Y, Liu Y (2003) The baroclinic circulation structure of Yellow Sea Cold Water Mass. Sci China 46(2):117–126
Yang H, Cho Y, Seo G, You SH, Seo J (2014) Interannual variation of the southern limit in the Yellow Sea Bottom Cold Water and its causes. J Mar Syst 139:119–127
Yeh SW, Kim CH (2010) Recent warming in the Yellow/East China Sea during winter and the associated atmospheric circulation. Cont Shelf Res 30(13):1428–1434
Yuan C (2011) Forcing mechanisms of seasonal to decadal variations of oceanic temperature and circulation in the Yellow Sea. Dissertation, Ocean University of China
Zhan J, Wang Y, Cheng Y (2009) The analysis of China Sea level change. Chin J Geophys 52(07):1725–1733 (in Chinese with English abstract)
Zhang J, Du B (2000) The trend of tidal range enlarging along the coast of the Yellow Sea of China. Mar Sci Bull 19(1):1–9 (in Chinese with English abstract)
Zhang J, Fang M (2015) Sea level trends of China Seas from 1993 to 2012. J Ocean U China 45(01):121–126 (in Chinese with English abstract)
Zhang SW, Wang QY, Lu Y, Cui H, Yuan YL (2008) Observation of the seasonal evolution of the Yellow Sea Cold Water Mass in 1996–1998. Cont Shelf Res 28(3):442–457
Zhang J, Wang H, Fan W, Li W, Gao T, Liu Q (2018) Characteristics of tide variation/change along the China coast. In: The 28th international ocean and polar engineering conference, June 2018 (accepted)
Zhao B (1985) The fronts of the Huanghai Sea Cold Water Mass induced by tidal mixing. Oceanologia Limnologia Sinica 16(6):451–460 (in Chinese with English abstract)
Zhao B (1987) The continental shelf fronts induced by tidal mixing in the Huanghai Sea. Adv Mar Sci 5(2):16–23
Zhao P, Jiang W (2011) A numerical study of the effects of coastal geometry in the Bohai Sea on storm surges induced by cold-air outbreaks. J Ocean U China 10(1):9–15. https://doi.org/10.1007/s11802-011-1746-0

Zhao B, Cao DM, Li WF et al (2001) Tidal mixing characters and tidal fronts phenomenon in the Bohai Sea. Acta Oceanol Sin 23:113–118 (in Chinese with English abstract)
Zhu J, Shi J, Guo X, Gao H, Yao X (2018) Air-sea heat flux control on the Yellow Sea Cold Water Mass intensity and implications for its prediction. Cont Shelf Res. https://doi.org/10.1016/j.csr.2017.10.006,152:14-26

Chapter 8
Changing Nutrients, Dissolved Oxygen and Carbonate System in the Bohai and Yellow Seas, China

Wei-dong Zhai, Li-wen Zheng, Cheng-long Li, Tian-qi Xiong, and Song-yin Wang

Abstract The Bohai and Yellow Seas in the Northwest Pacific are semi-enclosed shallow marginal seas of ecological and economic significance. By reviewing and synthesizing literature data, basin-wide decadal changes in nutrients and bottom-water dissolved oxygen and carbonate system parameters in the two coastal oceans were investigated. Results showed that both of the two coastal oceans were subject to basin-wide increases in wintertime nitrate during the past 40 years. The present-day seawater N:P ratios are usually within the algae-favorable range of 14–19. Presumably due to these changes, the Bohai Sea exhibits a 33-year decline in summertime bottom-water dissolved oxygen and the associated suppression of pH and $CaCO_3$ saturation states in summer. The historically lowest bottom-water dissolved oxygen in the Bohai Sea was recorded at 67 μmol O_2 L^{-1} in early September 2015, which was very close to the threshold value of hypoxia. In the Yellow Sea, periodical suppression of pH and $CaCO_3$ saturation states occurs in its central basin area, where the net community carbonate dissolution was detectable in bottom waters in late summer and autumn, threatening marine calcifiers inhabiting there and with potentially severe consequences for valuable shellfish fisheries.

Keywords Bohai sea · Yellow sea · Eutrophication · Deoxygenation · Coastal acidification

W. Zhai (✉) · L. Zheng · C. Li · T. Xiong · S. Wang
Institute of Marine Science and Technology, Shandong University, Qingdao 266237, China
e-mail: wdzhai@126.com

L. Zheng
e-mail: zhengliwen516@163.com

C. Li
e-mail: clli23@126.com

T. Xiong
e-mail: xiongtianqi0701@sina.com

S. Wang
e-mail: 2511936284@qq.com

C.-T. A. Chen and X. Guo (eds.), *Changing Asia-Pacific Marginal Seas*, Atmosphere, Earth, Ocean & Space, https://doi.org/10.1007/978-981-15-4886-4_8

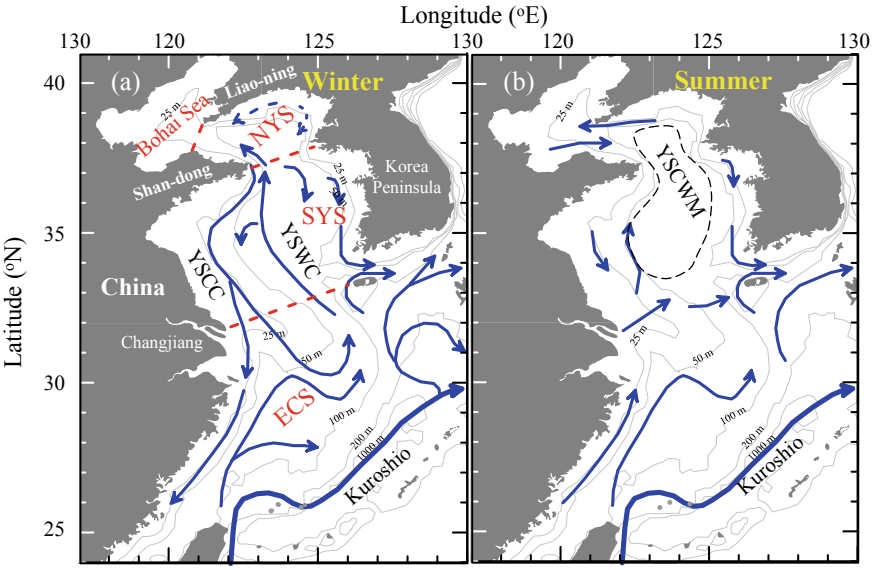

Fig. 8.1 Maps showing geography and circulations. NYS = North Yellow Sea. SYS = South Yellow Sea. ECS = East China Sea. YSCC = Yellow Sea Coastal Current. YSWC = Yellow Sea Warm Current. YSCWM = Yellow Sea Cold Water Mass

The Bohai and Yellow Seas are two western North Pacific marginal seas of major ecological and economic importance (Fig. 8.1). Both of them sustained many commercially valuable fishery species, and they are teeming with fast-developing marine aquaculture activities, including acid-sensitive scallops and clams.

The Bohai Sea has an area of 77000 km^2 and a mean depth of only 18 m, with a maximum depth of approximately 60 m. It is surrounded by China's Hebei, Liaoning, and Shandong provinces, and Tianjin.

The Yellow Sea has a total area of ~0.37×10^6 km^2. It is geographically divided into two basins, i.e., the North Yellow Sea and the South Yellow Sea. The North Yellow Sea is surrounded by Liaoning and Shandong provinces of China, and the Democratic People's Republic of Korea, as well as being connected to the Bohai Sea to the west. The South Yellow Sea is connected to the East China Sea to the south. The North Yellow Sea has an area of ~70×10^3 km^2 and a mean water depth of 38 m, while the South Yellow Sea has an area of ~300×10^3 km^2 and a mean water depth of 44 m. The deepest water depth of 103 m occurs within the eastern basin of the South Yellow Sea, near the Republic of Korea.

Climatic variations of the Bohai and Yellow Seas are primarily dominated by the East Asian Monsoon (Chen 2009). The rain-bearing southwest monsoon lasts from June to early September, while the strong northeast monsoon prevails in autumn, winter, and early spring, from November to March of each year (Zhai et al. 2014). During the northeast monsoon period, the general circulation is characterized by a strong southward-moving coastal current and the northward-moving Yellow Sea

Warm Current (YSWC) within its central basin area. The YSWC is considered a compensating current to the northeast monsoon-driven Yellow Sea coastal current (YSCC), transporting saline open ocean waters into the Yellow Sea (Fig. 8.1a; Chen 2009). During the southwest monsoon period, the summertime hydrography across the Yellow Sea is characterized by a pronounced stratification in its deeper regions. A cold pool develops, typically with water temperatures of 8–11 °C, which is overlain by 15 to 25 m of warm water. It is regarded as being the remnant of the previous winter's cooling and is known as the Yellow Sea cold water mass (Fig. 8.1b).

Since the 1980s, the Bohai Sea fishery resources have experienced a continuing decline (e.g. Deng et al. 1988; Jin 2000; Li et al. 2008). Moreover, there has been a basin-wide nitrate enrichment in the Bohai Sea over the past 40 years (Zhao et al. 2002; Wang and Li 2006; Wang et al. 2019). Consequently, the frequency of algae blooms in the Bohai Sea increased since 1999 (Song et al. 2016), and summertime bottom-water DO decreased (Ning et al. 2010; Shi 2016; Zhai et al. 2019). Recently, quite low summertime bottom-water concentrations of dissolved oxygen (DO) were detected at 67 to 90 μmol O_2 L^{-1} in parts of the central Bohai Sea in August 2014 (Zhang et al. 2016; Zhao et al. 2017) and in early September 2015 (Zhai et al. 2019), close to hypoxia. The latter is a DO threshold of lower than 63 μmol O_2 L^{-1}, i.e. 2 mg L^{-1} or 1.4 mL O_2 L^{-1} (Rabalais et al. 2010). These phenomena suggest that the Bohai Sea is on a critical path of environmental degradation.

The Yellow Sea is fed by nutrient inputs from both atmospheric dry/wet deposition (Zhang 1994; Shi et al. 2012; Tan and Wang 2014) and subsurface regeneration processes (Zhang et al. 2002). In a year, algal blooms are observed from April to October (He et al. 2013), while green tides of macroalgae *Ulva prolifera* recur from May to July (Hu et al. 2010). These blooms undoubtedly cause sinking particulate organic matters, leading to seasonal subsurface oxygen consumption, CO_2 accumulation and pH decline (Zhai et al. 2014; Zhai 2018).

In this chapter, we synthesized relevant literature data. We aimed to describe basin-scale changes in nutrients and dissolved oxygen during the past $30-40$ years, emphasizing the recent emergence of hypoxia in the Bohai Sea. Also we characterized seasonal variations in subsurface carbonate system parameters, including fugacity of CO_2 (fCO_2), $CaCO_3$ saturation state of aragonite (Ω_{arag}), and pH, highlighting the metabolism-enhanced ocean acidification in the Bohai and Yellow Seas.

8.1 Changing Nutrients in the Bohai and Yellow Seas

In the Bohai and Yellow Seas, both biological assimilation and respiration/remineralization can result in complex seasonal variations in nutrient contents and structures (Chen 2009). To show the basin-wide eutrophication, only wintertime nutrient data are presented in this chapter.

In the central Bohai Sea (excluding the Yellow River Estuary, the Bohai Bay, the Laizhou Bay, and the Liaodong Bay), wintertime dissolved inorganic nitrogen (DIN) rose from 4.6 ± 3.0 μmol L^{-1} in the 1980s to 9.4 ± 5.3 μmol L^{-1} in the

2010s (Fig. 8.2a), while wintertime phosphate decreased from 1.9 ± 0.5 μmol L^{-1} in the 1980s to 0.6 ± 0.1 μmol L^{-1} in the 2010s (Fig. 8.2b). It is also notable that wintertime DSi declined from from 15 ± 5 μmol L^{-1} in the 1980s to 6 ± 3 μmol L^{-1} in the 1990s and 8 ± 3 μmol L^{-1} in the 2000s (Fig. 8.2c). Recently the wintertime DSi rose again to 11.3 ± 0.3 μmol L^{-1} in 2016 (Fig. 8.2c). The wintertime DIN:DIP ratio increased from 2.4 ± 2.0 in 1983 to 7.6 ± 4.7 in 1993 and 8.5 ± 3.2 in 2001 (Fig. 8.2d). From 2006 to 2016, the central Bohai Sea wintertime DIN:DIP ratio varied limitedly between 16.1 ± 3.0 and 16.9 ± 3.4 (Fig. 8.2d).

Similarly, wintertime DIN in the Yellow Sea rose during past three decades (e.g. He et al. 2013; Wei et al. 2015; Yang et al. 2018). For example, the wintertime concentration of nitrate increased by 1–2 folds from the 1980s to 2000s in the North Yellow Sea (Yang et al. 2018). In this chapter, we integrated basin-wide nutrient data collected by us in the North Yellow Sea with literature data collected in the South Yellow Sea along the 36°N transect (Fig. 8.2e–h), since the two areas are closely coupled with each other through the YSWC and YSCC in winter (Fig. 8.1a). The results showed that Yellow Sea wintertime DIN increased from 1.3 ± 0.7 μmol L^{-1} in 1985 to 6.3 ± 5.3 μmol L^{-1} during the 2000s and 2010s (Fig. 8.2e). From the 1980s to the 2010s, the mean concentration of phosphate varied limitedly between 0.2 μmol L^{-1} and 0.6 μmol L^{-1} (Fig. 8.2f), while DSi increased from usually 2–6 μmol L^{-1} in the 1980s and 1990s to frequently 8–12 μmol L^{-1} in the 2000s and 2010s (Fig. 8.2g). The Yellow Sea wintertime DIN:DIP ratio increased from a quite low level of ~4.5 in 1985 to the algae-favorable range of 14–19 in the 2000s and 2010s (Fig. 8.2h).

Causes underlying the decadal changes in basin-wide nutrients are quite complex. According to Wang et al. (2019), the phosphate decrease in the Bohai Sea from the 1980s to 1990s may result from the sediment load decrease of the Yellow River during that period, and the increasing sewage discharges and nonpoint nutrient sources contribute the DIN increase. Moreover, the widespread anthropogenic nitrogen via atmospheric deposition may also supply sea surface excess DIN (relative to previous phosphate) since the 1980s (Kim et al. 2014; Kim et al. 2017). Although subsurface regeneration processes undoubtedly provide nutrients (especially for phosphate), some researchers have provided evidences showing causal relationship between the Yellow Sea springtime algae blooms with nutrient supply from the deposition of Asian dust (e.g. Zhang 1994; Shi et al. 2012; Tan and Wang 2014). In a research spanning the North Pacific Ocean, Kim et al. (2014) found that sea surface DIN in the vicinity of the Asian dust source area increased by ~0.24 μmol L^{-1} per year from 1980 to 1999. Therefore, the increasing DIN that appeared in the Bohai and Yellow Seas (Fig. 8.2) may reflect a combined effect of local human activities (such as the increasing sewage discharge and marine aquaculture) and the regional environment changes (e.g. the inland land-use and land-cover changes and the Asian dust dynamics).

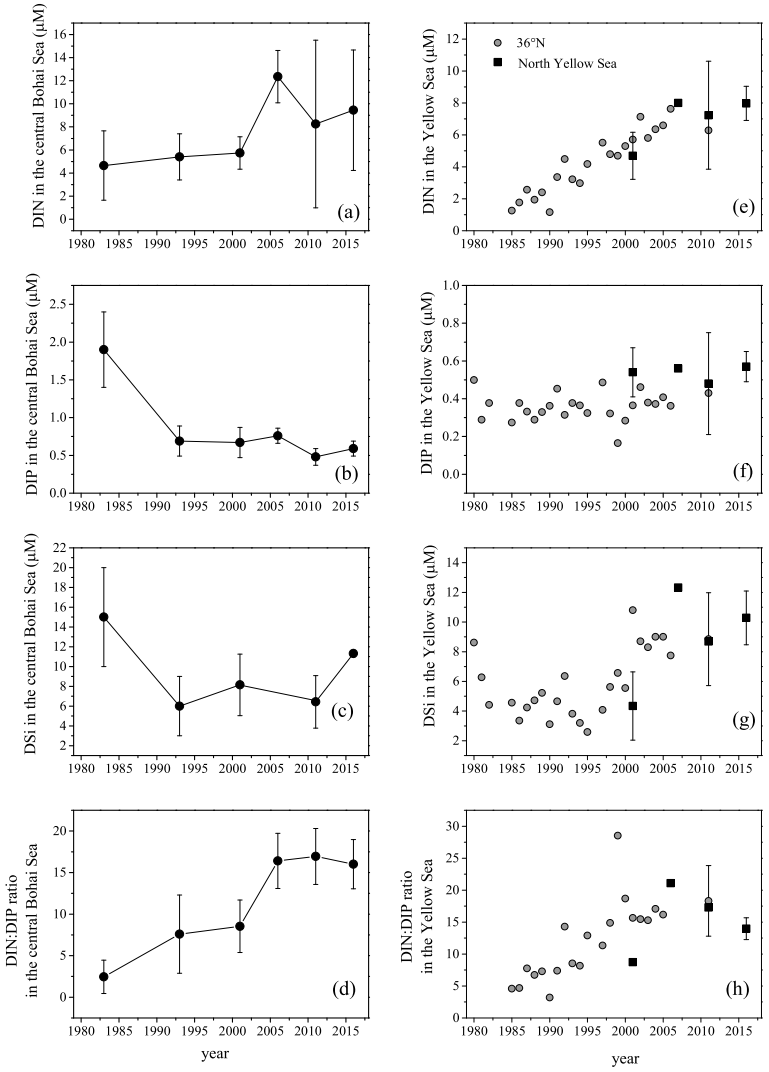

Fig. 8.2 Evolutions of wintertime/autumnal nutrient concentrations and the DIN:DIP ratio in the Bohai Sea (**a**–**d**) and in the Yellow Sea (**e**–**h**) from the 1980s to 2010s. Data were presented using the survey-based arithmetic average values, although they may cover different stations and different salinity of each year. Error bars denote standard deviations. In panels (**a**–**d**), the basin-wide data in 1982 and 1992 are from Tang and Meng (1997), while the basin-wide data in 2001 and 2006 are from Li et al. (2003) and Wang et al. (2012b), respectively. In panel (**e**–**h**), the 1985–2006 data in the South Yellow Sea along the 36°N transect are from Wei et al. (2015), while the North Yellow Sea basin-wide data in 2001 and 2007 are from Li et al. (2003) and Zhao et al. (2012), respectively. The North Yellow Sea basin-wide data in 2011 and 2016 were collected by the authors

8.2 Changing Dissolved Oxygen in the Bohai and Yellow Seas

To address long-term variations of summertime bottom-water DO in the Bohai Sea since the early 1980s, several historical snap-shot data sets were replotted (Fig. 8.3). Although the DO data were collected by different researchers, sea surface DO values usually varied in a tight range of 210–255 μmol O_2 L^{-1} (Fig. 8.3a–e), indicating that

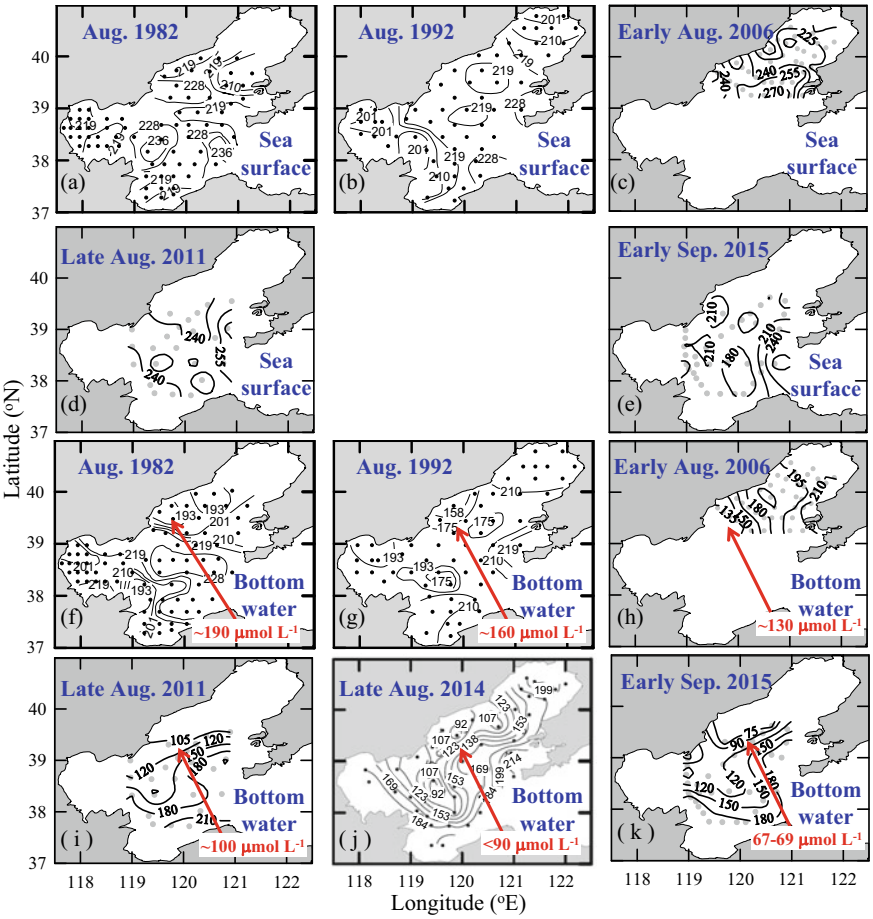

Fig. 8.3 Summertime sea surface dissolved oxygen concentration (DO, μmol O_2 L^{-1}) from the 1980 s to mid-2010s (**a**–**e**) and bottom-water DO (**f**–**k**) in the central Bohai Sea. The 1982 and 1992 data are from Tang and Meng (1997), while the 2006 and 2014 data are from Wang et al. (2012a) and Zhao et al. (2017), respectively. The 2011 and 2015 data are from Zhai et al. (2012) and Zhai et al. (2019), respectively. Data from Tang and Meng (1997) have been converted using the relationship 1 ml L^{-1} = 44.64 μmol O_2 L^{-1}. An edited version of this chart was published by Zhai et al. (2019) as Supporting Information. Copyright (2019) American Geophysical Union

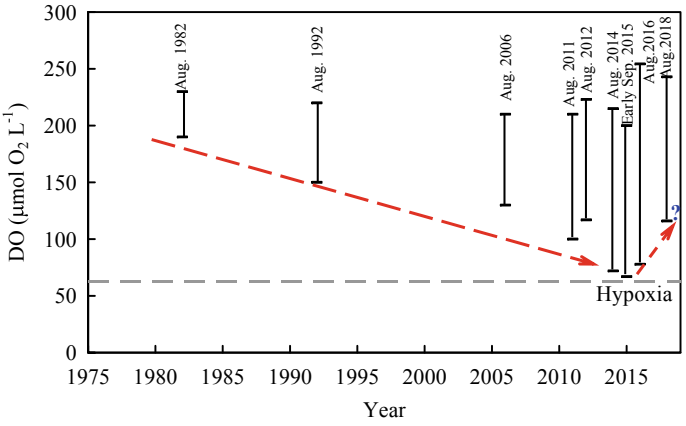

Fig. 8.4 Evolution of the survey-based range of summertime bottom-water dissolved oxygen concentration (DO, μmol O_2 L^{-1}) in the central Bohai Sea from the 1980s to 2018. Besides data presented in Fig. 8.3, the 2012 data were from Zhai et al. (2019), the 2016 data from Zang (2018), and the 2018 data obtained by Zhang et al. (2020)

those field data sets are generally comparable. However, the lowest measured value of summertime bottom-water DO for each survey-year shows a remarkable decline from the 1980s to mid-2010s (Fig. 8.4).

In the early years after the launch of the China "Reform and Openness" policy (in 1978), the Bohai Sea had rather high levels of summertime bottom-water DO at over 190 μmol O_2 L^{-1} in 1982 and over 160 μmol O_2 L^{-1} in 1992 (Tang and Meng 1997; Figs. 8.3f–g). In early August 2006, however, the lowest bottom-water DO decreased to ~130 μmol O_2 L^{-1} (Wang et al. 2012a; Wei et al. 2019a; Fig. 8.3h). In 2011 and 2014, the lowest summertime DO further dropped to ~100 μmol O_2 L^{-1} (Zhai et al. 2012; Fig. 8.3i) and 72–90 μmol O_2 L^{-1} (Zhang et al. 2016; Zhao et al. 2017; Fig. 8.3j), respectively. In late summer 2015, the historically lowest bottom-water DO was recorded at 67 μmol O_2 L^{-1} (very close to the threshold value of hypoxia) in the Bohai Sea (Zhai et al. 2019; Fig. 8.3k), while the survey-based lowest DO was slightly elevated to 78 μmol O_2 L^{-1} in August 2016 (Zang 2018; Fig. 8.4). The survey-based lowest summertime bottom-water DO values were usually obtained along the northern coast of the central Bohai Sea (Fig. 8.3f–k), where a marine aquaculture zone was highly developed, and extensive blooms of the brown tide microalgae, *Aureococcus anophagefferens*, occurred every summer during 2009 to 2014 (Zhang et al. 2012; Song et al. 2016), provided plenty of oxygen-consuming organic particles to the sea.

Based on a field study carried out from June to August in 2011 (Zhai et al. 2012), a quite high bimonthly bottom-water net DO consumption rate of 2.0–2.8 μmol O_2 kg^{-1} per day was estimated in the Bohai Sea summertime DO depletion area. This rate is comparable to the lower limit of net community respiration rates found

by Chen et al. (2006) off the Changjiang Estuary in the East China Sea, a well-documented summertime hypoxia zone (e.g. Li et al. 2002). According to this net DO consumption rate, it takes only 66–93 days (i.e. 2–3 months) to form the hypoxia level (i.e. <63 μmol O_2 L^{-1}) from the late spring DO saturated level (~250 μmol O_2 L^{-1}). This is a reasonable time lag between the stratification formation in early summer (in June) and the stratification collapse in early autumn (in mid-September). According to Zhao et al. (2017), the emergence of hypoxia in the Bohai Sea may shape one of the large oxygen-deficient areas in China's coastal zones.

In 2012 and 2018, however, extratropical cyclones (Damrey in August 2012 and Yagi in August 2018) entered the Bohai Sea (http://agora.ex.nii.ac.jp/digital-typhoon/), leading to bottom-water ventilation in summer. Correspondingly, quite high bottom-water DO values of no less than 116 μmol O_2 L^{-1} were observed in these two summers (Fig. 8.4). To better define the newly developed hypoxia in this shallow-water coastal ocean of ecological and economic importance, more efforts are needed in the future.

In the Yellow Sea, we have no enough data to examine decadal changes in DO, although the western part of the North Yellow Sea was subject to a 30-year decline of August bottom-water DO by 1.4 ± 0.3 μmol O_2 kg^{-1} per year from 1976 to 2006 (Wei et al. 2019b). In the 2010s, the wintertime and springtime Yellow Sea had the nearly air-saturated DO, while the summertime and autumnal Yellow Sea was characterized by undersaturated subsurface/bottom-water DO of 60 − 88 and 45 − 98% (relative to the air-equilibrium levels), respectively (Zhai 2018). This seasonal DO decline suggests a net community respiration rate of ~1 μmol O_2 kg^{-1} per day in the Yellow Sea Cold Water Mass (Zhai et al. 2014; Zhai 2018).

8.3 Carbonate System in the Bohai and Yellow Seas and the Locally-Intensified Ocean Acidification in Subsurface Waters

In the Yellow Sea, 90% of field data of total alkalinity (TAlk) obtained in winter, spring, and summer were around 2290 ± 25 μmol kg^{-1} (Zhai et al. 2014; Zhai 2018). In autumn, however, a relatively low survey-averaged TAlk of 2253 ± 25 μmol kg^{-1} was measured in the Yellow Sea (Fig. 8.5), likely due to an open ocean water intrusion via the YSWC during the northeast monsoon season (Fig. 8.1; Chen 2009; Zhai et al. 2014). Field data of dissolved inorganic carbon (DIC) were not presented in this chapter, since its distribution was usually similar to TAlk. However, our earlier studies had revealed positive correlations between excess DIC (relative to the air-equilibrated DIC calculated from the air-equilibrated partial pressure of CO_2 and field-measured TAlk) and apparent oxygen utilization (Zhai 2018), indicating the sea surface removal of DIC via photosynthesis and the subsurface addition of DIC via respiration/remineralization.

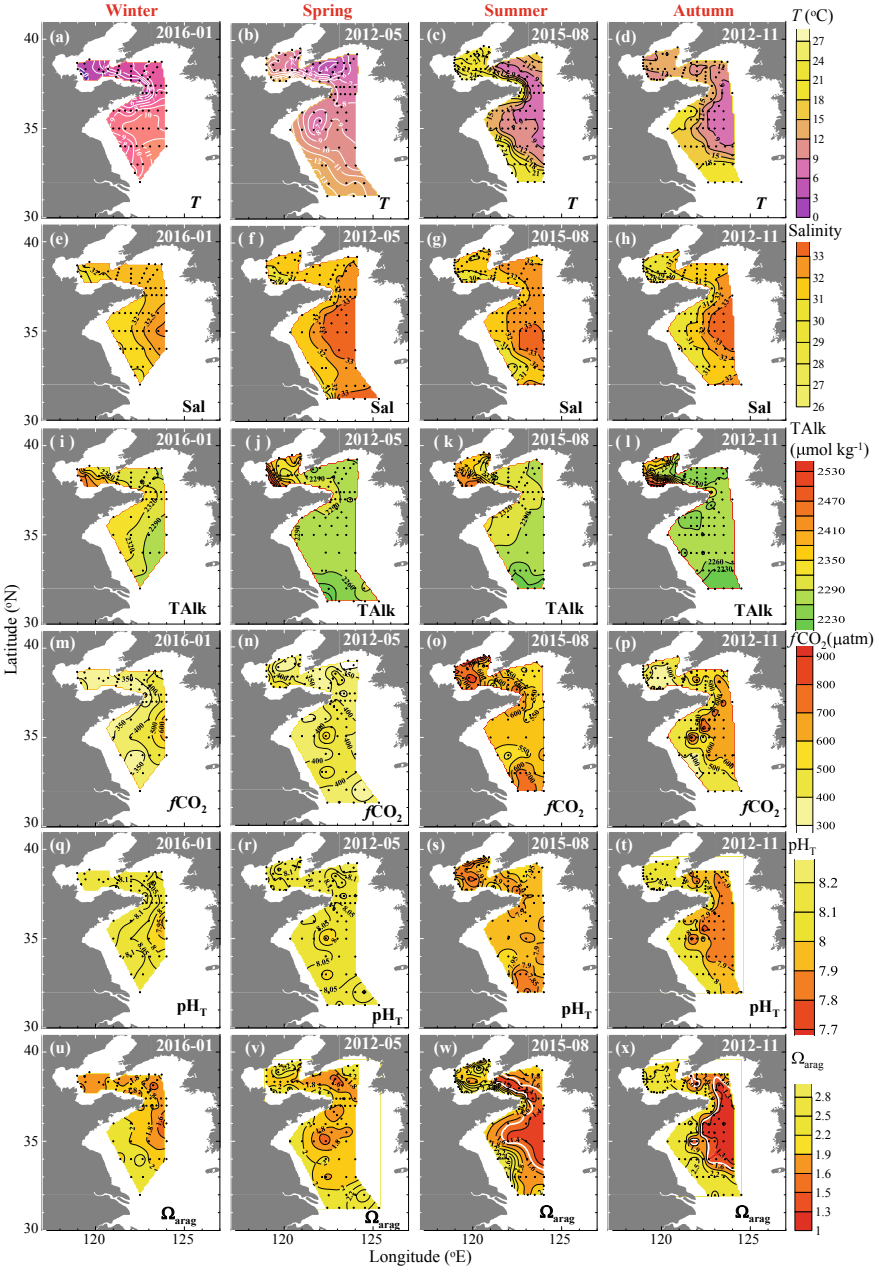

Fig. 8.5 Distributions of bottom-water temperature, salinity, total alkalinity (TAlk), fugacity of CO_2 (fCO_2), pH_T in situ, and $CaCO_3$ saturation of aragonite (Ω_{arag}) in winter, spring, summer, and autumn. The Yellow Sea data were from Zhai (2018), while the Bohai data were from Zhai et al. (2019). In panels (w) and (x), contours of bottom-water $\Omega_{arag} = 1.5$ are plotted as white curves

As a consequence of respiration and/or remineralization induced DIC accumulation in subsurface waters in stratified seasons, the Yellow Sea bottom-water fCO_2 data varied from the air-equilibrated level of usually 350−450 μatm in winter and spring to relatively high values of usually 500−700 μatm in summer and autumn (Fig. 8.5). Correspondingly, summertime/autumnal Yellow Sea bottom waters exhibited relatively low pH and quite low Ω_{arag} values (Zhai et al. 2014; Zhai 2018; Choi et al. 2020). At many Yellow Sea sampling sites, bottom water pH_T varied from 7.98 to 8.19 in winter and spring, but from 7.79 to 7.98 in summer, and from 7.74 to 7.94 in autumn. The corresponding bottom water Ω_{arag} decreased from values of 1.57–2.19 in winter and spring to values of 1.13–2.00 in summer and values of 1.02–2.21 in autumn. It is worth noting that the low Ω_{arag} values of less than 1.5 occupied 65000 and 67000 km^2 in summer and autumn, representing areas of one third of the surveyed Yellow Sea area (Zhai 2018), where net community $CaCO_3$ dissolution could be detected (Fig. 8.6; Li 2019; Li and Zhai 2019). Near an ocean dumping site in the central South Yellow Sea, even aragonite-undersaturated bottom waters have been observed in autumn (Choi et al. 2020). Thus, this seasonal acidification in the Yellow Sea undoubtedly threatens benthic calcifiers inhabiting there, and clearly deserves further study.

In the Bohai Sea, TAlk values were usually 100 μmol kg^{-1} higher than those in the Yellow Sea (Fig. 8.5i–l), likely due to discharges from more than a dozen rivers having moderate or high alkalinity of 1470 to 6300 μmol kg^{-1} (Xia and Zhang 2011), including the significant contributions from the Yellow River (Liu et al. 2014a). Summertime bottom-water fCO_2 was revealed at 600–900 μatm (Fig. 8.5o), much

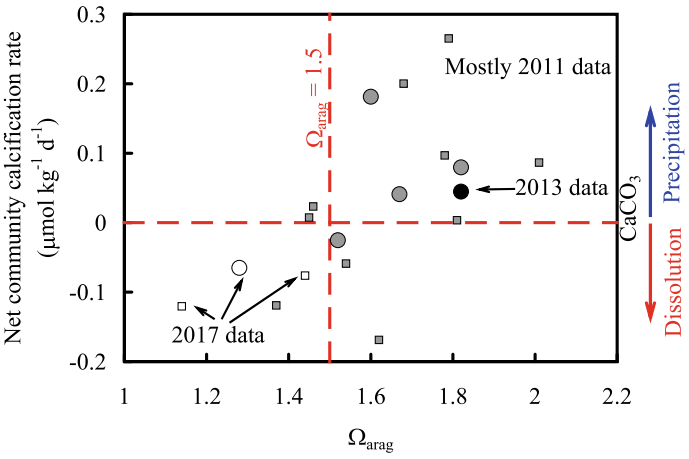

Fig. 8.6 Net community calcification rate versus bottom-water $CaCO_3$ saturation of aragonite (Ω_{arag}) in the North Yellow Sea cold water mass, showing that the local net calcification rate declines to nearly zero (as indicated by the horizontal dashed line) when Ω_{arag} reaches a critical level of 1.5–1.6 (Li and Zhai 2019). Circles show survey-average-based results, while squares indicate results calculated from monthly/bimonthly changes at selected nearby stations. Data were updated from Li and Zhai (2019), including our 2017 data reported by Li (2019)

higher than the air-equilibrated level (~400 μatm) in winter, spring, and autumn, indicating that net community respiration had induced a DIC accumulation in summer (Zhai et al. 2019). The quite high fCO_2 suppressed bottom-water pH_T (to the lowest value of 7.66) and Ω_{arag} (to the lowest value of 1.3) in a part of the central Bohai Sea (Zhai et al. 2019).

To investigate influences of the atmospheric CO_2 increase on local seawater chemistry in the recent decade, we plotted time series of basin-wide averaged carbonate system parameters in bottom waters in the North Yellow Sea (Fig. 8.7) from literatures (Li 2019; Li and Zhai 2019). Unlike the rising trend of atmospheric CO_2 mol fraction (xCO_2) from ~ 400 ppm (ppm = parts of CO_2 per million dry air) in 2011–2012 to values higher than 410 ppm in 2016–2017 (Fig. 8.7a), the air-equilibrated partial pressure of CO_2 varied irregularly between 385 μatm in July 2011 and 409 μatm in May 2013 in North Yellow Sea bottom waters (Fig. 8.7b). Meanwhile, the North Yellow Sea bottom-water air-equilibrated Ω_{arag} had recurrent seasonal values, fluctuating between winter values of around 1.62 (in 2012) and summer ones of 1.93 (in 2011) (Fig. 8.7c). In contrast, the North Yellow Sea bottom-water air-equilibrated pH_T varied negligibly, having the lowest value of 8.04 in May 2013 and the highest of 8.06 in August 2011 (Fig. 8.7d).

The North Yellow Sea bottom-water carbonate parameters showed different seasonal patterns to the air-equilibrated ones. Briefly, the North Yellow Sea bottom-water fCO_2 regularly fluctuated between springtime 350 ± 18 μatm (in May 2011) and autumnal 660 ± 71 μatm (in October 2011) (Fig. 8.7b). Correspondingly, the North Yellow Sea bottom-water Ω_{arag} varied from autumnal 1.25 ± 0.12 (in October 2011) to springtime 1.81 ± 0.10 (in May 2011) (Fig. 8.7c), and pH_T fluctuated from autumnal 7.86 ± 0.04 (in October 2011) to springtime 8.10 ± 0.02 (in May 2011) (Fig. 8.7d).

Considering the combined effect of a constant or accelerating community respiration levels and the long-term atmospheric CO_2 rise on the ocean, severely subsurface acidified waters with very low Ω_{arag} of 1.0–1.5 may develop within the next several decades (Zhai 2018; Li and Zhai 2019; Zhai et al. 2019), rather than a century. This change may bring enormous stress to benthic faunal communities in the Bohai and Yellow Seas by the 2050s. To manage and document such chemical changes, immediate and regular monitoring should be carried out.

8.4 Summary and Potential Ecological Effects

The Bohai and Yellow Seas are subject to basin-wide increases in wintertime nitrate and the DIN:DIP ratio during the past 40 years. Likely due to these changes, algae blooms frequently occurs in the Bohai Sea since 1999 (Song et al. 2016), leading to the recent occurrence of summertime bottom-water DO shortage in the central Bohai Sea (e.g. Zhai et al. 2019). In the Yellow Sea, however, summertime/autumnal community respiration resulted in a large amount of CO_2 accumulation in subsurface

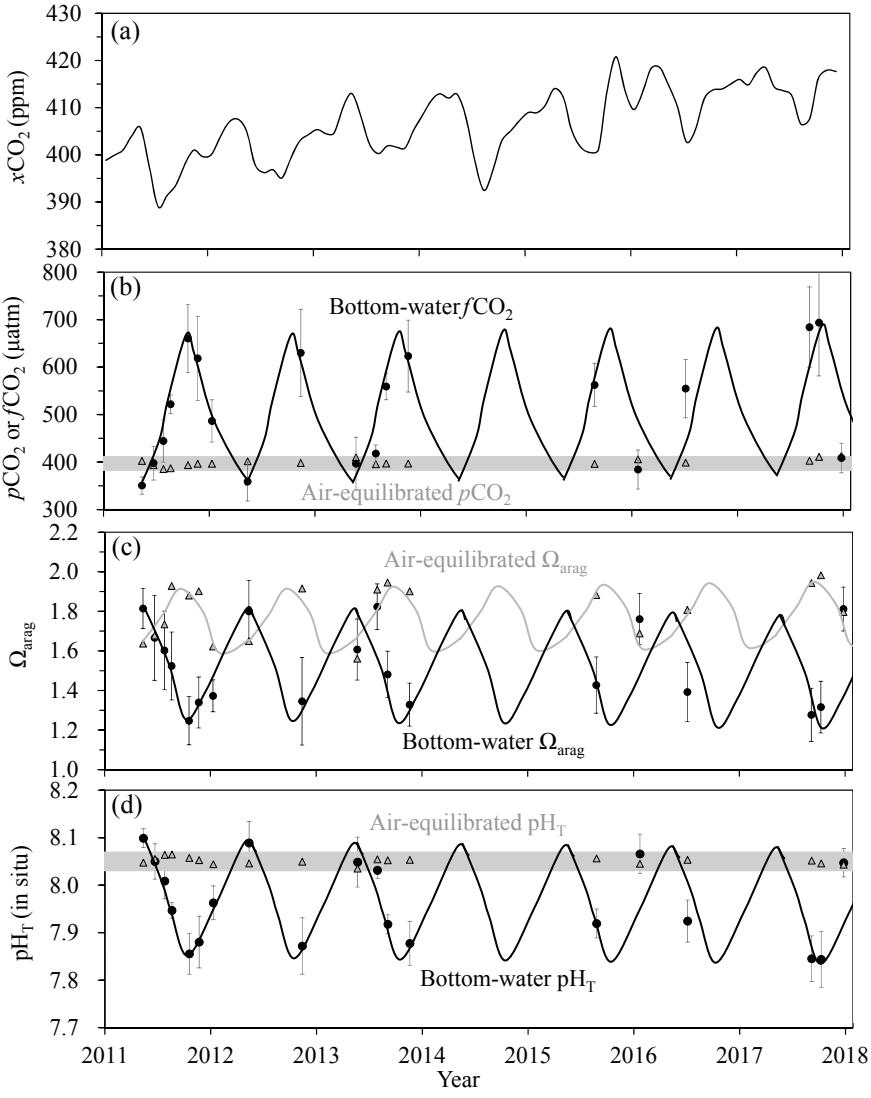
(a)
xCO_2 (ppm)
430
420
410
400
390
380
(b)
Bottom-water fCO_2
Air-equilibrated pCO_2
pCO_2 or fCO_2 (µatm)
800
700
600
500
400
300
(c)
Air-equilibrated Ω_{arag}
Bottom-water Ω_{arag}
Ω_{arag}
2.2
2.0
1.8
1.6
1.4
1.2
1.0
(d)
Air-equilibrated pH_T
Bottom-water pH_T
pH_T (in situ)
8.2
8.1
8.0
7.9
7.8
7.7
2011
2012
2013
2014
2015
2016
2017
2018
Year

◀**Fig. 8.7** Time series of the North Yellow Sea bottom-water carbonate system parameters during 2011–2017, comprising **a** flask analysis data of CO_2 mol fraction (xCO_2) for the adjacent Tae-ahn Peninsula (TAP) site (36°44′N 126°08′E) (data from NOAA/ESRL's Global Monitoring Division http://www.esrl.noaa.gov/gmd/); **b** bottom-water fugacity of CO_2 (fCO_2, connected with a black solid curve) and the air-equilibrated partial pressure of CO_2 (pCO_2), which was corrected to a constant barometric pressure of 1013 hPa and 100% humidity at bottom-water temperature and salinity; **c** bottom-water aragonite saturation state (Ω_{arag}, black circles connected with a black solid curve) and the air-equilibrated Ω_{arag} (grey triangles connected with a grey solid curve); **d** bottom-water pH_T and the air-equilibrated pH_T. This is an update from Li and Zhai (2019), including our 2017 data reported by Li (2019). Data were presented using the survey-based arithmetic average values, although they may cover different stations and different salinity of each survey. Error bars denote standard deviations. The air-equilibrated Ω_{arag} and pH_T were calculated from the air-equilibrated pCO_2 and survey-averaged TAlk, using the software CO2SYS.xls (Ver 24) (Pelletier et al. 2015), an updated version of the original CO2SYS.EXE (Lewis and Wallace 1998). The dissociation constants for carbonic acid were those determined by Millero et al. (2006), and the dissociation constant for the HSO_4^- ion was determined as per Dickson (1990). Phosphate and silicate concentrations required by the program were replaced by zero. The K_{sp}* values for aragonite were taken from Mucci (1983), and the Ca^{2+} concentrations were assumed to be proportional to salinity, as presented in Millero (1979)

waters, leading to substantial carbonate mineral suppression to critical levels in one third of the areas.

Although the DO-deficient and/or $CaCO_3$-suppressing waters may only continue for one or several months every year, and the susceptibility of marine organisms to acidified waters is affected by many other factors such as the nourishment status (Ramajo et al. 2016; Leung et al. 2019) and the protective mechanism of organic matrix (e.g. Glover and Kidwell 1993), the short-term CO_2-induced acidification may even damage adult bivalves by affecting important physiological functions such as food intake, oxygen consumption, and ammonia excretion (Liu and He 2012; Xu et al. 2013). Furthermore, hypoxia-induced metabolic depression in the Bohai Sea may decrease shellfish's tolerance to acidification (Jansson et al. 2015; Gobler and Baumann 2016; Sui et al. 2016). Therefore, the combined occurrence of DO shortage and seasonal acidification may lead to profound consequences for shellfish aquaculture industries.

If native shellfishes have to endure higher energetic costs than before to fight against DO shortage and shell dissolution, their ecosystem functions such as filtering and habitat building must decrease. In the Bohai Sea, recent field surveys showed that local shrimps and crabs with larger sizes and longer life spans have been replaced by more tolerant bivalve species with smaller sizes and shorter life spans (Zhou et al. 2007; Cai et al. 2013; Liu et al. 2014b). These changes highlight the combined stress of increasing human activities and the unfavorable aquatic chemistry on macrozoobenthos in this area. In addition to overfishing, seasonal DO shortage and acidification may play an important role.

Acknowledgments This research was supported by the Natural Science Foundation of Shandong Province (grant no. ZR2018MD019). Sampling surveys were mostly supported by the National Natural Science Foundation of China via Open Ship-time projects in the Bohai and Yellow Seas (2011–2018). We appreciate constructive comments and suggestions from three anonymous reviewers, which have improved the quality of this chapter.

References

Cai W-Q, Meng W, Liu L-S et al (2013) Long-term trends of the dominant macro-zoobenthos in Bohai Bay (in Chinese). Acta Sci Circumst 33:2332–2340

Chen C-TA (2009) Chemical and physical fronts in the Bohai, Yellow and East China seas. J Mar Syst 78:394–410. https://doi.org/10.1016/j.jmarsys.2008.11.016

Chen C-C, Chiang K-P, Gong G-C et al. (2006) Importance of planktonic community respiration on the carbon balance of the East China Sea in summer. Glob Biogeochem Cyc 20. https://doi.org/10.1029/2005gb002647

Choi Y, Cho S, Kim D (2020) Seasonal variation in aragonite saturation states and the controlling factors in the southeastern Yellow Sea. Mar Poll Bull 150:110695. https://doi.org/10.1016/j.marpolbul.2019.110695

Deng J-Y, Meng T-X, Ren S-M et al (1988) Species composition, abundance and distribution of fishes in the Bohai Sea (in Chinese). Mar Fish Res 9:11–89

Dickson AG (1990) Standard potential of the reaction: $AgCl(s) + 1/2\ H_2(g) = Ag(s) + HCl(aq)$, and the standard acidity constant of the ion HSO_4^- in synthetic sea water from 273.15 to 318.15 K. J Chem Thermodyn 22:113–127. https://doi.org/10.1016/0021-9614(90)90074-Z

Glover CP, Kidwell SM (1993) Influence of organic matrix on the post-mortem destruction of molluscan shells. J Geol 101:729–747. https://doi.org/10.1086/648271

Gobler CJ, Baumann H (2016) Hypoxia and acidification in ocean ecosystems: coupled dynamics and effects on marine life. Biol Lett 12:20150976. https://doi.org/10.1098/rsbl.2015.0976

He X, Bai Y, Pan D et al (2013) Satellite views of the seasonal and interannual variability of phytoplankton blooms in the eastern China seas over the past 14 yr (1998–2011). Biogeosciences 10:4721–4739. https://doi.org/10.5194/bg-10-4721-2013

Hu C-M, Li D-Q, Chen C-S et al (2010) On the recurrent *Ulva prolifera* blooms in the Yellow Sea and East China Sea. J Geophys Res 115:C05017. https://doi.org/10.1029/2009JC005561

Jansson A, Norkko J, Dupont S et al (2015) Growth and survival in a changing environment: Combined effects of moderate hypoxia and low pH on juvenile bivalve *Macoma balthica*. J Sea Res 102:41–47. https://doi.org/10.1016/j.seares.2015.04.006

Jin X-S (2000) The dynamics of major fishery resources in the Bohai Sea (in Chinese). J Fish Sci China 7(4):22–26

Kim H, Lee K, Lim D et al (2017) Widespread anthropogenic nitrogen in northwestern Pacific Ocean sediment. Environ Sci Technol 51:6044–6052. https://doi.org/10.1021/acs.est.6b05316

Kim I-N, Lee K, Gruber N et al (2014) Increasing anthropogenic nitrogen in the North Pacific Ocean. Science 346:1102–1106. https://doi.org/10.1126/science.1258396

Leung JYS, Doubleday ZA, Nagelkerken I et al (2019) How calorie-rich food could help marine calcifiers in a CO_2-rich future. Proc Roy Soc B Biol Sci 286:20190757. https://doi.org/10.1098/rspb.2019.0757

Lewis E, Wallace DWR (1998) Program developed for CO_2 system calculations. ORNL/CDIAC-105, Carbon Dioxide Information Analysis Center, Oak Ridge National Laboratory. U.S. Department of Energy, Oak Ridge, Tennessee

Li C-L (2019) A comparative study of seasonal acidification in southern nearshore and central offshore waters of the North Yellow Sea (in Chinese). Master thesis, Shandong University

Li C-L, Zhai W-D (2019) Decomposing monthly declines in subsurface-water pH and aragonite saturation state from spring to autumn in the North Yellow Sea. Cont Shelf Res 185:37–50. https://doi.org/10.1016/j.csr.2018.11.003

Li D-J, Zhang J, Huang D-J et al (2002) Oxygen depletion off the Changjiang (Yangtze River) Estuary. Sci China Ser D 45:1137–1146

Li X-S, Niu M-X, Dai F-Q (2008) Characteristics of structure and distribution of spawning stock of fishery species in the Bohai Sea (in Chinese). Mar Fish Res 29(4):15–21

Li Z, Bai J, Shi J et al (2003) Distributions of inorganic nutrients in the Bohai Sea of China. J Ocean Univ China 2(1):112–116. https://doi.org/10.1007/s11802-003-0038-8

Liu Z-Y, Zhang L-J, Cai W-J et al (2014a) Removal of dissolved inorganic carbon in the Yellow River Estuary. Limnol Oceanogr 59:413–426. https://doi.org/10.4319/lo.2014.59.2.0413

Liu X-S, Fan Y, Shi S-J et al (2014b) Studies on the species composition and community structure of macrofauna in the Bohai Sea, China (in Chinese). Acta Oceanol Sin 36(12):53–66

Liu W-G, He M-X (2012) Effects of ocean acidification on the metabolic rates of three species of bivalve from southern coast of China. Chin J Oceanol Limnol 30(2):206–211. https://doi.org/10.1007/s00343-012-1067-1

Millero FJ, Graham TB, Huang F et al (2006) Dissociation constants of carbonic acid in seawater as a function of salinity and temperature. Mar Chem 100:80–94. https://doi.org/10.1016/j.marchem.2005.12.001

Millero FJ (1979) The thermodynamics of the carbonate system in seawater. Geochim Cosmochim Acta 43:1651–1661. https://doi.org/10.1016/0016-7037(79)90184-4

Mucci A (1983) The solubility of calcite and aragonite in seawater at various salinities, temperatures, and one atmosphere total pressure. Am J Sci 283:780–799. https://doi.org/10.2475/ajs.283.7.780

Ning X-R, Lin C-L, Su J-L et al (2010) Long-term environmental changes and the responses of the ecosystems in the Bohai Sea during 1960–1996. Deep Sea Res II 57:1079–1091. https://doi.org/10.1016/j.dsr2.2010.02.010

Pelletier GJ, Lewis E, Wallace DWR (2015) CO2SYS.XLS: A calculator for the CO_2 system in seawater for Microsoft Excel/VBA (Ver 24). Washington State Department of Ecology, Olympia, Washington

Rabalais NN, Díaz RJ, Levin LA et al (2010) Dynamics and distribution of natural and human-caused hypoxia. Biogeosciences 7:585–619. https://doi.org/10.5194/bg-7-585-2010

Ramajo L, Pérez-León E, Hendriks IE et al (2016) Food supply confers calcifiers resistance to ocean acidification. Sci Rep 6:19374. https://doi.org/10.1038/srep19374

Shi Q (2016) Spatio-temporal mode for inter-annual change of dissolved oxygen and apparent oxygen utilization in summer Bohai Sea (in Chinese). J Appl Oceanogr 35:243–255

Shi J-H, Gao H-W, Zhang J et al (2012) Examination of causative link between a spring bloom and dry/wet deposition of Asian dust in the Yellow Sea, China. J Geophys Res 117:D17304. https://doi.org/10.1029/2012JD017983

Song N-Q, Wang N, Lu Y et al (2016) Temporal and spatial characteristics of harmful algal blooms in the Bohai Sea during 1952–2014. Cont Shelf Res 122:77–84. https://doi.org/10.1016/j.csr.2016.04.006

Sui Y-M, Kong H, Huang X-Z et al (2016) Combined effects of short-term exposure to elevated CO_2 and decreased O_2 on the physiology and energy budget of the thick shell mussel *Mytilus coruscus*. Chemosphere 155:207–216. https://doi.org/10.1016/j.chemosphere.2016.04.054

Tan S-C, Wang H (2014) The transport and deposition of dust and its impact on phytoplankton growth in the Yellow Sea. Atmos Environ 99:491–499

Tang Q-S, Meng T-X (1997) Atlas of the ecological environment and living resources in the Bohai Sea (in Chinese). Qiangdao Press, Qiangdao

Wang J, Yu Z, Wei Q et al (2019) Long-term nutrient variations in the Bohai Sea over the past 40 years. J Geophys Res Oceans 124:703–722. https://doi.org/10.1029/2018JC014765

Wang J-T, Tan L-J, Li K-Q (2012a) Dissolved oxygen and pH in the Bohai Sea (in Chinese). In Hong H-S (ed) Regional Oceanography of China Seas—Chemical Oceanography. China Ocean Press, Beijing, p 7–17

Wang J-T, Tan L-J, Zhang W-H (2012b) Nutrients in the Bohai Sea (in Chinese). In Hong H-S (ed) Regional Oceanography of China Seas—Chemical Oceanography. China Ocean Press, Beijing, p 18–34

Wang X-L, Li K-Q (2006) Marine environmental capacity of pollutants in Bohai Sea (in Chinese). Science Press, Beijing

Wei Q-S, Wang B-D, Yao Q-Z et al (2019a) Spatiotemporal variations in the summer hypoxia in the Bohai Sea (China) and controlling mechanisms. Mar Poll Bull 138:125–134. https://doi.org/10.1016/j.marpolbul.2018.11.041

Wei Q-S, Yao Q-Z, Wang B-D et al (2019b) Deoxygenation and its controls in a semienclosed shelf ecosystem, northern Yellow Sea. J Geophys Res Oceans 124:9004–9019. https://doi.org/10.1029/2019JC015399

Wei Q-S, Yao Q-Z, Wang B-D et al (2015) Long-term variation of nutrients in the southern Yellow Sea. Cont Shelf Res 111:184–196. https://doi.org/10.1016/j.csr.2015.08.003

Xia B, Zhang L-J (2011) Carbon distribution and fluxes of 16 rivers discharging into the Bohai Sea in summer. Acta Oceanol Sin 30(3):43–54. https://doi.org/10.1007/s13131-011-0118-3

Xu X-M, Zhai W-D, Wu J-H (2013) Effects of CO_2-driven ocean acidification on the calcification and respiration of *Ruditapes philippinarum* (in Chinese). Acta Oceanol Sin 35(5):112–120

Yang F-X, Wei Q-S, Chen H-T et al (2018) Long-term variations and influence factors of nutrients in the western North Yellow Sea, China. Mar Poll Bull 135:1026–1034. https://doi.org/10.1016/j.marpolbul.2018.08.034

Zang K-P (2018) Seasonal variations and regulatory mechanisms of dissolved methane concentration and its sea-to-air fluxes in the seasonal oxygen deficient zones in Bohai Sea (in Chinese). Doctoral dissertation, Chinese Academy of Meteorological Sciences

Zhai W-D, Zhao H-D, Su J-L et al (2019) Emergence of summertime hypoxia and concurrent carbonate mineral suppression in the central Bohai Sea, China. J Geophys Res Biogeosci 124:2768–2785. https://doi.org/10.1029/2019JG005120

Zhai W-D (2018) Exploring seasonal acidification in the Yellow Sea. Sci China Earth Sci 61:647–658. https://doi.org/10.1007/s11430-017-9151-4

Zhai W-D, Zheng N, Huo C et al (2014) Subsurface pH and carbonate saturation state of aragonite on the Chinese side of the North Yellow Sea: seasonal variations and controls. Biogeosciences 11:1103–1123. https://doi.org/10.5194/bg-11-1103-2014

Zhai W-D, Zhao H-D, Zheng N et al (2012) Coastal acidification in summer bottom oxygen-depleted waters in northwestern-northern Bohai Sea from June to August in 2011. Chin Sci Bull 57:1062–1068. https://doi.org/10.1007/s11434-011-4949-2

Zhang Y, Chen B, Zhai W-D (2020) Exploring sources and biogeochemical dynamics of dissolved methane in the central Bohai Sea in summer. Front Mar Sci 7:79. https://doi.org/10.3389/fmars.2020.00079

Zhang H, Li Y-F, Tang C et al (2016) Spatial characteristics and formation mechanisms of bottom hypoxia zone in the Bohai Sea during summer (in Chinese). Chin Sci Bull 61:1612–1620. https://doi.org/10.1360/N972015-00915

Zhang Q-C, Qiu L-M, Yu R-C et al (2012) Emergence of brown tides caused by *Aureococcus anophagefferens* Hargraves et Sieburth in China. Harmful Algae 19:117–124. https://doi.org/10.1016/j.hal.2012.06.007

Zhang S-W, Xia C-S, Yuan Y-L (2002) A physical-biochemical coupling model of Yellow Sea cold water mass (in Chinese). Prog Nat Sci 12:315–319

Zhang J (1994) Atmospheric wet deposition of nutrient elements: Correlation with harmful biological blooms in Northwest Pacific coastal zones. Ambio 23:464–468

Zhao H-D, Kao S-J, Zhai W-D et al (2017) Effects of stratification, organic matter remineralization and bathymetry on summertime oxygen distribution in the Bohai Sea, China. Cont Shelf Res 134:15–25. https://doi.org/10.1016/j.csr.2016.12.004

Zhao Q, Zang L, Zhang C et al (2012) The seasonal changes of nutrients and interfering factors in the west of the North Yellow Sea (in Chinese). Adv Mar Sci 30(1):69–76

Zhao L, Wei H, Feng S-Z (2002) Annual cycle and budgets of nutrients in the Bohai Sea (in Chinese). Environ Sci 23:78–81

Zhou H, Zhang Z-N, Liu X-S et al (2007) Changes in the shelf macrobenthic community over large temporal and spatial scales in the Bohai Sea, China. J Mar Syst 67:312–321. https://doi.org/10.1016/j.jmarsys.2006.04.018

Chapter 9
The Changing East China Sea—A Physical View

Takeshi Matsuno

Abstract Long-term trends, along with various time-scale variations in the physical properties, in the East China Sea (ECS) are summarized. Long-term variations in sea surface temperature (SST) shows a clear trend after the year 1900 with a 1.2 °C per century variation. However, it includes relatively shorter interannual to multi-decadal time-scale variations. The SST increase rate is more distinct in winter than in summer. The Kuroshio is the most dominant oceanographic feature in the ECS, and it exhibits long-term variations. The Kuroshio volume transport in the PN section located in the central ECS, is known to have a slight long-term increase in 55 years after 1955. The expansion of Changjiang Diluted Water also shows long-term variations associated with climate indices caused by not only the amount of river discharge but also the movement of surface water driven by wind fields in the ECS. One of the symbolic factors related to global warming is sea level, and clear long-term variations in the sea level are found in the ECS, whereas the vertical land motion is noted using tide-gauge data. The long-term variation in the sea level is significantly correlated with climate indices particularly with the relatively regional wind fields.

Keywords Long term variations · East China Sea · SST · Kuroshio transport · Changjiang diluted water · Sea level

9.1 Introduction

The East China Sea (ECS) roughly consists of two parts: a wide continental shelf that is shallower than 200 m and deep Okinawa Trough. The northern part of the ECS is connected to the Yellow Sea (YS), whereas no topographically distinct boundary exists. The shelf region is strongly affected by land environment through the inflow of fresh water from rivers. On the other hand, a significant part of the deeper region is occupied by the Kuroshio and the subtropical water in the North Pacific. The East Asian monsoon directly affects the sea-water temperature, particularly in the shelf region, with large seasonal variations. Furthermore, current through the Taiwan

T. Matsuno (✉)
Research Institute for Applied Mechanics, Kyushu University, Kasuga, Japan
e-mail: matsuno@riam.kyushu-u.ac.jp

C.-T. A. Chen and X. Guo (eds.), *Changing Asia-Pacific Marginal Seas*, Atmosphere, Earth, Ocean & Space, https://doi.org/10.1007/978-981-15-4886-4_9

Strait transports water from the South China Sea. Therefore, the long-term variations in the marine environment in the ECS result from the complicated contribution of various factors. In terms of physical oceanography, we are interested in the long-term variations in the sea level, tidal motions, temperature, salinity, and current system. As expected, because the short-term variability in the different factors is very large, determining the long-term variations using limited observational data is difficult, whereas long-term monitoring can provide statistically significant variations. In this chapter, we briefly summarize the long-term variations in the physical factors in the ECS, such as temperature, salinity, sea level, and currents, according to the literature. We should note that the average values over the area according to the literature sometimes include the YS data.

Temperature is the most fundamental of the various components in an ocean because heat is a huge reservoir of energy and strongly controls the climate and ecosystem. Therefore, we started by summarizing the long-term variations in the ECS using the sea surface temperature (SST) and then summarized the vertical structure of temperature by focusing on the YS Cold Water (YSCW), the variations in salinity for which are also presented briefly. As mentioned earlier, because the Kuroshio is the dominant factor in the ECS and transports significant heat energy, we consider it relevant to temperature change. We then present an overview of the other major factor, the variation in the Changjiang diluted water (CDW). Finally, the variation in the sea level, which partly reflects the temperature via the steric height, is summarized and the variations in tidal motion are added.

9.2 Sea Surface Temperature

Temperature is the most common factor of the physical properties in an ocean to investigate its long-term variations because a large number of data have been historically obtained all over the world. A similar situation is true for the ECS. In particular, long-term variations in SST in the ECS have been reported by various researchers because the SST data, which include in situ hydrographic and satellite remote-sensing data, are well archived in various datasets, although the ECS is divided into complicated exclusive economic zones of surrounding countries.

Long-term variations in SST in the ECS, based on historical data since 1900, have been reported on the Japan Meteorological Agency (JMA) website and summarized in the annual "Climate Change Monitoring Report" (JMA 2017). The JMA divides the ECS into two parts, the northern and southern areas, where SST increased by 1.23 and 1.18 °C per century, respectively, in the 117 years from 1900. The rates of increase were quite faster than the global mean of 0.73 °C per century (JMA 2017).

The JMA reports that SST in the ECS generally increases as a long-term trend. Recent studies, for example by Yeh and Kim (2010), Wang et al. (2013), and Wu et al. (2016), have shown that long-term increases in SST in the ECS followed a linear trend. However, various time-scale variations were also reported. Yeh and Kim (2010) showed that there was a distinct increase in SST in winter in the area,

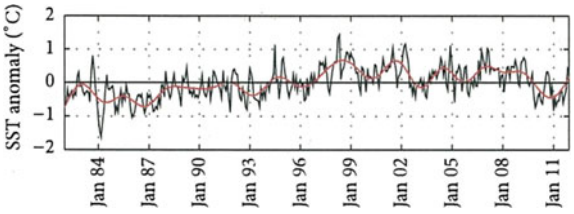

Fig. 9.1 Long-term SST variation averaged over the region of 25°N–40°N, 118°E–127°E in the ECS in winter from 1950 to 2008 reprinted from Yeh and Kim (2010) with permission from Elsevier. The red line indicates the nine-year running-mean time series

averaged over the ECS and YS, after the mid-1980s; this was based on the Hadley Center SST dataset (HadISST) from 1950 to 2008 (Fig. 9.1). They compared the long-term variation in SST with that of the sea level pressure in the North Pacific and suggested that the increase in SST after the mid-1980s could be related to the intensification of the anti-cyclonic atmospheric circulation in the North Pacific, which corresponded to the weakening of the northerly wind in winter in the ECS. In other words, weakening the latent and sensible heat fluxes would result in increases in SST in winter, which could be a reasonable explanation for the SST increase after the mid-1980s. Jin and Wang (2011) used a longer time series, based on HadISST since 1870, and observed that warming was dominant in the last 20 years in the marginal seas along the Chinese coast. In particular, the strongest warming was found off Changjiang Estuary in the ECS.

These inter-decadal variations in SST was also demonstrated by Wu et al. (2016) where reanalyzed data based on shipboard, buoy, and satellite SST measurements were used. Similar to the results by Yeh and Kim (2010), the increase in the SST anomaly was indicated to be observed after the mid-1980s, whereas Wu et al. (2016) used the data over the east marginal sea of China (EMSC), including Bohai, YS, and ECS, and presented the SST anomaly relative to climatology, which means that their data contained these anomalies through all seasons. Wu et al. (2016) showed a slight decrease in the SST anomaly after the mid-2000s (Fig. 9.2), which was not shown by Yeh and Kim (2010) because of the record length. Wu et al. (2016) revealed a sub-decadal variation in SST and a significant periodical variation in 3.3 years

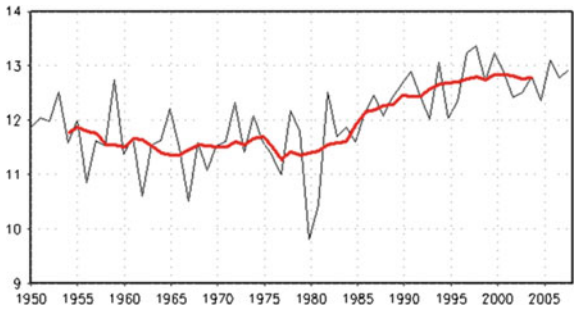

Fig. 9.2 Temporal variation in the SST anomaly from the climatological monthly mean in the ECS from 1982 to 2011 along with (red line) the two-year low-pass-filtered one presented by Wu et al. (2016)

using wavelet analysis. The variations in the SST anomaly with a significant energy peak around 3.3 years were compared with the sea surface heat flux (SSHF) in the EMSC, along with the El Niño-Southern Oscillation (ENSO) index. There was a clear correlation between the SSHF and SST anomalies with SSHF leading three months lag. The relationship between the SSHF and SST anomalies with the ENSO index showed significant correlation with one- and six-month time lags, respectively. Wu et al. (2016) concluded that the interannual variations in SST were significantly correlated with the SSHF and ENSO-scale climate phenomena.

Wang et al. (2013) also demonstrated a long-term increase in SST in the ECS for approximately 40 years after 1957 using the Ocean Science Database of the Institute of Oceanology, Chinese Academy of Sciences, which includes various international databases. They showed a clear increase in SST after 1985, whereas the SST decreased for 10 years before the mid-1980s. They showed a spatial pattern of long-term SST variations in the seas east of China where a clear SST increase was observed in central ECS and northeast of Taiwan in February but not in August. The spatial pattern of SST increase in February indicated a spatial distribution similar to the result obtained by Yeh and Kim (2010), particularly the large enhancements in central ECS. Meanwhile, the cause of the SST increase was different from that proposed by Yeh and Kim (2010). Wang et al. (2013) discussed how the long-term trend could arise and compared the SST trend with the meridional SST gradient in each grid. The significant correlation between the SST trend and meridional SST gradient, particularly in winter, suggested that the SST increase could have resulted from the increase in ocean circulation. Intensification of the Kuroshio was also suggested because an increase in the warm water advected by the Kuroshio would result in SST increase. The net onshelf Kuroshio intrusion northeast of Taiwan was positively correlated with the Kuroshio volume transport (Liu et al. 2014).

9.3 Yellow Sea Cold Water

Long-term variations in temperature have been reported by various researchers, and most of them have investigated SST. However, studies on long-term variations at the subsurface are limited. On the vertical structure of temperature in the ECS, one of the factors that interest the researchers is the YSCW, although the main part of it is located in the YS instead of the ECS, as summarized by Wei et al. in Chap. 7 in this book. The YSCW is an important feature related to the vertical structure of the ECS and can control the current fields and biological environment in the northeastern part of the ECS. The YSCW is known as bottom cold water that appears in the YS and the northeastern region of ECS, particularly in spring and summer. Seasonal variations in the YSCW are well known, and the YSCW is reported to expand southward from spring to summer, forming clear bottom cold water below the pycnocline in southern YS and northern ECS (e.g., Li et al. 2016). The intensity of the northerly wind in winter influences the Yellow Sea Warm Current (YSWC) and results in the formation of the YSCW in summer (Oh et al. 2013), indicating that an external atmospheric

condition can change the spatial distribution of YSCW, which may cause long-term variations.

Park et al. (2011) demonstrated interannual-to-interdecadal variabilities in the YSCW using the Korea Oceanographic Data Center dataset from 1967 to 2008. The area in the dataset covers west of Korea, and the southern end of the area that they considered is located at the northern end of ECS. They exhibited long-term variations in the bottom water temperature in the YSCW with periods of 2–7 and 10–20 years, revealing three cold events in 1967–1971, 1983–1988, and after 1996, along with two warm events in 1972–1980 and 1990–1995. The time series of the bottom water-temperature anomaly showed a distinct increase from 1985 to 1992, which was a similar trend to the SST in the ECS mentioned earlier. They discussed the relationship between the YSCW and climate indices such as the North Pacific and Pacific Decadal Oscillation (PDO) indices. The behavior of the YSCW responds to the climate change through changes in its wind and current fields.

The YSCW shows long-term variation not only in temperature but also in salinity. Li et al. (2017) demonstrated that the salinity of the YSCW has exhibited a long-term decreasing trend in summer since the mid-1970s. It could be related to the decrease in salinity of the YSWC flowing into the YS west of Jeju Island, although it is dominant in winter. They also compared the decrease in salinity in the YSCW with the decrease in salinity in the Taiwan Strait. Whereas YSCW, YSWC and the water around Taiwan exhibited a similar trend of decreasing salinity over 30 years, the decrease in salinity in the YSCW was much larger than those of YSWC and the water around Taiwan. This result could suggest that long-term freshening occurred over the marginal seas around ECS, which is possibly caused by the influence of the climate change that may result in an increase in precipitation and Changjiang discharge (CD). Therefore, a salinity-reduction trend significantly occurred in the YSCW rather than in YSWC and the water around Taiwan.

9.4 The Kuroshio

One of the largest features that control the ocean structure in the ECS is the Kuroshio. Although many studies are available concerning the variabilities of the Kuroshio with a time-scale shorter than an annual variation, studies concerning long-term variations are limited due to lack of long-term data. Whereas direct-observation data for investigating the Kuroshio long-term variations are limited, the sea surface height (SSH) detected from satellites can cover a wide area to examine the behavior of the Kuroshio and has been used by various researchers to investigate long-term variation in the Kuroshio in the ECS.

The vertically integrated Kuroshio transport (KT) in the ECS was discussed by Andres et al. (2009) using climate indices. They demonstrated clear correlation between KT and the PDO index. They used altimeter data from satellites along with the relationship between SSH and the volume transport obtained using in situ measurements from pressure-sensor-equipped inverted echo sounders and current

meters, including acoustic Doppler current profilers and hydrocasts. They concluded that KT in the ECS was well correlated with the PDO index with no lag, whereas the data length was only 15 years from 1993. Because the PDO index is an index of an SST pattern in the Pacific and a positive value of the PDO index corresponds to a low temperature in the northern North Pacific and strong westerly, KT was explained to be related to the Sverdrup balance associated with intensified wind system in the subtropical region.

Wei et al. (2013) calculated the long-term variation in KT by applying an inverse method to historical dataset along the PN section and Tokara Strait. They demonstrated a long-term trend of KT with a 0.47-Sv increase during the 55 years from 1955 to 2010, which was much lesser than that presented by Zhang et al. (2011) where KT increased to 8.5 Sv from 1956 to 2003 using historical data along the PN section. The large difference appeared to be caused by the spatial interval of the used data. The data interval used by Zhang et al. (2011) was sparse for the earlier period in the PN section in which the calculated volume transport could be underestimated compared with the fine-interval data. Wei et al. (2013) also demonstrated large fluctuations in KT with interannual and decadal time scales whose ranges were 5.60 and 0.65 Sv, respectively. The interannual variations appeared to have increased in the recent decades compared with those in the period from the 1950s to 1980s (Fig. 9.3).

Wang and Oey (2014) investigated long-term variations in the Kuroshio path (KP) in the ECS using SSH from 1992 to 2013 and demonstrated relatively large on- and off-shore migrations of the KP northeast of Taiwan. The onshore Kuroshio intrusion

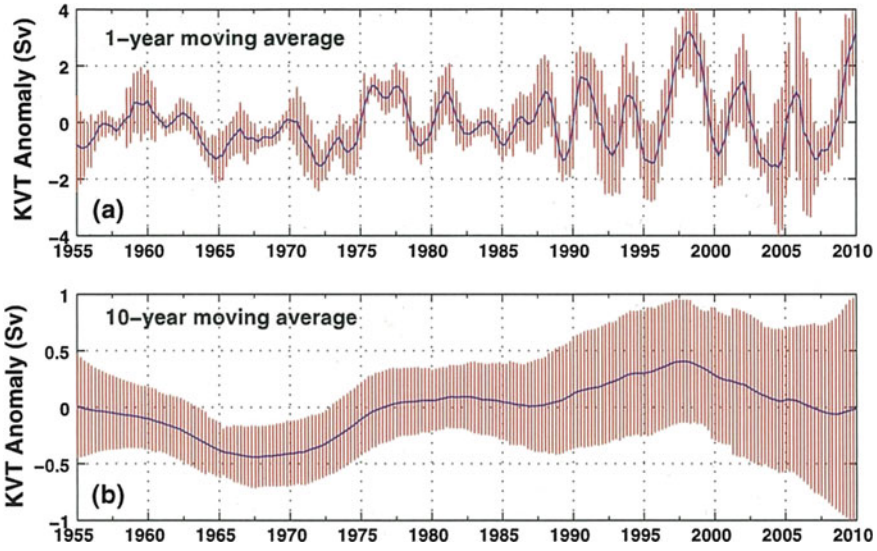

Fig. 9.3 Temporal variation in the Kuroshio transport (KT) anomaly presented by Wei et al. (2013) with (upper) one-year moving average and (lower) 10-year moving average. The red bars indicate standard errors. Reprinted by permission from Springer

contributed to the increase in temperature in the shelf region in the southern ECS. The fluctuation in the KP was revealed to have interannual and decadal variations and a significant correlation was found with the Philippine–Taiwan Oscillation (PTO) rather than with the PDO or KT. The PTO demonstrated a wind stress curl pattern in the subtropical western North Pacific. Because the onshore shift of the KP in northeast Taiwan is a relatively local phenomena, the KP can be more reasonably correlated with the local wind field (PTO) compared to the global-scale oscillation (PDO). Hsin et al. (2013) also demonstrated an interannual variation in the Kuroshio east of Taiwan based on satellite altimeter data for 20 years after 1993.

The locations of the KP and KT east of Taiwan were well correlated, and the timing of the KT peak coincided with the cold phase of the PDO index. Therefore, the KT and its position east of Taiwan could be connected to PDO-related eddy activities in the subtropical counter current region. The variations in the KT and KP east of Taiwan could significantly influence those in the ECS northeast of Taiwan and the heat flux in the shelf region in the ECS. A detailed explanation is presented in Chap. 15.

Similarly, Chang and Oey (2011) demonstrated that slow fluctuations in PTO could play a crucial role in the interannual fluctuation of KT east of Taiwan. The activity of the mesoscale eddies was suggested to be an important factor that contributed to local KT. Chang and Oey (2011) and Wang and Oey (2014) suggested a correlation of the Kuroshio northeast of Taiwan to PTO instead of PDO. This result was different from that of Andres et al. (2009) where a close relationship between KT and the PDO index in the PN section, a little downstream of the Kuroshio from northeast of Taiwan, was observed. As mentioned earlier, Hsin et al. (2013) also suggested a significant correlation between KT and the PDO index east of Taiwan, whereas they presented the importance of eddy activities associated with PDO as well as correlation with wind stress curl near Taiwan and Philippines. The difference in the relationship between KT and the PDO index could be caused by the location of calculated KT or the period of the data; however, the reason has not yet been clarified.

A data-assimilative numerical model presented by Soeyanto et al. (2014) suggested that KT is influenced by mesoscale eddy activities, along with a large-scale climate index such as the PDO index. Meanwhile, as reported in other works, KT was positively correlated with the PDO index for the time series from 1993 to 2002. When a longer dataset from 1993 to 2012 was used, the correlation was reduced by the influence of the mesoscale eddies. Actually, after 2002, the activities of the mesoscale eddies have been enhanced. Furthermore, the tendency depended on the location along the Kuroshio in the ECS. They concluded that the combination of PDO- and eddy-related signals could determine the interannual variations in KT in the ECS.

9.5 Changjiang Diluted Water

The other component of the external factors that control the physical properties of the ECS is the fresh water discharged from Changjiang. As well known, CDW expands to the central area in the ECS shelf region, particularly in summer, accompanied with distinct seasonal variation in CD. The interannual fluctuation in the monthly mean CD in summer is large from less than 40,000 to more than 70,000 $m^3\ s^{-1}$, whereas the range is less than the seasonal variation. The climatological monthly mean CD is from 10,000 to 50,000 $m^3\ s^{-1}$ (e.g., Siswanto et al. 2008). Siswanto et al. (2008) presented the long-term variation in surface salinity in the northern ECS using the salinity data from 1950 to 2002 from the Japan Oceanographic Data Center. They demonstrated that the expansion of low-salinity water influenced by CD exhibited a large interannual variation. They also compared the sea surface salinity (SSS) between 31°N and 32°N in the shelf in northern ECS with the amount of CD. As expected, SSS was correlated with the amount of CD; however, it showed large variability, which was caused by various external forces such as the wind effect, Taiwan Warm Current, and tidal motions. Despite the large variability, SSS exhibited a long-term decrease, which could reflect the increase in the amount of CD. Actually, they concluded that the long-term decrease in SSS was caused by the increase in the amount of CD. Using a slightly longer dataset, Zhang et al. (2014) presented a slight long-term increase in the amount of CD, and they concluded that the increase in CD corresponded to PDO or ENSO. Although the warm phase of PDO in the eastern Pacific could be related to the reduced precipitation over the Changjiang basin, the increase in temperature also in the continent of China could be related to the ice melting in glacier, resulting in the increase in CD. In reality, the shift in the PDO index from negative to positive phase during the 1970s was related to the CD increase. However, the trend was actually slight, and the processes appeared to be complicated. Whereas Zhang et al. (2014) demonstrated a slight linear trend in CD for 60 years, CD appears to decrease or is stable if we look at the time series after 2000, which could be caused by the partial completion of the Three Gorges Dam (TGD) in 2003 when CD became partly regulated compared with the previous period. However, further studies are needed to determine the influence of TGD on the long-term variation in the oceanic structure in the ECS.

The interannual variation in the CDW expansion was estimated from the ocean color detected by satellites (Kim et al. 2009) using the relationship in which low-salinity water is correlated with chlorophyll, as observed by the satellites. Kim et al. (2009) concluded that the CDW area varied corresponding to the interannual variation in the amount of CD using the data from 1998 to 2007. The area of the CDW expansion in late summer was significantly correlated with CD in July and August and exhibited a relationship with the southerly wind. This result indicates that climate indices such as the PDO index can affect the expansion of CDW caused by not only the precipitation in the drainage basin but also the wind fields in the shelf region associated with the Ekman transport.

9.6 Sea Level

Long-term variations in the ocean are often discussed based on sea level because sea level data from tide gauges are acquired over long periods. However, in the recent decades altimeter data from satellites have been used to monitor sea level not only in the open ocean but also in coastal waters. Han and Huang (2008) used both tide-gauge data at 8 stations along the Chinese and Korean coasts as well as Ishigaki Island, and SSH data over Bohai, YS and ECS from TOPEX/Poseidon (T/P) to investigate the interannual and decadal variations in sea level for a relatively short period from 1992 to 2002. They compared the satellite altimetry data with the tide-gauge data and found a good correlation between them for the annual variation (Fig. 9.4). However, for the interannual and decadal variations, the tide-gauge data exhibited much larger fluctuations than the satellite altimeter data did; this could have been caused by the geographic location of the selected tide gauge. The altimeter and tide-gauge data used in their study showed a linear trend in the sea level from 1992 to 2002, with the relatively similar rates of increase of 0.64 and 0.60 cm per year, respectively. However, when longer-term tide-gauge data were used, the rate of increase decreased, to 0.2–0.3 cm per year, as given in previous studies. Actually, their T/P data period appeared to be equivalent to a distinct increase in the abovementioned SST, and a significant part of the sea level variation corresponded to the steric height. Therefore, they concluded that the long-term rate of increase in sea level depends on the length of the data analyzed. Han and Huang (2008) stated that because the interannual variations in the sea level appear to be correlated with the climate indices such as PDO index, a long-time dataset, beyond multi-decadal oscillation, is necessary to evaluate the long-term trend.

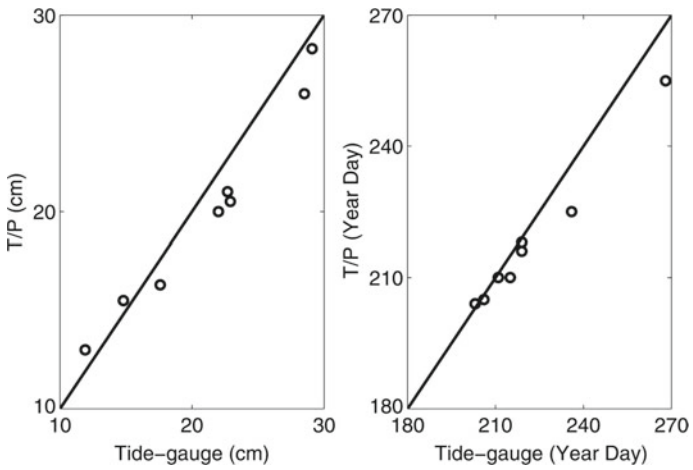

Fig. 9.4 Correlation of the annual sea level harmonics between T/P and tide-gauge observations of the **a** amplitude and **b** phase presented by Han and Huang (2008). The phase indicates the time (year–day) when the annual sea level is the highest

Chen et al. (2018) examined the long-term trend of sea level using tide-gauge data around the ECS after the 1950s, which showed an increase in the sea level at various stations around the ECS with significant regional variations from 0.1 to 0.5 cm per year. They noted that the regional variation was mainly associated with the vertical land motion, which could not be accounted by Glacial Isostatic Adjustment and could be due to various local land motions. Figure 9.5 shows examples of the sea level trend around the ECS obtained by Chen et al. (2018) in which the significant difference in the increase rate in the sea level depended on the location. The difference was mainly caused by individual vertical land motion at each site. Therefore, although the length of the tide-gauge data is usually long, we should note that the results must be relative to the land motion, and combined analysis with the satellite altimeter data is necessary.

Cheng et al. (2016) presented the sea level acceleration in the ECS, along with Bohai Sea, using long-term data since 1950 and demonstrated that the sea level in the ECS appeared to rise with increasing rate at constant acceleration of 0.074 ± 0.032 mm per square year), which was calculated after removing the multi-decadal oscillation. They stated that because the variation in the sea level includes various types of long-period oscillations correlated with the climate indices such as PDO, ENSO, and North Pacific Gyre Oscillation (NPGO), removing the long-period oscillation using a satisfactorily long-term dataset is important to identify the change in the sea level due to global warming.

From a different viewpoint, Xu et al. (2015) discussed the role of the Kuroshio on the sea level in the shelf region in the ECS mainly using satellite altimeter data from 1993 to 2010. They concluded that the Kuroshio could be a barrier that blocked the

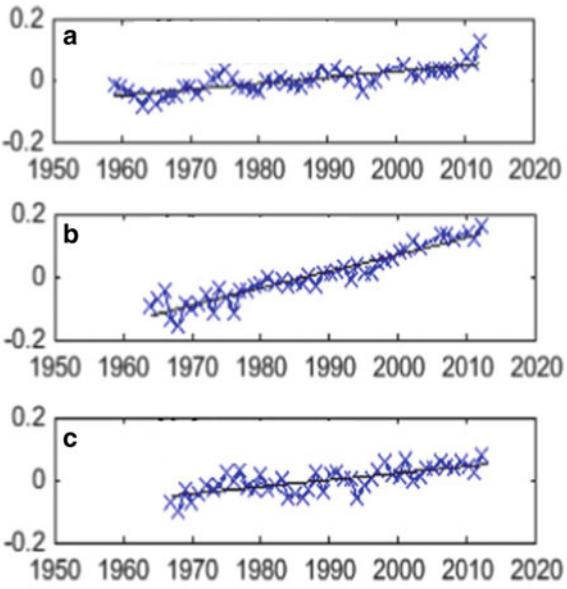

Fig. 9.5 Temporal variations in the sea level observed using the tide gauge at **a** Kahmen, on the east coast of China in the central ECS, **b** Jeju, in the north end of the ECS, and **c** Naha, in the eastern end of central ECS, reprinted from Chen et al. (2018) with permission from Elsevier

influence of the Pacific Ocean on the shelf region; that is, the correlation between the sea level in the Pacific Ocean and the coastal region was reduced by the existence of the Kuroshio. This result indicated that the long-term variation in the sea level in the shelf region in the ECS was associated mainly with local systems, such as the coastal current system, instead of global changes. Further, the sea level in the coastal region was shown to be rising at a rate slower than the global average. This result appeared to be slightly different from those of other studies in which the sea level change was correlated with climate indices such as PDO or ENSO.

Moon and Song (2017) showed two multi-decadal regional sea level trends after 1960, which decreased from 1960 to 1985 and increased from 1986 to 2010 after the global mean sea level trend has been removed, using tide-gauge data, satellite altimeter data, and the non-Boussinesq Ocean General Circulation Model (Fig. 9.6). The trends were more dominant in the Kuroshio region compared with those in the

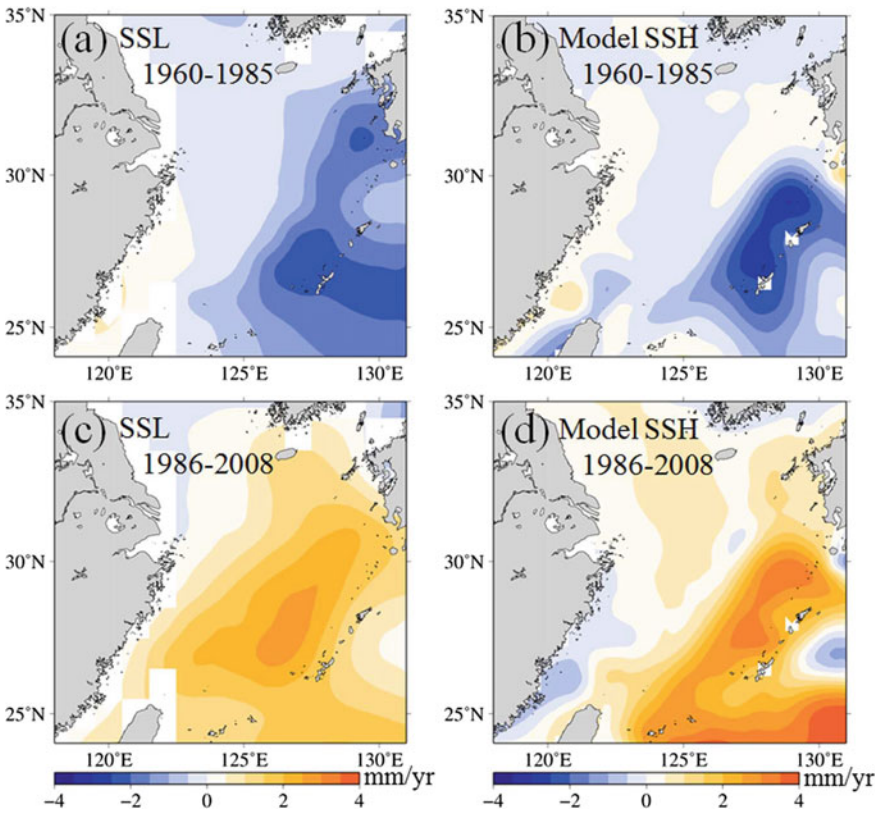

Fig. 9.6 Sea level trends over the ECS during the two multi-decadal periods: **a** and **b** 1960–1985 and **c** and **d** 1986–2008, which are derived from **a** and **c** the steric sea level (SSL) and **b** and **d** Ocean General Circulation Model where the global-mean sea level rise has been removed. This figure was reprinted from Moon and Song (2017) with permission from Elsevier

shelf region in the ECS, which appeared to be consistent with the explanation by Xu et al. (2015) that the Kuroshio plays a role as a barrier to block the influence of the Pacific Ocean on the shelf region. However, when the sea level change significantly corresponded to the steric height, the fluctuation range was small in the shallow region compared with that in the deep ocean. Furthermore, Moon and Song (2017) presented that the decadal fluctuations in the sea level were more closely related to NPGO than PDO. NPGO is a climate index explained by the second mode of the empirical orthogonal function principal component of the North Pacific SSH (Di Lorenzo et al. 2008). Whereas NPGO exhibited a dominant pattern in the eastern North Pacific, the significant inter-decadal oscillation found in the wind stress curl in the western subtropical North Pacific was well correlated with NPGO (Moon and Song 2017). The inter-decadal oscillation found in the sea level in the ECS was explained to be caused by convergence and divergence due to the wind fields.

Whereas the sea level variation from the satellite altimeter offers an advantage of being free from land motion, the multi-decadal oscillation cannot be well removed yet because the data length is shorter than 30 years. However, combined analysis of the altimeter and historical tide-gauge data could provide a long-term trend of the sea level. Various studies suggest a long-term rise in the sea level in the ECS, whereas the rising rate exhibits variations due to the area, period, method of analysis, data length, and so on.

The long-term rise in the mean sea level may influence tidal motion in shallow water. Feng et al. (2015) investigated the long-term variations in the major semidiurnal and diurnal constituents at several stations along the China coast from Bohai to South China seas. Whereas they demonstrated 18.61 years of nodal modulation in which some discrepancies existed between the observed amplitudes and equilibrium theory, they did not present a significant long-term trend in the ECS. They found no convincing evidence between the tidal motion and rise in the sea level.

9.7 Discussion

To observe how the ECS has been changing in the recent decades, we reviewed literature that examined the long-term variations in the SST, the YSCW, the Kuroshio, the CDW, and sea level. When we consider long-term trends, our focus is usually on the influence of global warming. In reality, various researchers have shown that SST tended to display a long-term increasing trend in the recent century. For example, the JMA report (JMA 2017) indicated a linear trend of approximately 1.2 °C per century in the ECS. However, in general, the long-term trends in various factors are difficult to identify because of decadal and/or multi-decadal oscillations, which means that the results could depend on the length of the recorded observations.

When we use a data from an observation period of a limited length, we need to discuss long-term trends by including oscillations on an interannual to multi-decadal time scale. This process means that part of the oscillations should be recognized as a long-term trend when the data length is shorter than the oscillation period.

We have observed long-term variations in various factors in the ECS, such as the temperature, salinity, sea level, and current velocity of the Kuroshio, based on the literature mainly published in recent decades. However, they are not independent factors but are related to one another. As expected, SST and the sea level height appear to be correlated with the climate indices mainly through the wind system. Furthermore, SST, sea level, KT and the expansion of CDW are correlated with climate indices including the relatively global-scale indices, PDO and ENSO, or regional-scale PTO, and NPGO, whereas they are simply indices of oscillations. If we consider the long-term trends associated with global warming, various time-scale oscillations can be removed by considering different climate indices, whereas the climate indices themselves may also be influenced by global warming.

Whereas different interpretations on the long-term trend in the physical factors in the ECS exist, we can briefly summarize the trend qualitatively as follows: SST and the sea level in the ECS have exhibited a rising trend during the recent several decades. The salinity in YSCW and KT has shown a decreasing trend and a slight increase, respectively, during these periods. However, determining a reliable magnitude of the trends is difficult except for that of SST, as shown earlier.

Acknowledgements This study is partly supported by Grant-in-Aid for Scientific Research on Innovative Areas (MEXT KAKENHI grants: JP15H05821). Figure 9.1, Fig. 9.5 and Fig. 9.6 were reprinted from Conti Shelf Res 30(13), Yeh S-W, Kim C-H, Recent warming in the Yellow/East China Sea during winter and the associated atmospheric circulation, p. 1429, Copyright (2010), from Conti Shelf Res. 152, Chen N, Han G, Yang J, Mean relative sea level rise along the coasts of the China Seas from mid-20th to 21st centuries, p. 29, Copyright (2017) and from Conti Shelf Res 143, Moon JH, Song YT, Decadal sea level variability in the East China Sea linked to the North Pacific Gyre Oscillation, p. 280, Copyright (2016), respectively, with permission from Elsevier. And also Fig. 9.3 was reprinted from J Oceanogr 69, Wei Y, Huang D, Zhu X-H, Interannual to decadal variability of the Kuroshio current in the East China Sea from 1955 to 2010 as indicated by in situ hydrographic data, p. 584, Copyright (2013), with permission from Springer.

References

Andres M, Park J-H, Wimbush M, Zhu X, Nakamura H, Kim K, Chang K-I (2009) Manifestation of the Pacific decadal oscillation in the Kuroshio. Geophys Res Lett 36:L16602. https://doi.org/10.1029/2009GL039216

Chang Y-L, Oey L-Y (2011) Interannual and seasonal variations of Kuroshio transport east of Taiwan inferred from 29 years of tide gauge data. Geophys Res Lett 38:L08603. https://doi.org/10.1029/2011GL047062

Chen N, Han G, Yang J (2018) Mean relative sea level rise along the coasts of the China Seas from mid-20th to 21st centuries. Cont Shelf Res 152:27–34. https://doi.org/10.1016/j.csr.2017.12.002

Cheng Y, Ezer T, Hamlington BD (2016) Sea level acceleration in the China Seas. Water 8:293. https://doi.org/10.3390/w8070293

Di Lorenzo E, Schneider N, Cobb KM, Franks PJS, Chhak K, Miller AJ, McWilliams JC, Bograd SJ, Arango H, Curchitser E, Powell TM, Rivière P (2008) North Pacific gyre oscillation links ocean climate and ecosystem change. Geophys Res Lett 35:L08607. https://doi.org/10.1029/2007GL032838

Feng X, Tsimplis MN, Woodworth PL (2015) Nodal variations and long-term changes in the main tides on the coasts of China. J Geophys Res: Oceans 120(2):1215–1232
Han G, Huang W (2008) Pacific decadal oscillation and sea level variability in the Bohai, Yellow, and East China Seas. J Phys Oceanogr 38:2772–2783. https://doi.org/10.1175/2008JPO3885.1
Hsin Y-C, Qiu B, Chiang T-L, Wu C-R (2013) Seasonal to interannual variations in intensity and central position of the surface Kuroshio east of Taiwan. J Geophys Res Oceans 118:4305–4316. https://doi.org/10.1002/jgrc.20323
Japan Meteorological Agency (2017) Climate change, Chapter 2. In: Climate change monitoring report. http://www.jma.go.jp/jma/en/NMHS/ccmr/4_ccmr2017_chapter2.pdf
Jin Q, Wang H (2011) Multitime scale variations of sea surface temperature in the China seas based on the HadISST dataset. Acta Oceanol Sin 30(4):14–23
Kim H, Yamaguchi H, Yoo S, Zhu J, Okamura K, Kiyomoto Y, Tanaka K, Kim S-W, Park T, Oh I-S, Ishizaka J (2009) Distribution of Changjiang Diluted Water detected by satellite chlorophyll-a and its interannual variation during 1998–2007. J Oceanogr 65:129–135
Li J, Li G, Xu J, Dong P, Qiao L, Liu S, Sun P, Fan Z (2016) Seasonal evolution of the Yellow Sea Cold Water Mass and its interactions with ambient hydrodynamic system. J Geophys Res Oceans 121:6779–6792. https://doi.org/10.1002/2016JC012186
Li A, Yu F, Si G, Wei C (2017) Long-term variation in the salinity of the Southern Yellow Sea Cold Water Mass, 1976–2006. J Oceanogr 73:321–331. https://doi.org/10.1007/s10872-016-0405-x
Liu C, Wang F, Chen X, von Storch J-S (2014) Interannual variability of the Kuroshio onshore intrusion along the East China Sea shelf break: effect of the Kuroshio volume transport. J Geophys Res Oceans 119:6190–6209. https://doi.org/10.1002/2013JC009653
Moon JH, Song YT (2017) Decadal sea level variability in the East China Sea linked to the North Pacific Gyre Oscillation. Cont Shelf Res 143:278–285. https://doi.org/10.1016/j.csr.2016.05.003
Park S, Chu PC, Lee JH (2011) Interannual-to-interdecadal variability of the Yellow Sea Cold Water Mass in 1967–2008: characteristics and seasonal forcings. J Mar Syst 87(3):177–193
Oh KH, Lee S, Song KM, Lie HJ, Kim YT (2013) The temporal and spatial variability of the Yellow Sea Cold Water Mass in the southeastern Yellow Sea, 2009–2011. Acta Oceanol Sin 9:1–10. https://doi.org/10.1007/s13131-013-0346-9
Siswanto E, Nakata H, Matsuoka Y, Tanaka K, Kiyomoto Y, Okamura K, Zhu J, Ishizaka J (2008) The long-term freshening and nutrient increases in summer surface water in the northern East China Sea in relation to Changjiang discharge variation. J Geophys Res 113:C10030. https://doi.org/10.1029/2008JC004812
Soeyanto E, Guo X, Ono J, Miyazawa Y (2014) Interannual variations of Kuroshio transport in the ECS and its relation to the PDO and mesoscale eddies. J Geophys Res Oceans 119:3595–3616. https://doi.org/10.1002/2013JC009529
Wang J, Oey L-Y (2014) Inter-annual and decadal fluctuations of the Kuroshio in East China Sea and connection with surface fluxes of momentum and heat. Geophys Res Lett 41:8538–8546. https://doi.org/10.1002/2014GL062118
Wang F, Meng Q, Tang X, Hu D (2013) The long-term variability of sea surface temperature in the seas east of China in the past 40 a. Acta Oceanol Sin 32(3):48–53. https://doi.org/10.1007/s13131-013-0288-2
Wei Y, Huang D, Zhu X-H (2013) Interannual to decadal variability of the Kuroshio current in the East China Sea from 1955 to 2010 as indicated by in-situ hydrographic data. J Oceanogr 69:571–589. https://doi.org/10.1007/s10872-013-0193-5
Wu R, Lin J, Li B (2016) Spatial and temporal variability of sea surface temperature in Eastern Marginal Seas of China. Adv Meteorol 2016(Article ID 3820720):9. http://dx.doi.org/10.1155/2016/3820720
Xu Y, Lin M, Zheng Q, Ye X, Li J, Zhu B (2015) A study of long-term sea level variability in the East China Sea. Acta Oceanol Sin 34(11):109–117. https://doi.org/10.1007/s13131-015-0754-0
Yeh S-W, Kim C-H (2010) Recent warming in the Yellow/East China Sea during winter and the associated atmospheric circulation. Cont Shelf Res 30(13):1428–1434. https://doi.org/10.1016/j.csr.2010.05.002

Zhang X, Fan D, Wang H, Yang Z (2014) Water discharge variability of Changjiang (Yangtze) and Huanghe (Yellow) Rivers and its response to climatic changes. Chin J Oceanol Limnol 32(6):1392–1405. https://doi.org/10.1007/s00343-015-4034-9

Zhang Q-L, Hou Y-J, Yan T-Z (2011) Inter-annual and inter-decadal variability of Kuroshio heat transport in the East China Sea. Int J Climatol. https://doi.org/10.1002/joc.2295

Chapter 10
Changing Nutrients, Oxygen and Phytoplankton in the East China Sea

Jianfang Chen, Dewang Li, Haiyan Jin, Zhibing Jiang, Bin Wang, Bin Wu, Qiang Hao, and Xiangyu Sun

Abstract Biogeochemical processes in the East China Sea are substantially affected by anthropogenic nutrient inputs. The dramatic decadal changes in nutrient concentrations were mainly due to the increases of DIN and DIP in the Changjiang (Yangtze) River since 1980s. As a result, phytoplankton abundance increased dramatically between 1958 and 2016 in both the Changjiang Estuary and the East China Sea. Before 1980s, chain-forming diatoms were dominant, while increasing of large-cell dinoflagellates is probably related to increasing DIN/silicate ratio. Increasing nutrient input and phytoplankton abundance greatly impact seasonal hypoxia condition in the East China Sea. Hypoxia is relatively sporadic and patchy before 2013. In 2016 and 2017, hypoxic events were more severe, occurring over larger areas with dramatically lower minimum values of dissolved oxygen. Notwithstanding, occurrences of bottom hypoxia in the East China Sea are highly dynamic and are significantly influenced by episodic events such as wind mixing.

J. Chen (✉) · D. Li · H. Jin · Z. Jiang · B. Wang · B. Wu · Q. Hao
Key Laboratory of Marine Ecosystem Dynamics, Second Institute of Oceanography, Ministry of Natural Resources, Hangzhou 310012, China
e-mail: jfchen@sio.org.cn

D. Li
e-mail: dwli@sio.org.cn

H. Jin
e-mail: jinhaiyan@sio.org.cn

Z. Jiang
e-mail: jzb@sio.org.cn

B. Wang
e-mail: wangbin@sio.org.cn

B. Wu
e-mail: wubin@sio.org.cn

Q. Hao
e-mail: haoq@sio.org.cn

X. Sun
Ocean College, Zhejiang University, Zhoushan 316021, China
e-mail: xiangyusun@126.com

C.-T. A. Chen and X. Guo (eds.), *Changing Asia-Pacific Marginal Seas*, Atmosphere, Earth, Ocean & Space, https://doi.org/10.1007/978-981-15-4886-4_10

Keywords East china sea · Nutrients · Phytoplankton · Dissolved oxygen · Decadal change

10.1 Introduction

The East China Sea, which borders the East Asia mainland, is a marginal sea of the northwest Pacific Ocean. To the south, the sea connects to the South China Sea through the Taiwan Strait; to the northeast, to the Japan/East Sea through the Tsushima Strait. Kuroshio waters intruding through north-east Taiwan and eastbound shelf break are the major water sources. The interactions of these waters with shelf waters significantly influence the East China Sea water budget (Hsueh et al. 1992; Zhou et al. 2015), and biogeochemical cycles (Chen and Wang 1999; Lui et al. 2015). The East China Sea also receives massive inputs of fresh water, nutrients, and suspended organic matter from the Changjiang (Yangtze) River and the Qiantang River. The tremendous inputs of riverine materials trigger harmful algal blooms, and hypoxia (Liu et al. 2015a, b; Wang et al. 2017a, b; Zhou et al. 2008; Zhu et al. 2011), greatly affect carbon cycles (Chou et al. 2013; Li et al. 2018; Tseng et al. 2014), and the shelf ecosystem (Gong et al. 2011; Jiang et al. 2014), especially in plume waters.

Over the past few decades, the East China Sea shelf has experienced dramatic environmental change. Since the 1980s, the ever-expanding population and economic growth of East China, including the Changjiang River Basin have caused three to six fold increase of nutrient (nitrogen and phosphate) inputs to the Changjiang Estuary and the East China Sea (Li et al. 2007; Zhou et al. 2008). As a result, phytoplankton standing stocks and the frequency of harmful algal blooms in the sea have increased (Jiang et al. 2014; Wang and Wu 2009). In bottom waters, large-scale hypoxia has occurred frequently due to the enhanced input of organic matter from the surface phytoplankton blooms (Zhu et al. 2011; Wang et al. 2017a).

In this chapter, we review decadal changes of nutrients, phytoplankton community, and dissolved oxygen (DO) characteristic in the East China Sea (Fig. 10.1), based on data obtained from multiples research cruises. Some of these data have been reported in the literatures. For this overview, we focus on the northern East China Sea, which is strongly affected by the Changjiang River.

10.2 Nutrients

National marine surveys of Chinese seas in the 1950s (OIOSC 1964a), 1980s (Wang et al. 1991), and 2000s (Wang et al. 2011), as well as others scientific surveys have provided valuable snapshots of the spatial distributions of nutrients in the East China Sea (Chen 2009; Gong et al. 1996; Wang et al. 2003). The temporal variations, especially the decadal variations are less well documented (Chai et al. 2006; Wang et al. 2018), even though such changes are important for evaluating shelf ecosystem

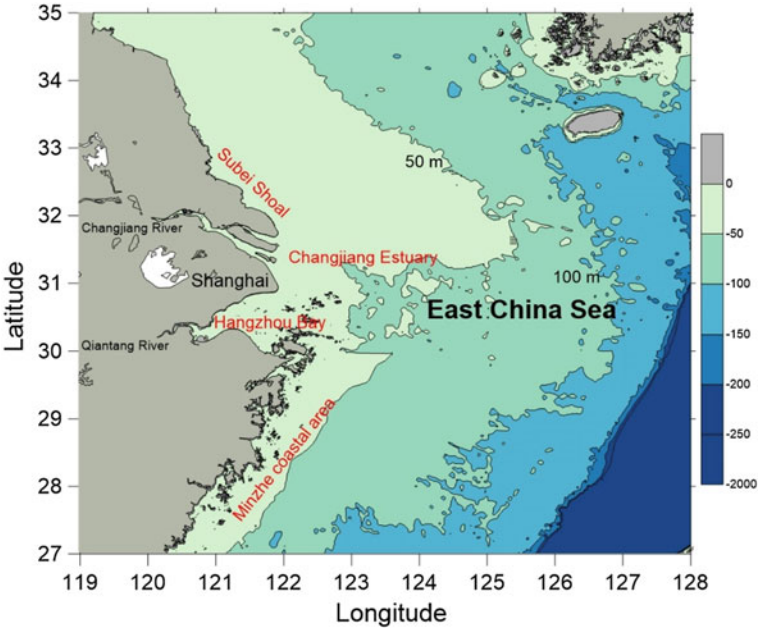

Fig. 10.1 Map of the East China Seas

status, and projecting future scenarios (Ducklow et al. 2009). In surveying historical data, we found that discussions of decadal changes in nutrient concentrations did not always include the corresponding values of salinity, which are significantly important in understanding coastal and shelf process. Here, we compare nutrient data from the 1980s and the 2000s in the East China Sea across a wide salinity range.

10.2.1 East China Sea

In the East China Sea, concentrations of dissolved inorganic nitrogen (DIN, sum of nitrate, nitrite, and ammonium) in the 2000s were much higher than that in the 1980s (Fig. 10.2a). At salinity <5, DIN concentrations in the 2000s exceeded 100 μmol L^{-1}, up from less than 60 μmol L^{-1} in the 1980s. This increase is likely caused by increasing DIN concentrations in the Changjiang River. On river-dominated shelf, where a large plume is formed by the mixing of nutrient-replete river water and relatively nutrient-poor oceanic water, plume DIN concentrations decrease sharply with increasing salinity. A salinity of 31 is often used to define the outer edge of the plume, which can sometimes reach the South Korean peninsula (Isobe and Matsuno 2008; Wang et al. 2003) and during flood years may cover an area of 141,000 km^2 (Gong et al. 2011). As shown in Fig. 10.2a, the maximum DIN concentration at the plume edge was ~16 μmol L^{-1} in the 1980s and ~25 μmol L^{-1} in the 2000s. This

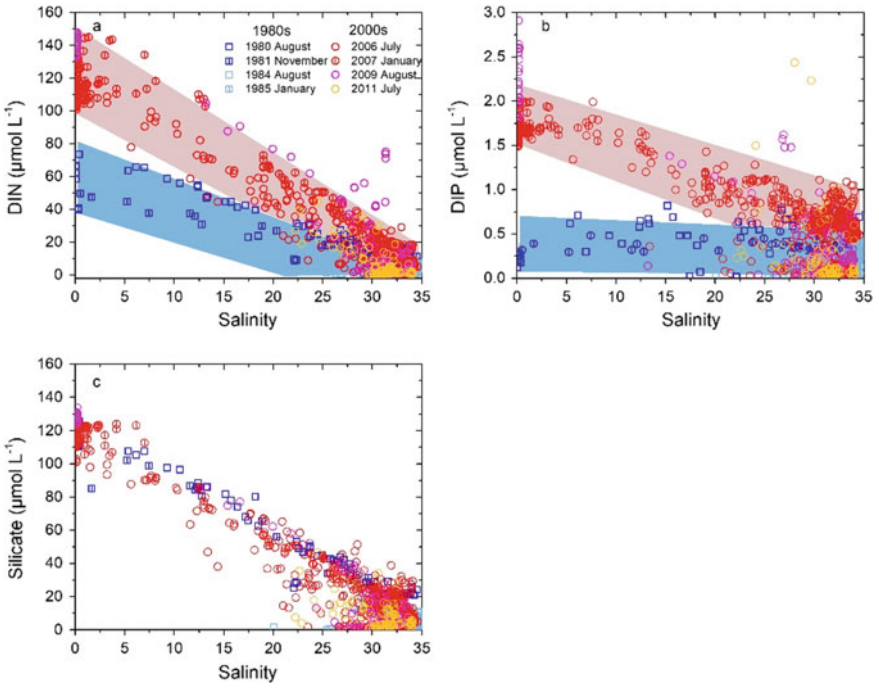

Fig. 10.2 Nutrient concentrations in the East China Sea during the 1980s and 2000s, plotted as a function of salinity: **a** DIN, **b** DIP, and **c** silicate. The blue and red envelopes on the top two panels showed concentration limits along salinity during 1980s and 2000s, respectively. Data were obtained from Edmond et al. (1985), Wang et al. (2011), Li et al. (2016), and our own unpublished work

30-year DIN increase of plume waters could be reasonably expected to significantly influence oxygen dynamics and phytoplankton community structure in the East China Sea (as discussed below) and even the Japan Sea (Chang et al. 2015). For salinity >33, no significant DIN decadal trend was found from our data set.

Similar to the case of DIN, the mixing of nutrient-poor oceanic surface waters and river waters high in dissolved inorganic phosphate (DIP) has been important in regulating concentrations in the East China Sea. DIP concentrations in the 2000s were higher than those of the 1980s (Fig. 10.2b). At low salinities, DIP concentrations in the 2000s were >1.5 μmol L^{-1}, up from <0.8 μmol L^{-1} in the 1980s. In the early 1980s, DIP concentrations were relatively constant across the wide salinity range of 5–15. In the 2000s, however, DIP generally decreased with increasing salinity over that range. Desorption of DIP from suspending sediments could also have been important (Edmond et al. 1985; Liu et al. 2016; Zhang 1996). In Changjiang Estuary surface waters, concentrations of particulate inorganic phosphate accounts for about half the concentration of DIP (Liu et al. 2016; Wang et al. 2009). At the outer edge of the river plume, DIP concentrations are usually undetectable due to phytoplankton uptake, while nitrate is still available; thus, phytoplankton growth is usually limited

by the depletion of DIP (Harrison et al. 1990; Tseng et al. 2013). Phosphate-enrich bottom waters and waters transport from Taiwan Strait can be an important phosphate source to upper waters (Chen and Wang 1999; Huang et al. 2019; Li et al. 2016).

Silicate concentrations, unlike those of DIN and DIP, exhibit no notable decadal changes in the fresh water endmember (Fig. 10.2c), while they show a dramatically decreasing trend in the oceanic water endmember, indicating diatom bloom has increased because of increasing of DIN and DIP (Wang et al. 2017a). This difference seems reasonable in light of the different sources and biogeochemical processes of these nutrients. DIN and DIP concentrations have been strongly influenced by anthropogenic nutrient sources (increasing), whereas the main source of silicate is the weathering of rocks within the Changjiang river basin. The Three Gorges Dam, which was constructed across the river in 2003, has reportedly reduced downstream river sediment loads significantly (Dai et al. 2010) and possibly also river water silicate concentrations (Dai et al. 2010; Gong et al. 2006). In our East China Sea data set, however, no significant trend of decreasing silicate was found in the fresh water endmember. A longer period of observation is perhaps needed to document the potentially more subtle decadal variations of silicate concentrations in shelf waters.

10.2.2 Hangzhou Bay

Sharp increases of DIN were observed in Hangzhou Bay over the three decades of observation (Fig. 10.3a), similar to the case of the East China Sea (Fig. 10.2a). At salinity = 10, DIN concentrations were ~140 μmol L^{-1} in the 2000s, up from 20 to 80 μmol L^{-1} in the 1980s. At the mid-range salinities of 10–27, concentrations increased by a factor of 2–3, from ~30 μmol L^{-1} in the 1980s to ~70 μmol L^{-1} in the 2000s. This increase of mid-bay DIN was caused primarily by increasing concentrations in not only the Qiantang River, which flows directly into Hangzhou Bay, but also the Changjiang River to the north (Dai et al. 2014; Su and Wang 1989). In the low-salinity zone of upper Hangzhou Bay, the Changjiang influence was not likely a primary driver, as DIN concentrations there were even higher than those in the Changjiang estuary (Figs. 10.2a and 10.3a). At salinity = 10, for example, recent DIN concentrations were 100 μmol L^{-1} in the East China Sea and ~140 μmol L^{-1} in Hanghzou Bay.

The decadal variations of Hangzhou Bay DIP (Fig. 10.3b) are more complex than those of DIN. The majority of DIP concentrations measured in the 1980s were lower than those seen at the same salinities during the 2000s, but an exception is seen in the extremely high concentrations of some samples collected in winter 1981 (2.5–3.0 μmol L^{-1}). The processes regulating DIP concentrations are also more complicated those associated with DIN, with DIP being strongly influenced by not only Qiangtang River outflow and Changjiang plume intrusion, but also adsorption and desorption of DIP onto and off of suspended particles (Edmond et al. 1985).

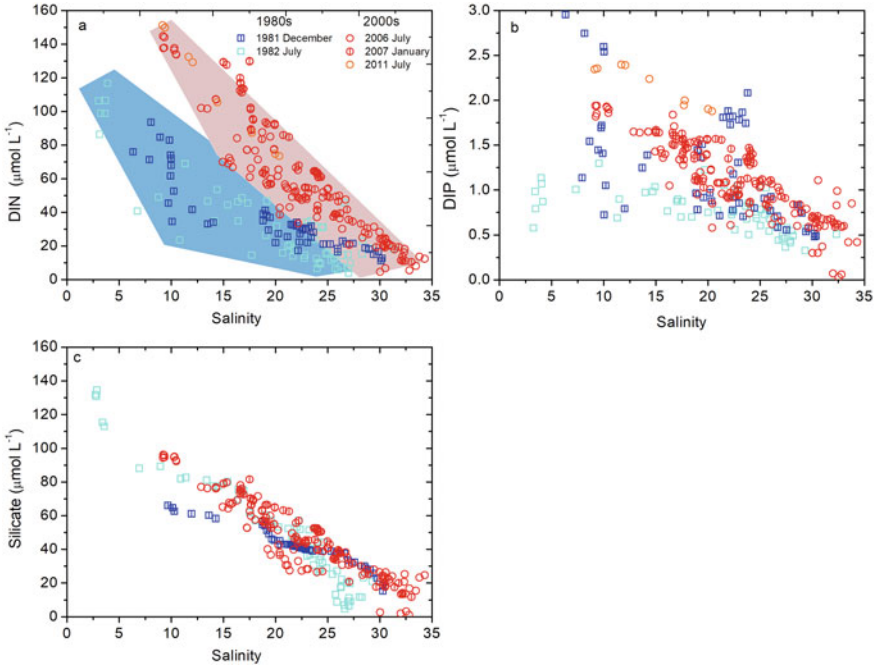

Fig. 10.3 Nutrient concentrations in Hangzhou Bay during the 1980s and 2000s, plotted as a function of salinity: **a** DIN, **b** DIP, and **c** silicate. The blue and red envelopes on panel (**a**) showed concentration limits along salinity during 1980s and 2000s, respectively. Data were obtained from Gao et al. (1993), Wang et al. (2011), Tseng et al. (2013) and Wu et al. (2019)

Both DIN and DIP are influenced by strong tidal mixing within the bay, which results in sediment resuspension and the mixing of nutrients released from the sediment pore waters. Sediment suspension also contributes extreme high particulate organic carbon flux (720–7300 mg C m^{-1} day^{-1}) in the inner shelf of the East China Sea (Hung et al. 2013), which could possibly enhance nutrient regeneration. The role of tidal resuspension on decadal nutrient variations in the bay are largely unknown.

For silicate concentrations in Hangzhou Bay, there was no obvious decadal concentration trend (Fig. 10.3c), similar to the case of the East China Sea.

10.2.3 N/P and N/Si Ratios

In East China Sea coastal waters, extremely high N/P ratios were measured, due to the inflow of high-N/P Changjiang river waters. Classical biogeochemical theory suggests that phytoplankton take up nutrients with a N/P ratio of 16 (Redfield 1958), with slight variations in different systems (Anderson and Sarmiento, 1994; Deutsch and Weber 2012). In both the 1980s and the 2000s, the N/P ratios of most East China

Sea water samples were well above the Redfield ratio (Figs. 10.4a, c) (Harrison et al. 1990; Tseng et al. 2013; Wang et al. 2013a, b). For waters of salinity <15, N/P ratios in the 2000s (~60) were lower than in the 1980s (~100). However, it is hard to say whether this decrease was ecologically significant because even the later N/P ratios were still much greater than 60. For waters of salinity >25, N/P ratios can be much higher than those seen in low-salinity waters because of the intense phytoplankton uptake of phosphorus in marine waters (Wang et al. 2013a, b). For the most productive plume waters (salinity ranges from 25 to 31), the N/P ratio was sometimes >150, as DIP concentrations were usually below the detection limit of 0.01 μmol L^{-1}. It should be noted that Kuroshio Subsurface Water significantly influences the chemical characteristics of subsurface water on the Changjiang shelf. With an N/P ratio of ~16, Kuroshio Subsurface Water could potentially alleviate phosphate limitation in shelf waters (Chen 1996; Chen and Wang 1999; Li et al. 2016; Tseng et al. 2013).

The N/Si (DIN/silicate) ratio in the 1980s was ~0.5, doubling to ~1 by the 2000s (Fig. 10.4b, d). Such an increase can be explained by the steady increase of DIN over the decades (Chai et al. 2009; Li et al. 2007; Wang et al. 2018). It is usually assumed that silicate is not a limiting nutrient in the Changjiang estuary and the East China Sea. However, as the N/Si ratio increased, the phytoplankton community characteristic may be changed over time. Previous studies suggested that dinoflagellate increased

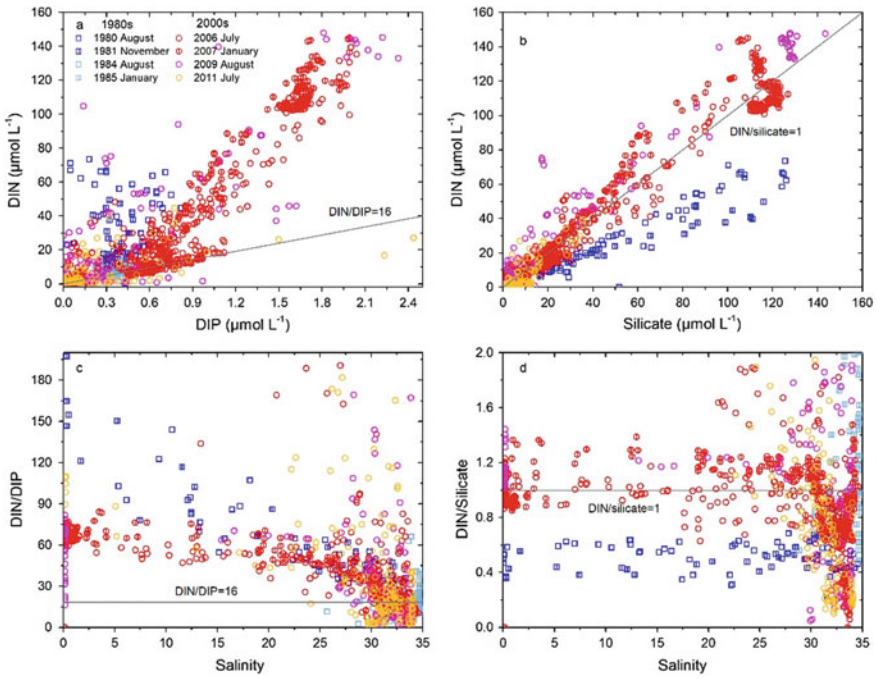

Fig. 10.4 Relationships between nutrtients in the East China Sea during the early 1980s and the 2000s: **a** DIN and DIP, **b** DIN and silicate, **c**, DIN/DIP and salinity, and **d** DIN/silicate and salinity

over past decades (Zhou et al. 2008, and discussion below). Notwithstanding, during the summer, diatoms (with shells of silica) are the dominant phytoplankton group in the Changjiang Estuary (Jiang et al. 2014), and remineralization of their sinking remains is the major consumer of bottom-water oxygen in the outer estuary (Wang et al. 2017a).

10.2.4 Changing Nutrient Inputs

Sources of nutrients to the East China Sea have been discussed in previous studies (Chen and Wang 1999; Kim et al. 2013; Liu et al. 2000 Zhang et al. 2007). Briefly, offshore waters are the major sources of phosphate and silicate to the shelf, with rivers contributing significant nitrogen (Chen and Wang 1999). For the Changjiang River plume waters specifically, nutrient dynamics are influenced mostly by riverine materials. The Changjiang River is the major supplier of fresh water.

Nutrient fluxes in the Changjiang River have risen sharply in recent decades (Fig. 10.5) due to increasing anthropogenic inputs (Dai et al. 2010; Li et al. 2007; Liu et al. 2003; Wang et al. 2018; Zhou et al. 2008). In the early 1960s, Changjiang DIN concentrations (as measured at the Datong hydrological station, approximately 624 km upstream from the river mouth) were ~20 μmol L^{-1} (Fig. 10.5a). Over the next 20 years there was little change, but in the 1980s DIN began to increase sharply. By the 1980s, concentrations had increased to ~80 μmol L^{-1}, and in the 2000s, values of 100–120 μmol L^{-1} were measured. The most recent measurements, from the 2000s, were ~120–160 μmol L^{-1}. A critical part of this story is the 1980s launch of the Reform and Opening policy by the Chinese government. Over the next four decades, the use of nitrogen fertilizer increased by a factor of about four in China (Liu et al. 2013).

DIP concentrations in the river (Fig. 10.5b) fluctuated around ~0.5 μmol L^{-1} before 1980, then increased sharply to ~1.5 μmol L^{-1} in the 1990s and ~1.5 μmol

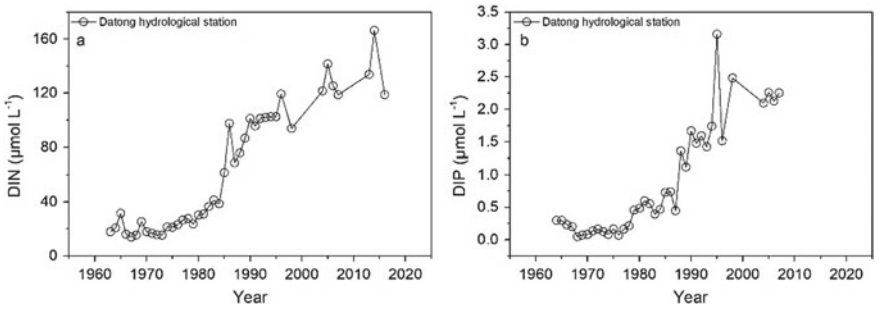

Fig. 10.5 Long term nutrient data in the Changjiang. **a** DIN, **b** DIP. Nutrient data in Datong hydrological station were obtained from Li et al. (2007) and Wang et al. (2018)

L^{-1} in the 2000s. As with DIN, increasing concentrations of DIP in the Changjiang River were caused by increasing anthropogenic inputs.

Surface offshore waters in the East China Sea (salinity > 34) are generally oligotrophic, with nutrient-rich subsurface waters beneath. When this deeper waters are upwelled onto the East China Sea shelf, massive amounts of nutrients are also transported onto the shelf (Chen 1996). Because subsurface upwelling and advection are strongly influenced by diverse events of various scales—such as meandering of the Kuroshio Current (James et al. 1999) and the passage of eddies and typhoons (Hsin et al. 2010)—decadal trends in offshore nutrient concentrations are difficult to evaluate from the available data. Lui et al. (2014), based on long-term nutrient data from the Japan Meteorological Agency, concluded that the nitrate concentration of Kuroshio Intermediate Waters at 400 m increased at a rate of 0.197 ± 0.0295 μmol kg^{-1} $year^{-1}$ (1987–2010) due to reduced ventilation of North Pacific Intermediate Water. The influence of increasing nutrient concentrations in source waters to the East China Sea shelf merit further study, especially in the context of ongoing global change.

10.3 Phytoplankton Communities

Eutrophication profoundly influences phytoplankton communities, and has led to an increase in the occurrence of harmful algal blooms in the China coastal seas (Jiang et al. 2014; Wang and Wu 2009; Zhou et al. 2008), thereby exacerbating hypoxia in terms of its frequency, range, persistence, and destructive capability (Wang et al. 2017; Zhu et al. 2011). Understanding long-term changes in phytoplankton communities is useful in the assessment and management of large estuaries and marginal seas. Several studies have reported phytoplankton community variations in the Changjiang Estuary in response to environmental forcing (Li et al. 2010; Jiang et al. 2010; 2014; Zhou et al. 2008), but few studies have focused on phytoplankton community change across the entire East China Sea.

Since 1958, a large number of phytoplankton studies have been conducted using plankton nets (76 μm mesh) in the Changjiang Estuary and East China Sea (Guo and Yang 1992; Jiang et al. 2014 and references therein; OIOSC 1964b; Zheng et al. 2003). In accord with Chinese government's specifications for marine monitoring, most early phytoplankton collections in the area were conducted using this type of net, and until recently, few samples were collected using water sampling (Jiang et al. 2014 and references therein).

Early phytoplankton studies in the Changjiang Estuary were conducted mostly during summer (Huang et al. 2018; Jiang et al. 2014 and references therein). This section therefore focuses on summer phytoplankton community variations in the Changjiang Estuary from 1959 to 2016, as seen in net-collected phytoplankton samples. Such samples likely reflect time-of-collection losses of noncolonial species with small cell sizes (e.g., cryptophytes, coccolithophores, and some diatoms and dinoflagellates). We also compiled data regarding phytoplankton communities in the

East China Sea during other seasons, 1958–2011. We examined changes in abundance, dominant species, and community composition of phytoplankton using net collection method. Our objective was to explore phytoplankton community change in the Changjiang Estuary and East China Sea in response to extensive human activity and ongoing climate change.

10.3.1 Phytoplankton Abundance

Over the period of record for the Changjiang Estuary, the abundance of net-collected phytoplankton (1959–2016) increased significantly (Mann-Kendall test, $Z = 2.26$; $p < 0.05$) (Fig. 10.6). In the East China Sea as well (Table 10.1), net-collected phytoplankton abundance (1958–1959 to 2009–2011) increased, with large variations among the different seasons. These results are consistent with reports of increased

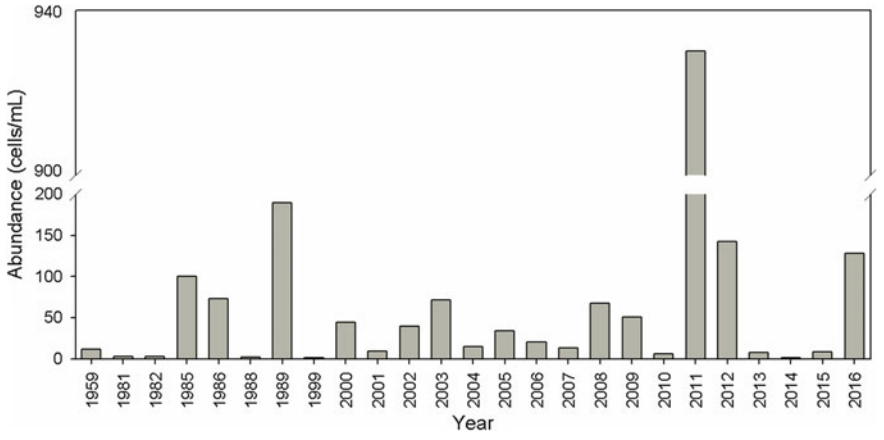

Fig. 10.6 Time-series of abundance of net-collected phytoplankton from the Changjiang Estuary, 1959–2016 (approximately 30–32°N, 121.5–124°E). Data were obtained from Huang et al. (2018), Jiang et al. (2014) and references therein, and also our own unpublished results

Table 10.1 East China Sea phytoplankton abundance (cells L^{-1}), based on net-collected samples. Data were obtained from Liu et al. (2015a), Zheng et al. (2003), and our own unpublished results

Year	Winter	Spring	Summer	Autumn	Average
1958–1959	–	–	–	–	1120
1981–1982	120	1400	12000	1700	3805
1997–2000	114	20	504	2119	689
2006–2007	908	5290	50200	18400	18700
2009–2011	831	816	17266	8814	6932

concentrations of chlorophyll *a* in both field measurements (Jiang et al. 2014) and remote-sensing studies (He et al. 2013). Previous studies have linked increased phytoplankton biomass to the nutrient enrichment of recent decades (Jiang et al. 2010, 2014; Zhou et al. 2008).

10.3.2 Phytoplankton Community Composition

In the Changjiang Estuary, the contribution of diatoms to phytoplankton cell abundance has decreased in recent decades (Mann-Kendall test, $Z = -1.09$), while the contribution of dinoflagellates has slightly increased (Mann-Kendall test, $Z = 0.33$) (Fig. 10.7a). Similarly, the proportion of diatom species within the total number of species has decreased (Mann-Kendall test, $Z = -2.26$, $p < 0.05$) while the proportion of dinoflagellate species has increased (Mann-Kendall test, $Z = 1.86$) (Fig. 10.7b). In the East China Sea (Fig. 10.8), the story is the same: decreasing dominance of diatoms and increasing dominance of dinoflagellates. This widespread community shift is likely attributable to changing nutrient ratios and rising water temperatures. In the Changjiang Estuary and elsewhere, under conditions of increased DIN/Si (Fig. 10.4) and regional warming (Belkin 2009; Jiang et al. 2014), non-siliceous phytoplankton, particularly dinoflagellates, have gradually became more dominant (Jiang et al. 2010; 2014; Sellner et al. 2001).

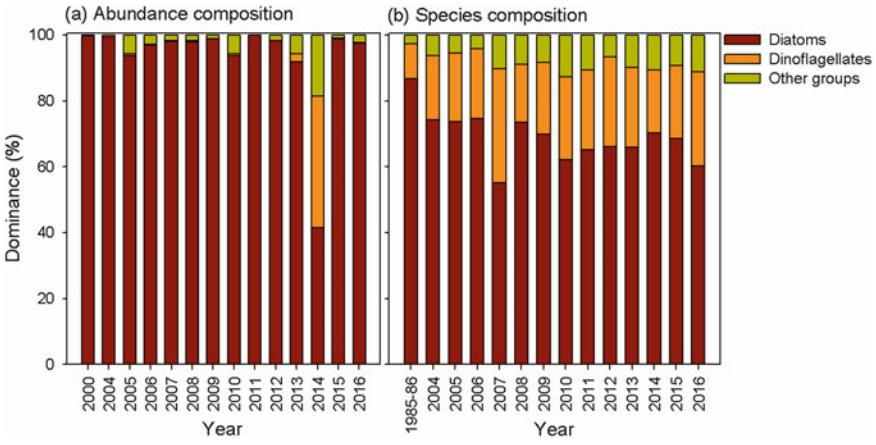

Fig. 10.7 Time-series of community composition of net-collected phytoplankton from the Changjiang Estuary (approximately 30.5–32°N, 121.5–123°E): percent occurrence in terms of **a** cell numbers, 2000 to 2016 and **b** species numbers, 1985–1986 to 2016) Data were obtained from Guo and Yang (1992), Huang et al. (2018), Wang et al. (2008), and our own unpublished results

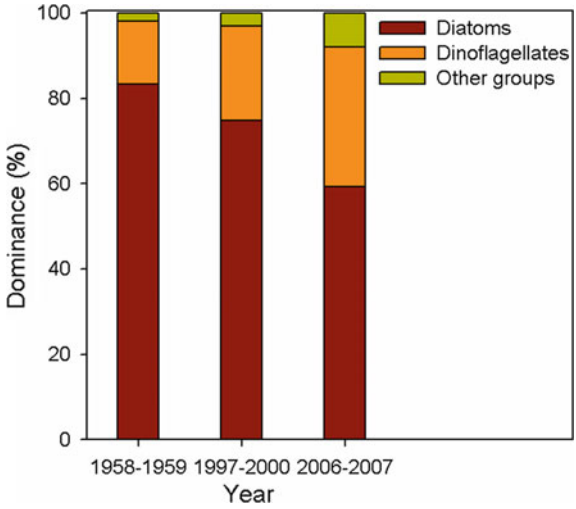

Fig. 10.8 Time-series of species composition of net-collected phytoplankton from the East China Sea. Data were obtained from OIOSC (1964b), Zheng et al. (2003), and our own unpublished results

10.3.3 Dominant Phytoplankton Species

In the Changjiang Estuary, the dominant species (dominance here is calculated the same as percentage) in the summertime phytoplankton samples (net-collected) have most consistently been the chain-forming diatoms, mainly within the genera *Skeletonema*, *Chaetoceros*, and *Pseudo-nitzschia* (Table 10.2). Recently, the proportions of large-celled dinoflagellates (*Ceratium*) and filamentous cyanobacteria (*Trichodesmium*) have been growing, although their percentages are still small. In the East China Sea, recent phytoplankton samples have been similarly dominated by colonial diatoms, dinoflagellates (e.g., *Ceratium* spp., *Dinophysis caudata*, *Noctiluca scintillans*, and *Prorocentrum donghaiense*), and *Trichodesmium* spp. (Table 10.3). Despite the eutrophication occurring in the Changjiang Estuary and East China Sea (Fig. 10.2 through Fig. 10.5), the trichome densities of *Trichodesmium* (which usually thrives in oligotrophic warm waters) have increased considerably in both areas (Jiang et al. 2017, 2018), In addition, the northern range boundary of this warm water species has shifted northward since the 1970s (Jiang et al. 2018). We therefore speculate that the shifts of dominant species seen in the Changjiang Estuary and East China Sea are closely related to not only eutrophication but also warming.

Table 10.2 Changjiang Estuary summertime phytoplankton species dominance, 1959–2011 (30–33°N, 122–124°E; net-collected). Diatom species are listed in red, dinoflagellates in organge, and cyanobacteria in green. The grid-cell colors indicate percent dominance, with warmer colors indicating greater dominance (see key at end of table). Data were obtained from Jiang et al. (2014) and references therein, as well as our own unpublished results

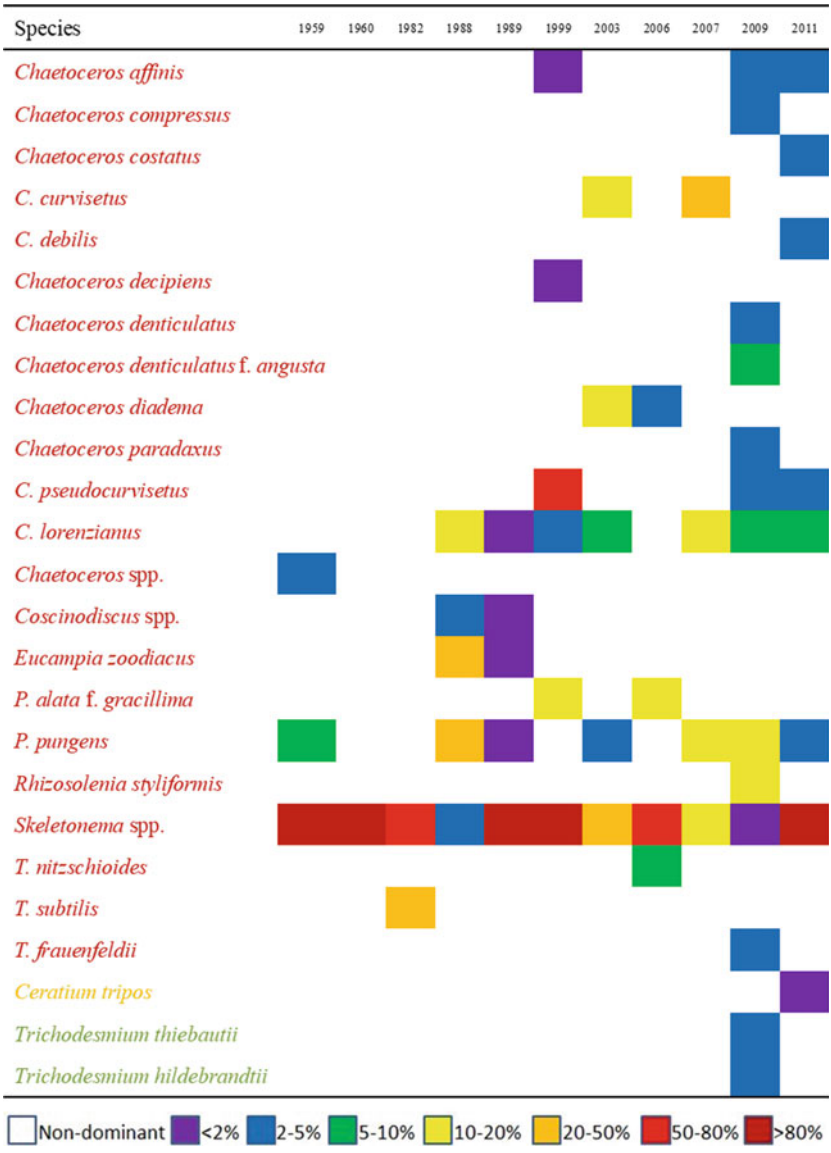

Table 10.3 East China Sea dominant phytoplankton species by season, 1958–2011 (net-collected). Diatom species are listed in red, dinoflagellates in organge, and cyanobacteria in grey. The seasons are indicated by W (winter, shaded by blue), Sp (spring), Su (summer, shaded by red), and A (autumn). The green color blocks mark which species were dominant in each time segment. Data were obtained from Liu et al. (2015a) and Zheng et al. (2003)

10.4 Dissolved Oxygen and Hypoxia

10.4.1 Dissolved Oxygen

DO concentration is controlled by the thermophysical properties of seawater (temperature, salinity, and pressure) and physical/biogeochemical processes such as diffusion and aeration, photosynthesis, and respiration. Globally, oxygen concentrations have been declining faster in coastal waters (-0.28 μmol L^{-1} $year^{-1}$) than in open ocean waters (-0.02 μmol L^{-1} $year^{-1}$) (0–300 m depth, 1976–2000; Gilbert et al. 2010). Changing ocean circulation, mixing, and biogeochemical processes (rather than direct thermally induced solubility effects) are the main drivers (Ito et al. 2017; Keeling et al. 2010). In coastal waters, deoxygenation is exacerbated by global warming (Keeling et al. 2010; Meier et al. 2011) and anthropogenic inputs of excess nutrients (Breitburg et al. 2018; Fennel and Testa 2018; Laurent et al. 2018).

DO in the East China Sea has been declining, just as in other seas around the world. Along a 32°N transect (122°–127°E), average annual rates of change of DO (1975–1995) were -0.448 (surface samples), -0.608 (water column samples), and -0.736 μmol kg^{-1} $year^{-1}$ (bottom samples) (Ning et al. 2011). At the sea surface, declining concentrations were due mainly to rising temperatures, which decreases oxygen solubility. At the sea bottom, declining concentrations were due mainly to biologically mediated summertime oxygen depletion, which was triggered by surface phytoplankton blooms and the subsequent sinking and remineralization of organic matter (Ning et al. 2011). Estimated summer bulk oxygen depletion in the hypoxic bottom water (based on absolute apparent oxygen utilization, AOU, relative to the fully saturated state) was 4.7×10^6 tons DO in 1999, 7.2×10^6 tons in 2006, and 5.1×10^6 tons in 2013 (Zhu et al. 2017). On the outer shelf, estimated rates of DO change in Kuroshio Intermediate Water (1982–2010) ranged from -0.11 ± 0.07 to -0.19 ± 0.02 μmol kg^{-1} $year^{-1}$ (based on data from line PN: 126°E, 29°N to 128.3°E, 27.5°N). This decline was caused by reduced ventilation of North Pacific Intermediate Water (Lui et al. 2014), where DO had a maximum rate of decline (1985–2010) of -0.36 ± 0.08 μmol kg^{-1} $year^{-1}$ on the potential density surface of $\sigma = 27.3$ (Takatani et al. 2012). The DO of Kuroshio Tropical Water has, despite the effects of warming and freshening, increased due to enhanced productivity (Lui et al. 2014).

10.4.2 Seasonal Hypoxia

Bottom hypoxia occurs frequently in estuaries and coastal waters where high rates of photosynthetic production contribute massive amounts of organic matter to bottom waters. This input of organic carbon results in high rates of oxygen consumption in the subsurface waters and sediments. Such hypoxia can be exacerbated by global

warming (Keeling et al. 2010), decreasing ocean ventilation, and, mostly importantly, the eutrophication of coastal waters (Liu et al. 2015a, b), which is caused by increasing nitrogen fertilizer usage and sewage inputs (Breitburg et al. 2018; Diaz and Rosenberg 2008; Zhang et al. 2010).

Hypoxia in the Changjiang Estuary occurs below the pycnocline and is seasonal in character. Low-oxygen conditions develop in late spring and early summer, reaching maximum spatial extent during mid-summer or sometimes early autumn, and then disappearing in late autumn (Li et al. 2011; Wang et al. 2012). Usually, there are two zones of hypoxia: one off the Changjiang Estuary and inner Subei Shoal and one near the Minzhe coastal area (Fig. 10.9). The northern zone is likely associated with low-salinity water detached from the Changjiang Diluted Water (Xuan et al. 2012). The southern zone is in an area influenced by the upwelling of Kuroshio Subsurface Water. Oxygen depletion in the northern zone is severe but short-lived, whereas depletion in the southern zone is milder but longer in duration (Zhu et al. 2011). At Subei Shoal, hypoxic waters are found at depths shallower than 20 m and are usually well mixed vertically (Luo et al. 2018; Zhou et al. 2017). Outside the shoal area, the northern hypoxia occurs in waters deeper than 30 m (depth of ~45 m).

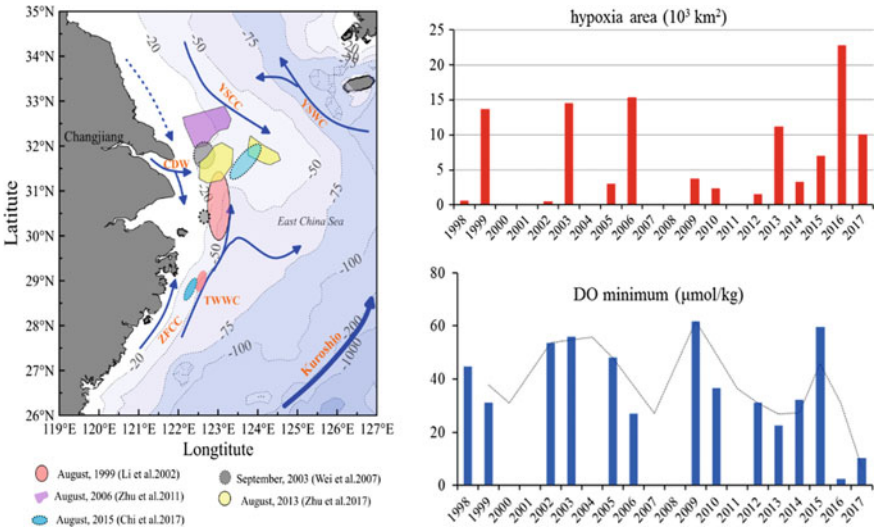

Fig. 10.9 Hypoxia in the East China Sea. **a** Map of East China Sea bathymetry and observed large (>5000 km^2) areas of hypoxia, 1999–2013. The blue arrows show major currents in the East China Sea: CDW = Changjiang Diluted Water, YSCC = Yellow Sea Coastal Current, YSWC Yellow Sea Warm Current, ZFCC = Zhejiang-Fujian Coastal Current, and TWWC = Taiwan Warm Current, and Kuroshio. **b** Time series of hypoxia areal extent, 1998–2017. **c** Time series of DO minima, 1998–2017. The dotted gray line shoes moving average result of the data. For events before 2013, data were obtained from Zhu et al. (2011) and Luo et al. (2018) and references therein. For years 2014, 2016, and 2017, data were obtained on recent field cruises (unpublished data, Jianfang Chen, principal investigator). For 2015, data were obtained from Chi et al. (2017)

Summer hypoxia in the vicinity of the estuary (in areas centered at 31.5°N, 123°E) was first reported in the late 1950s and 1960s, with an average coverage of 3,000–4,000 km^2 (Wang et al. 1991). In the summer of 1999, Li et al. (2002) found a much larger hypoxic area of 13,700 km^2 (Fig. 10.9a). Since the 1990s, many researchers have reported an increasing incidence of hypoxia and adverse effects (Zhu et al. 2011 and references therein).

Large areas of hypoxia (>5,000 km^2) occurred in years 1999, 2003, and 2006, with smaller events every 3–4 years (Fig. 10.9b). Between 2009 and 2012, while nutrient inputs continued to increase, three more events of smaller extent were observed. In August 2013, a hypoxic area of 11,500 km^2 was documented (Zhu et al.2017). In 2016, the largest hypoxic area ever recorded, >22,808 km^2, was discovered during a late August research cruise. The following year, in August 2017, the hypoxic area was observed to be 10,071 km^2. These two recent years were also a time of dramatically lower DO minimum values within the hypoxic areas (Fig. 10.9c). The DO minima approximately 10 years earlier were 27.0 $\mu mol\ kg^{-1}$ (2006) and 61.7 $\mu mol\ kg^{-1}$ (2009). The 2016 and 2017 minimum values were 2.5 $\mu mol\ kg^{-1}$ and 10.2 $\mu mol\ kg^{-1}$, respectively.

Recent studies have linked this seasonal hypoxia to water-column stratification (Zhou et al. 2009; Zhu et al. 2016), bottom bathymetry (Wang et al. 2012), water residence time (Rabouille et al. 2008), upwelling of subsurface water (Chen et al. 2007), lateral advection (Wei et al. 2007), decomposition of marine-origin particulate organic matter (Chen et al. 2007; Wang et al. 2017a), and sedimentary oxygen comsumption (Song et al. 2016; Zhang et al. 2017). Bottom hypoxia has usually been coupled with the presence of Changjiang plume water and surface phytoplankton blooms (Chen et al. 2017), specifically diatom blooms (Wang et al. 2017a). As shown in the conceptual model of Fig. 10.10, waters in the outer region (seaward of the turbidity maximum zone) are clear; thus, light limitation of phytoplankton growth is alleviated. When nutrients and light are both suitable for algal growth (Ning et al. 2004), phytoplankton blooms, especially diatom blooms, consume dissolved nutrients and carbon dioxide (CO_2) in surface waters through photosynthesis. The result is deficits of nutrients and dissolved inorganic carbon and oversaturation with respect to oxygen. With strong summer stratification, organic matters (mostly contributed by diatom blooms in the East China Sea) sink quickly to the sea bottom, where they decompose and deplete oxygen from the bottom water. If oxygen consumption exceeds supply, the bottom waters will become hypoxic. In this way, surface blooms and bottom hypoxia are strongly coupled (Wang et al. 2017a). The occurrence of diatom blooms could thereby be a determining factor for the development of summer hypoxia in the East China Sea.

The full story is complex, though, with hypoxia in this marginal sea being highly dynamic and episodic. Disturbance by one of the frequent episodic events of summer (e.g., strong northeast winds, typhoons, tides, or eddies) may destroy one episode of hypoxia (Ni et al. 2016) while also triggering the onset of a subsequent one by mixing bloom-fueling nutrients upward from bottom waters into well-lit surface waters. Thus, hypoxia in the East China Sea, while seasonal in character, also displays highly dynamic spatial and temporal variations within the summer season.

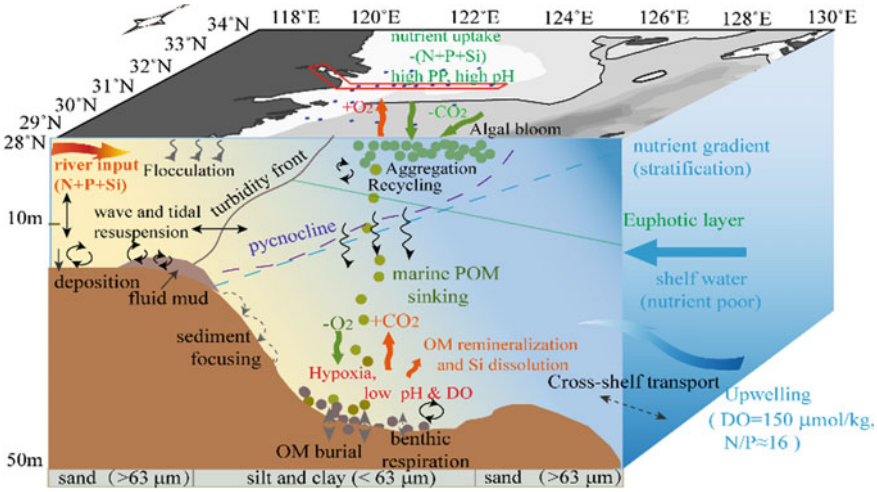

Fig. 10.10 Conceptual model for the formation of summer hypoxia in bottom waters due to surface diatom blooms off the Changjiang Estuary. Under optimal conditions of light and nutrients, diatom blooms may form, with high primary production in surface waters and large fluxes of rapidly sinking biogenic silica and labile organic carbon. Other potentially significant physical and biogeochemical processes include riverine input, aggregation, flocculation, desorption, resuspension, respiration, and intrusion (upwelling) of Kuroshio Subsurface Water. OM = organic matter Figure reproduced from Wang et al. (2017a)

Predicting future hypoxia remains difficult. Integrated multidisciplinary approaches are required to advance the current understanding of oxygen dynamics in the East China Sea.

10.5 Conclusions

Decadal average concentrations of DIN and DIP have significantly increased in the East China Sea and Hangzhou Bay since 1980s, especially in waters of salinity <31. At the outer edge of the Changjiang plume water (defined by salinity = 31), the maximum DIN concentration was ~16 μmol L^{-1} in the 1980s and ~25 μmol L^{-1} in the 2000s. DIN concentrations in waters of salinity >33 did not exhibit notable decadal change. DIP concentrations (for a given salinity) in the East China Sea were higher in the 2000s than the 1980s. Silicate concentrations did not exhibit notable decadal change. Some nutrient ratios changed. The DIN/silicate ratio doubled, from ~0.5 in the 1980s to ~1 in the 2000s. The dramatic decadal changes of nutrient concentrations and ratios were caused mostly by increasing DIN and DIP concentrations in the Changjiang River.

Phytoplankton communities in the Changjiang Estuary and East China Sea have experienced remarkable changes. The overall phytoplankton abundance increased

over the past 50 years. In the 1950s and the 1980s, chain-forming diatoms were the dominant species. In recent years, large-cell dinoflagellates and filamentous cyanobacteria have been growing, although their percentages are still small. All of these changes are strongly associated with eutrophication and warming, but quantitatively defining those linkages is difficult because of the limited availability of time-series data. These changes in phytoplankton community structure may profoundly influence local food-web dynamics and biogeochemical processes, thus exacerbating the occurrence of harmful algal blooms and hypoxia in the Changjiang Estuary and East China Sea.

DO concentrations in the East China Sea have been generally declining due to global warming and eutrophication. Reduced regional ventilation and the remineralization of the products of locally boosted productivity have together tended to promote oxygen depletion. Before 2013, summer hypoxia in the East China Sea was relatively limited in terms of spatial coverage and severity. In 2016, hypoxia occurred over an expanded area of the sea (>22808 km^2), with dramatically lower values of minimum DO (~2.5 $\mu mol\ L^{-1}$). Occurrences of hypoxia are highly dynamic and are tied to a variety of events over a wide range of scales. Therefore, multidisciplinary approaches are required to evaluate present conditions and predict future changes. Summer hypoxia is affected by both climate change and anthropogenic activity.

Acknowledgments This work was jointly funded by the National Key Research and Development Program of China (2018YFD0900901), Natural Science Foundation of China (No. U1709201, 41706183, 41706120, 41806095, 41876198), and Long Term Observation and Research Plan in the Changjiang Estuary and the Adjacent East China Sea Project (LORCE) established by the Second Institute of Oceanography, MNR. Two anonymous reviewers provided very comprehensive and constructive comments which helped strengthening the manuscript.

References

Anderson LA, Sarmiento JL (1994) Redfield ratios of remineralization determined by nutrient data analysis. Global Biogeochem Cy 8:65–80

Belkin IM (2009) Rapid warming of large marine ecosystems. Prog Oceanogr 81(1–4):207–213

Breitburg D, Levin LA, Oschlies A et al (2018) Declining oxygen in the global ocean and coastal waters. Science 359:7240. https://doi.org/10.1126/science.aam7240

Chai C, Yu ZM, Shen ZL et al (2009) Nutrient characteristics in the Yangtze River Estuary and the adjacent East China Sea before and after impoundment of the Three Gorges Dam. Sci Total Environ 407(16):687–695

Chai C, Yu ZM, Song XX et al (2006) The status and characteristics of eutrophication in the Yangtze River (Changjiang) Estuary and the adjacent East China Sea, China. Hydrobiologia 563:313–328

Chang KI, Zhang C-I, Park C et al (2015) Oceanography of the East Sea (Japan Sea). Springer International Publishing, Switzerland

Chen C-TA (1996) The Kuroshio intermediate water is the major source of nutrients on the East China Sea continental shelf. Oceanolo Acta 19:523–527

Chen C-TA (2009) Chemical and physical fronts in the Bohai, Yellow and East China seas. J Mar Syst 78:394–410

Chen C-TA, Wang SL (1999) Carbon, alkalinity and nutrient budgets on the East China Sea continental shelf. J Geophys Res 104(C9):20675–20686. https://doi.org/10.1029/1999JC900055
Chen C-C, Gong G-C, Shiah F-K (2007) Hypoxia in the East China Sea: one of the largest coastal low-oxygen areas in the world. Mar Environ Res 64:399–408. https://doi.org/10.1016/j.marenvres.2007.01.007
Chen JY, Pan DL, Liu ML et al (2017) Relationships between long-term trend of satellite-derived chlorophyll-*a* and hypoxia off the Changjiang Estuary. Estuar Coast 40:1055–1065. https://doi.org/10.1007/s12237-016-0203-0
Chi LB, Song XX, Yuan YQ et al (2017) Distribution and key influential factors of dissolved oxygen off the Changjiang River Estuary (CRE) and its adjacent waters in China. Mar Pollut Bull 125(1–2):440–450
Chou W-C, Gong G-C, Cai W-J et al (2013) Seasonality of CO_2 in coastal oceans altered by increasing anthropogenic nutrient delivery from large rivers: evidence from the Changjiang-East China Sea system. Biogeosciences 10:3889–3899
Dai ZJ, Du JZ, Zhang XL et al (2010) Variation of riverine material loads and environmental consequences on the Changjiang (Yangtze) Estuary in recent decades (1955–2008). Environ Sci Technol 45:223–227
Dai ZJ, Liu JT, Xie HL et al (2014) Sedimentation in the outer Hangzhou Bay, China: the influence of Changjiang sediment load. J Coastal Res 298:1218–1225
Deutsch C, Weber T (2012) Nutrient ratios as a tracer and driver of ocean biogeochemistry. Annu Rev Mar Sci 4:113–141
Diaz RJ, Rosenberg R (2008) Spreading dead zones and consequences for marine ecosystems. Science 321:926–929. https://doi.org/10.1126/science.1156401
Ducklow HW, Doney SC, Steinberg DK (2009) Contributions of long-term research and time-series observations to marine ecology and biogeochemistry. Annu Rev Mar Sci 1:279–302
Edmond J, Spivack A, Grant B et al (1985) Chemical dynamics of the Changjiang estuary. Cont Shelf Res 4:17–36
Fennel K, Testa JM (2018) Biogeochemical controls on coastal hypoxia. Annu Rev Mar Sci 11(1):1–26
Gao SQ, Yu GH, Wang YH (1993) Distributional features and fluxes of dissolved nitrogen, phosphorus and silicon in the Hangzhou Bay. Mar Chem 43:65–81
Gilbert D, Rabalais NN, Díaz RJ et al (2010) Evidence for greater oxygen decline rates in the coastal ocean than in the open ocean. Biogeosciences 7:2283–2296. https://doi.org/10.5194/bg-7-2283-2010
Gong G-C, Lee Chen Y-L, Li K-K (1996) Chemical hydrography and chlorophyll a distribution in the East China Sea in summer: implications in nutrient dynamics. Cont Shelf Res 16:1561–1590
Gong G-C, Chang J, Chiang K-P et al (2006) Reduction of primary production and changing of nutrient ratio in the East China Sea: effect of the three gorges dam? Geophys Res Lett 33:L07610
Gong G-C, Liu K-K, Chiang K-P et al (2011) Yangtze River floods enhance coastal ocean phytoplankton biomass and potential fish production. Geophys Res Lett 38:L13603. https://doi.org/10.1029/2011GL047519
Guo YJ, Yang ZY (1992) Quantitative variation and ecological analysis of phytoplankton in the estuarine area of the Changjiang River (in Chinese). Studia Marina Sin 33:167–189
Harrison P, Hu MH, Yang YP et al (1990) Phosphate limitation in estuarine and coastal waters of China. J Exp Mar Biol Ecol 140:79–87
He XQ, Bai Y, Pan DL et al (2013) Satellite views of the seasonal and interannual variability of phytoplankton blooms in the eastern China seas over the past 14 years (1998–2011). Biogeosciences 10:4721–4739
Hsin Y-C, Qu TD, Wu C-R (2010) Intra-seasonal Variation of the Kuroshio southeast of Taiwan and its possible forcing mechanism. Ocean Dynam 60:1293–1306
Hsueh Y, Wang J, Chern CS (1992) The intrusion of the Kuroshio across the continental shelf northeast of Taiwan. J Geophys Res 97:14323–14330

Huang HY, Wang QL, Yan X et al (2018) Distribution of summer community of net-collected phytoplankton from 2004 to 2016 and the factors in the Changjiang river estuary. Oceanol Et Limnol Sin 49:319–330

Huang T-H, Chen C-TA, Lee J et al (2019) East China Sea increasingly gains limiting nutrient P from South China Sea. Sci Rep 9:5648

Hung C-C, Tseng C-W, Gong G-C et al (2013) Fluxes of particulate organic carbon in the East China Sea in summer. Biogeosciences 10(10):6469–6484

Isobe A, Matsuno T (2008) Long–distance nutrient–transport process in the Changjiang River plume on the East China Sea shelf in summer. J Geophys Res 113:C04006

Ito T, Minobe S, Long MC et al (2017) Upper ocean O_2 trends: 1958–2015. Geophys Res Lett 44:4214–4223

James C, Wimbush M, Ichikawa H (1999) Kuroshio meanders in the east China Sea. J Phys Oceanogr 29:259–272

Jiang T, Yu ZM, Song XX et al (2010) Long-term ecological interactions between nutrient and phytoplankton community in the Changjiang estuary. Chinese J Oceanol Limnol 28(4):887–898

Jiang ZB, Liu JJ, Chen JF et al (2014) Responses of summer phytoplankton community to drastic environmental changes in the Changjiang (Yangtze River) estuary during the past 50 years. Water Res 54:1–11

Jiang ZB, Chen JF, Zhou F et al (2017) Summer distribution patterns of *Trichodesmium* spp. in the Changjiang (Yangtze River) Estuary and adjacent East China Sea shelf. Oceanologia 59:248–261

Jiang ZB, Li HL, Zhai HC (2018) Seasonal and spatial changes in *Trichodesmium* associated with physicochemical properties in East China Sea and southern Yellow Sea. J Geophys Res-Biogeo 123:509–530

Keeling RF, Körtzinger A, Gruber N (2010) Ocean Deoxygenation in a Warming World. Annu Rev Mar Sci 2:199–229

Kim SK, Chang KI, Kim B et al (2013) Contribution of ocean current to the increase in N abundance in the Northwestern Pacific marginal seas. Geophys Res Lett 40:143–148

Li DJ, Zhang J, Huang DJ et al (2002) Oxygen depleted off the Changjiang (Yangtze River) Estuary. Sci China Ser D-Earth Sci 45(12):1137–1146

Li DW, Chen JF, Ni XB et al (2018) Effects of biological production and vertical mixing on sea surface pCO_2 variations in the Changjiang River plume during early autumn: a buoy-based time series study. J Geophys Res-Oceans 123:6156–6173. https://doi.org/10.1029/2017JC013740

Li DW, Chen JF, Wang K et al (2016) Contribution of outer-shelf deep water to the nutrient inventories in the euphotic zone of the Changjiang River plume during Summer. J Coast Res 32:1081–1091

Li MT, Xu KQ, Watanabe M et al (2007) Long-term variations in dissolved silicate, nitrogen, and phosphorus flux from the Yangtze River into the East China Sea and impacts on estuarine ecosystem. Estuar Coast Shelf Sci 71:3–12

Li XA, Yu ZM, Song XX et al (2011) The seasonal characteristics of dissolved oxygen distribution and hypoxia in the Changjiang Estuary. J Coast Res 27(6A):52–62

Li Y, Li D, Tang JL et al (2010) Long-term changes in the Changjiang Estuary plankton community related to anthropogenic eutrophication. Aquat Ecosyst Health 13(1):66–72

Liu HJ, Fu WC, Sun J (2015a) Seasonal variations of netz-phytoplankton community in East China Sea continental shelf from 2009–2011. Acta Oceanol Sin 37:106–122

Liu K-K, Tang TY, Gong G-C et al (2000) Cross-shelf and along-shelf nutrient fluxes derived from flow fields and chemical hydrography observed in the southern East China Sea off northern Taiwan. Cont Shelf Res 20(4–5):493–523

Liu K-K, Yan WJ, Lee H-J et al (2015b) Impacts of increasing dissolved inorganic nitrogen discharged from Changjiang on primary production and seafloor oxygen demand in the East China Sea from 1970 to 2002. J Mar Syst 141:200–217

Liu SM, Qi XH, Li XA et al (2016) Nutrient dynamics from the Changjiang (Yangtze River) estuary to the East China Sea. J Mar Syst 154:15–27

Liu SM, Zhang J, Chen HT et al (2003) Nutrients in the Changjiang and its tributaries. Biogeochemistry 62(1):1–18

Liu XJ, Zhang Y, Han WX et al (2013) Enhanced nitrogen deposition over China. Nature 494:459–462

Laurent A, Fennel K, Ko DS et al (2018) Climate change projected to exacerbate impacts of coastal eutrophication in the northern Gulf of Mexico. J Geophys Res-Oceans 123:3408–3426

Lui H-K, Chen C-TA, Lee J et al (2014) Looming hypoxia on outer shelves caused by reduced ventilation in the open oceans: case study of the East China Sea. Estuar Coast Shelf Sci 151:355–360

Lui H-K, Chen C-TA, Lee J et al (2015) Acidifying intermediate water accelerates the acidification of seawater on shelves: an example of the East China Sea. Cont Shelf Res 111(Part B):223–233

Luo XF, Wei H, Fan RF et al (2018) On influencing factors of hypoxia in waters adjacent to the Changjiang estuary. Cont Shelf Res 152:1–13. https://doi.org/10.1016/j.csr.2017.10.004

Meier H, Andersson H, Eilola K et al (2011) Hypoxia in future climates: a model ensemble study for the Baltic Sea. Geophys Res Lett 38(24). https://doi.org/10.1029/2011gl049929

Ni XB, Huang DJ, Zeng DY et al (2016) The impact of wind mixing on the variation of bottom dissolved oxygen off the Changjiang Estuary during summer. J Mar Syst 154:122–130. https://doi.org/10.1016/j.jmarsys.2014.11.010

Ning XR, Lin C, Su J et al (2011) Long-term changes of dissolved oxygen, hypoxia, and the responses of the ecosystems in the East China Sea from 1975 to 1995. J Oceanogr 67:59–75. https://doi.org/10.1007/s10872-011-0006-7

Ning XR, Shi JX, Cai YM et al (2004) Biological productivity front in the Changjiang Estuary and the Biological productivity front in the Changjiang and Hangzhou Bay and its ecological effects (in Chinese with English abstracts). Acta Oceanol Sin 26:96–106

Office of Integrated Oceanographic Survey of China (OIOSC) (1964a) Dataset of the national integrated oceanographyic survey (in Chinese). Vol 6. Distribution of dissoloved oxygen, phosphate, silicate and alkalinity in Chinese coastal seas. Beijing

Office of Integrated Oceanographic Survey of China (OIOSC) (1964b) Dataset of the national integrated oceanographyic survey (in Chinese), vol 8. Survey report of Chinese coastal plankton, Beijing

Redfield AC (1958) The biological control of chemical factors in the environment. Am Sci 46:205–221

Rabouille C, Conley DJ, Dai MH et al (2008) Comparison of hypoxia among four river-dominated ocean margins: The Changjiang (Yangtze), Mississippi, Pearl, and Rhône rivers. Cont Shelf Res 28:1527–1537. https://doi.org/10.1016/j.csr.2008.01.020

Sellner KG, Sellner SG, Lacouture RV et al (2001) Excessive nutrients select for dinoflagellates in the stratified Patapsco River estuary: Margalef reigns. Mar Ecolo Prog Ser 220:93–102

Song GD, Liu SM, Zhu ZY et al (2016) Sediment oxygen consumption and benthic organic carbon mineralization on the continental shelves of the East China Sea and the Yellow Sea. Deep-Sea Res Pt II 124:53–63

Su JL, Wang KS (1989) Changjiang river plume and suspended sediment transport in Hangzhou Bay. Cont Shelf Res 9:93–111

Takatani Y, Sasano D, Nakano T et al (2012) Decrease of dissolved oxygen after the mid-1980s in the western North Pacific subtropical gyre along the 137°E repeat section. Global Biogeochem Cy 26(2). https://doi.org/10.1029/2011gb004227

Tseng CM, Shen PY, Liu KK (2014) Synthesis of observed air-sea CO_2 exchange fluxes in the river-dominated East China Sea and improved estimates of annual and seasonal net mean fluxes. Biogeosciences 11:3855–3870. https://doi.org/10.5194/bg-11-3855-2014

Tseng Y-F, Lin J, Dai MH et al (2013) Joint effect of freshwater plume and coastal upwelling on phytoplankton growth off the Changjiang River. Biogeosciences 10:10363–10397

Wang B, Chen JF, Jin HY et al (2017a) Diatom bloom-derived bottom water hypoxia off the Changjiang estuary, with and without typhoon influence. Limnol Oceanogr 62:1552–1569. https://doi.org/10.1002/lno.10517

Wang B-D, Wang X-L, Zhan R (2003) Nutrient conditions in the Yellow Sea and the East China Sea. Estuar Coast Shelf Sci 58:127–136
Wang B-D, Wei QS, Chen JF et al (2012) Annual cycle of hypoxia off the Changjiang (Yangtze River) Estuary. Mar Environ Res 77:1–5. https://doi.org/10.1016/j.marenvres.2011.12.007
Wang B-D, Xin M, Wei QS et al (2018) A historical overview of coastal eutrophication in the China Seas. Mar Pollut Bull 136:394–400
Wang, YL, Yuan Q, Shen XQ (2008) Distribution status and change tendency of phytoplankton during summer in Changjiang Estuary and adjacent waters (in Chinese). Mar Environ Sci 27:169–172
Wang F, Meng QJ, Tang XH et al (2013a) The long-term variability of sea surface temperature in the seas east of China in the past 40 a. Acta Oceanol Sin 32(3):48–53
Wang JH, Wu JY (2009) Occurrence and potential risks of harmful algal blooms in the East China Sea. Sci Total Environ 407(13):4012–4021
Wang K, Chen JF, Jin HY et al (2011) The four seasons nutrients distribution in Changjiang River Estuary and its adjacent East China Sea (in Chinese with English abstract). J Mar Sci 29:18–35
Wang K, Chen JF, Jin HY et al (2013b) Nutrient structure and relative limitation in Changjiang River Estuary and adjacent East China Sea (in Chinese with English abstract). Acta Oceanol Sin 35:128–136
Wang K, Chen JF, Ni XB et al (2017b) Real-time monitoring of nutrients in the Changjiang Estuary reveals short-term nutrient-algal bloom dynamics. J Geophys Res-Oceans 122:5390–5403. https://doi.org/10.1002/2016JC012450
Wang WL, Chen JF, Jin HY et al (2009) The distribution characteristics and influence factors of some species phosphorus in waters of the Changjiang River Estuary in summer (in Chinese with English abstract). J Mar Sci 27:32–41
Wang YH, Lu SY, Huang SG et al (1991) Marine atlas of Bohai Sea, Yellow Sea, East China Sea: Chemistry, Beijing
Wei H, He YC, Li QJ et al (2007) Summer hypoxia adjacent to the Changjiang Estuary. J Mar Syst 67:292–303. https://doi.org/10.1016/j.jmarsys.2006.04.014
Wu B, Jin HY, Gao SQ et al (2019) Nutrient Budgets and Recent Decadal Variations in a Highly Eutrophic Estuary: Hangzhou Bay. J Coastal Res, China. https://doi.org/10.2112/JCOASTRES-D-18-00071.1
Xuan J-L, Huang DJ, Zhou F et al (2012) The role of wind on the detachment of low salinity water in the Changjiang Estuary in summer. J Geophys Res-Oceans 117:C10004
Zhang HY, Zhao L, Sun Y et al (2017) Contribution of sediment oxygen demand to hypoxia development off the Changjiang Estuary. Estuar Coast Shelf Sci 192:149–157
Zhang J (1996) Nutrient elements in large Chinese estuaries. Cont Shelf Res 16(8):1023–1045
Zhang J, Gilbert D, Gooday AJ et al (2010) Natural and human-induced hypoxia and consequences for coastal areas: synthesis and future development. Biogeosciences 7(5):1443–1467
Zhang J, Liu SM, Ren JL et al (2007) Nutrient gradients from the eutrophic Changjiang (Yangtze River) Estuary to the oligotrophic Kuroshio waters and re-evaluation of budgets for the East China Sea Shelf. Prog Oceanogr 74:449–478
Zheng YJ, Chen XZ, Cheng JH et al (2003) Biological resource and environment in the East China Sea continental shelf. Shanghai Science and Technology Press, Shanghai, pp 472–488
Zhou F, Chai F, Huang DJ et al (2017) Investigation of hypoxia off the Changjiang Estuary using a coupled model of ROMS-CoSiNE. Prog Oceanogr 159:237–254. https://doi.org/10.1016/j.pocean.2017.10.008
Zhou F, Xue HJ, Huang DJ et al (2015) Cross-shelf exchange in the shelf of the East China Sea. J Geophys Res-Oceans 120:1545–1572
Zhou F, Xuan JL, Ni XB et al (2009) A preliminary study of variations of the Changjiang Diluted Water between August of 1999 and 2006. Acta Oceanol Sin 28:1–11
Zhu JR, Zhu ZY, Lin J et al (2016) Distribution of hypoxia and pycnocline off the Changjiang Estuary, China. J Mar Syst 154:8–40. https://doi.org/10.1016/j.jmarsys.2015.05.002

Zhou M-J, Shen Z-L, Yu R-C (2008) Responses of a coastal phytoplankton community to increased nutrient input from the Changjiang (Yangtze) River. Cont Shelf Res 28:1483–1489
Zhu Z-Y, Zhang J, Wu Y et al (2011) Hypoxia off the Changjiang (Yangtze River) Estuary: oxygen depletion and organic matter decomposition. Mar Chem 125:108–116
Zhu Z-Y, Wu H, Liu S-M et al (2017) Hypoxia off the Changjiang (Yangtze River) estuary and in the adjacent East China Sea: quantitative approaches to estimating the tidal impact and nutrient regeneration. Mar Pollut Bull 125:103–114

Chapter 11
The Changing Circulation of Asia-Pacific Marginal Seas in the South China Sea: A Physical View

Jianping Gan, Zhiqiang Liu, Chiwing Rex Hui, Yao Tang, Zhongya Cai, and Junlu Li

Abstract The South China Sea (SCS) is the largest marginal sea in the western Pacific Ocean. The overall change of marine environment in the SCS is mainly regulated by the variation of ocean circulation, which is, in turn, governed by the geophysical fluid dynamics in the circulation. This chapter provides an overview and analysis on the predominant cyclonic-anticyclonic-cyclonic (CAC) circulation, and the associated processes and responses of the hydrography and pathway of the water masses in the SCS. We present the changing CAC circulation and transport in the SCS during the last 20-year, and reason the changes by investigating the underlying mechanism of external forcing associated with the water exchange with adjacent ocean, and internal dynamic response to the external forcing in the SCS. This study links the changing ocean with fundamental circulation physics, which validate scientifically the changing evidences and provide a solid theoretical foundation to foresee the future changing trend.

Keywords South China Sea circulation · Circulation physics · Changing circulation · Changing forcing

J. Gan (✉) · C. R. Hui · Y. Tang · Z. Cai · J. Li
Department of Ocean Science and Department of Mathematics, Hong Kong University of Science and Technology, Kowloon, Hong Kong, China
e-mail: magan@ust.hk

C. R. Hui
e-mail: macwhui@ust.hk

Y. Tang
e-mail: ytangba@connect.ust.hk

Z. Cai
e-mail: zcaiaa@connect.ust.hk

J. Li
e-mail: jliaw@connect.ust.hk

Z. Liu
Department of Ocean Science and Engineering, Southern University of Science and Technology, Shenzhen 518055, China
e-mail: liuzq@sustech.edu.cn

C.-T. A. Chen and X. Guo (eds.), *Changing Asia-Pacific Marginal Seas*, Atmosphere, Earth, Ocean & Space, https://doi.org/10.1007/978-981-15-4886-4_11

11.1 Introduction

The South China Sea (SCS) is a semi-enclosed marginal sea in the tropical northwest Pacific Ocean (NPO, Fig. 11.1). Four restricted openings connect the SCS to surrounding seas. The shallow (<100 m) Taiwan and Karimata Straits connect the northern (NSCS, north of 13° N) and southern SCS (SSCS) to the East China Sea (ECS) and Java Sea, respectively. The channels (<200 m) in the Palawan Archipelago join the southeastern SCS to the Sulu Sea with the strongest water exchange in those channels occurring through Mindoro Strait. Because of the strong exchange through Mindoro Strait, this strait aptly represents the flow through the channels of the Palawan Archipelago. Lastly, Luzon Strait (LS), northeast of the SCS, is the deepest passage (~2500 m) connecting the SCS to the NPO.

The maximum water depth of the deep SCS basin is over 4000 m, and below 2500 m, the basin is enclosed. There are broad continental shelves on the western sides of the NSCS and the SSCS, and the central basin is surrounded by a semi-enclosed continental slope between the 200 and 3000 m isobaths. The topography of the slope is highly variable containing valleys, canyons, seamounts, and ridges. The SCS has a deep basin in the northeast and a shallower basin south of 9° N in the

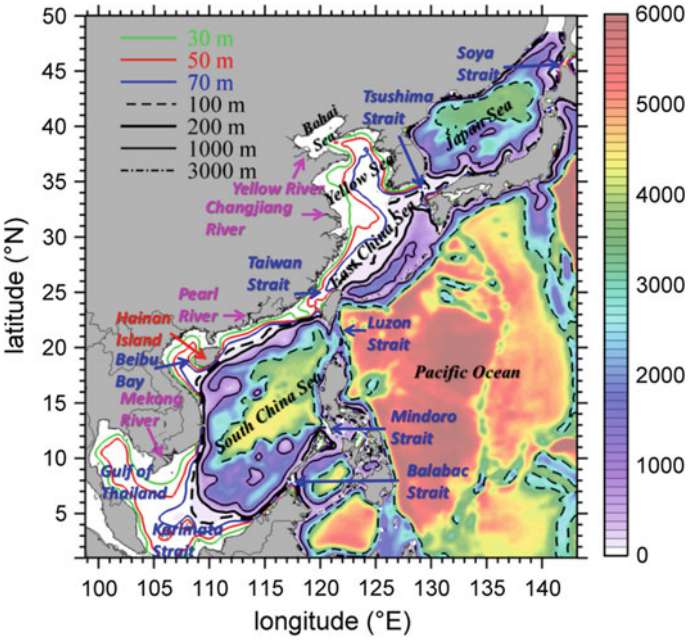

Fig. 11.1 Bathymetry (m) in the Northwest Pacific Ocean and China Seas with the 30, 50, 70, 100, 200, 1000, and 3000 m isobaths contours. The locations of seas, islands, rivers, and straits are marked (adapted from Gan et al. 2016b)

SSCS (Fig. 11.1). The 3000 m isobath enclosing the southern basin is shaped like a rhombus with a moderate slope that is oriented northeastward.

The mean annual SCS circulation flows cyclonically in the upper layer (<~750 m) along the sea's surrounding slope (Gan et al. 2016b). This circulation pattern comes from the intrusion of the Kuroshio Current through LS in the upper layer and from positive vorticity caused by the monsoonal wind stress curl. The circulation weakens along the southwestward mainstream over the slope in the NSCS. The mainstream bifurcates near the Xisha Islands and forms an even weaker southeastward branch that flows towards Mindoro Strait. The main branch flows further southward along the slope and intensifies over the narrow slope east of Vietnam. Part of this relatively weak western boundary current in the SCS basin veers northeastward in the southernmost SSCS, joins the southeastward branch from the Xisha Islands, and exits the SCS through Mindoro Strait (Liu and Gan 2017). The southward transport across the SCS basin is called the SCS Throughflow (SCSTF) (Qu et al. 2006), and it conveys the NPO waters through LS to the Java Sea, ECS, and the Sulu Sea (Qu 2000; Qu et al. 2000). In addition, the circulation in the upper layer of the SCS has strong seasonal variation that is subject to the controlling variability of the Kuroshio intrusion through LS and of the monsoonal wind stress (Gan et al. 2006).

The monsoonal wind and the water intrusions/extrusions through the surrounding straits, especially through the LS, jointly drive the SCSTF (Gan et al. 2006, 2016a). Through LS, there is a three-layered exchange flow that connects with the three-layered circulation in the SCS basin (Gan et al. 2016a, b; Xu and Oey 2014). In the upper layer of LS, the Kuroshio carries the NPO water and branches westward (Wu and Hsin 2012) connecting to the other surrounding seas via the SCSTF (Fang et al. 2009). In the intermediate layer of LS, there is an eastward outflow of SCS water (Gan et al. 2016b; Li and Qu 2006). Finally, in the lower layer of LS (1500–2500 m), the intrusion of denser NPO water regulates the thermal dynamics in the deep basin (Nan et al. 2015). The intrusive denser NPO water sinks in the NSCS and causes an energetic cyclonic circulation in the closed deep basin (Lan et al. 2013). There is extensive upwelling over the slope in the northwestern SCS and east of Vietnam to compensate for these subducted waters (Chao et al. 1996), and the SCSTF is partly maintained by the upwelled denser waters (Qu et al. 2009).

In this chapter, we use recent observations and model results from the China-Seas Multi-scale Ocean Modeling System (CMOMS, https://odmp.ust.hk/cmoms/) (Gan et al. 2016b) to present characteristics of the circulation in the SCS. We describe new knowledge of the mean states, multiscale variabilities, and forcing mechanisms. Section 11.2 introduces the mean state of internal and external forces that drive the SCS circulation. Section 11.3 discusses the general nature of SCS circulation and the hydrographic properties. Section 11.3 also highlights the circulation pathways in the SCS basin indicated by residence time of different water masses. Section 11.4 presents the variability of the forcing and the changing SCS circulation. We discuss the mechanism that governs the SCS circulation and its variability in Sect. 11.5, and, finally, in Sect. 11.6, we summarize the contents of the chapter.

11.2 Characteristics of Internal and External Forces in the SCS

First, we introduce the characteristics of forces that drive the circulation in the SCS. We focus on the major external drivers: wind forcing and volume transport through the straits around the basin.

11.2.1 The Monsoonal Wind

The East Asia Monsoon is the primary influence on the upper layer circulation. In winter, the northeasterly wind prevails over the entire SCS basin with an average wind speed of ~9 m s^{-1} (Hellerman and Rosenstein 1983). In summer, the southwesterly wind has an average speed of ~6 m s^{-1}. The winter monsoon is much stronger than the southwesterly summer wind. The line of zero wind stress curl orients northeast to southwest over the central basin and forms a dipole wind stress curl pattern with negative/positive values in the northern/southern part of basin. In winter, the positive wind stress curl is stronger than in summer; for example, over the slope east of Vietnam. In summer, a dipole wind stress curl also exists, but with positive/negative values in the northern/southern part of basin, opposite to the winter dipole.

11.2.2 External Transport Through Straits

The exchange flows around the periphery of the SCS vary coherently with the current in the NPO. In the tropical NPO, the westward North Equatorial Current (NEC) between 8° N and 18° N bifurcates at ~11° N east of the Philippines in summer and at ~14° N in winter. The bifurcation is shown by the transport stream function in the upper 750 m in Fig. 11.2. The annual mean transport of the NEC is ~59 Sv. The bifurcation of the NEC forms the northward Kuroshio (~23 Sv) and the southward Mindanao Current (~35 Sv) (Fig. 11.2). Because of the weakened NEC transport and the northward displacement of its stream-axis, in winter there is a weaker Kuroshio transport with a stronger westward intrusion into the SCS through LS (Qu 2000; Qu et al. 2000) and across the slope of the ECS (Liu and Gan 2012).

Figure 11.3 illustrates the exchange between the SCS and adjacent seas and the transport coherencies. An ~5.5 Sv (annual and depth-integrated transport) westward transport enters the SCS basin through LS from the NPO. Conveyed by the slope in the SCS, an ~1.2 Sv of this intrusive transport exits the basin through Taiwan Strait in the north, an ~1.16 Sv exits through Karimata Strait, and an ~3.2 Sv exits through the Mindoro Strait in the south. These transports around the periphery of the SCS are closely connected with the transports in neighboring seas because of mass conversation and constraining shelf topography of the East Asia marginal sea. For

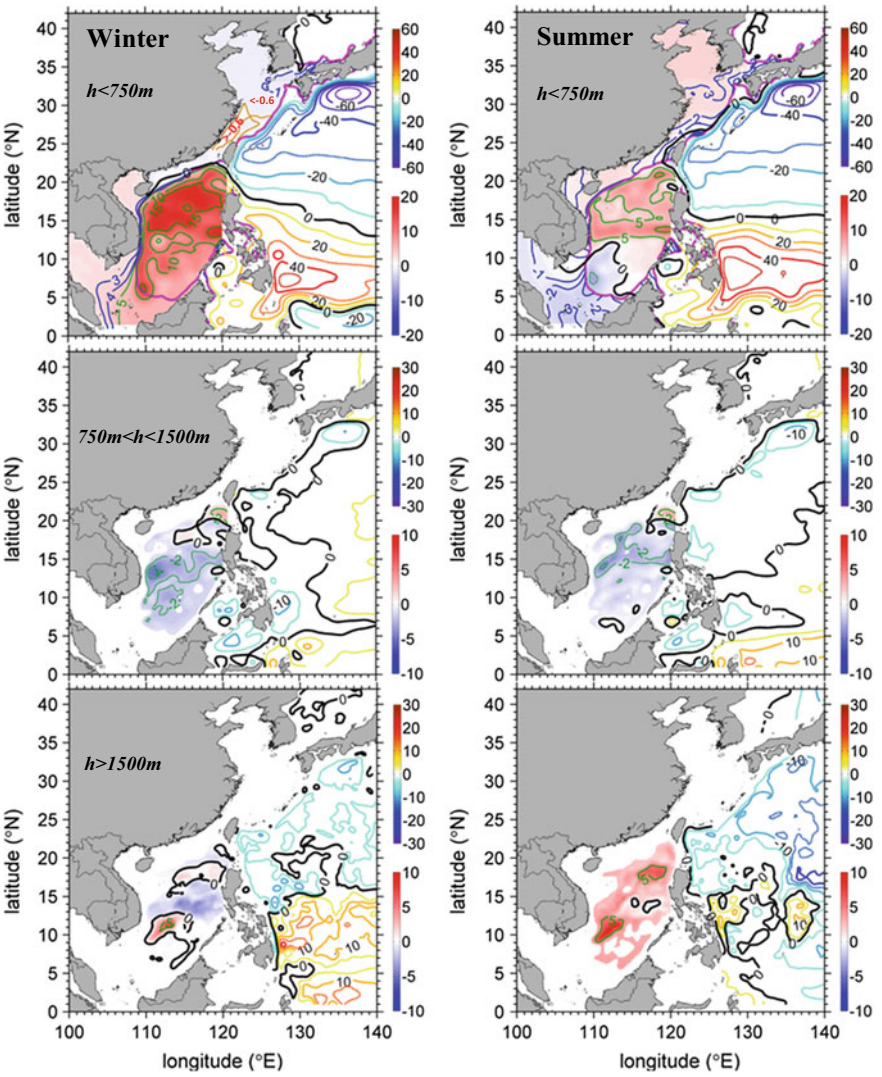

Fig. 11.2 Transport (Sv) stream functions in the upper layer (<750 m), middle layer (750–1500 m), and deep layer (>1500 m) in the winter (left column) and summer (right column), respectively. The upper and lower scales are for the western Pacific (east of the 200 m isobath) and the SCS, respectively (adapted from Gan et al. 2016b)

example, an ~1.2 Sv northward transport in Taiwan Strait is closely linked with the shoreward transport across the slope off the ECS and the northward transport through Tsushima Strait. These linked transports interact with the wind-forced currents and shape the circulation in the SCS (Gan et al. 2016b).

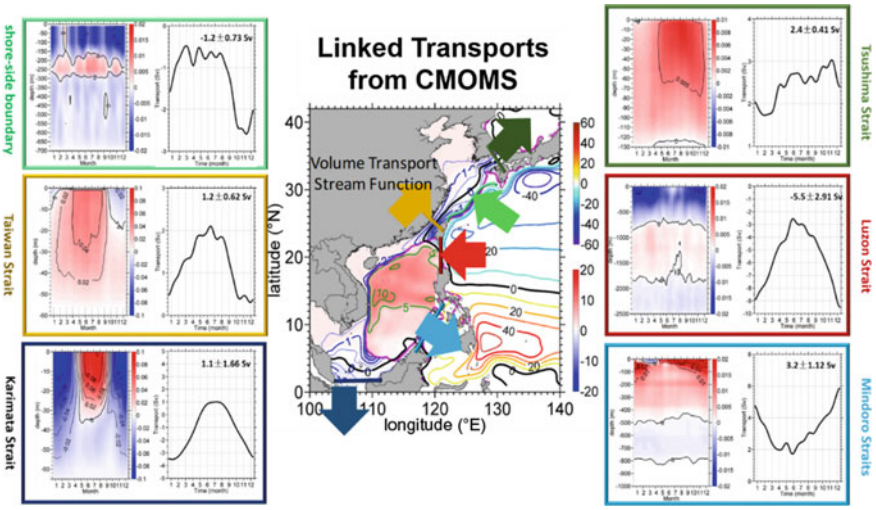

Fig. 11.3 Time series of depth-integrated transport (Sv) and depth-dependent volume flux ($m^2\ s^{-1}$) through the straits around the South China Sea. Each strait and shore-side-boundary of Kuroshio along the ECS slope is represented by a specific color bar and the result for each strait is shown by a corresponding colored box. The background contours in the surrounding China Seas represent the annual mean transport stream function for the upper 750 m. A positive value refers to northward flow in the Taiwan, Karimata, and Tsushima Straits, and out-flows in Luzon and Mindoro Straits. The pink line represents the 200 m isobath (redrawn from Gan et al. 2016b)

The different flow exchanges have strong seasonality around the periphery of the SCS. In addition, the transports in the four straits concurrently exhibit a strong annual *U*-shaped (or inverted *U*-shaped) time variation, with weaker inflows/outflows in summer and stronger ones during the other seasons (Fig. 11.3). We extrinsically link the *U*-shaped variation of the transports with the variable strength of the Kuroshio separation at the entrance of LS (Hsin et al. 2012; Qu et al. 2000; Wu and Hsin 2012) and intrinsically link the same variation with the interaction between the transports and the SCS circulation (Gan et al. 2016a, b).

Not only do the transports that cross through the straits and slope vary geographically and seasonally, but these transports also vary vertically. The transports in the deeper layer are much weaker than the ones in the upper layer. In LS, the inflow-outflow-inflow structure is evident in the upper-middle-deep layers. Although the complete mechanism governing the three-layer structure is still unclear, it is conceivable that this sandwich structure is responsible for the alternating three-layer cyclonically-anticyclonically-cyclonically (CAC) spinning circulation in the SCS (Gan et al. 2016a). We estimate that the transports in the upper, middle, and deep layers of LS are ~−5.9 Sv, 1.4 Sv, and −0.9 Sv, respectively. An ~3.2 Sv outward transport in the Mindoro Strait occurs in the upper 400 m while there is a weak inflow of ~0.1 Sv in the deep channels of the main Mindoro Strait channel. The inflow from LS in the upper layer of the SCS basin balances the outflows through

Taiwan Strait, Karimata Strait, and Mindoro Strait. Liu and Gan (2017) found that a downward momentum flux from the upper layer of LS and an upward momentum flux from the deep layer compensate for the outflow in the middle layer of LS. On the domain-averaged scale, little of the deep intrusive water reaches the upper layer, but a strong upward motion can occur in isolated locations in the SCS because of local topography, eddies, waves, and other local processes. By generating the upward motion in the semi-closed basin, deep transport, such as the one in LS, is important in maintaining the three-dimensional SCS circulation.

11.3 Circulation and Physical Characteristics in the SCS

In this section, we introduce the general oceanic response of the SCS to forcing conditions.

11.3.1 SCS Layered Circulation

The time-dependent, three-dimensional circulation of the China Seas in winter and summer are represented in Fig. 11.2 by the depth-integrated stream function (ψ) for the upper, middle, and deep layers. The time series of depth-dependent horizontally averaged vorticity in the SCS is shown in Fig. 11.4. The circulation in the SCS is characterized by a three-layer alternating spinning CAC circulation in the upper

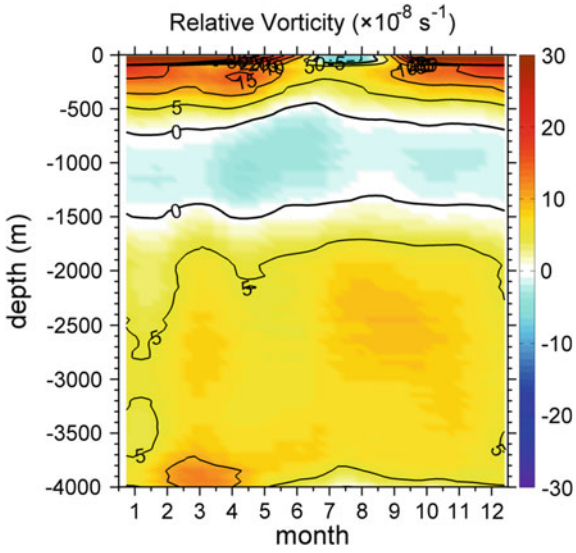

Fig. 11.4 Time series of domain-averaged depth-dependent relative vorticity in the SCS basin (>100 m) (adapted from Gan et al. 2016b)

(<750 m), middle (750–1500 m), and deep layers (>1500 m). The CAC circulation is closely linked with the external transports through the surrounding straits and the monsoonal wind (Gan et al. 2016a). We present an overview of flow in the three layers in the following paragraphs.

Upper layer (0–750 m): In the NPO, the NEC and the Kuroshio are major currents adjacent to the SCS. The two currents exhibit strong seasonality, as indicated by ψ in Fig. 11.2, and the currents strongly influence the upper layer flow in the SCS because of the NEC's bifurcation.

In winter, a weakened NEC bifurcates further north than in summer. This bifurcation, in turn, weakens the Kuroshio and enhances the westward intrusion of the Kuroshio into the SCS through LS (Gan et al. 2006; Qu 2000; Qu et al. 2000). As a result, the SCS winter circulation in the upper layer flows cyclonically and spans the entire basin more strongly in the northern part of the SCS basin than in the south (Fig. 11.2). In addition to the stronger winter Kuroshio intrusion, this upper layer circulation is forced by the northeasterly monsoon and its associated positive wind stress curl (Gan et al. 2006; Qu 2000).

In summer, a southwestward current along the northern slope and an eastward returning current at ~13° N form a cyclonic circulation in the northern part of the basin and a weak anticyclonic circulation in the southern part of the basin. Together, the basin dipole wind stress curl and the recirculation of a coastal jet separation east of Vietnam (Gan and Qu 2008) govern the summer circulation.

The half-basin circulation patterns in both seasons produce a larger outflow through Mindoro Strait than through Karimata Strait and Taiwan Strait. This larger outflow indicates that the LS inflow exits the SCS mainly through Mindoro Strait which is the main pathway of the SCSTF (Qu et al. 2006).

Middle layer (750–1500 m): In the middle layer, the current in the NPO is generally weak in winter and summer. The circulation in the middle layer of the SCS itself flows anticyclonically, though it is not as circular as in the upper layer. The seasonality of the mid-layer circulation is also much weaker than in the upper layer. The main external forcing for the anticyclonic circulation is the outflow in LS, while the internal forcing is complex and involves the interaction among the layers and the effect of slope topography. More details about the forcing mechanism are presented in Sect. 11.5.

Deep layer (>1500 m): In the deep layer, a cyclonic circulation prevails in the basin in winter and summer (Lan et al. 2013). There is cyclonic basin circulation in this layer, despite a weak anticyclonic circulation in the deepest central basin in winter. The cyclonic circulation is stronger in summer than in winter, which is different from the upper layer where the cyclonic circulation is stronger in winter. The seasonality correlated well in time with the deep intrusion through LS.

All three layers have seasonal variability. We examine the seasonal variation of the layered circulation more closely using the time series of domain-averaged vorticity obtained from the numerical solution to Stokes' theorem:

$$C = \oint \vec{V} \cdot dl = \iint \zeta dS, \tag{11.1}$$

where $\vec{V}$ is the horizontal velocity vector and ζ is the vertical relative vorticity normal to S, which is the area of the sea having the layered circulation, C. We exclude the shelf where the depth is less than 100 m in the SCS to rule out the influence of shelf circulation (Gan et al. 2009a, b). The numerical model results for Eq. (11.1) are displayed in Fig. 11.4 showing the vertical circulation patterns of the SCS.

The layered circulation in the SCS is physically valid only under the principles governing Stokes' Theorem (Eq. 11.1) with a geopotential coordinate system. The 'layered circulation' observed in other studies is detected by an overhead view of the circulation pattern over only part of the basin which was never physically sufficient. Meanwhile, the circulation exposed by Eq. (11.1) in an isopycnal coordinate system might not be valid for proving the existence of CAC circulation because the area-integrated vorticity perpendicular to the isopycnal surface cannot adequately represent the layered circulation in the SCS. Details about the physical definition of the layered circulation in a basin are presented in Cai et al. (2020).

As we previously stated, the time series of domain-averaged depth-dependent relative vorticity in Fig. 11.4 presents a three-layer alternating CAC rotating circulation in the SCS. Furthermore, Figs. 11.4 and 11.2 illustrate the seasonality of the circulation. In the upper layer, vorticity input from the wind stress curl and a positive horizontal shear vorticity on the seaward side of the slope current jointly form the cyclonic circulation. In winter, the slope current and the basin circulation is much stronger (Fig. 11.2). The stronger slope current and basin circulation result in a thicker (thinner) upper layer during winter (summer) because of the first order conservation of potential vorticity. However, in the middle layer, the basin circulation is anticyclonic for the entire year, and it is relatively strong in late spring and early summer. In the deep layer, the cyclonic circulation strengthens from July to October, and a relatively strong circulation occurs between 2000 and 3000 m.

11.3.2 Characteristics of Thermohalines

Figure 11.5a displays the horizontal distribution of the density anomaly, $\rho_\theta{}'$, at representative layers of the World Ocean Atlas 2013 (WOA13). We use this horizontal distribution to identify hydrographic properties of SCS water.

At different locations (x, y, z) in the SCS, $\rho_\theta{}'$ is expressed as

$$\rho_\theta{}'(x, y, z) = \rho_\theta(x, y, z) - \overline{\rho_\theta}(z), \tag{11.2}$$

where $\overline{\rho_\theta}(z) = \frac{\iint_{SCS} \rho_\theta(x,y,z)dxdy}{\iint_{SCS} dxdy}$ represents the horizontally averaged $\overline{\rho_\theta}$.

Figure 11.5b illustrates the zonally averaged $\rho_\theta{}'$ in the basin.

In Fig. 11.5a, we see that upwelling of denser intermediate water occurs in the northern and western SCS, immediately beneath the mixed layer (200 and 500 m), where there is positive $\rho_\theta{}'$. It is possible for the lighter water in the upper layer to be subducted into the intermediate layer in the SSCS where $\rho_\theta{}'$ is negative at

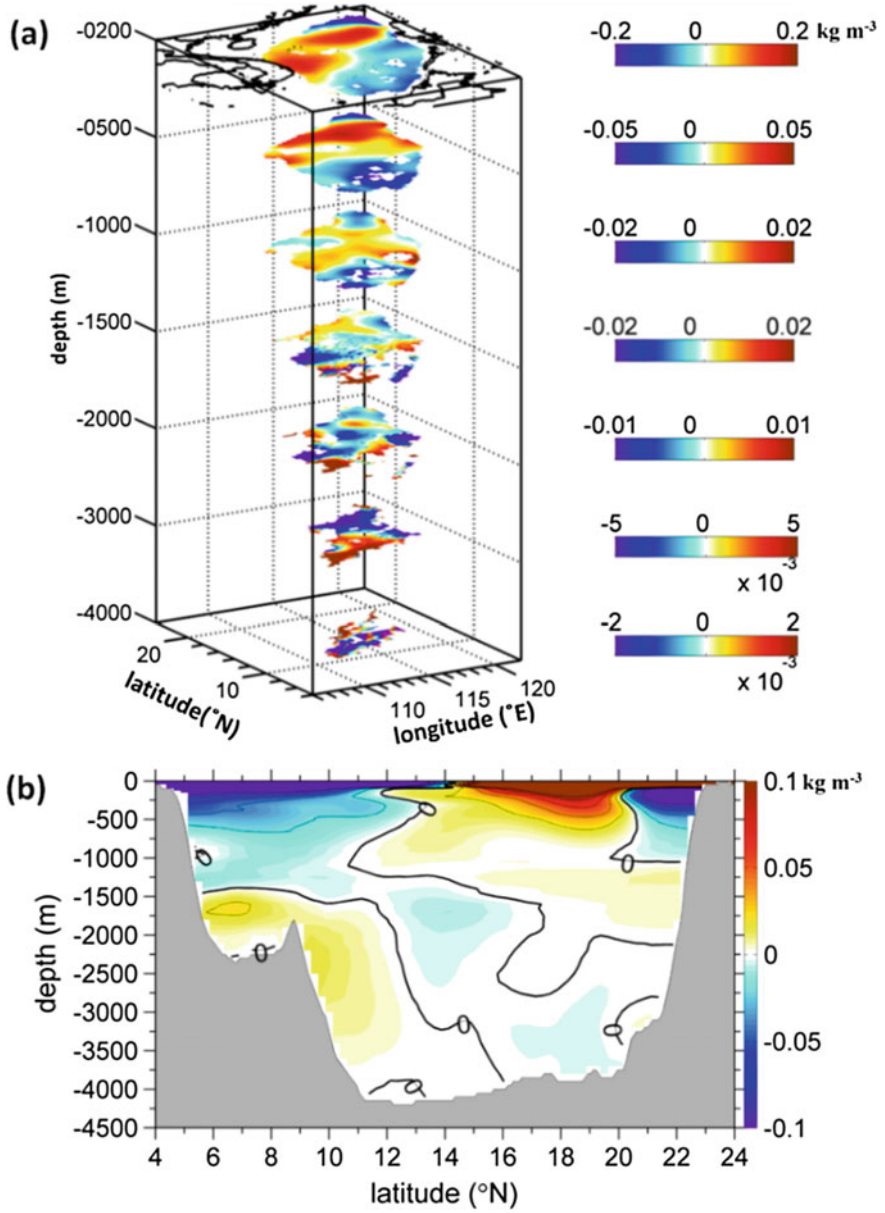

Fig. 11.5 **a** Three-dimensional view of $\rho_\theta{}'$ at selected, but representative, layers of the SCS and **b** zonally averaged $\rho_\theta{}'$ (kg m^{-3}) as a function of depth and latitude in the SCS. $\rho_\theta{}'$ is retrieved from the annual means of the WOA13 dataset (adapted from Liu and Gan 2017)

200 and 500 m. However, the figure shows that there is extensive subduction of the upper layer water into the intermediate layer at 1000 m (negative $\rho_\theta{}'$), and notable upwelling (positive $\rho_\theta{}'$) in the lower layer in the SSCS. More vertical migrations of water masses in the SSCS are indicated by the respective negative and positive $\rho_\theta{}'$ in the intermediate and lower (>1500 m) layers in Fig. 11.5b. Similarly, extensive downwelling of intermediate water towards the lower layer occurs in the NSCS, where $\rho_\theta{}'$ is negative (Fig. 11.5a).

11.3.3 Circulation Pathways and Residence Time

Studying the circulation pathways and knowing the residence time of the different water masses inform us about physical mechanisms driving the circulation in semi-enclosed systems. The residence times (*ReT*) of the different SCS waters have complicated spatial variability because the circulation is driven by internal and external forces and the circulation and thermal dynamics within the basin itself. Liu and Gan (2017) investigated the spatial variability of the residence time with a numerical Eulerian analysis on the Lagrangian characteristics of the SCS water masses. Figure 11.6 is from Liu and Gan (2017) and illustrates the time series of the percentage of SCS water being replaced by the invasive non-SCS water as a function of the water depth. In Fig. 11.6, the 100% contour (bold black line) represents the time when the basin is completely occupied by non-SCS waters at certain depths and is called the maximum *ReT* (ReT_{max}). The relationship between the *ReT* and ReT_{max} is

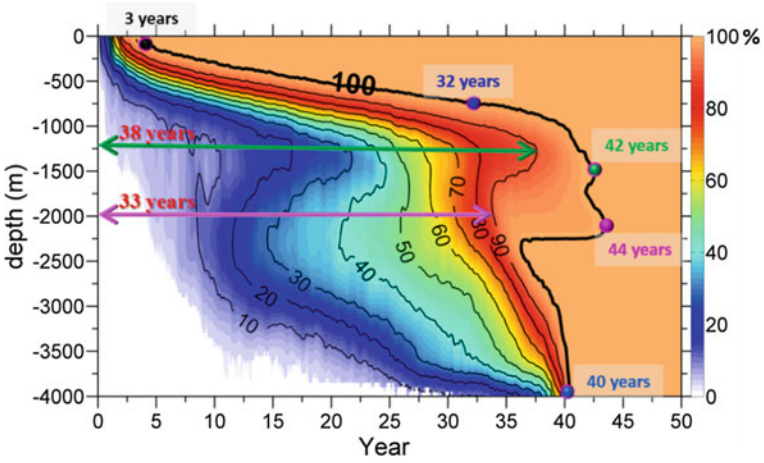

Fig. 11.6 Time series of the percentage of water that is refreshed in the SCS as a function of depth (adapted from Liu and Gan 2017)

$$ReT_{max}(\mathrm{z}) = \max[ReT(x, y, z)] \tag{11.3}$$

ReT_{max} for the entire SCS is generally shorter than 45 years. Figure 11.6 illustrates that ReT_{max} increases with depth. It takes about three years for the water in the near-surface layer (<200 m) to refresh. These SCS waters are replaced by the Kuroshio water cyclonically spreading over the upper layer.

ReT_{max} in the upper layer, where the pycnocline is located, rapidly increases to approximately 32 years at 750 m. ReT_{max} keeps increasing to its maximum in the intermediate layer (~42 years) and the upper part of the lower (~44 years) layer. In the closed less stratified basin, ReT_{max} reduces to approximately 40 years.

There is a narrow but deep trough (~2430 m) between 114–117° E and 6–8° N in the southernmost of the intermediate SSCS water. The water in the trough has limited communication with the rest of the SCS waters. This limitation causes a sharp increase of ReT_{max} at ~2200 m.

The amount of time needed to replace 90% of the SCS water masses in the water column further confirms that the longest ReT_{max} mainly occurs in the intermediate layer, because it takes ~38 years for 90% of the intermediate water to be refreshed, while it takes ~33 years to refresh the water in the lower layer. Unlike results from previous studies (for example, Yang et al. (2012)), the ReT_{max} increases monotonically with depth, and the maximum ReT_{max} in the intermediate layer suggests that the formation of intermediate water is deferred if the prevailing circulation is anticyclonic.

11.4 The Changing SCS Circulation

Having described the fundamental characteristics and physics of the SCS circulation, we now discuss bi-decadal changes in the SCS circulation from 1992 to 2011.

11.4.1 Changes in Horizontal Plane

To discuss the recent changes in the circulation of the SCS, we use the surface velocity vectors averaged over 20 years from 1992 to 2011and the standard deviation from the mean velocity for that period. We present the surface vectors and standard deviations in Fig. 11.7. The figure illustrates the major characteristics and variability in the SCS circulation that link the westward intrusion of the Kuroshio through LS with the pathways of the SCSTF.

The mean circulation pattern is like the pattern we presented in the previous sections with a relatively large variance of the surface flow occurring near the entrance of LS and in the southwestern basin. Furthermore, the magnitudes of the variances in these two locations were comparable with their mean values, but the influences on the variability in the two locations are different.

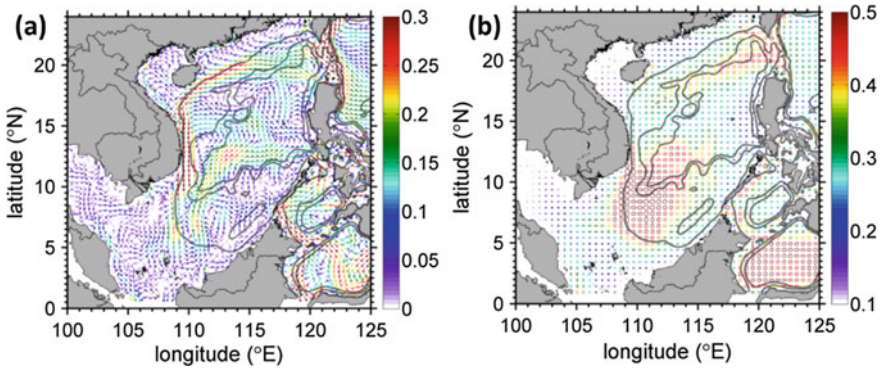

Fig. 11.7 **a** Long-term (1992–2011) averaged surface velocity vectors (m s^{-1}) and **b** associated standard deviation of the velocity vector in the SCS. The black contours are the 200, 2000, and 3000 m isobaths. The size and color of the circles in (**b**) indicate the magnitude of the standard derivation

The variability of the circulation near LS is associated with the variations of intensity and the path of Kuroshio intrusion at inter-annual, seasonal, and smaller temporal scales (Gan et al. 2016b). In the southwestern basin, the variability is associated with an opposing seasonal variation that is governed by a separating along-slope current off Vietnam associated with the southward slope current in winter and with the local wind stress curl dipole in summer (Gan and Qu 2008). The strong southwestward slope current has a weak standard deviation in the northwestern slope and suggests that the current on the northwestern slope prevails all year.

Seasonal cyclonic circulation in the upper layer is attributed to the positive vorticity in the slope current along the SCSTF. Like the surface velocity fields in Fig. 11.7, the larger variance of the cyclonic circulation occurs along the basin-wide slope current (Fig. 11.8). Variabilities from the Kuroshio intrusion and wind stress curl are the major drivers for the cyclonic circulation variabilities in the upper layer. In addition, spatial variation of the vorticity variance suggests that the local dynamics, such as the seasonally reversed jet along the steep slope off Vietnam (Gan and Qu 2008), contribute substantially to the upper layer circulation variability in the SCS. The circulation in the middle and deep layers (not shown) varies similarly to the upper layer.

11.4.2 SCS Layered Circulation Trends

As we have already discussed, the CAC circulation in the SCS has strong seasonal variability related to the Kuroshio intrusion and wind stress curl seasonality. However, the variability in the circulation also occurs in different frequency bands that are subject to the external controls of the Kuroshio intrusion and wind stress curl.

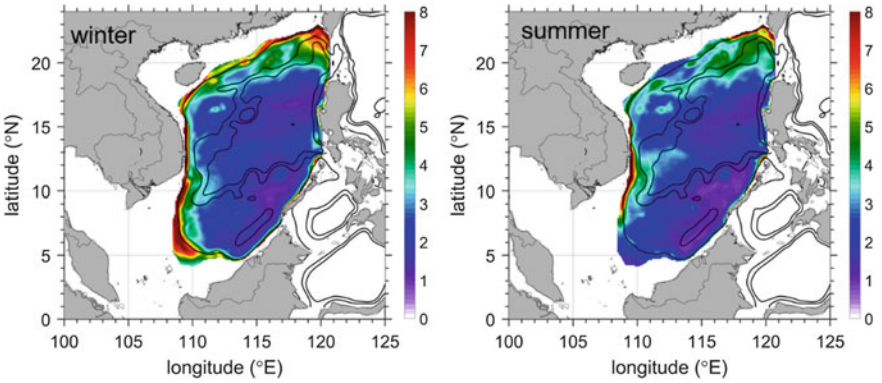

Fig. 11.8 Seasonal standard deviation of relative vorticity (10^{-6} s^{-1}) in the upper layer during the winter and summer from 1992 to 2011. The black contours are the 200, 2000, and 3000 m isobaths

Figure 11.9 shows the time series of the CAC circulation anomaly in the water column from 1992 to 2011 that we derived from the daily-averaged velocities from CMOMS output. While the CAC circulation prevails during these 20 years, the circulation exhibits a strong temporal variability at different frequencies. For the upper layer, the associated power spectrum density (not shown) indicates that the basin-averaged vorticity in that layer has significant periods of variation at six months, annual, and five-year cycles, which might be related to the annual and inter-annual variations of the circulation. Similar conditions exist in the middle and deep layers with the addition of a significant period at 2.5-years.

The cyclonic layers in the CAC circulation intensify over the 20 years (Fig. 11.9) while the anticyclonic circulation in the middle layer weakens. The increasing rates of vorticity for the cyclonic circulation in the upper (2.95×10^{-12} s^{-1} day^{-1}) and deep (2.35×10^{-12} s^{-1} day^{-1}) layers have similar magnitudes. However, the weakening rate of the anticyclonic circulation in the middle (7.19×10^{-13} s^{-1} day^{-1}) layer is one order of magnitude smaller than the rates in the other layers. Despite the difference, the rate in the middle layer is still significant for those 20 years. The intensities of the domain- and time-averaged vorticities are stronger in the upper (1.45×10^{-7} s^{-1}) and deep (1.29×10^{-7} s^{-1}) layers, than in the middle (-1.04×10^{-9} s^{-1}) layer.

Gan et al. (2020) validated the trends in vorticity described in the previous paragraph by using geostrophic currents derived from hydrographic data from the World Ocean Database (Boyer et al. 2018) and from the Archiving, Validation, and Interpretation of Satellite Oceanographic Data (AVISO; https://www.aviso.altimetry.fr/en/home.html) dataset. The changing CAC circulation has rarely been studied, and the cause of the changes is largely unclear. Nevertheless, there is the belief that the circulation changes are controlled by corresponding changes in the wind stress curl and the net planetary vorticity influx from the SCS's surrounding straits (Gan et al. 2016a). It should be noted that the uncertainty of the layered circulation trends in the SCS remains, largely due to the uncertainty from the wind stress curl which is

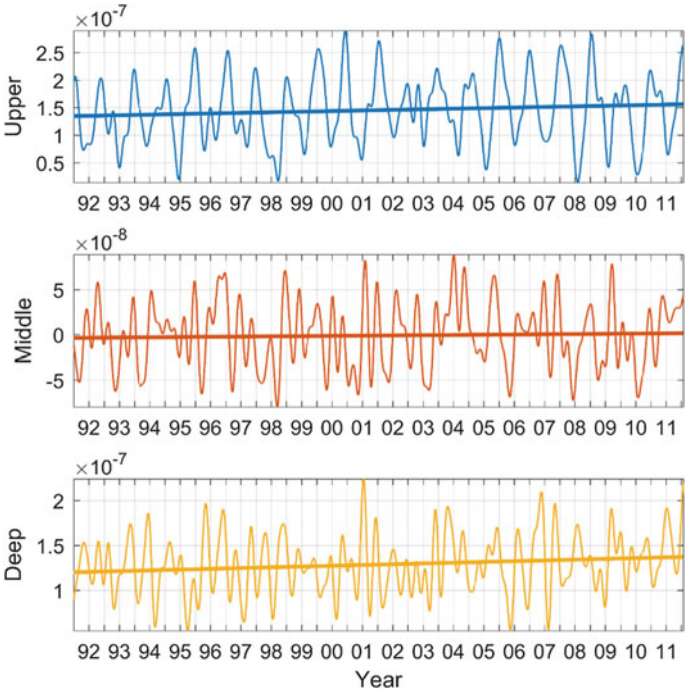

Fig. 11.9 Time series of 90-day filtered, layer-integrated, and basin-averaged vorticity (s^{-1}) from the upper, middle, and deep layers. The straight lines are the corresponding trends with rates of $k_1 = 2.95 \times 10^{-12}$, $k_2 = 7.19 \times 10^{-13}$, and $k_3 = 2.35 \times 10^{-12}$ s^{-1} day^{-1} from 1992 to 2011. All trend rates (k) pass 95% significance. Areas with water depth shallower than 100 m in the basin are excluded in the calculation

obtained from atmosphere circulation model and lack of validation with wind data over the vast SCS basin.

11.5 Dynamics for the Changing SCS Circulation

11.5.1 Vorticity Dynamics

In this section, we describe the fundamental forcing mechanism for the SCS circulation using vorticity dynamics (Gan et al. 2016a).

With Stokes' theorem, the circulation is expressed as the sum of the vertical relative vorticity over that region (Eq. 11.4). Integrating the Layer-Integrated Vorticity Equation (LIVE) (Gan et al. 2016a) over the entire domain identifies the multi-forcing mechanisms of wind, lateral fluxes, and the intrinsic dynamics of the flow-topography interaction, and identifies their contribution to the circulation.

LIVE is written as:

$$\overbrace{\int_A \Omega_t dA}^{\Omega^{\text{acce}}} = \overbrace{-\int_A \left[(f\bar{u}D)_x + (f\bar{v}D)_y\right]dA}^{\Omega^{cor}}$$
$$\overbrace{-\int_A \nabla_H \times (\mathbf{HNL})dA + \int_A \nabla \times \int_{Lb}^{Lu} \mathbf{hvisc}\, dz dA}^{\Omega^{hadv}} \overbrace{-\int_A \nabla_H \times (\mathbf{VNL})dA}^{\Omega^{vadv}}$$
$$\overbrace{+\int_A -\frac{1}{\rho_o}\left[J\left(LB, P^{Lb}\right) + J\left(Lu, P^{Lu}\right)\right]dA}^{\Omega^{pgf}} + \overbrace{\int_A \nabla_H \times \int_{Lb}^{Lu} (K_v(\bar{\mathbf{v}})_z)_z dz dA}^{\Omega^{vvis}}; \tag{11.4}$$

for the upper layer, $Lu = \eta$ and $Lb = \begin{cases} h(x, y), -750 < h < -100\,\text{m} \\ -750\ \text{m}, \quad h \geq -750\,\text{m} \end{cases}$;

for the middle layer, $Lu = -750\,\text{m}$ and $Lb = \begin{cases} h(x, y), -1500 < h < -750\,\text{m} \\ -1500\,\text{m}, \quad h \geq -1500\,\text{m} \end{cases}$;

and for the bottom layer, $Lu = -1500$ and $Lb = h(x, y)$.

f is the Coriolis parameter. D is the total layer depth. u and v are the zonal (x) and meridional (y) velocities, respectively. Lu and Lb are the depths of the top and bottom for each specific layer, respectively. η is the sea surface elevation. **HNL** is the horizontal nonlinear advection. **hvisc** is the horizontal viscous term, which is generally very small. **VNL** is the vertical advection term. P^{Lu} and P^{Lb} are the pressure at the top and bottom of each specific layer, respectively. J is a Jacobian operator. K_v is the vertical viscous coefficient. The suffix represents derivation, and the overbar refers to the layer average.

The physical meaning of each term in LIVE, from left to right, is the acceleration Ω^{acce}, divergence Ω^{cor} (vortex stretching and β-effect), the horizontal advection Ω^{hadv}, tilting Ω^{vadv}, pressure torque Ω^{pgf}, and vertical viscosity Ω^{vvis}. Ω^{vvis} can be expressed as $\Omega^{vvis} = \Omega^{sstr}$ (wind stress curl)—Ω^{bstr} (bottom stress curl) in the upper layer. The bottom pressure torque, Ω^{pgf}, forms when the baroclinic induced pressure interacts with the variable slope topography (Mertz and Wright 1992). The nonuniform vertical velocity field generates tilting horizontal components of the vorticity into the vertical and causes tilting Ω^{vadv}. Figure 11.10 demonstrates how the terms in Eq. (11.4) balance for each layer.

11.5.2 Dynamic Driver for the CAC Circulation

In this section, we discuss the balance of the LIVE terms using the model results from CMOMS forced with climatological mean atmospheric fluxes (Gan et al. 2016b).

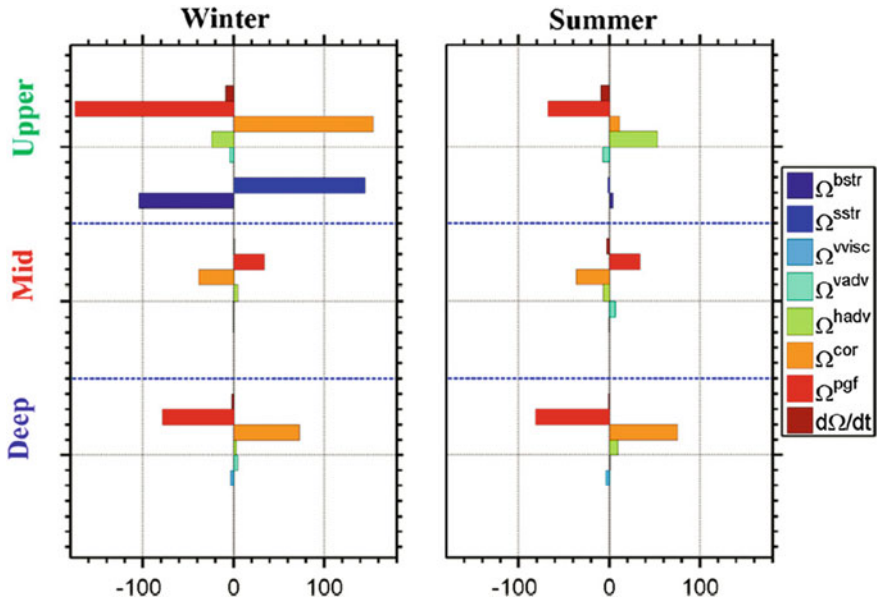

Fig. 11.10 Terms $\left(\mathrm{m}^3\mathrm{s}^{-2}\right)$ of the domain and layer integrated vorticity equation in the upper, middle (mid), and deep layers during (left) winter and (right) summer: Ω^{acce} is acceleration; Ω^{cor} is divergence or vortex stretching; Ω^{hadv} is horizontal advection; Ω^{vadv} is tilting; Ω^{pgf} is the bottom pressure torque; Ω^{vvis} is vertical viscosity (middle and deep layers); Ω^{sstr} is wind stress curl; and Ω^{bstr} is bottom stress curl in the upper layer (adapted from Gan et al. 2016a)

The winter model results attribute the major sources of the SCS upper layer cyclonic circulation to Ω^{cor} and Ω^{sstr}. The two terms are mainly balanced by Ω^{pgf} and Ω^{bstr}. The main sources for the relatively weak cyclonic circulation in summer is Ω^{hadv} and Ω^{cor}. The Ω^{sstr} has a very small influence, and it is mainly balanced by Ω^{pgf}. The negative value of Ω^{acce}, in winter and summer, suggests that the cyclonic circulation weakens following accelerations in autumn and spring (Fig. 11.3).

In the middle and deep layers, the Ω^{cor} is the main source of the anticyclonic and cyclonic circulation. The bottom pressure torque Ω^{pgf} primarily balances Ω^{cor}, while the remaining terms are relatively small. Almost all the signs of the terms in the middle layer oppose those in the upper and deep layers.

Ω^{cor} is the dominant source of the CAC circulation in each layer, while Ω^{pgf} acts as the major response to CAC circulation in the SCS basin. According to the divergence theorem, the Ω^{cor} could be related to the planetary vorticity fluxes that cross the meridionally oriented section of LS. The same relationship could exist for the meridionally (*Si*) and zonally (*Sj*) oriented sections along Mindoro Strait and along the 100-m isobath. Equation 11.5 represents this relationship between Ω^{cor} and planetary vorticity fluxes. These planetary vorticity fluxes provide extrinsic vorticity sources for the CAC circulation in the SCS.

$$\Omega^{cor} = -\int_{Si} f\bar{u}\,dSi - \int_{Sj} f\bar{v}\,dSj. \tag{11.5}$$

Figure 11.11 shows that the planetary vorticity flux through LS mainly contributes to Ω^{cor} in all the layers during winter and summer, while the planetary vorticity flux through Mindoro Strait and the 100-m isobath mainly offsets Ω^{cor}.

Therefore, we attribute the CAC circulation to vortex stretching from the planetary vortex that is extrinsically induced by the inflow-outflow-inflow in the upper-middle-deep layers through LS. Furthermore, we attribute the cyclonic circulation in the upper layer to wind stress curl in winter and nonlinear advection in summer (Gan et al. 2016a).

Overall, our results suggest that the changing CAC circulation in the SCS is largely controlled by the corresponding changes in planetary fluxes through the straits around the SCS and wind stress curl. However, the variability of the CAC circulation can also arise from the response of flow to the slope topography and from the nonlinearity of the circulation itself, as the relatively large magnitudes of bottom pressure torque Ω^{pgf} and horizontal advection Ω^{hadv} show.

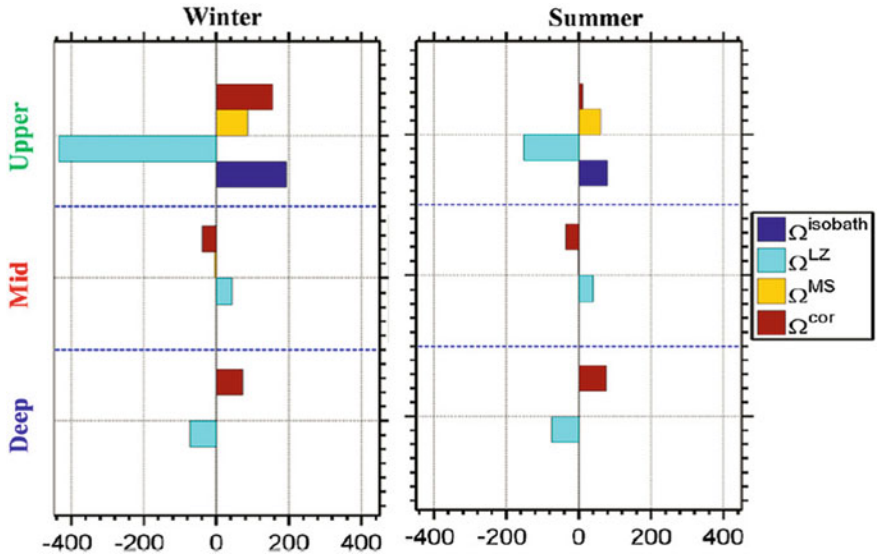

Fig. 11.11 Mean values of Ω^{cor} terms $\left(\mathrm{m^3 s^{-2}}\right)$ in the upper, middle (mid), and deep layers and the respective contributions by planetary vorticity flux through Luzon Strait Ω^{LZ}, Mindoro Strait Ω^{MS}, and across the 100-m isobath $\Omega^{isobath}$ in winter and summer (adapted from Gan et al. 2016a)

11.5.3 Mechanism for the Changing Layered Circulation

Equations 11.4 and 11.5 show us that external forcing of monsoonal wind stress curl and planetary vorticity flux from the external inflow/outflow through the straits around the SCS mainly drive the circulation in the SCS (also see Gan et al. 2016b). We also see that corresponding internal responses include bottom pressure torque arising from the flow interacting with the continental slope, a vertical exchange of vorticity among layers, and other nonlinear dynamic processes. We now discuss the mechanism that drives the changes in the CAC circulation occurring over our 20-year study period.

During our 20-year study period, the net planetary vorticity flux in the upper layer through all straits weakens (Gan et al. 2020). This weakening is due to the decreased Kuroshio intrusion into the basin from LS, because of an intensifying Kuroshio (Fig. 11.12). We found that the Kuroshio intrusion increased at the rate of $k = 7.11 \times 10^{-5}$ Sv day^{-1} over the 20 years. Nan et al. (2016) observed that the upper layer freshened in the SCS from 1993 to 2012, which they attributed to the weakening of the Kuroshio intrusion through LS. The decreasing trend of the planetary vorticity influx would weaken the cyclonic circulation in the upper CAC circulation according to Eqs. 11.4 and 11.5, so decreasing planetary vorticity cannot account for the strengthened cyclonic circulation in the upper layer shown in Fig. 11.9.

Equation 11.3 shows that a change of wind stress curl can alter vorticity. Our data show that the basin-averaged wind stress curl is positive in all seasons (Gan et al. 2016b). During the 20-year period, the basin-integrated wind stress curl ($\nabla \times \frac{\tau^s}{\rho}$) strengthens at a rate of $k = 0.0044$ m^{3}s^{-2} day^{-1} (with 95% significance). The increasing wind stress curl imparts positive vorticity to strengthen the upper cyclonic circulation and modulates the dynamic height at the surface which could affect the overall changing circulation in the water column through a spin-up/spin-down of the barotropic pressure gradient.

The strengthening cyclonic circulation in the deep layer of the semi-closed basin (Fig. 11.9) is due to the increase in deep planetary vorticity influx through LS (Table 11.1, Gan et al. 2020). The reason for the increasing deep intrusion through LS is unknown.

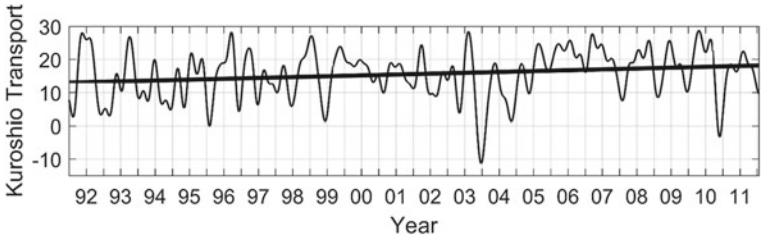

Fig. 11.12 Time series of Kuroshio transport (Sv) along 18° N from the coast to 130° E. The thick black line indicates the trend of the transport which has a rate of $k = 7.11 \times 10^{-5}$ Sv day^{-1} with 95% significance

Table 11.1 Trends of basin-averaged vorticity, net planetary vorticity flux (F flux) into the basin, and wind stress curl. The symbol "+" indicates an increasing rate and "−" denotes a decreasing trend

Layer	Variables		
	Vorticity	F flux into basin	Wind stress curl
Upper	+	–	+
Middle	+	–	
Deep	+	+	

The strengthening middle layer outflow through LS represents a loss of planetary vorticity for the layer so it cannot account for the weakening anticyclonic circulation in the middle layer. The viscous drag curl (Ω^{vvis} in Eq. 11.4) from the increasing cyclonic circulation in the neighboring upper and deep layers would contribute to the decelerating anticyclonic in the middle layer. In addition, the vertical vorticity flux from the neighboring layers could contribute to the weakening anticyclonic circulation in the middle layer.

The changing external forcing for the CAC circulation has been related to the Pacific Decadal Oscillation (PDO) in previous studies (Nan et al. 2016), but more analyses are required before we can provide a holistic understanding of the mechanism that changes the CAC circulation, in particular the change in the middle and deep layers. We still lack understanding of the deep circulation pattern in the tropical NPO off LS.

Table 11.1 summarizes the trends of the CAC circulation, the corresponding planetary vorticity flux through LS, and the domain-averaged wind stress curl. Gan et al. (2020) present the detailed mechanism governing the variability and long-term trend in the CAC circulation in the SCS.

11.6 Summary

In this chapter, we outline the characteristics of the SCS circulation based on recent research derived from observations and numerical simulations. We present the three-layer alternating CAC circulation in the SCS based on Stokes' Theorem. We dynamically link the CAC circulation with the extrinsic forcing of winds and lateral momentum/vorticity fluxes through the straits around the SCS. We also bridge the extrinsic forcing and intrinsic dynamic response in the CAC circulation in the SCS basin. We use the CAC circulation to derive the pathways and residence time of the water masses in the SCS.

Our new fundamental knowledge about the SCS circulation shows us the long-term trends and variability of the CAC circulation. The changing circulation provides a broad dynamic overview of the response of a regional ocean such as SCS to changing forcing in the large-scale tropical NPO and atmospheric fluxes. These findings provide new understanding of the changing circulation patterns, hydrographic properties, energy, and biogeochemical substances in the SCS.

The three-dimensional SCS circulation characterized by the vertically alternating spinning CAC circulation in the upper, middle, and deep layers, is mainly driven by the net planetary vorticity influx/outflux through the straits surrounding the SCS. We find that the CAC circulation is mainly composed of basin-wide slope currents. The vorticity of the CAC circulation comes primarily from the vorticities arising along the route of the SCSTF in the slope current, the Kuroshio intrusion near LS, and outflow near Mindoro Strait in the upper and middle layers. A larger contribution to the cyclonic circulation in the deep layer is from the circulation in the southwestern deep basin.

The CAC circulation displays strong spatiotemporal variability over a 20-year study period, from 1992 to 2011. The largest variances are mainly along the stream of the SCSTF over the slope, and there is a strengthening trend of the CAC circulation in the SCS. This changing circulation is mainly attributed to the strengthening positive wind stress curl which is stronger than the weakening planetary influx through the Luzon Strait. However, due to uncertainty of the wind data derived from atmosphere model, the uncertainty in the layered circulation trends remains inevitably. The mechanism that leads to the strengthening of the circulation in the middle and deep layers is not obvious and needs further investigation. The underlying driver(s) for the changing CAC circulation is complex and may be associated with the changing oceanic circulation in the tropical NPO, influx/outflux through the straits, and the changing vertical exchanges among the three layers.

Understanding the fundamental dynamics that regulate the CAC circulation is essential for identifying the process that leads to the changing CAC circulation. We use a dynamic tool, based on LIVE to bridge extrinsic and intrinsic forcing, to diagnose the underlying physics. This tool is critical in forecasting the trend of the changing SCS circulation. We find that the CAC circulation forms, because of the vorticity imparted by wind stress curl of the East Asia monsoon and, the input of planetary vorticity flux from the inflow-outflow-inflow in LS after the input has been offset by the vorticity induced by the interacting baroclinic flow and basin topography or bottom pressure torque.

We find that the inflow-outflow-inflow in LS persisted for our 20-year study from 1992 to 2011, and the variability occupies different frequency bands. The variation of the inflow/outflow in LS is related to the intensity of the Kuroshio in the upper layer, which, in turn, is linked with the NPO currents: the NEC, Kuroshio, and Mindanao Current. Similarly, the CAC circulation in the middle and deep layers link to the corresponding under currents of the North Equatorial Undercurrent, Luzon Undercurrent, and Mindanao Undercurrent. The results derived from LIVE show that the changing extrinsic fluxes would alter the total budget of the planetary vorticity and trigger corresponding intrinsic dynamics of the interacting flow topography and associated nonlinear processes in the CAC circulation.

In the end, though, we still have little knowledge about how the responses of the intrinsic dynamics interact with the extrinsic forcing to regulate the changing SCS circulation. We lack understanding about the variability of the current system in the NPO, particularly regarding the role of undercurrents on the CAC circulation.

Understanding the interaction between the forcing and resulting flow and the variable NPO currents are essential for us to completely understand the changing ocean circulation, the regional climate variability, transport of biogeochemical substances in the SCS and overall understanding of ocean science development in this marginal sea.

Acknowledgements This research was supported by the Key Research Project of the National Science Foundation, China (41930539, 41906016), and the Hong Kong Research Grants Council (GRF16204915, GRF16206516).

References

Boyer TP, Baranova OK, Coleman C et al (2018) World ocean database 2018. In: Mishonov AV Technical Editor NOAA Atlas NESDIS 87

Cai ZY, Gan JP, Liu ZQ et al (2020) Progress on the formation dynamics of the layered circulation in the South China Sea. Prog Oceanogr 181(202):102246

Chao SY, Shaw PT, Wu SY (1996) Deep water ventilation in the South China Sea. Deep-Sea Res Pt I 43(4):445–466. https://doi.org/10.1016/0967-0637(96)00025-8

Fang G, Wang Y, Wei Z et al (2009) Interocean circulation and heat and freshwater budgets of the South China Sea based on a numerical model. Dyn Atmos Oceans 47(1):55–72

Gan JP, Qu T (2008) Coastal jet separation and associated flow variability in the southwest South China Sea. Deep-Sea Res Pt I 55(1):1–19. https://doi.org/10.1016/j.dsr.2007.09.008

Gan JP, Li H, Curchitser EN et al (2006) Modeling South China Sea circulation: response to seasonal forcing regimes. J Geophys Res Oceans 111(C6)

Gan JP, Cheung A, Guo XG et al (2009a) Intensified upwelling over a widened shelf in the northeastern South China Sea. J Geophys Res Oceans 114(C9)

Gan JP, Li L, Wang DX et al (2009b) Interaction of a river plume with coastal upwelling in the northeastern South China Sea. Cont Shelf Res 29(4):728–740

Gan JP, Liu ZQ, Hui CR (2016a) A three-layer alternating spinning circulation in the South China Sea. J Phys Oceanogr 46(8):2309–2315

Gan JP, Liu Z Q, Liang L L (2016b) Numerical modeling of intrinsically and extrinsically forced seasonal circulation in the China Seas: a kinematic study. J Geophys Res Oceans 121(7):4697–4715

Gan JP, Cai Z, Tang Y et al (2020) Chaniging layered circulation in the South China Sea and adjacent northwestern Pacific Ocean (1992–2011) (to be submitted to Nat Geosci)

Hellerman S, Rosenstein M (1983) Normal monthly wind stress over the world ocean with error-estimates. J Phys Oceanogr 13(7):1093–1104

Hsin YC, Wu CR, Chao SY (2012) An updated examination of the Luzon Strait transport. J Geophys Res Oceans 117:C03022

Lan J, Zhang NN, Wang Y (2013) On the dynamics of the South China Sea deep circulation. J Geophys Res Oceans 118(3):1206–1210

Li L, Qu TD (2006) Thermohaline circulation in the deep South China Sea basin inferred from oxygen distributions. J Geophys Res Oceans 111(C5)

Liu ZQ, Gan JP (2012) Variability of the Kuroshio in the East China Sea derived from satellite altimetry data. Deep-Sea Res Pt I 59:25–36. https://doi.org/10.1016/j.dsr.2011.10.008

Liu Z, Gan J (2017) Three-dimensional pathways of water masses in the South China Sea: a modeling study. J Geophys Res Oceans 122(7):6039–6054

Mertz G, Wright DG (1992) Interpretations of the JEBAR term. J Phys Oceanogr 22(3):301–305

Nan F, Xue HJ, Yu F (2015) Kuroshio intrusion into the South China Sea: a review. Prog Oceangr 137:314–333

Nan F, Yu F, Xue H, Zengb L et al (2016) Freshening of the upper ocean in the South China Sea since the early 1990s. Deep-Sea Res I 118:20–29

Qu T (2000) Upper-layer circulation in the South China Sea. J Phys Oceanogr 30(6):1450–1460

Qu TD, Du Y, Sasaki H (2006) South China Sea throughflow: a heat and freshwater conveyor. Geophys Res Lett 33(23)

Qu T, Mitsudera H, Yamagata T (2000) Intrusion of the North Pacific waters into the South China Sea. J Geophys Res Oceans 105(C3):6415–6424

Qu TD, Song YT, Yamagata T (2009) An introduction to the South China Sea throughflow: its dynamics, variability, and application for climate. Dyn Atmos Oceans 47(1–3):3–14

Wu CR, Hsin YC (2012) The forcing mechanism leading to the Kuroshio intrusion into the South China Sea J Geophys Res Oceans (1978–2012) 117(C7)

Xu FH, Oey LY (2014) State analysis using the Local Ensemble Transform Kalman Filter (LETKF) and the three-layer circulation structure of the Luzon Strait and the South China Sea. Ocean Dyn 64(6):905–923

Yang SC, Lee DC, Ho TY (2012) The isotopic composition of Cadmium in the water column of the South China Sea. Geochim Cosmochim Acta 98:66–77

Chapter 12
Changing Biogeochemistry in the South China Sea

Chen-Tung Arthur Chen, Shujie Yu, Ting-Hsuan Huang, Hon-Kit Lui, Yan Bai, and Xianqiang He

Abstract The tropical/subtropical South China Sea (SCS) is the largest marginal sea in the world. Like other warm bodies of water, its sea surface temperature (SST) is rising, albeit more slowly (0.012 °C/yr between 1998 and 2016) than that of cold-water regions at high latitudes. The chlorophyll concentration increased at 0.0012 μg/L/yr during that period, and the Secchi disk depth (SDD) increased by 0.035 m/yr. The changes of SST, chlorophyll concentration and SDD, the factors governing changes in ocean biogeochemistry, in the SCS exhibit high temporal-spatial variability, and these parameters varied in opposite directions during the periods 1998–2008 and 2008–2016. The first period witnessed declining SST and SDD and increasing chlorophyll concentration, referring to enhancing primary productivity. The second period witnessed increasing SST and SDD but falling chlorophyll concentration, referring to declining primary productivity. These changes and increasing anthropogenic activities on land may be related to changing biogeochemistry such as decreasing dissolved oxygen concentration in coastal regions. In the SCS basin, however, particulate organic carbon and nitrogen seem to be on the rise.

C.-T. A. Chen (✉) · T.-H. Huang · H.-K. Lui
Department of Oceanography, National Sun Yat-Sen University, Kaohsiung 804, Taiwan
e-mail: ctchen@mail.nsysu.edu.tw

T.-H. Huang
e-mail: thhuang@mail.nsysu.edu.tw

H.-K. Lui
e-mail: hklui@mail.nsysu.edu.tw

S. Yu · Y. Bai · X. He
State Key Laboratory of Satellite Ocean Environment Dynamics, Second Institute of Oceanography, Ministry of Natural Resources, Hangzhou 310012, China
e-mail: yvshujie@126.com

Y. Bai
e-mail: baiyan@sio.org.cn

X. He
e-mail: hexianqiang@sio.org.cn

C.-T. A. Chen and X. Guo (eds.), *Changing Asia-Pacific Marginal Seas*, Atmosphere, Earth, Ocean & Space, https://doi.org/10.1007/978-981-15-4886-4_12

Keywords South China Sea · Sea surface temperature · Salinity · Chlorophyll · Secchi disk depth · pH · Temporal changes

12.1 Introduction

The South China Sea (SCS), with an area of 3.5×10^6 km^2, is the largest marginal sea in the world (Fig. 12.1). Like the oceans, it is undergoing the consequences of the global environmental change. Although the SCS encompasses a large area and an average depth of about 1350 m, it is actually semi-enclosed because the Sunda Shelf and the Gulf of Thailand in its southern and southwestern regions are rather shallow, with an average depth of only 50 m. The wide Sunda Shelf connects to the Indian Ocean via the Strait of Malacca to the southwest, but the major connection is with the Java Sea to the southeast through the Karimata and Gelasa Straits which are less than 50 m deep. The northern and northwestern regions of the SCS are also wide shelves that connect to the East China Sea (ECS) via the shallow Taiwan Strait, which has an average depth of only 50 m (Fig. 12.1).

The central and northeastern parts of the SCS are as deep as 5500 m but the only deep linkages to areas beyond the sea are the 400 m-deep Mindoro Strait, which connects to the Sulu Sea, and the 2200 m-deep Luzon Strait, which opens into the West Philippine Sea (WPS). Since the ridge that separates the Sulu Sea from the water beyond it is only approximately 100 m deep, water that is deeper than about 100 m in the Pacific Ocean can only enter the SCS through the Luzon Strait. Monsoon

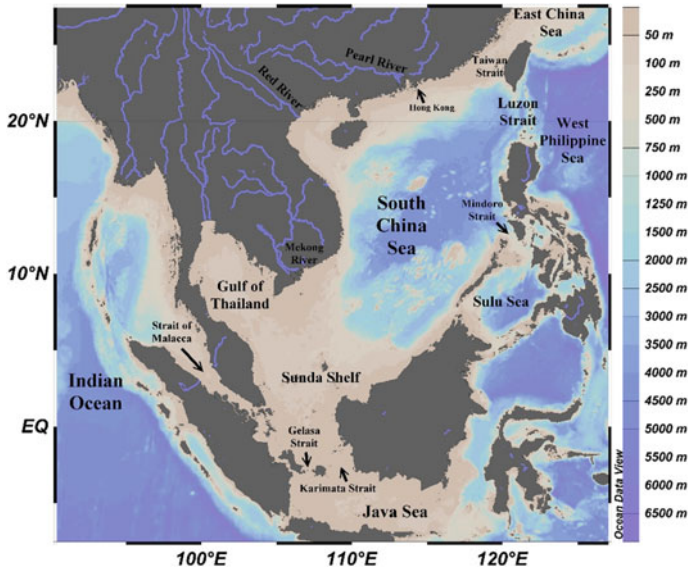

Fig. 12.1 Map of the South China Sea

winds dominate the circulation in the SCS and exchanges of seawater with the water outside it (Chao et al. 1996a, b; Qu 2000; Wu and Chang 2005). Since no deep or intermediate water forms in the SCS because cooling in winter is too little to make the water very dense, unique subsurface features, such as extreme salinity are brought in from the WPS. Subsequent vertical mixing and upwelling diminish these features (Chen and Huang 1996).

The anthropogenic release of CO_2 undoubtedly caused the problem of so-called global environmental change. The oceans are a major sink of excess anthropogenic CO_2, some of which has penetrated to the bottom of the oceans (Chen and Millero 1979; Chen and Pytkowicz 1979; Chen 2003; Chen et al. 2006a, b). Like the global oceans, the SCS has experienced a fall in pH as a result of the increase in the concentration of CO_2 in the atmosphere (Chai et al. 2009; Liu et al. 2014; Lui and Chen 2015). Perhaps owing to the upwelling, however, anthropogenic CO_2 penetrates to a depth of only roughly 1500 m in the SCS (Chen et al. 2006a, b) although signals near the detection limit have also been reported below 1500 m (Huang et al. 2016). As the saturation horizon of calcite exceeds a depth of 2000 m in the SCS (Chen and Huang 1995), excess CO_2 penetration is expected to enhance its dissolution only slightly. The saturation horizon of aragonite, however, is only 600 m, which is less than the depth of excess CO_2 penetration but greater than the aragonite saturation horizon in the Bering Sea (Chen et al. 2020a). As a result, an upward migration of the saturation horizon affects the aragonite deposits on the SCS shelf, but less than it affects the deposits in the Bering Sea.

The salinity of the SCS surface water has reportedly been declining during the last two decades (Fig. 12.2; Nan et al. 2016), consistent with the general trend that relatively fresh seas, including several marginal seas, are experiencing falling salinity while more saline regions, such as the North Pacific Subtropical Water have been increasing in salinity (Durack and Wijffels 2010). Interestingly, the freshening of the upper waters of the SCS is not caused by increasing river discharge, because all three major rivers that enter the SCS—the Mekong, Pearl and Red Rivers—experienced a declining outflow between 1993 and 2012 (Nan et al. 2016). Precipitation increased

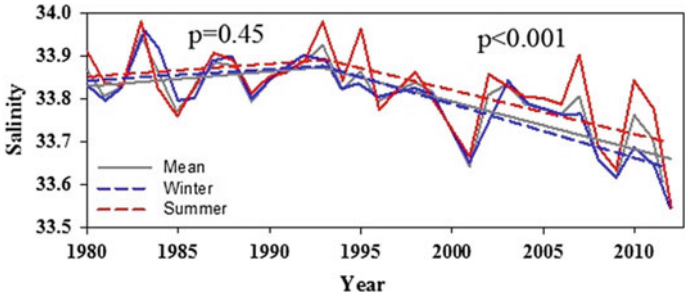

Fig. 12.2 Time series of salinity in the winter (Dec.–Feb.; blue), the summer (Jun.–Aug.; red), and mean (black) averaged above 100 m in the SCS. Dotted lines represent the linear trends before/after 1993 that best fit the data (modified from Nan et al. 2016)

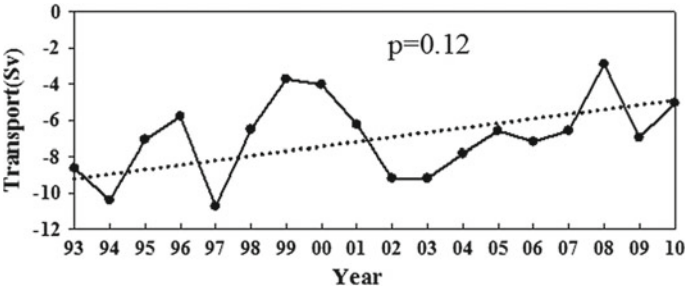

Fig. 12.3 Annual time series and linear trend of flux of Luzon Strait based on ROMS. Data taken from Nan et al. 2015 (Negative values represent westward flow)

to exceed evaporation during that period but the increase was responsible for only 15% of the seawater freshening (Nan et al. 2016). The major cause of 85% of the freshening was reportedly a decrease in the intrusion of salty Kuroshio water in those years (Nan et al. 2013, 2015; Fig. 12.3). Lui et al. (2018), however, reported an increase in Kuroshio intrusion in the Luzon Strait transport since 2012. Since the nutrient inventories in the euphotic layer of the WPS are significantly lower than that in the SCS, the intrusion of the WPS seawater decreases the nutrient inventories of the euphotic layer, and hence reduces primary production and export production in the SCS. These complicated processes influence the biogeochemistry of the SCS, but the impact of such factors as the El Nino-Southern Oscillation (ENSO) and the Pacific Decadal Oscillation (PDO) is unknown. For example, Fig. 12.4 plots a time series of anomalies of alkalinity, dissolved inorganic carbon, nitrogen, phosphorus and silicate concentrations as well as water transport from the SCS to the ECS. Overall, they tend to rise, and this trend is clearly related to anomalous change in sea surface height (Fig. 12.4h). These signals correlate with PDO (Fig. 12.4j). Recent changes in SST, chlorophyll, Secchi disk depth (SDD) and related carbonate chemistry will be discussed below.

12.2 Changing Sea Surface Temperature

The SST data for the period from 1998 to 2016 were taken from the AVHRR_OI dataset, which is a product of the Group for High-Resolution Sea Surface Temperature (GHRSST), and can be obtained from the National Center for Environmental Information (NCEI), NOAA (https://data.nodc.noaa.gov/ghrsst/L4/GLOB/NCEI/AVHRR_OI/ghrsst/L4/GLOB/NCEI/AVHRR_OI/). Data were averaged monthly from 1998 to 2016. Details can be found in Chen et al. (2020a).

Figure 12.5a displays a climatological map of the SST, which typically exceeds 26 °C except in the coastal region southeast of China, mainly because the cold Chinese coastal water flows southward from September to May when the NE monsoon

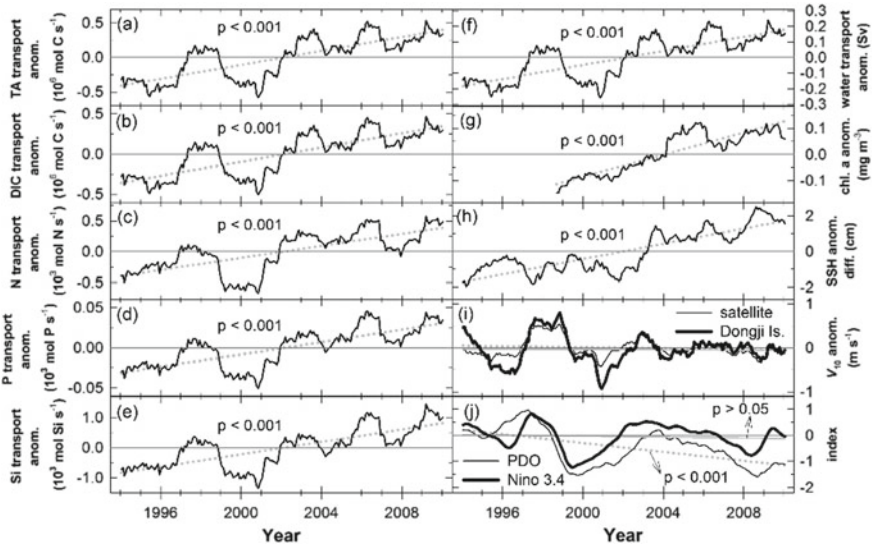

Fig. 12.4 Twenty-four month moving average time series of anomalies and their regression lines in the Taiwan Strait for **a** TA flux, **b** DIC flux, **c** N flux, **d** P flux, **e** Si flux, **f** water flux, **g** satellite chl. a concentration, **h** difference in SSH between southern and northern entrances, **i** wind speed measured by the satellite and at the weather station in the south-north direction at a height of 10 m, and **j** PDO and Niño 3.4 indices. Dashed and solid lines in (**i**) are regression lines from satellite data and weather station data, respectively. Dashed and solid lines in (**j**) are regression lines of PDO and Niño 3.4, respectively (taken from Huang et al. 2019)

prevails. This cold water brings nutrients from the ECS to the SCS (Chen 2003; Naik and Chen 2008; Han et al. 2013).

Figure 12.6a plots the temporal variation of the SST. Unlike in high-latitude seas, where the SST exhibits a large seasonal variation (Chen et al. 2020a, b), in the SCS, the mean SST varies only between about 25 and 30 °C. Also, whereas the temperature from 1998 to 2016 in the high-latitude seas generally increased (0.055 °C/yr for the Bering Sea (Chen et al. 2020a); 0.045 °C/yr for the Okhotsk Sea (Chen et al. 2020b)), that in the SCS exhibited only a statistically insignificant linear increase of 0.12 °C/yr ($p = 0.46$). The quadratic polynomial fit of the SST has a lower p value of 0.14 (better correlation) than the linear fit (Fig. 12.6a). The quadratic fit seems to indicate that the SST initially fell after the strong El Nino year of 1998 when basin-wide warming occurred in the SCS (Wu and Chang 2005), and increased in subsequent years. The mixed layer, however, seems to have become shallower from 1992 to 2000 (Li et al. 2017) consistent with a rise in SST, especially during the strong El Nino years of 1997 and 1998.

Many reports of interannual SST variations in the SCS have been published, but the results vary with the time span considered. He et al. (2017) reported little change in the SST between 1998 and 2010. Giuliani et al. (2019) reported an increase of 0.028 ºC/yr from 1960 to 2011, which is close to that obtained by Bai et al. (2018)

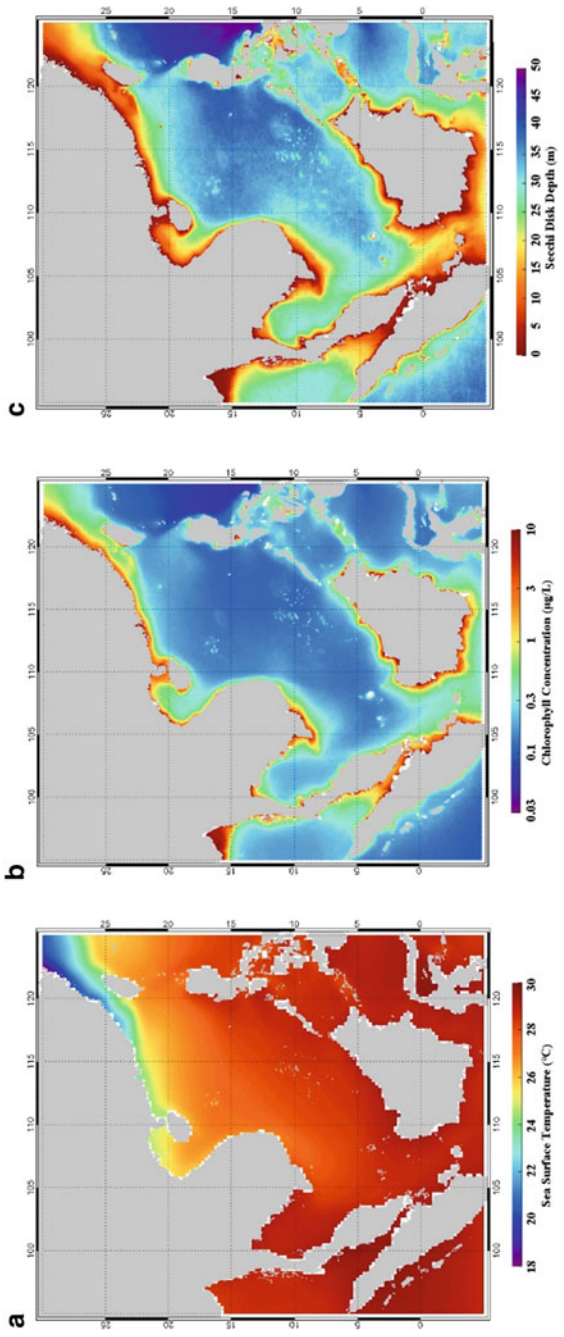

Fig. 12.5 Climatological map of **a** SST, **b** chlorophyll concentration and **c** SDD in the South China Sea

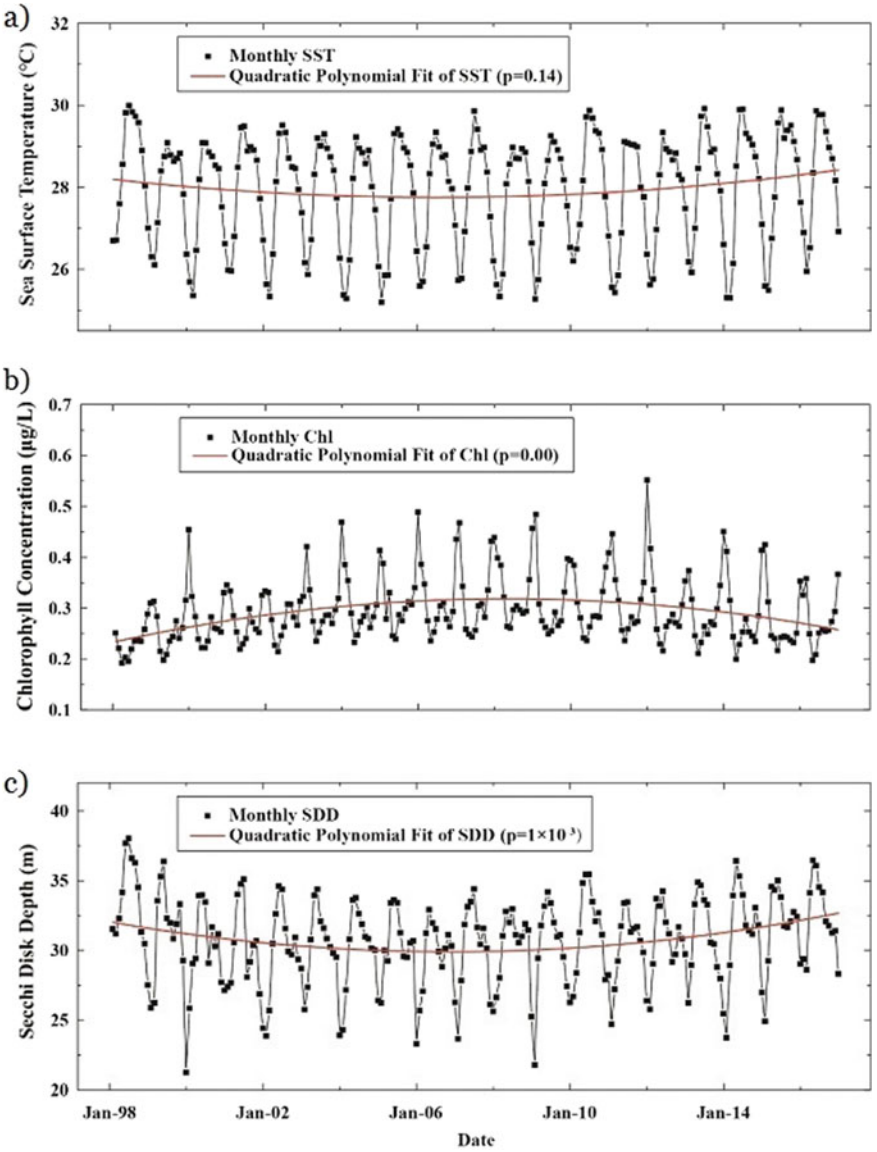

Fig. 12.6 Time series of **a** SST, **b** chlorophyll concentration and **c** SDD in the SCS during 1998–2016

(around 0.03 °C or 0.1%/yr from 2003 to 2014) in low-latitude marginal seas around the Eurasian continent, including the SCS, the Java-Banda Sea, the Bay of Bengal and the Arabian Sea. Chapter 1 noted that higher-latitude marginal seas exhibited larger temperature increases.

Geographically, the region off SE China where the average SST is the lowest of any part of the SCS saw a decrease in the SST, while the warmest regions in the southern SCS saw an increase in the SST. Figure 12.7a demonstrates that the SST in the mid- and southern SCS increased at a significant rate of 0.01–0.02 °C per year over the period 1998–2016. Notably, the SST fell remarkably both off SE China and in the Taiwan Strait, where the chlorophyll concentration significantly increased (Fig. 12.7b). The cooling may suggest strengthening of coastal upwelling, which would have resulted in an increase of surface nutrient supply, favoring the growth of phytoplankton.

12.3 Changing Chlorophyll Concentration

The chlorophyll concentration data for the period 1998–2016 were obtained from the Ocean Colour project of the ESA Climate Change Initiative (CCI) (http://www.esa-oceancolour-cci.org). Details can be found in Chen et al. (2020a).

As expected, because of riverine input of nutrients, entrainment by river plumes, coastal upwelling, and more effective wind and tidal mixing, the coastal regions in the SCS had higher chlorophyll concentrations than more open, deeper waters (Fig. 12.5b; Chen 2008; Chen et al. 2020a, b). In 1998–2016, chlorophyll concentrations rose significantly on the northern shelf of the SCS and off the Indochina Peninsula (Fig. 12.7b). In the Taiwan Strait and in the northern SCS, the chlorophyll concentration generally increased at the rate of 2.5% per year (Fig. 12.7b). Increased anthropogenic nutrient inputs might have contributed to the increase in chlorophyll concentration in these coastal waters. Patches of decreasing chlorophyll concentration formed sporadically in the central basin of the SCS, in which the chlorophyll concentration fell at 1–1.5% per year. Overall, the whole SCS exhibited a very small average annual increase of 0.0012 μg/L ($p = 0.11$) from 1998 to 2016 (Fig. 12.6b). The quadratic polynomial fitting indicates that chlorophyll concentration in the SCS firstly rose and then fell. Figure 12.6b shows an increase from Jan. 1998 to Apr. 2008 and a decrease from Apr. 2008 to Dec. 2016. In contrast, from 1998 to 2016, the chlorophyll concentration increased steadily in the Bering Sea (0.011 μg/L/yr, Chen et al. 2020a) and the Okhotsk Sea (0.01 μg/L/yr, Chen et al. 2020b).

He et al. (2017) reported no apparent change in chlorophyll concentration in the SCS between 1997 and 2010, whereas Palacz et al. (2011) reported an increase of 0.04 μg/L (9%) over that period. The data that were generated by modeling of Li et al. (2015) indicate an increase between 2000 and 2014 although the lead author of that paper, Q. P. Li (personal communication, 12/1/2018) identified no clear trend. They also did not consider lateral transports. Bai et al. (2018), reported a very small rate of increase of <0.001 μg/L per year between 2003 and 2014, in contrast to

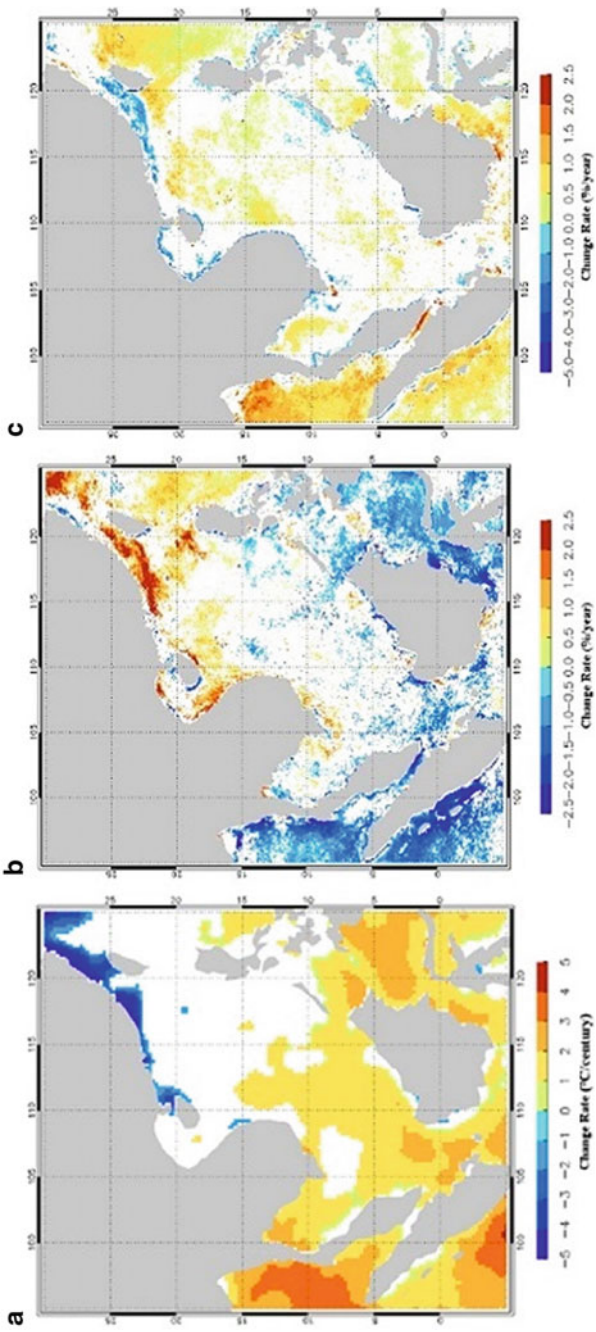

Fig. 12.7 Temporal variations of **a** SST, **b** chlorophyll concentration and **c** SDD in the SCS during 1998–2016 (Only pixels that are associated with significance at $P < 0.1$ are shown in bright colors)

decreases in other tropical marginal seas, such as the Arabian Sea, the Java-Banda Sea, the Red Sea, the Persian Gulf and the Bay of Bengal. In fact, a close look at the interannual variability of chlorophyll concentration in the SCS (Fig. 12.6b) suggests that the concentration increased between 1998 and 2008 but decreased thereafter. As mentioned earlier, 1998 was a strong El Nino year in which the SST was high. The high SST resulted in relatively low-density surface water and a relatively high density gradient. Therefore vertical mixing was less than in other years, so fewer nutrients were pumped to the surface layer, resulting in lower primary productivity, chlorophyll, diatom biomass and biological productivity in general (Lu et al. 2018). Future changes are, however, difficult to predict as a higher SST would impede the upward transport of nutrients whereas riverine input is rising. The physiological responses of many marine organisms, to variables other than nutrient availability, such as those caused by typhoons, eddies, atmospheric deposition and nitrogen fixation, may also change (Li et al. 2015; Wu and Chang 2005; Wong et al. 2002). Notably, oxygen inventories have been increasing in the SCS contrary to most other oceans (Schmidtko et al. 2017; Breitburg et al. 2018). The oxygen inventory increased perhaps because of the decreasing SST (higher oxygen solubility) and enhanced productivity, as revealed by the increasing chlorophyll concentration there. Ito et al. (2017) also reported increasing oxygen concentration between 100 and 700 m.

Interestingly, the collection of particles in sediment traps at 2,000 m and 3,500 m depths in the basin of the SCS indicates that proportions of the particulate organic carbon (POC) and particulate organic nitrogen (PON) increased with time but the POC/PON ratio decreased (Fig. 12.9) probably because of increasing anthropogenic nutrient outflows with the consequence that the chlorophyll concentration off Hong Kong has been increasing since 1990 (Fig. 12.8a). The dissolved oxygen concentration in the bottom layer, however, seems to be falling (Fig. 12.8b), perhaps due to an increase in the decomposition of phytoplankton from 2008 to 2016 (Fig. 12.8; Lui et al. 2018). Intuitively, this finding seems to be inconsistent with the fall in chlorophyll concentration that was observed during the same period. The result is interesting because in the basin of the SCS, lower the net primary productivity corresponds to higher export efficiency (Li et al. 2018). In the SCS, primary productivity correlates positively with chlorophyll concentration (Chen 2005) so the decreasing chlorophyll concentration between 2008 and 2016 reflects a fall in net primary productivity. As a result, the export efficiency increased, resulting in higher proportions of POC and PON in the sediment traps. The increases in the POC and PON percentages are probably not caused by an increase in riverine outflow. A larger amount of terrestrial organic matter would have corresponded to a higher POC/PON ratio but this was not observed (Fig. 12.9c). Notably, the increasing POC percentage that was reported by Lui et al. (2018) covered only a relatively short period from 2008 to 2016. The POC flux (Li et al. 2017) actually seems to have decreased between 1992 and 1999. Multi-decadal data are required to identify any genuine long-term trend.

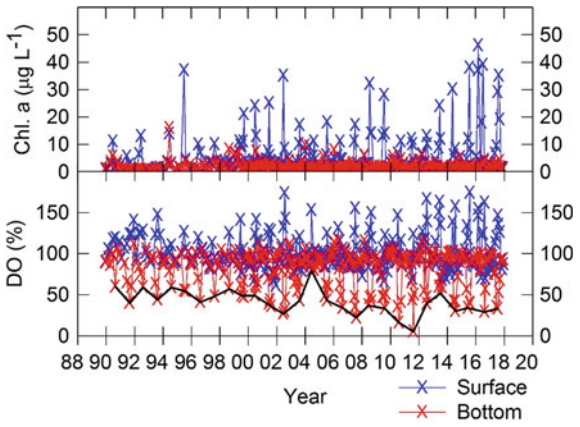

Fig. 12.8 Time series of **a** chlorophyll concentration and **b** dissolved oxygen off Hong Kong (taken from Lui et al. 2020)

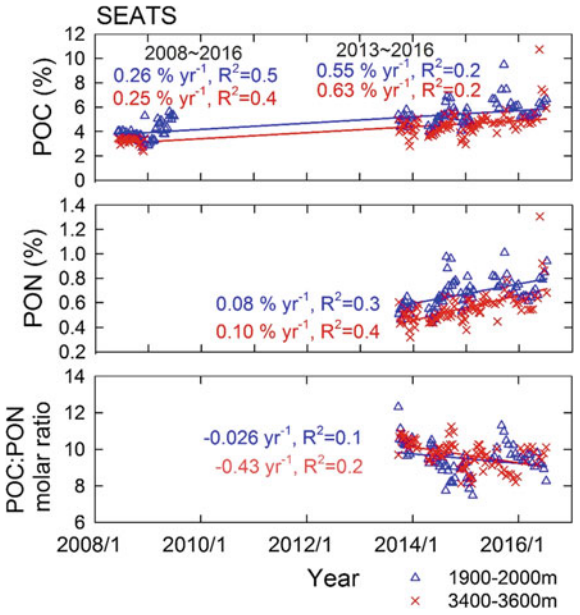

Fig. 12.9 Percentages of **a** POC and **b** PON in sinking particles, and the **c** POC:PON molar ratio at various depths at SEATS between 2008 and 2016. The POC data between 2008/6/10 and 2009/6/30 were taken from Wei et al. 2017. Solid lines and numbers are regression lines, slopes, and coefficient of determination. All regression lines have $p < 0.0001$, apart from that for POC:PON ratio at 2000 m for which $p = 0.04$ (taken from Lui et al. 2018)

12.4 Changing Secchi Disk Depth

The SDD is a good index of water transparency, and pertinent data for the period 1998–2016 were provided by the Globcolour project (http://globcolour.info/). Details can be found in Chen et al. (2020a). Figure 12.5c displays the distribution of the SDD. As expected, the SDD is shallow close to the coast because of the relatively high phytoplankton biomass there, as indicated by the high chlorophyll concentration (Fig. 12.5b), and the large amount of suspended sediment due to river transport.

Mixing by winds and tides in shallow waters also reduces the SDD, which throughout almost the entire SCS increased during the period 1998–2016 (0.35 m/yr, p = 0.35, Fig. 12.7c), showing that the SCS water became more transparent. The fitting revealed that the SDD in the SCS decreased from Jan. 1998 to Nov. 2008 and then increased from Nov. 2008 to Dec. 2016 (Fig. 12.6c). However, the SDD in coastal waters substantially decreased (Fig. 12.7c), especially off the coast of SE China and in the Taiwan Strait, perhaps because of the increase in chlorophyll concentration (Fig. 12.7b).

He et al. (2017) reported a decrease in the SDD in the SCS of about 0.08 m/yr from 1998 to 2010. A close look at the temporal change of the SDD from 1998 to 2016 (Fig. 12.6c) indicates that it decreased from 1998 to about 2008, consistent with the findings of He et al. (2017). The SDD increased after 2008. Bai et al. (2018) recently found that the SDD in all 12 marginal seas around the Eurasian continent increased from 2003 to 2014. They reported a rate of increase of 0.05 m/yr, which is slightly higher than the value obtained herein, which is 0.035 m/yr. The difference between the rates of increasing may be a result of a difference in the study periods. Chen et al. (2020a) reported no significant change in the SDD in the Bering Sea, and Chen et al. (2020b) reported a slight increase in the SDD (0.018 m/yr) in the Okhotsk Sea.

12.5 Conclusions

From 1998 to 2016, the SST in the SCS increased by 0.012 °C/yr, which is much less than the rate of warming of high-latitude oceans. This result is consistent with the generally declining salinity of the surface water of the SCS. The chlorophyll concentration increased at an overall rate of 0.0012 μg/L/yr. The significant increase in chlorophyll concentration occurred mainly on the northern shelf of the SCS and off the Indochina Peninsula. The SDD throughout the SCS increased by 0.035 m/yr in the same period. However, the SST, chlorophyll concentration and SDD in the SCS changed in opposite directions in the two periods 1998–2008 and 2008–2016. In the first period, the SST and SDD decreased while the chlorophyll concentration increased. In the second period, the SST and SDD increased but the chlorophyll concentration decreased. Since in the SCS basin, a lower net primary productivity corresponded to higher export productivity, reduced chlorophyll concentration yielded higher observed percentages of POC and PON that collected in sediment traps. All such changes might have altered the biogeochemical processes in the SCS.

Acknowledgements Preparation of this chapter was supported by the Ministry of Science and Technology (MOST 107-2611-M-110-006 and 107-2611-M-110-021) and the Ministry of Education (Higher Education Sprout Program) of Republic of China. Two anonymous reviewers provided valuable comments which strengthened the manuscript.

References

Bai Y, He XQ, Yu SJ, Chen CTA (2018) Changes in the ecological environment of the marginal seas along the Eurasian Continent from 2003 to 2014. Sustainability 10(3):635. https://dx.doi.org/10.3390/su10030635

Breitburg D, Levin LA, Oschlies A, Gregoire M, Chavez FP, Conley DJ, Garcon V, Gilbert D, Gutierrez D, Isensee K, Jacinto GS, Limburg KE, Montes I, Naqvi SWA, Pitcher GC, Rabalais NN, Roman MR, Rose KA, Seibel BA, Telszewski M, Yasuhara M, Zhang J (2018) Declining oxygen in the global ocean and coastal waters. Science 359:46 (6371), eaam7240

Chai F, Liu GM, Xue HJ, Shi L, Chao Y, Tseng CM, Chou WC, Liu KK (2009) Seasonal and interannual variability of carbon cycle in South China Sea: a three-dimensional physical-biogeochemical modeling study. J Oceanogr 65(5):703–720

Chao SY, Shaw PT, Wu SY (1996a) El Nino modulation of the South China Sea circulation. Prog Oceanogr 38(1):51–93

Chao SY, Shaw PT, Wu SY (1996b) Deep water ventilation in the South China Sea. Deep-Sea Res Pt I 43(4):445–466

Chen CT, Millero FJ (1979) Gradual increase of oceanic CO_2. Nature 277(5693):205–206

Chen CT, Pytkowicz RM (1979) Total CO_2 titration alkalinity oxygen system in the Pacific ocean. Nature 281(5730):362–365

Chen CTA (2003) Rare northward flow in the Taiwan Strait in winter: a note. Cont Shelf Res 23(3–4):387–391

Chen CTA (2008) Buoyancy leads to high productivity of the Changjiang diluted water: a note. Acta Oceanol Sin 27(6):133–140

Chen CTA, Huang MH (1995) Carbonate chemistry and the anthropogenic CO_2 in the South China Sea. Acta Oceanolog Sin 14:47–57

Chen CTA, Huang MH (1996) A mid-depth front separating the South China Sea water and the West Philippine Sea water. J Oceanogr 52:17–25

Chen CTA, Hou WP, Gamo T, Wang SL (2006a) Carbonate-related parameters of subsurface waters in the West Philippine, South China and Sulu Seas. Mar Chem 99(1–4):151–161

Chen CTA, Wang SL, Chou WC, Sheu DD (2006b) Carbonate chemistry and projected future changes in pH and $CaCO_3$ saturation state of the South China Sea. Mar Chem 101(3–4):277–305

Chen CTA, SJ Yu, TH Huang, Y Bai, XQ He (2020a) Changes in temperature, chlorophyll concentration, and Secchi Disk Depth in the Bering Sea from 1998 to 2016. In: Chen CTA, Guo XY (eds) Changing Asia-Pacific marginal seas. Springer International Publishing (in press)

Chen CTA, SJ Yu, TH Huang, Y Bai, XQ He (2020b) Changes in temperature, chlorophyll concentration, and Secchi Disk Depth in the Okhotsk Sea from 1998 to 2016. In: Chen CTA, Guo XY (eds) Changing Asia-Pacific marginal seas. Springer International Publishing (in press)

Chen YLL (2005) Spatial and seasonal variations of nitrate-based new production and primary production in the South China Sea. Deep-Sea Res Pt I 52(2):319–340

Durack PJ, Wijffels SE (2010) Fifty-year trends in global ocean salinities and their relationship to broad-scale warming. J Climate 23(16):4342–4362

Giuliani S, LG. Bellucci, DH Nhon (2019) The coast of Vietnam: present status and future challenges for sustainable development. In: Sheppard C (ed) World seas: an environmental evaluation, 2nd edn, Chapter 19. Academic Press, pp 415–435

Han AQ, Dai MH, Gan JP, Kao SJ, Zhao XZ, Jan S, Li Q, Lin H, Chen CTA, Wang L, Hu JY, Wang LF, Gong F (2013) Inter-shelf nutrient transport from the East China Sea as a major nutrient source supporting winter primary production on the northeast South China Sea shelf. Biogeosciences 10(12):8159–8170

He XQ, Pan DL, Bai Y, Wang TY, Chen CTA, Zhu QK, Hao ZZ, Gong F (2017) Recent changes of global ocean transparency observed by SeaWiFS. Cont Shelf Res 143:159–166

Huang P, Zhang M, Cai M, Ke H, Deng H, Li W (2016) Ventilation time and anthropogenic CO_2 in the South China Sea based on CFC-11 measurements. Deep Sea Res Part I 116:187–199

Huang T-H, Chen C-TA, Lee J, Wu C-R, Wang Y-L, Bai Y, He X, Wang S-L, Kandasamy S, Lou J-Y, Tsuang B-J, Chen H-W, Tseng R-S, Yang YJ (2019) East China Sea increasingly gains limiting nutrient P from South China Sea. Sci Rep 9:5648. https://doi.org/10.1038/s41598-019-42020-4

Ito T, Minobe S, Long MC, Deutsch C (2017) Upper ocean O_2 trends: 1958–2015. Geophys Res Lett 44(9):4214–4223

Li QP, Wang YJ, Dong Y, Gan JP (2015) Modeling long-term change of planktonic ecosystems in the northern South China Sea and the upstream Kuroshio Current. J Geophys Res-Oceans 120(6):3913–3936

Li HL, Wiesner MG, Chen JF, Ling Z, Zhang JJ, Ran LH (2017) Long-term variation of mesopelagic biogenic flux in the central South China Sea: impact of monsoonal seasonality and mesoscale eddy. Deep-Sea Res Pt I 126:62–72

Li T, Bai Y, He XQ, Chen XY, Chen CTA, Tao BY, Pan DL, Zhang X (2018) The relationship between POC export efficiency and primary production: opposite on the Shelf and basin of the northern South China Sea. Sustainability 10(10): 3634. https://doi.org/10.3390/su10103634

Liu Y, Peng ZC, Zhou RJ, Song SH, Liu WG, You CF, Lin YP, Yu KF, Wu CC, Wei GJ, Xie LH, Burr GS, Shen CC (2014) Acceleration of modern acidification in the South China Sea driven by anthropogenic CO_2. Sci Rep 4:5148. https://doi.org/10.1038/srep05148

Lu W, Luo Y, Yan X, Jiang Y (2018) Modeling the contribution of the microbial carbon pump to carbon sequestration in the South China Sea. Sci China Earth Sci 11:1594–1604

Lui HK, Chen CTA (2015) Deducing acidification rates based on short-term time series. Sci Rep 5:11517. https://doi.org/10.1038/srep11517

Lui HK, Chen KY, Chen CTA, Wang BS, Lin HL, Ho SH, Tseng CJ, Yang Y, Chan JW (2018) Physical forcing-driven productivity and sediment flux to the deep basin of northern South China Sea: a decadal time series study. Sustainability 10(4): 971. https://doi.org/10.3390/su10040971

Lui HK, CTA Chen, WP Ho, SJ Yu, JW Chan, Y Bai, XQ He (2020) Transient carbonate chemistry in the expanded Kuroshio region, In: Chen CTA, Guo XY (eds) Changing Asia-Pacific marginal seas. Springer International Publishing (in press)

Naik H, Chen CTA (2008) Biogeochemical cycling in the Taiwan Strait. Estuar Coast Shelf S 78(4):603–612

Nan F, Xue HJ, Chai F, Wang DX, Yu F, Shi MC, Guo PF, Xiu P (2013) Weakening of the Kuroshio Intrusion into the South China Sea over the past two decades. J Climate 26(20):8097–8110

Nan F, Xue HJ, Yu F (2015) Kuroshio intrusion into the South China Sea: a review. Prog Oceanogr 137:314–333

Nan F, Yu F, Xue HJ, Zeng LL, Wang DX, Yang SL, Nguyen KC (2016) Freshening of the upper ocean in the South China Sea since the early 1990s. Deep-Sea Res Pt I 118:20–29

Palacz AP, Xue HJ, Armbrecht C, Zhang CY, Chai F (2011) Seasonal and inter-annual changes in the surface chlorophyll of the South China Sea. J Geophys Res-Oceans 116:C09015. https://doi.org/10.1029/2011jc007064

Qu TD (2000) Upper-layer circulation in the South China Sea. J Phys Oceanogr 30(6):1450–1460

Schmidtko S, Stramma L, Visbeck M (2017) Decline in global oceanic oxygen content during the past five decades. Nature 542(7641):335. https://doi.org/10.1038/nature21399

Wong GTF, SW Chung, FK Shiah, CC Chen, LS Wen, KK Liu (2002) Nitrate anomaly in the upper nutricline in the northern South China Sea-Evidence for nitrogen fixation. Geophys Res Lett 29(23):12-1–12-4

Wei CL, Chia CY, Chou WC, Lee WH (2017) Sinking fluxes of Pb-210 and Po-210 in the deep basin of the northern South China Sea. J Environ Radioactiv 174:45–53

Wu CR, Chang CWJ (2005) Interannual variability of the South China Sea in a data assimilation model. Geophys Res Lett 32:L17611. https://doi.org/10.1029/2005gl023798

Chapter 13
Interdecadal Variations of the Oyashio and Extreme Cold Water Events Near the Japanese Coast from the 1960s to the 2010s

Hiroshi Kuroda, Yuko Toya, Shigeho Kakehi, and Takashi Setou

Abstract This chapter reviews interdecadal variations of the Oyashio from the 1960s to the 2010s and the impacts of the Oyashio on coastal waters with a focus on the Extreme Cold Water Events (ECWEs) that occur during winter–spring near the Japanese coast adjacent to the Oyashio. The southernmost latitude of the First Oyashio Intrusion migrated southward in response to the basin-scale wind stress from the mid-1960s to the mid-1980s, while it changed less interdecadally from the mid-1990 to the mid-2010s. For the latter period, the Oyashio transport/velocity, including the intensity of the Western Subarctic Gyre, decreased interdecadally. Representative ECWEs occurred during winter–spring in 1963, 1974, 1981, 1984, 2006, and 2014. These ECWEs occurred under different conditions during the two periods; the ECWEs in 1963, 1974, 1981, and 1984 were accompanied by extreme southward intrusions of the Oyashio, whereas the ECWEs in 2006 and 2014 were not. The ECWEs in 2006, 2014, 1974, and 1984 occurred concomitantly with an extreme intensification of wind-induced circulation in the Okhotsk Sea that lasted a few months. Hence, the ECWEs could be caused by either or both of extreme southward intrusion of the Oyashio and extreme intensification of wind-induced circulation in the Okhotsk Sea.

H. Kuroda (✉) · Y. Toya
Hokkaido National Fisheries Research Institute, Japan Fisheries Research and Education Agency, Hokkaido 085-0805, Japan
e-mail: kurocan@affrc.go.jp

Y. Toya
e-mail: toya108@affrc.go.jp

S. Kakehi
Tohoku National Fisheries Research Institute, Japan Fisheries Research and Education Agency, Miyagi 985-0001, Japan
e-mail: kakehi@affrc.go.jp

T. Setou
National Research Institute of Fisheries Science, Japan Fisheries Research and Education Agency, Kanagawa, Japan
e-mail: setou@affrc.go.jp

C.-T. A. Chen and X. Guo (eds.), *Changing Asia-Pacific Marginal Seas*, Atmosphere, Earth, Ocean & Space, https://doi.org/10.1007/978-981-15-4886-4_13

Keywords Interdecadal variability · Westerlies · First Oyashio Intrusion · Extreme southward intrusion of the Oyashio (ESIO) · Extreme cold water event (ECWE) · Coastal Oyashio water

13.1 Introduction

The Oyashio and East Kamchatka Current are the western boundary currents of the Western Subarctic Gyre (WSAG) in the North Pacific Ocean (Fig. 13.1). The East Kamchatka Current is renamed the Oyashio south of the Bussol Strait. The Oyashio transports cold, low-salinity, subarctic water that is referred to as Oyashio water. This water is formed by mixing of Okhotsk Sea water with WSAG water around the central and southern regions of the Kuril Islands and Four Islands (Fig. 13.1) (e.g., Ohtani 1989; Yasuda et al. 2002), where there are strong tidal currents (e.g., Nakamura and Awaji 2004; Nakamura et al. 2004; Tanaka et al. 2007). For the intermediate layer

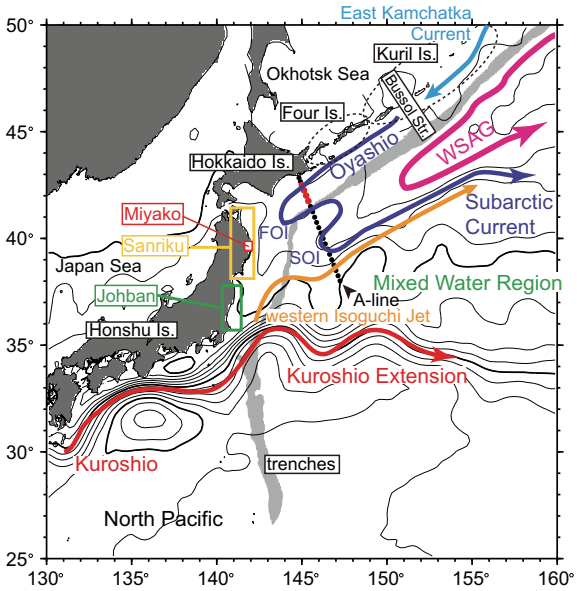

Fig. 13.1 Schematic map of the Kuroshio-Oyashio system. The abbreviations "WSAG", "FOI", ad "SOI" stand for the Western Subarctic Gyre and the First and Second Oyashio Intrusion, respectively. Contour lines with an interval of 10 cm indicate 22-year (1993–2014) mean absolute dynamic topography estimated from daily maps of absolute dynamic topography distributed from the Archiving, Validation and Interpolation of Satellite Oceanographic data group (AVISO) (SSALTO/DUACS 2004). Light gray region denotes water depths >6500 m associated with the Kuril–Kamchatka and Japan trenches. Regular monitoring stations on the A-line are depicted by closed circles (red, Stns. A03–A06; black, Stns. A01, A02, and A07–A21). The Four and Kuril islands are encircled by dashed black lines; the Sanriku and Joban districts facing the Oyashio are surrounded by yellow and green squares, respectively; Miyako is denoted by a red open square

(e.g., potential density of 26.7–26.8 kg m^{-3}), the two origin waters were identified by difference in potential vorticity; low and high potential vorticity for Okhotsk Sea and WSAG water, respectively (Yasuda 1997). The Oyashio flows along the Kuril, Four, Hokkaido, and Honshu islands, intrudes southward into the Kuroshio-Oyashio Mixed Water Region east of Honshu Island and then typically veers to the east with meanders. The first and second meander peaks from nearshore eastward are called the First Oyashio Intrusion (FOI) and the Second Oyashio Intrusion (SOI), respectively (Kawai 1972a). The Oyashio, together with the western Isoguchi Jet, then returns northeastward to the subarctic region along the offshore Oyashio front (Isoguchi et al. 2006; Sugimoto et al. 2014; Wagawa et al. 2014; Kakehi et al. 2017). This northeastward flow is referred to as the Oyashio Return Flow (Kuroda et al. 2017a) or the Subarctic Current (Ohtani 1970; Qiu 2001). Part of the Oyashio water, however, is entrained into the subtropical gyre and does not return to the subarctic region. Instead, it feeds the North Pacific Intermediate Water, which is characterized by a salinity minimum within a potential density range of about 26.6–26.9 kg m^{-3} in the subtropical gyre (e.g., Yasuda et al. 1996; Shimizu et al. 2003; Yasuda 2004). Namely, part of the Oyashio intrusion extends southward beyond the wind-driven gyre boundary, where it is associated with cross-gyre transport (Tatebe and Yasuda 2004).

Oyashio water is gradually modified along its transport pathway by mixing with surrounding water, particularly the warm and high-salinity Kuroshio water, which is spatially distributed such as warm-water streamers, tongues, or clockwise eddies (e.g., Yasuda et al. 1996; Kono 1997; Okuda et al. 2001). The spatiotemporal distribution of the Oyashio water also changes in a very complex manner (e.g., Fig. 13.2) because of the intensity of the Oyashio (e.g., Sekine 1988; Hanawa 1995; Sekine 1999); fluctuations of mesoscale eddies along its pathway (e.g., Mitsudera et al. 2004); interactions of the Oyashio with mesoscale eddies (e.g., Uehara et al. 2004; Kuroda et al. 2015); and the mesoscale eddy structure of Oyashio water itself (Shimizu et al. 2001). To roughly comprehend the Oyashio conditions, the southern boundaries of the Oyashio have been conventionally delineated by an isotherm at a depth of 100 m that differs from month to month (Kawai 1972b) (e.g., Fig. 13.2), a 5 °C isotherm at a depth of 100 m (Yoshida 1992), an isohaline of 33.7 at a depth of 100 m (Kawai 1972a), or an isohaline of 33.6 at depths of 50–200 m (Shimizu et al. 2009). The southernmost positions of the FOI and SOI are geometrically determined from the southern boundary of the Oyashio.

The southernmost position of the FOI, which is basically located on the slope inshore of the Japan and Kuril-Kamchatka trenches (e.g., Ogawa et al. 1987; Murakami 1994; Kuroda et al. 2017a; Fig. 13.2), can seriously affect coastal and shelf environments from Hokkaido through Sanriku to the Joban coast of Japan (e.g., Ishida and Ogawa 1989; Takasugi 1991). A particularly large southward intrusion may occur during the spring in some years. Such an intrusion is referred to as an "Extreme Southward Intrusion of the Oyashio (ESIO)". The alternative designation, "Anomalous Southward Intrusion of the Oyashio", has instead been used in some studies (e.g., Sekine 1988; Sekine 1999). However, in this chapter the designation ESIO is used because the occurrence of such an extremely large southward intrusion

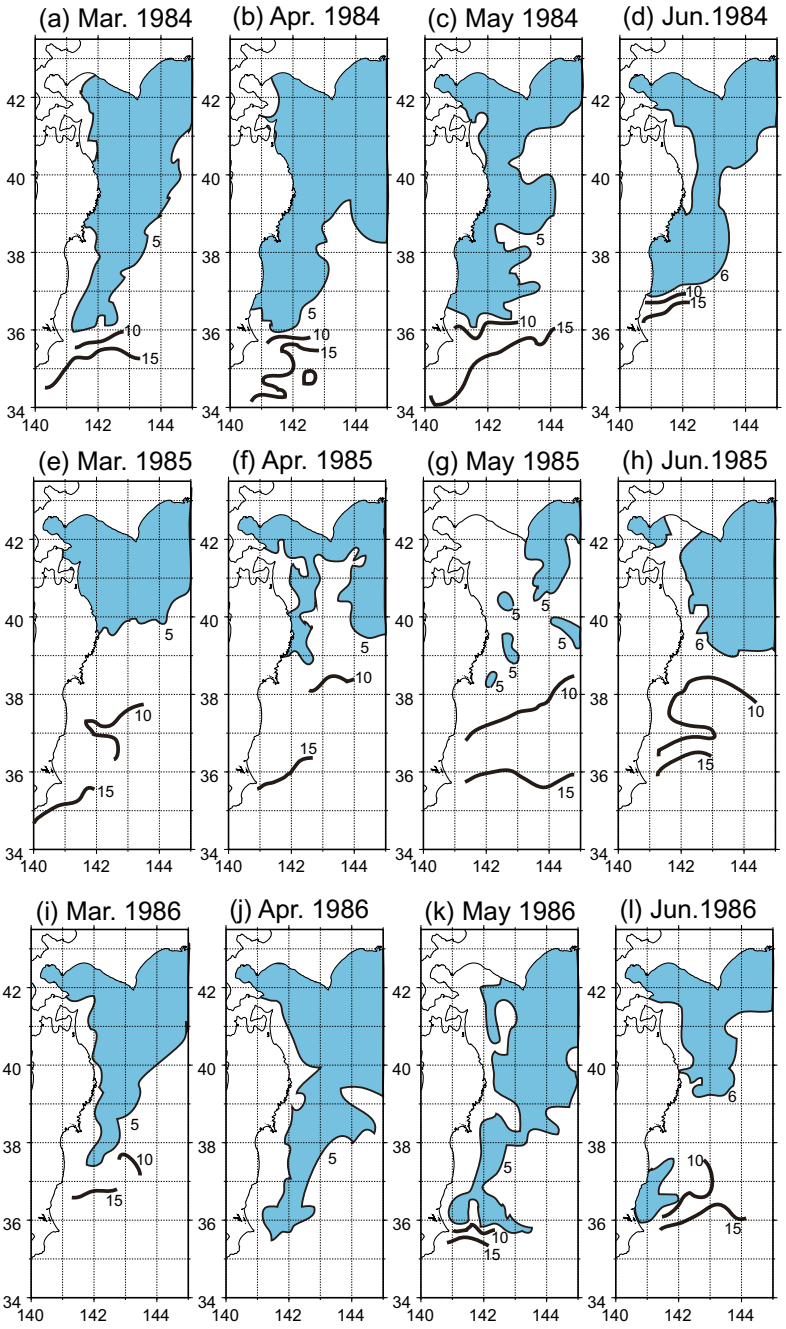

Fig. 13.2 Map of 100-m temperatures in March–June of 1984–1986, redrawn on the basis of Kiso et al. (1987). Light blue areas represent the Oyashio water <5 °C for March–May and <6 °C for June

is not abnormal; rather, it has been historically recorded numerous times at intervals of a few years to about 10 years (Okuda and Mutoh 1986; Ogawa et al. 1987; Ogawa 1989). The most famous ESIO occurred during the spring of 1984 (Fig. 13.2a–d).

When the impacts of the Oyashio water upon coastal and shelf waters along the Japanese coast are described, it should be noted that there is a very cold water during winter–spring near the sea surface that is supplied from the Okhotsk Sea to the North Pacific. There is a coastal boundary current (Hanawa 1984; Kubokawa and Hanawa 1984), inshore of the Oyashio, flowing mainly along the Pacific coast of Hokkaido (Fig. 13.3a, b). This current flows throughout the year on the shelf in the same direction that the Oyashio flows on the slope and is referred to as the Coastal Oyashio (Ogasawara 1987; Rosa et al. 2007, 2009; Kusaka et al. 2016). The seasonality and dynamics of the Coastal Oyashio have been examined in some studies (Kono et al. 2004; Kuroda et al. 2006; Sakamoto et al. 2010), but its interannual variability has received less attention, except for the study of Isoda et al. (1998).

During winter–spring, the Coastal Oyashio on the Pacific shelf off the southeastern coast of Hokkaido transports mainly Coastal Oyashio water that originates in the Okhotsk Sea (Isoda et al. 2003; Kusaka et al. 2009, 2013) (Fig. 13.3a, b). The Coastal Oyashio water is generally defined by a temperature of <2 °C and salinity of <33 (Ohtani 1971). Coastal Oyashio water is clearly colder, fresher, and less dense than Oyashio water at the sea surface. The origins of this water are still controversial and may include sea-ice meltwater, East Sakhalin Current water, and river discharge (Ohtani 1971; Isoda et al. 2003; Oguma et al. 2008; Mizuno et al. 2018). High-resolution modeling with a grid of about 2 km has made it clear that the majority of this water originates in the East Sakhalin Current area in the Okhotsk Sea (e.g., Fig. 13.3a) (Sakamoto et al. 2010; Kuroda et al. 2014). After outflowing from the Okhotsk Sea to the North Pacific, Coastal Oyashio water is transported extensively southward on the shelf–slope adjacent to the Oyashio and may reach the vicinity of the Sanriku coast (e.g., Hanawa and Mitsudera 1987) during winter–spring in years when an Extreme Cold Water Event (ECWE) occurs near the Sanriku-to-Joban coast (Okuda 1986; Okuda and Mutoh 1986; Wagawa et al. 2015). Analyses of historical temperature and salinity profiles (Fig. 13.3c) reveal that Coastal Oyashio water is climatologically distributed near the Sanriku coast during January–March less than 10% of the time. The most famous ECWE occurred during winter–spring 1984, concurrently with the most famous ESIO (Fig. 13.2a–d). That is, Coastal Oyashio water from the Okhotsk Sea spreaded extremely to the south concomitantly with the ESIO, came into contact extensively with the Sanriku-to-Joban coast, and generated the massive ECWE in 1984.

The genesis and possible causes of ECWEs were intensively studied until the 1980s because some studies hypothesized that ocean-atmosphere interactions might relate ECWEs to cold summer weather and result in poor rice harvests and famines in northeastern Japan (e.g., Arakawa 1955; Kondo 1988). Some studies have also related ECWEs to the combined effects of the ESIO and the southward intrusion of very cold sea-ice meltwater (e.g., Coastal Oyashio water) to the Sanriku-to-Joban coast from the Okhotsk Sea (Iida and Katagiri 1974; Akagawa 1980; Okuda 1986). The discharge of large amounts of sea ice or sea-ice meltwater from the Okhotsk

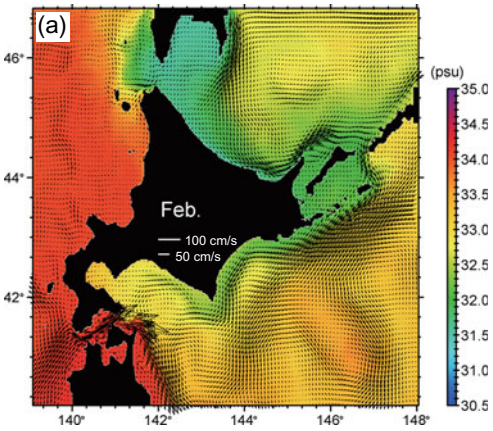
(a)
Feb.
100 cm/s
50 cm/s
(psu)
35.0
34.5
34.0
33.5
33.0
32.5
32.0
31.5
31.0
30.5
46°
44°
42°
140°
142°
144°
146°
148°

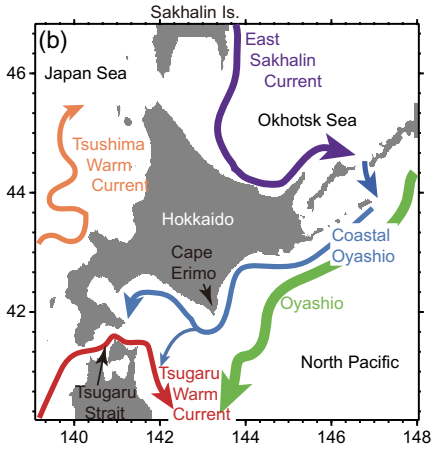
(b)
Sakhalin Is.
Japan Sea
East
Sakhalin
Current
Okhotsk Sea
Tsushima
Warm
Current
Hokkaido
Cape
Erimo
Coastal
Oyashio
Oyashio
North Pacific
Tsugaru
Warm
Current
Tsugaru
Strait
46
44
42
140
142
144
146
148

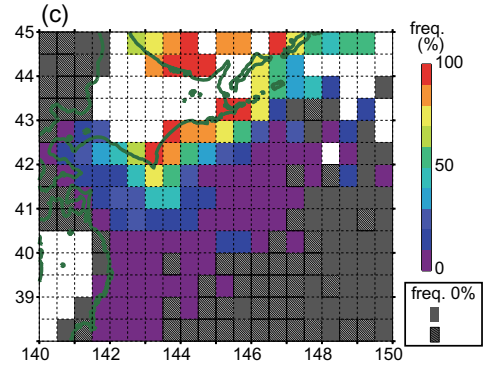
(c)
freq.
(%)
100
50
0
freq. 0%
45
44
43
42
41
40
39
140
142
144
146
148
150

◀**Fig. 13.3** **a** Mean salinities and current velocities in February and **b** schematic view of currents at the sea surface in February. **a** and **b** were based on simulation by a 1/50° ocean model with climatological monthly mean forcings. The diagram is modified from Kuroda et al. (2014), Fisheries Science, 80: 127–138 (license number 4510141259002). **c** Frequency with which the Coastal Oyashio water (temperature <2 °C and salinity <33) appeared in temperature-salinity (TS) profiles for January–March. Historical TS data were collected from the National Oceanographic Data Center (World Ocean Database 2013) and the Japan Oceanographic Data Center (http://www.jodc.go.jp). TS data that were managed by the Hokkaido National Fisheries Research Institute have also been added to the analysis

Sea is thought to be controlled by meteorological conditions in the Far East, such as meanders of westerly winds (Matsukura 1975). Since the 1980s, however, there have been fewer studies of ECWEs, although the quality and quantity of oceanographic data have increased.

This chapter aims to describe the dominant long-term variations, particularly interdecadal variations of the Oyashio from the 1960s to the 2010s, and their impacts on coastal waters along the Sanriku-to-Joban coast, with a focus on the ECWE. Many papers regarding these coastal impacts have been written in Japanese, but there is little information in the international literature. This chapter presents important results from the major studies of the Oyashio and their impacts.

The chapter is organized as follows. Section 13.2 briefly introduces the seasonality and dynamics of the Oyashio, which can be helpful to readers without adequate knowledge of the Oyashio. In Sect. 13.3, the southernmost latitude of the FOI, the basin-scale wind stress curl in the North Pacific that is the major driving force of the Oyashio, and the relationship between them are explained in the context of interdecadal variations. Interdecadal variations of the southernmost position of the FOI corresponded (did not correspond) to interdecadal variations of the basin-scale wind stress curl from the mid-1960s to the mid-1980s (the mid-1990s to the mid-2010s). Interdecadal variations of the Oyashio are therefore summarized separately for the above two periods in Sect. 13.4. Section 13.5 explains impacts of Oyashio variations on coastal and shelf waters, with a special focus on the ECWE. A remarkable point is that ECWEs occurred (did not occur) concurrently with ESIOs in the mid-1960s to mid-1980s (mid-1990s to mid-2010s), and a few factors that may control the ECWE are discussed. Section 13.6 concerns a few important issues that remain to be clarified in future work.

13.2 Seasonality and Dynamics of the Oyashio

Prior to describing the long-term variations of the Oyashio, it is instructive to mention the seasonal variations and dynamics of the Oyashio. The Oyashio exhibits remarkable seasonality with respect to its velocity (Isoguchi et al. 1997), transport (Kono and Kawasaki 1997; Ito et al. 2004; Kuroda et al. 2017a), southward intrusions (Ogawa 1989; Kuroda et al. 2017a), and area of cold water (<5 °C) at a depth

of 100 m (Yoshida 1992). The Oyashio transport off the southeast Hokkaido coast is most intense and weakest in February and November, respectively. These months precede by one month the meridional migration of the southernmost latitude of the FOI and SOI (Kuroda et al. 2017a). The seasonal variations of the Oyashio are also accompanied by analogous variations of the WSAG (Qiu 2002; Isoguchi and Kawamura 2006a). In addition, the altimetry-derived Oyashio velocity exhibits a secondary small local minimum and maximum around April and June, respectively (Isoguchi and Kawamura 2006b), which can also be identified in the Oyashio transport off the Hokkaido coast (see Fig. 8b in Kuroda et al. 2017a). The adjustment of the subarctic ocean to the wind stress curl on the North Pacific by barotropic Rossby waves has been thought to exert a major control on the seasonality of the Oyashio. A different explanation, however, has been proposed by Tatebe and Yasuda (2005a), who have suggested that baroclinic coastal-trapped waves may contribute to seasonal variations of the Oyashio. The adjustment time by coastal-trapped waves is a few months, longer than the adjustment time of at most 6–50 days by barotropic Rossby waves (Sekine 1988; Isoguchi et al. 1997). It should be noted that seasonal adjustments of baroclinic Rossby waves with a period of one year are almost negligible because they become evanescent in the subarctic region north of about 40° N (Qiu et al. 1997).

A controversial topic is whether the Emperor Seamounts at around 170° E influence barotropic Rossby waves and meridional transport of the Oyashio. Qiu (2002) and Isoguchi and Kawamura (2006a) neglected effects of the seamounts on seasonality of the Oyashio and East Kamchatka Current. However, Kono and Kawasaki (1997) have argued that the Emperor Seamounts may block propagation of barotropic Rossby waves and that integration of the wind stress curl from the seamounts to the western boundary of the North Pacific is comparable to the observed Oyashio transport. Ito et al. (2004) and Kuroda et al. (2017a) obtained consistent results using long-term Oyashio transport data generated by combining CTD-derived geostrophic velocities with altimetry data. Nonaka et al. (2008) used an eddy-resolving ocean general circulation model and briefly reported that westward propagating sea surface height anomalies associated with barotropic Rossby waves are sometimes halted or weakened around the seamounts. A simple theoretical study by Wagawa et al. (2010) examined effects of the seamounts on wind-driven seasonal variations of the subarctic gyre. They proposed several possible effects that depend on the timescale of variation. Although some idealizations in their theoretical study need to be validated before their theory can be applied to the actual ocean, it is certain that, apart from the seasonal component of the streamfunction, the time-independent component was free from the seamounts after adjustment of the baroclinic Rossby waves due to establishment of isostacy. The adjustment time was about 20 years, i.e., an interdecadal timescale.

It is noteworthy that Mitsudera et al. (2018) and Miyama et al. (2018) have recently proposed a new framework for the dynamics around the WSAG, including the Oyashio and the western Isoguchi Jet. The largest difference from previous studies is that they focus on baroclinic Rossby wave characteristics over bottom topography. Westward propagation of baroclinic Rossby waves, which many previous studies assumed, is deflected by advection of ambient barotropic flow, particularly along

low seafloor rises around the WSAG. Although these theoretical studies have been limited at this stage to a steady state of the WSAG, it is expected that the theory will be applied to temporal variations of the Oyashio on seasonal, interannual, multi-year, decadal, and interdecadal timescales.

13.3 Basin-Scale Wind Stress and the Southernmost Latitude of the FOI

Wind stress curl is the major force that drives the Oyashio, and features of the interdecadal variations of the basin-scale wind stress in the North Pacific during winter (December–February) are here shown by the North Pacific Index (NPI) (Trenberth and Hurrell 1994) (Fig. 13.4a), Sverdrup transport at 40–44° N integrated from the eastern to the western boundary of the ocean basin (Fig. 13.4b), and the meridional position of the zero-line contour of Sverdrup transport zonally averaged from 146° E–140° W (Fig. 13.4c). According to Sugimoto and Hanawa (2009), the NPI reflects the intensity and longitudinal position of the Aleutian low (AL) and the intensity of the westerlies, which are related to the activity of the Pacific-North American teleconnection pattern. In a strengthening (weakening) phase of the AL, the AL shifts eastward (westward), and the westerlies strengthen (weaken). Sverdrup transport has also been estimated under the assumption that the response of the ocean to wind stress curl is linear and barotropic. In the real ocean, because there is a delay of ocean adjustment via propagation of baroclinic Rossby waves, a concurrent response of the ocean to wind stress curl is not necessarily the dominant response. Nonetheless, examination of Sverdrup transport can facilitate comprehension of the features of basin-scale wind stress curl and wind-driven gyre boundary (e.g., Ishi and Hanawa 2005).

The NPI exhibited relatively high values (i.e., weak AL and westerlies) in the 1960s and decreased gradually from the 1970s to negative values in the mid-1980s (Fig. 13.4a). After being briefly positive around 1990, the NPI increased gradually from the mid-1990s to the mid-2010s. Some studies have regarded the abrupt decrease and increase of the NPI around 1976/1977 and 1988/1989, respectively, as regime shifts (Mantua et al. 1997; Minobe 1999; Hare and Mantua 2000). From the standpoint of interdecadal variations, there were contrasting changes of the NPI between the period from the mid-1960s to the mid-1980s and the period from the mid-1990s to the mid-2010s. These two periods corresponded to intensification and weakening, respectively, of both westerlies and the AL. Moreover, the winter Sverdrup transport at latitudes where the Oyashio is expected to flow increased gradually from the mid-1960s to the mid-1980s and decreased from the mid-1990s to the mid-2010s (Fig. 13.4b). This pattern is consistent with the NPI variation. In addition to the long-term variation of the intensity of the westerlies, the wind-driven gyre boundary migrated gradually southward (northward) from the mid-1960s to the mid-1980s (the mid-1990s to the mid-2010s) (Fig. 13.4c).

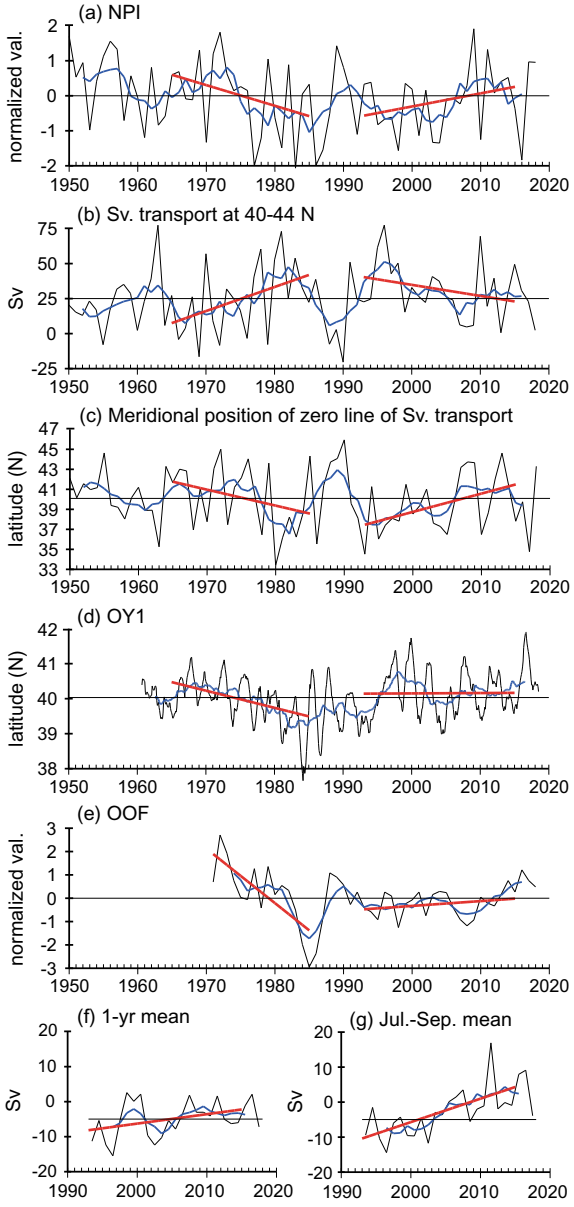
(a) NPI
normalized val.
(b) Sv. transport at 40-44 N
Sv
(c) Meridional position of zero line of Sv. transport
latitude (N)
(d) OY1
latitude (N)
(e) OOF
normalized val.
(f) 1-yr mean
Sv
(g) Jul.-Sep. mean
Sv

◀**Fig. 13.4** Time series of atmospheric/oceanographic data. Thin black (thick blue) line denotes annual (5-year running) mean; bold red line indicates linear regression line for 1965–1985 and 1993–2015; and horizontal line represents the mean value. **a** Winter North Pacific Index (NPI) averaged for December–February and normalized by the mean and standard deviation. The NPI is defined as the sea level pressure averaged within the area of (30°–65° N, 160° E–140° W). **b** Winter Sverdrup transport integrated from the eastern to the western boundary at 40–44° N. **c** Meridional positions of the zero-line contour of the winter Sverdrup transport that were zonally averaged from 146° E to 140° W. Monthly mean sea level pressure and wind stress from the National Centers for Environmental Prediction (NCEP) and National Center for Atmospheric Research (NCAR) (Kalnay et al. 1996) were used for estimating (**a**)–(**c**). **d** Monthly time series of the southernmost latitude of the First Oyashio Intrusion (OY1), which was smoothed with 1-year (thin black line) and 5-year running means (thick blue line). The Oyashio domain was initially determined on a 100-m temperature map as a cold-water area that was surrounded by 5 °C isotherms and distributed continuously off the eastern coast of Hokkaido. The OY1 was specified as a trough of the southern boundary of the Oyashio domain that was the closest to the Japanese coast. Monthly observed maps of 100-m temperature were used for 1960–2014, and roughly 10-day mean maps of 100-m temperature based on the FRA-ROMS (Kuroda et al. 2017b) were employed for 2015–2018. **e** Meridional position of the offshore Oyashio front (OOF), which was defined by 6 °C isotherms at a depth of 100 m in August and detected by the method of Yasuda and Watanabe (1994). The time series of the OOF based on Yasuda (2003) and Kuroda and Yokouchi (2017) was extended from 2015 to 2018 using 100-m temperature based on the FRA-ROMS. **f** Annual mean volume transport through Stn. A03–A06 (red closed circles in Fig. 13.1) on the slope off the southeastern coast of Hokkaido, which was estimated from altimetry-derived daily mean transport integrated from the sea surface to 3100 dbar or the sea bottom (Kuroda et al. 2017a). Negative transport means southwestward transport. **g** Same as (**f**), but means for July–September

It is instructive to compare the NPI time series (Fig. 13.4a) with the corresponding time series of the southernmost latitude of the FOI (hereafter "OY1") (Fig. 13.4d) and the meridional position of the offshore Oyashio front (hereafter "OOF") (Fig. 13.4e). The OY1 was identified from 5 °C isotherm at a depth of 100 m, and the meridional position of the OOF was defined by that of 6 °C isotherm at a depth of 100 m in August that was averaged between 146 and 155° E (Yasuda and Watanabe 1994). The OOF is thus equivalent to the western part of the subarctic front (Yasuda 2003). The legend of Fig. 13.4 provided details of methods to estimate the OY1 and OOF. The correlation coefficient between the NPI and OY1 for 1965–2018 was −0.12 for the annual mean time series and 0.39 for the 5-year running means. The OY1 was highly correlated with the NPI in the mid-1960s to mid-1980s ($r = 0.82$ for the 5-year running means in 1965–1985), whereas it was virtually uncorrelated with the NPI in the mid-1990s to mid-2010s ($r = 0.01$ for 5-year running means in 1993–2015). Similar interdecadal contrasts for their correlation were pointed out by Yasuda (2003). The gradual southward movement of the OY1 corresponded to a decrease of the NPI from the mid-1960s to the mid-1980s, whereas there was little interdecadal movement of the OY1 from the mid-1990s to the mid-2010s, despite the interdecadal increase of the NPI. The OOF also exhibited similar relationships with the OY1; there was a relatively high correlation between the NPI and OOF from the mid-1960s to the mid-1980s ($r = 0.66$ for the 5-year running means in 1973–1985), when the OOF fluctuated meridionally with a large amplitude, but the correlation was weak

from the mid-1990 to the mid-2010s ($r = -0.16$ for the 5-year running means in 1993–2015), when the OOF fluctuated only a little around its mean position. These results indicate that both the OY1 and the OOF responded to the basin-scale wind stress in the North Pacific differently on an interdecadal timescale between the two periods. Characteristics of the Oyashio variations are therefore described separately for these two periods in the following discussion.

It is noteworthy that the OY1 includes dominant interannual variations with a period of about 3 years (Fig. 13.4d). Similar variations with periods of 3–4 years have been identified by Kutsuwada et al. (2008) for temperature at a depth of 10 m off the Sanriku coast, by Takasugi and Yasuda (1994) for the occupancy ratio of Oyashio water area at a depth of 100 m in an area off the Sanriku coast, and by Iwao and Chotoku (1995) for Oyashio water properties at depths of 500–800 m along a monitoring line at 40.5° N. The two possibilities have been proposed for the interannual variations. Some studies have related these periodic variations to the El Niño-Southern Oscillation (Kutsuwada 1990; Takasugi and Yasuda 1994; Iwao and Chotoku 1995), whereas Hanawa (1995) and Nonaka et al. (2008) have pointed out that the wind field in the North Pacific has a similar 3-year periodicity.

13.4 Long-Term Variations of the Oyashio

13.4.1 Mid-1960s to Mid-1980s

The gradual southward movement of the OY1 from the mid-1960s to the mid-1980s (Fig. 13.4d) was first reported by Ogawa (1989). In addition to the OY1 migration, Nakanowatari et al. (2015) have reported that the gradual freshening of North Pacific Intermediate Water over the subtropical gyre from the mid-1960s to the mid-1980s was related to the increase in southward transport of the Oyashio. Hanawa (1995) has related the interdecadal variation of the OY1 to Sverdrup transport (Fig. 13.4b) and has proposed use of multiple linear regression models to predict interannual variations of the OY1. One of the models uses Sverdrup transports with 0- and 3-year time lag as explanatory variables. These transports are associated with combination of barotropic and baroclinic response of the ocean to basin-scale wind stress curl.

Two studies based on ocean modeling have successfully reproduced the gradual southward movement of the OY1 from the mid-1960s to the mid-1980s (Tatebe and Yasuda 2005b; Nonaka et al. 2008), but the proposed mechanisms differed. Using a three-layer eddy-permitting model, Tatebe and Yasuda (2005b) concluded that the OY1 was determined primarily by a baroclinic response of the subarctic ocean to basin-scale wind stress curl. The baroclinic response differed between bi-decadal and penta-decadal variations of wind stress, the resonance of which accounted for climate regime shifts (Minobe 1999). Wind-induced baroclinic Rossby waves with bi-decadal periods were seriously attenuated by anomalies of the local wind stress curl, which changed their signs on the characteristics of the Rossby waves, whereas

baroclinic Rossby waves with penta-decadal periods propagated successfully to the western boundary with less attenuation and resulted in intensification of the Oyashio. They also speculated that small-scale eddies might contribute to weakening of the Rossby waves via nonlinear processes.

In an eddy-resolving ocean general circulation model (Nonaka et al. 2008), the gradual southward migration of the Oyashio from the mid-1960s to the mid-1980s seemed to occur synchronously with the gradual enhancement of the baroclinic velocity of the Oyashio at a depth of 100 m. Lag correlation analyses between the Oyashio velocity and sea level pressure revealed that the enhancement of the baroclinic velocity of the Oyashio tended to occur concomitantly with anomalous upward Ekman pumping in the region around 45° N, 160° E, west of the Emperor Seamounts. This Ekman pumping could impact the strength of the Oyashio through propagation of baroclinic Rossby waves on a time frame of three years.

It is noteworthy that these two modeling studies likely failed to reproduce the northward migration of the OY1 that occurred on a decadal timescale during the 1990s (Fig. 13.4d). Tatebe and Yasuda (2005b) have briefly explained the possible contribution of mesoscale eddies to the observed decadal northward migration of the OY1 during the 1990s. As described in Sect. 13.4.2, mesoscale eddies, particularly clockwise eddies with Kuroshio water, interacted with the Oyashio and affected variations of the OY1.

13.4.2 Mid-1990s to Mid-2010s

Great progress has been made in understanding the dynamics of the Oyashio and WSAG thanks to a series of satellite altimetry missions that began in 1992. Isoguchi and Kawamura (2006a) have accounted for interannual/seasonal variations of the WSAG, including the Oyashio during 1992–2001, primarily based on the barotropic response of the subarctic ocean to basin-scale wind stress curl. Qiu (2002) has used altimetry data to examine variations of the WSAG during 1992–2000 with respect to its intensity and circulation pattern. He has pointed out that the western boundary currents of the WSAG (i.e., the East Kamchatka Current and Oyashio) were more intense in 1997–1999, when the gyre was contracted, than in 1993–1995, when the gyre was elongated. Baroclinic Rossby waves with damping timescales of six years have played important roles in adjustment of the subarctic ocean to basin-scale wind stress. Ito et al. (2004) have reported that an altimetry-based net Oyashio transport that crosses between the Hokkaido coast and the approximate position of the offshore Oyashio front is consistent with the results of Qiu (2002), except for a one-year time lag.

Kuroda et al. (2015) have analyzed long-term (1993–2011) altimetry data and in situ CTD data on the A-line off the southeastern coast of Hokkaido (see Fig. 13.1) on an interdecadal timescale. They estimated the total decrease of Oyashio transport

on the slope during those 19 years to be 8.9 Sverdrups (Sv).[1] Time series of the altimetry-derived Oyashio transport on the slope (i.e., through Stns. A03–A06) was re-estimated here by the method of Kuroda et al. (2017a) and extended to 2017 (Fig. 13.4f). A total decrease of Oyashio transport was apparent and was estimated to be 6.20 Sv for the 23-year period from 1993 to 2015. Kuroda et al. (2015) have proposed two mechanisms that control the interdecadal decrease of the annual mean Oyashio transport: one is adjustment by propagation of baroclinic Rossby waves that have been generated by basin-scale wind stress curl and attenuated by damping with a time constant of six years (i.e., the same mechanism proposed by Qiu 2002); the other is mesoscale clockwise eddies that have stagnated near the Kuril-Kamchatka Trench off the southeastern coast of Hokkaido more frequently after 2008 than before that time.

Kuroda and Yokouchi (2017) have indicated that the distribution of the clockwise eddies and Oyashio transport on the slope off the Hokkaido coast have exhibited remarkable seasonality on an interdecadal timescale. That is, interdecadal decrease in Oyashio transport on the slope were more apparent during summer than winter (e.g., Figure 13.4g). In addition, warm, clockwise eddies approached the Hokkaido coast more frequently during summer than winter after 2010. The clockwise eddies blocked the Oyashio as it flowed along the slope and deflected it offshore upstream of the Hokkaido coast. This deflection has resulted in an interdecadal decrease of the Oyashio transport in recent summers on the slope off the Hokkaido coast (Fig. 13.4g). Kuroda and Yokouchi (2017) focused on a specific clockwise eddy with a lifetime >5 years. The generation area of the eddy was just a little south of the Kuril-Kamchatka Trench, and the trajectory of the eddy center was roughly clockwise around the trench. The generation area and trajectory of the eddy were clearly different from those of typical clockwise eddies with a lifetime >5 years. A so-called Kuroshio Warm Core Ring that approaches the southeastern coast of Hokkaido is typically generated near the Kuroshio Extension and moves northward/northeastward to the Hokkaido coast along the Japan and Kuril-Kamchatka trenches (Kitano 1975; Yasuda et al. 1992; Itoh and Yasuda 2010).

A question arises as to how the Oyashio and a part of the East Kamchatka Current off the Kuril Islands changed from the mid-1990s to the mid-2010s, because seasonality of the interdecadal decrease of the Oyashio transport seems to have been localized on the slope off the Hokkaido coast. Figure 13.5a shows the annual mean of the dynamic topography around the outer edge of the WSAG along the Kuril Islands (148° E, 45° N to 156° E, 50° N) (green line with closed circle) and within the interior of the WSAG (156° E, 45° N to 164° E, 50° N) (blue line with closed circle). Both dynamic topographies increased gradually from the mid-1990s to the mid-2010s on an interdecadal timescale. The rate of increase of the dynamic topography within the interior of the WSAG was approximately constant and about twice as large as the rate of increase along the outer edge. The sea level difference between the outer edge and interior, which is equivalent to the intensity of the western boundary currents at the sea surface, was a maximum around 1997, when the pattern of the WSAG

[1] One Sv $= 10^6$ m^3 s^{-1}.

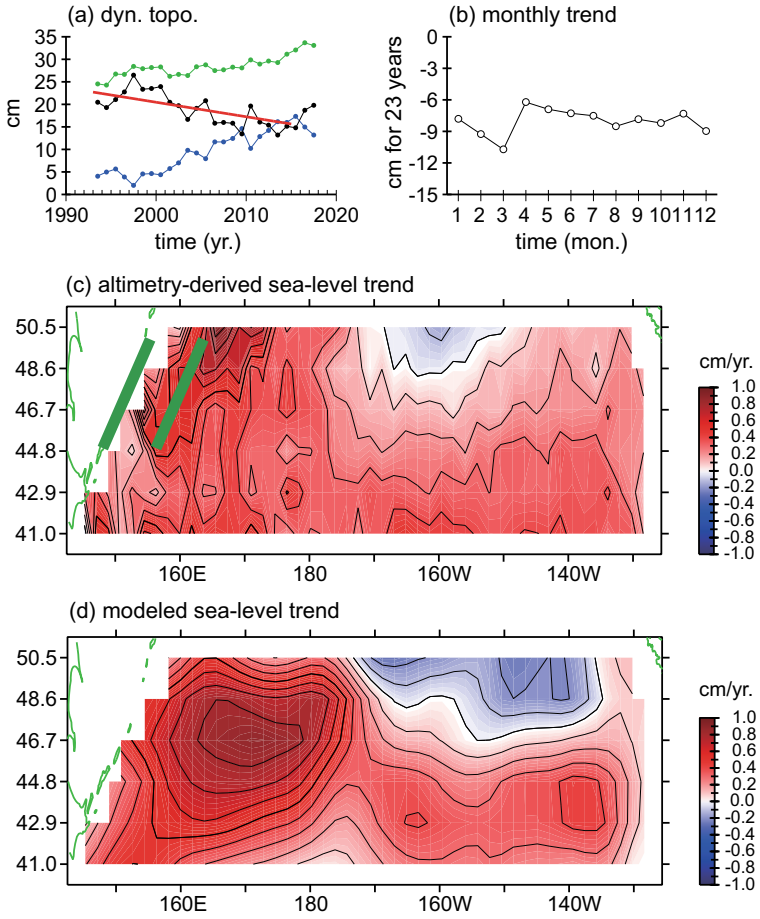

Fig. 13.5 **a** Annual means of absolute dynamic topography around the outer edge of the WSAG (148° E, 45° N to 156° E, 50° N) (green line with closed circles) and within the interior of the WSAG (156° E, 45° N to 164° E, 50° N) (blue line with closed circles). The positions of both the outer edge and interior are depicted by green bold lines in (**c**). Their difference (i.e., the outer edge minus interior) and the linear regression line for 1993–2015 are shown by the black line with closed circles and red thick line, respectively. The absolute dynamic topography was estimated by superimposing an altimetry-derived sea level anomaly (dataset name "two-sat-merged") from AVISO (SSALTO/DUCS 2014) with a mean dynamic topography referred to as "CNES-CLS13 MDT" (Rio et al. 2013). **b** Monthly trends for 1993–2015 of the sea-level difference between the outer edge and interior of the WSAG. **c** Trends of AVISO altimetry-based sea level anomalies for 1993–2015 that were subsampled onto grid points of the reduced-gravity Rossby wave model. **d** Same as (**c**), but for trends of sea level anomaly estimated with a 1.5-layer, reduced-gravity model of Rossby waves with a 6-year dissipation term that was forced by monthly mean wind stress curl based on NCEP/NCAR. The same model settings as in Kuroda et al. (2015) were used, except for propagation speeds of the first-mode baroclinic Rossby waves, which were determined on the basis of Qiu (2002); 1.42 cm s^{-1} for 41.0° N, 1.28 cm s^{-1} for 42.9° N, 1.16 cm s^{-1} for 44.8° N, 1.05 cm s^{-1} for 46.7° N, 0.95 cm s^{-1} for 48.6° N, and 0.86 cm s^{-1} for 50.5° N

was contracted (Qiu 2002). The sea level difference then decreased gradually to the mid-2010s on an interdecadal timescale. The gradual decrease was detected as a significant linear trend during 1993–2015 ($p < 0.05$). The decrease of sea level difference from 1993 to 2015 was apparent not only in summer but also in each month of the year (Fig. 13.5b). The implication is that seasonality of the interdecadal decrease of the western boundary currents along the Kuril Islands was different from that of the Oyashio transport on the slope off the Hokkaido coast (Fig. 13.4g; Kuroda and Yokouchi 2017), and, thus, that the seasonality of the interdecadal variation of the Oyashio localized off the Hokkaido coast (Fig. 13.4g) is due mainly to the clockwise mesoscale eddies that approach the Hokkaido coast rather than to basin-scale variations of the WSAG.

In Fig. 13.5c and d, maps of the linear trend of sea level during 1993–2015 are compared between altimetry observations and the reduced-gravity model of Rossby waves forced by monthly wind stress curl. The same approach was used by Kuroda et al. (2015), except for the propagation speeds of the baroclinic Rossby waves. In Fig. 13.5c, rates of observed sea level increase >0.5 cm/year around the WSAG west of 170° W, particularly around the center of the WSAG, indicated an interdecadal weakening of the WSAG during 1993–2015. In contrast, sea level decreased to the northeast of the WSAG. The spatial correlation coefficient of 0.61 between the observed and modeled linear trends suggests that, to first-order approximation, the model of baroclinic Rossby waves is valid, although the model overestimated both the increase and decrease of sea level. Some discrepancies between the observed and modeled trends (e.g., their difference in spatial position of the maximum sea level rises) might be related to deflection of propagation of baroclinic Rossby waves by ambient barotropic flows (Mitsudera et al. 2018). At any rate, the interdecadal decreases of the Oyashio and WSAG from the mid-1990s to the mid-2010s could be accounted for mainly by a baroclinic response of the subarctic ocean to basin-scale wind stress curl. It should be emphasized, in conclusion, that the OY1 hardly seemed to respond to basin-scale wind stress curl from the mid-1990s to the mid-2010s (Fig. 13.4a–d), but the Oyashio velocity and transport, including the intensity of the WSAG, responded to this wind stress curl (Fig. 13.5).

13.5 Impacts of the Oyashio on Coastal Waters

In this section we focus on ECWEs as an example of the impact of Oyashio variations on the coastal and shelf water. As described in Sect. 13.3, the OY1 responded to basin-scale wind stress curl differently from the mid-1960s to the mid-1980s versus the mid-1990s to the mid-2010s. Likewise, ECWEs occurred under different OY1 conditions during the two periods (vide infra); ECWEs occurred (did not occur) concomitantly with the ESIOs during the mid-1960s to the mid-1980s (the mid-1990s to the mid-2010s). This is partly because the ESIOs occurred in the mid-1960s to the mid-1980s more frequently than in the mid-1990s to the mid-2010s.

After 1960, a typical ECWE occurred near the Sanriku coast and in some cases expanded to the Joban coast during winter–spring in 1963, 1974, 1981, 1984, and 2006 (Iida and Katagiri 1974; Matsukura 1975; Mutoh 1975; Okuda 1986; Okuda and Mutoh 1986; Ohtani 1987; Wagawa et al. 2015). The year 2014 has also been added to the representative ECWE years in this chapter for reasons that will be explained later. It should be borne in mind that representative ECWE years have not been defined by an objective criterion but rather have been recorded historically as winter–spring events when there was especially serious damage to the fisheries near the Sanriku-to-Joban coast. This pattern of recorded ECWE years resembles that of cold summers that were determined based on poor rice harvests and famines, as pointed out by Tomosada (1986). In addition, it is difficult to determine an ECWE by using a single criterion based on a temperature mean and standard deviation (hereafter "SD"), because ECWEs have occurred during both cold and warm temperature regimes. There was definitely a cold (warm) regime before (after) 1990 near the Sanriku coast (Fig. 13.6a). For example, if a general threshold of an extreme event, namely 2 SD below the mean sea surface temperature (SST) from 1965–2018 (left-side axis in Fig. 13.6a) is used as the criterion of an ECWE, then the SST in 2014 at Miyako on the Sanriku coast is excluded from the ECWEs. In contrast, if 2 SD below the mean SST during the warm regime of 1990–2018 is used as the criterion (not shown), the minimum monthly SST at Miyako during January–May of 2014 is 2.07 SD below the mean and hence satisfies the criterion, in which case the winter–spring of 2014 could be regarded as a representative ECWE year. Generally, spring 2014 is known to have been extremely cold during a warm regime; during 2014 sea ice that escaped from the Okhotsk Sea reached further south in the North Pacific during April than during any other year since 1971 (SDMO-JMA 2014).

The normalized minimum value of the OY1 during January–May exhibited large negative values <-2 in 1963, 1974, 1977, 1981, 1984, 1986, and 2010 (blue bar in Fig. 13.6b). This study defines these seven years when the ESIOs occurred. Namely, the ESIOs occurred during the mid-1960s to the mid-1980s more frequently than during the mid-1990s to the mid-2010s. The defined years of the ESIO are not identical to those by Okuda and Mutoh (1986) because of some differences in analysis period and definition, but the ESIOs in 1963, 1974, 1981 and 1984 are consistent for the analyzed period of 1960–1984. In addition, note that the winter Sverdrup transport at 40–44° N (Fig. 13.4b) did not have a local maximum with a relatively large value (>50 Sv) for 1974, 1977, 1984, and 1986, when the ESIOs occurred (Fig. 13.6b). This fact suggested that the ESIOs were not necessarily caused by barotropic response of the subarctic ocean to basin-scale wind stress curl.

Previous studies have suggested two factors that may control the ECWE: the OY1 and the Far Eastern Zonal Index (FEZI). The FEZI is equated to the difference of the geopotential height anomaly on the 500-hPa surface between 40° N and 60° N and zonally averaged from 90° E to 170° E. This index is generally used as a metric of the condition of mid-latitude westerlies (Kawamura 1984). A low value of the index signifies that the westerlies are meandering. When the FEZI is low, a low-pressure system tends to frequently appear around the Kuril Islands, which are south of its normal location, and brings northerly winds in the Okhotsk Sea (Matsukura

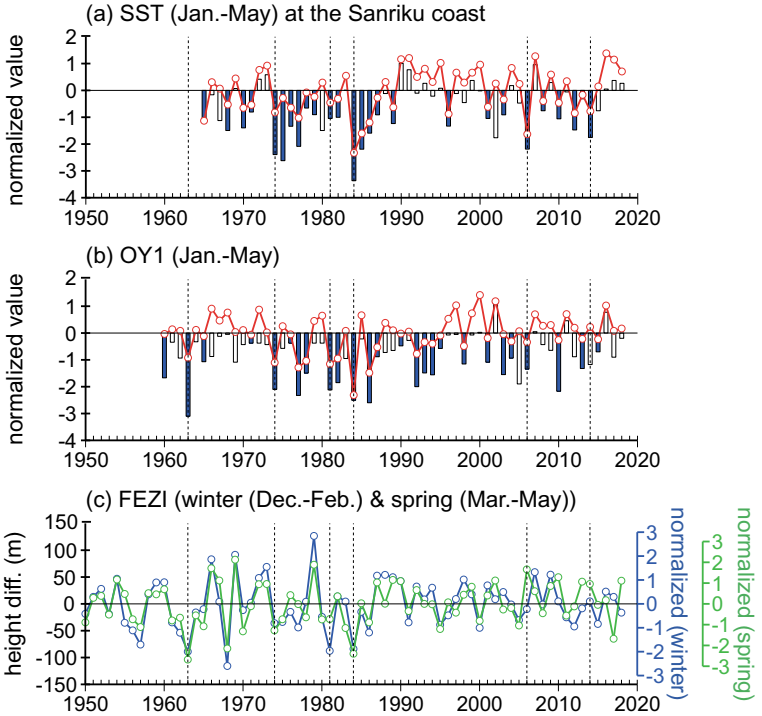

Fig. 13.6 **a** Sea surface temperatures (SSTs) at Miyako on the Sanriku coast (the location is shown in Fig. 13.1) averaged over January–May in each year (red line with open circles). Bar chart denotes the minimum monthly value of SST between January and May in each year normalized by the monthly mean and standard deviation. When the SST averaged for January–May was negative—associated with a winter–spring colder than the normal year—the color of the bar is blue. Monthly mean SST data for 1965–2006 were derived from CMDC (1965–2006). For 2007–2018, the monthly mean SST at Miyako was estimated by linear regression models (Miyako versus Yamada Bay or Miyako versus Noda Bay) based on SSTs recorded in 1994–2018 at Yamada and Noda Bay by the Iwate Fisheries Technology Center (SST data were downloaded from the website http://www.suigi.pref.iwate.jp/). **b** Same as (**a**), but for the southernmost latitude of the FOI (i.e., OY1) based on the same data as in Fig. 13.4d. **c** FEZI averaged over the winter (December–February; blue line with open circles) and spring (March–May; green line with open circles). The FEZI was estimated from the geopotential height at 500 h Pa based on the NCEP/NCAR (Kalnay et al. 1996). Vertical thin dashed lines in (**a**)–(**c**) represent occurrences of representative ECWEs in 1963, 1974, 1981, 1984, 2006, and 2014

1975; Akagawa 1980). These winds tend to force sea ice to actively flow out from the Okhotsk Sea to the North Pacific. Akagawa (1980) has suggested that for the decade of 1965–1975, a low (high) FEZI corresponded to a high (low) frequency of occurrence of water with a salinity <33, associated with Coastal Oyashio water, during March–April in the North Pacific off the southeastern Hokkaido coast.

Figure 13.6c shows winter and spring FEZIs, which fluctuated less after than before the mid-1980s. The ECWEs in 1963, 1974, 1981, and 1984 corresponded

to low FEZIs, including some local minima (Fig. 13.6c). In contrast, the ECWEs in 2006 and 2014 did not. Moreover, the ECWEs in 1963, 1974, 1981, and 1984 corresponded to large southward migrations of the FOI (Fig. 13.6b). The ECWEs before the mid-1980s therefore occurred concurrently with the ESIO during a time of low FEZIs, as suggested by Matsukura (1975) and Akagawa (1980). The ECWEs in 2006 and 2014, however, did not correspond to ESIOs and low FEZIs (Fig. 13.6c). In other words, the ECWEs occurred under different conditions from the mid-1960s to the mid-1980s versus the mid-1990s to the mid-2010s. The implication is that factors other than the OY1 and FEZI may be needed to explain the occurrence of ECWEs after the mid-1990s.

Kuroda et al. (2018) have reported that the volume transport of the source water for the Coastal Oyashio water along the east Sakhalin coast may have been a useful indicator of the occurrence of the ECWE near the Sanriku coast in 2006. The long-term volume transport was estimated as follows. The source water in the Okhotsk Sea was defined by the same criterion as the Coastal Oyashio water in the North Pacific (i.e., temperature <2 °C and salinity <33) (e.g., Figure 13.3c). The transport of the source water across a zonal section at 46° N between the eastern coast of Sakhalin Island and 145° E was estimated by using daily mean reanalysis data from the operational ocean forecasts of the Fisheries Research and Education Agency Regional Ocean Modeling System (FRA-ROMS) during 2003–2011 (Kuroda et al. 2017b). The important point is that the modeled transport in October–April was determined mainly by barotropic response to the wind stress in the Okhotsk Sea because the model temperature and salinity in the Okhotsk Sea were restored to the monthly climatology on a 30-day timescale instead of being coupled with a sea-ice model in the FRA-ROMS (Kuroda et al. 2013). The volume transport across the 46° N section was highly correlated with Ekman transport estimated from alongshore wind stress and integrated in a counterclockwise direction along the coastline from the northern coast of the Okhotsk Sea to 46° N. This correlation indicates barotropic dynamics of arrested topographic wave, that is, adjustment by shelf waves (Csanady 1978; Simizu and Ohshima 2002). Dominance of the barotropic response in the Okhotsk Sea is consistent with results of Nakanowatari and Ohshima (2014) (see Chap. 3). The volume transports from October to April of 1958–2018 were generated from the JRA55 wind stress data (Kobayashi et al. 2015) by using linear regression models to relate the volume transport across the 46° N section based on the FRA-ROMS (objective variable) and the integrated Ekman transport based on wind stress data 3.25 days before (explanatory variable) for individual months from October to April. The legend of Fig. 13.7 provides details of the regression models.

The generated volume transports were integrated from 1 October of each year and normalized by the climatological mean and SD for each day (Fig. 13.7). For 1974, 1984, 2006, and 2014, the integrated transport exceeded the mean plus 1.65 SD (equivalent to the argument of the normal distribution function below which the integrated probability is 0.90) for several months during January–April. This result enables us to expect that in the winter–spring of those four years, a large amount of the source water for the Coastal Oyashio water that had been transported southward along the Sakhalin coast was discharged to the North Pacific and transported to the

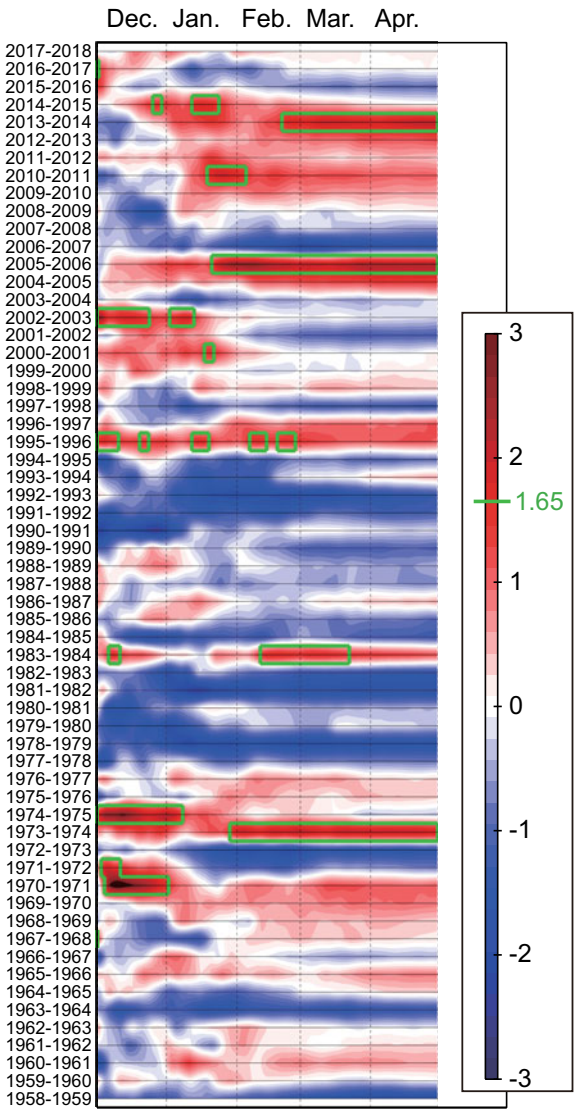

Fig. 13.7 Volume transport of source water for Coastal Oyashio water across the 46° N section between the eastern coast of Sakhalin Island and 148° E, which was estimated from the 6-hourly wind stress of JRA55 using a monthly linear regression model. The data were smoothed with a 5-day running mean, integrated from 1 October, and normalized using the mean and standard deviation estimated in 1958–2018 for each day. Relatively large positive anomalies >1.65 are surrounded by green bold boxes. In the monthly regression model, a linear equation of the form $Y = a_i X + b_i$ was used, where Y is the volume transport, X is the Ekman transport based on the JRA55 along-shelf wind stress 3.5 days prior to Y, which was integrated counterclockwise along the coastline from the northern coast of the Okhotsk Sea to 46° N. The subscript i is month, and a_i and b_i are a pair of coefficients for each month; $a_{10} = 0.109$, $b_{10} = 0.0514$, $a_{11} = 0.185$, $b_{11} = 0.0565$, $a_{12} = 0.658$, $b_{12} = 0.173$, $a_1 = 1.129$, $b_1 = 0.795$, $a_2 = 1.231$, $b_2 = 0.764$, $a_3 = 0.826$, $b_3 = 0.388$, and $a_4 = 0.532$, $b_4 = -0.0293$. The coefficient of determination and root-mean-squared error were 0.799 and 0.487 Sv, respectively, for October–April in 2003–2011 between the 5-day running mean of volume transports based on the FRA-ROMS and statistically estimated from the JRA55 wind stress

vicinity of the Sanriku coast, where this Coastal Oyashio water caused the ECWEs (Okuda 1986; Okuda and Mutoh 1986; Wagawa et al. 2015). The ECWEs of 2006 and 2014 were therefore generated mainly by extreme intensification for a few months of the wind-driven circulation in the Okhotsk Sea from winter to spring, even though an ESIO did not occur. Interestingly, the ECWEs in 1974 and 1984 were generated by a combination of an ESIO during a time of low FEZI and an extreme intensification for a few months of the wind-driven circulation in the Okhotsk Sea.

It is noteworthy that a low FEZI, ESIO, and a high integrated transport of the source water was not necessarily limited to the ECWE years (Figs. 13.6 and 13.7). The implication is that some factors that were not represented by the three indices could prevent occurrence of an ECWE. For instance, the ESIO that occurred during the winter–spring of 1986 was comparable to the ESIO that accompanied the ECWE in 1984 (Fig. 13.6b), but an ECWE did not occur in 1986. The explanation for this difference is mainly that the contact between the cold water and the Sanriku-to-Joban coast was less extensive in 1986 (Fig. 13.2i–l). An important factor in preventing contact of the cold water with the Sanriku-to-Joban coast is the spread of warm water masses such as the Tsugaru Warm Current water and Kuroshio water in the vicinity of the Sanriku-to-Joban coast. Okuda and Mutoh (1986) have reported that the spatial coverage of the two warm water masses was small during the period of the ECWE in 1984. Coastal sea level differences across the Tsugaru Strait (Ohtani 1987) also suggest that the Tsugaru Warm Current through the strait weakened during the winter–spring of 1984, mainly because of a depression of sea level in the Japan Sea caused by severe winter cooling in 1984. The Tsugaru Warm Current at that time might also weaken through adjustment that is initiated by high sea levels at the shelf of the Soya Strait (Kida et al. 2016), which were determined by dynamics of arrested topographic wave in this study. Additional indices are therefore expected to improve understanding and prediction of the occurrence of ECWEs. Nevertheless, it is not surprising that the FEZI, ESIO, and integrated transport of the source water roughly explain the occurrence of typical ECWEs.

13.6 Future Perspectives

This chapter has provided an overview of the interdecadal variations of the Oyashio from the 1960s to the 2010s and the influences of the Oyashio on coastal and shelf waters, with a special focus on the ECWE in winter–spring. The OY1 responded (did not seem to respond) interdecadally to the basin-scale wind stress curl in the North Pacific in the mid-1960s to the mid-1980s (the mid-1990s to the mid-2010s). Unlike the OY1, the transport and velocity of the Oyashio, including the intensity of the WSAG, decreased interdecadally and responded to the basin-scale wind stress curl during the latter period. A specific cause and the dynamical mechanism for the discrepancy between the behavior of the Oyashio velocity/transport and the OY1 in the mid-1990s to the mid-2010s have not been clarified, although mesoscale eddies seemed to affect them. Moreover, to clarify these points might give a clue to reveal

why the ESIOs occurred during the mid-1990s to the mid-2010s less frequently than during the mid-1960s to the mid-1980s.

It should also be kept in mind that one of the clockwise eddies with a lifetime >5 years that stagnated off the Hokkaido coast after 2010 exhibited a characteristic clockwise trajectory around the Kuril-Kamchatka Trench. This eddy changed seasonally in intensity through eddy split/coalescence processes and interacted with the Oyashio off the Hokkaido coast (Kuroda and Yokouchi 2017). It is important to note that the eddy trajectory seemed to be along an eddy-driven barotropic flow around a low ocean-floor rise just south of the trench (Mitsudera et al. 2018). The implication is that the eddy trajectory might be affected by the barotropic flow around the low ocean-floor rise. Likewise, if baroclinic Rossby waves are deflected by ambient barotropic flows around the WSAG, as suggested by recent advances in understanding of their dynamics, the baroclinic response of the subarctic ocean to the basin-scale wind stress curl under ambient barotropic flows should be meticulously examined. There is now a need to apply these recent advances to verify/revise our understanding of long-term variations of the Oyashio as well as to elucidate the dynamical linkage between the OY1 and Oyashio velocity/transport in the mid-1990s to mid-2010s.

This chapter has focused only on the Okhotsk Sea water near the sea surface (i.e., the Coastal Oyashio water). That water causes the ECWEs near the Sanriku-to-Joban coast. In contrast, this chapter neglected influences of the Okhotsk Sea and Okhotsk Sea water on long-term variations of the Oyashio, although many studies have pointed out the importance of these influences. For example, Tatebe and Yasuda (2004) have indicated that upward diapycnal transport from the deep to intermediate layer along the Kuril Islands, which is associated with strong tidal mixing, is an important factor in determining the OY1 and cross-gyre transport. Likewise, Nakamura et al. (2006) have indicated that the tidal mixing there makes the intermediate layer deeper and thicker, and the thickening and deepening strengthen the Oyashio, which crosses over the zero-line contour of climatological Sverdrup transport into the subtropical gyre. In recent years, moreover, many studies have focused on the influences of the astronomical lunar 18.6-year tidal cycle via diurnal tidal mixing on water properties in the intermediate layer (e.g., Osafune and Yasuda 2006, 2012). An important issue is how oceanographers can precisely evaluate effects of the Okhotsk Sea and its water masses on the Oyashio transport/velocity/intrusion on an interdecadal timescale. A combination of continued ocean monitoring and coupled ice-ocean modeling, such as in Nakanowatari et al. (2015), will hopefully provide a clue.

Acknowledgments This work was supported by a Grant-in-Aid for Scientific Research KAKENHI (A) (17H00775) from the Japan Society for the Promotion of Science. We would like to thank editors, Dr. Chen-Tung Arthur and Dr. Guo Xinyu for giving us opportunity of summarizing this manuscript. Thanks are extended to reviewers for many constructive comments.

References

Arakawa H (1955) Meteorological conditions of the great famines in the last half of the TOKUGAWA period, Japan. Pap Meteorol Geophys 6:101–115. https://doi.org/10.2467/mripapers1950.6.2_101

Akagawa M (1980) Relations between pack-ice in the Okhotsk Sea and oceanographic conditions off Hokkaido and Tohoku distinct. Umi to Sora 55:169–181 (in Japanese with English abstract)

CMDC [Coastal Movement Data Center]: Annual Report of Tidal Data (in Japanese) (1965–2006)

Csanady GT (1978) The arrested topographic wave. J Phys Oceanogr 8:47–62. https://doi.org/10.1175/1520-0485(1978)008%3c0047:TATW%3e2.0.CO;2

Hanawa K (1984) Coastal boundary current. Bull Coast Oceanogr 22:67–82 (in Japanese)

Hanawa K, Mitsudera H (1987) Variations of water system distribution in the Sanriku coast area. J Oceanogr Soc Japan 42:435–446. https://doi.org/10.1007/BF02110194

Hanawa K (1995) Southward penetration of the Oyashio water system and the wintertime condition of midlatitude westerlies over the North Pacific. Bull Hokkaido Nat Fish Res Inst 59:103–120

Hare SR, Mantua NJ (2000) Empirical evidence for North Pacific regime shifts 1977 and 1989. Prog Oceanogr 47:103–145. https://doi.org/10.1016/S0079-6611(00)00033-1

Iida H, Katagiri K (1974) Abnormal spreading of cold water along the east coast of Honshu Island in February, 1974. The Oceanogr Mag 26:41–47

Ishi Y, Hanawa K (2005) Large-scale variabilities of wintertime wind stress curl field in the North Pacific and their relation to atmospheric teleconnection pattern. Geophys Res Lett 32:L10607. https://doi.org/10.1029/2004GL022330

Ishida T, Ogawa Y (1989) Hydrographic influences of the first Oyashio Intrusion on temperature fields in the Pacific waters along the Sanriku coast. Bull Tohoku Reg Fish Res Lab 51:183–190 (in Japanese with English abstract)

Isoda Y, Shimizu M, Ueoka A, Matsuo Y, Ohtani K, Nakatani T (1998) Interannual variations of oceanic conditions related to the walleye pollock population around the Pacific Sea area. South of Hokkaido. Bull Japan Soc Fish Oceanogr 62:1–11 (in Japanese with English abstract)

Isoda Y, Kuroda H, Myousyo T, Honda S (2003) Hydrographic feature of Coastal Oyashio and its seasonal variation. Bull Coast Oceanogr 41:5–12 (in Japanese with English abstract)

Isoguchi O, Kawamura H, Kono T (1997) A study on wind-driven circulation in the subarctic North Pacific using TOPEX/POSEIDON altimeter data. J Geophys Res 102:12457–12468. https://doi.org/10.1029/97JC00447

Isoguchi O, Kawamura H (2006a) Seasonal to interannual variations of the western boundary current of the subarctic North Pacific by a combination of the altimeter and tide gauge sea levels. J Geophys Res 111(C4). https://doi.org/10.1029/2005jc003080

Isoguchi O, Kawamura H (2006b) Oyashio seasonal intensification and its effect on subsurface temperature variation off the Sanriku coast. J Geophys Res 111:C10006. https://doi.org/10.1029/2006JC003628

Isoguchi O, Kawamura H, Oka E (2006) Quasi-stationary jets transporting surface warm waters across the transition zone between the subtropical and the subarctic gyres in the North Pacific. J Geophys Res 111:C10003. https://doi.org/10.1029/2005JC003402

Ito S, Uehara K, Miyao T, Miyake H, Yasuda I, Watanabe T, Shimizu Y (2004) Characteristics of SSH anomaly based on TOPEX/POSEIDON altimeter and in situ measured velocity and transport of Oyashio on OICE. J Oceanogr 60:425–437. https://doi.org/10.1023/B:JOCE.0000038059.54334.6b

Itoh S, Yasuda I (2010) Characteristics of mesoscale eddies in the Kuroshio-Oyashio Extension region detected from the distribution of the sea surface height anomaly. J Phys Oceanogr 40:1018–1034. https://doi.org/10.1175/2009JPO4265.1

Iwao T, Chotoku H (1995) Long term trends and ENSO events-related variability of the oceanic conditions on the vertical profile along 41°30'N in the sea south of Hokkaido. Umi to Sora 71:25–32 (in Japanese with English abstract)

Kakehi S, Ito S, Wagawa T (2017) Estimating surface water mixing ratios using salinity and potential alkalinity in the Kuroshio-Oyashio mixed water regions. J Geophys Res 122:1927–1942. https://doi.org/10.1002/2016JC012268

Kalnay E, Kanamitsu M, Kistler R, Collins W, Deaven D, Gandin L, Iredell M, Saha S, White G, Woollen J, Zhu Y, Chelliah M, Ebisuzaki W, Higgins W, Janowiak J, Mo KC, Ropelewski C, Wang J, Leetmaa A, Reynolds R, Jenne R, Joseph D (1996) The NCEP/NCAR 40-year reanalysis project. Bull Am Meteor Soc 77:437–472. https://doi.org/10.1175/1520-0477(1996)077%3c0437:TNYRP%3e2.0.CO;2

Kawai H (1972a) Hydrography of the Kuroshio extension. In: Stommel H, Yoshida K (eds) Kuroshio: its physical aspects. University of Tokyo Press, Tokyo, pp 235–352

Kawai H (1972b) Hydrography of the Kuroshio and the Oyashio. In: Physical oceanography II: Kaiyokagaku Kiso Koza (Fundamental lectures of oceanography). Tokai University Press, Tokyo, pp 129–320 (in Japanese)

Kawamura R (1984) Relation between atmospheric circulation and dominant sea surface temperature anomaly patterns in the North Pacific during the northern winter. J Meteor Soc Japan Ser. II 62:910–916. https://doi.org/10.2151/jmsj1965.62.6_910

Kida S, Qiu B, Yang J, Lin X (2016) The annual cycle of the Japan Sea throughflow. J Phys Oceanogr 46:23–39. https://doi.org/10.1175/JPO-D-15-0075.1

Kiso K, Kumagai I, Kaeriyama M (1987) Spring migration of Masu Salmon (*Oncorhynchus masou*) as determined by the tagging experiments performed in Shizugawa Bay, the east coast of Honshu, Japan. Bull Tohoku Reg Fish Res Lab 49:89–101 (in Japanese with English abstract)

Kitano K (1975) Some properties of warm eddies generated in confluence zone of Kuroshio and Oyashio currents. J Phys Oceanogr 5:245–252. https://doi.org/10.1175/1520-0485(1975)005%3c0245:SPOTWE%3e2.0.CO;2

Kobayashi S, Ota Y, Harada Y, Ebita A, Moriya M, Onoda H, Onogi K, Kamahori H, Kobayashi C, Endo H, Miyaoka K, Takahashi K (2015) The JRA-55 reanalysis: general specifications and basic characteristics. J Meteor Soc Japan 93:5–48. https://doi.org/10.2151/jmsj.2015-001

Kondo J (1988) Volcanic eruption, cool summers, and famines in the Northwestern part of Japan. J Climate 1:775–788. https://doi.org/10.1175/1520-0442(1988)001%3c0775:VECSAF%3e2.0.CO;2

Kono T (1997) Modification of the Oyashio Water in the Hokkaido and Tohoku areas. Deep-Sea Res 44:669–688. https://doi.org/10.1016/S0967-0637(96)00108-2

Kono T, Kawasaki Y (1997) Results of CTD and mooring observations southeast of Hokkaido: 1. Annual velocity and transport variations in the Oyashio. Bull Hokkaido Nat Fish Res Inst 61:65–81

Kono T, Foreman M, Chandler P, Kashiwai M (2004) Coastal Oyashio south of Hokkaido, Japan. J Phys Oceanogr 34:1477–1494. https://doi.org/10.1175/1520-0485(2004)034%3c1477:COSOHJ%3e2.0.CO;2

Kubokawa A, Hanawa K (1984) A theory of semigeostrophic gravity waves and its application to the intrusion of a density current along a coast. J Oceanogr Soc Japan 40:260–270

Kuroda H, Isoda Y, Takeoka H, Honda S (2006) Coastal current on the eastern shelf of Hidaka Bay. J Oceanogr 62:731–744. https://doi.org/10.1007/s10872-006-0090-2

Kuroda H, Setou T, Aoki K, Takahashi D, Shimizu M, Watanabe T (2013) A numerical study of the Kuroshio-induced circulation in Tosa Bay, off the southern coast of Japan. Cont Shelf Res 53:50–62. https://doi.org/10.1016/j.csr.2012.12.005

Kuroda H, Takahashi D, Mitsudera H, Azumaya T, Setou T (2014) A preliminary study to understand the transport process of the eggs and larvae of Japanese Pacific walleye pollock *Theragra chalcogramma* using particle-tracking experiments based on a high-resolution ocean model. Fish Sci 80:127–138. https://doi.org/10.1007/s12562-014-0717-y

Kuroda H, Wagawa T, Shimizu Y, Ito S, Kakehi S, Okunishi T, Ohno S, Kusaka A (2015) Interdecadal decrease of the Oyashio transport on the continental slope off the southeastern coast of Hokkaido, Japan. J Geophys Res Oceans 120:2504–2522. https://doi.org/10.1002/2014JC010402

Kuroda H, Toya Y, Wagawa T, Kuwata A, Setou T, Development of a high-resolution ocean model around Hokkaido: To evaluate effects of the Okhotsk Sea on ecosystem in the North Pacific. Low Temp Sci 74:115–125 (in Japanese with English abstract). https://doi.org/10.14943/lowtemsci.74.115

Kuroda H, Yokouchi K (2017) Interdecadal decrease in potential fishing areas for Pacific saury off the southeastern coast of Hokkaido, Japan. Fish Oceanogr 26:439–454. https://doi.org/10.1111/fog.12207

Kuroda H, Wagawa T, Kakehi S, Shimizu Y, Kusaka A, Okunishi T, Hasegawa D, Ito S (2017a) Long-term mean and seasonal variation of altimetry-derived Oyashio transport across the A-line off the southeastern coast of Hokkaido, Japan. Deep-Sea Res. Part I 121:95–109. https://doi.org/10.1016/j.dsr.2016.12.006

Kuroda H, Setou T, Kakehi S, Ito S, Taneda T, Azumaya T, Inagake D, Hiroe Y, Morinaga K, Okazaki M, Yokota T, Okunishi T, Aoki K, Shimizu Y, Hasegawa D, Watanabe T (2017b) Recent advances in Japanese fisheries science in the Kuroshio-Oyashio region through development of the FRA-ROMS ocean forecast system: overview of the reproducibility of reanalysis products. Open J Mar Sci 7:62–90. https://doi.org/10.4236/ojms.2017.71006

Kuroda H, Toya Y, Wagawa T, Kodama T, Yamanome T (2018) Development of some practical methods to predict oceanographic conditions. Monthly Kaiyo 50:506–510 (in Japanese)

Kusaka A, Ono T, Azumaya T, Kasai H, Oguma S, Kawasaki Y, Hirakawa K (2009) Seasonal variations of oceanographic conditions in the continental shelf area off the eastern Pacific coast of Hokkaido, Japan. Oceanogr Japan 18:135–156 (in Japanese with English abstract)

Kusaka A, Azumaya T, Kawasaki Y (2013) Monthly variations of hydrographic structures and water mass distribution off the Doto area, Japan. J Oceanogr 69:295–312. https://doi.org/10.1007/s10872-013-0174-8

Kusaka A, Shimizu Y, Sato T, Yoshida J (2016) Temporal variations in the current structure and volume transport of the Coastal Oyashio revealed by direct current measurement. J Oceanogr 72:601–615. https://doi.org/10.1007/s10872-016-0356-2

Kutsuwada K (1990) Long-term variability of oceanic and atmospheric condition off Sanriku coast. Umi to Sora 66:15–25 (in Japanese with English abstract)

Kutsuwada K, Hattori M, Yamada Y (2008) Long-term variability of upper oceanic condition off the Sanriku coast. Oceanogr Japan 17:19–38 (in Japanese with English abstract)

Mantua NJ, Hare SR, Zhang Y, Wallace JM, Francis RC (1997) A Pacific interdecadal climate oscillation with impacts on salmon production. Bull Am Meteor Soc 76:1069–1079

Matsukura H (1975) Occurrence of an extreme oceanographic condition in 1974 along the Sanriku–to–Joban coast and its linkage with meteorological condition around Japan. Bull Japan Soc Fish Oceanogr 26:79–87 (in Japanese)

Minobe S (1999) Resonance in bidecadal and pentadecadal climate oscillations over the North Pacific: Role in climatic regime shifts. Geophys Res Lett 26:855–858. https://doi.org/10.1029/1999GL900119

Mitsudera H, Taguchi B, Yoshikawa Y, Nakamura H, Waseda T, Qu T (2004) Numerical study on the Oyashio water pathways in the Kuroshio-Oyashio confluence. J Phys Oceanogr 34:1174–1196. https://doi.org/10.1175/1520-0485(2004)034%3c1174:NSOTOW%3e2.0.CO;2

Mitsudera H, Miyama T, Nishigaki H, Nakanowatari T, Nishikawa H, Nakamura T, Wagawa T, Furue R, Fujii Y, Ito S (2018) Low ocean-floor rises regulate subpolar sea surface temperature by forming baroclinic jets. Nature Comm 9:1190. https://doi.org/10.1038/s41467-018-03526-z

Miyama T, Mitsudera H, Nishigaki H, Furue R (2018) Dynamics of a quasi-stationary jet along the subarctic front in the North Pacific Ocean (the western Isoguchi Jet): An ideal two-layer model. J Phys Oceanogr 48:807–830. https://doi.org/10.1175/JPO-D-17-0086.1

Mizuno Y, Nishioka J, Tanaka T, Tada Y, Suzuki K, Tsuzuki Y, Sugimoto S, Yamashita Y (2018) Determination of the freshwater origin of Coastal Oyashio Water using humic-like fluorescence in dissolved organic matter. J Oceanogr 74:509–521. https://doi.org/10.1007/s10872-018-0477-x

Murakami M (1994) On long-term variations in hydrographic conditions in the Tohoku area. Bull Tohoku Reg Fish Res Lab 56:47–56 (in Japanese with English abstract)

Mutoh S (1975) Extreme cold water event in 1974 at the Sanriku to Joban coast. Bull Japan Soc Fish Oceanogr 26:68–78 (in Japanese)
Nakamura T, Toyoda T, Ishikawa Y, Awaji T (2004) Tidal mixing in the Kuril Straits and its impact on ventilation in the North Pacific Ocean. J Oceanogr 60:411–423. https://doi.org/10.1023/B:JOCE.0000038225.15056.c6
Nakamura T, Awaji T (2004) Tidally-induced diapycnal mixing in the Kuril Straits and its role in water transformation and transport: a three dimensional nonhydrostatic model experiment. J Geophys Res 109:C09S07. https://doi.org/10.1029/2003jc001850
Nakamura T, Toyoda T, Ishikawa Y, Awaji T (2006) Effects of tidal mixing at the Kuril Straits on North Pacific ventilation: adjustment of the intermediate layer revealed from numerical experiments. J Geophys Res 111:C04003. https://doi.org/10.1029/2005JC003142
Nakanowatari T, Ohshima KI (2014) Coherent sea level variation in and around the Sea of Okhotsk. Prog Oceanogr 126:58–70. https://doi.org/10.1016/j.pocean.2014.05.009
Nakanowatari T, Mitsudera H, Motoi T, Ishikawa I, Ohshima KI, Wakatsuchi M (2015) Multidecadal-scale freshening at the salinity minimum in the western part of North Pacific: importance of wind-driven cross-gyre transport of subarctic water to the subtropical gyre. J Phys Oceanogr 45:988–1008. https://doi.org/10.1175/JPO-D-13-0274.1
Nonaka M, Nakamura H, Tanimoto Y, Kagimoto T, Sasaki H (2008) Interannual-to-decadal variability in the Oyashio and its influence on temperature in the subarctic frontal zone: an eddy-resolving OGCM simulation. J Climate 21:6283–6303. https://doi.org/10.1175/2008JCLI2294.1
Ogasawara J (1987) Oyashio and Doto coastal current. Monthly Kaiyo 19:21–25 (in Japanese)
Ogawa Y, Hirai M, Yasuda I (1987) Fluctuations of the first Oyashio Intrusion and it's influences on coastal fishery-resources. Bull Tohoku Reg Fish Res Lab 49:1–15 (in Japanese with English abstract)
Ogawa Y (1989) Variation of the southern end latitude of the First Oyashio Intrusion. Bull Tohoku Reg Fish Res Lab 51:1–9 (in Japanese with English abstract)
Oguma S, Ono T, Kusaka A, Kasai H, Kawasaki Y, Azumaya T (2008) Isotopic tracers for water masses in the coastal region of eastern Hokkaido. J Oceanogr 54:525–539. https://doi.org/10.1007/s10872-008-0044-y
Ohtani K (1970) Relative transport in the Alaskan Stream in winter. J Oceanogr Soc Japan 26:271–282. https://doi.org/10.1007/BF02769468
Ohtani K (1971) Studies on the change of the hydrographic conditions in the Funka Bay. II. Characteristics of the waters occupying the Funka Bay. Bull Fac Fish Sci Hokkaido Univ 22:58–66 (in Japanese with English abstract)
Ohtani K (1987) Westward inflow of the Coastal Oyashio Water into the Tsugaru Strait. Bull Fac Fish Hokkaido Univ 38:209–220 (in Japanese with English abstract)
Ohtani K (1989) The role of the Sea of Okhotsk on the Oyashio Water. Umi to Sora 65:63–83 (in Japanese with English abstract)
Okuda K (1986) Occurrence of extremely low-temperature in the coastal region of the Tohoku area associated with interannual variations of the Oyashio. Bull Japan Soc Fish Oceanogr 50:231–238 (in Japanese)
Okuda K, Mutoh S (1986) Features of the abnormally cold water phenomena in the Tohoku sea area and its cause. Bull Tohoku Reg Fish Res Lab 48:87–96 (in Japanese with English abstract)
Okuda K, Yasuda I, Hiroe Y, Shimizu Y (2001) Structure of subsurface intrusion of the Oyashio water into the Kuroshio Extension and formation process of the North Pacific intermediate water. J Oceanogr 57:121–140. https://doi.org/10.1023/A:1011135006278
Osafune S, Yasuda I (2006) Bidecadal variability in the intermediate waters of the northwestern subarctic Pacific and the Okhotsk Sea in relation to 18.6-year period nodal tidal cycle. J Geophys Res 111:C05007. https://doi.org/10.1029/2005jc003277
Osafune S, Yasuda I (2012) Numerical study on the impact of the 18.6-year period nodal tidal cycle on water-masses in the subarctic North Pacific. J Geophys Res Oceans 117:C05009. https://doi.org/10.1029/2011jc007734

Qiu B, Miao W, Müller P (1997) Propagation and decay of forced and free baroclinic Rossby waves in off-equatorial oceans. J Phys Oceanogr 27:2405–2417. https://doi.org/10.1175/1520-0485(1997)027%3c2405:PADOFA%3e2.0.CO;2

Qiu B (2001) Kuroshio and Oyashio currents. In: Encyclopedia of ocean sciences. Academic Press, pp 1413–1425

Qiu B (2002) Large-scale variability in the midlatitude subtropical and subpolar North Pacific Ocean: observations and causes. J Phys Oceanogr 32:353–375. https://doi.org/10.1175/1520-0485(2002)032%3c0353:LSVITM%3e2.0.CO;2

Rio M-H, Mulet S, Picot N (2013) New global mean dynamic topography from a GOCE geoid model, altimeter measurements and oceanographic in-situ data. In: Proceedings of 'ESA living planet symposium 2013' (ESA SP-722). European Space Agency (ESA), Edinburgh, UK

Rosa AL, Isoda Y, Uehara K, Aiki T (2007) Seasonal variations of water system distribution and flow patterns in the southern sea area of Hokkaido, Japan. J Oceanogr 63:573–588. https://doi.org/10.1007/s10872-007-0051-4

Rosa AL, Isoda Y, Kobayashi N (2009) Seasonal variations of shelf circulation in Hidaka Bay, Hokkaido, Japan, with an interpretation of the migration route of juvenile walleye pollock. J Oceanogr 65:615–626. https://doi.org/10.1007/s10872-009-0052-6

Sakamoto K, Tsujino H, Nishikawa S, Nakano H, Motoi T (2010) Dynamics of the coastal Oyashio and its seasonal variation in a high-resolution western North Pacific ocean model. J Phys Oceanogr 40:1283–1301. https://doi.org/10.1175/2010JPO4307.1

SDMO-JMA [Sapporo District Meteorological Observatory, Japan Meteorological Agency] (2014) Operating Report of Sea Ice. pp 20 (in Japanese)

Sekine Y (1988) A numerical experiment on the anomalous southward intrusion of the Oyashio east of Japan. Part I. barotropic model. J Oceanogr Soc Japan 44:60–67. https://doi.org/10.1007/BF02303121

Sekine Y (1999) Anomalous southward intrusions of the Oyashio east of Japan: 2. Two-layer numerical model. J Geophys Res 104(C2):3049–3058. https://doi.org/10.1029/1998JC900044

Shimizu Y, Yasuda I, Ito S (2001) Distribution and circulation of the coastal Oyashio intrusion. J Phys Oceanogr 31:1561–1578. https://doi.org/10.1175/1520-0485(2001)031%3c1561:DACOTC%3e2.0.CO;2

Shimizu Y, Yasuda I, Okuda K, Hanawa K, Ito S (2003) ADCP-referenced Kuroshio and Oyashio transports for the North Pacific Intermediate Water formation. J Phys Oceanogr 33:220–233. https://doi.org/10.1175/1520-0485(2003)033%3c0220:ARKAOW%3e2.0.CO;2

Simizu D, Ohshima KI (2002) Barotropic response of the Sea of Okhotsk to wind forcing. J Oceanogr 58:851–860. https://doi.org/10.1023/A:1022879314764

Shimizu Y, Takahashi K, Ito S, Kakehi S, Tatebe H, Yasuda I, Kusaka A, Nakayama T (2009) Transport of subarctic large copepods from the Oyashio area to the mixed water region by the coastal Oyashio intrusion. Fish Oceanogr 18:312–327. https://doi.org/10.1111/j.1365-2419.2009.00513.x

SSALTO/DUACS (2004) User Handbook: (M)SLA and (M)ADT near-real time and delayed time products. CLS-DOS-NT-06-034 Nomenclature: SALP-MU-P-EA-21065-CLS Issue: 4rev 2

Sugimoto S, Hanawa K (2009) Decadal and interdecadal variations of the Aleutian low activity and their relation to upper oceanic variations over the North Pacific. J Meteor Soc Japan 87:601–614. https://doi.org/10.2151/jmsj.87.601

Sugimoto S, Kobayashi N, Hanawa K (2014) Quasi-decadal variation in intensity of the western part of the winter subarctic SST front in the western North Pacific: The influence of Kuroshio Extension path state. J Phys Oceanogr 44:2751–2760. https://doi.org/10.1175/JPO-D-13-0265.1

Takasugi S (1991) Characteristics of surface temperature variations measured at coastal hydrographic stations around northern part of Japan. Bull Japan Soc Fish Oceanogr 55:329–337 (in Japanese with English abstract)

Takasugi S, Yasuda I (1994) Variation of the Oyashio water in the Iwate coastal region and in the vicinity of the east coast of Japan. Bull Japan Soc Fish Oceanogr 58:253–259 (in Japanese with English abstract)

Tanaka Y, Hibiya T, Niwa Y (2007) Estimates of tidal energy dissipation and diapycnal diffusivity in the Kuril Straits using TOPEX/POSEIDON altimeter data. J Geophys Res Oceans 112(C10). https://doi.org/10.1029/2007jc004172

Tatebe H, Yasuda I (2004) Oyashio southward intrusion and cross-gyre transport related to the diapycnal upwelling in the Okhotsk Sea. J Phys Oceanogr 34:2327–2341. https://doi.org/10.1175/1520-0485(2004)034%3c2327:OSIACT%3e2.0.CO;2

Tatebe H, Yasuda I (2005a) Numerical experiments on the seasonal variations of the Oyashio near the east coast of Japan. J Phys Oceanogr 35:2309–2326. https://doi.org/10.1175/JPO2818

Tatebe H, Yasuda I (2005b) Interdecadal variations of the coastal Oyashio from the 1970s to the early 1990s. Geophys Res Lett 32:L10613. https://doi.org/10.1029/2005GL022605

Tomosada A (1986) 3-3. Long-term ocean variation and extreme cold water event. Bull Japan Soc Fish Oceanogr 50:37–40 (in Japanese)

Trenberth KE, Hurrell JW (1994) Decadal atmosphere-ocean variations in the Pacific. Climate Dyn 9:303–319. https://doi.org/10.1007/BF00204745

Uehara K, Ito S, Miyake H, Yasuda I, Shimizu Y, Watanabe T (2004) Absolute volume transports of the Oyashio referred to moored current meter data crossing the OICE. J Oceanogr 60:397–409. https://doi.org/10.1023/B:JOCE.0000038224.77418.91

Wagawa T, Yoshikawa Y, Masuda A (2010) Bathymetric influences of the Emperor Seamounts upon the subarctic gyre of the North Pacific: Examining boundary current dynamics along the eastern side of the mountain ridge with an idealized numerical model. J Oceanogr 66:259–271. https://doi.org/10.1007/s10872-010-0023-y

Wagawa T, Ito S, Shimizu Y, Kakehi S, Ambe D (2014) Currents associated with the quasi-stationary jet separated from the Kuroshio Extension. J Phys Oceanogr 44:1636–1653. https://doi.org/10.1175/JPO-D-12-0192.1

Wagawa T, Kuroda H, Ito S, Kakehi S, Yamanome T, Tanaka K, Endoh Y, Kaga S (2015) Variability in water properties and predictability of sea surface temperature along Sanriku coast, Japan. Cont Shelf Res 103:12–22. https://doi.org/10.1016/j.csr.2015.04.016

Yasuda I, Okuda K, Hirai M (1992) Evolution of a Kuroshio warm-core ring—variability of the hydrographic structure. Deep-Sea Res Part A 39:S131–S161. https://doi.org/10.1016/S0198-0149(11)80009-9

Yasuda I, Watanabe Y (1994) On the relationship between the Oyashio front and saury fishing grounds in the north-western Pacific: a forecasting method for fishing ground locations. Fish Oceanogr 3:172–181. https://doi.org/10.1111/j.1365-2419.1994.tb00094.x

Yasuda I, Okuda K, Shimizu Y (1996) Distribution and modification of North Pacific Intermediate Water in the Kuroshio-Oyashio interfrontal zone. J Phys Oceanogr 26:448–465

Yasuda I (1997) The origin of the North Pacific Intermediate Water. J Geophys Res 102:893–909. https://doi.org/10.1029/96JC02938

Yasuda I, Koketsu S, Katsumata K, Ohiwa M, Kawasaki Y, Kusaka A (2002) Influence of intermediate Okhotsk Sea water on the Oyashio and North Pacific Intermediate Water. J Geophys Res 107(C12):3237. https://doi.org/10.1029/2001JC001037

Yasuda I (2003) Hydrographic structure and variability in the Kuroshio-Oyashio transition area. J Oceanogr 59:389–402. https://doi.org/10.1023/A:1025580313836

Yasuda I (2004) North Pacific Intermediate Water: progress in SAGE (SubArctic Gyre Experiment) and related projects. J Oceanogr 60:385–395

Yoshida T (1992) Climatological seasonal variations of the distribution of the Oyashio cold water. Umi to Sora 68:79–88 (in Japanese with English abstract)

Chapter 14
Multidecadal Variations of Sea Surface CO_2 Fugacity (fCO_2) in the Oyashio Current-Influenced Ocean Margin

Hongjie Wang and Xinping Hu

Abstract Oyashio Current-influenced northwestern North Pacific Ocean margin (the Oyashio Region, east of Japan) represents an important area for intermediate water mass formation, hence the transport of anthropogenic CO_2 into the interior North Pacific. Currently, it is unclear how the air-sea CO_2 fugacity gradient in the climatically sensitive Oyashio Region has been behaving in recent decades. Taking advantage of a community-based Surface Ocean CO_2 Atlas (SOCAT, Version 5), we examined the sea surface fCO_2 trends in 0.5° × 0.5° grids in the east Japanese margin (32.0°N–43.5°N, 140.0°E–147.0°E). In the Oyashio Region, seawater fCO_2 increased significantly at a rate of 2.86 ± 0.92 μatm yr^{-1}, greater than the atmospheric fCO_2 increase rate (1.95 ± 0.03 μatm yr^{-1}). Because of lower oceanic fCO_2 values in this region compared with the atmosphere, the faster seawater fCO_2 increase suggests that the Oyashio Region probably represents a decreasing CO_2 sink in the past decades. Furthermore, the trend of the non-temperature controlled fCO_2 change (3.22 ± 1.11 μatm yr^{-1}) suggests that processes such as (1) enhanced respiration based on the increasing export of organic carbon from the neighboring Okhotsk Sea, and (2) reduced primary production in the Oyashio Region itself due to increased water column stratification, may have contributed to the faster surface fCO_2 increase.

Keywords Surface ocean CO_2 fugacity (fCO_2) · Anthropogenic CO_2 · Generalized additive mixed modeling · Oyashio Current · Ocean margin

H. Wang (✉) · X. Hu
Department of Physical and Environmental Sciences, Texas A&M University-Corpus Christi, Corpus Christi, TX, USA
e-mail: hwangwa@uw.edu

X. Hu
e-mail: xinping.hu@tamucc.edu

Present Address:
H. Wang
Joint Institute for the Study of the Atmosphere and Ocean, University of Washington, Seattle, WA, USA

C.-T. A. Chen and X. Guo (eds.), *Changing Asia-Pacific Marginal Seas*, Atmosphere, Earth, Ocean & Space, https://doi.org/10.1007/978-981-15-4886-4_14

14.1 Introduction

Sea surface primary productivity, including production of organic carbon and, to a lesser extent, inorganic carbon (i.e., carbonate), plays the dominant role in transporting CO_2 from the atmosphere into the ocean interior (Ducklow et al. 2015; Honjo et al. 2008; Longhurst and Glen Harrison 1989; Rost and Riebesell 2004). However, despite the relatively smaller role of direct CO_2 uptake by the ocean due to thermodynamic gradient (i.e., air-sea CO_2 disequilibrium) (Sarmiento and Gruber 2006), the evolution of this gradient is an important subject of study given the increasing CO_2 level in the atmosphere since the industrial revolution, as CO_2 dissolution is the dominant mechanism for the ocean's uptake of anthropogenic CO_2 (McKinley et al. 2017; Wanninkhof and McGillis 1999; Sabine et al. 2004). This uptake is especially relevant under the changing ocean biogeochemistry in the context of global climate change.

It is known that the open ocean in general has been largely trailing the increasing atmospheric CO_2 over the past decades (Takahashi et al. 2009). Nonetheless, regional changes in the CO_2 sink/source capacity over time do exist (Wanninkhof et al. 2013). For example, in the Southern Ocean decadal oscillation in surface ocean CO_2 levels has been observed. This oscillation resulted in a shift in CO_2 uptake intensity over the past decades (Landschützer et al. 2015; McKinley et al. 2017; Lenton et al. 2012). In comparison, due to large spatial and temporal variability, changes in ocean margin CO_2 balance (i.e., source vs. sink) in the global ocean carbon budget have remained poorly understood. In recent years, several studies on global ocean margin CO_2 trends based on the newly available community-based data synthesis effort (such as the Surface Ocean CO_2 Atlas, or SOCAT, https://www.socat.info/) were published (Wang et al. 2016, 2017), and detailed interpretations of how different ocean margins behave (Huthnance et al. 2002) have begun. It is imperative to examine seawater CO_2 dynamics using the newer dataset in the context of previous findings, which were mostly derived from either smaller scale studies or based on shorter temporal data coverages.

The Oyashio Current is a cold western boundary current that originates in the subarctic Pacific known as East Kamchatka Current, and it carries signatures of the Okhotsk Sea and the Japan Sea Outflow (Saito et al. 2002; Kono 1997; Yasuda 2003). While flowing to the south, the Oyashio Current meets the Soya Warm Current and the Tsugaru Warm Current, both of which are separated from the Kuroshio Current, a northward flowing western boundary current coming from the tropical North Pacific (Saito et al. 2002). The Oyashio Current-influenced east Japanese margin (the Oyashio Region) exhibits substantial seasonal and interannual variability in hydrographic structure as well as significant long-term changes in its ecosystem characteristics (Yatsu et al. 2013; Yasuda 2003). For example, from the 1970s to the late 1990s, this area experienced a decrease in phytoplankton biomass, Chl a, and diatoms (Sakurai 2007), and showed substantial changes in annual surface primary productivity (Saito et al. 2002). Because of deep convection that results in the formation of North Pacific Intermediate Water (NPIW), the Oyashio Region is an

important area where anthropogenic CO_2 is entrained into the ocean interior (Ono et al. 2000, 2003; Masujima et al. 2003). Currently, the Oyashio Region is a sink for anthropogenic CO_2 at a capacity on the order of 0.025–0.045 Gt-C yr^{-1} (Ono et al. 2000, 2003).

Seasonal variations of seawater CO_2 system have been extensively studied in the past on small scale influences such as eddies in the Oyashio Region (Kusakabe et al. 2002; Rogachev et al. 1996). Biological modulation of CO_2 partial pressure (pCO_2) was studied and primary production was thought to be the dominant cause for winter-spring pCO_2 reduction, from supersaturation (winter) to undersaturation (spring) with respect to the atmospheric CO_2 (Midorikawa et al. 2003). Note that both fCO_2 and pCO_2 are used in the literature for studying air-sea gas exchange, although the numerical values of these two parameters are close to each other under normal seawater conditions, i.e., $\Delta < 0.4\%$ (Zeebe and Wolf-Gladrow 2001). Therefore, trend analyses using both parameters would produce largely the same results.

14.2 Prior Results on Changes in fCO_2 in the Japanese Margin

In developing a new statistical method, Wang et al. (2016) used SOCAT Version 3 data from a 1° × 1° grid at the Japanese margin (34°N–35°N, 138°E–139°E) as an example to illustrate the application of a generalized additive mixed modeling (GAMM) in interpreting multidecadal fCO_2 changes. Average fCO_2 increasing trend in the Japanese Margin is 2.1 ± 0.6 μatm yr^{-1} (with a range of 0.3–4.0 μatm yr^{-1}) based on data during the 1992–2013 period. Subsequently, Wang et al. (2017) took an average of fCO_2 trends in all 1° × 1° grid in the broad Kuroshio and Oyashio area (22°N–45°N, 130°E–148°E) and concluded that seawater fCO_2 trend is 2.30 ± 1.71 μatm yr^{-1}. Furthermore, the decomposed thermal fCO_2 trend (−0.19 ± 1.26 μatm yr^{-1}), i.e., fCO_2 trend due to temperature change only, suggested that enhanced upwelling may have led to a cooling effect in this area in the past decades (also see Liu et al. 2010). In contrast, the non-thermal fCO_2 trend (i.e., fCO_2 change due to non-temperature variations) is 2.55 ± 1.75 μatm yr^{-1}. Both of these studies suggested that the seawater fCO_2 trend in this expansive area is not significantly different from the global atmospheric fCO_2 increase rate, i.e., ~1.90 ± 0.06 μatm yr^{-1} (Wang et al. 2017). In comparison, Laruelle et al. (2018) took a different approach by calculating the trend of wintertime pCO_2 gradient between the atmosphere and sea surface ($pCO_{2,air} - pCO_{2,water}$) in 0.5° × 0.5° grids. Using two types of margin definition (narrow vs. wide), they calculated the rates of change in ΔpCO_2 in the coast of Japan is 0.77 ± 0.69 μmol yr^{-1} and 0.22 ± 0.70 μatm yr^{-1}, respectively (Laruelle et al. 2018). These large-scale studies showed that fCO_2 trends along the Japanese margin exhibit a spatial pattern, i.e., lower toward the south but higher in the north (Oyashio Region). Similar to this region-wide distribution pattern, Ishii et al. (2011) observed pCO_2 increase rate of 1.54 ± 0.33 μatm yr^{-1} between 31°N and 34°N

along 137°E using data collected in 1994–2008. However, a detailed examination of fCO_2 signal changes in the highly dynamic Oyashio Region is still lacking. Given its climate sensitivity, associated deep water formation, and potentially long-term changes in primary production, elucidating fCO_2 changes will be useful in understanding both anthropogenic CO_2 uptake capacity and primary production change in this region.

14.3 Analysis of the fCO_2 Trends Using the SOCAT Version 5 Data

Quality controlled fCO_2 and associated coordinates, date, sea surface temperature (SST), and sea surface salinity (SSS) are obtained from the SOCAT Version 5 coastal databases (Bakker et al. 2016). We focus on the northern section of Japanese margin where there are SOCAT data record (32.0°N–43.5°N, 140.0°E–147.0°E), overlapping with the western Kuroshio-Oyashio Confluence Region (KOCR, 142°–160°E, 35°–40°N, Sugimoto and Hanawa 2011). The grid size for our calculation is 0.5° × 0.5°. Note that the SOCAT coastal dataset covers the ocean margin areas within 400 km from the coastline (Pfeil et al. 2013). Because of the narrow continental shelf in the studied area, we do not limit the dataset by removing areas with deeper water. In fact, the broad inclusion of the SOCAT is useful in revealing large-scale ocean behaviors regarding boundary current activities.

Monthly dry air CO_2 (xCO_2, ppm) data are downloaded from NOAA's Earth System Research Laboratory (http://www.esrl.noaa.gov/gmd/ccgg/trends/), and the in situ monthly air fCO_2 is calculated based on averaged SSS, SST, and atmospheric pressure in each 0.5° × 0.5° grid (Wang et al. 2016).

$$fCO_{2,\mathrm{air}} = xCO_2 \times [P_b - P_w] \times e^{\left(\frac{P_b(B+2\delta)}{RT}\right)} \tag{14.1}$$

where P_b is the monthly average barometric pressure in the study area. P_w is saturated water vapor pressure calculated using monthly average salinity and temperature in the study area (Weiss and Price 1980). B, the first virial coefficient of CO_2, and the cross virial coefficient δ are both functions of temperature (Weiss 1974).

We adopt the GAMM method to analyze the fCO_2 trend in each selected grid (Wang et al. 2016). Briefly, this method predicts fCO_2 mainly based on three terms: seasonal cycle, the additional fCO_2 variations caused by the SST and SSS changes, and the long-term sea surface fCO_2 change. A cyclic penalized spline is used to fit the seasonal cycle with the entire time series data in each grid. Second-order polynomial models are then used to fit the non-linear relationships of fCO_2 variation with SST and SSS. With the best fitted seasonal cycle and environmental variability, we then assume the residual fCO_2 variation (fCO_2 × Day) is a linear function of sampling date, and its coefficient represents the temporal fCO_2 trend.

In the GAMM method, a correction for autocorrelation is included to account for the lack of independence of consecutive observations taken close together in time. The method also weighs the observations using explicit models for heteroscedasticity to account for unequal variance in sampling date, SSS, or SST (Wang et al. 2016). Because of high variability, temporal trends based on short records (such as 10-year or less) are very sensitive to the beginning and ending dates (McKinley et al. 2011). Therefore, we only calculate the trend in grids that have more than 10 years of data record, and we report the slope of trends with a significant regression ($p < 0.05$). Grubbs' test (Grubbs 1969) is adopted to detect and remove the fCO_2 trend outliers at significance level of 0.05 in the studied area.

In order to separate the influence of temperature from the influence of all other physical, chemical, and biological processes on fCO_2 trend, we adopt an empirical relationship between temperature and fCO_2 ($\partial \ln fCO_2/\partial T = 0.0423\ ^\circ C^{-1}$) (Takahashi et al. 2002) to calculate the thermal fCO_2 (T-fCO_2) and non-thermal fCO_2 (NT-fCO_2) in each grid. The two components are calculated following Eqs. 14.2 and 14.3, in which the over bar represents the mean value of SST, SSS, or fCO_2 in each grid.

$$\text{T-}fCO_2 = \overline{fCO_2} \times \exp\left[0.0423\left(\text{SST} - \overline{\text{SST}}\right)\right] \tag{14.2}$$

$$\text{NT-}fCO_2 = fCO_2 \times \exp\left[0.0423\left(\overline{\text{SST}} - \text{SST}\right)\right] \tag{14.3}$$

Then T-fCO_2 and NT-fCO_2 trends are calculated in the same manner as that for the fCO_2 trend analysis with the exception that SST was not used for these trend calculations, because the temperature effect is removed by normalizing to a common temperature in each grid. SSS and SST trends are directly calculated after removing the seasonal cycle, which is fitted by a cyclic penalized spline.

For each grid, the mean fCO_2 level in surface ocean ($fCO_{2,\,ocean}$) is compared with the mean fCO_2 level in the atmosphere ($fCO_{2,\,air}$) during the same period. If $fCO_{2,\,ocean}$ is lower than $fCO_{2,\,air}$, the ocean is a CO_2 sink; otherwise the ocean is a CO_2 source. This study assesses the CO_2 sink/source changes by only comparing the sea surface and atmospheric fCO_2 trends. The examined grid would become a decreasing (or increasing) CO_2 sink when the oceanic fCO_2 trend is higher (or lower) than atmospheric fCO_2 trend. In contrast, the ocean would become an increasing (or decreasing) CO_2 source when the fCO_2 trend in the surface ocean is higher (or lower) than in the atmosphere.

14.4 Time Scales for the Trend Calculations

The start year of fCO_2 records in the examined grids ranges from 1990 to 2000, while the end year ranges from 2012 to 2016. As a result, the temporal spans in all studied grids are mostly between 15 and 25 years with the majority of grids sampled

more than 10 unique months across the time span (Fig. 14.1). Ideally, fCO_2 trend calculations should be done using a fixed period across a studied area. In reality, coastal CO_2 data usually have quite heterogenous spatial coverages and longer data records are rarer due to earlier technological and logistical constraints. Meanwhile, new observations increased substantially especially in the past two decades. Thus our goal is to include as many data points as possible so that we could report the largest temporal coverage of this margin area and adjacent boundary current influenced regions.

14.5 Spatial Distribution of fCO_2, SST, and SSS

The southernmost latitude of the Oyashio Current intrusion is around 38.8°N (Qiu 2001; Yasuda 2003). In order to examine the processes that dominate the CO_2 change, we divide the study area into two zones: north (≥39°N, i.e., Oyashio Region, the focus of this study) and south (<39°N). Average sea surface fCO_2 across the entire time span shows general lower values (~ 300 μatm) in the Oyashio Region (Fig. 14.2a), and it coincides with a lower temperature and salinity there (Fig. 14.2b, c); whereas the highest average fCO_2 values (nearly 390 μatm) appear near the coast of Tohoku region of the Honshu Island. In the Kuroshio Current-influenced area in the south, even though SST and SSS are both higher, average fCO_2 levels are moderate (330–350 μam). Nevertheless, both SST and SSS have significant correlation with average fCO_2 ($r = 0.57$ and 0.33, respectively, $p \ll 0.001$).

14.6 Seawater fCO_2 Trends

The surface oceanic fCO_2 trends in the Oyashio Region are significantly higher than the rest of the Japanese Margin (2.86 ± 0.92 vs. 2.10 ± 0.59 μatm yr^{-1}, $p \ll 0.001$, Fig. 14.3a). However, the average fCO_2 trend in this entire area is 2.36 ± 0.81 μatm yr^{-1}, which is not significantly different from the previously calculated value for this margin (2.3 ± 1.7 μatm yr^{-1}, Wang et al. 2017), a result based on an earlier version of the SOCAT data (Version 3). The average increase rate of atmospheric fCO_2 in this area is 1.95 ± 0.03 μatm yr^{-1}.

The entire east Japanese margin exhibits strong spatial heterogeneity in both fCO_2 levels and their multidecadal trends. The cooler Oyashio Region in the north that has lower fCO_2 experiences a faster increase in fCO_2, while the warmer southern region (under the Kuroshio Current influence) experiences a lag in seawater fCO_2 increase relative to the atmosphere. Due to the decreasing air-sea fCO_2 gradient in the Oyashio Region, a decrease in anthropogenic CO_2 uptake potential may be expected, while the Kuroshio Current-influenced area exhibits variable changes, i.e., some grids show increasing sink and some show decreasing sink (Fig. 14.3b).

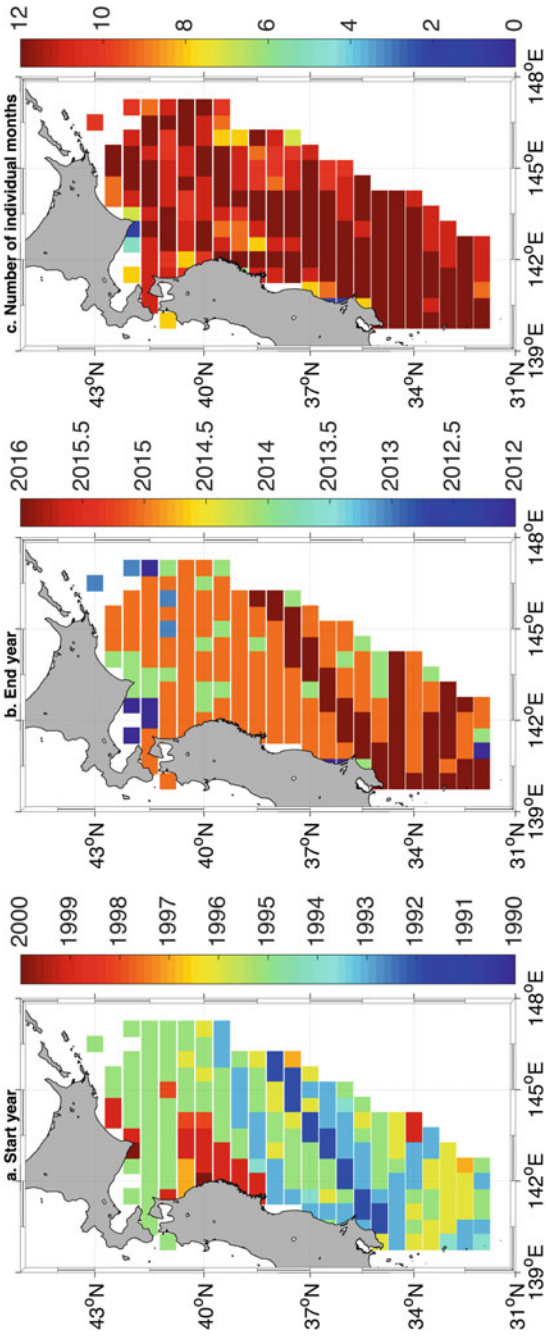

Fig. 14.1 The time span of fCO_2 record in Oyashio-Kuroshio currents-influenced Japanese margin. **a** start year, **b** end year, and **c** number of individual months across the entire time span

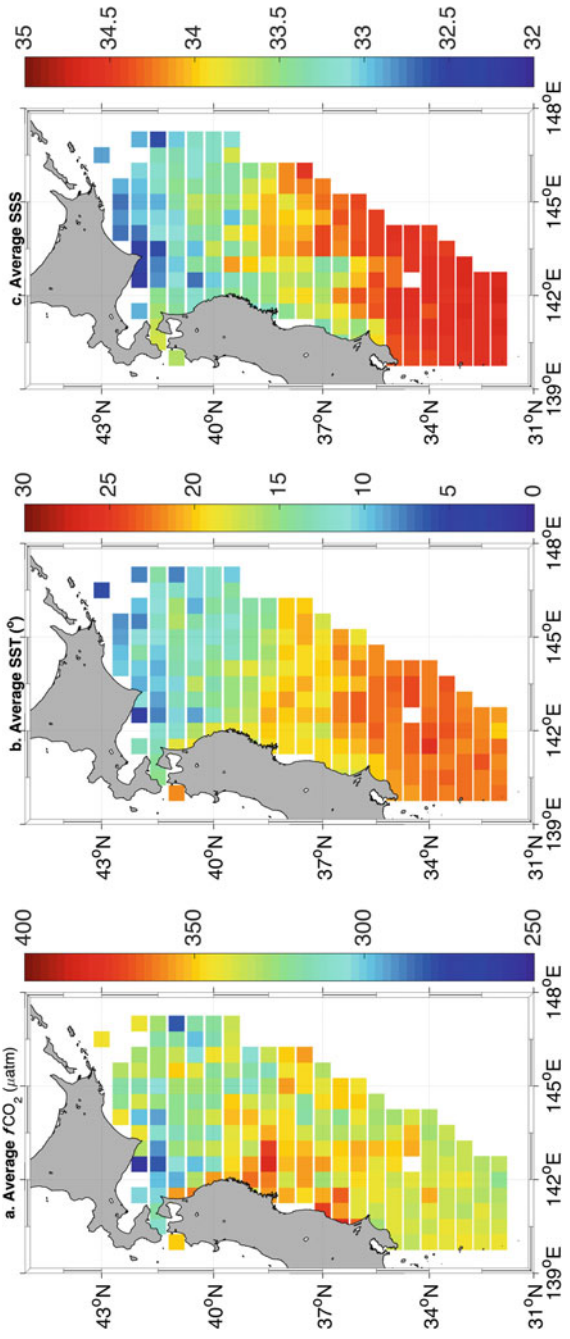

Fig. 14.2 **a** Average fCO_2, **b** average sea surface temperature—SST, and **c** average surface salinity—SSS in the Oyashio-Kuroshio currents-influenced margin

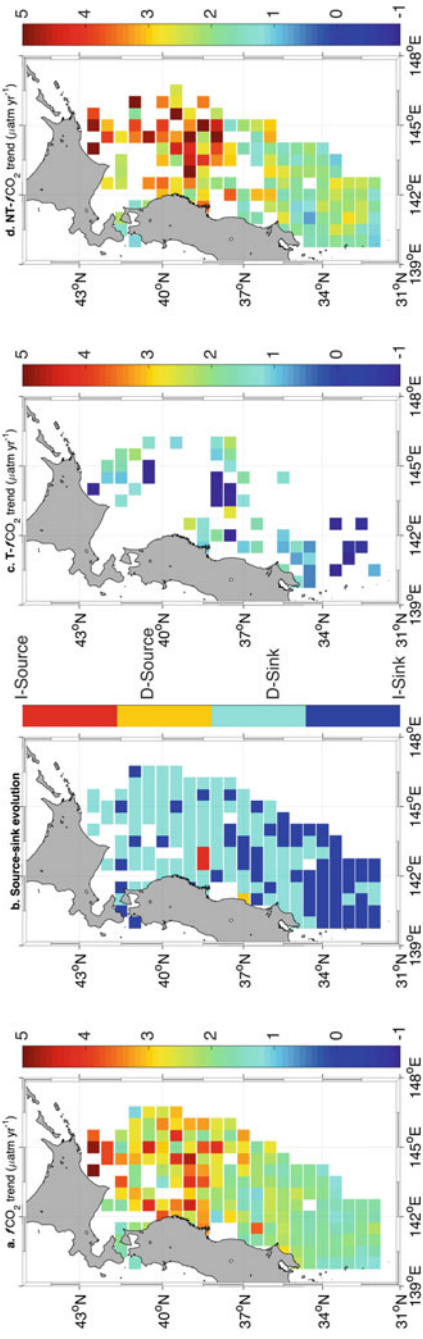

Fig. 14.3 **a** fCO_2 trend, **b** CO_2 sink/source change, **c** thermal fCO_2 (T-fCO_2) trend, **d** non-thermal fCO_2 (NT-fCO_2) trend in the Oyashio-Kuroshio currents-influenced margin

There are a much smaller number of grids that have significant T-fCO_2 trends than those that have significant NT-fCO_2 trends (Fig. 14.3c, d). The average thermal fCO_2 (T-fCO_2) trend is 0.6 ± 1.3 μatm yr^{-1}, significantly lower than the average non-thermal fCO_2 (NT-fCO_2) trend (2.5 ± 1.0 μatm yr^{-1}, $p << 0.001$). These results suggest that non-thermal effects are much greater than thermal effects in controlling sea surface fCO_2 changes in the studied area.

14.7 Temporal and Spatial Changes in SST and SSS and Their Effect on fCO_2

Because fCO_2 variation in surface ocean is a function of the SST, SSS, and biological activities that may change total dissolved inorganic carbon and total alkalinity balances, we attempt to address the potential mechanisms that have caused the spatial heterogeneities of fCO_2 by examining decomposed fCO_2 trends and interpreting potential changes in the context of changing physical (SSS and SST) and biogeochemical conditions.

SST trends in the north and south of 39°N do not exhibit significant difference (Fig. 14.4a, c, $p > 0.05$), even though slightly higher variability in the SST trend can be observed in the Oyashio Region (-0.03 ± 0.16 °C yr^{-1}) than the rest of the studied margin (0.01 ± 0.13 °C yr^{-1}). In comparison, SSS trends in the Oyashio Region are significantly lower than that in the south (-0.022 ± 0.046 yr^{-1} vs. 0.002 ± 0.028 yr^{-1}, Fig. 14.4b, d). Despite the fact that the average changes in both areas are not significantly different from zero due to the patchy distribution of these trend values, "freshening" of the coastal Tohoku region can be seen (Fig. 14.4b).

By definition, T-fCO_2 reflects temperature controlled fCO_2 change, whereas NT-fCO_2 reflects changes due to physical (other than temperature), chemical, and biological processes (Takahashi et al. 2002). Despite that there are only a small number of grids that show significant changes in both T-fCO_2 (Fig. 14.3c) and SST trends (Fig. 14.4a), these changes are highly correlated in their respective grids (Fig. 14.5a), indicating that decadal temperature change has had significant effect on sea surface fCO_2. Note the apparent sign differences between the average SST trends and average T-fCO_2 trends for both the Oyashio region and the entire studied area are likely caused by the different numbers of grids that have significant results (Table 14.1). On the other hand, there is no significant relationship between the SSS trend and the NT-fCO_2 trend (Fig. 14.5b). Further analysis shows that NT-fCO_2 trends are significantly greater than those of atmospheric fCO_2 (paired t-test, $p \ll 0.001$). The high NT-fCO_2 increase rates suggest that other processes other than air-sea gas exchange must have contributed to the sea surface fCO_2 increase.

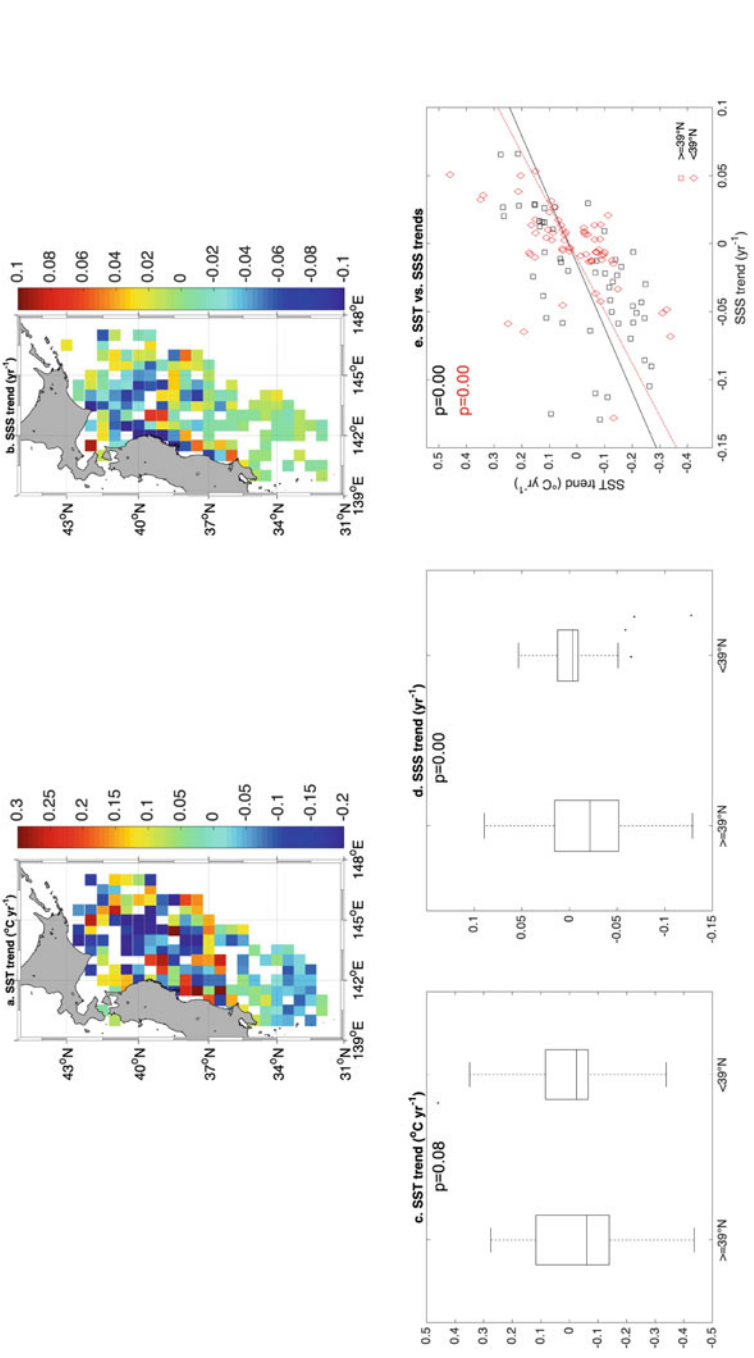

Fig. 14.4 Spatial distributions of calculated SST (**a**) and SSS (**b**) trends, comparison of SST (**c**) and SSS (**d**) between the north (≥39°N) and the south (<39°N) of the two areas as well as the correlation analyses between the two trends in both areas (**e**)

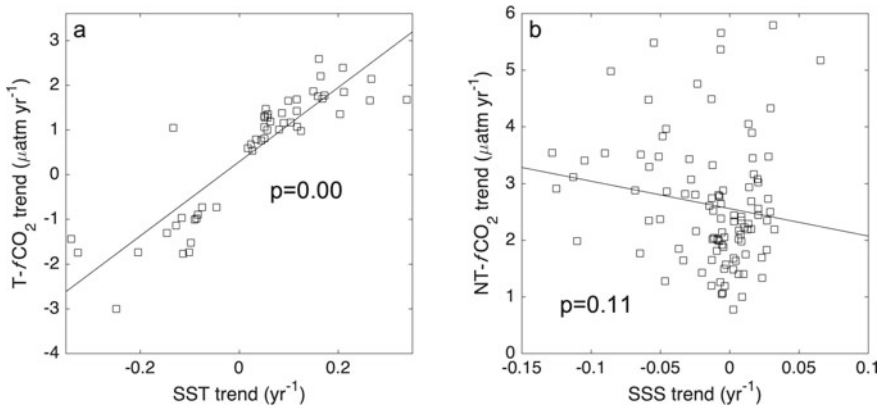

Fig. 14.5 Correlation analysis between **a** T-fCO_2 and SST trends, **b** NT-fCO_2 and SSS trends. See Figs. 14.3 and 14.4 for the spatial distributions of these trend values

Table 14.1 A summary of temporal trends for SST, SSS, fCO_2, T-fCO_2, and NT-fCO_2 in the Kuroshio-Oyashio currents-influenced east Japanese margin. Values in the parentheses represent number of grids with significant regression ($p \leq 0.05$). Units are SST (°C yr^{-1}), SSS (yr^{-1}), fCO_2 and decomposed trends (μatm yr^{-1})

	SST	SSS	fCO_2	T-fCO_2	NT-fCO_2
≥39°N	−0.03 ± 0.16 (66)	−0.02 ± 0.05 (64)	2.86 ± 0.92 (62)	0.74 ± 1.59 (14)	3.22 ± 1.11 (44)
<39°N	0.01 ± 0.13 (92)	−0.002 ± 0.03 (83)	2.10 ± 0.59 (112)	0.53 ± 1.27 (39)	2.20 ± 0.85 (98)
Overall	−0.004 ± 0.14 (158)	−0.01 ± 0.04 (147)	2.36 ± 0.81 (178)	0.58 ± 1.35 (53)	2.51 ± 1.05 (142)

14.8 Effect of Changing Boundary Current Conditions on fCO_2 Trend

Compared to our earlier calculations in the broader Japanese Margin (Wang et al. 2017), in which T-fCO_2 is −0.19 ± 1.26 μatm yr^{-1} and NT-fCO_2 is 2.55 ± 1.75 μmol yr^{-1}, the values calculated in this study are not significantly different (0.58 ± 1.35 μatm yr^{-1} and 2.51 ± 1.05 μatm yr^{-1}, Table 14.1). Average SST trend in the grids where T-fCO_2 trends are also significant (see Fig. 14.3c) is 0.03 ± 0.5 °C (n = 51), while that for the entire studied area (Fig. 14.4a) is −0.004 ± 0.14 °C (n = 158) (Table 14.1). Nevertheless, this area as a whole does not appear to show a warming trend as found in the Gulf Stream influenced margin (Wu et al. 2012; Yang et al. 2016).

Different from the Gulf Stream-influenced North America ocean margin where NT-fCO_2 is significantly lower than the atmospheric fCO_2 trend (0.61 ± 2.37 μatm yr^{-1}), for which Wang et al. (2017) interpreted the lower NT-fCO_2 as a result of increasing primary productivity due to anthropogenic nutrient input, the Oyashio

Region has higher NT-fCO_2 trend than the atmospheric one. Therefore, instead of enhanced primary production, the Oyashio Region must have been experiencing changes that have elevated sea surface fCO_2 over the past a few decades.

There are three major causes for sea surface fCO_2 increase (aside from temperature that has been accounted for in NT-fCO_2 calculations), changes in biological activities (primary production and respiration), enhanced upwelling that brings up CO_2-rich subsurface water, and fCO_2 increase in the atmosphere. The fact that NT-fCO_2 trend is greater than the atmospheric trend indicates that either biological activities or upwelling may have contributed to the elevated NT-fCO_2 over time.

The Oyashio Region features abundant warm and cold eddies (Shimizu et al. 2001; Itoh and Yasuda 2010). The presence of eddies is consistent with the higher SST and SSS fluctuation in the north than in the south (Fig. 14.4a, c). The anticyclonic eddies in the northern hemisphere can lead to downwelling, and the interaction between downwelling currents and the continental slope could generate shelf break upwelling, which makes the Oyashio Current-influenced area highly productive (Matano and Palma 2008). The presence of mesoscale eddies potentially can significantly increase primary productivity (Kusakabe et al. 2002). However, the monthly satellite Chl a does not show significant decadal increase in the Oyashio Region for the period spanning from 2002 to 2017 (https://neo.sci.gsfc.nasa.gov/view.php?datasetId=MY1DMM_CHLORA). Therefore, the short-term fluctuation of biological activities does not appear to have exerted significant impact on decadal fCO_2 trends. Nonetheless, biological changes may need further examination in the future as this area has experienced anthropogenic nitrogen enrichment that could enhance primary production (Kim et al. 2011; 2014). Other than organic matter production, calcification also increases fCO_2. However, the pelagic coccolithophores are not in large presence (a few percent or less) compared to diatom in both the Oyashio Region (Nosaka et al. 2017) and the southern end of our study area (Fassbender et al. 2017), therefore they should have minimal control on decadal fCO_2 changes. Wang et al. (2017) speculated that upwelling could be the cause for higher NT-fCO_2 (2.55 ± 1.75 μatm yr^{-1}) in the broader expanse of the Japanese margin (22°N–45°N, 130°E–148°E), which encompasses the area under this investigation. Based on the updated data, the smaller spatial coverage, and the fact that T-fCO_2 trends are positive (Table 14.1, vs. -0.19 ± 1.26 μatm yr^{-1} in Wang et al. 2017), it is unlikely that increasing upwelling has maintained the higher NT-fCO_2 trend.

Using data from both Russian cruises during the 1949–1952 period and a World Ocean Circulation Experiment (WOCE) cruise in 1993, Hill et al. (2003) found basin-wide freshening (salinity decrease by 0.05–0.1) and warming (0.1–0.3 °C) over the latter half of the 20th century in the Okhotsk Sea, an important source of water to the Oyashio Region. Within the Oyashio Region itself, Sasano et al. (2018) observed slight warming trend (0.0187 ± 0.0086 °C yr^{-1}) using winter data only (1954–2014) at the 10 m depth. Despite the fact that their salinity data did not exhibit a long-term trend, sea surface density has decreased at a rate of -0.0018 ± 0.0006 kg m^{-3} yr^{-1}, hence increasing upper water column stratification. During the winter-spring transition, Midorikawa et al. (2003) found that primary production is the greatest contributor to CO_2 drawdown. However, water column stratification

resulted in a decrease in nutrient levels in the surface mixed layer from February to August, subsequently decreasing net community production (NCP) on an annual basis (Chiba et al. 2004) as well as *Neocalanus* copepod biomass (Tadokoro et al. 2005). Therefore, a reduction in primary production may have contributed to the increase in NT-fCO_2.

On the other hand, sea ice decline in the Okhotsk Sea (Ohshima et al. 2014) may have increased surface primary production within the Okhotsk because melting sea ice alleviates both light and iron limitations (Zappa et al. 2007; Kanna et al. 2014), similar to observations in other high latitude regions (e.g., Brown and Arrigo 2012). The Okhotsk Sea is known to export organic carbon from primary production to the east Japanese margin through the Kruzenshterna Strait and Bussol Strait (Seki et al. 2006; Yasuda et al. 2002; Nakatsuka et al. 2004). Therefore, the changing Okhotsk Sea could have led to enhanced respiration in the Oyashio Region that is driven by the imported allochthonous organic carbon, leading to elevated NT-fCO_2, compared to its lower latitude counterpart (<39°N).

14.9 CO_2 Sink/Source Evolution

Based on the differences in the atmospheric and ocean fCO_2 levels (seawater fCO_2 is lower than the atmospheric values, Fig. 14.2a) and trends (seawater fCO_2 trends are greater in the north than in the south, Fig. 14.3a), the Oyashio Region has become a weaker CO_2 sink, while part of the area south of 39°N has become a stronger CO_2 sink (Fig. 14.3b). In the entire studied area, there are ~60% grids that have become a decreasing CO_2 sink (mostly in the Oyashio Region), while the rest (~40%, south of 39°N) have become a stronger CO_2 sink (Fig. 14.3b). However, thermodynamic gradient ($\Delta fCO_{2,\,\text{air-sea}} = \Delta fCO_{2,\,\text{air}} - \Delta fCO_{2,\,\text{sea}}$) can only tell the tendency of the CO_2 source/sink, wind speed record needs to be considered in evaluating how air-sea CO_2 exchange kinetics has changed over time (Wanninkhof 2014). Nevertheless, Watanabe et al. (2013) also observed decrease in anthropogenic CO_2 uptake in the Okhotsk Sea, due to the enhanced stratification as a result of warming. As a result, NPIW could have experienced a reduction in anthropogenic CO_2 uptake as well.

14.10 Conclusions

Based on SCOAT fCO_2 (Version 5) data, temporal and spatial distributions of sea surface fCO_2 are examined in the climatically sensitive northwestern North Pacific region, which is under the influences of western boundary currents (Oyashio and Kuroshio). fCO_2 in this general area has been largely lower than the atmospheric value, although its trends show a clear latitudinal difference (Fig. 14.3a), higher in the Oyashio Region to the north and lower to the south that is under the Kuroshio

Current influence. This difference is expected to result in different behaviors in CO_2 source/sink evolution over time.

The fCO_2 signals are decomposed to thermal- (T-fCO_2) and non-thermal (NT-fCO_2) components to aid the time series analysis. The T-fCO_2 trends (with limited data) show a small increase, although the NT-fCO_2 trends indicate much higher values in the Oyashio Region than the rate of atmospheric CO_2 increase. There are two processes that may have contributed to the elevated NT-fCO_2 in the Oyashio Region: (1) reduction in surface primary production in the Oyashio Region due to stronger upper ocean stratification; (2) possibly enhanced export of primary production from the Okhotsk Sea due to sea ice decline, which alleviates light and iron limitation within the Okhotsk Sea.

To further examine whether the present anthropogenic CO_2 uptake will change in the future, continued effort in data synthesis such as the SOCAT as well as in situ monitoring such as that in Sutton et al. (2018) is needed. In addition, climate variables (e.g., wind speed) and further advances in ocean modeling (Qiu et al. 2017) are also required to calculate actual CO_2 fluxes and carbon budget in this climatically sensitive region.

Acknowledgements The authors were partially supported by an NSF grant (OCE#1654232) during the development of this manuscript. The SOCAT Version 5 Coastal databases used here was downloaded from https://www.socat.info/index.php/2017/06/19/v5-release/. The many researchers and funding agencies responsible for the collection of data and quality control are thanked for their contributions that made the SOCAT available. We also thank Larissa Dias for providing helpful editorial assistance, and Drs. Kitack Lee and Hon-Kit Lui for their helpful comments on an earlier draft of this manuscript.

References

Bakker DCE, Pfeil B, Landa C, Metzl N, O'Brien KM, Olsen A, Smith K, Cosca C, Harasawa S, Jones SD, Nakaoka S, Nojiri Y, Schuster U, Steinhoff T, Tilbrook B, Wanninkhof R, Alin SR, Barbero L, Bates NR, Bianchi AA, Bonou F, Boutin J, Bozec Y, Burger E, Cai W-J, Castle RD, Chen L, Chierici M, Currie K, Evans W, Featherstone C, Feely RA, Fransson A, Greenwood N, Gregor L, Hankin S, Hardman-Mountford NJ, Harlay J, Hauck J, Hoppema M, Humphreys M, Hunt CW, Ibánhez JSP, Johannessen T, Keeling R, Kitidis V, Körtzinger A, Kozyr A, Krasakopolou E, Kuwata A, Landschʊtzer P, Lauvset SK, Lefèvre N, Lo Monaco C, Manke AB, Mathis JT, Merlivat L, Monteiro P, Munro D, Murata A, Newberger T, Omar AM, Ono T, Paterson K, Pierrot D, Robbins LL, Sabine CL, Saito S, Salisbury J, Schneider B, Schlitzer R, Schweitzer R, Sieger R, Skjelvan I, Sullivan KF, Sutherland SC, Sutton AJ, Sweeney C, Tadokoro K, Takahashi T, Telszewski M, Tuma M, Vandemark D, Van Heuven SMAC, Wada C, Ward B, Watson AJ, Xu S (2016) A multi-decade record of high-quality fCO_2 data in version 3 of the Surface Ocean CO_2 Atlas (SOCAT). Earth Syst Sci Data 8:383–413. https://doi.org/10.5194/essd-6-69-2014

Brown ZW, Arrigo KR (2012) Contrasting trends in sea ice and primary production in the Bering Sea and Arctic Ocean. ICES J Mar Sci 69(7):1180–1193. https://doi.org/10.1093/icesjms/fss113

Chiba S, Ono T, Tadokoro K, Midorikawa T, Saino T (2004) Increased stratification and decreased lower trophic level productivity in the Oyashio Region of the North Pacific: a 30-year retrospective study. J Oceanogr 60(1):149–162. https://doi.org/10.1023/B:JOCE.0000038324.14054.cf

Ducklow HW, Steinberg DK, Buesseler KO (2015) Upper ocean carbon export and the biological pump. Oceanography 14(4):50–58

Fassbender AJ, Sabine CL, Cronin MF, Sutton AJ (2017) Mixed-layer carbon cycling at the Kuroshio Extension Observatory. Glob Biogeochem Cycles 31(2):272–288. https://doi.org/10.1002/2016GB005547

Grubbs FE (1969) Procedures for detecting outlying observations in samples. Technometrics 11(1):1–21. https://doi.org/10.1080/00401706.1969.10490657

Hill KL, Weaver AJ, Freeland HJ, Bychkov A (2003) Evidence of change in the sea of okhotsk: Implications for the North Pacific. Atmos-Ocean 41(1):49–63. https://doi.org/10.3137/ao.410104

Honjo S, Manganini SJ, Krishfield RA, Francois R (2008) Particulate organic carbon fluxes to the ocean interior and factors controlling the biological pump: a synthesis of global sediment trap programs since 1983. Prog Oceanogr 76(3):217–285. https://doi.org/10.1016/j.pocean.2007.11.003

Huthnance JM, Aken HMV, White M, Barton ED, Cann BL, Coelho EF, Fanjul EA, Miller P, Vitorino J (2002) Ocean margin exchange—water flux estimates. J Mar Sys 32:107–137

Ishii M, Kosugi N, Sasano D, Saito S, Midorikawa T, Inoue HY (2011) Ocean acidification off the south coast of Japan: a result from time series observations of CO_2 parameters from 1994 to 2008. J Geophys Res 116(C6):C06022. https://doi.org/10.1029/2010jc006831

Itoh S, Yasuda I (2010) Characteristics of mesoscale eddies in the Kuroshio-Oyashio Extension Region detected from the distribution of the sea surface height anomaly. J Phys Oceanogr 40(5):1018–1034. https://doi.org/10.1175/2009jpo4265.1

Kanna N, Toyota T, Nishioka J (2014) Iron and macro-nutrient concentrations in sea ice and their impact on the nutritional status of surface waters in the southern Okhotsk Sea. Prog Oceanogr 126:44–57. https://doi.org/10.1016/j.pocean.2014.04.012

Kim I-N, Lee K, Gruber N, Karl DM, Bullister JL, Yang S, Kim T-W (2014) Increasing anthropogenic nitrogen in the North Pacific Ocean. Science 346(6213):1102–1106. https://doi.org/10.1126/science.1258396

Kim T-W, Lee K, Najjar RG, Jeong H-D, Jeong HJ (2011) Increasing N abundance in the Northwestern Pacific Ocean due to atmospheric nitrogen deposition. Science 334(6055):505–509. https://doi.org/10.1126/science.1206583

Kono T (1997) Modification of the Oyashio Water in the Hokkaido and Tohoku areas. Deep-Sea Res Part I 44(4):669–688. https://doi.org/10.1016/S0967-0637(96)00108-2

Kusakabe M, Andreev A, Lobanov V, Zhabin I, Kumamoto Y, Murata A (2002) Effects of the anticyclonic eddies on water masses, chemical parameters and chlorophyll distributions in the Oyashio Current Region. J Oceanogr 58(5):691–701. https://doi.org/10.1023/a:1022846407495

Landschützer P, Gruber N, Haumann FA, Rödenbeck C, Bakker DCE, van Heuven S, Hoppema M, Metzl N, Sweeney C, Takahashi T, Tilbrook B, Wanninkhof R (2015) The reinvigoration of the Southern Ocean carbon sink. Science 349(6253):1221–1224. https://doi.org/10.1126/science.aab2620

Laruelle GG, Cai W-J, Hu X, Gruber N, Mackenzie FT, Regnier P (2018) Continental shelves as a variable but increasing global sink for atmospheric carbon dioxide. Nat Commun 9(1):454. https://doi.org/10.1038/s41467-017-02738-z

Lenton A, Metzl N, Takahashi T, Kuchinke M, Matear RJ, Roy T, Sutherland SC, Sweeney C, Tilbrook B (2012) The observed evolution of oceanic pCO_2 and its drivers over the last two decades. Glob Biogeochem Cycles 26(2):GB2021. https://doi.org/10.1029/2011gb004095

Liu K-K, Atkinson L, Quiñones R, Talaue-McManus L (2010) Biogeochemistry of continental margins in a global context. In: Liu K-K, Atkinson L, Quiñones R, Talaue-McManus L (eds) Carbon and nutrient fluxes in continental margins: a global synthesis. Springer, p 500

Longhurst AR, Glen Harrison W (1989) The biological pump: profiles of plankton production and consumption in the upper ocean. Prog Oceanogr 22(1):47–123. https://doi.org/10.1016/0079-6611(89)90010-4

Masujima M, Yasuda I, Hiroe Y, Watanabe T (2003) Transport of Oyashio Water across the subarctic front into the mixed water region and formation of NPIW. J Oceanogr 59(6):855–869. https://doi.org/10.1023/B:JOCE.0000009576.09079.f5

Matano RP, Palma ED (2008) On the upwelling of downwelling currents. J Phys Oceanogr 38(11):2482–2500. https://doi.org/10.1175/2008jpo3783.1

McKinley GA, Fay AR, Lovenduski NS, Pilcher DJ (2017) Natural variability and anthropogenic trends in the ocean carbon sink. Annu Rev Mar Sci 9(1):125–150. https://doi.org/10.1146/annurev-marine-010816-060529

McKinley GA, Fay AR, Takahashi T, Metzl N (2011) Convergence of atmospheric and North Atlantic carbon dioxide trends on multidecadal timescales. Nat Geosci 4(9):606–610. https://doi.org/10.1038/ngeo1193

Midorikawa T, Iwano S, Saito K, Takano H, Kamiya H, Ishii M, Inoue HY (2003) Seasonal changes in oceanic pCO_2 in the Oyashio region from winter to spring. J Oceanogr 59(6):871–882

Nakatsuka T, Toda M, Kawamura K, Wakatsuchi M (2004) Dissolved and particulate organic carbon in the Sea of Okhotsk: transport from continental shelf to ocean interior. J Geophys Res-Oceans 109(C9). https://doi.org/10.1029/2003jc001909

Nosaka Y, Yamashita Y, Suzuki K (2017) Dynamics and origin of transparent exopolymer particles in the Oyashio region of the western subarctic Pacific during the spring diatom bloom. Front Mar Sci 4(79). https://doi.org/10.3389/fmars.2017.00079

Ohshima KI, Nakanowatari T, Riser S, Volkov Y, Wakatsuchi M (2014) Freshening and dense shelf water reduction in the Okhotsk Sea linked with sea ice decline. Prog Oceanogr 126:71–79. https://doi.org/10.1016/j.pocean.2014.04.020

Ono T, Sasaki K, Yasuda I (2003) Re-Estimation of annual anthropogenic carbon input from Oyashio into North Pacific Intermediate Water. J Oceanogr 59(6):883–891. https://doi.org/10.1023/B:JOCE.0000009578.19174.d4

Ono T, Watanabe YW, Sasaki K (2000) Annual anthropogenic carbon transport into the North Pacific intermediate water through the Kuroshio/Oyashio Interfrontal Zone: an estimation from CFCs distribution. J Oceanogr 56(6):675–689. https://doi.org/10.1023/a:1011177717139

Pfeil B, Olsen A, Bakker DCE, Hankin S, Koyuk H, Kozyr A, Malczyk J, Manke A, Metzl N, Sabine CL, Akl J, Alin SR, Bates N, Bellerby RGJ, Borges A, Boutin J, Brown PJ, Cai WJ, Chavez FP, Chen A, Cosca C, Fassbender AJ, Feely RA, González-Dávila M, Goyet C, Hales B, Hardman-Mountford N, Heinze C, Hood M, Hoppema M, Hunt CW, Hydes D, Ishii M, Johannessen T, Jones SD, Key RM, Körtzinger A, Landschützer P, Lauvset SK, Lefèvre N, Lenton A, Lourantou A, Merlivat L, Midorikawa T, Mintrop L, Miyazaki C, Murata A, Nakadate A, Nakano Y, Nakaoka S, Nojiri Y, Omar AM, Padin XA, Park GH, Paterson K, Perez FF, Pierrot D, Poisson A, Ríos AF, Santana-Casiano JM, Salisbury J, Sarma VVSS, Schlitzer R, Schneider B, Schuster U, Sieger R, Skjelvan I, Steinhoff T, Suzuki T, Takahashi T, Tedesco K, Telszewski M, Thomas H, Tilbrook B, Tjiputra J, Vandemark D, Veness T, Wanninkhof R, Watson AJ, Weiss R, Wong CS, Yoshikawa-Inoue H (2013) A uniform, quality controlled Surface Ocean CO_2 Atlas (SOCAT). Earth Syst Sci Data 5(1):125–143. https://doi.org/10.5194/essd-5-125-2013

Qiu B (2001) Kuroshio and Oyashio currents. In: Steele J, Thorpe S, Turekian K (eds) Ocean currents: a derivative of the encyclopedia of ocean sciences. Academic Press, pp 61–72. https://doi.org/10.1038/s41558-018-0263-1

Qiu B, Chen S, Schneider N (2017) Dynamical links between the decadal variability of the Oyashio and Kuroshio Extensions. J Climate 30(23):9591–9605. https://doi.org/10.1175/jcli-d-17-0397.1

Rogachev K, Tishchenko PY, Pavlova G, Bychkov A, Carmack EC, Wong CS, Yuraso GI (1996) The influence of fresh-core rings on chemical concentrations (CO_2, PO_4, O_2, alkalinity, and pH) in the western subarctic Pacific Ocean. J Geophys Res-Oceans 101(C1):999–1010. https://doi.org/10.1029/95JC02924

Rost B, Riebesell U (2004) Coccolithophores and the biological pump: responses to environmental changes. In: Thierstein HR, Young JR (eds) Coccolithophores: from molecular processes to global impact. Springer, Berlin, pp 99–125. https://doi.org/10.1007/978-3-662-06278-4_5

Sabine CL, Feely RA, Gruber N, Key RM, Lee K, Bullister JL, Wanninkhof R, Wong CS, Wallace DWR, Tilbrook B, Millero FJ, Peng T-H, Kozyr A, Ono T, Rios AF (2004) The oceanic sink for anthropogenic CO_2. Science 305(5682):367–371

Saito H, Tsuda A, Kasai H (2002) Nutrient and plankton dynamics in the Oyashio region of the western subarctic Pacific Ocean. Deep-Sea Res Part II 49(24):5463–5486. https://doi.org/10.1016/S0967-0645(02)00204-7

Sakurai Y (2007) An overview of the Oyashio ecosystem. Deep-Sea Res Part II 54(23):2526–2542. https://doi.org/10.1016/j.dsr2.2007.02.007

Sarmiento JL, Gruber N (2006) Ocean biogeochemical dynamics. Princeton University Press, Princeton

Sasano D, Takatani Y, Kosugi N, Nakano T, Midorikawa T, Ishii M (2018) Decline and bidecadal oscillations of dissolved oxygen in the Oyashio region and their propagation to the western North Pacific. Glob Biogeochem Cycles 32(6):909–931. https://doi.org/10.1029/2017GB005876

Seki O, Yoshikawa C, Nakatsuka T, Kawamura K, Wakatsuchi M (2006) Fluxes, source and transport of organic matter in the western Sea of Okhotsk: stable carbon isotopic ratios of n-alkanes and total organic carbon. Deep-Sea Res Part I 53(2):253–270. https://doi.org/10.1016/j.dsr.2005.11.004

Shimizu Y, Yasuda I, Ito S-I (2001) Distribution and circulation of the coastal Oyashio intrusion. J Phys Oceanogr 31(6):1561–1578. https://doi.org/10.1175/1520-0485(2001)031%3c1561:Dacotc%3e2.0.Co;2

Sugimoto S, Hanawa K (2011) Roles of SST anomalies on the wintertime turbulent heat fluxes in the Kuroshio-Oyashio Confluence Region: influences of warm eddies detached from the Kuroshio Extension. J Clim 24(24):6551–6561. https://doi.org/10.1175/2011jcli4023.1

Sutton AJ, Feely RA, Maenner-Jones S, Musielwicz S, Osborne J, Dietrich C, Monacci N, Cross J, Bott R, Kozyr A (2018) Autonomous seawater pCO_2 and pH time series from 40 surface buoys and the emergence of anthropogenic trends. Earth Syst Sci Data Discuss 2018:1–23. https://doi.org/10.5194/essd-2018-77

Tadokoro K, Chiba S, Ono T, Midorikawa T, Saino T (2005) Interannual variation in Neocalanus biomass in the Oyashio waters of the western North Pacific. Fish Oceanogr 14(3):210–222. https://doi.org/10.1111/j.1365-2419.2005.00333.x

Takahashi T, Sutherland SC, Sweeney C, Poisson A, Metzl N, Tilbrook B, Bates N, Wanninkhof R, Feely RA, Sabine C, Olafsson J, Nojiri Y (2002) Global sea–air CO_2 flux based on climatological surface ocean pCO_2, and seasonal biological and temperature effects. Deep-Sea Res Part II 49(9–10):1601–1622. https://doi.org/10.1016/s0967-0645(02)00003-6

Takahashi T, Sutherland SC, Wanninkhof R, Sweeney C, Feely RA, Chipman DW, Hales B, Friederich G, Chavez F, Sabine C, Watson A, Bakker DCE, Schuster U, Metzl N, Yoshikawa-Inoue H, Ishii M, Midorikawa T, Nojiri Y, Körtzinger A, Steinhoff T, Hoppema M, Olafsson J, Arnarson TS, Tilbrook B, Johannessen T, Olsen A, Bellerby R, Wong CS, Delille B, Bates NR, de Baar HJW (2009) Climatological mean and decadal change in surface ocean pCO_2, and net sea-air CO_2 flux over the global oceans. Deep-Sea Res Part II 56(8–10):554–577

Wang H, Hu X, Cai W-J, Sterba-Boatwright B (2017) Decadal fCO_2 trends in global ocean margins and adjacent boundary current-influenced areas. Geophys Res Lett 44(17):8962–8970. https://doi.org/10.1002/2017GL074724

Wang H, Hu X, Sterba-Boatwright B (2016) A new statistical approach for interpreting oceanic fCO_2 record. Mar Chem 183:41–49

Wanninkhof R (2014) Relationship between wind speed and gas exchange over the ocean revisited. Limnol Oceanogr-Meth 12(6):351–362. https://doi.org/10.4319/lom.2014.12.351

Wanninkhof R, McGillis WR (1999) A cubic relationship between air-sea CO_2 exchange and wind speed. Geophys Res Lett 26(13):1889–1892. https://doi.org/10.1029/1999GL900363

Wanninkhof R, Park GH, Takahashi T, Sweeney C, Feely R, Nojiri Y, Gruber N, Doney SC, McKinley GA, Lenton A, Le Quéré C, Heinze C, Schwinger J, Graven H, Khatiwala S (2013) Global ocean carbon uptake: magnitude, variability and trends. Biogeosciences 10(3):1983–2000. https://doi.org/10.5194/bg-10-1983-2013

Watanabe YW, Nishioka J, Nakatsuka T (2013) Decadal time evolution of oceanic uptake of anthropogenic carbon in the Okhotsk Sea. Geophys Res Lett 40(2):322–326. https://doi.org/10.1002/grl.50113

Weiss RF (1974) Carbon dioxide in water and seawater: the solubility of a non-ideal gas. Mar Chem 2(3):203–215. https://doi.org/10.1016/0304-4203(74)90015-2

Weiss RF, Price BA (1980) Nitrous oxide solubility in water and seawater. Mar Chem 8(4):347–359

Wu L, Cai W, Zhang L, Nakamura H, Timmermann A, Joyce T, McPhaden MJ, Alexander M, Qiu B, Visbeck M, Chang P, Giese B (2012) Enhanced warming over the global subtropical western boundary currents. Nat Clim Change 2:161. https://doi.org/10.1038/nclimate1353

Yang H, Lohmann G, Wei W, Dima M, Ionita M, Liu J (2016) Intensification and poleward shift of subtropical western boundary currents in a warming climate. J Geophys Res-Oceans 121(7):4928–4945. https://doi.org/10.1002/2015JC011513

Yasuda I (2003) Hydrographic structure and variability in the Kuroshio-Oyashio transition area. J Oceanogr 59(4):389–402. https://doi.org/10.1023/a:1025580313836

Yasuda I, Kouketsu S, Katsumata K, Ohiwa M, Kawasaki Y, Kusaka A (2002) Influence of Okhotsk Sea intermediate water on the Oyashio and North Pacific intermediate water. J Geophys Res-Oceans 107(C12):30-31–30-11. https://doi.org/10.1029/2001jc001037

Yatsu A, Chiba S, Yamanaka Y, Ito S, Shimizu Y, Kaeriyama M, Watanabe Y (2013) Climate forcing and the Kuroshio/Oyashio ecosystem. ICES J Mar Sci 70(5):922–933. https://doi.org/10.1093/icesjms/fst084

Zappa CJ, McGillis WR, Raymond PA, Edson JB, Hintsa EJ, Zemmelink HJ, Dacey JWH, Ho DT (2007) Environmental turbulent mixing controls on air-water gas exchange in marine and aquatic systems. Geophys Res Lett 34(10). https://doi.org/10.1029/2006gl028790

Zeebe RE, Wolf-Gladrow D (2001) CO_2 in seawater: equilibrium, kinetics, isotopes, vol 65. Elsevier Oceanography Series. Elsevier, Amsterdam

Chapter 15
Changing Kuroshio and Its Affected Shelf Sea: A Physical View

Hirohiko Nakamura

Abstract Since around 2010, there have been numerous studies on seasonal, interannual, and longer timescale variations in the path and volume transport of the Kuroshio over its entire length because sufficiently long time series data from satellites and reanalysis datasets have been accumulated. This review provides an overview of the integrated features of these variations, which have historically been investigated separately in geographically distinct regions. Specifically, we focus on keystone phenomena that are representative of separate regions, which include Kuroshio volume transport variations off Luzon Island, off Taiwan, and in the East China Sea. Additionally, we examine Kuroshio path variations such as the meridional shift in the bifurcation latitude of the North Equatorial Current off the Philippines, the Kuroshio intrusion into the South China Sea through the Luzon Strait, the Kuroshio on-shelf intrusion northeast of Taiwan, and the Kuroshio path states around Kyushu Island. The principle pieces of knowledge obtained through this review are as follows. The El Niño-Southern Oscillation (ENSO) and the Pacific Decadal Oscillation (PDO) regulate these phenomena to a greater or lesser degree, with the PDO tending to provide a more dominative driver than the ENSO.

Keywords Kuroshio path · Kuroshio volume transport · Seasonal variation · Interannual and longer timescale variations · ENSO · PDO · Mechanisms

15.1 Introduction

The Kuroshio, which is the western boundary current of the North Pacific subtropical gyre, originates from the east of the Philippines as a northward branch current bifurcated from the North Equatorial Current (NEC) and flows northeastward along the continental slope in the western boundary region (Fig. 15.1). The western boundary region of the subtropical North Pacific has a complicated coastal geometry that is composed of island arcs accompanied by marginal seas at their west, such as the South China Sea (SCS), the East China Sea (ECS), and the Japan/East Sea (JES). The

H. Nakamura (✉)
Faculty of Fisheries, Kagoshima University, 4-50-20 Shimoarata, Kagoshima 890-0056, Japan
e-mail: nakamura@fish.kagoshima-u.ac.jp

C.-T. A. Chen and X. Guo (eds.), *Changing Asia-Pacific Marginal Seas*, Atmosphere, Earth, Ocean & Space, https://doi.org/10.1007/978-981-15-4886-4_15

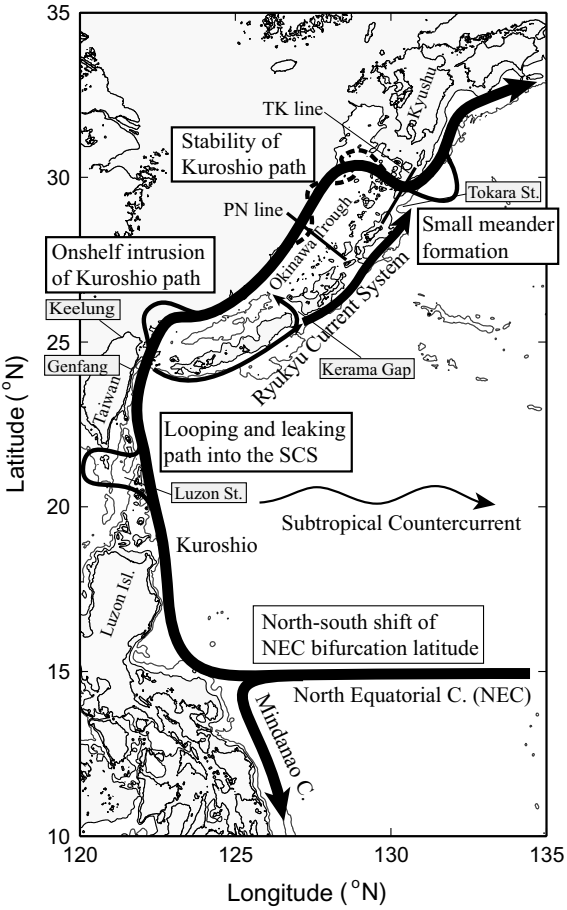

Fig. 15.1 Overview of distinct phenomena concerning seasonal, interannual, and longer timescale variations for Kuroshio volume transports and paths, which are shown in the figure, along with brief comments within rectangles

Kuroshio, therefore, passes through several geographically distinct regions along the complicated continental slope, including the waters east of Luzon Island, the Luzon Strait, the east of Taiwan, the ECS, and the south of Japan. Up to now, numerous scientists have investigated the Kuroshio in each separate region and have focused on its various physical aspects such as seasonal, interannual, and longer timescale variations in volume transport, path, and water properties. This is not only because they are fundamental problems for physical oceanography, but also because they are important factors in understanding environments in the coastal seas over the west of the Kuroshio, as well as in understanding regional climates around the Kuroshio current field. In this chapter, we concentrate on reviewing interannual and longer timescale variations of the volume transport and path over the entire Kuroshio region, while other chapters will undertake detailed reviews about their impacts on the region's coastal seas. In the following parts of this section, we provide an overview of the contents reviewed in this chapter with respect to these topics.

In 2010, nearly 20 years after satellites measuring sea surface height (SSH) were first launched in 1992, our understanding of interannual and longer timescale variations of surface geostrophic velocities over the global oceans began progressing remarkably because an amount of data sufficiently large to analyze long-term variations had been accumulated. In addition, recent developments in the field of ocean reanalysis datasets have provided well-organized information on interannual and longer timescale variations in velocity and temperature/salinity, even under the sea surface, thereby allowing us to incorporate several types of observational data, such as in situ temperature and salinity profiles, with satellite SSH anomalies using a data assimilation system. Because of this, we believe it is now an appropriate time to review recent studies on interannual and longer timescale variations of the Kuroshio volume transport and path.

Although we will focus primarily on interannual and longer timescale variations, seasonal variations will not be excluded from this review, not only because such variations are fundamental components of Kuroshio temporal variations, but also because they can generate interannual and longer timescale variations via phase and/or amplitude modulations. Furthermore, an understanding of seasonal variation mechanisms is vitally important for understanding interannual and longer timescale variations. Long time series from satellite altimetry and reanalysis data have remarkably improved the statistical reliability of seasonal variation data in the Kuroshio velocity field, and thus have advanced our understanding of seasonal as well as longer timescale variations. Therefore, it can now be said that seasonal variations can provide fundamental knowledge for better understanding interannual and longer timescale variations.

Historically, seasonal, interannual, and longer timescale variations concerning the Kuroshio have been investigated separately in geographically distinct regions, as shown in Fig. 15.1. Hence, their integrated features have not yet been established. Accordingly, herein, we will devote our effort to constructing integrated features that incorporate the individual features that have already been revealed in several geographical distinct regions. For this purpose, in Sect. 15.2 we focus on keystone phenomena that are representative of those separated regions and which have attracted scientists over a long period of time. These include the meridional shift in the bifurcation latitude of the NEC off the Philippines and its relationship to the Kuroshio volume transport variation off Luzon Island, which is discussed in Sect. 15.2.1; the Kuroshio intrusion into the SCS through the Luzon Strait, which is discussed in Sect. 15.2.2; the Kuroshio volume transport variation off Taiwan, which is discussed in Sect. 15.2.3; the eddy activity in the subtropical countercurrent (STCC) zone, which influences the Kuroshio path state and volume transport near Taiwan and is discussed in Sect. 15.2.4; the Kuroshio intrusion onto the continental shelf northeast of Taiwan, which is discussed in Sect. 15.2.5; the Kuroshio volume transport variation in the ECS, which is discussed in Sect. 15.2.6; and the Kuroshio path states around Kyushu and their relationship to the small meander formation southeast of the island and frontal eddy development southwest of the island, which are discussed in Sect. 15.2.7.

Interannual and longer timescale variations of the key stone phenomena mentioned above have been examined with relation to several climate indices. The following climate signals, therefore, appear in this review: El Niño and Southern Oscillation (ENSO) (e.g., Wang et al. 2016a), Pacific Decadal Oscillation (PDO) (Mantua et al. 1997), Philippines-Taiwan Oscillation (PTO) (Chang and Oey 2012), and Western Pacific (WP) pattern (Wallace and Gutzler 1981). Although the explanation of these climate signals is beyond the scope of this review, it is worth summarizing the changes in prevailing winds over the North Pacific due to these climate variations because those changes significantly affect Kuroshio volume transport and path variations. ENSO events are associated with a weakening (strengthening) of the Trades over the tropical Pacific during El Niño (La Niña) years. The PDO consists of a strengthening (weakening) of the Westerlies due to the stronger (weaker) Aleutian low and a weakening (strengthening) of the Trades in the western tropical Pacific during the warm (cold) phase. The PTO is a regional climate signal over the subtropical and tropical western North Pacific, which is an oscillation of the wind stress curl difference between east of the Philippines and east of Taiwan; in the positive (negative) PTO phase, the thermocline rises (deepens) east of the Philippines while deepens (rises) east of Taiwan, which are partially connected with the El Niño (La Niña) event and/or positive (negative) PDO phase. The WP pattern is a climate signal that represents intensity of the East Asian jet stream; positive (negative) WP phase is associated with stronger (weaker) East Asian jet stream over the western North Pacific.

In Sect. 15.2, we demonstrate how the interannual and longer timescale variations of the Kuroshio transports and paths show regionally different characteristics. This suggests that variations in different regions are governed by several mechanism types rather than a single mechanism. In order to construct an integrated feature, in Sect. 15.3 we reconsider the regional phenomena in the separate regions from the mechanism viewpoint. For example, interannual and longer timescale variations in Kuroshio volume transport are basically governed by the Sverdrup response to the changes in wind stress curl over the North Pacific interior region, but the actual variations observed cannot be explained solely by the Sverdrup response. One of the reasons for this is believed to be because they are formed with additional processes near or within the western boundary region, such as (1) downstream advection by the Kuroshio (e.g., Akitomo et al. 1996), (2) upstream propagation along the continental slope by the combined effect of planetary and topographic Rossby waves (e.g., Andres et al. 2011; Wu et al. 2019a), and (3) eddy-organized recirculation gyres (e.g., Hsin et al. 2013; Yan et al. 2016). Section 15.4 is devoted to summarizing present problems and future subjects related to physical aspects of the Kuroshio study, especially interannual and longer timescale variations.

15.2 Description of Regional Features of the Kuroshio

15.2.1 East of the Philippines

The NEC, which flows westward on the 10–15°N band, bifurcates off the Philippines into the Mindanao Current flowing southward and the Kuroshio flowing northward (Nitani 1972). Many scientists have studied temporal variations in the bifurcation latitude of the NEC because that location affects the seawater exchange process between tropical and subtropical ocean circulations, possibly resulting in changes to climate and marine ecosystems (Hu et al. 2015). For example, the southward shift of the bifurcation latitude injects more tropical water into the Kuroshio, which may change the meridional heat flux in the North Pacific and subtropical marine ecosystem (Gordon et al. 2014). Interannual and longer time scale variations in the bifurcation latitude are an important factor of those variations in the stock abundance of Japanese ell larvae that arrive from the NEC region to East Asian countries' coasts via the Kuroshio (Kim et al. 2007; Zenimoto et al. 2009; Chang et al. 2015; Lin et al. 2017; Lin and Wu 2019). Accordingly, in this section, we will first review the seasonal variations and then the interannual and longer timescale variations in the bifurcation latitude of the NEC as well as their relationships to the Kuroshio and Mindanao Current volume transports off the Philippines.

15.2.1.1 Seasonal Variations

Seasonal variations of the bifurcation latitude have been characterized by depth-integrated geostrophic velocity fields derived from hydrographic data (Qu and Lukas 2003; Yaremchuk and Qu 2004), at approximately the northernmost position (16–17°N) in winter (November–December) and the southernmost position (14–15°N) in summer (June–July). Such seasonal variations have also been evaluated using surface geostrophic velocity fields derived from satellite SSH data (Qiu and Chen 2010a), giving different values for northernmost position (12.5°N) in winter (December-January) and southernmost position (11.5°N) in summer. Both seasonal variations are consistent in amplitude and phase, but different in the absolute bifurcation latitude. Differences in the absolute bifurcation latitude are based on the vertical structure of the bifurcation whose position shifts northward with increasing depth (Qu and Lukas 2003; Yaremchuk and Qu 2004; Qiu et al. 2015).

It has been considered likely that seasonal variations of the bifurcation latitude are accompanied by seasonal volume transport variations of the NEC, Kuroshio, and Mindanao Current, according to observational results (Yaremchuk and Qu 2004), as well as numerical results and theoretical considerations (Qiu and Lukas 1996; Yang et al. 2013). However, the two types of result do not seem to be completely consistent. For example, the former (observational results) shows a somewhat ambiguous relationship among them with respect to the phase (Fig. 4 in Yaremchuk and Qu (2004)). However, Yang et al. (2013) summarized bifurcation latitude shifts northward and

found that the Kuroshio weakens in the fall and then moves southward, thereby causing Mindanao Current transport to decrease in the summer. Additionally, Hu et al. (2015) stated that the NEC, Mindanao Current, and Kuroshio transports are all at their seasonal maximum during summer (June–July) when bifurcation occurs at the southernmost latitude, but are at their minimum during winter (November–December) when bifurcation occurs at the northernmost latitude, although Yang et al. (2013) pointed out that this has not yet been established by observational facts. On the other hand, the latter (numerical and theoretical results) clearly shows that the NEC is partitioned into the weaker (stronger) Kuroshio and the stronger (weaker) Mindanao Current at the northernmost (southernmost) position of the bifurcation latitude. This mechanism will be described in Sect. 15.2.2.

A fundamental mechanism underlying seasonal variations of the NEC bifurcation latitude was considered in Qiu and Lukas (1996) and Qu and Lukas (2003), focusing on the following issue. The zero wind-stress curl line, which acts to separate the tropical from subtropical gyres, has a large amplitude meridional shift (~8°) in its seasonal variations, while its amplitude of the NEC bifurcation latitude is ~2°, which is significantly smaller than the meridional shift of the zero wind-stress curl line. In their interpretation, Qiu and Lukas (1996) said that the first baroclinic mode planetary Rossby wave has a propagation time longer than 1 year (estimated as ~3 years in Qiu and Chen (2010a)) from the eastern to western boundary on the ~15°N band, which meant that the external forcing effect due to seasonally varying wind stress curl was cancelled out during signal propagation. Although the reduction in amplitude was interpreted well, the phase in the seasonal variation was not explained. Pointing out this deficiency, Qu and Lukas (2003) claimed that the local Ekman pumping off the Philippines due to the Southeast Asia Monsoon plays an important role in seasonal variations of the bifurcation latitude because both variations have a nearly consistent phase relationship. Based on results obtained from a high-resolution numerical model, Kim et al. (2004) showed that the local Ekman pumping process is necessary to form seasonal variations in the NEC bifurcation latitude.

15.2.1.2 Interannual and Longer Timescale Variations

It is known that interannual variations of the NEC bifurcation latitude are driven by the El Niño-Southern Oscillation (ENSO) (Wang et al. 2016a), taking the northmost position in El Niño years and the southernmost position in La Niña years (Qiu and Lukas 1996; Kim et al. 2004; Kashino et al. 2009; Qiu and Chen 2010a; Chen et al. 2015). Qiu and Chen (2010a) indicated that the bifurcation latitude migration has a ~5.5° latitude range, using a low-pass filtered time series (>~1 year) derived from monthly mean SSH data during 1992 and 2010. As the timescale in variation becomes increasingly long, the remote response in the NEC bifurcation latitude (which is the response due to the first baroclinic mode planetary Rossby wave) becomes increasingly dominant. This is because wind stress curl anomalies over the interior region can persist during the time in which such a wave transvers the North Pacific basin. Because of these dynamics, Qiu and Chen (2010a) successfully reconstructed a long

time series of bifurcation latitude shifts using wind stress curl time series results obtained from the atmospheric reanalysis over ~60 years and showed that variations in the NEC bifurcation latitude are strongly nonstationary and undergo interdecadal timescale modulations. For example, there was relatively low variance in the bifurcation latitude prior to 1970s but prominent changes occurred within a 3–5-year period during the 1980s and prominent quasi-decadal variations were noted in the 1990s and 2000s. As a result, they concluded that a positive (negative) Nino-3.4 index could be utilized as a general indicator for northerly (southerly) NEC bifurcations, but that the exact NEC bifurcation latitude depends on the surface wind forcing over the western tropical North Pacific Ocean, thus indicating that containing variability was not fully representable by the commonly used ENSO indices.

Chen and Wu (2012) examined long-term trends of the NEC bifurcation latitude in the period from 1958 to 2008 using SSH data obtained from the Simple Ocean Data Assimilation (SODA) system and found that the bifurcation latitude shifts had a linear trend that followed a southward shift from 15.5 to 13.9°N over the past six decades. Associated with multidecadal variability, the bifurcation latitude shifted southward from 1950 to the late 1960s, while it migrated northward slightly from 1970 to 1992. After the early 1990s, it shifted southward again following the same pattern seen in the first 20 years, and this trend was confirmed with data during 1993–2014 in Wu et al. (2016). This southward bifurcation latitude shift trend was associated with changes in the wind stress curl over the tropical Pacific Ocean between 10 and 20°N, which strengthened the Kuroshio at its origin.

Although Wu (2013) also examined interannual variations of the NEC bifurcation latitude in relation to ENSO and the Pacific Decadal Oscillation (PDO) (Mantua et al. 1997), he followed a different process than Qiu and Chen (2010a) and Chen and Wu (2012) by addressing the effects of monsoon winds off the Philippines on the bifurcation instead of focusing on the trade winds over the tropical interior ocean. More specifically, he stated that a southerly anomalous wind off the Philippines causes a northward shift of the NEC bifurcation latitude in the warm PDO phase, thereby leading to a weakened Kuroshio off Luzon and a Kuroshio intrusion into the SCS. He further insisted that the PDO plays an important role in interannual variability in the low-latitude western North Pacific because the influence of the ENSO is not stationary. Furthermore, he said that the ENSO has little effect on monsoonal winds during the warm PDO phase, even though it has a strong impact on the monsoon and meridional migration of the NEC bifurcation latitude during the cold PDO phase. Wang et al. (2014) confirmed the above-mentioned facts, and pointed out that in the positive PDO phase, neither ENSO nor PDO has a significant influence on westward propagating Rossby wave generations through the wind stress curl anomaly over the low-latitude North Pacific. As a latest study, Wu et al. (2019b) insisted that the Atlantic Multidecadal Oscillation is an ultimately essential driver to govern the North Pacific climate system.

15.2.2 Luzon Strait

The Luzon Strait, which is located between Luzon Island (~18.5°N for the northern tip) and Taiwan (~22°N for the southern tip) where the Philippine Sea is connected with the SCS, is a passage with a width of ~400 km and a sill depth of ~2200 m (Qu et al. 2006). It is known that the Kuroshio takes three different current paths around the Luzon Strait (Caruso et al. 2006; Nan et al. 2011): following the latter paper, a leaping path where the Kuroshio flows northward on the eastern slope of the Luzon Strait sill, a looping path where the Kuroshio flows into the SCS at the southern part of the strait and flows out at its northern part, and a leaking path where a branch current separated from Kuroshio intrudes into the SCS through the Luzon Strait. The Kuroshio intrusion into the SCS has an important influence on mass, heat, salinity, and nutrient balances between the Pacific Ocean and the SCS (Wu et al. 2017). This section discusses the intrusion phenomenon of the Kuroshio into the SCS through the Luzon Strait and its seasonal, interannual, and longer timescale variations. Readers should note that an excellent review paper by Nan et al. (2015) thoroughly explains this topic from observational and theoretical aspects.

15.2.2.1 Seasonal Variations

According to Nan et al. (2011), which examined the three path types (leaking, looping, and leaping paths) in order to ascertain the seasonal features of their occurrence frequencies, the leaking path is predominant in winter at the rate of 69%, followed by the looping path at 25%. In contrast, the leaping path dominates in summer by 82%. The mechanisms of such seasonal variations have been considered historically from two dynamical aspects: the horizontal shift of the Kuroshio path around the Luzon Strait and the inter-basin transport budget between the SCS and the Philippine Sea. The former aspect is composed of two primary mechanisms: (1-1) the steering effect on the Kuroshio induced by wind stress (e.g., Farris and Wimbush 1996), and (1-2) the gap-leaping effect on the Kuroshio induced by upstream current speed (e.g., Sheremet 2001). The latter aspect is determined primarily by (2-1) the circulation integral around the Philippines (e.g., Yang et al. 2013) rather than the traditional island rule (e.g., Qu et al. 2005), and (2-2) the combined effect of the geostrophic and hydraulic controls in the straits (e.g., Song 2006). In the following paragraphs, major papers dealing with these mechanisms are reviewed, not considering the sporadic effect such as an influence of westward propagating mesoscale eddy (Chen et al. 2011).

Over the last several decades, the Kuroshio intrusions into the SCS and its connections to the Northeast Asian Monsoon have been examined by numerous scientists (e.g., Shaw 1991; Farris and Wimbush 1996). The mechanism for (1-1), which is related to the above-listed pioneering works, is connected to the westward Ekman transport by the southward wind stress over the Kuroshio in winter. This transport shifts the Kuroshio path into the SCS as the looping or leaking path. Based on this

mechanism, Farris and Wimbush (1996) proposed an empirical law by which the loop current in winter is formed when the southward component of 4-day averaged local wind stress in the Luzon Strait exceeds 0.08 N m^{-2}. Following Hsin et al. (2012), Wu and Hsin (2012), based on numerical experiments, investigated the Kuroshio path responses to different distributions of local wind stress and wind stress curl over the SCS and the Philippine Sea and showed that, independent of seasonal wind stress variations over the Philippine Sea, only the local seasonal wind stress variation on and west of the Luzon Strait contributes to seasonal Kuroshio path variations around the Luzon Strait. They regarded its driving force as the westward Ekman transport in winter, which steers the Kuroshio current toward the SCS north of the Luzon Strait. However, considering that the surface Ekman layer is only ~10–20 m thick, it is doubtful that the Ekman transport acts directly to shift the Kuroshio, which is a thick current occupying the permanent thermocline under the surface boundary layer. With respect to this point, Nakamura et al. (2015) pointed out the effect of vorticity input due to the nonlinear Ekman pumping over the Kuroshio by the Northeast Asia Monsoon (see Sect. 15.2.7 for more details).

The mechanism for (1-2) is based on theoretical works by Sheremet (2001) and Sheremet and Kuehl (2007), which examined general characteristics of the western boundary current flowing over a gap embedded along the western boundary. Using a single-layer quasi-geostrophic model, Sheremet (2001) examined the response of the jet flowing over the gap to two parameters: γ (the ratio of the gap width to the Munk layer width) and *Re* (the Reynolds number). The results indicated that a larger *Re* is responsible for the leaping path, while a smaller *Re* generates a looping path, and that a multiple equilibrium state exists between them. These results imply that the Kuroshio normally takes the leaping path but switches to the looping path when the current speed declines significantly. Sheremet considered it likely that this situation normally appears in winter when the southward wind blows against the Kuroshio current, although the mechanism by which the wind caused the current speed reduction was not explained. With respect to seasonal surface velocity variations over the entire Kuroshio path, Zhang et al. (2020) pointed out that they are stronger in summer and weaker in winter, based on observational data analysis. Furthermore, through numerical experiments, they also showed that its essential driving force is the local wind stress over the Kuroshio (see Sect. 15.2.6 for more details). This study supports the speculative mechanism proposed by Sheremet (2001) for the winter looping path formation, the mechanism of which will be considered in Sect. 15.3.

In addition to the horizontal shift of the Kuroshio path around the Luzon Strait, the inter-basin transport budget between the SCS and the Philippine Sea is discussed here. Qu (2000) calculated the seasonal change in geostrophic transport across the Luzon Strait using historical hydrographic data, which resulted in a finding that the maximum transport is 5.3 Sv (1 Sv = 1×10^6 m^3 s^{-1}) in winter (January–February) and that the minimum transport is 0.2 Sv in summer (June–July). Qu also stated that seasonal pressure gradient changes across the Luzon Strait are generated by seasonal changes in the local wind stress, which act to pile up water off the southern tip of Taiwan and reduce it off the northern tip of Luzon Island in winter, although his paper did not clarify the dynamics underlying the pile-up. According to Metzger

and Hurlburt (2001), the local Ekman pumping around the Luzon Strait is regarded as the force that forms seasonal changes in the meridional pressure gradient across the Luzon Strait. Furthermore, Qu (2000) pointed out that seasonal Ekman Transport changes contribute little to the seasonal geostrophic volume transport changes related to the intrusion of the Kuroshio water into the SCS.

Based on the estimate of seasonal transport variations in the Luzon Strait throughflow by Qu (2000), Yang et al. (2013) examined the mechanism of (2-1), i.e., the circulation integral around the Philippines for information on the current system regarding the NEC, Mindanao Current, Kuroshio, Luzon Strait throughflow, and so on. Their main result was the finding that the intensity of an anomalous circulation from the steady state around the Philippines depends linearly on the NEC bifurcation latitude and the transport ratios of the Kuroshio and Mindanao Current, based on a circulation integral constraint according to friction around an island (see Eq. 12 in their paper). This idea is consistent with observational evidence with respect to the following points: the northward (southward) shift of the NEC bifurcation latitude leads to a strong (weak) Luzon Strait throughflow and a weak (strong) Kuroshio current, or a strong (weak) Mindanao Current induces a strong (weak) Luzon Strait throughflow. However, a problem with this concept is that both processes cannot exist simultaneously without causing a discrepancy.

On the other hand, Song (2006) tested the mechanism for (2-2), which is the combined effect of the geostrophic and hydraulic control in the straits. By diagnosing the global ocean model outputs using a theoretical formula based on geostrophic and hydraulic control theories, they successfully reproduced seasonal volume transport variations of the throughflows passing through the main straits such as the Karimata-Makassar, Luzon, Taiwan, and Korea/Tsushima Straits. In this mechanism, seasonal inter-basin transports are driven by the SSH difference and the bottom pressure (hence, the vertical density profile) difference at the sill depth between the two basins connected by the strait. This implies that a key mechanism underlying the inter-basin transports is the adjustment process for the SSH and the density distributions over the entire western North Pacific with Asian marginal seas.

15.2.2.2 Interannual and Longer Timescale Variations

In contrast to seasonal variations, the interannual and longer timescale variations of the Kuroshio intrusion into the SCS are less well documented by observational evidence because there is a limited amount of long-time observational records. Here, we refer to Yuan et al. (2014), who analyzed comprehensive datasets consisting of moored current meter records (July 2009–March 2011), Argo float trajectories (2010/11 wintertime), absolute surface geostrophic velocity fields from satellite, and so on. They revealed that the Kuroshio intrusion into the SCS was more remarkable in the winter of the El Niño year for 2009/10 than in the winter of the La-Niña year for 2010/11. Furthermore, using a reanalysis dataset (Global Ocean Forecast System Version 3.0), they pointed out that the Kuroshio was weaker off the eastern coast of Luzon Island for the El Niño year of 2009/10 and regarded that the stronger intrusion

was caused by the weakening of the Kuroshio upstream of the Luzon Strait, based on the theory proposed by Sheremet (2001). As explained in Sect. 15.2.1, it is generally known that the Kuroshio weakens off Luzon Island in El Niño years, and thus the scenario, i.e., that interannual variations of the Kuroshio intrusion into the SCS are related to El-Niño events, is reasonable. It is worth noting that Yuan et al. (2014) pointed out that local wind stress caused by the Northeast Asia Monsoon is responsible for the seasonal variations in the Kuroshio intrusion, but not for the interannual variations. Before Yuan et al. (2014), Qu et al. (2004) proposed this scenario using a high-resolution ocean general circulation model in which he addressed the point that the Luzon Strait throughflow plays an important role in transporting heat from the North Pacific to the SCS with respect to the ENSO event.

Further long-timescale features of the Kuroshio intrusion into the SCS have been investigated by Tsui and Wu (2012), Wu (2013), and Wu et al. (2017) with relation to climate signals such as the PDO index, using the Kuroshio intrusion (KI) index time series from 1992, which is the satellite-derived SSH averaged over the area west of Luzon Island. A low KI index corresponds to an intrusion event. These studies emphasized that the Kuroshio intrusions into the SCS with interannual and longer timescales conform with the PDO index rather than the El Niño indices, as shown in Sect. 15.2.1. The deep intrusion occurs during the warm PDO phase because the southerly anomalous wind off the Philippines shifts the bifurcation latitude of the NEC northward and weakens the Kuroshio off Luzon Island. Furthermore, Nan et al. (2013) and Wu et al. (2016) revealed that the Kuroshio intrusion in the SCS showed a weakening trend over more than two decades from the 1990s to the early 2010s. This is consistent with the results shown by Chen and Wu (2012), Wu et al. (2016, 2019b), in which a long-term trend of the NEC bifurcation latitude observed in the period from the 1990s to 2010s had a linear southward shift (see Sect. 15.2.1 for details). This southward bifurcation latitude shift was associated with changes in the wind stress curl over the tropical Pacific Ocean between 10 and 20°N in Qiu and Chen (2010a) and Chen and Wu (2012), while it was connected with the monsoon wind off the Philippines in Wu et al. (2016).

15.2.3 East of Taiwan

The Kuroshio path and volume transport east of Taiwan are significantly affected by impingements of westward propagating mesoscale eddy with a period of about 100–200 days (Johns et al. 2001; Hsin et al. 2008, 2013), which emanates from the area around the subtropical countercurrent (STCC). This means that their seasonal variations are much smaller in amplitude than variations caused by the mesoscale eddy impingement. Therefore, in order to estimate their seasonal variations, we need long-term records with short time intervals (~10 days or less) in order to remove mesoscale eddy's influences precisely. Although identifying the exact seasonal path and transport variations east of Taiwan used to be a primary difficulty, recent studies (Hsin et al. 2013; Chang et al. 2015; Yan et al. 2016) have overcome this problem by

using satellite altimetry and reanalysis data accumulated over more than 20 years, which provide an observation period long enough for seasonal variation analyses.

When estimating seasonal volume transport variations, another basic problem comes from barotropic responses to seasonal wind stress curl variations in the interior region. This makes it necessary to measure velocity sections in the whole water column. On the other hand, the interannual and longer timescale variations in volume transport can be estimated more easily than its seasonal variations because, unlike the seasonal variations, interannual and longer timescale variations are caused primarily by the baroclinic process. Therefore, they are dynamically equivalent to those variations within the permanent thermocline when the first baroclinic mode response, which can be estimated by using satellite-derived sea surface geostrophic velocity, is assumed. In the following parts of this section, the seasonal, interannual, and longer timescale variations east of Taiwan are reviewed primarily for Kuroshio volume transport. Readers, therefore, should take the above-mentioned issues into consideration when reading the subsection below. Finally, it is worth emphasizing that this section should be read together with Sect. 15.2.6, in which the Kuroshio volume transport variations in the ECS are reviewed.

15.2.3.1 Seasonal Variations

In order to examine volume transport variations in the Kuroshio southeast of Taiwan, Gilson and Roemmich (2002) constructed a long time series of upper-layer geostrophic volume transport (0–800 m depths), using volunteer-ship based expendable bathythermograph/expendable conductivity-temperature-depth (XBT/XCTD) probes of sections that had been observed forth each year from 1993 to 2001. Analyzing this time series, they revealed seasonal volume transport variations with a maximum in July (25.6 Sv) and a minimum in April (17.2 Sv) (amplitude of an annual cycle is 8.4 $\pm$ 6 Sv), which were consistent with conventional estimates (Tang and Yang 1993; Chuang and Liang 1994). On the other hand, Chang and Oey (2011), using the sea level differences between two tide gauge stations for Keelung (the northern tip of Taiwan) and Ishigaki-Jima Island (the southern end of Ryukyu Islands), constructed a 29-year time series of the Kuroshio volume transport index. Contrary to the results of Gilson and Roemmich (2002), their result indicated a maximum in November and a minimum in May. This discrepancy was at first ascribed to the fact that the 8.5-year time series analyzed by Gilson and Roemmich (2002) was too short to remove mesoscale eddy disturbances. In order to verify the results from Chang and Oey (2011), Hsin et al. (2013) examined multiple sea level data from tide gauge stations located on the eastern coast of Taiwan (excluding Keeling) and Ishigaki-Jima Island, together with satellite SSH anomaly data, and concluded that seasonal volume transport variations east of Taiwan have a maximum in summer and minimum in winter, in the almost same way as described in the conventional literature (Tang and Yang 1993; Gilson and Roemmich 2002). They also pointed out that the seasonal variations derived by Chang and Oey (2011) result from Keeling's particular geographical location.

15.2.3.2 Interannual and Longer Timescale Variations

Since almost 2010, there have been many studies on interannual and longer timescale variations in Kuroshio path and volume transport east of Taiwan (Chang and Oey 2011, 2012; Hsin et al. 2013; Chang et al. 2015; Yan et al. 2016; Wang et al. 2016b; Jifeng et al. 2018; Wang and Wu 2018). All the studies listed above pointed out that the interannual and longer timescale variations are related to variations in eddy kinetic energy (EKE) due to baroclinic instability of the STCC. More specifically, in periods with high (low) EKE around the STCC, the anticyclonic (cyclonic) eddy field is more dominant than the cyclonic (anticyclonic) eddy field, so the Kuroshio volume transport east of Taiwan increases (decreases). Although this process is commonly understood among the scientists concerned with these studies, there are two different ideas about how the physical anticyclonic (cyclonic) eddy field becomes more dominant than the cyclonic (anticyclonic) one. Hsin et al. (2013) and Jifeng et al. (2018) insist that the number ratio of the anticyclonic to cyclone eddy impinging the Kuroshio does not change in the interannual timescale, but the intensity ratio (vorticity in the center of eddy) does change. In contrast, Chang et al. (2015) and Yan et al. (2016) take the opposite position, stating that the number ratio of anticyclonic to cyclone eddy impinging the Kuroshio does change in the interannual timescale. This discrepancy has yet to be solved. Besides these studies, Wang and Wu (2018) examined the trend of the Kuroshio intensity during 1993–2013 along its path in terms of eddy impinging, and revealed that the Kuroshio is weakened east of Taiwan relating to positive vorticity trend along the STCC, while it is strengthened east of Luzon Island connecting with negative vorticity trend along the zone south of the STCC. In this study, the positive vorticity trend corresponds to the condition that the cyclonic eddy number takes an increasing trend while the anticyclonic eddy number has a decreasing trend, and vice versa for the negative vorticity trend. In the next section, eddy activity around the STCC will be reviewed for seasonal, interannual, and longer timescale variations.

15.2.4 Subtropical Countercurrent Zone

The STCC is a shallow eastward current on a subtropical front existing in the southwestern subtropical gyre (Yoshida and Kidokoro 1967; Uda and Hasunuma 1969; Hasunuma and Yoshida 1978). There are three distinct STCCs in the southwestern subtropical North Pacific, which are maintained near the southern rims of pycnostads associated with subtropical and central mode water (Kobashi and Kubokawa 2012).

15.2.4.1 Seasonal Variations

Using satellite-derived SSH data, Qiu (1999) showed that areas around STCCs are characterized as with high eddy kinetic energy (EKE) and that the EKE values in

those regions are about half as large as that around the Kuroshio Extension. Moreover, they show remarkable seasonal variations with maximums in spring (April–May) and minimums in winter (December–January). These seasonal variations are related to baroclinic instability of the STCCs, which is enhanced in spring and diminished in fall, depending on the stratification and associated vertical velocity shear in the upper thermocline. More specifically, the seasonal surface heat flux forcing makes a greater contribution to the seasonal vertical velocity shear signals, accounting for 80% of their amplitude, than the seasonal Ekman flux convergence forcing (Qiu and Chen 2013).

Chang and Oey (2011) inferred that seasonal EKE variations around the STCCs cause seasonal Kuroshio transport variations off Taiwan based on the idea that the Kuroshio is enhanced (diminished) by impingements of the anticyclonic (cyclonic) eddy. This process is based on the fact that the number of the anticyclonic eddies is 1.35 times larger than that of the cyclonic eddies around the STCCs (Hwang et al. 2004). Although this process is attractive, it has not been established because Hsin et al. (2013) pointed out that the seasonal Kuroshio transport variations off Taiwan that were used in their paper were wrong regarding its phase (see Sect. 15.2.3). In addition to this fact, there are another reasons why the eddy process may be not regarded as a main driving force of seasonal volume transport variations off Taiwan. If we consider that the period of the eddy impinging the Kuroshio east of Taiwan is about 100 days (e.g., Yang et al. 1999), it seems to be difficult that the eddies impinging the Kuroshio drive the seasonal transport change in the Kuroshio through the stochastic process. In other respects, a recent study by Zhang et al. (2020) showed that seasonal changes in local wind stress over the Kuroshio are likely to be a driving force behind seasonal surface velocity variations over the entire Kuroshio path (see Sect. 15.2.6 for more details). However, it remains unclear whether seasonal EKE variations around the STCCs affect the seasonal Kuroshio transport variations off Taiwan.

15.2.4.2 Interannual and Longer Timescale Variations

Interannual and longer timescale EKE variations around the STCCs have been investigated in numerous studies and in connection with several climate signals. These include the Western Pacific (WP) index (Wallace and Gutzler 1981) in Qiu and Chen (2010b); the PDO index in Chen and Qiu (2010), Yoshida et al. (2011), and Wu et al. (2017); and the Philippines–Taiwan Oscillation (PTO) index in Chang and Oey (2012). Qiu and Chen (2013), using SSH data from October 1992 to June 2012, examined the PDO, WP, and PTO time series for the decadal STCC EKE time series and found that the PDO and PTO indices could represent the EKE changes around the STCCs favorably at lead times of 6 and 12 months, respectively. However, the WP index can only be used for low-frequency EKE changes prior to 2007. Furthermore, it is known that the ENSO indices are not good indicators of the interannual EKE variations around the STCCs (Kazmin and Rienecker 1996; Chen and Qiu 2010).

Qiu and Chen (2013) examined the mechanism of EKE variations around the STCCs from two aspects based on their upper-ocean temperature budget analysis of MOAA-GPV data (Hosoda et al. 2008), which are a combined dataset of quality-controlled Argo-profiling data and other available moored and ship observations. Their results showed that vertical velocity shear around the STCCs varies in the decadal timescale, largely depending on the meridional distribution of surface heat flux forcing, but not on the convergent Ekman flux forcing. This is the same driving mechanism seen in seasonal variations of the EKE around the STCCs. The surface heat flux forcing is not only crucial for seasonal modifications in vertical shear of the STCC eastward flow, it also plays a determinant role in their decadal modulations (Kazmin and Rienecker 1996; Yoshida et al. 2011).

15.2.5 Northeast of Taiwan

The Kuroshio flows into the ECS passing through the channel between Taiwan and Yonaguni-Jima Island (often called the East Taiwan Channel), and then it turns eastward largely along the continental slope. It tends to intrude on the continental slope near this turning place and numerous scientists have paid particular attention to this phenomenon because it has important influences on the mass, heat, salinity, and nutrient balances between the Pacific Ocean and the shelf region of the ECS (Wu et al. 2017). Since the pioneering work by Sun (1987), it has become well known that the on-shelf intrusion northeast of Taiwan tends to occur more often in winter than in summer. Furthermore, using available satellite-derived SSH data that now cover nearly 20 years, our understanding of the interannual and longer timescale variations of the on-shelf intrusion has remarkably progressed in the 2010s. In this section, we will review seasonal, interannual, and longer timescale variations for on-shelf Kuroshio intrusions northeast of Taiwan.

In addition to the on-shelf intrusions of the Kuroshio, there is another interesting phenomenon, which is the cold dome northeast of Taiwan, which often occurs in summer but rarely in winter (e.g., Wu et al. 2008; Cheng et al. 2009). Although this phenomenon has been studied by numerous scientists, its review is beyond the scope of this paper, so the latest study by Cheng et al. (2018) is only briefly introduced here. They revealed that cold dome variations correlate best with the Oceanic Niño index and poorly with the PDO index. Finally, it is worth emphasizing that this section should be read together with Sect. 15.2.7, in which the Kuroshio path states around Kyushu Island are reviewed.

15.2.5.1 Seasonal Variations

As for seasonal variations, the mechanisms for the on-shelf Kuroshio intrusions that have been proposed up to this point are classified into local processes of two types. One is related to the Ekman flow due to the Northeast Asian Monsoon (e.g., Chen

et al. 1996), in which the northeasterly monsoonal wind in winter blows against the Kuroshio and shifts the surface of the current shelf-ward, while the southerly summer wind shifts it offshore-ward. This idea is shared with the local wind mechanism adopted for the winter loop current formation in the Luzon Strait (e.g., Farris and Wimbush 1996). However, Oey et al. (2010) rejected this local wind mechanism because the seasonal on-shelf intrusions do not correlate well with the seasonal wind variations (e.g., Tang and Yang 1993). Additionally, the set-up time for the on-shelf intrusion after strong northeasterly winds is significantly longer than the response time (~5–10 days) of a typical wind-driven upwelling/downwelling, and the on-shelf intrusion remains in place even after the winter winds have declined. Based on these reasons, they proposed another mechanism that is related to surface heat flux forcing on the Kuroshio.

The surface heat flux forcing mechanism discussed in Oey et al. (2010) is explained as follows. The winter monsoon wind over the Kuroshio near Taiwan is stronger than that in other surrounding regions, which results in stronger surface cooling over the Kuroshio near Taiwan. This strong surface cooling changes the density stratification within the Kuroshio over the continental slope near the northeast of Taiwan and causes the Kuroshio to intrude onto the shelf through the joint effects of baroclinicity and bottom relief (JEBAR). This hypothetical mechanism was confirmed in Oey et al. (2010) using a general circulation model with an idealized bottom topography near Taiwan.

In order to verify which forcing, wind stress or surface shear flux, is more effective for the winter on-shelf Kuroshio intrusion northeast of Taiwan, Wu et al. (2014) classified the sea surface velocity patterns northeast of Taiwan into four groups via the self-organizing mapping method, using surface geostrophic velocity dataset from the Archiving Validation and Interpretation of Satellite Oceanography (AVISO) Data Center. After matching the Kuroshio index time series with the on-shelf intrusion, they concluded that large-scale intrusions are likely to occur in late winter and are related to the surface heat flux, while small-scale intrusions tend to occur in early winter and are related to the wind stress. The summer flow pattern without on-shelf intrusions is connected with the southeast summer monsoon winds.

15.2.5.2 Interannual and Longer Timescale Variations

Interannual and longer timescale variations have been examined by Wu et al. (2014) and Wang and Oey (2014). In the same way as seasonal variations, Wu et al. (2014) examined the Kuroshio index time series representing the on-shelf intrusion for longer timescale variations from 1993 to 2011. Unlike the seasonal variations, they concluded that the Kuroshio index time series (positive: intrusion event) are unrelated to the wind stress variations, but have a relatively strong negative correlation with Kuroshio volume transport variations off Taiwan (specifically, the sea level difference between Genfang at the eastern coast of Taiwan and Ishigaki-Jima Island) and have a relatively strong positive correlation with surface heat flux variations over the Kuroshio near Taiwan. Investigating the relationships between the Kuroshio index

and several climate indices, Wu et al. (2014) showed that the Kuroshio index has statistically significant relationships with both the Niño 3.4 and the PDO indices, and proposed a scenario in which both climate signals affect longer timescale variations of the on-shelf intrusion through Kuroshio volume transports and surface heat flux variations over the Kuroshio near Taiwan.

In addition, after examining the PTO index for interannual and longer timescale variations of the on-shelf Kuroshio intrusion, Wang and Oey (2010) insisted that, with a time lag of 4 months, the PTO index has a strong correlation ($r = 0.65$) with the on-shelf intrusion (see Fig. 14 in their paper). This indicates that the PTO index is a better forcing factor than the Kuroshio volume transport off Taiwan ($r = 0.48$; time lag = 0 months), the PDO index ($r = 0.48$; time lag = 1 month), and other climate signals such as the ENSO. Here, they pointed out that the barotropic response to the changes in PDO-related wind stress curl over the North Pacific, such as those examined in Andres et al. (2011) (see Sect. 15.2.6), are not responsible for the on-shelf Kuroshio intrusion, because there are some cases in which the intrusion precedes the PDO index. Instead of forcing related to the PDO, they proposed PTO-related local wind stress around Taiwan as the forcing that generates the on-shelf intrusion. More specifically, since both the northeasterly wind stress and associated cooling occur approximately 4–7 months after a negative PTO peak, the upper layer depth of the Kuroshio tends to become shallower as the current enters the ECS, thereby generating an on-shelf intrusion through JEBAR via the same mechanism as described in Oey et al. (2010). They further suggested that the spatial pattern of a PTO-related wind stress curl is similar to that of the PDO-related wind stress curls observed in the North Pacific Ocean, but noted that those stress curls are clearly different from the ones observed in the western boundary region near Taiwan. However, Wu et al. (2017) recently pointed out that the on-shelf intrusion is unrelated to the PDO index, based on their original time series of the Kuroshio index representing the on-shelf intrusion that was produced during almost the same period, as shown in Wang and Oey (2014). The exact cause of this discrepancy is uncertain, but it may depend partially on differences of the Kuroshio index type defined in each study. Following Wu et al. (2017, 2019a) revealed that, after 1999, the PDO index looks like losing influence on the Kuroshio transport and path variations with interannual and longer timescale, because those timescale variation pattern of wind stress curl changed systematically over the North Pacific. It is, therefore, worth examining whether the PTO is a robust climate index on the Kuroshio transport and path variations in the area from east of the Philippines to the ECS.

Using the output from a high-resolution general circulation model with realistic forcing and bottom topography, Liu et al. (2014) examined interannual on-shelf Kuroshio intrusion variation mechanisms over the entire continental slope region from the northeast of Taiwan to the southwest of Kyushu. They then proposed a mechanism in which the interannual Kuroshio volume transport variations near Taiwan provide a driving force for interannual on-shelf Kuroshio intrusion variations over the entire continental slope. More specifically, the increase (decrease) of the Kuroshio transport shifts the Kuroshio path offshore-ward (inshore-ward) near the slope area with the convoluted shape northeast of Taiwan by strengthening (weakening) the

inertial effect caused by the current speed increase (decrease), as shown in Sheremet (2001). This offshore-ward (inshore-ward) shift results in a vorticity balance that generates a cyclonic (anticyclonic) circulation in that location. This, in turn, results in a modal structure with a cyclonic-anticyclonic-cyclonic (anticyclonic-cyclonic-anticyclonic) pattern along the continental slope between Taiwan and Kyushu where the Kuroshio path tends to separate from (attach to) the slope around its southern and northern ends. In this scenario, interannual volume transport variations can be remotely driven over the North Pacific interior region. This mechanism is different from that described in Oey et al. (2010) because the forcing is independent of the local surface heat flux forcing. Finally, it is worth mentioning a recent study by Gan et al. (2019) in which the lateral shift of the Kuroshio path with an interannual timescale over the continental slope region in the ECS, as shown in Liu et al. (2014), affects summertime precipitation around the ECS.

15.2.6 East China Sea

The ECS has the vast continental shelf on the west and the Okinawa Trough on the east. The Okinawa Trough, which reaches depths greater than 2000 m, is separated from the Philippine Sea by a submarine ridge associated with the Ryukyu Island chain. The Kuroshio flows in through the channel east of Taiwan (sill depth 775 m) and out through the Tokara Strait (sill depth 690 m), and thus exchanges water shallower than ~700 m between the Okinawa Trough and the Philippine Sea. In contrast, there is a current, called the Ryukyu Current, which carries water at intermediate depths over the eastern slope of the Ryukyu Island chain (Zhu et al. 2003; Ichikawa et al. 2004; Zhu et al. 2005; Nakamura et al. 2007; Thoppil et al. 2016). In this section, we focus primarily on the seasonal, interannual, and longer timescale variations of the Kuroshio volume transport. Note, however, that variations of the Ryukyu Current and other branches from the Kuroshio, such as the Taiwan and Tsushima Warm Currents, are not explained in this review. Readers who are interested in variation processes for the circulation over the vast continental shelf including branch currents from the Kuroshio can refer to the following articles: Guo et al. (2006), Isobe (2008), Takahashi and Morimoto (2013) and Lie and Cho (2016) for the seasonal variation, and Gordon and Giulivi (2004) and Han and Huang (2008) for the decadal variation.

Seasonal, interannual, and longer timescale variations of the Kuroshio volume transport were well investigated in the ECS even before the 2000s when satellite-derived SSH data had first been accumulated sufficiently to allow us to analyze interannual variations. This is because long time series of Kuroshio volume transports have been reproduced in the ECS since the early 1990s using hydrographic measurements collected in the PN and TK sections (see Fig. 15.1 for their locations) by the Japan Meteorological Agency (e.g., Ichikawa and Beardsley 1993; Kawabe 1995; Oka and Kawabe 1998; Guo et al. 2012; Wei et al. 2013), and also by using sea level records obtained over long periods of time at several islands in the Tokara Strait and Ryukyu Island chain (e.g., Yamashiro and Kawabe 1996, 2002; Kawabe 2001).

Some of these studies, such as Kawabe (1995), focused on the bimodal path states south of Japan, namely, large and non-large meander paths, and their relationships to long-term ECS Kuroshio volume transport variations. This is because the Kuroshio volume transport in the ECS was regarded as one of the upstream boundary conditions to the bimodal Kuroshio path states south of Japan (Kawabe 1996). However, since the upstream conditions at the Tokara Strait have not recently been considered to be essential factors when analyzing the ocean reanalysis dataset (Usui et al. 2013), we will not explain the details of these studies in this review, and will instead focus on solely on seasonal, interannual, and longer timescale variations of the Kuroshio transport in the ECS, with particular attention paid to their mechanisms. Readers who are interested in the bimodal path states south of Japan can refer to Usui et al. (2013) for a recent study.

15.2.6.1 Seasonal Variations

Kuroshio transport in the ECS reaches a maximum in summer and a minimum in autumn (Ichikawa and Beardsley 1993; Kagimoto and Yamagata 1997; Andres et al. 2008a). This seasonal cycle is roughly similar to that off the south coast of Japan. The driving mechanisms of the seasonal transport variations in the ECS and south of Japan have been examined by numerous scientists (Greatbatch and Goulding 1989, 1990; Sekine and Kutsuwada 1994; Kubota et al. 1995; Sakamoto and Yamagata 1996; Kagimoto and Yamagata 1997) in relation to the following two problems. The first problem is that observed seasonal Kuroshio transport variations are much smaller in amplitude than Sverdrup transport variations. The other is that the observed variations are about 180° out of phase with Sverdrup transport variations.

These two problems have been examined primarily from two dynamical aspects. One aspect is the local dynamics in the western boundary region. Using a linear barotropic model, Kubota et al. (1995) focused on the effect of vorticity input over the continental slope caused by seasonal along-slope wind stresses, which are due to spatial variations of water column thickness over the slope. The phases of the annual cycle transport variations have been well reproduced, but their amplitudes were much smaller than those recorded in the observations. Other dynamics that are related to the effects of variable bottom topography include the continental slope effect due to the JEBAR (Sakamoto and Yamagata 1996), the blocking effect of the Izu-Ogasawara Ridge on westward-propagating barotropic Rossby waves (Greatbatch and Goulding 1989, 1990; Sekine and Kutsuwada 1994; Isobe and Imawaki 2002), and a combination of both of these topographies (Kagimoto and Yamagata 1997). However, none of the studies examining those issues clearly explained the seasonal variation phase discrepancies that exist between the observed and Sverdrup volume transports, even though they did mention the volume transport reductions. On the other hand, Kagimoto and Yamagata (1997) succeeded in reproducing seasonal Kuroshio volume transport variations both in amplitude and phase by using a numerical model with a realistic bottom topography. However, while they tied the seasonal variation mechanisms to the JEBAR, they did not investigate the specific

processes involved. Here, it should be noted that although the bottom topography certainly plays an important role in seasonal Kuroshio volume transport variations, it cannot be the definitive mechanism, especially when their summer maximum and winter minimum phases are considered.

In an effort to solve this problem, Zhang et al. (2020) recently examined a different approach in which, instead of volume transport, the seasonal velocity variations at different depths along the entire Kuroshio path are analyzed. This is because they sought to understand the individual processes relating to volume transport, which is a vertically integrated characteristic of those seasonal variations. Their data analysis conducted using satellite altimetry and reanalysis datasets show that seasonal velocity variations in the upper layer (from 0 to approximately 500 m) reach a maximum in July and a minimum in autumn (October to November) or winter (December to February), with different tendencies noted in each region. However, the lower layer velocity (>~500 m depth) shows reversed seasonal variations—reaching a maximum in winter—especially in the continental slope area from Luzon Island to the Ryukyu Island chain. This difference between the upper and lower layers was confirmed for the Kuroshio across the Tokara Strait in Liu et al. (2019), based on long-term ferryboat ADCP data. Using a realistic general circulation model, Zhang et al. (2020) showed that seasonal Kuroshio velocity variations in the upper layer are caused primarily by local responses to wind stress upon the current itself while the lower layer seasonal Kuroshio velocity variations can be explained by the Sverdrup theory, in which barotropic responses to the wind stress curl over the area west of the Izu-Ogasawara Ridge are responsible. They pointed out that if seasonal Kuroshio transport variations are estimated for the water column from the sea surface to depths over 1000 m, a semiannual cycle with maxima in winter and summer will be detected for a combined feature of the two responses, as shown for the region south of Japan by Isobe and Imawaki (2002) and for the Tokara Strait by Zhu et al. (2017).

15.2.6.2 Interannual and Longer Timescale Variations

During 2002 and 2004, a collaborative international observational study involving Japan, the U.S.A., and Korea was performed to obtain accurate Kuroshio volume transport variation measurements in the northeastern ECS. In this study, a mooring array consisting of pressure-sensor equipped echo sounders (PIESs) and current meters was constructed around the PN line and the absolute volume transport over the whole water column was estimated (Andres et al. 2008a). Using this 2-year study of absolute volume transport measurements as a reference, a long time series (1993–2007) for the Kuroshio volume transport was constructed using satellite-derived SSH data (Andres et al. 2008b). Analyzing this time series, Andres et al. (2009) showed that Kuroshio volume transport variations had a high correlation with the PDO index without a lag time ($r = 0.76$ over a 15-year period), thereby suggesting the barotropic responses to wind stress curl over the central North Pacific near ~35° N. Further analysis by Andres et al. (2011) separated volume transport variations into barotropic and baroclinic responses by using the cross-current gradients of the

satellite-derived SSH and the 26.5 σ_θ isopycnal. In their results, they showed that the SSH gradient and PDO index have a positive correlation without lag time and a negative correlation with a 7-year lag, while the 26.5 σ_θ isopycnal gradient and PDO index have a negative correlation with a 7-year lag. Investigating forcing regions, it was suggested that positive correlations without lag time are related to wind stress curl over the central North Pacific near ~35° N, as discussed in Andres et al. (2009), while negative correlations with a 7-year lag are connected with wind stress curl over the central North Pacific near ~27° N, which is on the same latitude as the ECS. The reason why the SSH gradients respond to signals emanating from two forcing regions is explained as follows. Nondispersive barotropic Rossby waves propagate along the f/H contours as a waveguide (f: Coriolis parameter; H: water depth), while nondispersive baroclinic Rossby waves tend to propagate zonally with an isostatic lower layer.

Using data after 2000s, some researchers have been aware that the PDO index does not behave as the cause of the interannual variation of the Kuroshio transport in the ECS (Nakamura et al. 2012; Soeyanto et al. 2014; Wu et al. 2019a). Using reanalysis data collected until 2012, Soeyanto et al. (2014) reconsidered the point made by Andres et al. (2009). Specifically, they validated that the Kuroshio volume transport in the ECS was highly correlated with the PDO index in the period from 1993 to 2007, and pointed out that the correlation was actually strong during the period from 1993 to 2002, but weakened in the period from 2002 to 2012. This was because the variation range of the PDO index became smaller after 2002 when the westward propagating mesoscale eddies caused larger variations in the Kuroshio transport. They concluded that the combination of PDO- and eddy-related signals determine the interannual Kuroshio transport variations in the ECS. More clearly, Wu et al. (2019a) pointed out that the reason why the PDO index lost influence on the Kuroshio transport variations with interannual and longer timescales. Namely, the leading mode governing atmospheric circulation in the North Pacific has changed from Type A (PDO-like) pattern to Type B (northeast-southwest dipole) pattern since 1999.

15.2.7 Around Kyushu Island

The Kuroshio flows northeastward on the continental slope of the ECS, turns clockwise upon leaving the continental slope, and extends out of the ECS through the Tokara Strait. After passing through the Tokara Strait, the current turns anticlockwise and flows to an area off the southeastern coast of Kyushu where it rejoins and follows the continental slope. Similar to the northeast of Taiwan (Sect. 15.2.5), this region (from the flow-separation point on the continental slope in the ECS to the southeast coast of Kyushu) has various Kuroshio path states. Here, we focus on two different phenomena in order to characterize the Kuroshio path states in this region. One is the Kuroshio small meander southeast of Kyushu (e.g., Nakamura et al. 2015), and the other is the wintertime Kuroshio path destabilization phenomenon southwest of

Kyushu (e.g., Nakamura et al. 2012). Both phenomena have been examined well for seasonal features, but poorly for interannual and longer timescale features. Therefore, we here primarily review the seasonal variations of these phenomena, while touching lightly on their interannual and longer timescale features.

15.2.7.1 Small Meander Formation in Wintertime

The small meander appears about once a year off the southeastern coast of Kyushu. It then propagates downstream and sometimes develops into large meanders off the southern coast of Honshu. Numerous scientists have been intrigued by the processes that govern the formation of small meanders and their development into large types (e.g., Ichikawa 2001; Ebuchi and Hanawa 2003; Usui et al. 2008, 2013; Endoh and Hibiya 2009). In addition to the physical aspects that trigger large meander developments south of Honshu, data collected during the 1960s and 1970s show that small meanders are likely to appear in the winter-spring period (Moriyasu 1961; Solomon 1978; Sekine and Toba 1981). Later, Nagano and Kawabe (2004) examined the occurrence of small meanders using coastal sea level records recorded south of Japan during from 1961 to 1995 and concluded that, in contrast to the findings of previous studies, small meanders tended to occur in summer and autumn rather than in winter and spring. Recently, Nakamura et al. (2015) reported that small meanders experience phase-locking with the seasonal cycle, as occurs in the winter-spring period, even though the intensity of such phase-locking is modulated on decadal timescales.

Nakamura et al. (2015), after analyzing monthly mean surface geostrophic current and wind stress fields, indicated that the southwestward wind blowing against the Kuroshio in the autumn and early winter is responsible for the small meander formation. Furthermore, assuming that the Kuroshio is a surface inertial jet with a double-exponential velocity profile, they showed that nonlinear Ekman pumping over the jet with strong velocity shear (Niiler 1969) results in the inshore-ward shift of the jet. Here, nonlinear Ekman pumping means the vertical velocity due to divergence of the Ekman transport that is calculated from a momentum balance of Coriolis term, wind stress term and nonlinear advection term, which is not negligible within the strong jet stream like the Kuroshio. The nonlinear Ekman pumping acts to strengthen the convoluted Kuroshio path pattern around Kyushu and promotes the development of a small meander southeast of the same island. A two-layer shallow water model with idealized topography shows that the response of the modeled Kuroshio to the local wind stress is consistent with observational and theoretical results. This mechanism is similar to the Ekman transport hypothesis proposed by Chen et al. (1996), Farris and Wimbush (1996) and Wu and Hsin (2012) for the winter loop current formation in the Luzon Strait, but it has an essential development that is explained in the following point; the Ekman transport cannot shift the Kuroshio main body because the surface Ekman layer thickness is only ~10–20 m, while the nonlinear Ekman pumping can change the main body structure of the Kuroshio via vorticity input.

15.2.7.2 Kuroshio Path Destabilization Phenomenon in Wintertime

Between the continental slope and Tokara Strait in the ECS, the Kuroshio exhibits meanders associated with a spatially growing frontal cyclonic eddy that propagates downstream along the continental slope (Nakamura et al. 2003). It is known that such Kuroshio path variations, which are characterized by dominant periods of 30–90 days, tend to occur with larger amplitudes in the winter–spring period and diminish in the summer-autumn period (Nakamura et al. 2006, 2010). In addition, its seasonal amplitudes are modulated by interannual variations that have a weakly coherent tendency with the PDO index (Nakamura et al. 2006, 2012).

Nakamura et al. (2010) showed that a similar feature was reproduced by a realistic high-resolution simulation in the OGCM for the Earth Simulator (OFES). In this study, the driving force of the seasonal path destabilization phenomenon was regarded as the Northeast Asian Monsoon prevailing over the Okinawa Trough. According to this driving mechanism, the interannual amplitude modulation for this destabilization phenomenon may be caused by interannual variations of winter monsoon wind intensity, which are related to the PDO index to some degree.

In this study, the mechanism that causes path destabilization was considered to be nonlinear Ekman upwelling caused by winter northerly wind blowing against the Kuroshio, much as seen in the formation of small meanders. This mechanism has, however, remained unclear with respect to the dynamics of how the horizontal shift due to the upwelling causes the Kuroshio path destabilization (Nakamura et al. 2015). The other dynamics, which are likely to govern the winter Kuroshio path destabilization, are considered from a point of view of mixed layer instability (Boccaletti et al. 2007). In that regard, by analyzing a model output from the OFES with a 1/30° horizontal resolution, Sasaki et al. (2014) showed that sub-mesoscale instability is enhanced in wintertime over the entire North Pacific Ocean by mixed layer instability. The intensity of this mixed layer instability may be controlled by the intensity of Northeast Asian Monsoon, not only for seasonal variations but also for the interannual and longer timescale variations.

15.3 Comprehensive View of Mechanisms Driving Regional Kuroshio Variations

In the previous section, the seasonal, interannual, and longer timescale variations of the Kuroshio volume transport and path were described for each individual region from the east of Luzon Island to the southeast of Kyushu Island. In this section, using Tables 15.1, 15.2, 15.3 and 15.4, the regional features are integrated in order to clarify the essential dynamics underlying these variations. In Sect. 15.3.1, we summarize the regional features for seasonal variations (Table 15.1) and for interannual and longer timescale variations (Table 15.2). In Sect. 15.3.2, we then discuss the mechanisms

Table 15.1 A summary of seasonal variations of the Kuroshio volume transport, Kuroshio path, and EKE in the STCC zone

	Region	Phenomenon	Description
Kuroshio volume transport	East of Luzon Island	Upper layer	Fall or winter: minimum
			Summer: maximum
	East of Taiwan	Upper layer	Winter: minimum
			Summer: maximum
	ECS	Upper layer	Fall or winter: minimum
			Summer: maximum
Kuroshio path	East of the Philippines	NEC bifurcation latitude	Winter: northernmost position
			Summer: southernmost position
	Luzon Strait	Kuroshio intrusion into the SCS	Winter: yes (looping path)
			Summer: no (leaping path)
	Northeast of Taiwan	Kuroshio on-shelf intrusion	Winter: yes
			Summer: no
	Southeast of Kyushu Island	Small Kuroshio meander	Winter: yes
			Summer: no
STCC EKE	STCC zone	Upper layer	Spring (Apr.–May): maximum
			Winter (Dec.–Jan.): minimum

Table 15.2 A summary of interannual and longer time scale variations of the Kuroshio volume transport, Kuroshio path, and EKE in the STCC zone

	Region	Phenomenon	Description	Analyzed yr.	Remarks	Typical articles
Kuroshio volume transport	East of Luzon Island	Upper layer	El Niño: smaller La Niña: larger			Qu et al. (2004) Yuan et al. (2014)
			PDO+: smaller (lag: ~0 yr.) PDO−: larger	1993–2009	ENSO-related signal is unclear ENSO-related signal is clear	Wu (2013)
	East of Taiwan	Upper layer	El Niño: larger (lag: ~0 yr.) La Niña: smaller	1993–2010	Driven by eddies off Taiwan	Shen et al. (2014)
			PDO+: larger (lag: ~0 yr.) PDO−: smaller	1993–2012	Driven by eddies off Taiwan: positive PDO phase corresponds to high EKE phase in STCC zone	Hsin et al. (2013)
	ECS	Upper layer	El Niño: no reports La Niña:			
			PDO+: larger (lag: ~0 yr.) PDO−: smaller	1993–2007 1993–2012	Non-stationary interacting with eddy organization: after 2002, eddy plays an important role	Andres et al. (2011) Soeyanto et al. (2014)
Kuroshio Path	East of the Philippines	NEC bifurcation latitude	El Niño: north (lag: ~6 mon.) La Niña: south	1993–2009	Contaminated by variability not represented by ENSO indices	Qiu and Chen (2010a)

(continued)

Table 15.2 (continued)

	Region	Phenomenon	Description	Analyzed yr.	Remarks	Typical articles
			PDO+: north (lag: ~0 yr.) PDO−: south	1993–2009	ENSO-related signal is unclear ENSO-related signal is clear	Wu (2013)
	Luzon Strait	Kuroshio intrusion into the SCS	El Niño: enhanced (lag: ~0 yr.) La Niña: reduced			Qu et al. (2004) Yuan et al. (2014)
			PDO+: enhanced (lag: ~0 yr.) PDO−: reduced	1993–2013	PDO index is better than ENSO indices	Wu et al. (2017)
	Northeast of Taiwan	Kuroshio on-shelf intrusion	El Niño: low correlation La Niña:			
			PDO+: enhanced (lag: ~1 mon.) PDO−: reduced	1993–2013 1993–2013	PTO index (lag: 4 mon.) is better than PDO index Little correlation with PDO index	Wang and Oey (2014) Wu et al. (2017)
	Southeast of Kyushu Island	Small Kuroshio meander	No reports			
STCC EKE	STCC zone	Upper layer	El Niño: low correlation La Niña:			
			PDO+: larger (lag: ~6 mon.) PDO−: smaller	1993–2011	PTO index (lag: 12 mon.) is equivalent to PDO index	Qiu and Chen (2013)

Table 15.3 A summary of possible mechanisms for seasonal, interannual, and longer timescale variations of the Kuroshio volume transport. Note that the volume transport here is limited to the upper layer (the main thermocline) and does not cover the whole water column

Forcing type	Region	Time scale	Mechanism		Typical articles	Climate signal
Remote forcing	East of Luzon Island	Interannual to interdecadal	(1) Baroclinic RW response to WSC over the trade wind area (10–20° N) (2) Downstream advection of VT anomaly by the Kuroshio	(1)	Qiu and Chen (2010a)	ENSO (non-stational)
				(1)	Chen and Wu (2012)	Linear increasing trend
				(1) + (2)	Akitomo et al. (1996)	ENSO
	East of Taiwan	Interannual to interdecadal	(1) Impingements of mesoscale eddies from the STCC zone: (a) number ratio of anticyclonic and cyclonic eddy (b) intensity ratio of anticyclonic and cyclonic eddy	(1a)	Yan et al. (2016)	
				(1b)	Hsin et al. (2013)	PDO (its related EKE variation in the STCC)
	ECS	Interannual to interdecadal	(1) Barotropic RW response with the topographic β effect near the WBR to WSC over the westerly area (~35° N) (2) Baroclinic RW response to WSC over ~27° N (3) Impingements of mesoscale eddies from the STCC zone	(1) + (2)	Andres et al. (2011)	PDO
				(1) + (3)	Soeyanto et al. (2014)	PDO (non-stational)

(continued)

Table 15.3 (continued)

Forcing type	Region	Time scale	Mechanism		Typical articles	Climate signal
Local forcing	East of Luzon Island	Interannual to interdecadal	(1) Uncertain mechanism due to Northeast Asian Monsoon wind off the Philippines	(1)	Wu (2013)	PDO (non-stational)
	Entire Kuroshio path	Seasonal	(1) Nonlinear Ekman pumping over the jet by Northeast Asian Monsoon wind	(1)	Zhang et al. (2020)	

RW nondispersive Rossby wave over the flat bottom ocean
WSC wind stress curl
VT volume transport
WBR western boundary region

Table 15.4 A summary of possible mechanisms for seasonal, interannual and longer timescale variations of the Kuroshio path. Time scales of Kuroshio path variations are classified into (S) seasonal and (L) interannual to interdecadal time scales. The mechanisms underlying Kuroshio path variations are classified into four types, as stated along with the corresponding articles that first proposed the mechanisms below the table

Forcing type	Region	Time scale	Mechanism	Typical articles	Climate signal
Local forcing	Luzon Strait	(S)	(1)	Farris and Wimbush (1996)	
		(S)	(2)	Sheremet (2001)	
		(L)	(2)	Yuan et al. (2014) Wu et al. (2017)	ENSO PDO
	Northeast of Taiwan	(S)	(3)	Oey et al. (2010)	
		(S)	(1) + (3)	Wu et al. (2014)	
		(L)	(3)	Wang and Oey (2014)	PTO
		(L)	(2) + (3)	Wu et al. (2014)	PDO
		(L)	(2)	Liu et al. (2014)	Not specified
	ECS and around Kyushu	(S)	(4)	Nakamura et al. (2015)	

(1) Ekman transport due to wind stress over the Kuroshio: Chen et al. (1996)
(2) Current speed (inertia) of the Kuroshio: Sheremet (2001)
(3) Surface heat flux over the Kuroshio: Oey et al. (2010)
(4) Nonlinear Ekman pumping by wind stress over the Kuroshio: Nakamura et al. (2015)

underlying the volume transport (Table 15.3) and path variations (Table 15.4) for seasonal, interannual, and longer timescales.

15.3.1 Integrated Features Connecting Each Region

15.3.1.1 Seasonal Variations

Based on Table 15.1, integrated features connecting each region are given for seasonal variations as follows:

(1) The NEC bifurcation latitude tends to shift northward (southward) in winter (summer), which synchronizes with a decrease (increase) in the Kuroshio volume transport off Luzon Island.
(2) The relationships governing seasonal volume transport variations among the NEC, Mindanao Current, and Kuroshio off the Philippines have not yet been established (Yang et al. 2013).
(3) The Kuroshio is likely to take a meandering (straight) path in winter (summer) in the gap on the continental slope (Luzon Strait) and around the corners on the slope, which are characterized by convoluted shapes (northeast of Taiwan, and southeast of Kyushu Island).
(4) The upper-layer volume transport of the Kuroshio, which can be estimated from the SSH variation, is smaller (larger) in winter (summer) over the entire path. On the other hand, the lower-layer volume transport from the east of Taiwan to the east of the Ryukyu Island chain (as a route of the deeper Kuroshio flow) tends to be larger (smaller) in winter (summer) (Zhang et al. 2020).
(5) The EKE in the STCC zone has clear seasonal variations. However, it is unlikely that the seasonal EKE variations in the STCC zone drive the seasonal Kuroshio path or volume transport variations around Taiwan, because the period of the eddy impinging the Kuroshio east of Taiwan is about 100 days, which is almost equal to the seasonal timescale.
(6) A noticeable feature recognized in Table 15.1 is that the Kuroshio volume transport and path appear to vary coherently. Specifically, when the upper-layer Kuroshio is stronger (weaker) in summer (winter), the Kuroshio path takes a straight (meandering) form in the gap and around corners of the continental slope.

15.3.1.2 Interannual and Longer Timescale Variations

Table 15.2 yields integrated features connecting each region for interannual and longer timescale variations:

(1) The NEC bifurcation latitude tends to shift northward (southward) in the positive (negative) PDO period as well as during the El Niño (La Niña) period, which tends to synchronize with a decrease (increase) in the Kuroshio volume transport off Luzon Island and the enhanced (reduced) intrusion of the Kuroshio water into the SCS through Luzon Strait. For such relationships, the PDO index is a better control indicator than the ENSO indices, probably because the ENSO indices are modulated upon the PDO index time series.
(2) However, there is a controversy over whether the on-shelf intrusion of the Kuroshio northeast of Taiwan is correlated with the PDO index (or the PTO index). One group (Wang and Oey 2014) found a statistically significant correlation between them that the other group (Wu et al. 2017) did not find, even though the two groups analyzed data covering almost the same period. This discrepancy is uncertain, but it may depend partially on the difference of types

between the Kuroshio indices developed to represent the on-shelf intrusion northeast of Taiwan.

(3) The upper-layer volume transport of the Kuroshio tends to correlate with the PDO index, except that their correlation in the ECS is significant only for the limited period. Such a correlation is characterized by a reverse tendency between the upstream and downstream regions. More specifically, during the positive (negative) PDO period, the volume transport decreases (increases) off Luzon Island, while it increases (decreases) off Taiwan and the ECS. The reverse tendency has been pointed out by Hsin (2015) and Wang and Wu (2018). The volume transport is also correlated with the ENSO indices, but their correlation becomes increasingly unclear in the downstream Kuroshio region.

(4) The EKE variation in the STCC zone is larger (smaller) in the positive (negative) PDO period, but it is uncorrelated with the ENSO indices.

(5) After about 2000, the PDO index looks like losing influence on the Kuroshio transport and path variations with interannual and longer timescale, because those timescale variation pattern of wind stress curl changed systematically over the North Pacific (Wu et al. 2019a).

15.3.2 The Mechanisms

15.3.2.1 Kuroshio Volume Transport

We will begin by discussing the Kuroshio volume transport for the mechanisms underlying seasonal, interannual, and longer timescale variations. Note that the volume transport here refers to the upper-layer volume transport that is connected with the SSH data. According to Table 15.3, its mechanism is classified into remote and local forcing processes. As for the remote forcing process, there are two kinds of key mechanisms: the response to wind stress curl variations in the North Pacific interior region via barotropic and/or baroclinic Rossby waves, and the influence of mesoscale eddies impinging the Kuroshio, which are propagated from the STCC zone. Based on this framework, the mechanism is discussed as follows:

(1) Interannual and longer timescale variations off Taiwan are strongly affected by impingements of mesoscale eddies that emanate from the STCC zone. This is significantly different from the mechanisms governing upstream and downstream regions of Taiwan, which are basically related to the adjustment process under the Rossby wave excited by wind stress curl change over the interior ocean. This difference is responsible for the reverse tendency in which the volume transport decreases (increases) off Luzon Island, while it increases (decreases) off Taiwan during the positive (negative) PDO period (see Table 15.2). These phenomena are due to the fact that the positive (negative) PDO phase is characterized by stronger (weaker) westerlies and weaker (stronger) trades over the North Pacific. Off Luzon Island, the weaker (stronger) trades weakens (strengthens)

the Kuroshio current, because of the response due to baroclinic Rossby wave propagation between 10° N and 20° N. In contrast, off Taiwan, the stronger (weaker) westerlies strengthens (weakens) the Kuroshio current, because of increase (decrease) of the EKE in the STCC zone. This thought may be related to the finding in Wang and Wu (2018), who revealed that the Kuroshio had a weakening trend during 1993–2013 east of Taiwan relating to positive vorticity trend along the STCC, while it took a strengthening trend east of Luzon Island connecting with negative vorticity trend along the zone south of the STCC.

(2) The mechanism underlying interannual and longer timescale variations in the ECS is considered to be more complex than those variations off Luzon Island and Taiwan. This is because the variations in the ECS are likely to be affected by multiple forcing elements. Specifically, downstream advected anomalies from the low latitude by the Kuroshio, westward propagating mesoscale eddies and baroclinic Rossby waves from the interior region east of the ECS, and upstream propagating anomalies from the high latitude by barotropic Rossby waves along f/H contours. Furthermore, the presences of the Izu-Ogasawara Ridge and the Ryukyu Islands chain are responsible for the response in the ECS complex because they act to block westward propagating barotropic waves (Tanaka and Ikeda 2004). The baroclinic Rossby wave response also obscures the mechanism in the ECS because it is delayed by about 5–10 years to wind stress curl variations.

(3) The mechanism underlying seasonal variations of the upper-layer volume transport is primarily regarded as the response to local wind stress over the Kuroshio, according to the results from numerical experiments in Zhang et al. (2020). A plausible driving mechanism is the nonlinear Ekman pumping (see Sect. 15.2.7 for this term) over the jet caused by the Northeast Asian Monsoon. Here, note that they were convinced that the mechanism for the lower-layer volume transport is basically the barotropic-mode Sverdrup response to wind stress curl over the North Pacific interior region west of the Izu-Ogasawara Ridge. However, the issue of whether interannual and longer timescale variations are generated from phase and/or amplitude modulations of the seasonal variation by the local process has yet to be examined.

15.3.2.2 Kuroshio Path

Unlike the volume transport variations, all of the possible mechanisms underlying Kuroshio path variations are related to the local forcing processes (see Table 15.4). There exist four types of forcing: the Ekman transport due to wind stress over the Kuroshio, the current speed (inertia) of the Kuroshio, surface heat flux over the Kuroshio, and nonlinear Ekman pumping by wind stress over the Kuroshio. All of these forcing types can potentially drive both the seasonal variations and the interannual and longer timescale variations. Based on this framework, the mechanisms of the path variations are discussed as follows:

(1) As for seasonal variations, the path variations have a linkage with the upper-layer volume transport variations of the Kuroshio (see Table 15.1). The Kuroshio intrusion into the SCS through Luzon Strait, the Kuroshio on-shelf intrusion northeast of Taiwan, and the Kuroshio small meander formation southeast of Kyushu Island occur in winter in association with the reduction of the Kuroshio volume transport. Two distinct mechanisms are considered to explain this linkage. One mechanism is based on the current inertia, as shown in Sheremet (2001). This mechanism is not self-contained, because the reduction cause of the upper-layer volume transport in winter is not involved in the mechanism itself. The other mechanism is based on the vorticity input by nonlinear Ekman pumping caused by wind stress over the Kuroshio, as shown in Nakamura et al. (2015) and Zhang et al. (2020). This type of dynamics has an advantage because it can potentially generate both the change in upper-layer volume transport and the current path shift. In addition, it is well consistent with the current inertial effect. The JEBAR probably plays an important role in the seasonal path variations as a part of the mechanism, as shown in Oey et al. (2010).

(2) As for interannual and longer timescale variations of the Kuroshio path, it is difficult to propose a self-consistent and simple mechanism that governs those variations over the entire path. With respect to the Kuroshio intrusion into the SCS through the Luzon Strait, the enhanced intrusion is strongly related to the reduction of the upper-layer volume transport off Luzon Island. This fact is consistent with the mechanism due to the current inertia. On the other hand, with respect to the on-shelf intrusion northeast of Taiwan, two mechanisms exist, which are based on surface heat flux and the current inertia. However, according to Table 15.2, it appears that the two mechanisms cannot operate simultaneously, because the surface heat flux is enlarged and hence the on-shelf intrusion is enhanced in the positive PDO period, while the current inertia is likely to be weakened and hence the intrusion is enhanced in the negative PDO period. This discrepancy may be ascribed to the fact that the relationship between the on-shelf intrusion and the PDO index has not yet been established. Wu et al. (2017) actually pointed out that the on-shelf intrusion shows little in the way of correlation with the PDO index. As Wu et al. (2019a) reported that the PDO has lost influence on Kuroshio current variations since 1999, it is worth examining the PTO for its influence on the on-shelf intrusion since 1999.

15.4 Summary

Recently, our understanding of seasonal, interannual, and longer timescale variations concerning Kuroshio volume transports and paths has progressed remarkably for each geographically distinct region over the Kuroshio path because large amounts of data from satellites and reanalysis datasets have been accumulated. Because it is now an appropriate time, we have devoted our efforts in this review to constructing the

integrated features of these variations in the area from the east of the Philippines to the east of Kyushu Island. In this section, we finally summarize the present problems and future subjects related to these topics, especially the interannual and longer timescale variations.

Section 15.3 revealed that interannual and longer timescale variations of the Kuroshio volume transport off Luzon Island and Taiwan affect the Kuroshio path states in the Luzon Strait and northeast of Taiwan, respectively. We are now aware that the PDO regulates these phenomena to a greater or lesser degree. Off Luzon Island, the weaker (stronger) trades during the positive (negative) PDO phase weakens (strengthens) the Kuroshio current, accompanied by the northward (southward) shift of the NEC bifurcation latitude. In contrast, off Taiwan, the stronger (weaker) westerlies during the positive (negative) PDO phase strengthens (weakens) the Kuroshio current because of an increase (decrease) of the EKE in the STCC zone. Taking into consideration the information contained in this review, this relationship looks to be robust.

Furthermore, it is clear that the Kuroshio intrusion into the SCS through Luzon Strait is enhanced (reduced) during the positive (negative) PDO phase. This is well interpreted by the current inertia. Assuming that the Kuroshio on-shelf intrusion northeast of Taiwan is forced by the Kuroshio volume transport off Taiwan, we expect that the on-shelf intrusion northeast of Taiwan is out of phase with the Kuroshio intrusion through the Luzon Strait synchronizing with the PDO. However, it seems that the volume transport off Taiwan does not really regulate the on-shelf Kuroshio intrusion northeast of Taiwan, according to the PDO. This weaker synchronization with the PDO is probably caused by the PDO-related surface heat flux variation over the Kuroshio, which can enhance (reduce) the on-shelf intrusion during the positive (negative) PDO phase while the volume transport off Taiwan reduces (enhances) the on-shelf intrusion during the positive (negative) PDO phase. When working to construct a unified water exchange system between the North Pacific and the Asian marginal seas via the Kuroshio, it will be essentially important to clarify the tangled problem mentioned above.

Another important issue is the need to clarify interannual and longer timescale variations of the Kuroshio volume transport in the ECS. As seen in Sect. 15.3, this appears to be a particularly complicated problem because these variations are likely to be forced by multiple elements, such as a combination of barotropic Rossby wave propagation from the high-latitude interior region and baroclinic Rossby wave propagation from the mid-latitude interior region, westward propagating mesoscale eddies, and probably local wind stress. In order to solve this interwoven problem, approaches from several types of numerical experiments will be needed in the future. We can suppose that the volume transport variations in the ECS can potentially affect the Kuroshio path states around Kyushu Island, which may change the Tsushima Warm Current and the Kuroshio meanders south of Japan. If we presume these relationships, it is essentially important to make additional efforts to solve this problem.

Section 15.3 suggests that seasonal variations of the upper-layer Kuroshio volume transport are mainly forced by local wind stress over the entire Kuroshio path, but its

interannual and longer timescale variations are predominantly driven by remote processes. Such dynamical differences between seasonal and longer timescale variations appear reasonable because the response by the baroclinic Rossby wave responsible for the remote process needs a long time of about 5–10 years to develop in the middle latitudes. However, it is also worth examining how much interannual and longer timescale variations of the Kuroshio volume transport are influenced by amplitude and phase modulations of the Northeast Asian Monsoon. Assuming a 20% increase (decrease) in annual cycle amplitude for the sea-surface wind, we can expect a 44% increase (36% decrease) in wind stress amplitude because it is proportional to wind speed squared. Based on the fact that the seasonal amplitude variation of Kuroshio surface velocity is ~0.2 m/s off Taiwan, an amplitude of interannual modulation by ~40% wind stress change is estimated as ~0.08 m/s under the linear process, which is approximately comparable to that in observed interannual variations (e.g., Fig. 3 in Hsin (2015)). It is, therefore, meaningful to examine the role of local wind stress forcing in interannual and longer timescale variations of the Kuroshio volume transport.

In addition to oceanic responses to atmospheric forcing, it is important to understand the characteristics of atmospheric forcing such as the temporal and spatial variations of the wind stress over the North Pacific, including its western marginal seas. Conventional studies have mainly pointed out the importance of two types of North Pacific climate signals, ENSO for interannual timescale and PDO for interannual and longer timescales. However, because of the non-stationary features of these climate signals, Kuroshio volume transport and path variations cannot necessarily be explained by the same climate signals over several decades. Indeed, Wu et al. (2019a) claimed that the leading mode governing atmospheric circulation in the North Pacific has changed from the PDO-like pattern to the northeast-southwest dipole pattern since 1999. Therefore, exact information on climate states is necessary to a full understanding of interannual and longer timescale variations of the Kuroshio volume transport and path.

As a further (and even longer) timescale, scientists are now paying attention to the responses of the western boundary currents that may be due to global warming. Wu et al. (2012) reported that the sea surface temperatures of subtropical western boundary currents over the world oceans are warming at the highest rate among the world oceans, and this warming is associated with an intensification of subtropical western boundary currents caused by systematic changes in global wind. Although this problem is beyond the scope of this study, we believe that the pieces of knowledge obtained through this review will be of substantial assistance for researchers working to gain an understanding the response of the Kuroshio to global warming and its influences on the marginal seas.

Acknowledgements The author expresses his gratitude to two anonymous reviewers for their careful reading of the manuscript and important comments. This study was supported by the Japan Society for the Promotion of Science (JSPS) KAKENHI Grant Numbers 15H03725, 15H05821.

References

Akitomo K, Ooi M, Awaji T, Kutsuwada K (1996) Interannual variability of the Kuroshio transport in response to the wind stress field over the North Pacific: its relation to the path variation south of Japan. J Geophys Res-Oceans 101(C6):14057–14071

Andres M, Park JH, Wimbush M, Zhu XH, Chang KI, Ichikawa H (2008a) Study of the Kuroshio/Ryukyu Current system based on satellite-altimeter and in situ measurements. J Oceanogr 64:937–950

Andres M, Wimbush M, Park JH, Chang KI, Lim BH, Watts DR, Ichikawa H, Teague WJ (2008b) Observations of Kuroshio flow variations in the East China Sea. J Geophys Res-Oceans 113(C05013)

Andres M, Park JH, Wimbush M, Zhu XH, Nakamura H, Kim K, Chang KI (2009) Manifestation of the Pacific Decadal Oscillation in the Kuroshio. Geophys Res Lett 36(L16602)

Andres M, Kwon YO, Yang J (2011) Observations of the Kuroshio's barotropic and baroclinic responses to basin-wide wind forcing. J Geophys Res-Oceans 116(C04011)

Boccaletti G, Ferrari R, Fox-Kemper B (2007) Mixed layer instabilities and restratification. J Phys Oceanogr 38:2228–2250

Caruso MJ, Gawarkiewicz GG, Beardsley RC (2006) Interannual variability of the Kuroshio intrusion in the South China Sea. J Oceanogr 62(4):559–575

Chang YL, Oey LY (2011) Interannual and seasonal variations of Kuroshio transport east of Taiwan inferred from 29 years of tide-gauge data. Geophys Res Lett 38(L08603)

Chang YL, Oey LY (2012) The Philippines-Taiwan oscillation: monsoon-like interannual oscillation of the subtropical-tropical western North Pacific wind. J Clim 25:1597–1618

Chang Y, Miyazawa Y, Guo X (2015) Effects of the STCC eddies on the Kuroshio based on the 20-year JCOPE2 reanalysis results. Prog Oceanogr 135:64–76

Chen G, Hu P, Hou Y, Chu X (2011) Intrusion of the Kuroshio into the South China Sea, in September 2008. J Oceanogr 67(4):439–448

Chen HT, Yan XH, Shaw PT, Zheng Q (1996) A numerical simulation of wind stress and topographic effects on the Kuroshio current path near Taiwan. J Phys Oceanogr 26:1769–1802

Chen S, Qiu B (2010) Mesoscale eddies northeast of the Hawaiian archipelago from satellite altimeter observations. J Geophys Res-Oceans 115(C03016)

Chen Z, Wu L, Qiu B, Li L, Hu D, Liu C, Jia F, Liang X (2015) Strengthening Kuroshio observed at its origin during November 2010 to October 2012. J Geophys Res-Oceans 120:2460–2470

Cheng YH, Chung-Ru H, Zheng ZW, Lee YH, Kuo NJ (2009) An algorithm for cold patch detection in the sea off northeast Taiwan using multi-sensor data. Sensors 9(7):5521–5533

Cheng YH, Hu J, Zheng Q, Su FC (2018) Interannual variability of cold domes northeast of Taiwan. Int J Remote Sens 39(13):4293–4303

Chen Z, Wu L (2012) Long-term change of the Pacific North Equatorial Current bifurcation in SODA. J Geophys Res-Oceans 117(C06016)

Chuang WS, Liang WD (1994) Seasonal variability of intrusion of the Kuroshio water across the continental shelf northeast of Taiwan. J Oceanogr 50:531–542

Ebuchi N, Hanawa K (2003) Influence of mesoscale eddies on variations of the Kuroshio path south of Japan. J Oceanogr 59:25–39

Endoh T, Hibiya T (2009) Interaction between the trigger meander of the Kuroshio and the abyssal anticyclone over Koshu Seamount as seen in the reanalysis data. Geophys Res Lett 36(L18604)

Farris A, Wimbush M (1996) Wind-induced intrusion into the South China Sea. J Oceanogr 52:771–784

Gan B, Kwon Y, Joyce T, Chen K, Wu L (2019) Influence of the Kuroshio interannual variability on the summertime precipitation over the East China Sea and adjacent area. J Clim 15:2185–2205

Gilson J, Roemmich D (2002) Mean and temporal variability in Kuroshio geostrophic transport south of Taiwan (1993–2001). J Oceanogr 58:183–195

Gordon AL, Giulivi CF (2004) Pacific decadal oscillation and sea level in the Japan/East Sea. Deep Sea Res Part I 51:653–663

Gordon AL, Flament P, Villanoy C, Centurioni L (2014) The nascent Kuroshio of Lamon Bay. J Geophys Res-Oceans 119:4251–4263
Greatbatch RJ, Goulding A (1989) Seasonal variations in a linear barotropic model of the North Atlantic driven by the Hellerman and Rosenstein wind stress field. J Phys Oceanogr 19(5):572–595
Greatbatch RJ, Goulding A (1990) On the seasonal variation of transport through the Tokara Strait. J Oceanogr Soc Jpn 46(1):9–20
Guo X, Miyazawa Y, Yamagata T (2006) The Kuroshio onshore intrusion along the shelf break of the East China Sea: the origin of the Tsushima Warm Current. J Phys Oceanogr 36:2205–2231
Guo X, Zhu XH, Wu QS, Huang D (2012) The Kuroshio nutrient stream and its temporal variation in the East China Sea. J Geophys Res-Oceans 117(C01026)
Han G, Huang W (2008) Pacific decadal oscillation and sea level variability in the Bohai, Yellow and East China Seas. J Phys Oceanogr 38(2772–2783)
Hasunuma K, Yoshida K (1978) Splitting the subtropical gyre in the western North Pacific. J Oceanogr Soc Jpn 34:160–172
Hosoda S, Ohira T, Nakamura T (2008) A monthly mean dataset of global oceanic temperature and salinity derived from Argo float observations. JAMSTEC Rep Res Dev 8:47–59
Hsin YC, Wu CR, Shaw PT (2008) Spatial and temporal variations of the Kuroshio east of Taiwan, 1982–2005: a numerical study. J Geophys Res-Oceans 113(C04002)
Hsin YC, Wu CR, Chao SY (2012) An updated examination of the Luzon Strait transport. J Geophys Res-Oceans 117(C03022)
Hsin YC, Qiu B, Chiang TL, Wu CR (2013) Seasonal to interannual variations in the intensity and central position of the surface Kuroshio east of Taiwan. J Geophys Res-Oceans 118:4305–4316
Hsin YC (2015) Multidecadal variations of the surface Kuroshio between 1950s and 2000s and its impacts on surrounding waters. J Geophys Res-Oceans 120:1792–1808
Hu DX, Wu LX, Cai WJ, Sen-Gupta A, Ganachaud A, Qiu B, Gordon AL, Lin XP, Chen ZH, Hu SJ, Wang GJ, Wang QY, Sprintall J, Qu TD, Kashino Y, Wang F, Kessler WS (2015) Pacific western boundary currents and their roles in climate. Nature 522:299–308
Hwang C, Wu CR, Kao R (2004) TOPEX/Poseidon observations of mesoscale eddies over the subtropical countercurrent: kinematic characteristics of an anticyclonic eddy and a cyclonic eddy. J Geophys Res-Oceans 109(C08013)
Ichikawa H, Beardsley R (1993) Temporal and spatial variability of volume transport of the Kuroshio in the East China Sea. Deep-Sea Res Part I 40:583–605
Ichikawa H, Nakamura H, Nishina A, Higashi M (2004) Variability of northeastward current southeast of northern Ryukyu Islands. J Oceanogr 60:351–363
Ichikawa K (2001) Variation of the Kuroshio in the Tokara Strait induced by meso-scale eddies. J Oceanogr 57:55–68
Isobe A, Imawaki S (2002) Annual variation of the Kuroshio transport in a two-layer numerical model with a ridge. J Phys Oceanogr 32(3):994–1009
Isobe A (2008) Recent advances in ocean-circulation research on the Yellow Sea and East China shelves. J Oceanogr 64:569–584
Jifeng Q, Baoshu Y, Zhenhua X, Delei L (2018) Spatiotemporal variations of the surface Kuroshio east of Taiwan Island derived from satellite altimetry data. J Oceanol Limnol 36(1):77–91
Johns WE, Lee TN, Zhang D, Zantopp R, Liu CT, Yang Y (2001) The Kuroshio east of Taiwan: Moored transport observations from the WOCE PCM-1 array. J Phys Oceanogr 31:1031–1053
Kagimoto T, Yamagata T (1997) Seasonal transport variations of the Kuroshio: an OGCM simulation. J Phys Oceanogr 27:403–418
Kashino Y, Espana N, Syamsudin F, Richards KJ, Jensen T, Dutrieux P, Ishida A (2009) Observations of the North Equatorial Current, Mindanao Current, and the Kuroshio Current system during the 2006/07 El Niño and 2007/08 La Niña. J Oceanogr 65:325–333
Kawabe M (1995) Variations of current path, velocity, and volume transport of the Kuroshio in relation with the large meander. J Phys Oceanogr 25:3103–3117
Kawabe M (1996) Model study of flow conditions causing the large meander of the Kuroshio south of Japan. J Phys Oceanogr 26:2449–2461

Kawabe M (2001) Interannual variations of sea level at the Nansei Islands and volume transport of the Kuroshio due to wind changes. J Oceanogr 57:189–205
Kazmin AS, Rienecker MM (1996) Variability and frontogenesis in the large-scale oceanic frontal zones. J Geophys Res-Oceans 101(C1):907–921
Kim H, Kimura S, Shinoda A, Kitagawa T, Sasai Y, Sasaki H (2007) Effect of El Niño on migration and larval transport of the Japanese eel, Anguilla japonica. ICES J Mar Sci 64:1387–1395
Kim YY, Qu T, Jensen T, Miyama T, Mitsudera H, Kang HW, Ishida A (2004) Seasonal and interannual variations of the North Equatorial Current bifurcation in a high resolution OGCM. J Geophys Res-Oceans 109(C03040)
Kobashi F, Kubokawa A (2012) Review on North Pacific subtropical countercurrents and subtropical fronts: role of mode waters in ocean circulation and climate. J Oceanogr 68(113126)
Kubota M, Yokota H, Okamoto T (1995) Mechanism of the seasonal transport variation through the Tokara Strait. J Oceanogr 51(4):441–458
Lie HJ, Cho CH (2016) Seasonal circulation patterns of the Yellow and East China Seas derived from satellite-tracked drifter trajectories and hydrographic observations. Prog Oceanogr 146:121–141
Lin YF, Wu CR, Han YS (2017) A combination mode of climate variability responsible for extremely poor recruitment of the Japanese eel (Anguilla japonica). Sci Rep 7(44469)
Lin YF, Wu CR (2019) Distinct impacts of the 1997–98 and 2015–16 extreme El Niños on Japanese eel larval catch. Sci Rep 9(1384)
Liu C, Wang F, Chen X, Von Storch JS (2014) Interannual variability of the Kuroshio onshore intrusion along the East China Sea shelf break: effect of the Kuroshio volume transport. J Geophys Res-Oceans 119:6190–6209
Liu ZJ, Nakamura H, Zhu XH, Nishina A, Guo X, Dong M (2019) Tempo-spatial variations of the Kuroshio current in the Tokara Strait based on long-term ferryboat ADCP data. J Geophys Res-Oceans 124:6030–6049
Mantua NJ, Hare SR, Zhang Y, Wallace JM, Francis RC (1997) A Pacific interdecadal climate oscillation with impacts on salmon production. Bull Amer Meteor Soc 78:1069–1079
Metzger EJ, Hurlburt HE (2001) The nondeterministic nature of Kuroshio penetration and eddy shedding in the South China Sea. J Phys Oceanogr 31:1712–1732
Moriyasu S (1961) On the influence of the monsoon on the oceanographic conditions. J Oceanogr Soc Jpn 17:14–19
Nagano A, Kawabe K (2004) Monitoring of generation and propagation of the Kuroshio small meander using sea level data along the southern coast of Japan. J Oceanogr 60:879–892
Nakamura H, Ichikawa H, Nishina A, Lie HJ (2003) Kuroshio path meander between the continental slope and the Tokara Strait in the East China Sea. J Geophys Res-Oceans 108(3360)
Nakamura H, Yamashiro T, Nishina A, Ichikawa H (2006) Time-frequency variability of Kuroshio meanders in Tokara Strait. Geophys Res Lett 33(L21605)
Nakamura H, Ichikawa H, Nishina A (2007) Numerical study of the dynamics of the Ryukyu current system. J Geophys Res-Oceans 112(C04016)
Nakamura H, Nonaka M, Sasaki H (2010) Seasonality of the Kuroshio path destabilization phenomenon in the Okinawa Trough: a numerical study of its mechanism. J Phys Oceanogr 40:530–550
Nakamura H, Nishina A, Tabata K, Higashi M, Habano A, Yamashiro T (2012) Surface velocity time series derived from satellite altimetry data in a section across the Kuroshio southwest of Kyushu. J Oceanogr 68:321–336
Nakamura H, Hiranaka R, Ambe D, Saito T (2015) Local wind effect on the Kuroshio path state off the southeastern coast of Kyushu. J Oceanogr 5(71):575–596
Nan F, Xue H, Chai F, Shi L, Shi M, Guo P (2011) Identification of different types of Kuroshio intrusion into the South China Sea. Ocean Dyn 61:1291–1304
Nan F, Xue H, Chai F, Wang D, Yu F, Shi M, Guo P, Xiu P (2013) Weakening of the Kuroshio intrusion into the South China Sea over the past two decades. J Clim 26(20):8097–8110
Nan F, Xue H, Yu F (2015) Kuroshio intrusion into the South China Sea: an review. Progress Oceanogr 137:314–333

Niiler PP (1969) On the Ekman divergence in an oceanic jet. J Geophys Res-Oceans 74:7048–7052
Nitani H (1972) Beginning of the Kuroshio. In: Stommel H, Yashida K (eds) Kuroshio: Its physical aspects. University of Tokyo Press, pp 129–163
Oey LY, Hsin YC, Wu CR (2010) Why does the Kuroshio northeast of Taiwan shift shelfward in winter? Ocean Dyn 60:413–426
Oka E, Kawabe M (1998) Characteristics of variations of water properties and density structure around the Kuroshio in the East China Sea. J Oceanogr 54:605–617
Qiu B, Lukas R (1996) Seasonal and interannual variability of the North Equatorial Current, the Mindanao Current, and the Kuroshio along the Pacific western boundary. J Geophys Res-Oceans 101:12315–12330
Qiu B (1999) Seasonal eddy field modulation of the north Pacific STCC: TOPEX/Poseidon observations and theory. J Phys Oceanogr 29:2471–2486
Qiu B, Chen S (2010a) Interannual-to-decadal variability in the bifurcation of the North Equatorial Current off the Philippines. J Phys Oceanogr 40:2525–2538
Qiu B, Chen S (2010b) Interannual variability of the North Pacific STCC and its associated mesoscale eddy field. J Phys Oceanogr 40:213–225
Qiu B, Chen S (2013) Concurrent decadal mesoscale eddy modulations in the Western North Pacific subtropical gyre. J Phys Oceanogr 43:344–358
Qiu B, Chen S, Rudnick DL, Kashino Y (2015) A new paradigm for the North Pacific subthermocline low-latitude western boundary current system. J Phys Oceanogr 45:2407–2423
Qu T (2000) Upper-layer circulation in the South China Sea. J Phys Oceanogr 30:1450–1460
Qu T, Lukas R (2003) The bifurcation of the North Equatorial Current in the Pacific. J Phys Oceanogr 33:5–18
Qu T, Kim YY, Yaremchuk M, Tozuka T, Ishida A, Yamagata T (2004) Can Luzon Strait transport play a role in conveying the impact of ENSO to the South China Sea? J Clim 17:3644–3657
Qu T, Du Y, Meyers G, Ishida A, Wang D (2005) Connecting the tropical Pacific with Indian Ocean through South China Sea. Geophys Res Lett 32(L24609)
Qu T, Girton JB, Whitehead JA (2006) Deepwater overflow through Luzon Strait. J Geophys Res-Oceans 111(C01002)
Sakamoto T, Yamagata T (1996) Seasonal transport variations of the wind-driven ocean circulation in a two-layer planetary geostrophic model with a continental slope. J Mar Res 54(2):261–284
Sasaki H, Klein P, Qiu B, Sasai Y (2014) Impact of oceanic-scale interactions on the seasonal modulation of ocean dynamics by the atmosphere. Nat Commun 5:5636–5643
Sekine Y, Toba Y (1981) Velocity variation of the Kuroshio during formation of the small meander south of Kyushu. J Oceanogr Soc Jpn 37:87–93
Sekine Y, Kutsuwada K (1994) Seasonal variation in volume transport of the Kuroshio south of Japan. J Phys Oceanogr 24:261–272
Shaw PT (1991) The seasonal variation of the intrusion of the Philippine sea water into the South China Sea. J Geophys Res-Oceans 96:821–827
Shen ML, Tseng YH, Jan S, Young CC, Chiou MD (2014) Long-term variability of the Kuroshio transport east of Taiwan and the climate it conveys. Prog Oceanogr 121:60–73
Sheremet VA (2001) Hysteresis of a Western Boundary Current leaping across a gap. J Phys Oceanogr 31:1247–1259
Sheremet VA, Kuehl J (2007) Gap-leaping Western Boundary Current in a circular tank model. J Phys Oceanogr 37:1488–1495
Soeyanto E, Guo X, Ono J, Miyazawa Y (2014) Interannual variations of Kuroshio transport in the East China Sea and its relation to the Pacific Decadal Oscillation and mesoscale eddies. J Geophys Res-Oceans 119:3595–3616
Solomon H (1978) Occurrence of small "trigger" meanders of the Kuroshio off southern Kyushu. J Oceanogr Soc Jpn 34:81–84
Song YT (2006) Estimation of interbasin transport using ocean bottom pressure: theory and model for Asian marginal seas. J Geophys Res-Oceans 111(C11S19)

Sun X (1987) Analysis of the surface path of the Kuroshio in the East China Sea. In: Sun X (ed) Essays on investigation of Kuroshio. China Ocean Press, Beijing, pp 1–14
Takahashi D, Morimoto A (2013) Mean field and annual variation of surface flow in the East China Sea as revealed by combining satellite altimeter and drifter data. Prog Oceanogr 111:125–139
Tanaka K, Ikeda M (2004) Propagation of rossby waves over ridges excited by interannual wind forcing in a Western North Pacific model. J Oceanogr 60(2):329–340
Tang TY, Yang YJ (1993) Low frequency current variability on the shelf break northeast of Taiwan. J Oceanogr 49(19):193–210
Thoppil PG, Metzger EJ, Hurlburt HE, Smedstad OM, Ichikawa H (2016) The current system east of the Ryukyu Islands as revealed by a global ocean reanalysis. Prog Oceanogr 141:239–258
Tsui IF, Wu CR (2012) Variability analysis of Kuroshio intrusion through Luzon Strait using growing hierarchical self-organizing map. Ocean Dyn 62:1187–1194
Uda M, Hasunuma K (1969) The eastward subtropical countercurrent in the western North Pacific Ocean. J Oceanogr Soc Jpn 25(4):201–210
Usui N, Tsujino H, Fujii Y, Kamachi M (2008) Generation of a trigger meander for the 2004 Kuroshio large meander. J Geophys Res-Oceans 113(C01012)
Usui N, Tsujino H, Nakano H, Matsumoto S (2013) Long-term variability of the Kuroshio path south of Japan. J Oceanogra 69:647–670
Wallace JM, Gutzler DS (1981) Teleconnections in the geopotential height field during the Northern Hemisphere winter. Mon Wea Rev 109:784–812
Wang J, Oey LY (2014) Inter-annual and decadal fluctuations of the Kuroshio in East China Sea and connection with surface fluxes of momentum and heat. Geophys Res Lett 41:8538–8546
Wang LC, Wu CR, Qiu B (2014) Modulation of Rossby waves on the Pacific North Equatorial Current bifurcation associated with the 1976 climate regime shift. J Geophys Res-Oceans 119:6669–6679
Wang C, Deser C, Yu JY, DiNezio P, Clement A (2016a) El Niño-Southern Oscillation (ENSO): a review. In: Glymn P, Manzello D, Enochs I (eds) Coral reefs of the Eastern Pacific. Springer Science Publisher, pp 85–106
Wang YL, Wu CR, Chao SY (2016b) Warming and weakening trends of the Kuroshio during 1993–2013. Geophys Res Lett 43:9200–9207
Wang YL, Wu CR (2018) Discordant multi-decadal trend in the intensity of the Kuroshio along its path during 1993–2013. Sci Rep 8(14633)
Wei YZ, Huang D, Zhu XH (2013) Interannual to decadal variability of the Kuroshio Current in the East China Sea from 1955 to 2010 as indicated by in-situ hydrographic data. J Oceanogr 69:571–589
Wu CR, Lu HF, Chao SY (2008) A numerical study on the formation of upwelling off northeast Taiwan. J Geophys Res-Oceans 113(C08025)
Wu CR, Hsin YC (2012) The forcing mechanism leading to the Kuroshio intrusion into the South China Sea. J Geophys Res-Oceans 117(C07015)
Wu CR (2013) Interannual modulation of the Pacific Decadal Oscillation (PDO) on the low-latitude western North Pacific. Prog Oceanogr 110:49–58
Wu CR, Hsin YC, Chiang TL, Lin YF, Tsui IF (2014) Seasonal and interannual changes of the Kuroshio intrusion onto the East China Sea Shelf. J Geophys Res-Oceans 119:5039–5051
Wu CR, Wang YL, Lin YF, Chiang TL, Wu CC (2016) Weakening of the Kuroshio intrusion into the South China Sea under the global warming hiatus. IEEE J Sel Top Appl Earth Obs Remote Sens 9:5064–5070
Wu CR, Wang YL, Lin YF, Chao SY (2017) Intrusion of the Kuroshio into the South and East China Seas. Sci Rep 7(7895)
Wu C-R, Wang Y-L, Chao S-Y (2019a) Disassociation of the Kuroshio Current with the Pacific Decadal Oscillation since 1999. Remote Sens 11(3):276
Wu CR, Lin YF, Qiu B (2019b) Impact of the Atlantic multidecadal oscillation on the Pacific North Equatorial Current bifurcation. Sci Rep 9(2162)

Wu L et al (2012) Enhanced warming over the global subtropical western boundary currents. Nat Clim Change 2(3):161–166
Yamashiro T, Kawabe M (1996) Monitoring of position of the Kuroshio axis in the Tokara Strait using sea level data. J Oceanogr 52:675–687
Yamashiro T, Kawabe M (2002) Variation of the Kuroshio axis south of Kyushu in relation to the large meander of the Kuroshio. J Oceanogr 58:487–503
Yan X, Zhu XH, Pang C, Zhang L (2016) Effects of mesoscale eddies on the volume transport and branch pattern of the Kuroshio east of Taiwan. J Geophys Res-Oceans 121:7683–7700
Yang J, Lin X, Wu D (2013) On the dynamics of the seasonal variation in the South China Sea throughflow transport. J Geophys Res-Oceans 118:6854–6866
Yang Y, Liu CT, Hu JH, Koga M (1999) Taiwan Current (Kuroshio) and impinging eddies. J Oceanogr 55:609–617
Yaremchuk M, Qu T (2004) Seasonal variability of the large-scale currents near the coast of the Philippines. J Phys Oceanogr 34:844–855
Yoshida K, Kidokoro T (1967) A subtropical countercurrent (II)—a prediction of eastward flows at lower subtropical latitudes. J Oceanogr Soc Jpn 23:231–236
Yoshida S, Qiu B, Hacker P (2011) Low-frequency eddy modulations in the Hawaiian Lee Countercurrent: observations and connection to the Pacific Decadal oscillation. J Geophys Res-Oceans 116(C12009)
Yuan Y, Tseng YH, Yang C, Liao G, Chow CH, Liu Z, Zhu XH, Chen H (2014) Variation in the Kuroshio intrusion: Modeling and interpretation of observations collected around the Luzon Strait from July 2009 to March 2011. J Geophys Res-Oceans 119:3447–3463
Zenimoto K, Kitagawa T, Miyazaki S, Sasai T, Sasaki H, Kimura S (2009) The effects of seasonal and interannual variability of oceanic structure in the western Pacific North Equatorial Current on larval transport of the Japanese eel (Anguilla japonica). J Fish Biol 74:1878–1890
Zhang ZL, Nakamura H, Zhu XH (2020) Seasonal velocity variations over the entire Kuroshio path. J Phys Oceanogr, in review
Zhu XH, Han I, Park J, Ichikawa H, Murakami K, Kaneko A, Ostrovskii A (2003) The northeastward current southeast of Okinawa Island observed during November 2000 to August 2001 Geophys Res Lett 30(1071)
Zhu XH, Park JH, Kaneko I (2005) The northeastward current southeast of the Ryukyu Islands in late fall of 2000 estimated by an inverse technique. Geophys Res Lett 32(L05608)
Zhu XH, Nakamura H, Dong M, Nishina A, Yamashiro T (2017) Tidal currents and Kuroshio transport variations in the Tokara Strait estimated from ferryboat A DCP data. J Geophys Res-Oceans 122(3):2120–2142

Chapter 16
Transient Carbonate Chemistry in the Expanded Kuroshio Region

Hon-Kit Lui, Chen-Tung Arthur Chen, Wei-Ping Hou, Shujie Yu, Jui-Wen Chan, Yan Bai, and Xianqiang He

Abstract The Kuroshio is the most significant current in the western North Pacific Ocean and affects a wide area. This work shows that the intrusion of the oligotrophic upper-layer West Philippine Sea seawater into the South China Sea (SCS) as the branch of Kuroshio reduced the productivity and hence the fluxes of sinking particles in the SCS between 2013 and 2017. Conversely, the productivity in the SCS increased during a large scale Kuroshio intrusion in 1998–2006, indicating that other factors also affected the productivity. Further, the western North Pacific Ocean is acidifying, with the surface seawaters to the west having lower acidification rates. This phenomenon is likely a consequence of enhanced productivity owing to more anthropogenic nutrient inputs from the continent in the west, but needs further investigation. In the East China Sea, the Kuroshio Intermediate Water has increased nutrient concentrations, but decreased in both dissolved oxygen (DO) concentration and pH, most likely owing to reduced ventilation in the North Pacific Intermediate Water. Further warming of the surface oceans would strengthen the stratification of the surface

H.-K. Lui (✉) · C.-T. A. Chen
Department of Oceanography, National Sun Yat-Sen University, Kaohsiung 804, Taiwan
e-mail: hklui@mail.nsysu.edu.tw

C.-T. A. Chen
e-mail: ctchen@mail.nsysu.edu.tw

W.-P. Hou · J.-W. Chan
National Applied Research Laboratories, Taiwan Ocean Research Institute, Kaohsiung 80143, Taiwan
e-mail: ping@narlabs.org.tw

J.-W. Chan
e-mail: juwen@narlabs.org.tw

S. Yu · Y. Bai · X. He
State Key Laboratory of Satellite Ocean Environment Dynamics, Second Institute of Oceanography, Ministry of Natural Resources, Hangzhou 310012, China
e-mail: yvshujie@126.com

Y. Bai
e-mail: baiyan@sio.org.cn

X. He
e-mail: hexianqiang@sio.org.cn

C.-T. A. Chen and X. Guo (eds.), *Changing Asia-Pacific Marginal Seas*, Atmosphere, Earth, Ocean & Space, https://doi.org/10.1007/978-981-15-4886-4_16

ocean, weakening ventilation. Consequently, DO and pH would continue to decline while nutrients level increases.

Keywords Kuroshio · Intrusion · Intermediate water · South China sea · East China sea · Productivity

16.1 Introduction

The Kuroshio Current, or simply called Kuroshio, is a western boundary current in the western North Pacific Ocean. It originates in the northward bifurcation of the North Equatorial Current off the eastern Luzon Island, and its mainstream passes the east of the Luzon Strait and Taiwan (Fig. 16.1). The southward bifurcation forms the Mindanao Current. The Kuroshio flows northeastward along the shelf break of the East China Sea (ECS) and then passes the eastern coast of Japan. The current is about 85–135 km wide, 400–600 m thick, and has maximum velocities ranging between 0.7 and 1.4 m s^{-1} (Chen et al. 2016; Jan et al. 2015). The Kuroshio transports water, heat, salt, nutrients, dissolved oxygen (DO), dissolved inorganic carbon (DIC), and other dissolved and particulate materials northward from the tropical and subtropical regions of the West Philippine Sea (WPS). The Kuroshio mainstream occasionally

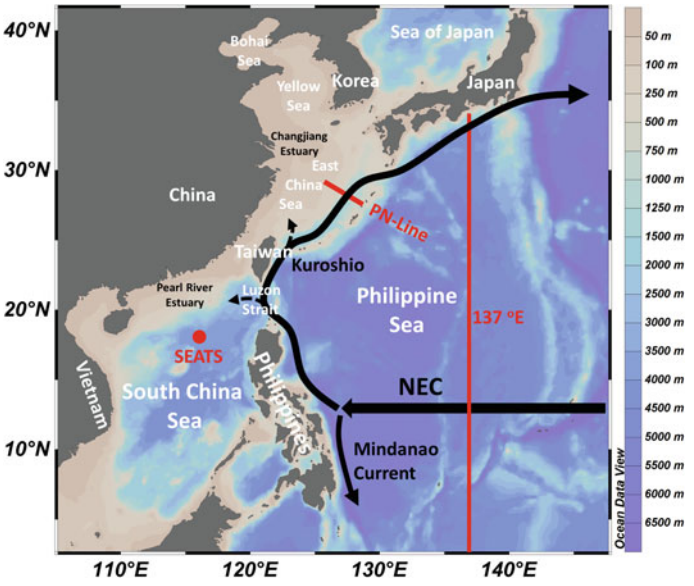

Fig. 16.1 Map of study area and station locations. The red solid circle shows the South East Asia Time Series Study (SEATS) station, and the red lines show the PN-Line and 137° E hydrographic lines. The black arrows indicate the Kuroshio, Mindanao current, and the North Equatorial Current (NEC)

intrudes into the South China Sea (SCS) through the Luzon Strait. It also intrudes into the continental shelves of the ECS across the shelf break northeast of Taiwan (Chen 1996, 2000; Wu et al. 2017).

Since the Kuroshio originates from the WPS, the current initially has the physical and chemical properties of the WPS seawaters, which contrast with those of waters of the SCS and the ECS. Certainly, the properties change by mixing with seawaters along its pathway (Chen et al. 2016; Jan et al. 2015; Qu et al. 2018). The potential temperature (θ) versus salinity (S) curve is the easiest and most convenient means to distinguish water masses in the regions influenced by the Kuroshio. The WPS generally has a maximum S (S_{max}) of about 34.9 when θ is about 21–23 °C at about 150 m water depth (Chen et al. 2016; Lui et al. 2014). On the other hand, the WPS Intermediate Water (WPSIW), originating from the North Pacific Intermediate Water (NPIW), is located at about 600–700 m depth with a S minimum (S_{min}) of about 34.15 when θ is about 7 °C. The WPSIW is the main source of the SCS Intermediate Water (SCSIW), yet the water mass in the SCS has a flatter θ/S curve than the WPS, largely due to strong vertical mixing. Therefore, the SCS has S_{max} of about 34.6 and S_{min} of about 34.45 when θ are at about 17–18 °C and 7–8 °C, respectively (Chen et al. 2016; Lui et al. 2014).

The WPS seawaters mix with the SCS seawaters off the Luzon Strait, and flow off the eastern coast of Taiwan into the ECS as the Kuroshio Current. For instance, the South China Sea Tropical Water (SCSTW) and the SCSIW are forced to enter the ECS by the northward flowing Kuroshio when they flow eastward off the Luzon Strait. The SCSTW and the SCSIW follow the same pathway as the Kuroshio, occupy the western half of the Okinawa Trough before existing it, and can be traced as far east as 140° E south of Japan (Chen 2005). The Kuroshio Tropical Water (KTW) is a mixture of surface and subsurface seawaters from the WPS and SCS, and has S_{max} of 34.85 or higher. Mixed with the WPSIW, the seawater with a S_{min} of 34.32 is the Kuroshio Intermediate Water (KIW) (Chen et al. 2016; Lui et al. 2014). Seawaters generally contain higher proportions of SCSTW and SCSIW west of the mainstream of the Kuroshio, and higher proportions of WPSTW and WPSIW east of the main stream (Chen 2005; Lui et al. 2014). In the wide ECS, the KTW with a maximum S of 34.85 centers at a depth of 150–200 m, extending westward to the shelf break. Meanwhile, the broad KIW with a minimum S of 34.32 centers at a depth between 600 and 800 m. The distributions of S and potential density (σ) are characterized by slanted isotherms, which tilt upward toward the west, reflecting upwelling of the subsurface waters (Fig. 16.2).

16.2 Increasing Nutrients but Decreasing DO and pH of the KIW

The Changjiang (Yantze) River contributes roughly 90% of all river water to the ECS, yet the upwelling of subsurface waters from the Kuroshio Current contributes the most nutrients to the ECS (Chen 1996, 2000; Chen and Wang 1999). For instance,

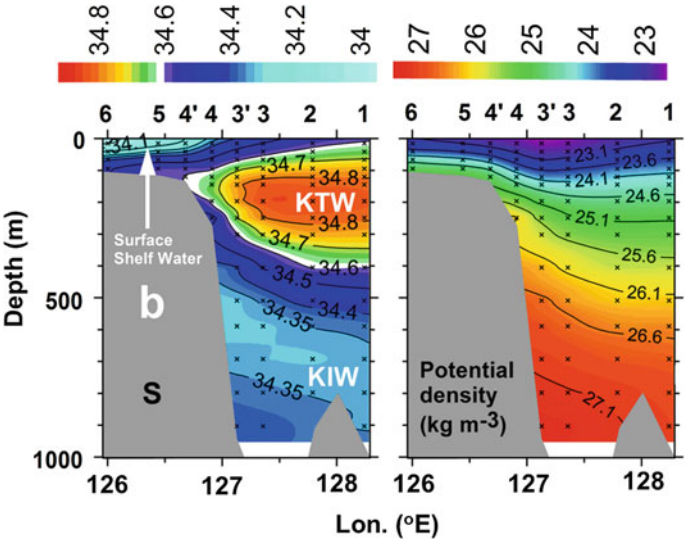

Fig. 16.2 Distribution of average salinity (left) and potential density (right) at various depths at the PN-Line between 1982 and 2010. The KTW refers to Kuroshio Tropical Water and the KIW is the Kuroshio Intermediate Water

the upwelled Kuroshio Current contributes ten times more PO_4^{3-} than all rivers entering the ECS combined, thus supporting high productivity in the ECS (Chen 1996, 2000). Using the PN-Line data taken from the Nagasaki Marine Observatory of the Japan Meteorological Agency (JMA), Lui et al. (2014) demonstrated that the KTW increased in DO but decreased in NO_3^- and PO_4^{3-} concentrations between 1982 and 2010, likely owing to the enhanced productivity (Figs. 16.2 and 16.3).

To have better understanding about the trend of change in productivity in the Kuroshio regions, the trend of changes in chlorophyll-a (Chl.-a) concentration between 2000 and 2018 is determined using the satellite-derived Chl.-a time-series data taken from the Ocean Colour Project of the ESA CCI (version 4 product). Data are resampled to the resolution of 1/6° from the original resolution of 1/24°. Trends in Chl.-a are assessed pixel by pixel and reported as percent per year, computed from the linear slope, with the average for the whole period. Only the pixels with more than 80 available data and significant change trend (The p value obtained by the f test is less than 0.1) are colored (Fig. 16.4). The result shows that the Chl.-a concentration increased in the ECS and in the Taiwan Strait (Fig. 16.4). Such a result is consistent with the finding of Lui et al. (2014) that at the PN-Line Chl.-a and DO concentrations of the KTW show increasing trends between the surface to 250 m depth. Meanwhile, nutrients show decreasing trends, suggesting enhanced productivity. In contrast, the Kuroshio regions off the Luzon Strait and Taiwan (Area 1), East of ECS (Area 2), south of Japan (Area 3) and its eastward extension (Area 4) show decreasing trends in Chl.-a concentration (Fig. 16.4). On average, Chl.-a concentrations in Areas 1–4

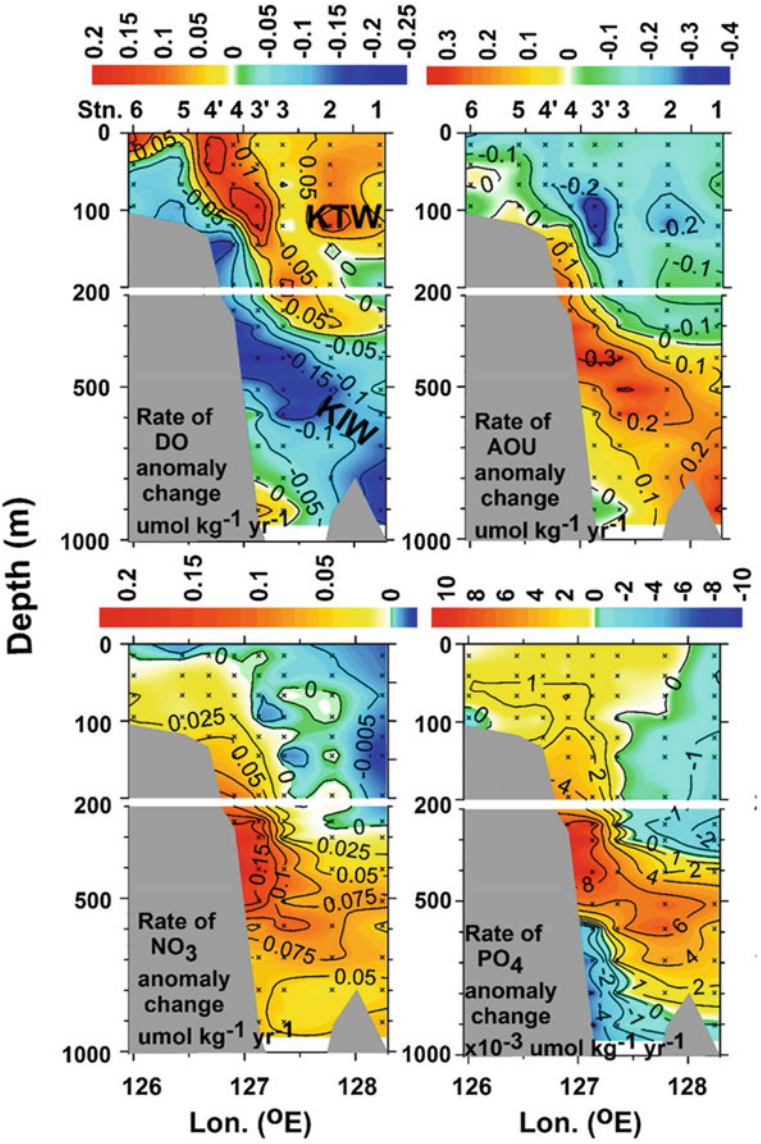

Fig. 16.3 Distributions of rates of temporal changes in anomalies of DO, appraent oxygen utilization (AOU), NO_3 and PO_4 concentrations along the PN-Line (taken from Lui et al. 2014). The anomalies are defined as observed data minus seasonal mean. The temporal changes are determined using the simple linear regression method. See Lui et al. (2014) for detail

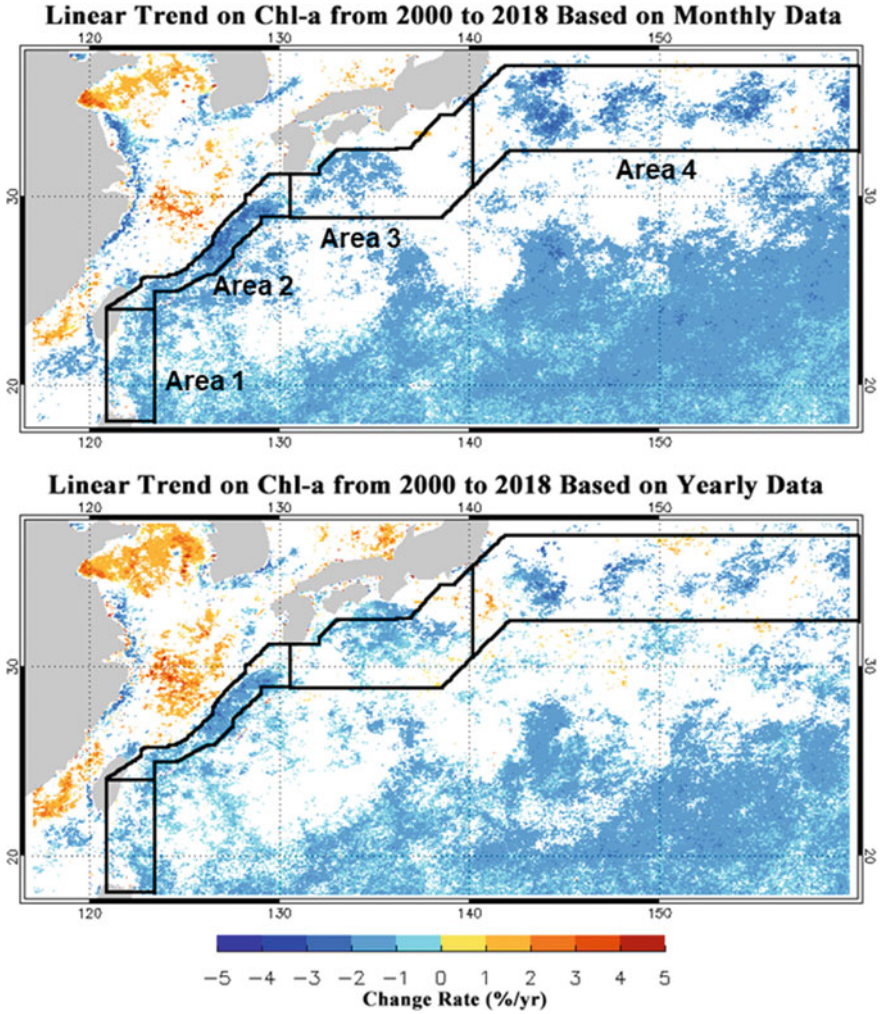

Fig. 16.4 Distribution of rate of percentage change in satellite-derived chlorophyll-a with respect to its average concentration based on monthly (top) or yearly (bottom) data between 2000 and 2018. Data are resampled to the resolution of 1/6° from the original resolution of 1/24°. Trends in chlorophyll-a are assessed pixel by pixel and reported as percent per year, computed from the linear slope, with the average for the whole period. Only the pixels with more than 80 available data and significant change trend (The p value obtained by the f test is less than 0.1) are colored

suffered decreasing trends of $-0.7\%\ yr^{-1}$, $-0.9\%\ yr^{-1}$, $-0.5\%\ yr^{-1}$ and $-0.8\%\ yr^{-1}$, respectively (Fig. 16.5).

In contrast, the KIW rose in NO_3^- and PO_4^{3-} concentrations but fell in DO (Guo et al. 2012; Lui et al. 2014) (Fig. 16.3). The NPIW is frequently observed around the σ of 26.6–27.4 (Talley 1997; Yasuda 1997). Notably, seawater with the maximum

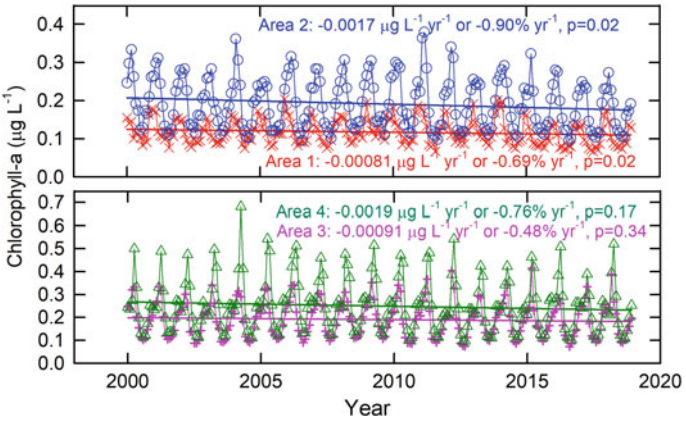

Fig. 16.5 Time series of average monthly satellite-derived chlorophyll-a concentrations in Kuroshio regions shown in Fig. 15.4. The solid lines show the linear trends, and the numbers show the rates of change ($\mu g\ L^{-1}\ yr^{-1}$ or % yr^{-1}) and the p values

DO decreasing rate ($-0.11 \pm 0.07\ \mu mol\ kg^{-1}\ yr^{-1}$) in the PN-Line had the same σ values ($\sigma = 26.7$–27.1) as the NPIW. At 20–25° N along the 137° E hydrographic line in the western North Pacific Ocean (Fig. 16.1), DO suffered the highest decreasing rate $-0.36 \pm 0.08\ \mu mol\ kg^{-1}\ yr^{-1}$ on the potential density level of $\sigma = 26.8$ between 1985 and 2010 (Takatani et al. 2012). In comparison, in the eastern North Pacific Ocean (33.5–41° N) the seawaters with σ between 26.5 and 27 (centered at 26.75) suffered the highest apparent oxygen utilization increment, or DO decrease (Chu et al. 2016). As mentioned above, the WPSIW originates from the NPIW. Changes found in the KIW, which originates from the mixing of the SCSIW and WPSIW, mostly resulted from the changes of the NPIW (Lui et al. 2014). The rise in nutrient concentrations but fall in DO of the NPIW was a likely consequence of reduced ventilation under the influence of seawater warming (Takatani et al. 2012; Ono et al. 2001; Whitney et al. 2007). As KIW contributes substantially to the upwelling, the NO_3^- and PO_4^{3-} in the bottom water of the ECS shelves are expected to increase, but the DO would decrease. On the other hand, Chen et al. (2020b) (this book) reports that nutrient concentrations of Changing River have risen since the 1960s. Given that the nutrient inputs from both the Changjiang River and the Kuroshio have rose, while the DO concentration in the Kuroshio has decreased, the ECS is likely to have more severe eutrophication and hypoxia than that in past decades. This is supported by the finding of Chen et al. (2020b) (this book) that hypoxia has continually occurred in the ECS since 2012. Notably, the SCSIW also originates from the NPIW. However, the chemical changes in the SCSIW in the past decades are heretofore unexplored.

16.3 Upper Layer Intrusion Reduces Productivity

The upper layer WPS seawater intrudes into the SCS through the Luzon Strait as a Kuroshio branch (Fig. 16.1). Nutrients are almost depleted in the euphotic zone in the mainstream of the Kuroshio. For instance, the PO_4^{3-} concentration is about 0.1 μM at 100 m depth in the WPS. In contrast, the concentration is as high as 1 μM in the SCS at the same depth (Du et al. 2013). That is, the degree of intrusion of the surface layer of WPS seawater as a Kuroshio branch is one of the main factors governing the changes in nutrients inventories and hence the productivity in the euphotic zone of the SCS (Du et al. 2013; Lui et al. 2018). The Kuroshio intrusion into the SCS weakened between 1993 and 2010 (Nan et al. 2013), while the salinity decreased (Nan et al. 2016). As expected, Chen et al. (2020a) (in this book) showed that the Chl.-a concentration in the northern shelf of the SCS rose between 1998 and 2016. Lui et al. (2018) showed that the increase in the WPS seawater proportions at the South East Asia Time Series Study (SEATS) station (18° N, 116° E) between 2014 and 2016, reflecting the Kuroshio intrusion into the SCS, resulted in a significant decrease in satellite-derived Chl.-a concentration and the fluxes of sinking particles collected at 2000 and 3500 m depths in 2013–2017 (Fig. 16.6). Certainly, the Kuroshio or Kuroshio branch did not reach the SEATS site directly, but the remnant did. Liu and Gan (2017) indicated that the intruded Kuroshio in the upper layer (0–750 m) had a residence time of about three years before subducting into deeper layers or flowing out from the SCS. Restated, the intruded Kuroshio could have interannual influences on the biogeochemical cycles in the SCS.

Data from the SEATS site indicates a strong Kuroshio intrusion into the SCS between 1998 and 2006, causing S, DIC and total alkalinity (TA) to rise significantly

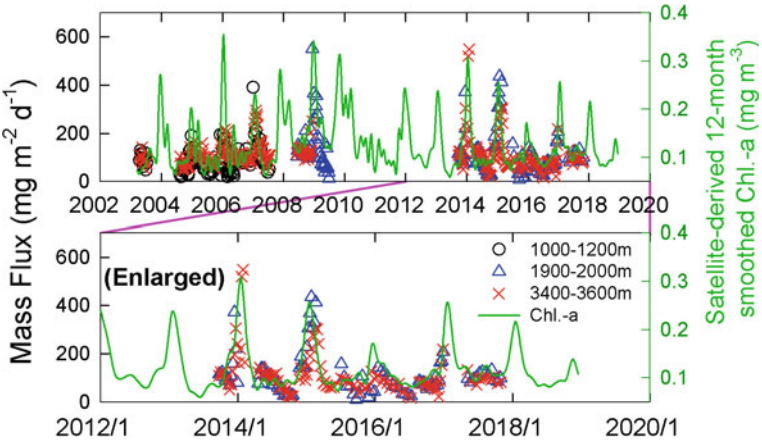

Fig. 16.6 Mass fluxes at various depths, and 12-month smoothing satellite-derived chlorophyll-a concentration with 50 × 50 km^2 in area (centered at SEATS site with 1 km^2 in resolution, green line), at SEATS between 2003 and 2017 (updated after Lui et al. 2018)

(Fig. 16.7). The intrusion of oligotrophic Kuroshio water into the SCS is expected to reduce the productivity in the SCS. Conversely, Chen et al. (2020a) (in this book) found a rising trend in Chl.-a concentration in the SCS between 1998 and 2006, suggesting that other factors were at play controlling the productivity in the SCS.

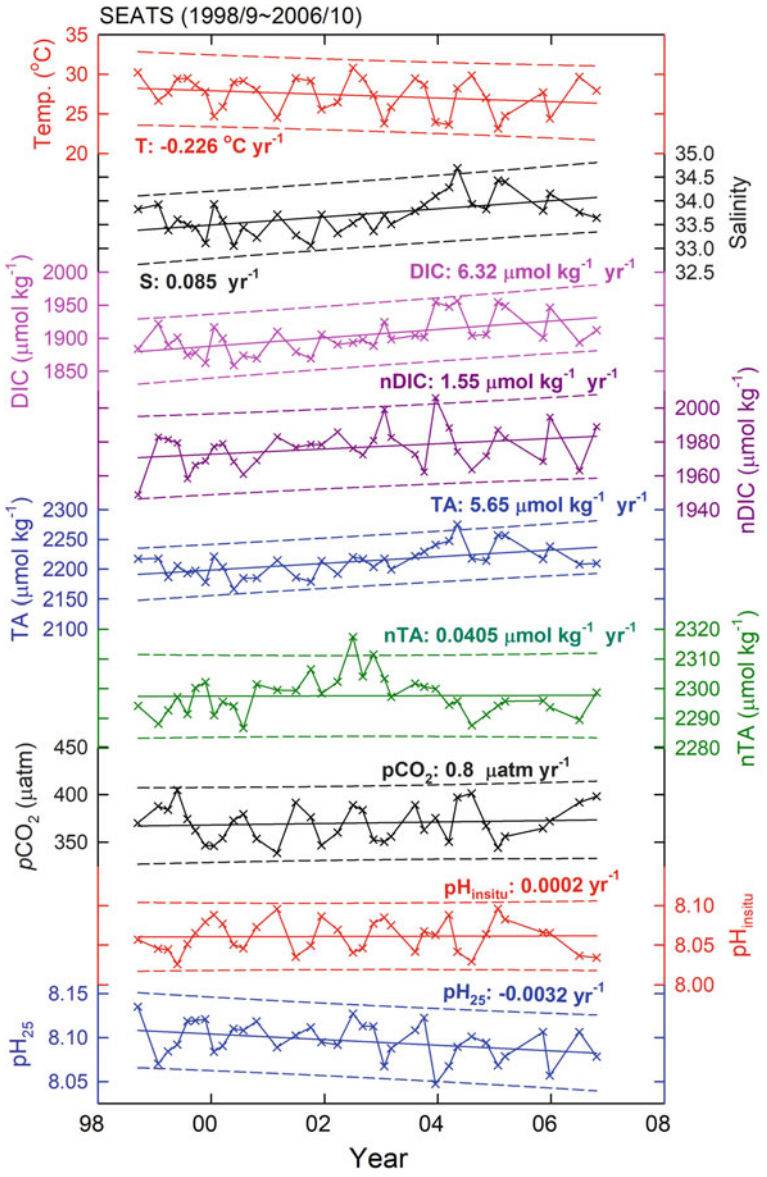

Fig. 16.7 Time series of temperature, DIC, TA, pCO_2, pH_{insitu} and pH_{25} at the surface of the SEATS station between 1998 and 2006. The numbers show the linear regression trends of changes

16.4 Changing Carbonate Chemistry

Influenced by the increasing atmospheric CO_2 in the past decades, the world surface oceans have partial pressure of CO_2 (pCO_2), DIC and pH changing rates (n = 7) of 1.89 ± 0.60 μatm yr^{-1}, 1.23 ± 0.40 μmol kg^{-1} yr^{-1} and −0.0018 ± 0.0005 pH unit yr^{-1}, respectively (Bates et al. 2014). As expected, TA remains constant. After normalizing the DIC (nDIC = DIC/S × 35) and TA (nTA = TA/S × 35) to S = 35 to minimize the influences of evaporation and precipitation on DIC and TA, the trends of changes in nDIC of 1.55 μmol kg^{-1} yr^{-1} and nTA of 0.04 μmol kg^{-1} yr^{-1} at SEATS were close to those in the open oceans (Fig. 16.7). Indeed, there was excess evaporation over precipitation during the study period, but this might contribute only 15% or even less of the salinity increase (Nan et al. 2016) (also see Chen et al. (2020a) in this book). The major cause of the increased S, DIC and TA was increased Kuroshio intrusion.

The relatively low rate of temporal change in pH under in situ temperature (pH_{insitu}) was due to an artifact resulting from uneven sampling distributions under the large seasonal pH_{insitu} variability. After correcting for the artifact using the method proposed by Lui and Chen (2015), surface seawater at the SEATS site yielded an acidification rate of −0.0015 ± 0.0009 pH unit yr^{-1}, which is almost the same as the expected value of −0.0017 pH unit yr^{-1} assuming air-sea CO_2 equilibrium. Lui and Chen (2017) further indicated that the change in the rate of temporal change in pH_{insitu} can be converted thermodynamically to the rate of temporal change in pH at 25 °C (pH_{25}) using the rate of seawater temperature change. The relatively high pH_{25} changing rate at the SEATS site between 1998 and 2006 was due to uneven sampling distributions under the strong seasonal variability. The relatively low pCO_2 changing rate shown in Fig. 16.7 could be explained in that way.

Seawaters at the PN-Line in the ECS clearly indicate that seawater suffered significantly higher acidification rates at the shelf break than in the Okinawa Trough or at the SEATS site (Fig. 16.8). Due to the enhanced productivity, the acidification rates of the KTW were lower than the anticipated −0.0017 pH unit yr^{-1} assuming an air-sea equilibrium (Lui et al. 2014, 2015). However, the KIW had higher acidification rates than the open oceans at the same depths (e.g. at the sites of Hawaii Ocean Time-series (HOT) in the north Pacific Ocean and the European Station for Time-series in the Ocean Canary Islands (ESTOC) in the north Atlantic Ocean), most likely owning to the reduced ventilation of the NPIW. Notably, the subsurface seawater had higher acidification rates at the HOT site than at the surface. This result could be a consequence of reduced ventilation. The Sea of Japan is a typical example in which the deep waters are acidifying faster than anticipated, largely due to reduced ventilation (Fig. 16.8). Consequently, the acidification rate is 27% higher near the bottom than at the surface (Chen et al. 2017). It is worth to mention that the changes in carbonate chemistry under the influence of a slow decline in seawater ventilation could be difficult to detect. Although results from climate models are consistent with that of observations that the oxygen inventories of the world oceans are declining, a quantitative attribution and mechanistic understanding between warming, changing

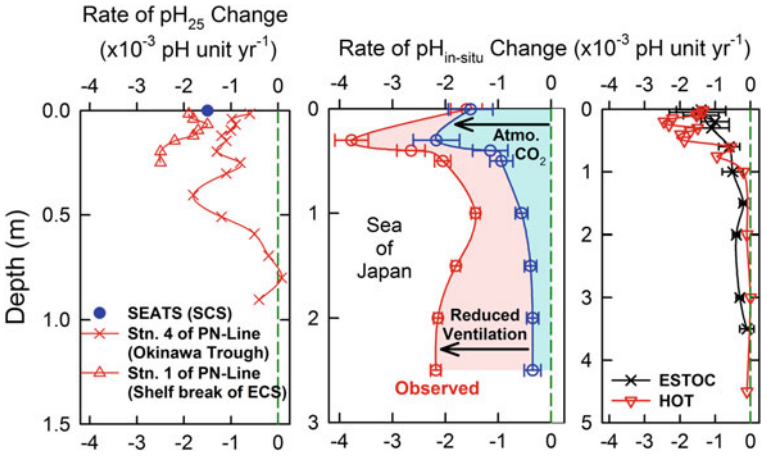

Fig. 16.8 Observed changes in pH at the surface of the SEATS site between 1998 and 2006 (taken from Lui and Chen 2015), at various depths at Stns 1 and 4 of the PN-Line between 1982 and 2007 (taken from Lui et al. 2015), and in the Sea of Japan (taken from Chen et al. 2017). Data from HOT (Dore et al. 2009) and ESTOC (Gonzalez-Davila et al. 2010) are presented for comparison. The solid dashed lines indicate zero rates of change

seawater ventilation and seawater chemistry need further investigation (Keeling et al. 2010; Schmidtko et al. 2017; Oschlies et al. 2018).

Ishii et al. (2011) showed that the surface water north (31.5–34° N) of the Kuroshio extension at 137° E had an acidification rate of -0.002 ± 0.007 pH unit yr^{-1} between 1994 and 2008, which is in line with the expected rate assuming air–sea CO_2 equilibrium. This rate is almost the same as that at 30° N (-0.021 pH unit yr^{-1}) (Fig. 16.9). The acidification rates declined gradually to -0.0013 pH unit yr^{-1} at 3° N. The decreasing CO_2 buffering capacity with increasing latitude might contribute 1/4 of the differences in the acidification rates (Feely et al. 2009). Compared with rates at 165° E hydrographic line, the acidification rates likely decreased towards the west (Fig. 16.9). Taking 18–20° N as an example, the rate is -0.0020 pH unit yr^{-1} at 165° E; -0.0018 pH unit yr^{-1} at 137° E, and only -0.0015 pH unit yr^{-1} at SEATS (18° N). Previous studies have shown that the coastal oceans had increased anthropogenic nitrogen inputs (Kim et al. 2014a, b). However, whether the westward decrease in acidification rates was due to the enhanced biological uptake from increased nutrient inputs needs further investigation.

16.5 Conclusions

Changes in Kuroshio pathways and the amount of water transport significantly influence the nutrient distributions in the SCS and the ECS. The surface seawaters in the regions affected by the Kuroshio are increasing in DIC concentrations but decreasing in pH, due to the influenced by the increasing atmospheric CO_2 concentration.

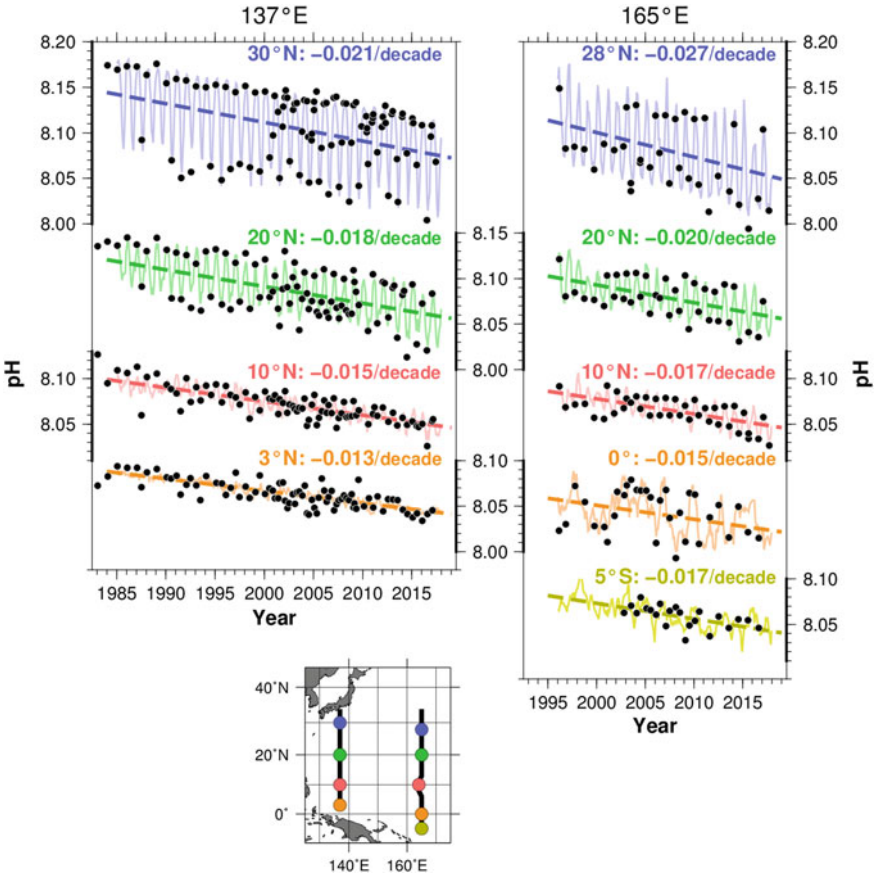

Fig. 16.9 pH_{insitu} time series at various latitudes in the JMA's repeat hydrographic lines at 137° E (left) and 165° E (right). The solid dots show pH values based on observed pCO_2 data. Solid lines represent reconstructed monthly pH values using the method of Ishii et al. (2011), whereas the dashed lines show the linear trends of changes of pH. The numbers refer to the rates of temporal changes at various latitudes (taken from the Global Environment and Marine Department, JMA.)

The WPSIW and the KIW increased in nutrient concentrations but decreased in DO, largely owing to the reduced ventilation of the NPIW. Consequently, the KIW has significantly higher acidification rates than the open oceans. Further warming may weaken the ventilation of the NPIW, resulting in higher nutrient concentrations but lower DO and pH in the WPSIW and KIW.

Acknowledgments This chapter was supported by the Ministry of Science and Technology of Taiwan under grant MOST 107-2611-M-110-026 and MOST 108-2611-M-110-025.

References

Bates NR, Astor Y, Church MJ, Currie K, Dore JE, Gonaález-Dávila M, Lorenzoni L, Muller-Karger F, Olafsson J, Santa-Casiano M (2014) A time-series view of changing ocean chemistry due to ocean uptake of anthropogenic CO_2 and ocean acidification. Oceanography 27(1):126–141. https://doi.org/10.5670/oceanog.2014.16

Chen CTA (1996) The Kuroshio intermediate water is the major source of nutrients on the East China Sea continental shelf. Oceanol Acta 19(5):523–527

Chen CTA (2000) The Three Gorges Dam: Reducing the upwelling and thus productivity in the East China Sea. Geophys Res Lett 27(3):381–383. https://doi.org/10.1029/1999gl002373

Chen CTA (2005) Tracing tropical and intermediate waters from the South China Sea to the Okinawa Trough and beyond. J Geophys Res 110 (C5). https://doi.org/10.1029/2004jc002494

Chen CTA, Lui HK, Hsieh CH, Yanagi T, Kosugi N, Ishii M, Gong GC (2017) Deep oceans may acidify faster than anticipated due to global warming. Nat Clim Change 7(12):890–894. https://doi.org/10.1038/s41558-017-0003-y

Chen CTA, Wang SL (1999) Carbon, alkalinity and nutrients budgets on the East China Sea continental shelf. J Geophys Res 104:20675–20686

Chen CTA, Yeh YT, Yanagi T, Bai Y, He X, Huang TH (2016) The tug-of-war between the West Philippine Sea and South China Sea Tropical Waters and Intermediate Waters in the Okinawa Trough. J Geophys Res 121(3):1736–1754. https://doi.org/10.1002/2015jc011274

Chen CTA, Yu S, Huang TH, Lui HK, Bai Y, He X (2020a) Changing biogeochemistry in the South China Sea. Changing Asia-Pacific marginal seas. Springer Nature, Chapter 12 of this book

Chen J, Li D, Jin H, Jiang Z, Wang B, Wu B, Hao Q, Sun X (2020b) Changing nutrients, oxygen and phytoplankton in the East China Sea. Changing Asia-Pacific marginal seas. Springer Nature, Chapter 10 of this book

Chu SN, Wang ZA, Doney SC, Lawson GL, Hoering KA (2016) Changes in anthropogenic carbon storage in the Northeast Pacific in the last decade. J Geophys Res 121(7):4618–4632. https://doi.org/10.1002/2016jc011775

Dore JE, Lukas R, Sadler DW, Church MJ, Karl DM (2009) Physical and biogeochemical modulation of ocean acidification in the central North Pacific. Proc Natl Acad Sci U S A 106(30):12235–12240. https://doi.org/10.1073/pnas.0906044106

Du C, Liu Z, Dai M, Kao SJ, Cao Z, Zhang Y, Huang T, Wang L, Li Y (2013) Impact of the Kuroshio intrusion on the nutrient inventory in the upper northern South China Sea: insights from an isopycnal mixing model. Biogeosciences 10(10):6419–6432. https://doi.org/10.5194/bg-10-6419-2013

Feely RA, Doney SC, Cooley SR (2009) Ocean acidification: present conditions and future changes in a high-CO_2 world. Oceanography 22(4):36–47. https://doi.org/10.5670/oceanog.2009.95

Gonzalez-Davila M, Santana-Casiano JM, Rueda MJ, Llinas O (2010) The water column distribution of carbonate system variables at the ESTOC site from 1995 to 2004. Biogeosciences 7(10):3067–3081. https://doi.org/10.5194/bg-7-3067-2010

Guo X, Zhu XH, Wu QS, Huang D (2012) The Kuroshio nutrient stream and its temporal variation in the East China Sea. J Geophys Res 117 (C1). https://doi.org/10.1029/2011jc007292

Ishii M, Kosugi N, Sasano D, Saito S, Midorikawa T, Inoue HY (2011) Ocean acidification off the south coast of Japan: a result from time series observations of CO_2 parameters from 1994 to 2008. J Geophys Res 116 (C6). https://doi.org/10.1029/2010jc006831

Jan S, Yang YJ, Wang J, Mensah V, Kuo TH, Chiou MD, Chern CS, Chang MH, Chien H (2015) Large variability of the Kuroshio at 23.75° N east of Taiwan. J Geophys Res 120(3):1825–1840. https://doi.org/10.1002/2014jc010614

Keeling RE, Kortzinger A, Gruber N (2010) Ocean deoxygenation in a warming world. Ann Rev Mar Sci 2:199–229. https://doi.org/10.1146/annurev.marine.010908.163855

Kim IN, Lee K, Gruber N, Karl DM, Bullister JL, Yang S, Kim TW (2014a) Increasing anthropogenic nitrogen in the North Pacific Ocean. Science 346(6213):1102–1106. https://doi.org/10.1126/science.1258396

Kim TW, Lee K, Duce R, Liss P (2014b) Impact of atmospheric nitrogen deposition on phytoplankton productivity in the South China Sea. Geophys Res Lett 41(9):3156–3162. https://doi.org/10.1002/2014gl059665

Liu Z, Gan J (2017) Three-dimensional pathways of water masses in the South China Sea: a modeling study. J Geophys Res 122(7):6039–6054. https://doi.org/10.1002/2016jc012511

Lui HK, Chen CTA (2015) Deducing acidification rates based on short-term time series. Sci Rep 5:11517. https://doi.org/10.1038/srep11517

Lui HK, Chen CTA (2017) Reconciliation of pH_{25} and pH_{insitu} acidification rates of the surface oceans: a simple conversion using only in situ temperature. Limnol Oceanogr Methods 15(3):328–335. https://doi.org/10.1002/lom3.10170

Lui HK, Chen CTA, Lee J, Bai Y, He X (2014) Looming hypoxia on outer shelves caused by reduced ventilation in the open oceans: case study of the East China Sea. Estuar Coast Shelf Sci 151:355–360. https://doi.org/10.1016/j.ecss.2014.08.010

Lui HK, Chen CTA, Lee J, Wang SL, Gong GC, Bai Y, He X (2015) Acidifying intermediate water accelerates the acidification of seawater on shelves: an example of the East China Sea. Cont Shelf Res 111:223–233. https://doi.org/10.1016/j.csr.2015.08.014

Lui HK, Chen KY, Chen CT, Wang BS, Lin HL, Ho SH, Tseng CJ, Yang Y, Chan J-W (2018) Physical forcing-driven productivity and sediment flux to the deep basin of northern South China Sea: a decadal time series study. Sustainability 10 (4). https://doi.org/10.3390/su10040971

Nan F, Xue H, Chai F, Wang D, Yu F, Shi M, Guo P, Xiu P (2013) Weakening of the Kuroshio intrusion into the South China Sea over the past two decades. J Clim 26(20):8097–8110. https://doi.org/10.1175/jcli-d-12-00315.1

Nan F, Yu F, Xue H, Zeng L, Wang D, Yang S, Nguyen K-C (2016) Freshening of the upper ocean in the South China Sea since the early 1990s. Deep-Sea Res Pt I 118:20–29. https://doi.org/10.1016/j.dsr.2016.10.010

Ono T, Midorikawa T, Watanabe YW, Tadokoro K, Saino T (2001) Temporal increases of phosphate and apparent oxygen utilization in the subsurface waters of western subarctic Pacific from 1968 to 1998. Geophys Res Lett 28(17):3285–3288. https://doi.org/10.1029/2001gl012948

Oschlies A, Brandt P, Stramma L, Schmidtko S (2018) Drivers and mechanisms of ocean deoxygenation. Nat Geosci 11(7):467–473. https://doi.org/10.1038/s41561-018-0152-2

Qu B, Song J, Yuan H, Li X, Li N (2018) Carbon chemistry in the mainstream of Kuroshio Current in eastern Taiwan and its transport of carbon into the East China Sea shelf. Sustainability 10 (3). https://doi.org/10.3390/su10030791

Schmidtko S, Stramma L, Visbeck M (2017) Decline in global oceanic oxygen content during the past five decades. Nature 542(7641):335–339. https://doi.org/10.1038/nature21399

Takatani Y, Sasano D, Nakano T, Midorikawa T, Ishii M (2012) Decrease of dissolved oxygen after the mid-1980s in the western North Pacific subtropical gyre along the 137° E repeat section. Global Biogeochem Cy 26(2). https://doi.org/10.1029/2011gb004227

Talley LD (1997) North Pacific Intermediate Water transports in the mixed water region. J Phys Oceanogr 27(8):1795–1803. https://doi.org/10.1175/1520-0485(1997)027%3c1795:npiwti%3e2.0.co;2

Whitney FA, Freeland HJ, Robert M (2007) Persistently declining oxygen levels in the interior waters of the eastern subarctic Pacific. Prog Oceanogr 75(2):179–199. https://doi.org/10.1016/j.pocean.2007.08.007

Wu CR, Wang YL, Lin YF, Chao SY (2017) Intrusion of the Kuroshio into the South and East China Seas. Sci Rep 7(1):7895. https://doi.org/10.1038/s41598-017-08206-4

Yasuda I (1997) The origin of the North Pacific Intermediate Water. J Geophys Res 102(C1):893–909. https://doi.org/10.1029/96jc02938